



HEAT TRANSFER DIVISION
Chair, R. D. SKOCYPEC
Vice Chair, M. K. JENSEN
Past Chair, Y. BAYAZITOGU
Secretary, T. W. TONG
Treasurer, CHANG H. OH
Member, RODNEY W. DOUGLASS

Editor, V. DHIR (2005)
Associate Editors,
S. ACHARYA (2006)
N. K. ANAND (2006)
G. CHEN (2005)
J. N. CHUNG (2005)
A. F. EMERY (2005)
B. FAROUK (2006)
S. V. GARIMELLA (2007)
C. P. GRIGORPOULOS (2006)
S. G. KANDLIKAR (2007)
J. M. KHODADADI (2007)
K. KIHM (2005)
J. H. LIENHARD V (2006)
P. M. LIGRANI (2006)
R. M. MANGLIK (2006)
C. H. OH (2007)
R. PITCHUMANI (2007)
V. PRASAD (2005)
R. P. ROY (2007)
K. A. THOLE (2007)
S. THYNELL (2005)
S. PRATAP VANKA (2005)

PUBLICATIONS DIRECTORATE
Chair, ARTHUR G. ERDMAN

OFFICERS OF THE ASME
President, HARRY ARMEN
Executive Director,
VIRGIL R. CARTER
Treasurer,
R. E. NICKELL

PUBLISHING STAFF
Managing Director, Engineering
THOMAS G. LOUGHLIN
Director, Technical Publishing
PHILIP DI VIETRO
Production Coordinator
COLIN McATEER
Production Assistant
MARISOL ANDINO

Transactions of the ASME, Journal of Heat Transfer (ISSN 0022-1481) is published bi-monthly (Feb., Apr., June, Aug., Oct., Dec.) by The American Society of Mechanical Engineers, Three Park Avenue, New York, NY 10016. Periodicals postage paid at New York, NY and additional mailing offices. POSTMASTER: Send address changes to Transactions of the ASME, Journal of Heat Transfer, c/o THE AMERICAN SOCIETY OF MECHANICAL ENGINEERS, 22 Law Drive, Box 2300, Fairfield, NJ 07007-2300. CHANGES OF ADDRESS must be received at Society headquarters seven weeks before they are to be effective. Please send old label and new address. STATEMENT from By-Laws. The Society shall not be responsible for statements or opinions advanced in papers or ... printed in its publications (B7.1, Para. 3). COPYRIGHT © 2004 by The American Society of Mechanical Engineers. For authorization to photocopy material for internal or personal use under those circumstances not falling within the fair use provisions of the Copyright Act, contact the Copyright Clearance Center (CCC), 222 Rosewood Drive, Danvers, MA 01923, tel: 978-750-8400, www.copyright.com. Request for special permission or bulk copying should be addressed to Reprints/Permission Department. INDEXED by Applied Mechanics Reviews and Engineering Information, Inc. Canadian Goods & Services Tax Registration #126148048.

Journal of Heat Transfer

Published Bimonthly by ASME

VOLUME 126 • NUMBER 5 • OCTOBER 2004

669 Editor's Note
Vijay K. Dhir

Conduction

670 On the Necessity of Positive Semi-Definite Conductivity and Onsager Reciprocity in Modeling Heat Conduction in Anisotropic Media
Joseph M. Powers

Evaporation, Boiling, and Condensation

676 Effects of Gravity, Shear and Surface Tension in Internal Condensing Flows: Results From Direct Computational Simulations
Q. Liang, X. Wang, and A. Narain

687 Pressure Drop During Refrigerant Condensation Inside Horizontal Smooth, Helical Microfin, and Herringbone Microfin Tubes
Jonathan A. Olivier, Leon Liebenberg, Mark A. Kedzierski, and Josua P. Meyer

Forced Convection

697 Three-Dimensional Numerical Simulation on Laminar Heat Transfer and Fluid Flow Characteristics of Strip Fin Surface With X-Arrangement of Strips
Z. G. Qu, W. Q. Tao, and Y. L. He

Heat and Mass Transfer

708 Second Law Based Optimization of Falling Film Single Tube Absorption Generator
S. Jani, M. H. Saidi, and A. A. Mozaffari

Heat Transfer in Manufacturing

713 Free Surface Flow in High Speed Fiber Drawing With Large-Diameter Glass Preforms
Zhiyong Wei, Kok-Meng Lee, Serge W. Tchikanda, Zhi Zhou, and Siu-Ping Hong

Micro/Nanoscale Heat Transfer

723 Observation of Femtosecond Laser-Induced Ablation in Crystalline Silicon
Tae Y. Choi and Costas P. Grigoropoulos

727 Molecular Dynamics Study of Phase Change Mechanisms During Femtosecond Laser Ablation
Xianfan Xu, Changrui Cheng, and Ihtesham H. Chowdhury

735 Modified Method of Characteristics for Simulating Microscale Energy Transport
Laurent Pilon and Kamal M. Katika

744 Thermal Characteristics of Microscale Fractal-Like Branching Channels
Ali Y. Alharbi, Deborah V. Pence, and Rebecca N. Cullion

753 Experimental Investigation of Gas Flow in Microchannels
Stephen E. Turner, Lok C. Lam, Mohammad Faghri, and Otto J. Gregory

Natural and Mixed Convection

764 Numerical Study of Mixed Convection Flow in an Impinging Jet CVD Reactor for Atmospheric Pressure Deposition of Thin Films
S. P. Vanka, Gang Luo, and Nick G. Glumac

(Contents continued on inside back cover)

This journal is printed on acid-free paper, which exceeds the ANSI Z39.48-1992 specification for permanence of paper and library materials. ©™
♻️ 85% recycled content, including 10% post-consumer fibers.

- 776 Solutions for Temperature Rise in Stationary/Moving Bodies Caused by Surface Heating With Surface Convection

Shuangbiao Liu, Sylvie Lannou, Qian Wang, and Leon Keer

Radiative Heat Transfer

- 786 Effects of Periodic Structures on the Coherence Properties of Blackbody Radiation
L. Hu, A. Schmidt, A. Narayanaswamy, and G. Chen

- 793 Mie Scattering Theory for Phonon Transport in Particulate Media
Ravi S. Prasher

- 805 An Integral Equation for the Dual-Lag Model of Heat Transfer
Vladimir V. Kulish and Vasily B. Novozhilov

Thermal Systems

- 809 Estimating Parameters and Refining Thermal Models by Using the Extended Kalman Filter Approach
Ashley F. Emery

- 818 Thermal Analysis of Laser-Densified Dental Porcelain Bodies: Modeling and Experiments
K. Dai, X. Li, and L. Shaw

Heat Exchangers

- 826 Local Heat Transfer and Pressure Drop for Finned-Tube Heat Exchangers Using Oval Tubes and Vortex Generators

James E. O'Brien, Manohar S. Sohal, and Philip C. Wallstedt

TECHNICAL NOTES

- 836 Three-Dimensional Forced Convection in Plane Symmetric Sudden Expansion
J. H. Nie and B. F. Armaly

- 840 The Nonlinear Increase of Nusselt Number With Friction Factor in Fully Developed Laminar Duct Flow
E. Van den Bulck

- 843 Convection Velocity of Temperature Fluctuations in a Turbulent Flume
G. Hetsroni, I. Tiselj, R. Bergant, A. Mosyak, and E. Pogrebnyak

- 849 An Experimental Correlation for Combined Convection and Radiation Between Parallel Vertical Plates
A. S. Krishnan, C. Balaji, and S. P. Venkateshan

- 852 Feasibility of High Speed Furnace Drawing of Optical Fibers
Xu Cheng and Yogesh Jaluria

- 858 Importance of Combined Lorentz-Doppler Broadening in High-Temperature Radiative Heat Transfer Applications
Anquan Wang and Michael F. Modest

- 862 Performance and Optimization Analysis for Fins of Straight Taper With Simultaneous Heat and Mass Transfer
B. Kundu and P. K. Das

- 869 Numerical and Experimental Investigations of Melting and Solidification Processes of High Melting Point PCM in a Cylindrical Enclosure

Ahmed Elgafy, Osama Mesalhy, and Khalid Lafdi

The ASME Journal of Heat Transfer is abstracted and indexed in the following:

Applied Science and Technology Index, Chemical Abstracts, Chemical Engineering and Biotechnology Abstracts (Electronic equivalent of Process and Chemical Engineering), Civil Engineering Abstracts, Compendex (The electronic equivalent of Engineering Index), Corrosion Abstracts, Current Contents, E & P Health, Safety, and Environment, Ei EncompassLit, Engineered Materials Abstracts, Engineering Index, Enviroline (The electronic equivalent of Environment Abstracts), Environment Abstracts, Environmental Engineering Abstracts, Environmental Science and Pollution Management, Fluidex, Fuel and Energy Abstracts, Index to Scientific Reviews, INSPEC, International Building Services Abstracts, Mechanical & Transportation Engineering Abstracts, Mechanical Engineering Abstracts, METADEX (The electronic equivalent of Metals Abstracts and Alloys Index), Petroleum Abstracts, Process and Chemical Engineering, Referativnyi Zhurnal, Science Citation Index, SciSearch (The electronic equivalent of Science Citation Index), Theoretical Chemical Engineering

We are pleased to inform our readers that the ASME JOURNAL OF HEAT TRANSFER will be published monthly beginning January 2005. As you know, the journal has been published bi-monthly since February 2001. By increasing the frequency of the journal, we hope to reduce the time from the submittal to the publication of archival papers. The increased frequency will also provide the technical community with rapid access to the latest research in thermal sciences and engineering thereby allowing researchers to reference the latest work in the field. Authors are urged to submit their new findings for quick dissemination to the technical com-

munity through the ASME JOURNAL OF HEAT TRANSFER. In addition, no mandatory page charges are levied on papers up to nine journal pages in length.

I would like to personally thank the readers, the reviewers, and the contributors to the Journal, and I look forward to receiving new and exciting works for publication.

Vijay K. Dhir
Editor

On the Necessity of Positive Semi-Definite Conductivity and Onsager Reciprocity in Modeling Heat Conduction in Anisotropic Media

Joseph M. Powers

e-mail: powers@nd.edu
Associate Professor,
Department of Aerospace and Mechanical
Engineering,
University of Notre Dame,
Notre Dame, Indiana 46556-5637

It is demonstrated by a concise standard derivation, motivated by principles of rational continuum mechanics and irreversible thermodynamics augmented by novel detailed examples, that for heat conduction in linearly anisotropic solids: (1) common restrictions placed on the form of the thermal conductivity tensor are insufficient to guarantee satisfaction of the second law of thermodynamics, and (2) satisfaction of the first and second laws of thermodynamics alone is still insufficient to insure agreement between heat flow predictions and observation. An additional constraint beyond that given in many standard studies, namely that all three principal invariants of the conductivity tensor be positive semi-definite, is imposed in order to guarantee satisfaction of the entropy inequality. Thus constrained, such a theory remains under-restricted and can admit purely cyclic heat fluxes, which are not observed in nature. Imposition of the conjectures of Duhamel and Stokes, which are in fact earlier specific incarnations of Onsager's reciprocity theory, on the constitutive model relating heat flux to temperature gradient is a sufficient remedy. [DOI: 10.1115/1.1798913]

Keywords: Analytical, Conduction, Heat Transfer, Second Law, Thermodynamics

Introduction

In this work, an exposition is given, accompanied by new illustrative examples and minor clarifications to some of the existing literature, to demonstrate that for energy diffusion in linearly anisotropic solids: (1) restrictions given in common heat transfer references are necessary but insufficient to guarantee satisfaction of the second law of thermodynamics, and (2) fully satisfied first and second laws of thermodynamics provide necessary but insufficient restrictions on the functional forms of common constitutive laws. An additional independent condition, such as that provided by Onsager reciprocity [1], which itself is a generalization of the earlier conjectures of Duhamel [2] and Stokes [3], is required to bring theory into agreement with experiment [4–6] for conduction in an anisotropic medium.

General discussions of issues relevant to Onsager reciprocity and anisotropic heat conduction are common in the communities of irreversible thermodynamics, cf. [7–12]; continuum mechanics, cf. [13–15]; and theoretical physics and statistical mechanics, cf. [16–19]. It is noted, moreover, that statistical mechanics gives an effective microscale based theory which casts macro-scale Onsager reciprocity and the second law of thermodynamics on a more fundamental theoretical foundation. Nevertheless, while often wide ranging, compact statements of theoretical restrictions on models of anisotropic heat conduction are often difficult to pinpoint in these sources; the useful [14] is the most relevant. The discussion in the traditional heat transfer community, cf. [20–31], is often more limited, and, as will be seen, incomplete. Understanding such issues can be of aid to anyone doing computational modeling of anisotropic materials, especially on nonorthogonal grids, designing experiments on materials with anisotropic microstructure, or wanting to build a strong classical foundation from

which to explore the implications of molecular dynamics on energy diffusion, especially relevant for energy transport on molecular lattice scales in solids.

In what follows, a simple model of diffusive energy transport in an anisotropic solid will be presented. The analysis is restricted to a classical, axiomatic, macro-scale approach with no detailed appeal to the underlying micro-scale physics; however, it is noted that the axioms employed here are consistent with conclusions which can be drawn from micro-scale models. For such a material, a general form of the first law of thermodynamics is posed along with constitutive models for internal energy and diffusive heat flux. A first set of restrictions on the form of the constitutive laws is found by a standard application of the second law of thermodynamics. It will then be shown that these necessary limitations alone nevertheless admit behavior which is not observed in experiment; this is remedied by further application of Onsager reciprocity.

How these principles may be unintentionally violated is then illustrated in three simple examples, which should be useful for pedagogical purposes. First, an anisotropic material which has a purely symmetric thermal conductivity tensor which also satisfies the limited second law requirements of [21], but has a third principal invariant with negative value, in fact violates the second law. Next, for an anisotropic material that has a purely antisymmetric thermal conductivity tensor, it will be shown that a temperature gradient in a given direction induces a heat flux in an orthogonal direction, all the while satisfying the first and second laws. This is demonstrated in two-dimensional geometries which are plane Cartesian and plane polar. In the plane polar geometry, it is seen that purely radial temperature gradients induce purely circumferential heat fluxes. A qualitative analogy is made between such a flux and (1) solid body rotation and (2) the so-called cyclic chemical reactions studied in the original work of Onsager.

Contributed by the Heat Transfer Division for publication in the JOURNAL OF HEAT TRANSFER. Manuscript received by the Heat Transfer Division January 29, 2004; revision received June 3, 2004. Associate Editor: R. Pitchumani.

Model and Analysis

Consider the first law of thermodynamics for an immobile, incompressible solid, posed in Cartesian index notation

$$\rho \frac{\partial e}{\partial t} = - \frac{\partial q_i}{\partial x_i} \quad (1)$$

Here, the standard Einstein convention, in which the repetition of the index i connotes a summation from $i=1$ to 3, is employed. The independent variables are distance x_i , where $i=1, 2, 3$, for each of the orthogonal directions in space, and time t . The dependent variables are internal energy per unit mass, e , and the heat flux vector, q_i . The density, ρ , is a constant parameter. For the incompressible immobile solid, which can undergo no deformation work process, classical thermodynamics provides a Gibbs equation for systems near equilibrium undergoing reversible heat transfer

$$de = Tds, \quad (2)$$

where T is the temperature and s is the entropy per unit mass. It is then postulated that such a relation is valid for more general systems which may be undergoing irreversible heat transfer. Consequently, one adopts the non-equilibrium $\partial e/\partial t = T\partial s/\partial t$, and the first law, Eq. (1), can be rewritten in terms of entropy as

$$\rho T \frac{\partial s}{\partial t} = - \frac{\partial q_i}{\partial x_i} \quad (3)$$

Next, use the product rule to expand the first law, Eq. (3), in a nonintuitive fashion to get

$$\rho \frac{\partial s}{\partial t} = - \underbrace{\frac{\partial}{\partial x_i} \left(\frac{q_i}{T} \right)}_{\text{reversible}} - \underbrace{\frac{q_i}{T^2} \frac{\partial T}{\partial x_i}}_{\text{irreversible}} \quad (4)$$

This formulation of the first law is written so as to segregate entropy generating terms into those associated with both reversible and irreversible heat transfer. This is seen upon consideration of the second law of thermodynamics, which for such a material is given by

$$\rho \frac{\partial s}{\partial t} \geq - \frac{\partial}{\partial x_i} \left(\frac{q_i}{T} \right) \quad (5)$$

Using Eq. (4) to eliminate the terms involving entropy and reversible heat transfer, the second law, Eq. (5), can be re-expressed as a Clausius-Duhem inequality

$$- \frac{q_i}{T^2} \frac{\partial T}{\partial x_i} \geq 0. \quad (6)$$

The only term which contributes to the Clausius-Duhem inequality is that associated with irreversible heat transfer. While reversible heat transfer does induce entropy changes, it makes no contribution to the irreversibility of the process.

Next two simple linear constitutive models are posed. First, the internal energy is taken to be a linear function of temperature so that the caloric state equation is

$$e = cT + e_o \quad (7)$$

where c is the constant specific heat and e_o is a reference energy. Second, the heat flux vector is given by Duhamel's generalization [2] of Fourier's law, i.e., it is taken to be a linear function of temperature gradient which vanishes when there is no temperature gradient. Thus,

$$q_i = - k_{ij} \frac{\partial T}{\partial x_j} \quad (8)$$

where k_{ij} is taken to be a constant nonisotropic asymmetric tensor of thermal conductivity. The asymmetric k_{ij} can be decomposed as $k_{ij} = k_{(ij)} + k_{[ij]}$, where the symmetric $k_{(ij)}$ and antisymmetric $k_{[ij]}$ are defined as

$$k_{(ij)} \equiv k_{(ji)} = \frac{1}{2}(k_{ij} + k_{ji}), \quad k_{[ij]} \equiv -k_{[ji]} = \frac{1}{2}(k_{ij} - k_{ji}) \quad (9)$$

With Eq. (9), Eq. (8) can be recast as

$$q_i = - k_{(ij)} \frac{\partial T}{\partial x_j} - k_{[ij]} \frac{\partial T}{\partial x_j} \quad (10)$$

Substituting Eq. (10) into the Clausius-Duhem relation (6), it is seen that the second law for this material becomes, after elimination of the nonzero temperature

$$k_{(ij)} \frac{\partial T}{\partial x_j} \frac{\partial T}{\partial x_i} + \underbrace{k_{[ij]} \frac{\partial T}{\partial x_j} \frac{\partial T}{\partial x_i}}_{=0} \geq 0 \quad (11)$$

Now the part of Eq. (11) involving $k_{[ij]}$ is identically zero for arbitrary values of temperature gradient and $k_{[ij]}$. This is because the tensor inner product of a symmetric tensor, such as $(\partial T/\partial x_j)(\partial T/\partial x_i)$ and an antisymmetric tensor, such as $k_{[ij]}$, always vanishes, which can be shown by direct expansion. So the second law reduces to

$$k_{(ij)} \frac{\partial T}{\partial x_j} \frac{\partial T}{\partial x_i} \geq 0 \quad (12)$$

which must hold for any value of temperature gradient. So it is seen that any nonzero antisymmetric component of k_{ij} cannot influence the evolution of entropy or the second law.

Using standard results from linear algebra, cf. Strang [32], it can further be stated that the entropy inequality, Eq. (12), will be satisfied if and only if $k_{(ij)}$ is positive semi-definite. This will be the case if and only if the eigenvalues λ of $k_{(ij)}$ are positive semi-definite. The eigenvalues are guaranteed to be real by the symmetry of $k_{(ij)}$. The eigenvalues of $k_{(ij)}$ can be shown to be positive semi-definite if and only if the so-called invariants of $k_{(ij)}$, I_1 , I_2 , and I_3 , are themselves positive semi-definite, which can be inferred from Fung [13]. The invariants reside in the characteristic polynomial of $k_{(ij)}$, which determines the eigenvalues λ

$$\lambda^3 - I_1 \lambda^2 + I_2 \lambda - I_3 = 0 \quad (13)$$

The three roots to Eq. (13) will be denoted as λ_1 , λ_2 , and λ_3 . Detailed analysis shows that the invariants, along with the necessary and sufficient conditions for positive semi-definiteness of symmetric matrices, are compactly summarized as

$$I_1 = k_{(ii)} = \text{tr}(k_{(ij)}) = \lambda_1 + \lambda_2 + \lambda_3 \geq 0 \quad (14)$$

$$I_2 = \frac{1}{2}(k_{(ii)}k_{(jj)} - k_{(ij)}k_{(ji)}) = \det(k_{(ij)})\text{tr}(k_{(ij)}^{-1}) \\ = \lambda_1 \lambda_2 + \lambda_2 \lambda_3 + \lambda_3 \lambda_1 \geq 0 \quad (15)$$

$$I_3 = \epsilon_{ijk} k_{(1j)} k_{(2j)} k_{(3j)} = \det(k_{(ij)}) = \lambda_1 \lambda_2 \lambda_3 \geq 0 \quad (16)$$

While it is likely the case that Eqs. (14)–(16) could be inferred from [20], it is certainly not transparent. The conditions in [21] are more clear, but the necessary Eq. (16) is unaccountably omitted. This omission propagates to other sources, e.g., [25].

When the special case in which $\partial T/\partial x_i = (1,0,0)^T$ is substituted into Eq. (12), one finds that $k_{(11)} \geq 0$. Equivalent results are obtained for the remaining two directions. As the symmetric part of a diagonal element is the diagonal element itself, one then has

$$k_{(11)} = k_{11} \geq 0, \quad k_{(22)} = k_{22} \geq 0, \quad k_{(33)} = k_{33} \geq 0 \quad (17)$$

It seems that no further significant simplifications can be made over those of Eqs. (14)–(17). However, it is useful to keep in mind the following imprecise, pragmatic, and rarely stated recipe: To insure positive definiteness of the conductivity tensor, terms on the diagonal must be positive and, relative to terms off the diagonal, large. In the two-dimensional limit, the conditions are simple and precise and reduce to $k_{(11)} \geq 0$, $k_{(22)} \geq 0$, and $\sqrt{k_{(11)}k_{(22)}} \geq k_{(12)}$, or, equivalently, $k_{11} \geq 0$, $k_{22} \geq 0$, and $\sqrt{k_{11}k_{22}} \geq (k_{12} + k_{21})/2$.

Just as antisymmetric terms do not influence the entropy inequality, it is easy to show that they do not influence the energy equation. Substituting Eq. (10) into Eq. (1), one finds

$$\rho \frac{\partial e}{\partial t} = k_{(ij)} \frac{\partial^2 T}{\partial x_i \partial x_j} + \underbrace{k_{[ij]} \frac{\partial^2 T}{\partial x_i \partial x_j}}_{=0} \quad (18)$$

Once again the tensor inner product of the symmetric $\partial^2 T / \partial x_i \partial x_j$ with the antisymmetric $k_{[ij]}$ identically vanishes, giving rise, after imposition of the caloric state equation (7), to a temperature evolution equation of

$$\rho c \frac{\partial T}{\partial t} = k_{(ij)} \frac{\partial^2 T}{\partial x_i \partial x_j} \quad (19)$$

Now while an antisymmetric component of k_{ij} cannot affect either the temperature field or the entropy inequality, it would induce a heat flux, and if such a flux existed, it could be measured with standard techniques. In fact in a hypothetical anisotropic material which had a purely antisymmetric thermal conductivity, one could imagine the following experiment. Take a thin rectangular plate and hold two parallel boundaries at two moderately different temperatures. The antisymmetric conductivity would then not induce a flux normal to the isothermal boundary, but would induce a parallel flux. This flux would induce as much energy to enter at one end and as to leave at the other. One could then put each of the nonisothermal boundaries in finite reservoirs of liquid water, and one would observe one reservoir solidify and the other boil. Such an observation has never been made, despite related careful attempts [4–6]. One might view this as a violation of the second law for the combined system of the reservoirs and the plate. If, however, the reservoirs were infinite, the energy flux would induce negligible temperature change, and thus no violation of the second law.

In [9] it is contended that nonzero $k_{[ij]}$ can have no observable consequences. It is then argued that this implies that one can choose $k_{[ij]}$ arbitrarily without resort to Onsager reciprocity. Reference [9] goes on to choose $k_{[ij]} = 0$, thus recovering Onsager reciprocity, while suggesting that other choices would be equally as valid. In light of the argument in the preceding paragraph, it is contended here that Onsager reciprocity

$$k_{[ij]} = 0 \quad (20)$$

is the unique choice to bring predictions of heat conduction in anisotropic materials into agreement with observation. This general conclusion is in agreement with Miller [11].

Counter Examples

Here three counterexamples are presented which illustrate the necessity of imposing the conditions described in the previous section.

Second Law Violation. Consider a conductivity tensor which is purely symmetric, as well as having positive diagonal elements, with a value of

$$k_{ij} = k_{(ij)} = \begin{pmatrix} 1 & 1 & 2 \\ 1 & 4 & -1 \\ 2 & -1 & 5 \end{pmatrix} \quad (21)$$

It is easily seen that the two conditions of [21], Eqs. (14)–(15), are satisfied as $I_1 = 10$ and $I_2 = 23$. However, the tensor is not positive semi-definite since it has eigenvalues of $\lambda = 6$, $\lambda = 2 + \sqrt{5} \sim 4.2361$, and $\lambda = 2 - \sqrt{5} \sim -0.2361$. Here, the neglected $I_3 = -6$, and thus Eq. (16) is not satisfied, rendering the tensor not positive semi-definite, and the second law violated.

That this would lead to a nonphysical prediction is clearly seen upon rotating the coordinate system to one aligned with the principal axes of the conductivity tensor. The principal axes are given by the eigenvectors of $k_{(ij)}$. The normalized eigenvectors are then cast into the columns of an orthogonal matrix ℓ_{mn} , which is the matrix of direction cosines of the rotation

$$\ell_{mn} = \begin{pmatrix} 0.3015 & 0.3868 & -0.8715 \\ -0.3015 & 0.9058 & 0.2977 \\ 0.9045 & 0.1730 & 0.3897 \end{pmatrix} \quad (22)$$

The transpose of this special matrix can be shown to be its inverse, and is also known as the rotation matrix, which results in $\ell_{jn} \ell_{mn} = \delta_{jm}$. Here, δ_{jm} is the Kronecker delta. As described in many sources, cf. [33], under rotation, a generic vector v_i is represented in the rotated, denoted by a prime superscript, coordinate system as $v'_p = \ell_{ip} v_i$. Likewise, a generic tensor a_{ij} is represented as $a'_{pn} = \ell_{ip} a_{ij} \ell_{jn}$. The relevant rotation operations are as follows:

$$\begin{aligned} q_i &= -k_{ij} \frac{\partial T}{\partial x_j} \\ \ell_{ip} q_i &= -\ell_{ip} k_{ij} \frac{\partial T}{\partial x_j} \\ \ell_{ip} q_i &= -\ell_{ip} k_{ij} \delta_{jm} \frac{\partial T}{\partial x_m} \\ \ell_{ip} q_i &= -(\ell_{ip} k_{ij} \ell_{jn}) \left(\ell_{mn} \frac{\partial T}{\partial x_m} \right) \\ q'_p &= -k'_{pn} \frac{\partial T}{\partial x'_n} \end{aligned} \quad (23)$$

The eigen-rotation of Eq. (22) renders $k'_{pn} = \ell_{ip} k_{ij} \ell_{jn}$ to be a purely diagonal tensor with the eigenvalues on the diagonal. Consequently, the generalized Fourier's law in this particular reference frame is that of an orthotropic material and can be written as

$$\begin{pmatrix} q'_1 \\ q'_2 \\ q'_3 \end{pmatrix} = - \begin{pmatrix} 6 & 0 & 0 \\ 0 & 4.2361 & 0 \\ 0 & 0 & -0.2361 \end{pmatrix} \begin{pmatrix} \frac{\partial T}{\partial x'_1} \\ \frac{\partial T}{\partial x'_2} \\ \frac{\partial T}{\partial x'_3} \end{pmatrix} \quad (24)$$

Such a conductivity tensor admits the non-physical $q'_3 = 0.2361 \partial T / \partial x'_3$; i.e., it predicts energy to be transported by random diffusion from regions of low temperature to regions of high temperature, in direct violation of Clausius' formulation of the second law.

Note that selection of a conductivity tensor which is more diagonally dominant can render the tensor to be positive semi-definite. For example, changing $k_{(11)}$ from 1 to 2 in Eq. (21) gives rise to satisfaction of the second law, as for this new tensor $\lambda_1 = 6.1135$, $\lambda_2 = 0.4829$, and $\lambda_3 = 4.4036$.

Onsager Reciprocity Violation, Plane Cartesian Case. Consider now a purely antisymmetric conductivity tensor applied to a strictly two-dimensional geometry. Take then

$$k_{ij} = \begin{pmatrix} 0 & -\kappa \\ \kappa & 0 \end{pmatrix} \quad (25)$$

where κ is a characteristic scalar value of thermal conductivity. Obviously for this tensor $k_{(ij)} = 0$ and $k_{[ij]} = k_{ij}$. From the generalized Fourier's law, Eq. (8), one then has

$$\begin{pmatrix} q_1 \\ q_2 \end{pmatrix} = - \begin{pmatrix} 0 & -\kappa \\ \kappa & 0 \end{pmatrix} \begin{pmatrix} \frac{\partial T}{\partial x_1} \\ \frac{\partial T}{\partial x_2} \end{pmatrix} \quad (26)$$

or more simply,

$$q_1 = \kappa \frac{\partial T}{\partial x_2}, \quad q_2 = -\kappa \frac{\partial T}{\partial x_1} \quad (27)$$

Substituting Eq. (26) into the Clausius-Duhem inequality, Eq. (6), the second law reduces to

$$\frac{1}{T^2} \begin{pmatrix} \frac{\partial T}{\partial x_1} & \frac{\partial T}{\partial x_2} \end{pmatrix} \begin{pmatrix} 0 & -\kappa \\ \kappa & 0 \end{pmatrix} \begin{pmatrix} \frac{\partial T}{\partial x_1} \\ \frac{\partial T}{\partial x_2} \end{pmatrix} \geq 0 \quad (28)$$

Expanding, one finds that the equality holds

$$\frac{1}{T^2} \underbrace{\left(-\kappa \frac{\partial T}{\partial x_1} \frac{\partial T}{\partial x_2} + \kappa \frac{\partial T}{\partial x_2} \frac{\partial T}{\partial x_1} \right)}_{=0} \geq 0 \quad (29)$$

and consequently the irreversibility is identically zero for such a conductivity.

Similarly the first law of thermodynamics, Eq. (1), after application of the caloric state equation, Eq. (7), and Eq. (26), is written as

$$\rho c \frac{\partial T}{\partial t} = \begin{pmatrix} \frac{\partial}{\partial x_1} & \frac{\partial}{\partial x_2} \end{pmatrix} \begin{pmatrix} 0 & -\kappa \\ \kappa & 0 \end{pmatrix} \begin{pmatrix} \frac{\partial T}{\partial x_1} \\ \frac{\partial T}{\partial x_2} \end{pmatrix} \quad (30)$$

This reduces to

$$\rho c \frac{\partial T}{\partial t} = -\kappa \frac{\partial^2 T}{\partial x_1 \partial x_2} + \kappa \frac{\partial^2 T}{\partial x_2 \partial x_1} = 0 \quad (31)$$

which holds that no temperature changes are induced by such a heat flux.

Consider now an initial boundary value problem for a plane Cartesian problem with a purely antisymmetric conductivity tensor. Consider the domain $x_1 \in (-\infty, \infty)$, $x_2 \in [0, H]$, $t \in [0, \infty)$, where H is the height of the domain. Next, take as Dirichlet boundary conditions and initial conditions

$$\begin{aligned} T(x_1, 0, t) &= T_o, & T(x_1, H, t) &= T_o, \\ T(x_1, x_2, 0) &= T_o + 4(T_{\max} - T_o) \left(\frac{x_2}{H} \right) \left(1 - \frac{x_2}{H} \right) \end{aligned} \quad (32)$$

Here, T_o is the boundary temperature, and T_{\max} is the maximum temperature, realized here at $x_2 = H/2$. Then Eq. (31) simply requires that the initial temperature distribution must hold for all time so that

$$T(x_1, x_2, t) = T_o + 4(T_{\max} - T_o) \left(\frac{x_2}{H} \right) \left(1 - \frac{x_2}{H} \right) \quad (33)$$

Application of Eq. (26) gives for the heat flux

$$q_1(x_1, x_2, t) = \frac{4\kappa(T_{\max} - T_o)}{H} \left(1 - 2 \frac{x_2}{H} \right), \quad q_2(x_1, x_2, t) = 0 \quad (34)$$

The temperature gradient in the 2 direction induces a heat flux in the 1 direction. At the midplane, $x_2 = H/2$, there is no heat flux, and the maximum amplitude of the heat flux occurs at the boundaries with a magnitude of $4\kappa(T_{\max} - T_o)/H$. In a rectangular control volume aligned with the domain, the same amount of energy enters at a given x_1 as exits at a downstream x_1 . Moreover, all the energy remains confined to the domain. Consequently, the spatially nonuniform temperature field has no variation in time. Had the conduction tensor been that of an ordinary isotropic material, energy flux through the boundaries at $x_2 = 0$ and $x_2 = H$ would have induced $T(x_1, x_2, t \rightarrow \infty) = 0$. In the absence of a driving potential difference in temperature at the boundaries, a positive isotropic conductivity causes the system to come to equilibrium with its environment.

Onsager Reciprocity Violation: Plane Polar Case. A similar result is obtained in non-Cartesian coordinates. Consider a problem related to the previous example in plane polar coordinates, for which one has

$$x_1 = r \cos \theta, \quad x_2 = r \sin \theta \quad (35)$$

Application of standard coordinate transformations leads one to formulate the generalized Fourier's law for the antisymmetric conductivity tensor as

$$q_r = \frac{\kappa}{r} \frac{\partial T}{\partial \theta}, \quad q_\theta = -\kappa \frac{\partial T}{\partial r} \quad (36)$$

It is trivial to show that the first law still reduces to $\partial T / \partial t = 0$, and that the second law is satisfied, with zero irreversibility. Consider now a similar initial boundary value problem on the domain of a circular disk for which $r \in [0, R]$, $\theta \in [0, 2\pi]$, $t \in [0, \infty)$:

$$\begin{aligned} T(R, \theta, t) &= T_o, & T(0, \theta, t) &< \infty, \\ T(r, \theta, 0) &= T_o + (T_{\max} - T_o) \left(1 - \left(\frac{r}{R} \right)^2 \right). \end{aligned} \quad (37)$$

Here, R is the outer radius of the disk. Once again the maximum temperature is T_{\max} , here realized at $r = 0$. The solution for the time-dependent temperature field and heat flux is straightforwardly found to be

$$T(r, \theta, t) = T_o + (T_{\max} - T_o) \left(1 - \left(\frac{r}{R} \right)^2 \right) \quad (38)$$

$$q_r(r, \theta, t) = 0 \quad (39)$$

$$q_\theta(r, \theta, t) = \frac{2\kappa(T_{\max} - T_o)}{R} \left(\frac{r}{R} \right) \quad (40)$$

Appropriately scaled temperature and heat flux fields are plotted in Fig. 1. Figure 1(a) shows the temperature field. Despite the lack of forcing either within the domain or at the boundary, the initial temperature disturbance persists for all time in the presence of purely antisymmetric conductivity. Figure 1(b) depicts the unusual consequence of a purely anti-symmetric conductivity: the heat flux vectors are tangent to the isotherms. This situation is analogous to velocity vectors and particle pathlines for a solid rotating about a central axis. In fact it is easy to show that the antisymmetric conductivity tensor has associated with it a vector which is analogous to the a solid body rotation vector; the equivalent vector here is $(1/2)\epsilon_{ijk}k_{[ij]} = (0, 0, \kappa)^T$. Here, ϵ_{ijk} is the alternating unit tensor. Another analog is found in a classical chemical kinetics problem described by Onsager [1]. There it was shown that if Onsager reciprocity were not imposed on constitutive laws for chemical kinetics, that so-called cyclic reactions, never ob-

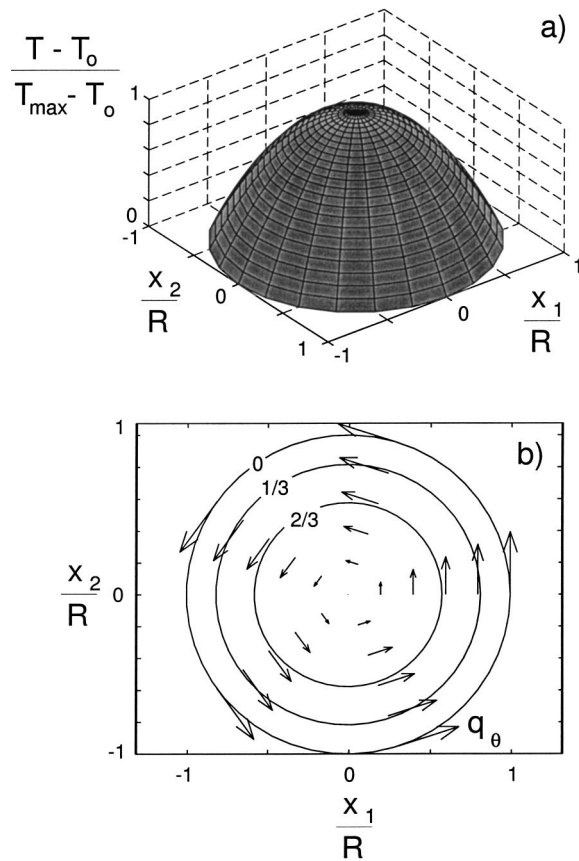


Fig. 1 Example solution for conductive heat transfer in an anisotropic material with a purely antisymmetric thermal conductivity tensor; (a) surface plot of temperature (dimensionless); and (b) isotherms of $(T - T_0)/(T_{\max} - T_0)$ and heat flux vectors (dimensionless)

served in closed adiabatic systems, could be predicted; for example, in a system with three components A , B , and C , one could predict a situation which at long time admitted the situation depicted in Fig. 2.

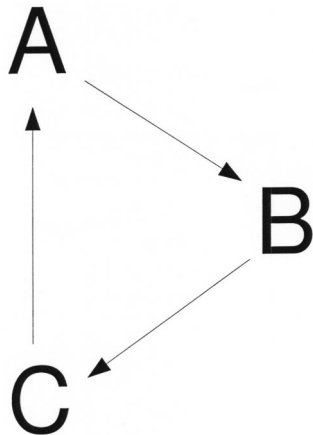


Fig. 2 Diagram of hypothesized cyclic chemical reaction for which Onsager reciprocity does not hold

Conclusions

As the scenario in the first example clearly violates the second law of thermodynamics, the necessity of the additional constraints for positive semi-definiteness is obvious. As the phenomenon predicted in the second two examples has never been observed in conductive heat transfer, despite the enforcement of first and second laws of thermodynamics, it is concluded that an additional condition is necessary. It is clear that Onsager reciprocity, equivalent to the Duhamel-Stokes conjecture, provides a sufficient condition.

Lastly, recent predictions such as those of [18] that Onsager reciprocity does not hold away from equilibrium suggest an interesting possibility. If this contention is correct, then it may be possible to repeat Soret's experiment [4], and with modern measurement devices, detect spiral components of heat fluxes in response to radial temperature gradients.

Acknowledgment

The author acknowledges the helpful comments of Prof. S. Paolucci of the University of Notre Dame.

Nomenclature

- A = generic chemical species
- B = generic chemical species
- C = generic chemical species
- H = domain height, [m]
- I_1 = first invariant of conductivity tensor, [W/m/K]
- I_2 = second invariant of conductivity tensor, [(W/m/K)²]
- I_3 = third invariant of conductivity tensor, [(W/m/K)³]
- R = domain outer radius, [m]
- T = temperature, [K]
- a_{ij} = generic tensor
- c = specific heat, [J/kg/K]
- e = specific internal energy, [J/kg]
- k_{ij} = thermal conductivity tensor, [W/m/K]
- ℓ_{ij} = direction cosine tensor
- q_i = heat flux vector, [W/m²]
- r = radial coordinate, [m]
- s = specific entropy, [J/kg/K]
- t = time, [s]
- v_i = generic vector
- x_i = Cartesian distance vector coordinate, [m]

Greek Symbols

- δ_{jm} = Kronecker delta
- ϵ_{ijk} = alternating unit tensor
- θ = circumferential coordinate
- κ = thermal conductivity scalar component, [W/m/K]
- λ = eigenvalue of conductivity tensor, [W/m/K]
- ρ = density, [kg/m³]

Subscripts

- i = Cartesian index
- j = Cartesian index
- m = Cartesian index
- max = maximum
- n = Cartesian index
- o = reference state
- p = Cartesian index
- r = radial direction
- θ = circumferential direction
- (\dots) = symmetric part of tensor
- $[\dots]$ = antisymmetric part of tensor

Superscript

- ' = rotated coordinate system

References

- [1] Onsager, L., 1931, "Reciprocal Relations in Irreversible Processes. I," Phys. Rev., 37(4), pp. 405–426.

- [2] Duhamel, J.-M.-C., 1832, "Sur les Équations Générales de la Propagation de la Chaleur dans les Corps Solides dont la Conductibilité n'est pas la Même dans Tous les Sens," *J. Ec. Polytech. (Paris)*, **13**(21), pp. 356–399.
- [3] Stokes, G. G., 1851, "On the Conduction of Heat in Crystals," *Cambridge and Dublin Math. J.*, **6**, pp. 215–238.
- [4] Soret, C., 1893, "Sur l'Étude Expérimentale des Coefficients Rotationnels de Conductibilité Thermique," *Arch. Sci. Phys. Nat.*, **29**, pp. 355–357.
- [5] Voigt, W., 1903, "Fragen der Kristallphysik I. Über die Rotatorischen Constanten der Wärmeleitung von Apatit und Dolomit," *Nachr. Ges. Wiss. Göttingen, Math.-Phys. Kl.*, **3**, pp. 87–89.
- [6] Voigt, W., 1910, *Lehrbuch der Kristallphysik*, Teubner, Leipzig.
- [7] Müller, I., and Ruggeri, T., 1998, *Rational Extended Thermodynamics*, Second ed., Springer, New York.
- [8] deGroot, S. R., and Masur, P., 1984, *Non-Equilibrium Thermodynamics*, Dover, New York.
- [9] Casimir, H. B. G., 1945, "On Onsager's Principle of Microscopic Reversibility," *Rev. Mod. Phys.*, **17**(2–3), pp. 343–350.
- [10] Prigogine, I., 1967, *Thermodynamics of Irreversible Processes*, Third ed., Wiley, New York.
- [11] Miller, D., 1960, "Thermodynamics of Irreversible Processes, the Experimental Verification of the Onsager Reciprocal Relations," *Chem. Rev. (Washington, D.C.)*, **60**, pp. 15–37.
- [12] Woods, L. C., 1975, *The Thermodynamics of Fluid Systems*, Clarendon, Oxford.
- [13] Fung, Y. C., 1965, *Foundations of Solid Mechanics*, Prentice-Hall, Englewood Cliffs, New Jersey.
- [14] Truesdell, C., 1969, *Rational Thermodynamics*, McGraw-Hill, New York.
- [15] Day, W. A., and Gurtin, M. E., 1969, "On the Symmetries of the Conductivity Tensor and Other Restrictions in the Nonlinear Theory of Heat Conduction," *Arch. Ration. Mech. Anal.*, **33**, pp. 26–32.
- [16] Oono, Y., 1993, "Onsager's Principle From Large Deviation Point of View," *Prog. Theor. Phys.*, **89**(5), pp. 973–983.
- [17] Sieniutycz, S., and Berry, R. S., 1993, "Canonical Formalism, Fundamental Equation, and Generalized Thermomechanics for Irreversible Fluids With Heat Transfer," *Phys. Rev. E*, **47**(3), pp. 1765–1783.
- [18] Allahverdyan, A. E., and Nieuwenhuizen, Th. M., 2000, "Adiabatic Steady State: Its Thermodynamics, Entropy Production, Energy Dissipation, and Violation of Onsager Relations," *Phys. Rev. E*, **62**(1), pp. 845–850.
- [19] LaCour, B. R., and Schieve, W. C., 2004, "Derivation of the Onsager Principle From Large Deviation Theory," *Physica A*, **331**(1–2), pp. 109–124.
- [20] Carslaw, H. S., and Jaeger, J. C., 1986, *Conduction of Heat in Solids*, Second ed., Clarendon, Oxford.
- [21] Özisik, M. N., 1993, *Heat Conduction*, Wiley, New York.
- [22] Bird, R. B., Stewart, W. E., and Lightfoot, E. N., 1960, *Transport Phenomena*, Wiley, New York.
- [23] Gebhardt, B., 1993, *Heat Conduction and Mass Diffusion*, McGraw-Hill, New York.
- [24] Mulholland, G. P., and Gupta, B. P., 1977, "Heat Transfer in a Three-Dimensional Anisotropic Solid of Arbitrary Shape," *ASME J. Heat Transfer*, **99**(1), pp. 135–137.
- [25] Chang, Y. P., 1977, "Analytical Solution for Heat Conduction in Anisotropic Media in Infinite, Semi-Infinite, and Two-Plane-Bounded Regions," *Int. J. Heat Mass Transfer*, **20**(10), pp. 1019–1028.
- [26] Sadd, M. H., and Miskioglu, I., 1978, "Temperatures in an Anisotropic Sheet Containing an Insulated Elliptical Hole," *ASME J. Heat Transfer*, **100**(3), pp. 553–555.
- [27] Chang, Y. P., and Poon, K. C., 1979, "Three-Dimensional, Steady-State Heat-Conduction in Cylinders of General Anisotropic-Media," *ASME J. Heat Transfer*, **101**(3), pp. 548–553.
- [28] Huang, S. C., and Chang, Y. P., 1984, "Anisotropic Heat-Conduction With Mixed Boundary Conditions," *ASME J. Heat Transfer*, **106**(3), pp. 646–648.
- [29] Zhang, X. Z., 1990, "Steady-State Temperatures in an Anisotropic Strip," *ASME J. Heat Transfer*, **112**(1), pp. 16–20.
- [30] Hsieh, M.-H., and Ma, C.-C., 2002, "Analytical Investigations for Heat Conduction Problems in Anisotropic Thin-Layer Media With Embedded Heat Sources," *Int. J. Heat Mass Transfer*, **45**(20), pp. 4117–4132.
- [31] Ma, C.-C., and Chang, S.-W., 2004, "Analytical Exact Solutions of Heat Conduction Problems for Anisotropic Multi-Layered Media," *Int. J. Heat Mass Transfer*, **47**(8–9), pp. 1643–1655.
- [32] Strang, G., 1988, *Linear Algebra and its Application*, Third ed., Harcourt Brace Jovanovich, Fort Worth, TX.
- [33] Aris, R., 1962, *Vectors, Tensors, and the Basic Equations of Fluid Mechanics*, Dover, New York.

Effects of Gravity, Shear and Surface Tension in Internal Condensing Flows: Results From Direct Computational Simulations

Q. Liang

X. Wang

A. Narain

Mem. ASME

e-mail: narain@mtu.edu

Department of Mechanical Engineering-
Engineering Mechanics,
Michigan Technological University,
Houghton, MI 49931

The paper presents accurate numerical solutions of the full two-dimensional governing equations for steady and unsteady laminar/laminar internal condensing flows. The results relate to issues of better design and integration of condenser-sections in thermal management systems (looped heat pipes, etc.). The flow geometry, in normal or zero gravity, is chosen to be the inside of a channel with film condensation on one of the walls. In normal gravity, film condensation is on the bottom wall of a tilted (from vertical to horizontal) channel. It is found that it is important to know whether the exit conditions are constrained or unconstrained because nearly incompressible vapor flows occur only for exit conditions that are unconstrained. For the incompressible vapor flow situations, a method for computationally obtaining the requisite exit condition and associated stable steady/quasi-steady solutions is given here and the resulting solutions are shown to be in good agreement with some relevant experimental data for horizontal channels. These solutions are shown to be sensitive to the frequency and amplitude of the various Fourier components that represent the ever-present and minuscule transverse vibrations (standing waves) of the condensing surface. Compared to a vertical channel in normal gravity, shear driven zero gravity cases have much larger pressure drops, much slower wave speeds, much larger noise sensitive wave amplitudes that are controlled by surface tension, and narrower flow regime boundaries within which vapor flow can be considered incompressible. It is shown that significant enhancement in wave-energy and/or heat-transfer rates, if desired, are possible by designing the condensing surface noise to be in resonance with the intrinsic waves. [DOI: 10.1115/1.1777586]

1 Introduction

Accurate numerical solutions of the full governing equations are presented for steady and unsteady laminar/laminar film condensation flows on one of the walls inside a channel. This is a good geometry for addressing the influence of shear and gravity by changing the channel inclination from vertical to horizontal (see Fig. 1) and is also a good geometry for consideration of flow behavior in the absence of gravity (space application). The results, based on simulations for channel heights in the 2–25 mm range and a specific choice of 4 mm in Table 1, are important for a qualitative understanding of condenser-section (typically of millimeter or sub-millimeter scale hydraulic diameters) behavior in applications (see Krotiuk [1] and Faghri [2]) such as Looped Heat Pipes, Capillary Pumped Loops, thermal management systems, and electronic-cooling devices.

This channel flow geometry is also a simple modification of the classical flat plate geometry associated with classical studies (Nusselt [3], Rohsenow [4], Koh [5], etc.) for external film condensation over vertical, horizontal, and tilted walls.

To address laminar/laminar flow issues that cannot be addressed by integral approaches (Chow and Parish [6], Narain et al. [7], etc.), direct numerical simulations are undertaken here to better understand the wave-phenomena and associated effects. Although the results presented here are strictly valid only for laminar vapor flows and laminar condensate, in practice, turbulent vapor at inlet (with inlet vapor Reynolds number as large as 7000) is allowed because of the much thicker laminar sub-layer encountered by the vapor flowing in the vicinity of the interface (i.e., $y_\delta^+ \gg 5$ as com-

pared to $y_\delta^+ \approx 5$ which yields the thickness y_δ^+ of the laminar sub-layer for zero interfacial mass transfer cases—see the definition of nondimensional y_δ^+ given in terms of the values of y^+ defined in Eq. (6.29) of White [8] and replace the wall shear stress by interfacial shear stress in the expression for nondimensional speed u^* that appears in this definition). This thickening is due to interfacial mass transfer and associated streamlines that pierce through the interface into a very slow laminar condensate flow. Under these semi-turbulent conditions, the vapor is laminar near the interface and turbulent outside the laminar layer. Therefore, for these cases ($Re_{in} < 7000$), the computational predictions (under laminar/laminar assumptions) of film thickness, heat transfer rates, etc.—though not the predictions for vapor velocity profile outside the interfacial laminar sub-layer—are, as expected, in good agreement with relevant experimental results of Lu [9] and Lu and Suryanarayana [10].

This paper briefly states some of the significant vertical channel results reported in Narain et al. [11] and utilizes its computational methodology to obtain new results for normal gravity (tilted to horizontal channels for gravity to shear dominated flows) and zero gravity. Among other new features of this paper is the fact that surface tension σ is not approximated as a constant (as in [11]) but is taken as $\sigma = \sigma(T)$ for pure vapor/liquid interface. Furthermore, at the interface, this paper retains the surface tension terms for not only the normal stress condition but also the tangential stress condition (the term responsible for Marangoni effects).

Unconstrained exit-condition cases associated with incompressible vapor flows and constrained exit-condition cases associated with compressible vapor flows physically arise from the fact that condenser-sections (such as the one in Fig. 1) are typically only a part of a closed flow-system (looped heat pipes, etc.) or a closed flow-loop (see, e.g., Fig. 2 in Narain et al. [11]). Therefore, pres-

Contributed by the Heat Transfer Division for publication in the JOURNAL OF HEAT TRANSFER. Manuscript received by the Heat Transfer Division October 4, 2003; revision received April 22, 2004. Associate Editor: J. Chung.

physical distances of a point with respect to the axes in Fig. 1 ($x=0$ is at the inlet and $y=0$ is at the condensing surface), we introduce a new nondimensional list of the fundamental variables through the following definitions

$$\{x, y, \delta, u_I, \dot{m}\} \equiv \left\{ \frac{x}{h}, \frac{y}{h}, \frac{\Delta}{h}, \frac{u_I}{U}, \frac{\dot{m}}{\rho_1 U} \right\} \quad (1)$$

$$\{v_I, \theta_I, \pi_I, t\} \equiv \left\{ \frac{y_I}{U}, \frac{T_I}{\Delta T}, \frac{p_I - p_0}{\rho_I U^2}, \frac{t}{(h/U)} \right\}$$

The nondimensional differential forms of mass, momentum (x and y -components), and energy equations for flow in the interior of either of the nearly incompressible phases ($I=1$ or 2) are the well-known equations

$$\frac{\partial u_I}{\partial x} + \frac{\partial v_I}{\partial y} = 0$$

$$\frac{\partial u_I}{\partial t} + u_I \frac{\partial u_I}{\partial x} + v_I \frac{\partial u_I}{\partial y} = - \left(\frac{\partial \pi_I}{\partial x} \right) + Fr_x^{-1} + \frac{1}{Re_I} \left(\frac{\partial^2 u_I}{\partial x^2} + \frac{\partial^2 u_I}{\partial y^2} \right) \quad (2)$$

$$\frac{\partial v_I}{\partial t} + u_I \frac{\partial v_I}{\partial x} + v_I \frac{\partial v_I}{\partial y} = - \left(\frac{\partial \pi_I}{\partial y} \right) + Fr_y^{-1} + \frac{1}{Re_I} \left(\frac{\partial^2 v_I}{\partial x^2} + \frac{\partial^2 v_I}{\partial y^2} \right)$$

$$\frac{\partial \theta_I}{\partial t} + u_I \frac{\partial \theta_I}{\partial x} + v_I \frac{\partial \theta_I}{\partial y} \approx \frac{1}{Re_I Pr_I} \left(\frac{\partial^2 \theta_I}{\partial x^2} + \frac{\partial^2 \theta_I}{\partial y^2} \right)$$

where $Re_I \equiv \rho_I U h / \mu_I$, $Pr_I \equiv \mu_I C_{pI} / k_I$, $Fr_x^{-1} \equiv g_x h / U^2$ and $Fr_y^{-1} \equiv g_y h / U^2$. The above equations are solved for each of the two phases under a complete and proper prescription of boundary conditions (inlet, exit, and the walls), initial conditions, and the interface conditions (see Delhay [20], etc.). These conditions are used in their exact forms and they are given in Eqs. (3)–(15) and Eqs. (A1)–(A9) of Narain et al. [11].

An inspection of all the nondimensional governing equations, interface conditions, and boundary conditions reveal the fact that the flows considered here are affected by the following set of nondimensional parameters

$$\left\{ Re_{in}, Ja, Fr_x^{-1}, \frac{\rho_2}{\rho_1}, \frac{\mu_2}{\mu_1}, Pr_1, x_e, Z_e(0), We, Fr_y^{-1} \right\} \quad (3)$$

where $Re_{in} \equiv \rho_2 U h / \mu_2 \equiv Re_2$, $Ja \equiv C_{p1} \Delta T h_{fg}^0$, and $h_{fg}^0 \equiv h_{fg}(T_s(p_0))$. Here Re_{in} , Fr_x^{-1} , and Ja are control parameters associated with inlet speed U , inclination α , and temperature difference ΔT . For unconstrained exit condition cases (i.e., incompressible vapor) considered here, it is seen later that $Z_e(0)$, the initial value of the exit vapor quality, is not important because it does not affect the naturally selected steady solution and its associated exit vapor quality $Z_e|_{Na}$. The density ratio ρ_2 / ρ_1 , viscosity ratio μ_2 / μ_1 , and Prandtl number Pr_1 are passive fluid parameters. Also, for unsteady or quasi-steady wavy-interface situations, the normal stress condition at the interface imply an additional dependence on a surface tension parameter, Weber number $We \equiv \rho_1 U^2 h / \sigma$. For superheated vapors, in the interface energy equation, there is a very weak dependence on the thermal conductivity ratio k_2 / k_1 . Furthermore, unlike in Narain et al. [11], in this paper, nonconstant surface tension $\sigma = \sigma(T)$ for pure vapors is allowed through $\nabla_s \sigma$ term in Eq. (A3) in the appendix of [11]. As a result, the term $[t]$ on the right side of the tangential stress condition given in Eq. (5) of [11] is modified by adding an additional term “ $Ma \partial \pi_2 / \partial x |^i \cdot 1 / \sqrt{1 + \delta_x^2}$ ” on the right side of Eq. (A9) of [11]. Here the Marangoni number $Ma \equiv \rho_2 U c_1 d_1 / \mu_1$ represents the surface tension contribution to tangential stress under the notation $c_1 \equiv dT_s / dp$ and $d_1 \equiv -d\sigma / dT$. For the cases considered here, a representative set of values of the new constants are: $c_1 \approx 0.0003$ K/Pa, $d_1 \approx 0.1046$ N/(m-K), and $Ma = 0.1963$.

It should be noted that negligible interfacial thermal resistance and equilibrium thermodynamics on either side of the interface is assumed to hold for values of x downstream of the origin (i.e., second or third computational cell onwards). And hence, as per discussions leading to Eq. (A8) in the appendix of Narain et al. [11], no model (see, Carey [16], Plesset and Prosperetti [21], etc.) is needed to supplement the known restrictions on the interfacial mass-flux \dot{m} (see Eq. (8) of Narain et al. [11]). However, reasonable initial estimates (from Nusselt [3] solution, etc.) for \dot{m} are used to obtain convergent solutions that are eventually shown to be independent of the initial guess.

Though $x \sim 0$ zone does not affect the results of this paper, ability to account for interfacial thermal resistances does become important when the liquid-vapor phase-change interface lies within 10–500 nm of a solid surface that is at a temperature different than the phase-change saturation temperature (say by more than 5°C). At such locations, boiling or condensation processes do require development of relevant thermodynamics and material-science knowledge base (suitably supported by experiments and molecular dynamic simulations) that would yield models of the type described in Carey [16], Plesset and Prosperetti [21], etc. This is an area of modern research that may provide key technological insights with regard to some key relevant processes (such as control of nucleation sites in boiling, sustenance of drop-wise condensation, etc.).

By dropping all time dependencies in the initial boundary value problem described above, the resulting steady equations (which are elliptic near exit) for any reasonable but arbitrarily prescribed exit condition Z_e (denoted as an initial value of $Z_e(t)$ at $t=0$), where

$$Z_e(0) = \int_{\delta_{steady}(x_e)}^1 u_2(x_e, y) \cdot dy \equiv Z_e \quad (4)$$

the steady solution is obtained. This solution is then assumed to apply at times $t \leq 0$. That is, if $\phi(x, y, t)$ is any variable (such as u_I , v_I , π_I , θ_I , etc.), the initial values of ϕ and film thickness $\delta(x, t)$ are such that

$$\phi(x, y, 0) = \phi_{steady}(x, y) \quad \text{and} \quad \delta(x, 0) = \delta_{steady}(x) \quad (5)$$

where ϕ_{steady} and δ_{steady} represent steady solutions. Although the prescription of Z_e within $0 < Z_e < 1$ is arbitrary (except that it should be such that it allows a steady computational solution in the stratified/annular regime assumed in Fig. 1), its natural value (denoted as $Z_e|_{Na}$) for the unconstrained cases is computationally found by the procedure outlined in section 4.

Using the initial condition in (5), the unsteady solutions for $t > 0$ are obtained by solving the full initial boundary value problem with appropriate boundary conditions (with or without the typically present minuscule vibrations of the condensing surface). Since an assumption of unconstrained exit conditions (i.e., incompressible vapor) are made for the unsteady computations in this paper, no exit conditions are prescribed for $t > 0$ as long term values of the exit condition (such as $Z_e|_{Na}$ for steady noise-free situations) are obtained as part of the solution.

3 Features of the Computational Approach

Details of the computational approach are given in Narain et al. [11] and Liang [12]. Some essential features and a broad outline are summarized here.

Between times “ t ” and “ $t + \Delta t$,” two types of adaptive grids (termed grid-A and grid-B) are employed. At time t , grid-A (see Fig. 3 of [11]) is based on a stair-step geometrical approximation of $\delta(x, t)$ as a function of x and it changes whenever the liquid and the vapor flow variables need to be recomputed for a changed interfacial configuration $\delta(x, t)$. The physical processes, however, employ a piecewise linear or higher (cubic splines) approximation of $\delta(x, t)$ based on their discrete values at marked locations in grid-A. In the interior of either the liquid or the vapor phase,

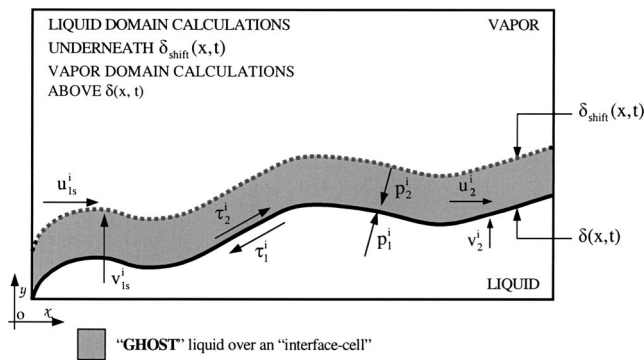


Fig. 2 The liquid domain calculations underneath $\delta_{\text{shift}}(x,t)$ with prescribed values of $(u_{1s}^i, v_{1s}^i, \theta_{1s}^i)$ on $\delta_{\text{shift}}(x,t)$ satisfy the shear and pressure conditions on the actual $\delta(x,t)$. Discarding all other calculations, only calculations underneath $\delta(x,t)$ are retained. The vapor domain calculations above $\delta(x,t)$ with prescribed values of $(u_2^i, v_2^i, \theta_2^i)$ on $\delta(x,t)$ satisfy $\dot{m}_{VK} = \dot{m}_{\text{Energy}}$ and the requirement of continuity of tangential velocities.

grid-A is used for all calculations. However, to make the best changes in $\delta(x,t)$ leading to its accurate prediction at time “ $t + \Delta t$,” a different grid (grid-B) is generated for spatially locating the variables ($\delta(x,t)$, $\bar{u}(x,t)$, and $\bar{v}(x,t)$) that appear in the interface tracking equation (see Eq. (7) below) for this problem. As discussed and shown in Fig. 3 of Narain et al. [11], grid-B needs to be defined for the x -domain alone because it is employed for the specific purpose of obtaining the best numerical predictions for changes in $\delta(x,t)$ through Eq. (7) described later on in this paper. The predictions made on grid-B are interpolated to obtain corresponding values on grid-A. At any time t , linear mappings suffice for spatial interpolation and exchange of the values of the relevant flow variables (viz. δ , \bar{u} , and \bar{v}) at locations between grid-A and grid-B. The approach broadly consists of the following:

- At discrete number of locations in Fig. 2, guess $\{\delta, u_{1s}^i, v_{1s}^i, \theta_{1s}^i, u_2^i, v_2^i, \theta_2^i\}$.
- Under the shifted interface depicted in Fig. 2, the liquid domain problem is solved by a finite-volume method (SIMPLER utilizing source term method described in Patankar [22] and Narain et al. [11]).
- Above the interface, the vapor domain problem (see Fig. 4(b) of [11]) is also solved by a finite-volume method (SIMPLER utilizing source term method described in Patankar [22] and Narain et al. [11]).
- The seven guesses are repeatedly updated to converge to their correct values with the help of seven interface conditions given in Narain et al. [11] (one each from Eqs. (3)–(5), two from Eq. (8), and two from Eq. (9) of [11]). For the steady problem for $t=0$, the exit condition Z_e needs to be prescribed and an additional eighth “condition” is created to satisfy this requirement.
- The above steps are repeated in such a way that all interface conditions, differential equations, etc., are satisfied.

One of the interface conditions, viz. the physical variable form of $\dot{m}_{LK} = \dot{m}_{\text{Energy}}$ in Eq. (8) of [11], also given as one of the equalities in Eq. (A7) of [11], is rewritten, with the help of Eqs. (A1) and (A5) of [11], in its popular interface tracking equation form

$$\frac{\partial H}{\partial t} + \mathbf{v}_1^i \cdot \nabla H \cong \frac{-k_1}{\rho_1 \cdot h_{fg}} \frac{\partial T_f^i}{\partial n} \cdot |\nabla H| \quad (6)$$

When the right side of Eq. (6) is zero, spatial extension of Eq. (6) leads to a color function H whose initial values $H=0$ and $H=1$ within each of the phases are retained for all times $t > 0$, and this forms the basis of the popular VOF (volume of fluids) techniques

(see Hirt and Nicholas [23], etc.) for air/water type flows. Similarly, a suitable spatial extension of Eq. (6), in conjunction with some other techniques, is used in the Level-Set method (Sussman et al. [24], etc.) for capturing the interface through iterative single-domain (consisting of both the phases) calculations. For boiling related phase change flows, the Level-Set technique has recently been used by Son and Dhir [25]. In order to overcome some of the problems (see, e.g., Li and Renardy [26]) associated with interface capturing techniques (be it Level-Set, VOF, etc.) that utilize Eq. (6), the limited goal here was to ensure that these problems do not give rise to spurious computationally generated waves when no physical disturbances or noise are present. This difficult requirement was met by looking at the existing knowledge base for the reduced form of Eq. (6) given in Eq. (7) below. By substituting $H = h \cdot \{y - \delta(x,t)\}$, $\partial H / \partial t = -U \cdot \partial \delta / \partial t$, $\partial H / \partial x = -\partial \delta / \partial x$, $\partial H / \partial y = 1$, etc. in Eq. (6) and properly nondimensionalizing the resulting equation, one obtains the following interface tracking problem

$$\frac{\partial \delta}{\partial t} + \bar{u}(x,t) \frac{\partial \delta}{\partial x} = \bar{v}(x,t) \quad (7)$$

$$\delta(0,t) = 0$$

$$\delta(x,0) = \delta_{\text{steady}}(x) \text{ or other prescriptions}$$

where $\bar{u} \equiv u_1^i + \{Ja / (\text{Re}_1 \cdot \text{Pr}_1)\} \partial \theta_1 / \partial x^i$ and $\bar{v} \equiv v_1^i + \{Ja / (\text{Re}_1 \cdot \text{Pr}_1)\} \partial \theta_1 / \partial y^i$ typically depend strongly, but indirectly, on δ . The computational issues for discretization and numerical solution of Eq. (7) are well understood and discussed in Narain et al. [11].

The computational approach defined above meets the following requirements: (i) the convergence criteria (i.e., smallness of “ b ” defined on p. 125 of Patankar [22]) in the interior of each fluid is satisfied, (ii) all the interface conditions are satisfied, (iii) grid independent solutions are obtained for grids that are sufficiently refined (see Fig. 14 of [11]), (iv) unsteady simulations yielding the sensitive interface locations are free of computational noise (this is achieved by ensuring that there is an absence of computational noise in the absence of physical noise), and (v) its predictions for the classical steady problems of condensation on vertical or horizontal plates (Nusselt [3], Koh [5], etc.) are in agreement (see Narain et al. [11] and Yu [27]) with the classical solutions. As per estimates described in Narain et al. [11], the sum total of errors in the solutions reported here is less than 6 percent.

4 Identification of Steady/Quasi-Steady Solutions and Their Compatibility With Experiments

For slow laminar/laminar internal condensing flows considered here, the steady governing equations are such that the behavior of the x -component of the velocity field are “elliptic” in the sense that downstream conditions are able to affect flow variables at an upstream location (see a representative point P in Fig. 1). This behavior of the steady equations allow the signature of degeneracy associated with a stationary saturated mixture in a closed container (i.e., the fluid, under equilibrium thermodynamics conditions, could have many vapor/liquid interfacial configurations associated with different mixtures—from all vapor to all liquid—with the actual quality being determined by the total amount of heat removed from an initial all vapor configuration) to be carried over to the steady solutions of the governing equations and one has many steady interfacial configurations for different exit-conditions (i.e., different exit vapor qualities Z_e in Eq. (4)) that represent different amounts of heat removed for any given inlet and wall conditions. As a result, as is seen in Fig. 5 of [11], there are different steady solutions for different exit vapor qualities. However, for incompressible steady vapor flows associated with unconstrained-exit cases, unsteady noise-free simulations in Fig. 3 (which are free of both physical and computational noise) show that these steady solutions seek out a naturally selected exit condition (denoted as $Z_e|_{\text{Na}}$) as $t \rightarrow \infty$. In other words, there is an

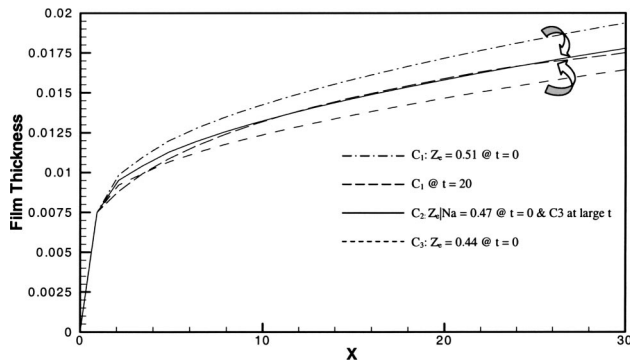


Fig. 3 For flow situation specified in Table 1 with $\alpha=90$ deg and $x_e=30$, the figure depicts two sets of steady solutions C_1 (for $Z_e=0.51$) and C_3 (for $Z_e=0.44$) that provide the initial conditions for solutions to be obtained for $t>0$ without any specification of exit conditions. The figure shows the resulting $\delta(x,t)$ predictions for $t>0$, the set of $\delta(x,t)$ curves C_1 start at $Z_e=0.51$ at $t=0$, and tend, as $t\rightarrow\infty$, to the solution for which $Z_{e|Na}=0.47$. The other set of curves C_3 start at $Z_e=0.44$ at $t=0$ and also tend, as $t\rightarrow\infty$, to the same $Z_{e|Na}$ solution.

attracting wave-free steady solution, which, in the qualitative representation of Fig. 4(a), is termed an attractor. The definition of an attractor among the steady solutions of a well-posed initial boundary value problem for a system of partial differential equations is qualitatively the same as that of a stable node (see Greenberg [28]) among the stationary solutions of a system of nonlinear ordinary differential equations. As shown later, this solution is stable but sensitive to noise. As a result, in practice, only a quasi-steady wavy solution of the type indicated in Fig. 4(b) is actually realized.

Since the above procedure requires consideration of the unsteady equations to identify the natural steady solution, it is obvious that this approach is both novel and different from steady incompressible single-phase or air/water flows where it typically suffices to work with steady equations to obtain steady solutions. The above approach for identifying stable quasi-steady incompressible vapor solutions is also found to be in good agreement (see Tables 2 and 3) with relevant experimental results of Lu [9] and Lu and Suryanarayana [10]. These experiments were done under unconstrained-exit conditions and filmwise condensation on the bottom surface of a horizontal duct (length=0.91 m) of rectangular cross-section (width=40 mm, height=25 mm). For comparisons with the simulations, the flow in the vertical midsection

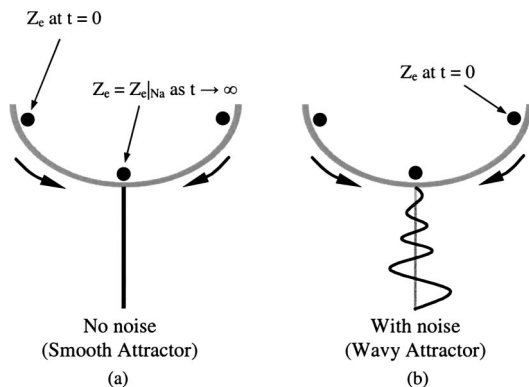


Fig. 4 Qualitative nature of the attracting steady/quasi-steady solution. The figure shows that different steady solutions associated with different exit conditions (Z_e at $t=0$) are attracted, under unconstrained exit conditions and as $t\rightarrow\infty$, to a special steady solution with $Z_e=Z_{e|Na}$.

Table 2 Comparison of experimental and computational $Z_{e|Na}$ values¹

Run #		$Z_e @ x_e = 12$	$Z_e @ x_e = 24$	$Z_e @ x_e = 36$	Mean Error %
220	Expt.	0.776	0.572	0.477	-2.13
	Theory	0.81	0.58	0.48	
221	Expt.	0.828	0.702	0.583	5.85
	Theory	0.85	0.66	0.5	
100	Expt.	0.908	0.824	0.761	-0.17
	Theory	0.92	0.84	0.74	
181	Expt.	0.884	0.796	0.718	3.97
	Theory	0.89	0.76	0.66	

¹Flow of saturated R113 condensing on the bottom plate of a horizontal channel of $h=25$ mm, $x_e=0.91$ m and measurements of $Z_{e|Na}$ at $x_e=12, 24$, and 36 .

of the experimental geometry (where ultrasound film thickness sensors, etc. were mounted) is modeled as a two-dimensional horizontal channel flow (with gap height $h=25$ mm). Furthermore, for experimental runs considered in Tables 2 and 3, the simulations ensured that the fluid (refrigerant called R-113), the average inlet velocity in the channel, bottom/top channel wall temperatures, and inlet pressure were specified to be the same as the specifications/values of the corresponding items/variables in the selected experimental runs. It is found in Tables 2 and 3 that, for horizontal channel flows considered, good agreement was obtained well beyond the typical laminar/laminar restriction of inlet vapor Reynolds number (based on channel height as characteristic length) being approximately less than 2000. It was found that the agreement was good for inlet vapor Reynolds number up to 7000. Perhaps, because of slow laminar condensate flows ($Re_\delta < 150$, where Re_δ is defined in Incropera and DeWitt [29]) and nonzero interfacial mass transfer through inclined or transverse vapor streamlines near the interface, the condensing vapor develops a sufficiently thick laminar sub-layer in the vicinity of the interface (see Narain et al. [11] or Liang [12]). This laminar layer allows computational predictions of film thickness, heat transfer rates, etc. under overall laminar/laminar assumptions to continue to remain in good agreement with the experiments of Lu and Suryanarayana [10] (though, perhaps, predictions of vapor velocity profile outside the laminar sub-layer of the vapor above the interface may not be good).

Effects of Gravity on Natural Steady Solutions. In Fig. 5(a) we see that gravity has a significant influence on film thickness. In the absence of gravity assisted condensate drainage that occurs for vertical/inclined configurations, condensate film is much thicker in zero gravity. However, zero gravity condensate is still slightly thinner than its values for the corresponding horizontal configuration. This is because, in the horizontal configuration, part of the vapor shear is used to deny the tendency of the condensate's hydrostatic-pressure distribution to cause a backward downhill flow and only the remaining vapor shear is used to keep it forward moving with a monotonically increasing film thickness. This monotonic increase of condensate thickness is due to a net balance that occurs between continuous accumulation of the liquid (under condensation mass transfer across the interface) and its forward flow. Despite the proximity of the horizontal and zero-gravity steady solutions, the absence of the transverse gravitational force in zero gravity makes the pressure variations in the liquid much more sensitive to the surface tension term in the normal stress condition (the second term on the right side of Eq. (4) in [11]) and this, as we see in the next section, causes much larger amplitude interfacial waves in response to ever present condensing surface noise. The significance of the magnitude of the transverse gravitational restoring force is best seen by observing that the liquid pressure variations $\pi_1(x,y,t)$ is affected both by its interfacial value π_1^i (as given by Eq. (4) in [11]) and its value required by the y -component of the momentum equation in Eq. (2). For example, if effects of $v_1(x,y,t)$ is ignored because of its smallness, the

Table 3 Comparison of experimental and computational mean film thickness values¹

Flow Speed U (m/s)	Run #	$\Delta T(^{\circ}C)$		$\delta(x_1)$	$\delta(x_2)$	$\delta(x_3)$	$\delta(x_4)$	$\delta(x_5)$	Average % Error
0.34	220	31.21	Expt.	0.010	0.015	0.016	0.018	0.020	-5%
			Comp.	0.012	0.014	0.015	0.017	0.019	
0.31	221	21.42	Expt.	0.008	0.013	0.014	0.015	0.017	2.9%
			Comp.	0.011	0.013	0.014	0.016	0.018	
0.42	100	14.76	Expt.	0.012	0.014	—	0.015	0.015	4.2%
			Comp.	0.010	0.013	—	0.016	0.018	
0.5	181	21.42	Expt.	0.008	0.012	0.013	0.014	0.016	3.0%
			Comp.	0.009	0.012	0.013	0.015	0.016	

¹Flow of saturated R113 condensing on the bottom plate of a horizontal channel of $h=25$ mm, $x_e=0.91$ m and measurements of film thickness values at $x=2.03, 6.10, 10.16, 18.29,$ and 32.51 .

y-momentum balance in Eq. (2) implies $\pi_1(x, y, t) \cong \pi_1^i + |Fr_y^{-1}|(\delta - y)$, where $|Fr_y^{-1}|$ is a positive constant and π_1^i satisfies Eq. (4) of [11].

Furthermore, Fig. 5(b) shows it is equivalent to prescribe exit pressure ($\bar{\pi}_2 \equiv 1/(1-\delta) \int_0^1 \pi_2 dy$) or exit quality Z_e at $x=x_e$ and that the natural exit conditions (exit quality $Z_{e|Na}$ or associated exit pressure) are different in different gravitational environments. The shear dominated cases (horizontal and zero gravity) have a much larger pressure drop and hence have a much narrower flow regime within which the compressibility of the vapor can be ig-

nored (this is because an increase in $\Delta p_2/p_0$ makes the underlying assumption “ $\Delta \rho_2/\rho_{20} \ll 1$ ” a poorer approximation). Figure 5(c-d) show that phase-speeds $\bar{u}_{steady}(x)$ (see Narain et al. [11]) for zero gravity and horizontal configurations are significantly smaller than gravity driven vertical cases, and, as a result, in Fig. 5(d), the characteristics curves along which disturbances propagate (see Narain et al. [11]) become very nearly vertical. This means that, for these shear dominated cases, effects of condensing surface noise are likely to accumulate around the location of the noise.

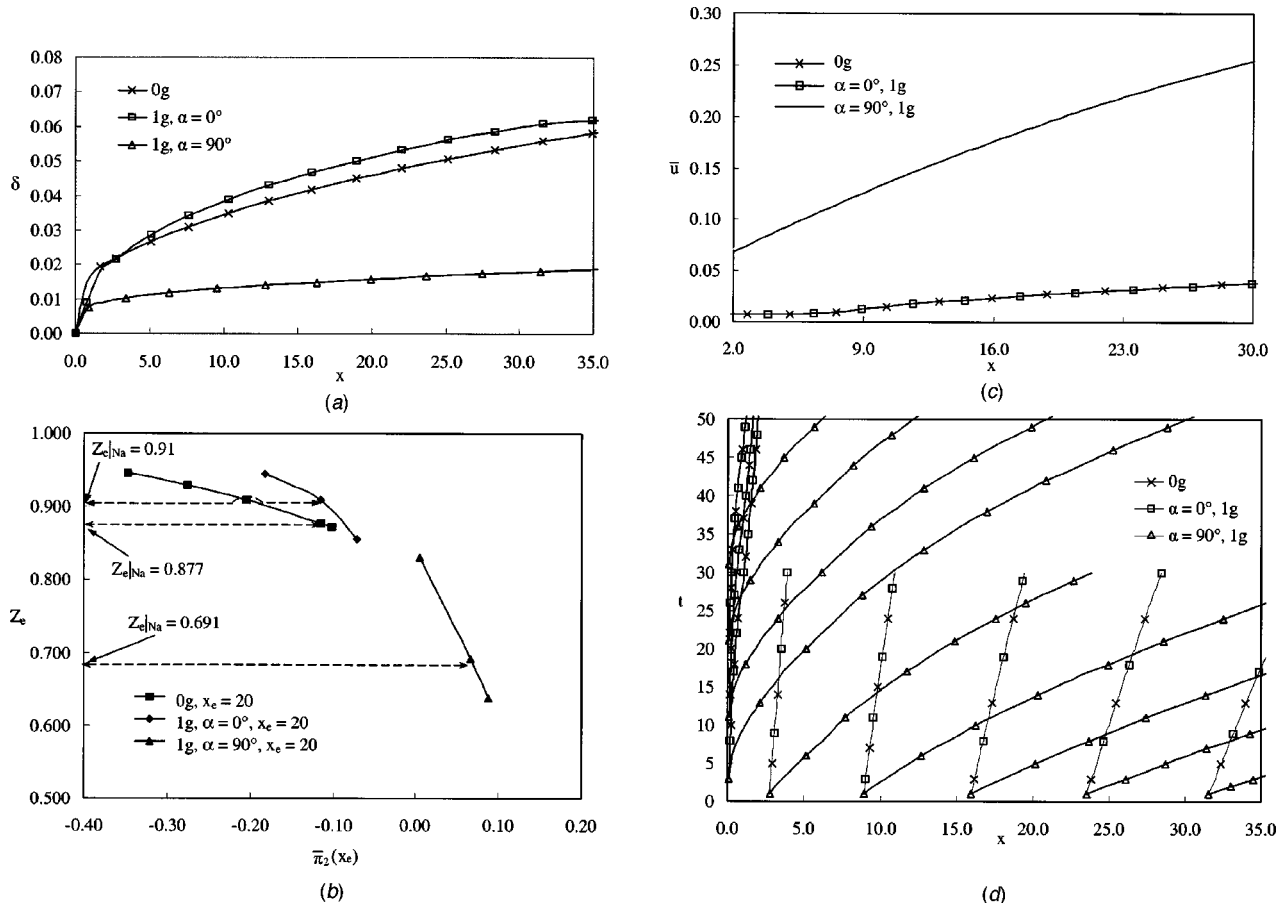


Fig. 5 (a) For flow situations specified in Table 1, the figure shows smooth steady condensate film thickness for vertical, horizontal and zero-gravity cases which have, for $x_e=20$, $Z_{e|Na}=0.691, 0.877,$ and 0.91 respectively. (b) For the flow situations specified in Table 1, the figure shows different exit pressure $\bar{\pi}_2(x_e)$ values associated with different Z_e values. In particular, it also shows $Z_{e|Na}$ and their corresponding exit pressure values for the cases considered in Fig. 5(a). (c) For flow situations specified in Table 1, the figure shows phase-speeds $\bar{u}_{steady}(x)$ for the cases considered in Fig. 5(a). (d) For flow situation specified in Table 1, the characteristics curves $x=x_e(t)$ denote curves along which infinitesimal initial disturbances naturally propagate (see [11]) on the stable steady solutions of Fig. 5(a). On characteristics that originate on $x=0$ line, there are no disturbances as $\delta(0,t) \cong 0$ implies $\delta' \cong 0$.

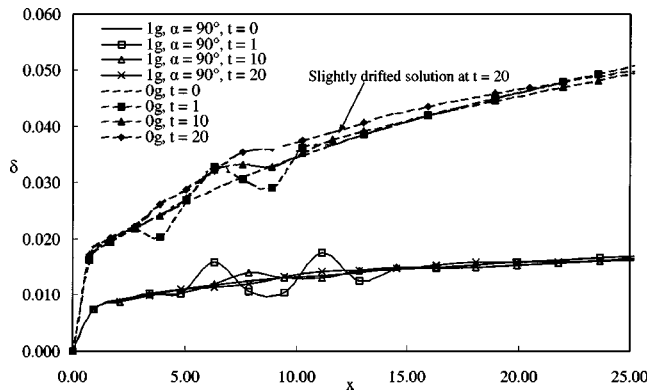


Fig. 6 For flow situations specified in Table 1, the above $\delta(x, t)$ predictions ($\Delta t = 10$) are for vertical and $0g$ cases with initial data $\delta(x, 0) = \delta_{\text{steady}}(x) + \delta'(x, 0)$, where a nonzero disturbance $\delta'(x, 0)$ has been superposed at $t = 0$ on the steady solution δ_{steady} . Here $\delta'(x, 0) = 0.004 \cdot \sin(2\pi x/5)$ for $3.5 \leq x \leq 13.5$ and $\delta' = 0$ elsewhere.

5 Discussion of Unsteady Simulation Results

Effects of Initial Disturbance. The behavior of natural exit-condition and associated smooth-interface steady solutions as obtained in Fig. 3 are qualitatively described in Fig. 4. In normal gravity, as shown in Narain et al. [11], these solutions are intrinsically wavy but stable to initial disturbances. However the stability of the natural ($Z_e = Z_e|_{\text{Na}}$) smooth-interface zero gravity solutions, as compared to stability of normal gravity solutions, is demonstrated by the results in Fig. 6. In Fig. 6, there is some separation between the $t \rightarrow \infty$ (i.e., large t , or $t = 20$) and $t = 0$ solutions for the zero gravity case. As the size of the amplitude of the disturbance used for the zero gravity case in Fig. 6 was reduced, it was found that the $t \rightarrow \infty$ (i.e., large t , or $t = 20$) solution stayed closer to the $t = 0$ solution associated with the natural exit condition. This large time behavior implies that the stability for the zero gravity case, as compared to normal gravity case, is weak. In other words, loosely speaking, for qualitative purposes, the bowl at the bottom of Fig. 4(a) is much flatter for zero gravity than the corresponding cases for normal gravity. This weak stability in zero gravity is observed even in the absence of surface tension and momentum transfer terms in the interfacial normal stress condition given in Eq. (4) of [11]. Therefore the weak stability to initial disturbances is a result of the mass transfer and the associated nature of the streamlines (which, at the interface, are more transverse in gravity driven flows and more slanted, as in Fig. 7, for shear dominated flows) rather than stabilizing or destabilizing effects of surface tension and/or momentum-transfer terms in the normal stress condition at the interface (see the right side of Eq. (4)).

Effects of Noise and Resonance. The noise-sensitivity of the solutions in Fig. 5(a) is shown in Figs. 7 and 8. These Figures show that the interface is quite sensitive to even minuscule standing wave vibrations of the bottom plate given by $v_1(x, 0, t) = \varepsilon \cdot \sin(2\pi x/\lambda) \cdot \sin(2\pi t/T)$ whose amplitude ε is in the range of $10^{-5} - 3 \cdot 10^{-5}$. This, in a way, is expected from Eq. (7) because interfacial disturbances are forced by the interfacial value v_1' of the transverse velocity v_1 that appears in \bar{v} . Furthermore, the extreme smallness of this forcing is consistent with the fact that, on average, $u_2 \gg u_1 \gg v_1$ with each dominance being at least two to three orders of magnitude (i.e., 10^2 or 10^3) bigger over the other. For the cases considered here (e.g., the case of $T \approx 24$, $\lambda \approx 10$, $h \approx 0.004$ m, and $U \approx 0.41$ m/s), the maximum displacement amplitude of the vibrations are about $0.25 \mu\text{m}$, maximum velocity amplitude are about $0.12 \mu\text{m/s}$, and maximum accelera-

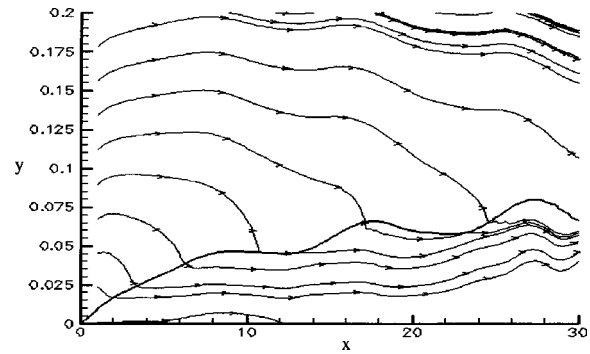


Fig. 7 Closer to the interface, the figure shows the interface location and vapor/liquid streamlines at $t = 300$ for a resonant bottom wall noise given as $v_1(x, 0, t) = \varepsilon \cdot \sin(2\pi x/\lambda) \cdot \sin(2\pi t/T)$ where $\varepsilon = 0.32E-5$, $\lambda = 10$, and $T(x) = \lambda/\bar{u}_{\text{steady}}(x)$. The underlying steady solution is for a zero gravity flow in Table 1 with $x_e = 30$, $Z_e|_{\text{Na}} = 0.91$ and $\sigma_0 = 15E-03$ N/m.

tion amplitude are about $6.25 \cdot 10^{-4} \text{ m/s}^2$ (which is less than $10^{-4}g$, $g \approx 10 \text{ m/s}^2$). Such vibrations are indeed commonly present as structural or coolant flow induced vibrations and these are in the 0–30 Hz range considered here. For the wavy cases discussed/studied here, these vibrations are often the primary cause of observed interfacial oscillations. Although the results shown in Figs. 7 and 8 are for sinusoidal standing waves on the condensing surface at $y = 0$, more complex two-dimensional or three-dimensional patterns will arise from a more general noise that would typically be present. Even if the noise itself is two-dimensional, any three-dimensional imperfection in the geometry can cause the waves to become three-dimensional.

For the resonance cases (vertical, horizontal, and zero-gravity) considered in Fig. 8(a) the resonance phenomena comes into play (see Narain et al. [11]) when the external noise frequency f_{ext} and wavelength λ associated with minuscule standing-wave noise of the bottom plate are chosen such that:

$$\lambda f_{\text{ext}}(x) \cong \bar{u}_{\text{steady}}(x) \quad (8)$$

where the steady problem's phase speeds $\bar{u}_{\text{steady}}(x)$ in Eq. (8) is well defined (see Fig. 5(c)) and is known from the steady solution for $Z_e = Z_e|_{\text{Na}}$. At a chosen operating condition, this large growth rate resonance condition can be actively achieved by placing vibration actuators along the condensing surface with well-defined frequency shifts or by a passive design (suitable variations in material thickness and/or composition) of the plate associated with the condensing surface. For zero gravity, the resonant noise-induced waves in Fig. 8(a) lead to enhanced pressure drops (see Fig. 8(b)).

The above-described effects of bottom wall standing-wave noise employ a product of a single wavelength spatial sinusoid and a single-frequency temporal sinusoid. In practice, there are several sinusoidal components of different wavelengths and frequencies. Once the actual components of bottom wall noise is experimentally known (with the help of accelerometers) and modeled (say as $v_1(x, 0, t)|_I = 2\varepsilon \cdot \sin(2\pi x/\lambda) \cdot \sin(2\pi t/T)$ and $v_1(x, 0, t)|_{II} = \varepsilon \cdot \sin(2\pi x/\lambda) \cdot \sin(2\pi t/T) + \varepsilon \cdot \sin(2\pi x/(\lambda/2)) \cdot \sin(2\pi t/T)$ in Fig. 9), the resulting shapes of the different free surface waves (see Fig. 9) and their effects can be assessed. Experimental measurements of both the bottom wall noise and real time film thickness values can be used for further validation and use of the resonance phenomena.

In Fig. 10, the waves in $0g$ (for $\sigma = \sigma_0$) have significantly greater amplitude for noise amplitude of $\varepsilon = 5\varepsilon^*$ as opposed to $\varepsilon = \varepsilon^*$. This is because forward wave speeds are very small and higher accumulation rates of local interfacial disturbances at higher amplitudes significantly dominate the damping rates of lo-

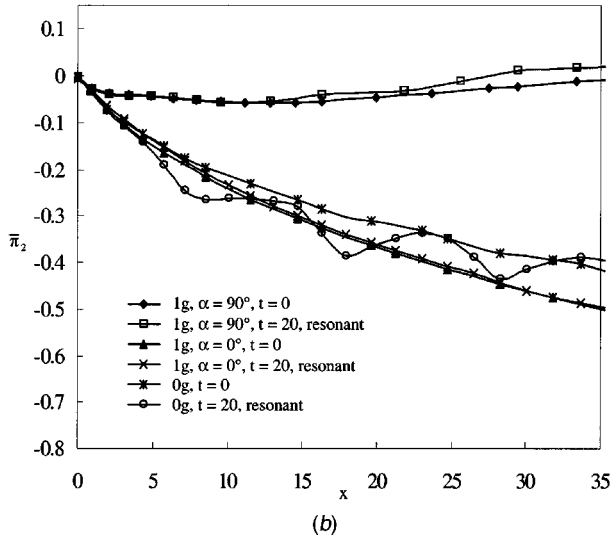
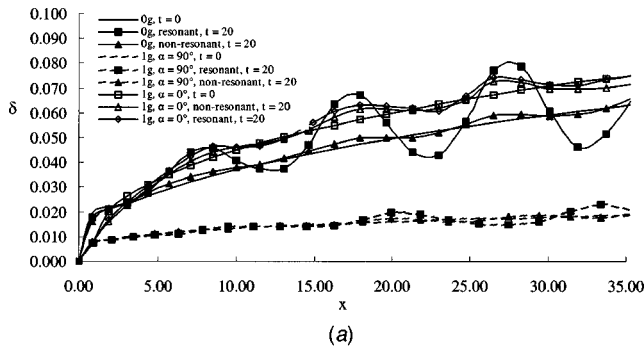


Fig. 8 (a) For flow situations specified in Table 1 and $x_e=35$, the above $\delta(x,t)$ values at $t=0$ (with $Z_e=Z_{elNa}$) and $t=20$ are for resonant and non-resonant bottom wall noise given as $v_1(x,0,t)=\varepsilon \cdot \sin(2\pi x/\lambda) \cdot \sin(2\pi t/T)$, $\varepsilon=0.24E-05$ and $\lambda=10$. For nonresonant cases $T=24$ and for resonant cases $T=T(x)=\lambda/\bar{u}_{steady}$. (b) For flow situations specified in Table 1 and $x_e=35$, the steady and unsteady values of exit pressures are shown as a function of x . The predictions are for case 1: vertical ($\alpha=90$ deg), case 2: horizontal in 1g ($\alpha=0$ deg, $Fr_y^{-1}=0.233$) and case 3: 0g ($Fr_y^{-1}=0$). The waves are due to bottom wall noise specified in Fig. 8(a).

cal disturbances. In the next section it is seen that surface tension forces eventually contain these larger amplitudes.

Effects of Surface Tension. For typical interfacial waviness associated with vertical to horizontal cases in the presence of gravity (e.g., the vertical case in Fig. 8(a)), it is found that the surface tension and momentum transfer terms in the relation for interfacial pressures (viz. the second and third terms on the right side of Eq. (4) in [11]) do not play a role over most of the condensing surface (a small leading edge zone over $0 \leq x \leq \varepsilon_0$, with $\varepsilon_0 \ll 1$, is excluded because flow physics in this region do not affect the rest of the flow). This was computationally verified. For example, in Fig. 8(a), waves for vertical and horizontal configurations, remain essentially the same (within 1–2 percent) as surface tension σ takes values over $0 \leq \sigma \leq 100\sigma^*$ and the momentum transfer term in Eq. (4) of [11] is retained or dropped. In other words, on earth, the value of the forcing v_1^i (see the right side of Eq. (7)) that influences δ is dominated, through $\pi_1(x,y,t)$, by gravitational forces $|Fr_x^{-1}|$ and/or $|Fr_y^{-1}|$ and surface tension is not influential. The interfacial value of $v_1(x,y,t)$, denoted as v_1^i , is influenced by $\pi_1(x,y,t)$ values which in turn are affected both by the interfacial liquid pressure π_1^i (see the surface tension term on the right side of Eq. (4) in [11]) and the x and y -momentum

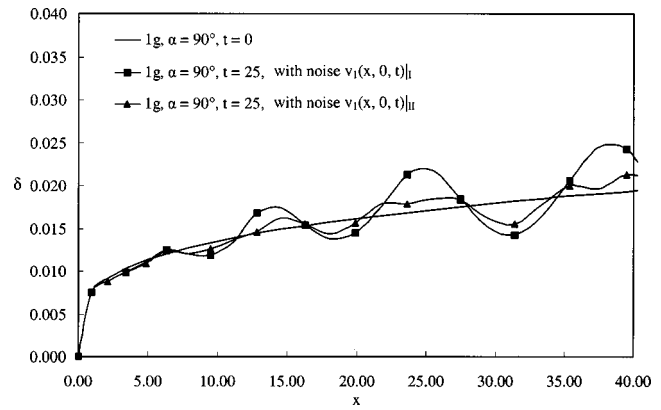


Fig. 9 For flow situations specified in Table 1, the $\delta(x,t)$ values at $t=0$ (with $Z_e=Z_{elNa}$) and $t=25$ are for different bottom wall noises defined as: $v_1(x,0,t)|_I=2\varepsilon \cdot \sin(2\pi x/\lambda) \cdot \sin(2\pi t/T)$, and $v_1(x,0,t)|_{II}=\varepsilon \cdot \sin(2\pi x/\lambda) \cdot \sin(2\pi t/T) + \varepsilon \cdot \sin(2\pi x/\lambda/2) \cdot \sin(2\pi t/T)$ where $\varepsilon=0.24E-05$, $\lambda=10$, $T=T(x)=\lambda/\bar{u}_{steady}$, and $\sigma_0=0.015$ N/m.

balance equations in Eq. (2) that play a role in the motion of the condensate. However, as seen in Fig. 8(a), effects of surface tension forces, in the interfacial normal stress condition (see Eq. (4) of [11]) are not masked in zero gravity where the surface tension term provides a key effect (which, for typically small surface tension values, becomes more significant whenever the curvature or δ_{xx} values become large). Thus surface tension particularly plays a significant role in 0g response to bottom wall noise of amplitude above certain values (compare $\varepsilon=\varepsilon^*$ with $\varepsilon=5\varepsilon^*$ for non-resonant 0g cases in Fig. 10). This is because higher noise amplitudes cause accumulation of interfacial disturbances to exceed their removal/damping rates and an unsteady situation is attained where the wave amplitudes are contained by just the right variations in curvature that are consistent with the role of surface tension forces in the normal stress condition. Furthermore, in Fig. 10, it is seen that the above-described dynamics is such that there is a wave amplitude decrease as surface tension values increase (for $\sigma_0=30\sigma^*$) and a wave amplitude increase with decrease in surface tension (for $\sigma_0=\sigma^*/30$). Computations also verify that an assumption of a hypothetical zero surface tension at the interface does not allow zero gravity flows to withstand average values of wall heat flux ($q_w''=-k_1 \cdot \partial T_1 / \partial y|_{y=0}$) are only slightly higher

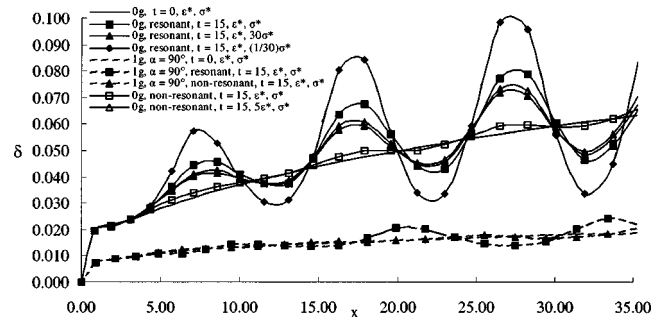


Fig. 10 For flow situations specified in Table 1, the $\delta_{steady}(x)$ and $\delta(x,t)$ predictions are for resonant and nonresonant bottom wall noise with different amplitudes ε (ε^* or $5\varepsilon^*$) and different surface tensions σ_0 (σ^* or $30\sigma^*$ or $\sigma^*/30$). The noise in the legend are specified by $v_1(x,0,t)=\varepsilon \cdot \sin(2\pi x/\lambda) \cdot \sin(2\pi t/T)$, $\varepsilon^*=0.24E-05$, $\lambda=10$, and $\sigma^*=0.015$ N/m. For nonresonant cases, $T=24$ and for resonant cases, $T=T(x)=\lambda/\bar{u}_{steady}$.

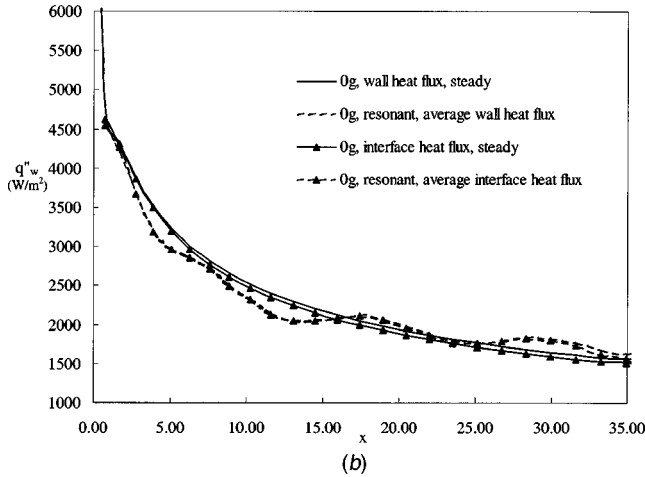
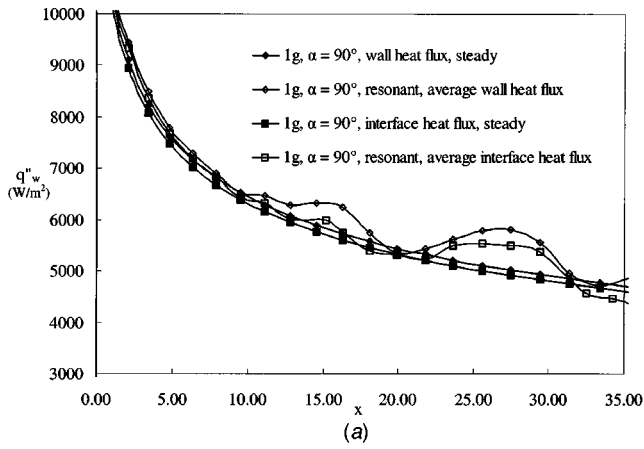


Fig. 11 (a) For the flow situations specified in Table 1, $x_e = 35$, and vertical configuration; the figure shows steady and time-averaged values of heat flux at the wall and at the interface; and (b) for the flow situations specified in Table 1, $x_e = 35$, and 0g configuration; the figure shows steady and time-averaged values of heat flux at the wall and at the interface

than time averaged values of interfacial heat-flux ($q''_i \equiv -k_1 \cdot \partial T_1 / \partial n|_i$). This is because transverse conduction heat transfer significantly dominates sensible cooling (i.e., mean liquid temperature drops somewhat with distance x).

It is recalled that heat transfer rates can also be increased under constrained exit conditions associated with compressible vapor flows—e.g., by increasing the exit pressure (or decreasing Z_e from 0.50 to 0.38 in Fig. 5 of [11]). The noise sensitivity analyses and flow regime (e.g., plug/churn versus annular flows) issues for these constrained cases are not studied here and are not fully understood at this point.

Effects on Shear Stress. Effects of noise-induced persistent waves are best reported as mean interfacial tangential stress $\bar{T}_{nt_0}^i$ on a representative or mean steady location $\delta_{\text{steady}}(x)$ of the interface ($\delta(x, t) \equiv \delta_{\text{steady}}(x) + \delta'(x, t)$). Replacing $\delta_{\text{steady}}(x)$ by steady interfacial location at $t=0$ (obtained, as in Fig. 5(a), under noise-free conditions for exit condition $Z_e = Z_{e|Na}$), a mean tangential stress (over time duration $[t_i, t_f]$, where t_i and “ $t_f - t_i$ ” are sufficiently large times) along the unit tangent $\hat{t}_0(x)$ at x is defined as

$$\bar{T}_{nt_0}^i \equiv \frac{1}{(t_f - t_i)} \int_{t_i}^{t_f} \{\mathbf{T}_1^i \cdot \hat{\mathbf{n}} \cdot \hat{\mathbf{t}}_0\} dt \equiv \rho_1 U^2 \cdot \bar{\tau}_{nt_0}^i, \quad (9)$$

where \mathbf{T}_1^i is the stress tensor value at the liquid interface ($\mathbf{T}_1^i \equiv -p_1^i \mathbf{1} + \mathbf{S}_1^i$) and $\hat{\mathbf{n}}$ is the unit normal on the interface (see defi-

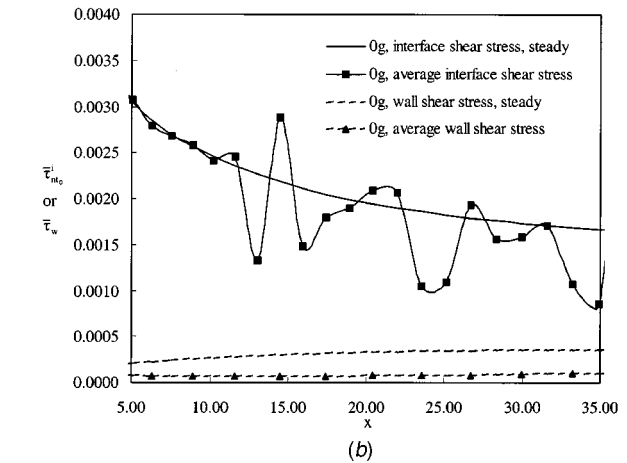
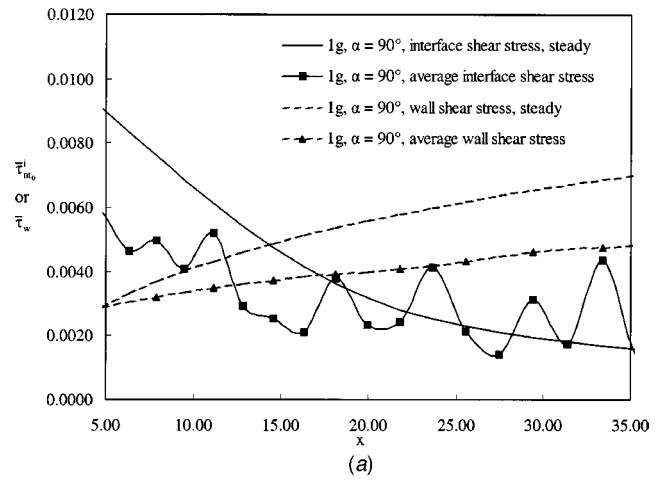


Fig. 12 (a) For the flow situations specified in Table 1, $x_e = 35$, and vertical configuration; the figure shows steady and time-averaged values of shear stress at the wall ($\bar{\tau}_w$) and the tangential stress ($\bar{\tau}_{nt_0}^i$) at the steady interface location; and (b) For the flow situations specified in Table 1, $x_e = 35$, and 0g configuration; the figure shows steady and time-averaged values of shear stress at the wall ($\bar{\tau}_w$) and the tangential stress ($\bar{\tau}_{nt_0}^i$) at the steady interface location

nitions given in the appendix of [11]). Clearly $\bar{\tau}_{nt_0}^i$ in Eq. (9) is the nondimensional value of the physical stress $\bar{T}_{nt_0}^i$. On the bottom wall, at $y=0$, with unit vectors $\hat{\mathbf{n}} = \hat{\mathbf{j}}$ and $\hat{\mathbf{t}}_0 = \hat{\mathbf{i}}$; the nondimensional wall shear stress $\bar{\tau}_w$ is similarly defined.

The interfacial and wall shear values are shown in Figs. 12(a,b). Under influence of gravity, as the condensate speeds up in Fig. 12(a), gravity driven waves cause a shear enhancement. It was verified that this enhancement is primarily due to viscous stresses and the pressure-drag contribution in Eq. (9) is very small. On the contrary, in the shear-dominated situation in Fig. 12(b), gravitational energy is not available; and, as a result, waves slightly decrease the mean interfacial shear as more of the instantaneous energy imparted to the condensate by the instantaneous values of the interfacial shear stress (i.e., vapor exerted traction on the liquid) must be used to sustain fluctuations on the liquid interface. However, unlike Fig. 12(a), in shear-dominated cases of Fig. 12(b), interfacial shears are much larger relative to wall shears.

Effects of Nonconstant Wall Temperatures. In most applications, the condensing surface temperature $T_w(x)$ is not a constant. As shown in Fig. 13, all else remaining the same, two different wall temperature variations $T_w(x)$ lead to predictions of

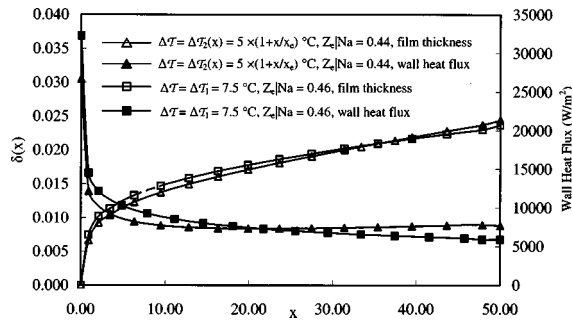


Fig. 13 For flow situation specified in Table 1 with $\alpha=90$ deg and $x_e=50$, the above figure depicts two different film thickness, wall heat flux, and natural exit condition $Z_{e|Na}$ predictions for two different wall temperature specifications $T_w(x)$ (and hence ΔT) which is, for case 1: $\Delta T_1=7.5^\circ\text{C}$ and case 2: $\Delta T_2(x)=5^\circ\text{C}\cdot(1+x/x_e)$

natural exit conditions $Z_{e|Na}$ which are somewhat different but close to one another because both temperature variations have the same average value between the inlet and the exit. As a consequence, as is seen in Fig. 13, on average, both the condensate thickness and wall heat flux values are also reasonably close to one another.

6 Conclusions/Results

In addition to a brief summary of the algorithm and vertical channel results reported in Narain et al. [11], the new results reported here are:

- For unconstrained exit conditions, the effectiveness (by way of showing compatibility with known experiments) of the unsteady noise-free simulation method for identifying the natural exit condition and associated attracting steady solution has been demonstrated for the shear-dominated cases (zero gravity and horizontal configurations) as well.
- The nonresonant and resonant effects of ubiquitous minuscule bottom plate vibrations on the stable steady solutions are demonstrated here for shear-dominated cases (zero gravity and horizontal configurations) and compared with the earlier results for gravity dominated vertical case.
- It is shown that, for suitably large (yet minuscule) amplitude bottom wall vibrations, the ability to sustain condensing surface noise in zero gravity is due only to normal stress effects of surface tension. Furthermore it is shown that zero gravity cases show significantly higher accumulation of noise-induced disturbances resulting in higher amplitude waves as compared to similarly induced waves in terrestrial environments.
- Effects of surface tension were shown to be insignificant for terrestrial environments (horizontal to vertical).
- Effects of surface tension in the tangential stress condition (the Marangoni effects) are found to be negligible in all environments.
- A weaker stability and higher noise-sensitivity of the zero gravity steady solutions is demonstrated. It is inferred that an active control for holding the natural exit condition fixed, active reductions in condensing surface noise levels, an increase in normal stress on the liquid interface by electrical or other means, etc. are needed for stable realizability of annular condensing flows in space-based applications.
- The proposed computational method's ability to predict significant flow variables (streamlines, interfacial and wall values of shear and heat-flux, etc.) for constant and non-constant wall temperatures is demonstrated.

The above results provide an understanding that is necessary for further enhancement of the reported simulation methods and codes. Future enhancements will allow considerations of: vapor compressibility effects for constrained exit cases, simulations for

longer channels and thicker condensates, and more general handling of the interface tracking equation (Eq. (6)) that allows predictions of phenomena that exhibit interfacial pinch-off and droplet formations.

Acknowledgment

This work was partially supported by the NSF grant CTS-0086988, and a grant (NNCO4GB52G) from NASA office of Biological and Physical Sciences.

Nomenclature

- C_p = specific heat, J/(kg-K)
 h = gap between the plates (see Fig. 1), m
 h_{fg} = latent heat ($h_g - h_f$), J/kg
 Ja = Jacob number, $C_{p1}\Delta T/h_{fg}$
 k = thermal conductivity, W/(m-K)
 p = pressure, N/m²
 p_0 = pressure at the inlet, N/m²
 q_w'' = bottom wall heat flux at any point and time, W/m²
 Re_1 = Reynolds numbers $\rho_1 U h / \mu_1$
 Re_{in} = inlet Reynolds number Re_2
 T = temperatures, K
 ΔT = temperature difference between the vapor and the wall, K
 U = value of the average vapor speed at the inlet, m/s
 (u, v) = values of x and y components of velocity, m/s
 (u, v) = nondimensional values of u and v
 (x, y, t) = physical distances along and across the bottom plate and time, (m, m, s)
 (x, y, t) = nondimensional values of (x, y, t)
 Z_e = ratio of exit vapor mass flow rate to total inlet mass flow rate

Greek Symbols

- δ = nondimensional value of condensate thickness
 Δ = physical value of condensate thickness, m
 ε = amplitude of nondimensional disturbances representing values of $v_1(x, 0, t)$
 μ = viscosity, Pa-s
 ν = kinematic viscosity μ/ρ , m²/s
 π = nondimensional pressure
 ρ = density, kg/m³
 σ = surface tension, N/m
 θ = nondimensional temperature
 $\bar{\tau}_w$ = steady or time-averaged nondimensional wall shear stress
 $\bar{\tau}_{nt_0}^i$ = steady or time-averaged nondimensional tangential shear stress at a point on a steady interface location

Subscripts

- I = it takes a value of 1 for liquid phase and 2 for vapor phase
 s = saturation condition
 w = wall

Superscripts

- i = value of a variable at an interface location

References

- [1] Krotiuk, W. J., 1990, *Thermal-Hydraulics for Space Power, Propulsion, and Thermal Management System Design*, American Institute of Aeronautics and Astronautics, Inc., Washington, D.C.
- [2] Faghri, A., 1995, *Heat Pipe Science and Technology*, Taylor and Francis, Washington D.C.
- [3] Nusselt, W., 1916, "Die Oberflächenkondensation des Wasserdampfes," *Z. Ver. Dt. Ing.*, **60**(27), pp. 541–546.
- [4] Rohsenow, W. M., 1956, "Heat Transfer and Temperature Distribution in Laminar Film Condensation," *Trans. ASME*, **78**, pp. 1645–1648.
- [5] Koh, J. C. Y., 1962, "Film Condensation in a Forced-Convection Boundary-Layer Flow," *Int. J. Heat Mass Transfer*, **5**, pp. 941–954.

- [6] Chow, L. C., and Parish, R. C., 1986, "Condensation Heat Transfer in Micro-Gravity Environment," *Proceedings of the 24th Aerospace Science Meeting*, AIAA, New York.
- [7] Narain, A., Yu, G., and Liu, Q., 1997, "Interfacial Shear Models and Their Required Asymptotic Form for Annular/Stratified Film Condensation Flows in Inclined Channels and Vertical Pipes," *Int. J. Heat Mass Transfer*, **40**(15), pp. 3559–3575.
- [8] White, F. M., 2003, *Fluid Mechanics*, Fifth Edition, McGraw Hill.
- [9] Lu, Q., 1992, "An Experimental Study of Condensation Heat Transfer With Film Condensation in a Horizontal Rectangular Duct," Ph.D. thesis, Michigan Technological University.
- [10] Lu, Q., and Suryanarayana, N. V., 1995, "Condensation of a Vapor Flowing Inside a Horizontal Rectangular Duct," *ASME J. Heat Transfer*, **117**, pp. 418–424.
- [11] Narain, A., Liang, Q., Yu, G., and Wang, X., 2004, "Direct Computational Simulations for Internal Condensing Flows and Results on Attainability/Stability of Steady Solutions, Their Intrinsic Waviness, and Their Noise-Sensitivity," *ASME J. Appl. Mech.*, **71**, pp. 69–88.
- [12] Liang, Q., 2003, "Unsteady Computational Simulations and Code Development for a Study of Internal Film Condensation Flows' Stability, Noise-Sensitivity, and Waviness," Ph.D. thesis, Michigan Technological University.
- [13] Traviss, D. P., Rohsenow, W. M., and Baron, A. B., 1973, "Forced-Convection Condensation Inside Tubes: A Heat Transfer Equation for Condenser Design," *ASHRAE J.*, **79**, Part 1, pp. 157–165.
- [14] Shah, M. M., 1979, "A General Correlation for Heat Transfer During Film Condensation Inside Pipes," *Int. J. Heat Mass Transfer*, **22**, pp. 547–556.
- [15] Hewitt, G. F., Shires, G. L., and Polezhaev, Y. V., Editors, 1997, *International Encyclopedia of Heat and Mass Transfer*, CRC Press, Boca Raton and New York.
- [16] Carey, V. P., 1992, *Liquid-Vapor Phase-Change Phenomena*, Series in Chemical and Mechanical Engineering, Hemisphere Publishing Corporation.
- [17] Palen, J. W., Kistler, R. S., and Frank, Y. Z., 1993, "What We Still Don't Know About Condensation in Tubes," in *Condensation and Condenser Design* J. Taborek, J. Rose, and I. Tanasawa, eds., United Engineering Trustees, Inc. for Engineering Foundation and ASME, New York, pp. 19–53.
- [18] Minkowycz, W. J., and Sparrow, E. M., 1966, "Condensation Heat Transfer in the Presence of Non-Condensibles, Interfacial Resistance, Superheating, Variable Properties, and Diffusion," *Int. J. Heat Mass Transfer*, **9**, pp. 1125–1144.
- [19] *ASHRAE Handbook*, 1985, Fundamentals SI Edition, American Society of Heating, Refrigeration and Air-Conditioning Engineers, Inc., Atlanta, GA.
- [20] Delhaye, J. M., 1974, "Jump Conditions and Entropy Sources in Two-Phase Systems; Local Instant Formulation," *Int. J. Multiphase Flow*, **1**, pp. 395–409.
- [21] Plesset, M. S., and Prosperetti, A., 1976, "Flow of Vapor in a Liquid Enclosure," *J. Fluid Mech.*, **78** (3), pp. 433–444.
- [22] Patankar, S. V., 1980, *Numerical Heat Transfer and Fluid Flow*, Hemisphere, Washington D.C.
- [23] Hirt, C. W., and Nichols, B. D., 1981, "Volume of Fluid (VOF) Method for the Dynamics of Free Boundaries," *J. Comput. Phys.*, **39**, pp. 201–255.
- [24] Sussman, M., Smereka, P., and Osher, S., 1994, "A Level Set Approach for Computing Solutions to Incompressible Two-Phase Flow," *J. Comput. Phys.*, **114**, pp. 146–159.
- [25] Son, G., and Dhir, V. K., 1998, "Numerical Simulation of Film Boiling Near Critical Pressures With a Level Set Method," *ASME J. Heat Transfer*, **120**, pp. 183–192.
- [26] Li, J., and Renardy, Y., 2000, "Numerical Study of Flows of Two Immiscible Liquids at Low Reynolds Number," *SIAM Rev.*, **42**(3), pp. 417–439.
- [27] Yu, G., 1999, "Development of a CFD Code for Computational Simulations and Flow Physics of Annular/Stratified Film Condensation Flows," Ph.D. thesis, ME-EM Department, Michigan Technological University.
- [28] Greenberg, M. D., 1978, *Foundations of Applied Mathematics*, Prentice-Hall, Inc., New Jersey.
- [29] Incropera, F. P., and DeWitt, D. P., 1996, *Fundamentals of Heat and Mass Transfer*, Fourth Edition, Wiley.
- [30] Di Marco, P., Grassi, W., and Trentavizi, F., 2002, "Pool Film Boiling Experiments on a Wire in Low Gravity," in *Microgravity Transport Processes in Fluid, Thermal, Biological, and Material Sciences*, S. S. Sadhal, ed., Annals of the New York Academy of Sciences, **974**, pp. 428–446.

Jonathan A. Olivier
e-mail: jonathan.olivier@up.ac.za

Leon Liebenberg
e-mail: lieb@up.ac.za

Department of Mechanical and Aeronautical
Engineering,
University of Pretoria,
Pretoria, 0002, South Africa

Mark A. Kedzierski
e-mail: mark.kedzierski@nist.gov
National Institute of Standards and Technology,
Gaithersburg, MD

Josua P. Meyer*
e-mail: jmeyer@up.ac.za
Department of Mechanical and Aeronautical
Engineering,
University of Pretoria,
Pretoria, 0002, South Africa

Pressure Drop During Refrigerant Condensation Inside Horizontal Smooth, Helical Microfin, and Herringbone Microfin Tubes

This paper presents a study of pressure drops during condensation inside a smooth, an 18-deg helical microfin, and a herringbone microfin tube. Measurements were conducted with refrigerant flowing through the tube of a concentric heat exchanger, with water flowing in a counterflow direction in the annulus. Each tube was part of a condenser consisting of eight subcondensers with instrumentation preceding each subcondenser. Three refrigerants were used, namely, R-22, R-407C, and R-134a, all operating at a saturation temperature of 40 °C with mass fluxes ranging from 400 to 800 kg/m² s. Inlet qualities ranged from 0.85 to 0.95 and outlet qualities ranged from 0.05 to 0.15. The test results showed that on average for the three refrigerants the pressure gradients of the herringbone microfin tube were about 79% higher than that of the smooth tube and about 27% higher than that of the helical microfin tube. Further, a correlation from the literature for predicting pressure drops inside a helical microfin tube was modified for the herringbone microfin tube. The modified correlation predicted the data to within an error of 1% and had an absolute mean deviation of 6.8%. This modified correlation compared well with a correlation from the literature that predicted the data to within an error of 7%. [DOI: 10.1115/1.1795240]

Keywords: Refrigerant Condensation, Smooth Tube, Helical Microfin Tube, Herringbone Microfin Tube, Pressure Drop, Flow Regime

Introduction

Many types of augmentation techniques exist today, with tubes having internal microfins being most common. A study conducted by Liebenberg [1], using helical microfin tubes with an inner diameter of 8.9 mm, showed that these tubes have a heat transfer coefficient increase of about 200% compared to that of a smooth tube. With this increase in heat transfer coefficients, however, there was also an increase in pressure drop. It was found, on average, that this increase was about 100% higher than that inside a smooth tube. These pressure drops were attributed to the increased vapor velocities in a helical microfin tube condenser, brought about by the greater regions of annular flow, which in turn increases the turbulence inside the tube compared to a smooth tube [1]. The fins redistribute the liquid layer around the circumference of the tube, forcing the flow to become annular rather than intermittent or stratified.

In the mid-1990s a new generation of microfin tube was being developed, one of them being the herringbone microfin tube. This tube consists of a double V-groove, as shown in Fig. 1(a), with grooves embossed on the inner surface. The orientation was chosen such that the liquid would converge at the top and bottom of the tube and diverge at the sides [Fig. 1(b)]. Due to the effect of gravity, especially at low velocities, the distribution of liquid at the bottom of the tube will be higher than at the top. The heat transfer enhancement, as explained by Miyara et al. [2], is due to the thin film layer on the sides and the mixing of the converging liquid at the top and bottom of the tube.

Table 1 gives a short summary of the experimental conditions used in previous work [3–5] on herringbone microfin tubes. The

mass fluxes ranged from 100 to 400 kg/m² s and in some cases are lower than required for heat-pump water-heater applications where the mass fluxes range up to 1000 kg/m² s. Although smaller tubes are being investigated by other researchers, especially in countries such as the US and Asia where tube diameters as low as 4 mm are being introduced, 3/8 in. (~9.5 mm) tubes are still the most common tubes used in residential and commercial air conditioners, heat pumps, and refrigeration systems.

The objective of this paper is to first introduce experimental findings of condensation pressure drops inside herringbone microfin tubes at mass fluxes higher than were published before (400–800 kg/m² s) and inside tubes with larger diameters (8.5 mm inside and 9.53 mm outside). The second objective is to compare the experimental data of the herringbone microfin tube to experimental data on smooth and helical microfin tubes. Third, the pressure-drop data were used to develop a modified pressure-drop correlation for a herringbone microfin tube.

Experimental Facility

The experimental test facility consisted of two main sub-systems: the vapor-compression loop and the water loops. A schematic of the experimental setup is given in Fig. 2. Each of the sub-systems was of the closed-loop type. The vapor-compression loop consisted of a hermetically sealed reciprocating compressor having a nominal cooling capacity of 9.6 kW, an oil separator with a maximum discharge volume of 2.6 m³/h, a manually adjustable expansion valve, a water-heated evaporator, and a water-cooled test condenser. Three test condensers were used, namely, a smooth tube, an 18-deg helical microfin tube, and a herringbone microfin tube. Geometric parameters of the tubes as well as their lengths are given in Table 2. The lengths of the tubes were chosen to obtain an energy balance better than 1%. The orientation of the herringbone microfin tube was chosen such that the liquid converges at the top and bottom of the tube and diverges at the sides.

*Corresponding author.

Contributed by the Heat Transfer Division for publication in the JOURNAL OF HEAT TRANSFER. Manuscript received by the Heat Transfer Division November 19, 2003; revision received June 15, 2004. Associate Editor: M. Jensen.

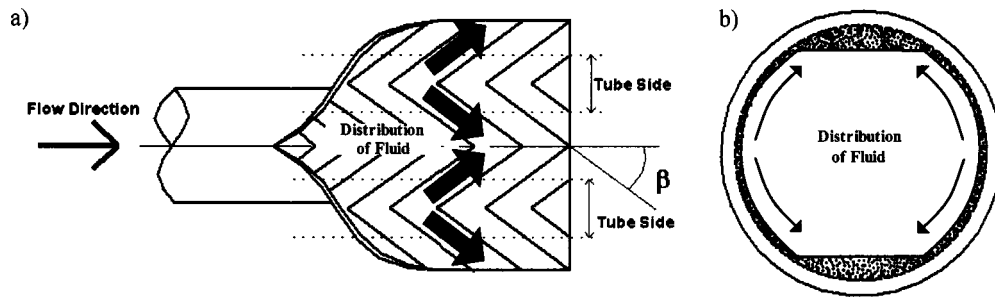


Fig. 1 a) Basic geometry of the herringbone microfin tube (not to scale) and b) an illustration of how condensate is distributed inside the tube for the adopted orientation (exaggerated)

Visual inspection ensured that the orientation of each tube was maintained during the manufacture of the condenser. Sight glasses, cylindrical in shape, were used to visualize the flow patterns inside the tubes. The inner diameter of these sight glasses was the same as the inner diameter of the condenser tubes. This was done so that the flow inside the tubes would not be affected.

The test condenser was of the tube-in-tube type with refrigerant flowing in the inner tube and water flowing in a counterflow direction in the annulus. The cold and hot water loops were connected to the condenser and evaporator, respectively. On the condensing side the cold water was used as a heat sink, removing the latent heat from the condensing refrigerant. The water temperature was kept constant in the range of 20–25°C (depending on the experiments conducted) in a 1000 l insulated reservoir connected to a 15 kW chiller. The water gauge pressure in the annulus was maintained between 70 and 140 kPa to prevent the formation of air bubbles, which could affect temperature readings and the heat transfer from the refrigerant to the water. A centrifugal pump pumped the chilled water to the double-tube condenser. A hand-controlled valve controlled the water flow rate through the test sections. After passing through the condenser, the water returned to the reservoir of the chiller unit.

A similar hot water flow loop was used on the evaporating side, also with an insulated 1000 l reservoir, but connected to a 12 kW electric resistance heater. The reservoir water temperature was varied between 30°C and 40°C depending on the experiments conducted. Increasing or decreasing the temperature of the water through the evaporator altered the refrigerant density at the compressor inlet and thus the refrigerant mass flow.

For the smooth and helical microfin tube, two resistance temperature detectors (RTDs) were used prior to each subsection, placed at the top and bottom of the inner tube. This was done to obtain an average temperature of the tube since the distribution of the liquid layer inside the tube would under- or overestimate the temperature measurement if only one RTD were used. For the herringbone microfin tube, however, the RTDs were placed at the top and on the side of the inner tube because the liquid film thickness on the top is much thicker than on the side. The absolute pressures of the condensing refrigerant were measured with piezoelectric pressure transducers, which were positioned at the inlet of each condenser subsection. Two Coriolis mass flow metres were used for the vapor compression loop and the cold-water loop. The

uncertainties of the instruments, given in Table 3, were calculated by using the method of Kline and McClintock [6].

Data Reduction

Deduction of Vapor Quality. The properties of the refrigerant at the inlet and outlet of the condenser were determined by temperature and pressure measurements. From these measurements the thermophysical properties of the condensing refrigerant were determined by interpolating the superheated (at the inlet of the condenser) and subcooled (at the outlet of the condenser) tables that were obtained from REFPROP [7]. The refrigerant properties for the rest of the condenser (two-phase sections) were determined by assuming that the calculated values of the heat transferred to the water was more accurate than the values calculated for the refrigerant. With this assumption the enthalpy values of the refrigerant could be deduced. In the first test subsection the water heat flux was equated to the refrigerant heat flux (due to the refrigerant enthalpy change) to obtain the outlet enthalpy h_o . This outlet enthalpy was then used as the inlet enthalpy h_i for the next subsection. This procedure was repeated for all eight subsections [1].

The average sectional vapor quality was thus obtained by

$$x_i = \frac{h_i - h_L}{h_L - h_V} \text{ with } h_L \text{ and } h_V \text{ measured at } T_i$$

$$x_o = \frac{h_o - h_L}{h_L - h_V} \text{ with } h_L \text{ and } h_V \text{ measured at } T_o \quad (1)$$

The average vapor quality of each test subsection was then determined as

$$x = \frac{x_i + x_o}{2} \quad (2)$$

Pressure Drop and Pressure Gradients. The total pressure drop was defined as

$$\Delta p_i = \Delta p_m + \Delta p_f + \Delta p_g \quad (3)$$

where the momentum pressure drop Δp_m is defined as

Table 1 Experimental conditions of previous work done on herringbone microfin tubes

	Ebisu and Torikoshi [3]	Miyara et al. [4]	Goto et al. [5]
Tube inside diameter [mm]	7	7	8
Total condenser length [m]	0.54	4	2
Refrigerant	R-22, R-407C	R-22, R-410A	R-22, R-410A
Saturation temperature [°C]	50	40	40
Mass flux range [kg/m ² s]	150–400	100–400	200–340
Pressure-drop measurements	Local	Average	Average
Correlation	No	Yes	No

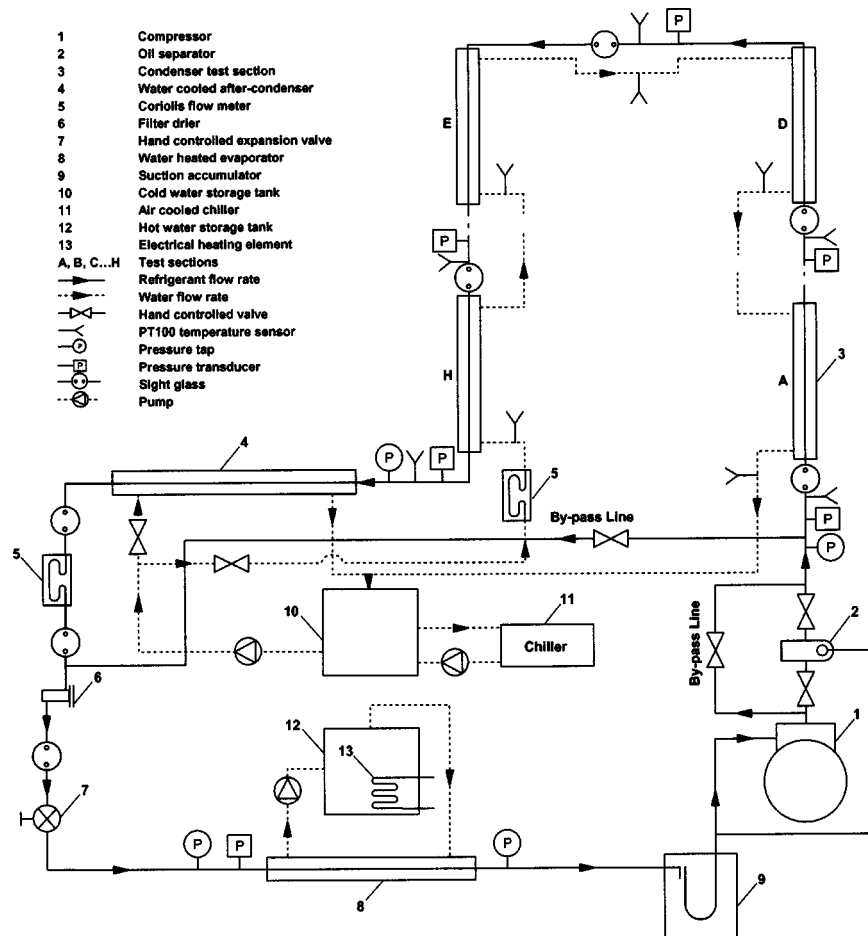


Fig. 2 Schematic of the experimental facility

$$\Delta p_m = G^2 \left\{ \left[\frac{(1-x)^2}{\rho_L(1-\varepsilon)} + \frac{x^2}{\rho_V \varepsilon} \right]_{out} - \left[\frac{(1-x)^2}{\rho_L(1-\varepsilon)} + \frac{x^2}{\rho_V \varepsilon} \right]_{in} \right\} \quad (4)$$

The void fraction ε used was that given by Rouhani and Axelsson [8]. Since the tubes were horizontally positioned, the gravitational pressure drop Δp_g was neglected. The frictional pressure drop Δp_f was calculated from known correlations obtained in the literature.

The measured pressure between each subsection that was in a two-phase region was subtracted from each other to obtain the total experimental pressure drop per subsection. This in turn was divided by the subsection length to obtain the pressure drop per unit condenser length, or the pressure gradient.

Penalty Factor. The parameter used to compare the pressure-drop characteristics of the herringbone microfin tubes to those of

Table 2 Inner tube geometric parameters of the test condensers

Type	Smooth	Helical	Herringbone
Material	Hard-drawn copper	Hard-drawn copper	Soft-drawn copper
Helix angle, β [°]	-	18	16
Apex angle, γ [°]	-	40	25
Number of fins, n [-]	-	60	70
Fin base thickness, t_b [mm]	-	1.672	0.0887
Outside diameter, D_o [mm]	9.52	9.55	9.51
Inside diameter, D_i [mm]	8.11	8.94	8.52
Tube wall thickness, t_w [mm]	1.4	0.307	0.3
Equivalent diameter, D_e [mm]	8.11	8.79	8.82
Fin height, e [mm]	-	0.209	0.2
Actual flow area, A_{fa} [m ²]	51.7×10^{-6}	60.64×10^{-6}	61.16×10^{-6}
Condenser subsection length [m]	1.5	1.13	0.563
Condenser total length [m]	12	9	4.5

Table 3 Estimated 95% uncertainties for the experimental instrumentation and Eq. (9) data

Measurements	Uncertainty
Refrigerant temperature	0.14 K
Water temperature	0.11 K
Saturation temperature	0.12 K
Pressure	0.23%
Refrigerant mass flow rate	0.23%
Water mass flow rate	0.28%
Average quality	3.02%
Viscosity	0.10%
Density	0.03%
Re	1.02%
X_{tt}	3.82%
Φ_L	4.46%
Δp_{Lo}	4.80%
Δp	6.80%

the smooth and helical microfin tube is the penalty factor PF . The penalty factor is defined as the ratio of the measured total pressure gradient in the herringbone microfin tube to the measured total pressure gradient in the smooth tube [Eq. (5)] and the ratio of the measured total pressure gradient in the herringbone microfin tube to the measured total pressure gradient in the helical microfin [Eq. (6)] as follows:

$$PF = \left(\frac{\Delta p_h}{\Delta p_s} \right) \quad (5)$$

$$PF = \left(\frac{\Delta p_h}{\Delta p_{he}} \right) \quad (6)$$

Flow Regimes. With the aid of mini digital video cameras and the flow regime maps developed by Thome [9], flow patterns were identified within the tubes, thus allowing the determination of flow regime transitions. The Froude rate, defined as

$$Ft = \left[\frac{G^2 x^3}{(1-x)\rho_v^2 g D_i} \right]^{1/2} \quad (7)$$

which is essentially the ratio relating the kinetic energy of the vapor to the amount of energy required to pump the liquid from the bottom to the top of the tube. In regions where gravitational drag becomes dominant, the Froude rate expresses how the energy dissipation due to liquid waves and liquid mass movement around the tube's diameter are related to the energy in the flow stream [1].

Experimental Results

Prior to obtaining experimental data on the herringbone microfin tube, experiments were conducted on the smooth and helical microfin tubes. These data were compared to pressure-drop correlations obtained from the literature. For the smooth tube the pressure-drop data were predicted on average for the three refrigerants to within 33% using the correlation of Lockhart and Martinelli [10]. The correlation of Cavallini et al. [11] was used for the helical microfin tube and predicted the pressure-drop data to within 13%.

Figure 3 shows the use of the flow regime maps of Thome [9]. For the smooth tube, the transition quality was calculated in the manner described by Thome [9] and is given in Fig. 3(a). This method was, however, only applicable for smooth tubes, and a new method needed to be developed for the helical and herringbone microfin tubes. The method used by Liebenberg [1] for determining the transition quality was implemented for the smooth tube, and the results differed by a quality of as little as 0.001. This meant that this new method could be used for the helical and herringbone microfin tubes. The flow regime maps for the helical and herringbone microfin tubes are given in Figs. 3(b) and 3(c). In these maps the transition quality from annular to intermittent

flow is different for each tube; the smooth tube having the highest transition quality and the herringbone microfin tube having the lowest.

Figure 4 shows a summary of the pressure gradients for the three refrigerants inside the smooth, helical microfin and herringbone microfin tubes as a function of the average vapor quality at mass fluxes of 400, 600, and 800 kg/m² s. The overall trend for the three refrigerants is that the pressure gradients increase with an increase in vapor quality. At high qualities where the pressure gradients are the highest, the flow was found to be annular, implying that the main reason for the drop in pressure was due to the increased turbulence formed by the high-velocity vapor-generating friction against the liquid annulus. Looking at Eq. (7), the Froude rate has a high value for high qualities, and thus, the flow is shear dominated. As the quality decreases a transition starts to occur between annular and intermittent flow and the vapor and liquid velocities become similar. For this reason the pressure gradients are much lower and from Eq. (7) the Froude rate has a small value, implying that the flow is gravity dominated.

For the smooth tube this transition region occurred at a quality of about 50% [12]. For the helical microfin and herringbone microfin tubes the transition occurred at a quality of 28% and 26% [12,13], respectively. This is characterized by a sharp increase in pressure gradient at qualities higher than the transition qualities. Thus, for the helical and herringbone microfin tubes, due to the increased turbulence generated by the fins, annular flow occurs over a larger vapor-quality region than for the smooth tube. This is visually shown in Table 4 from the captured video images. Looking at a quality of about 0.46, for the smooth tube the flow is intermittent, with slugs and plugs forming at the top of the tube, while the helical and herringbone microfin tubes are still in annular flow, noting that there is a liquid film layer around the circumference of the tube. This implies that the fins redistribute the liquid around the circumference of the tube, extending the annular flow regime down to lower qualities. This further implies that the average pressure gradients for these tubes will be higher due to the increase in turbulence found in annular flow. Since the transition quality for the herringbone microfin tube is lower than that of the helical microfin tube, one can expect the overall pressure drops (on average) for the herringbone microfin tube to be higher.

Figure 5 shows a summary of the average pressure gradients for condensation as a function of the mass flux. The overall trend is that the pressure gradients increase with an increase in mass flux. Further, it is noted that the local pressure gradients (Fig. 4) and the average pressure gradients (Fig. 5) of R-134a are always higher than that of R-22 and R-407C, with R-407C being the lowest. This concurs with expectations, as R-134a is a low-pressure refrigerant, which implies higher vapor velocities, resulting in higher relative pressure drops than those for the higher-pressure refrigerant.

Comparisons of Pressure-Drop Penalty Factors

The penalty factors for the herringbone microfin tube were determined by analyzing the ratio of the pressure drops of the herringbone microfin tube to the pressure drops of the smooth [Eq. (3)] and helical microfin tubes [Eq. (4)], reduced to equivalent lengths. The plots of the penalty factors are given in Fig. 6. For the plots against the smooth tube, Fig. 6(a), the penalty factors are always greater than one throughout the mass flux range, implying that the herringbone microfin tube overall has a higher pressure drop than that of the smooth tube. On average, when using R-22, the pressure drop is 84% higher than in the smooth tube, while when using R-407C and R-134a the pressure drops are 80% and 72% higher, respectively. On average for the three refrigerants the herringbone microfin tube has a 79% higher pressure drop than that of the smooth tube. This increase is due to the increase in turbulence generated by the fins. As was explained previously, the fins extend the annular flow regime to lower qualities by redistributing the liquid around the circumference of the tube. This is also shown visually in Table 4.

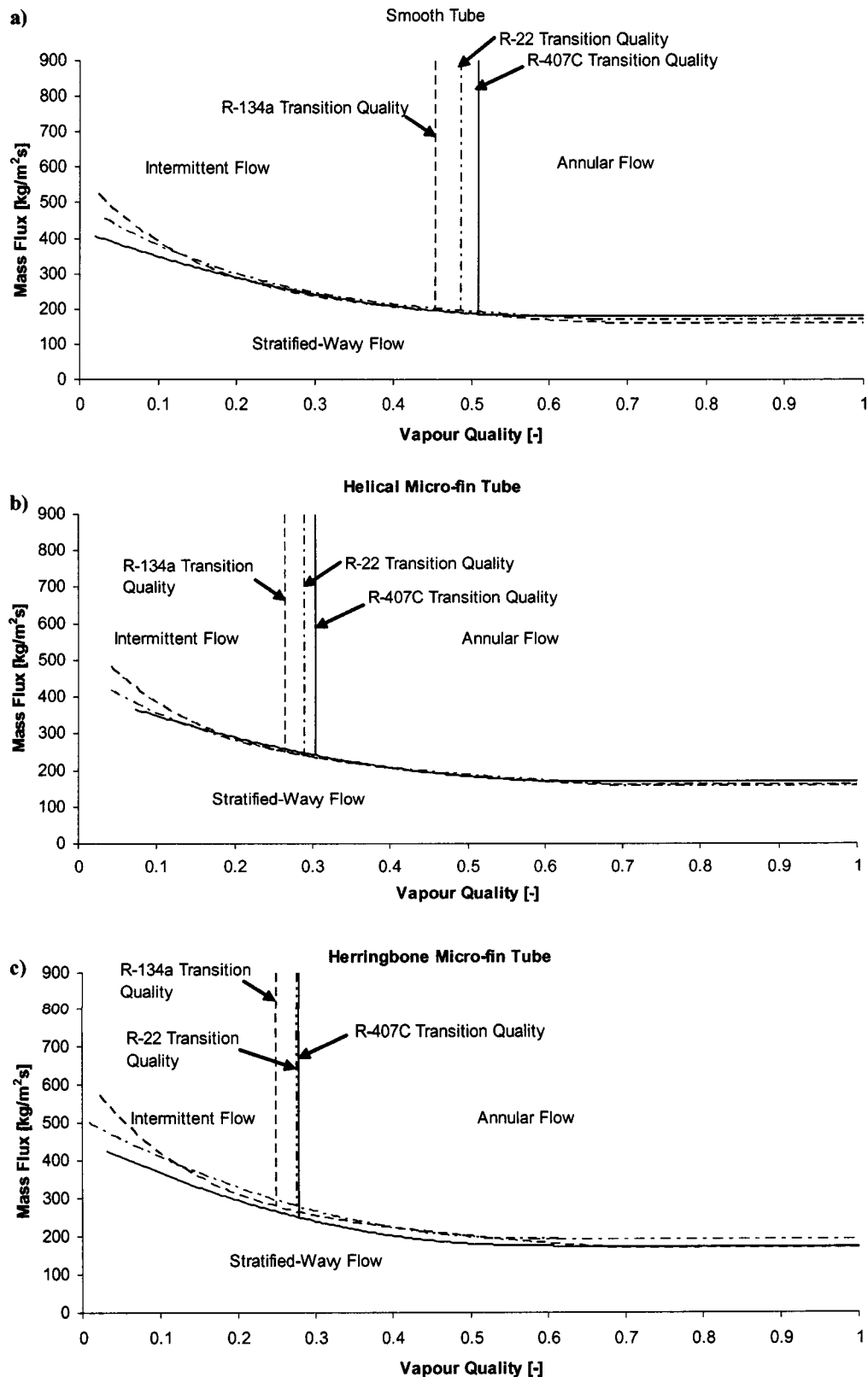


Fig. 3 Determining the transition qualities by making use of a) the Thome [9] map for the smooth tube, and the method used by Liebenberg et al. [13] for b) the helical microfin tube and c) the herringbone microfin tube

The penalty factors for the herringbone microfin tube against that of the helical microfin tube are given in Fig. 6(b). For R-22 the pressure drops of the herringbone microfin tube are about 41% higher than that of the helical microfin tube. This agrees well with

the work of other researchers [2–5,8]. For R-407C and R-134a, however, the penalty factors at lower mass fluxes (400–500 kg/m² s) are below one. An explanation is that the flow over the fins, as explained by Wang et al. [14], induces a viscous

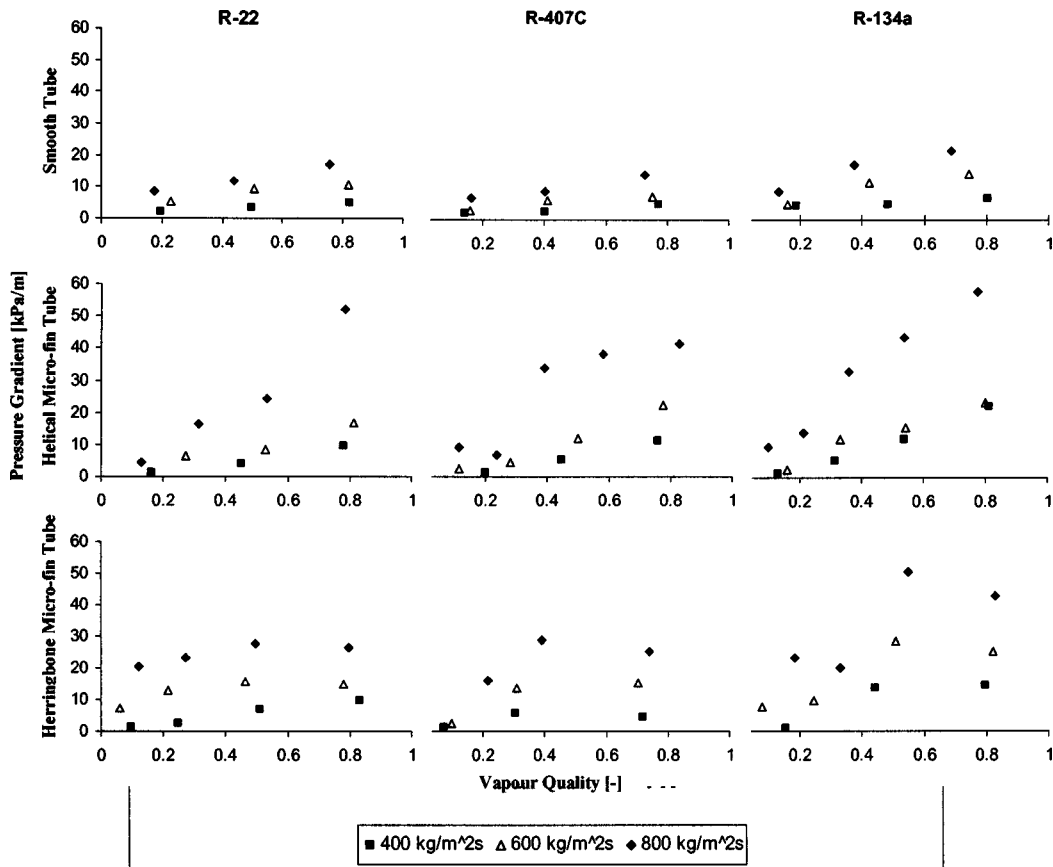


Fig. 4 Pressure gradients at mass fluxes of 400, 600, and 800 kg/m² s for the three tubes and refrigerants tested

sublayer thickness, buffer layer, and an integral constant in the log-law that is greater than that for the helical microfin tube, implying that the fins might have a drag reduction effect when compared to the helical microfin tube. At higher mass fluxes the pressure drops for these two refrigerants are, respectively, about 17% and 24% higher. On average for the three refrigerants the pressure drops of the herringbone microfin tube are about 27% higher than those of the helical microfin tube.

Comparisons With Other Pressure-Drop Correlations

Figure 5 gives plots of the correlation of Miyara et al. [4] with regard to the herringbone microfin tube experimental data. The deviations were calculated by

$$\text{Mean Deviation (\%)} = \frac{\Delta p_{pd} - \Delta p_{ex}}{\Delta p_{ex}} \times 100 \quad (8)$$

The experiments of Miyara et al. [4] were conducted at low mass fluxes (100 to 400 kg/m² s) with refrigerants R-22 and R-410A (see Table 1), also from where they derived their correlation. From Fig. 4 it follows that the correlation slightly deviates from the data at high mass fluxes, especially for R-407C and R-134a. On average, however, this correlation only underpredicted the data by 7%, implying that it could be used at mass fluxes higher than 400 kg/m² s and maybe even for refrigerants other than R-22 and R-410A.

Modification of a Pressure-Drop Correlation

The correlation developed by Carnavos [15] for finned tubes was modified for the herringbone microfin tube. The pressure drop due to friction is given by the product of the liquid-only pressure drop and a two-phase multiplier

$$\Delta p_f = \Delta p_{Lo} \Phi_L^2 \quad (9)$$

with the two-phase multiplier being that of Souza and Pimenta [16],

$$\Phi_L^2 = 1.376 + \frac{7.242}{X_{tt}^{1.655}} \quad (10)$$

The modified Darcy-Weisbach equation as obtained from Friedel [17] was calculated by

$$\Delta p_{Lo} = \frac{2 f_{Lo} G^2 (1-x)^2 L}{\rho_L D_i} \quad (11)$$

The liquid-only friction factor, as given by Carnavos [15] for a finned tube


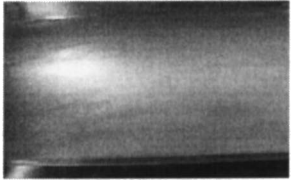
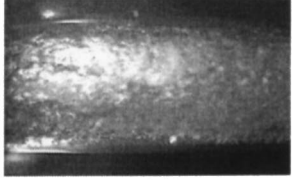
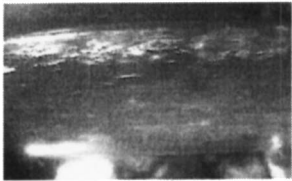
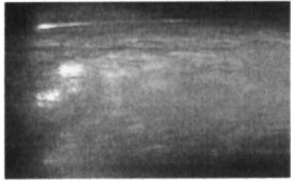
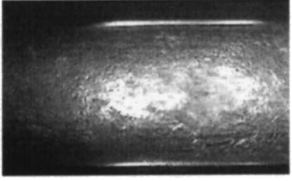
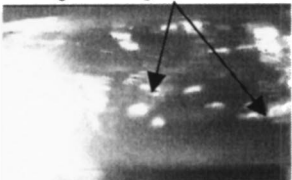
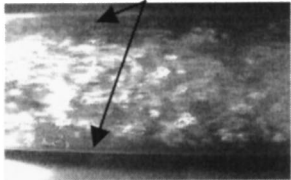
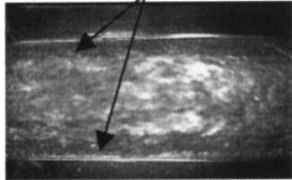
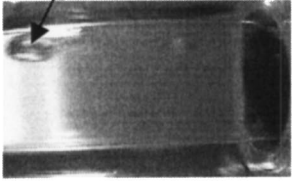
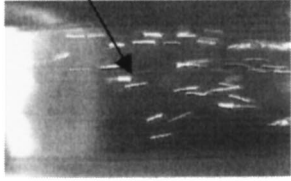
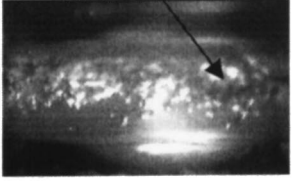
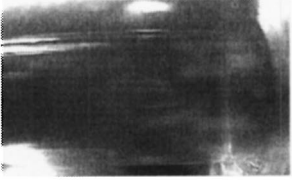


$$f_{Lo} = 0.046 \text{Re}_L^{-0.2} \left(\frac{D_i}{D_e} \right) \left(\frac{A}{A_n} \right)^{0.5} (\sec \beta)^{0.75} \quad (12)$$

with D_e being the equivalent inner tube diameter taking the fins into account, D_i the fin-root diameter, A_n the nominal flow area based on the fin-root diameter, and A the actual cross-sectional flow area of the tube. The area ratio for the microfin tube as given by Azer and Said [18] is

$$\frac{A}{A_n} = 1 - \frac{4ent}{\pi D_i^2 \cos \beta} \quad (13)$$

with e being the fin height, n the number of fins, t the fin thickness, and β the helix angle of the fins. The terms $\sec \beta$ and $\cos \beta$ in Eqs. (12) and (13) account for the swirling effect induced by the fins inside the helical microfin tube. By multiplying the cos

Table 4 Images of R-134a condensing at a mass flux of 500 kg/m² s for the three tubes tested

	Smooth Tube	Helical Micro-fin Tube	Herringbone Micro-fin Tube
	 x = 0.96	 x = 0.97	 x = 0.97
	 x = 0.77	 x = 0.79	 x = 0.79
↓ Decreasing Quality [-]	Plugs and Slugs  x = 0.46	Thick liquid film  x = 0.48	Thick liquid film  x = 0.46
	Plug flow  x = 0.21	Swirling of slugs and plugs  x = 0.20	Chaotic behaviour of slugs and plugs  x = 0.23
	 x = 0.06	 x = 0.06	Plug flow at very low quality  x = 0.06

and sec terms by a factor 2 and changing the power of the sec term in Eq. (12) from 0.75 to 1.1, the equations become, respectively,

$$f_{Lo} = 0.046 \text{Re}_L^{-0.2} \left(\frac{D_i}{D_e} \right) \left(\frac{A}{A_n} \right)^{0.5} (2 \sec \beta)^{1.1} \quad (14)$$

$$\frac{A}{A_n} = 1 - \frac{2ent}{\pi D_i^2 \cos \beta} \quad (15)$$

The experimental pressure-drop data using the modified correlation were predicted to within an error of 1%, having an absolute mean deviation of 6.8%; 94% of the data were predicted within $\pm 20\%$. This is visually shown in Fig. 7. The modified correlation is also visualized with the experimental data in Fig. 4. The uncertainties of Eq. (9) are given in Table 3.

To summarize, Eqs. (14) and (15) can be given in a more general form as follows:

$$f_{Lo} = 0.046 \text{Re}_L^{-0.2} \left(\frac{D_i}{D_e} \right) \left(1 - \frac{Xent}{\pi D_i^2 \cos \beta} \right)^{0.5} (X \sec \beta)^Y$$

For helical microfin tubes:

$$X = 1$$

$$Y = 0.75$$

$$(16)$$

For herringbone microfin tubes:

$$X = 2$$

$$Y = 1.1$$

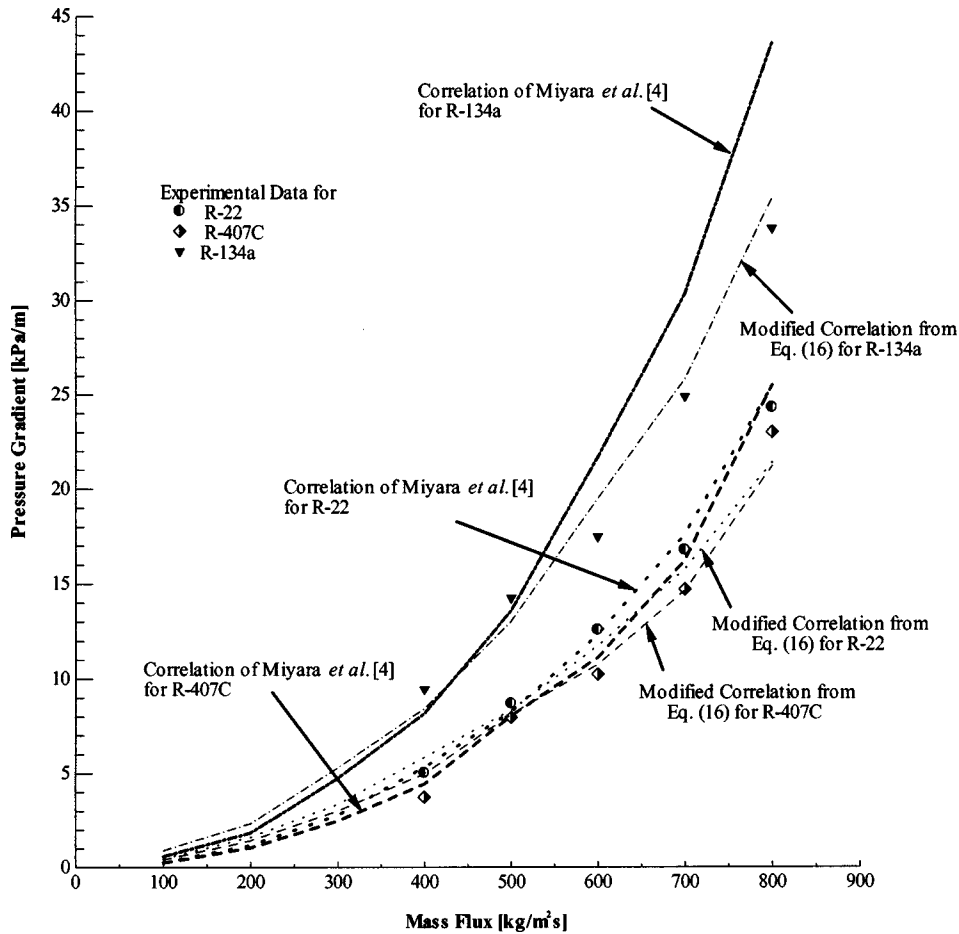


Fig. 5 Average pressure drops of the experimental data and that predicted by Miyara et al. [4] and the newly developed correlation for refrigerants R-22, R-407C, and R-134a

When comparing the proposed correlation with that of Miyara et al. [4] in Fig. 5, at high-mass fluxes the two differ by as much as 19%, but seem to converge to a point as the mass flux decreases. This is due to the fact that both correlations are strongly dependant on the mass flux. Further, the correlation of Miyara et al. [4] at high mass fluxes predicts higher pressure drops than the proposed correlation. This, however, changes from a mass flux lower than $500 \text{ kg/m}^2 \text{ s}$ where the proposed correlation predicts higher pressure drops. It is also noted that the two correlations are similar in form; the correlation of Miyara et al. [4] is defined in terms of a vapor-only pressure drop multiplied by a modified form of the Haraguchi et al. [19] two-phase multiplier.

Conclusion

Experiments for refrigerant pressure drops were conducted with herringbone microfin tubes during condensation and compared with the performance of their smooth and helical microfin counterparts. The condensers were of the tube-in-tube type with the refrigerant flowing in the inner tube and cooling water in a counterflow direction in the annulus. Three refrigerants were tested, namely, R-22, R-134a, and R-407C. All tests were conducted at a nominal saturation temperature of 40°C and at mass fluxes ranging from 400 to $800 \text{ kg/m}^2 \text{ s}$.

The results showed that for all three test condensers the pressure gradients increased with an increase in quality. The trends of the pressure gradients were due to the increase in turbulence from the intermittent to the annular region. These transitions occurred at an average vapor quality of 50%, 28%, and 26% for the smooth, helical microfin, and herringbone microfin tubes, respec-

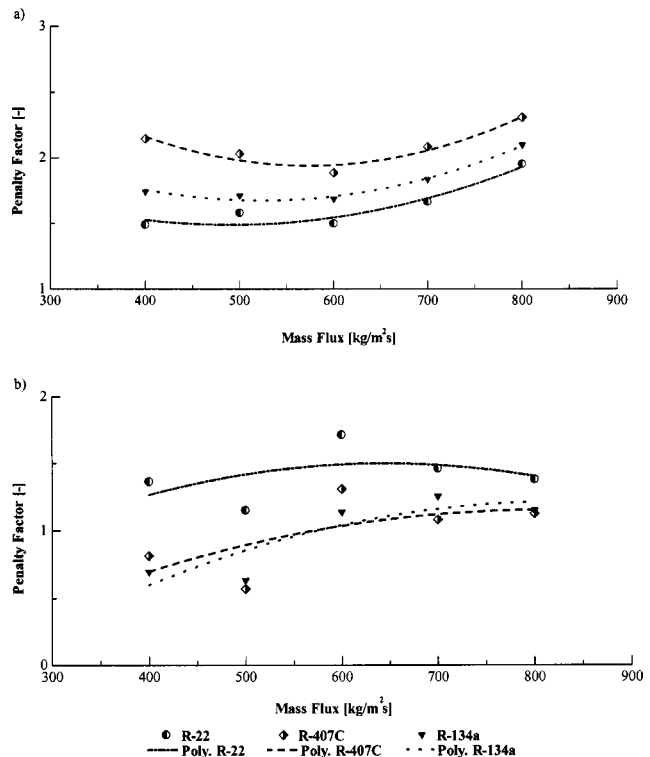


Fig. 6 Penalty factors for the herringbone microfin tube against a) the smooth tube and b) the helical microfin tube for R-22, R-407C, and R-134a

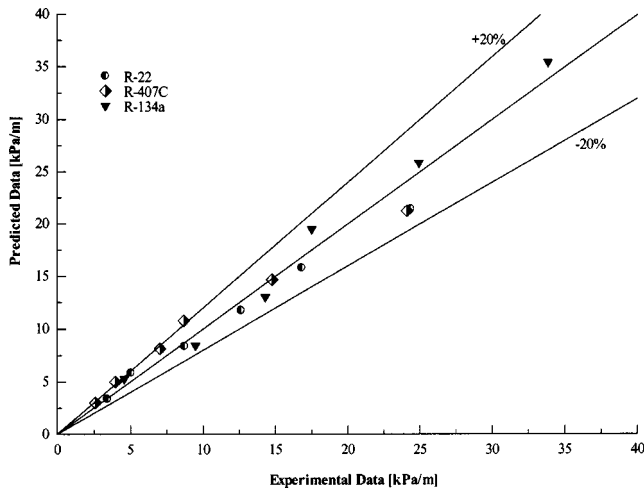


Fig. 7 Comparison of the experimental data with the modified prediction data for R-22, R-407C and R-134a

tively. The high pressure gradients, found at the high-quality regions (above the transition qualities), were due to the friction generated during annular flow by the high-velocity vapor core against the slow-moving liquid annulus. At low qualities where the flow was intermittent (below the transition qualities), and thus gravity dominated, the pressure gradients were lower and remained more or less constant. It was concluded that the fins on both the helical and herringbone microfin tubes redistributed the liquid layer around the circumference of the tube, extending the annular flow regime to lower qualities, thus having a longer range in which the flow is very turbulent.

With the pressure-drop data, the penalty factors of the herringbone microfin tube against that of the smooth and helical microfin tubes were calculated. The results indicated that, for the herringbone microfin tube against the smooth tube, the penalty factors were always above one. On average the pressure drops of the herringbone microfin tube were about 79% higher than those of the smooth tube. Results also indicated that the penalty factors for the three refrigerants were almost the same.

For the herringbone microfin tube against the helical microfin tube, the penalty factors for R-407C and R-134a were less than one for low mass fluxes. An explanation for this is that the fins might have a drag-reducing effect due to a larger viscous sublayer thickness, buffer layer, and a greater integral constant in the log-law. For R-22, however, the penalty factors were, on average, greater than one. For the three refrigerants, the pressure drops were, on average, about 27% higher.

The correlation of Miyara et al. [4], which was initially developed from R-22 and R-410A data inside a herringbone microfin tube, deviated from the measurements of this study on average by 7%, even though it was used to predict the pressure drops of not only R-22, but also R-407C and R-134a. This implied that this correlation could maybe be used for refrigerants other than R-22 and R-410A at higher mass fluxes.

An existing helical microfin tube correlation obtained from the literature was modified to predict the pressure drops inside the herringbone microfin tube. The results indicated that this modified correlation predicted the data within an average error of 1% and an average mean deviation of 6.8%.

Acknowledgments

Wolverine, Inc., Alabama, supplied the experimental helical microfin tubes, and Petur Thors is thanked for arranging the donation. Dr. Alex Kriegsmann of Wieland Werke also kindly donated several lengths of microfin tubing. The experimental herringbone microfin tube was donated by Professor Yasuyuki Takata of Ky-

ushu University, Japan, for which the authors are most grateful. The research work was performed with a South African National Research Foundation grant, under Grant No. 2053278.

Nomenclature

A = area
 D = diameter
 e = fin height
 Ft = Froude rate
 f = friction factor
 G = mass flux
 h = enthalpy
 L = length
 n = number of fins
 Δp = pressure drop
 PF = penalty factor
 Re = Reynolds number
 T = temperature
 t = thickness
 x = vapor quality
 X_{tt} = Lockhart-Martinelli parameter
 X, Y = constants, Eq. (16)

Greek Letters

β = helix angle
 ε = void fraction
 γ = apex angle
 ρ = density

Subscripts

b = base
 e = equivalent
 ex = experimental
 f = friction
 fa = actual flow
 g = gravitational
 h = herringbone
 he = helical
 i = inside, inlet
 L = liquid
 Lo = liquid only
 m = momentum
 n = nominal
 o = outside, outlet
 pd = predicted
 s = smooth
 V = vapor
 w = wall

References

- [1] Liebenberg, L., 2002, "A Unified Prediction Method for Condensation Performance in Smooth and Microfin Tubes," Ph.D. thesis, Rand Afrikaans University, Johannesburg.
- [2] Miyara, A., Otsubo, Y., Ohtsuka, S., and Mizuta, Y., 2003, "Effects of Fin Shape on Condensation in Herringbone Microfin Tubes," *Int. J. Refrig.*, **26**, pp. 417–424.
- [3] Ebisu, T., and Torikoshi, K., 1998, "Experimental Study on Evaporation and Condensation Heat Transfer Enhancement for R-407C Using Herringbone Heat Transfer Tube," *ASHRAE Trans.*, **104**(2), pp. 1044–1052.
- [4] Miyara, A., Nonaka, K., and Taniguchi, M., 2000, "Condensation Heat Transfer and Flow Pattern Inside a Herringbone-Type Microfin Tube," *Int. J. Refrig.*, **23**, pp. 141–152.
- [5] Goto, N., Inoue, N., and Ishiwatari, N., 2001, "Condensation and Evaporation Heat Transfer of R-410A inside Internally Grooved Horizontal Tubes," *Int. J. Refrig.*, **24**, pp. 628–638.
- [6] Kline, S. J., and McClintock, F. A., 1953, "Describing Uncertainties in Single-Sample Experiments," *Mech. Eng. (Am. Soc. Mech. Eng.)*, **75**, pp. 3–8.
- [7] REFPROP, 1999, "NIST Thermodynamic Properties of Refrigerants and Refrigerant Mixtures (REFPROP)," Version 6.0, *NIST Standard Reference Database 23*, National Institute of Standards and Technology, Gaithersburg, MD.
- [8] Rouhani, S. Z., and Axelsson, E., 1970, "Calculation of Volume Void Fraction in the Subcooled and Quality Region," *Int. J. Heat Mass Transfer*, **13**, pp. 383–393.

- [9] Thome, J. R., 2003, "On Recent Advances in Modeling of Two-Phase Flow and Heat Transfer," *Heat Transfer Engineering*, **24**(6), pp. 46–59.
- [10] Lockhart, R. W., and Martinelli, R. C., 1949, "Proposed Correlation of Data for Isothermal Two-Phase, Two-Component Flow in Pipe," *Chem. Eng. Prog.*, **45**, pp. 39–48.
- [11] Cavallini, A., Del Col, D., Doretti, L., Longo, G. A., and Rossetto, L., 2000, "Heat Transfer and Pressure Drop During Condensation of Refrigerants Inside Horizontal Enhanced Tubes," *Int. J. Refrig.*, **23**, pp. 4–25.
- [12] Owaga, D. C., 2003, "Flow Patterns during Refrigerant Condensation in Smooth and Enhanced Tubes," Master's dissertation, Rand Afrikaans University, Johannesburg.
- [13] Liebenberg, L., Thome, J. R., and Meyer, J. P., 2004, "Flow Pattern Identification With Power Spectral Density Distributions of Pressure Traces During Refrigerant Condensation in Smooth and Microfin Tubes," *ASME J. Heat Transfer*, submitted for review.
- [14] Wang, J., Lan, S., and Chen, G., 2000, "Experimental Study on the Turbulent Boundary Layer Flow Over Riblets Surface," *Fluid Dyn.*, **27**(4), pp. 217–229.
- [15] Carnavos, T. C., 1980, "Heat Transfer Performance of Internally Finned Tubes in Turbulent Flow," *Heat Transfer Eng.*, **4**(1), pp. 32–37.
- [16] Souza, A. L., and Pimenta, M. M., 1995, "Prediction of Pressure Drop During Horizontal Two-Phase Flow of Pure and Mixed Refrigerants," *ASME Conference on Cavitation and Multiphase Flow*, ASME, New York, Vol. 210, pp. 161–171.
- [17] Friedel, L., 1979, "Improved Friction Pressure Drop Correlation for Horizontal and Vertical Two-phase Two-component Flow in Pipes," E2, European Two-Phase Flow Group Meeting, Ispra.
- [18] Azer, N. Z., and Said, S. A., 1982, "Augmentation of Condensation Heat Transfer by Internally Finned Tubes and Twisted Tape Inserts," *Proc. of 7th Int. Heat Transfer Conference*, München, West-Germany, Hemisphere, **5**, pp. 33–38.
- [19] Haraguchi, H., Koyama, S., and Fujii, T., 1994, "Condensation of Refrigerants HCFC22, HFC134a and HCFC123 in a Horizontal Smooth Tube: 1st Report, Proposals of Empirical Expressions for the Local Frictional Pressure Drop," *Trans. JSME*, **60**, pp. 2111–2116.

Three-Dimensional Numerical Simulation on Laminar Heat Transfer and Fluid Flow Characteristics of Strip Fin Surface With X-Arrangement of Strips

Z. G. Qu

W. Q. Tao

e-mail: wqtao@mail.xjtu.edu.cn

Y. L. He

State Key Laboratory of Multiphase Flow
in Power Engineering,
School of Energy & Power Engineering,
Xi'an Jiaotong University,
Xi'an, Shaanxi 710049, China

In this paper, a numerical investigation of air side performance of strip fin surface is presented. Three-dimensional numerical computation was made for a model of a two-row finned tube heat exchanger. The tube configuration is simulated with step-wise approximation, and the fin efficiency is also calculated with conjugated computation. Four types of fin surfaces were studied: A-the whole plain plate fin; B-the strip fin with strips located in the upstream part of the fin; C-the strip fin with strips located in the downstream part of the fin; and D-the strip fin with strips covering the whole fin surface. It is found that the strip fin with strips located in the downstream part of the fin surface (fin C) has higher heat transfer rate than that with strips in the upstream part (fin B) at the same conditions, while the pressure drop of fin C is a bit lower than that of fin B. A comprehensive performance comparison was conducted by using the goodness factor and the pumping power consumption per unit surface area. It is revealed that between the two strip fins the performance of fin C is better than fin B with same strip number. Detailed discussion is provided from the view point of synergy between velocity and temperature gradient. It is shown that the synergy between velocity and temperature field becomes worse in the downstream part of the fin surface, and it is this place that enhancement technique is highly needed. The strip location of fin C just fits this situation. The present numerical work provides useful information on where the enhancement element should be positioned. [DOI: 10.1115/1.1798971]

Keywords: Convection, Enhancement, Finite Difference, Finned Surfaces, Heat Transfer

1 Introduction

Plate fin-and-tube heat exchangers are widely used in various engineering fields, such as HVAC&R (heating, ventilating, air-conditioning and refrigeration), automobiles, etc. It is an effective way to reduce the air-side thermal resistance which is often the major part of the overall thermal resistance of many industrial heat exchangers. Different types of plate-fin have been proposed, including the plain plate fin, the offset strip fin, the louver fin and the strip fin (slotted fin surface with protruding strips). According to traditional understanding of heat transfer enhancement mechanism, the major idea adopted in these fin surfaces is to interrupt the flow by repeated geometries or to reduce the thickness of the thermal boundary layers to enhance the heat transfer [1–4].

Experimental studies for different types of plate fins have been extensively performed, and to name a few recent publications, references [5–14] may be consulted. A comprehensive experimental investigation of the performance of plate fin-and-tube surface is very expensive because of the high cost of the tools needed to produce a wide range of geometric variations. For example, to investigate the influence of design parameters on the heat transfer and friction characteristics of slit fin surfaces, eighteen kinds of scaled-up models are specially made in [11]. Such study is of

course very useful, since the test data obtained not only can be used for design, but also for validating numerical simulation results. But high cost restricts its usage.

Numerical modeling, once validated by some test data, on the other hand, provides a cost-effective means for such a parametric study. Great deals of efforts have been paid in this regard. A comprehensive review of numerical investigations on heat transfer and pressure drop characteristics of plate fin-and-tube surfaces published before 2000 has been performed by Shah et al. [4]. In this paper only some related recent works are reviewed, and the emphasis is focused on the model of flow regime. In 1998, Jacobi and Shah [15] made a detailed discussion on heat transfer enhancement mechanisms and flow regime of air-side in compact heat exchanger. They indicated that for louvered and offset-strips fin the flow is laminar and steady ($Re < 400$), with increasing Re number ($400 < Re < 1000$), the flow remains laminar, but unsteadiness and vortex shedding become important, and for higher Re number ($Re > 1000$), the flow becomes turbulent. Meanwhile, they also pointed out that a basic definition of turbulence is difficult to formulate. In this paper we adopt laminar steady model for the flow with Re beyond 1000. Our basic considerations are as follows. First, the experimental observations and data for the flow regime transition in such complicated cases are not so well-accumulated and defined compared with the flow in a simple channel. If we regard the flow between two adjacent fin surfaces as a channel flow, the transition Reynolds number may take the

Contributed by the Heat Transfer Division for publication in the JOURNAL OF HEAT TRANSFER. Manuscript received by the Heat Transfer Division May 8, 2003; revision received June 24, 2004. Associate Editor: S. Acharya.

value around 2300, with the double spacing between the two fin surfaces as the reference dimension for the Reynolds number [16]. It is to be noted that the tube diameter is usually 10 times of the fin spacing, thus the value of $Re_\delta=2300$ (based on the fin spacing) corresponds to the value around 10,000 based on the tube diameter, Re_d . If we take the flow between two adjacent fin surface as the flow past a cylinder, then experimental data have shown that the turbulent flow occurs for $Re_d \geq 1.4 \times 10^5$ [16]. Therefore, from above discussion, the value of flow transition Reynolds number for the cases studied is still a problem open to discussion; Second, from engineering point of view, the most important information is the averaged friction factor and Nusselt number. For example, for flow past a single cylinder, flow visualization has shown that when the Reynolds number beyond 100, unsteady wake occurs behind the cylinder [17]. However, this fact does not prevent the usage of the time averaged drag coefficient and Nusselt number in engineering calculation. Third, recently, some authors performed a comparison study for flow in corrugated channels by using steady and transient models with the same conditions [18]. They found that when the flow reaches periodic unsteady regime, the time averaged heat transfer results are of good accuracy compared with the cycle-averaged steady results. Finally, many numerical studies in the existing literature adopted the steady and laminar models for plate fin-and-tube heat transfer surfaces when $Re_d > 1000$, and reasonably good results are obtained. To name a few, followings are some examples. Jang and Yang [19] conducted numerical studies on plain plate fin-and-tube surfaces with elliptic and round tubes, by using laminar and steady model. In their simulation the maximum frontal velocity is about 7.0 m/s, which corresponds a maximum $Re_d = 1.0 \times 10^4$. For louvered fin coils, there have been some numerical studies including EI-Hawat et al. [20], Leu et al. [21], which used laminar steady numerical model. In [20] the maximum Reynolds number based on the tube diameter is around 2900, in [21] the upper limit of Re_d is about 1800. For wavy fin configuration, Min and Webb [22], Comini and Groce [23] adopt laminar steady model, and the values of Re_d were both larger than 1000.

In spite of the very extensive study of numerical modeling, most previous works have studied the characteristics of the wavy fin, louver fin, offset strip fin on the whole fin surface or for a representative unit of the periodic fully developed region. The fin geometries so far numerically modeled do not include the strip fin with X-arrangement where the strips are positioned on the fin surface in the shape of "X" when viewed from the top of the fin surface. Among the above studies, only the work of Kang and Kim [9] experimentally studied the effect of strip location of X-arrangement on the heat transfer and pressure drop characteristics. The X-arrangement of the strips was first put forward by Hiroaki et al. in 1988 [24] and is probably one of the most widely used fin geometries nowadays in the air-conditioning engineering. One objective of this paper is to present a numerical study on the influence of strip location on heat transfer and pressure drop and to compare the numerical results with the experimental findings.

The reasons why the interrupted geometries can enhance heat transfer are usually attributed to the decrease in the thermal boundary layer and the increase of the disturbance in the fluid [1–4]. Recently Guo and his coworkers [25,26] proposed a novel concept of enhancing convective heat transfer. It is indicated that for the boundary layer flow the decrease of the intersection angle between the velocity and the temperature gradient is an effective way of enhancing heat transfer. Later Tao et al. [27] show by numerical examples that this principle also applies to elliptic flow and heat transfer provided that the Peclet number is not too small (greater than 100). Even for fluid flows whose Peclet number is less 100, the reduction of the intersection angle between velocity and temperature gradient is still an important way to enhance heat transfer, but not so significant as for the flows with Peclet number greater than 100, and, this principle is called as the field synergy (coordination) principle. In [28] more examples are provided to

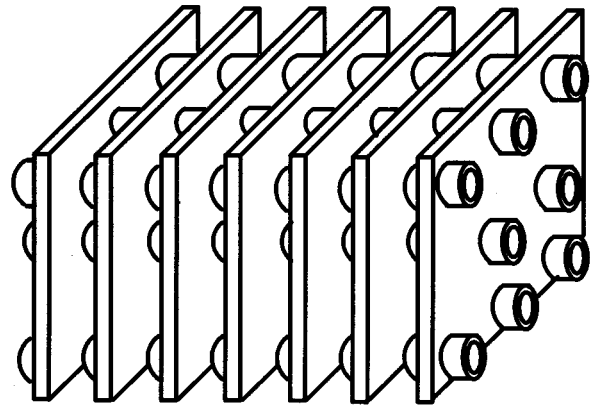


Fig. 1 Schematic diagram of fin-and-tube heat exchanger

show that the existing explanations of heat transfer enhancement can be unified by the field synergy principle. In [29,30] Tao and He reviewed on the recently-developed field synergy principle and its applications in enhancing convective heat transfer and improving the performance of pulse tube refrigerators. The second objective of this paper is to apply this principle to analyze our numerical results. We tried to make some analysis based on the numerical results on the heat transfer enhancement mechanism with field synergy principle and to find out where is the right place to locate the strips such that the heat transfer can be enhanced effectively with reasonable pressure drop penalty.

In the following presentation, the experimental results by Kang and Kim [9] are first numerically simulated and the numerical results are compared with their results to verify the reliability of the numerical model and code developed in this study. Based on the above results, we then study four fin patterns with different strip numbers and strip locations (types A, B, C, and D). The only difference between type B and C is in the strip location. The numerical results are then analyzed focusing on the interpretation of the numerical results from the point of view of field synergy principle. Finally some conclusions will be drawn which are helpful in the design of new enhancement surfaces.

2 Validation of Computational Model and Code

2.1 Physical Model. A schematic diagram of a plain plate fin-and-tube exchanger is shown in Fig. 1. The tube is usually made of copper and the fin surfaces are made of aluminum. The strip fin surface is alike except there are many pieces of strips existing in the fin surface. The fluid is assumed to be incompressible with constant property, and the flow is laminar and steady state. Some hot fluid, say freon refrigerant, is going through the tubes and heat is transmitted through the tube wall and the fin surfaces to the air. The heat transfer and pressure drop characteristics of the airside are solved by the numerical modeling. Because of the relatively high heat transfer coefficient of the inner fluid and the high thermal conductivity of the tube wall, the tube temperature is assumed to be constant. However, the fin surface temperature distribution is to be solved, hence, the problem is of conjugated type in which both the temperatures in the fin solid surface and in the fluid are to be determined simultaneously [31]. In the experimental work of Kang and Kim [9], four kinds of fin strip arrangement are studied: full plain plate fin, strip-plain fin, plain-strip fin and full strip fin. In strip-plain fin, the strips are located in the upstream part, while in plain-strip fin, the strips are arranged in the downstream part with the same strip number as the strip-plain fin, and for full strip fin strips are distributed in the whole plate. The main finding of their study is that the plain-strip plate fin can enhance transfer than strip-plain fin for about 10 percent with similarly pressure drop. The results show the impor-

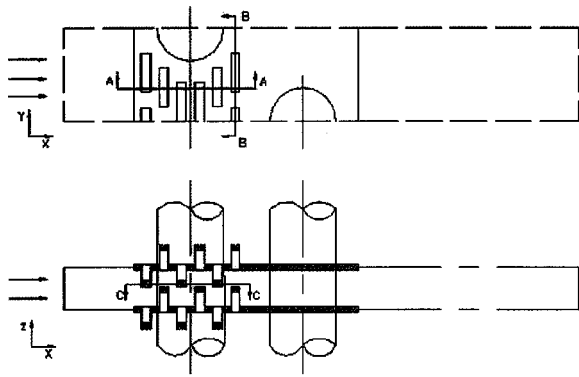


Fig. 2 Computational domain of strip plain fin geometry of reference [9]

tance of the strips arrangements. As the validation for our mathematical model and the code developed, we first simulated the characteristics of heat transfer and fluid flow for the above four types of fin surface.

2.2 Computational Domain. According to the geometry character of symmetry and periodicity, the cell between two neighboring fin surfaces in [9] is investigated. In the numerical simulation the tube wall temperature is specified, while the fin temperature distribution should be solved during the iterative process, making the problem of conjugated type. If we take the flow region as our computational domain, then not only the computational geometry is quite irregular but also the fin surface temperatures are unknown, making the solution process very complicated. However, if we take the whole region outlined by the dashed lines in Fig. 2 (typically for strip-plain fin) as the computational domain, we can easily use three dimensional Cartesian coordinates with sufficient fine grid system to simulate different parts of materials (air, tube and fin surface) by step-wise approximation for the tube surface. This is the practice we adopted in this study.

The computational domain is now described. In Fig. 2, x is the stream-wise coordinate, y is the span-wise one and z stands for the fin pitch direction. The fluid flows across the fin surface from the left to the right. It should be noted that ahead of the fin surface there is 1.5 times of stream-wise fin length as the inlet domain, and behind the fin surface there is 5 times of stream-wise fin length as the outlet domain. This implies that the whole stream-wise length of the computation domain is 7.5 times of the real fin length. The adoption of inlet and outlet regions is mainly for the execution of inlet and outlet boundary conditions, which will be addressed later. For saving space, the extended domain is not presented in scale in Fig. 2. The dashed lines show schematically such a computational domain in the x - y and z - x planes.

2.3 Numerical Treatment of Off-Set Strips in the Computation. In the conjugated computation, the solid regions including fin, strip, and tube are also meshed viewed as some special fluids. Since the physical properties of the different parts are very much different, the code should be able to identify during the computation which is which. To this regard, a special array called FLAG is introduced to identify different regions: fluid, fin and tube. We define the value of FLAG is 1 for fluid, and 2, 3, 4 for fin, tube, and strip, respectively. After the grid generation, the appropriate values of the elements in FLAG have to be input such that the above four regions can be identified correctly. The detailed computational method of conjugated heat transfer can be found in references [31–33]. In order to give a clear profile of the grid-topology and the role of the “identification” of FLAG, the structure of grid of $136 \times 107 \times 24$ is shown in Fig. 3, in which the inlet and outlet extended domain is omitted. This set of grid is the outcome of grid-independent examination. In the figure, it can be

found that in the x -direction, each strip is given four control volumes, while the grid of inlet and outlet extended regions is relatively sparser; In the y -direction, the grid is uniform and the dimension of each control volume in this direction is equal to the thickness of fin; In the z -direction (nonuniform), the thickness of fin holds two control volumes of this direction. The dark parts in the figure present solid parts, which are identified by the array FLAG as mentioned above.

2.4 Governing Equations and Boundary Conditions. The governing equations for continuity, momentum and energy in the computational domain can be expressed as follows:

$$\text{Continuity Equation} \quad \frac{\partial}{\partial x_i} (\rho u_i) = 0 \quad (1)$$

$$\text{Momentum Equations} \quad \frac{\partial}{\partial x_i} (\rho u_i u_k) = \frac{\partial}{\partial x_i} \left(\mu \frac{\partial u_k}{\partial x_i} \right) - \frac{\partial p}{\partial x_k} \quad (2)$$

$$\text{Energy Equation} \quad \frac{\partial}{\partial x_j} (\rho u_j T) = \frac{\partial}{\partial x_j} \left(\Gamma \frac{\partial T}{\partial x_j} \right) \quad (3)$$

where

$$\Gamma = \frac{\lambda}{c_p} \quad (4)$$

The governing equations are elliptic in the Cartesian coordinates, hence boundary conditions are required for all boundaries of the computation domain. Due to the conjugated type of the problem, the fin surfaces are considered as part of the solution domain and will be treated as a special type of fluid. The required conditions are described for the three regions (upstream extended region, fin coil region, down stream extended region), which are listed in Table 1. In the table USED means upstream extended domain, and DSED as downstream extended domain. With the extended region added, it is conveniently to adopt the so-called one-way coordinate or the fully developed assumption [31–33] for the treatment of the outlet boundary condition. It is to be noted that for unbounded hyperbolic flows Orlandi [34] proposed the so-called Sommerfeld radiation condition for the treatment of the outflow boundary. In this study the governing equations are of elliptic type and there is only one open boundary (the downstream outlet), hence, this method does not fit our situation and was not adopted. In addition, when there is no recirculation at the outflow boundary, the one-way coordinate or the fully developed assumption are the most-widely used practice in engineering computations, as can be witnessed from references [19–21,35–37].

2.5 Numerical Methods. The fluid-solid conjugated heat transfer problem is solved by full-field computation method. The solid in the computational domain is regarded as a special fluid of infinite viscosity. To guarantee the continuity of the flux rate at the interface, the thermal conductivity of fin and fluid adopts individual value, while the heat capacity of solid takes the value of the fluid [31]. A very large value of the thermal conductivity is assigned to the tube region to guarantee the tube temperature to be constant. The computational domain is discretized by nonuniform grids, with the grids of fin coils region being fine, and that in the extension domain being coarse. Governing equations are discretized by finite volume method, and the coupling of pressure and velocity is implemented by CLEAR algorithm in the staggered grids [38,39].

Before any computational results can be deemed enough to illuminate the physical phenomenon, the computational results must be justified through the grid-independent test, so a careful check for grid independence of the numerical solutions has been made. For this purpose, four different grid systems ($136 \times 107 \times 24$, $148 \times 107 \times 24$, $136 \times 157 \times 24$, $136 \times 107 \times 46$) were adopted and computations were performed for a case with a frontal velocity of 3 m/s. It was found that the maximum difference in heat

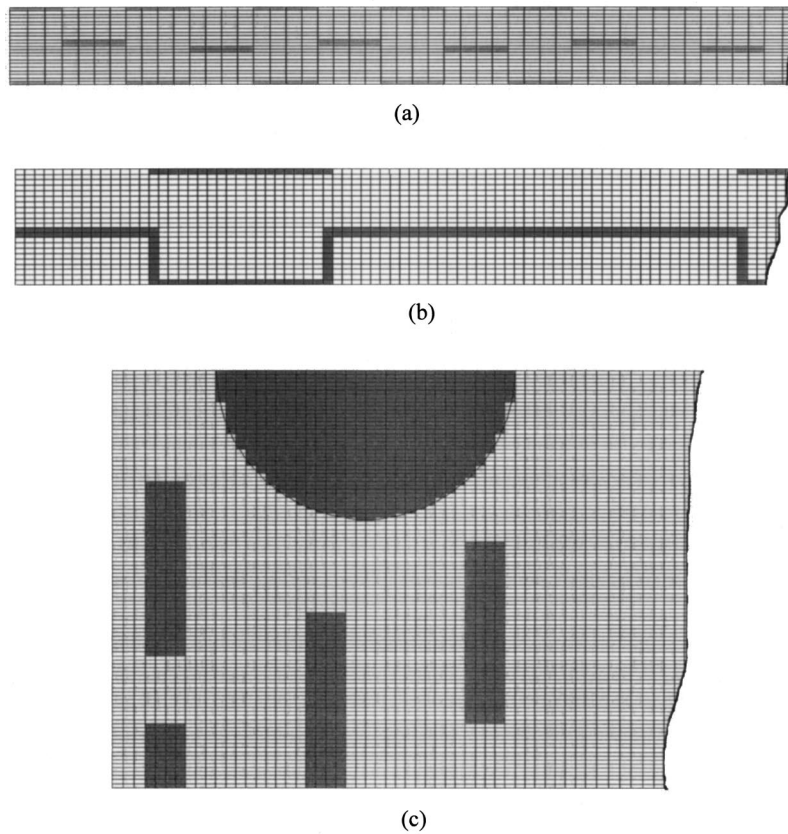


Fig. 3 Grid structure of computation of reference [9]: (a) A-A section view in Fig. 2; (b) B-B section view in Fig. 2; and (c) C-C section view in Fig. 2.

transfer coefficient between the results of grid systems of $136 \times 107 \times 24$ and $136 \times 107 \times 46$ is 1.5 percent. Considering the balance between economics and accuracy, the grid system of $136 \times 107 \times 24$ is regarded as the one for providing grid independence solutions. Computations were performed on a PC with CPU frequency of 2G, and typical CPU time was 7–8 hours for each case.

As has been discussed above, the computation is of a conjugated type in which the fin efficiency has to be determined during the computations and can not be obtained in advance. In the experiment of Kang and Kim [9], they only provided the parameter $h \cdot \eta_0$ not the pure heat transfer coefficient except the plain plate fin, whose fin efficiency was obtained from the empirical equation. In our numerical simulation the efficiency of the slit fin is computed as follows. According to heat transfer theory [1,3], the fin efficiency is defined by

$$\eta_f = \frac{Q_{\text{real}}}{Q_{\text{ideal}}} \quad (5)$$

where Q_{real} is the actual heat transfer rate between air and the fin surface; Q_{ideal} is the ideal heat transfer rate when the fin temperature is equal to the tube temperature T_w . To implement the ideal situation, we just artificially give the fin surface a very large value of thermal conductivity, say 1.0×10^{30} , which leads to the results of uniform temperature of the fin surface equal to the value of the tube wall.

2.6 Parameter Definitions. Some parameters are defined as follows:

$$\text{Re} = \frac{\rho u_m D_e}{\mu} \quad (6)$$

$$\text{Nu} = \frac{h D_e}{\lambda} \quad (7)$$

$$h = \frac{Q_{\text{real}}}{A \Delta T \eta_0} \quad (8)$$

$$\eta_0 = (A_{\text{tube}} + A_{\text{fin}} \eta_{\text{fin}}) / A \quad (9)$$

$$Q_{\text{real}} = \dot{m} c_p (T_{\text{out}} - T_{\text{in}}) \quad (10)$$

$$f = \frac{\Delta p}{\frac{1}{2} \rho u_m^2} \cdot \frac{D_e}{L} \quad (11)$$

$$\Delta T = \frac{T_{\text{max}} - T_{\text{min}}}{\log(T_{\text{max}} / T_{\text{min}})} \quad (12)$$

where u_m is the mean velocity of the minimum transverse area, D_e is the outside tube diameter, T_{in} , T_{out} are the fluid bulk temperature of inlet and outlet of the fin surface, respectively, $T_{\text{max}} = \max(T_w - T_{\text{in}}, T_w - T_{\text{out}})$, $T_{\text{min}} = \min(T_w - T_{\text{in}}, T_w - T_{\text{out}})$, η_f is the fin efficiency and η_0 stands for the overall fin efficiency defined by Eq. (9).

2.7 Computational Results. Numerical simulations were conducted for the four kinds fin pattern described above [9] with corresponding frontal velocity ranging from 0.2 m/s to 0.6 m/s. The wall temperature is set as 45°C with the inlet air temperature being 20°C. The pressure drop and heat transfer performance comparisons are shown in Fig. 4 and Fig. 5 respectively. In the above two figures, all the numerical data in this study are expressed with center-hollowed symbols, and the data in [9] are

Table 1 Boundaries conditions for numerical simulation in this study

			USED	Fin coil region						DSED
				Plain plate fin			Strip fin			
				Fin	Tube	Fluid	Fin	Tube	Fluid	
inlet	Velocity	u	$u=0$							
		v	$v=0$							
	Temperature	w	$w=0$							
		T	$T=T_{in}$							
Upper and Lower sides	Velocity	u	$\frac{\partial u}{\partial z}=0$	$u=0$	$u=0$		$u=0$	$u=0$	periodic	$\frac{\partial u}{\partial z}=0$
		v	$\frac{\partial v}{\partial z}=0$	$v=0$	$v=0$		$v=0$	$v=0$	periodic	$\frac{\partial v}{\partial z}=0$
		w	$w=0$	$w=0$	$w=0$		$w=0$	$w=0$	periodic	$w=0$
	Temperature	T	$\frac{\partial T}{\partial z}=0$	$\frac{\partial T}{\partial z}=0$	$T=T_W$		periodic	$T=T_W$	periodic	$\frac{\partial T}{\partial z}=0$
		u	$\frac{\partial u}{\partial y}=0$	$u=0$	$u=0$	$\frac{\partial u}{\partial y}=0$	$u=0$	$u=0$	$\frac{\partial u}{\partial y}=0$	$\frac{\partial u}{\partial y}=0$
		v	$v=0$	$v=0$	$v=0$	$v=0$	$v=0$	$v=0$	$v=0$	$v=0$
Front and back sides	Velocity	w	$\frac{\partial w}{\partial y}=0$	$w=0$	$w=0$	$\frac{\partial w}{\partial y}=0$	$w=0$	$w=0$	$\frac{\partial w}{\partial y}=0$	$\frac{\partial w}{\partial y}=0$
		T	$\frac{\partial T}{\partial y}=0$	$\frac{\partial T}{\partial y}=0$	$T=T_W$	$\frac{\partial T}{\partial y}=0$	$\frac{\partial T}{\partial y}=0$	$T=T_W$	$\frac{\partial T}{\partial y}=0$	$\frac{\partial T}{\partial y}=0$
		u								$\frac{\partial u}{\partial x}=0$
Outlet	Velocity	v								$\frac{\partial v}{\partial x}=0$
		w								$\frac{\partial w}{\partial x}=0$
		T								$\frac{\partial T}{\partial x}=0$

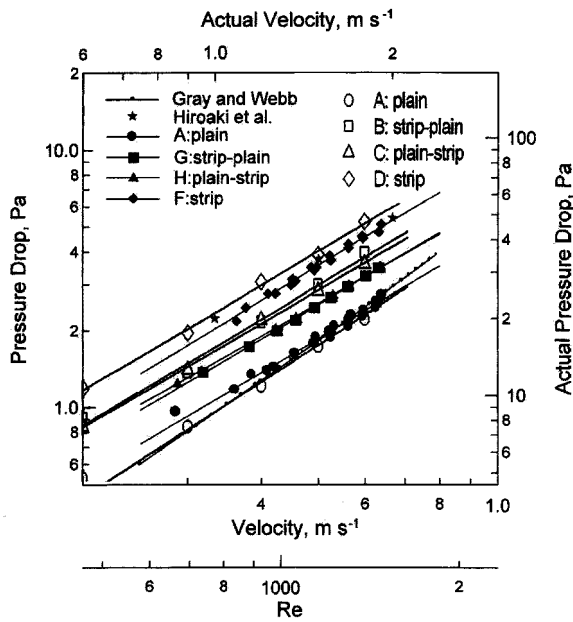


Fig. 4 Predicted pressure drop versus frontal velocity compared with reference [9]

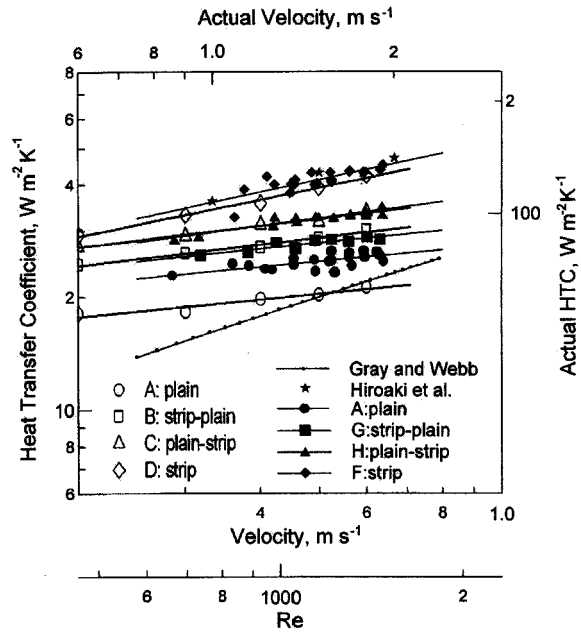


Fig. 5 Predicted $h\eta_0$ versus frontal velocity compared with reference [9]

expressed with center-solid symbols. For heat transfer coefficient comparison, the y -coordinate is $h \eta_0$ for strip fin surface and pure heat transfer coefficient h for plain plate fin. It can be observed from Fig. 4 that the numerical results of pressure drop is about 8–10 percent larger than the experimental ones for strip fins and the difference between predicted and experimental results is even smaller for plain plate fin. Such an agreement should be regarded reasonably well in the engineering computations. And for parameter $h \cdot \eta_0$, the two data sources are in good agreement (Fig. 5): the derivation of numerical results from the experimental ones is less than 6 percent for strip-plain fin, plain-strip fin, and for strip fin. The numerically predicted heat transfer coefficient for plain plate fin is 15–20 percent lower than the experimental results in [9]. This deviation is a bit too large, and the following fact may be one of the major reasons to account for this deviation. The plain plate fin in our numerical simulation is strictly smooth. However, in the real coil, there exist several mild wavy circles around the tube that were produced during the manufacturing process and they can enhance the air side heat transfer a bit. The effect of these wavy circles were not taken into account in the numerical simulation, leading to a lower numerical prediction. On the other hand, the deviation between the correlation provided by Gray and Webb and the test results of [9] (see Fig. 5) is, generally speaking, much larger than that of our numerical prediction. Therefore, our numerically predicted results might be still acceptable as an engineering computation.

From the above comparison, it is clear that within the framework of engineering numerical simulation the agreement between predicted and tested results is quite good, showing the reliability of the physical model and the code developed.

3 Numerical Simulation on the Fins of the Present Study

3.1 Four Fin Configurations Studied. In the above comparison study the strip arrangements are copied from the prototype tested in [9], where for fin B and fin C the strips are totally located within the upstream half and the downstream half of the fin surface respectively. In the present study, we make some changes for the two types of strip arrangement: the strips are mainly located in upstream half with a few strips being in the downstream for the fin B and vice versa for fin C. Figure 6 shows the details of fin configurations of the four strip arrangement patterns. Fin A is the whole plain plate fin. Fin D possess 12 pieces of strips arranged over the entire fin and protruded alternatively upward and downward along the flow direction, and each strip is punched with 1 mm width and 0.7 mm depth from the base sheet. The strip number is the same for B and C. The simulation conditions are listed in Table 2.

The computational domain is shown in Fig. 7 for fin D. The governing equations and the boundary conditions are similar to that presented in section 2. For this simulation we only need to redefine the array FLAG based on the configuration studied. The grid system used is $136 \times 116 \times 34$. The numerical methods used are the same as described in section 2 and will not be restated here.

3.2 Results and Discussion

3.2.1 Friction Factor Results. Figure 8 compare the friction factor of the four strip arrangement patterns shown in Fig. 8. The Re number ranges from 348 to 3480, and the corresponding frontal velocity ranges from 0.5 m/s to 5.0 m/s. It is revealed that the friction factor of whole plain fin (fin A) is the lowest, and the value of the whole strip fin (fin D) is the highest. The friction factor for the whole strip fin is 2.24 times than that of the whole plain fin (fin A) at $V=2.0$ m/s. This is mainly due to the frequent interruption of the flow created by the high-density strips. The pressure drops of half strip fins (fin B and fin C) are between the

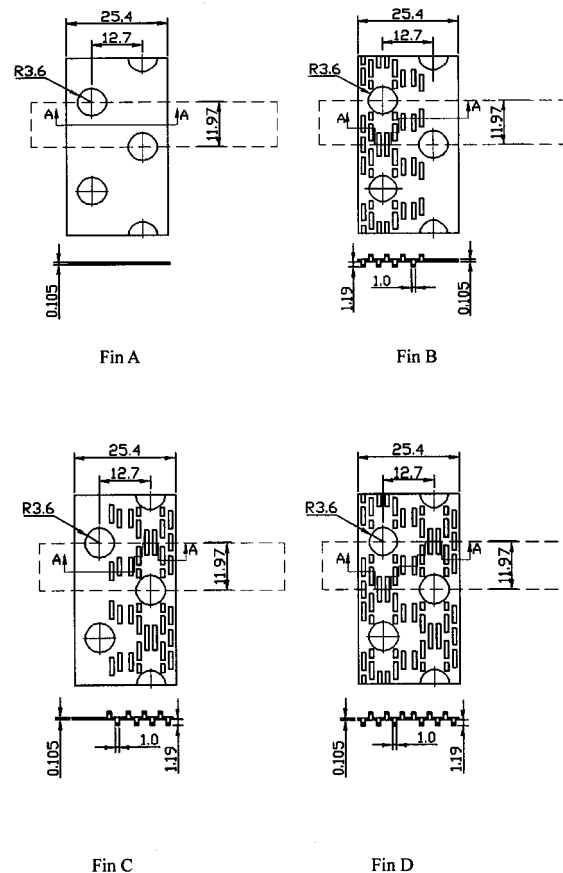


Fig. 6 Geometry configuration of the four patterns of slit arrangement

above two. It is to be noted that the pressure drop of fin B is 14 percent higher than fin C at frontal velocity of 2 m/s even though they possess the same number of strips.

3.2.2 Fin Efficiency. The fin efficiency of the four types of fins are presented in Fig. 9. It can be seen that in the low frontal velocity region the fin efficiency of the four types of surface are almost identical with the efficiency of the whole plain fin being a bit lower. The fin efficiency decreases with the increase of the Re number or the frontal velocity. This is consistent with the common understanding of the heat transfer theory. It should be noted that the decreasing trend of the fin efficiency of the whole plain fin (fin A) with the increase of frontal velocity is less steep than the other three ones, and at a relatively higher frontal velocity (>1.0 m/s), the fin efficiency of type A eventually becomes higher than that of fin B, C, D. The above variation characters of the fin efficiency can be explained as follows. From the tube wall to the air there are two thermal resistances in series to the heat transmission: one is

Table 2 Simulation conditions

Tube outside diameter	7.2 mm
Longitudinal tube pitch	12.7 mm
Transverse tube pitch	11.97 mm
Fin thickness	0.105 mm
Fin pitch	1.4 mm
Strip width	1.0 mm
Strip pitch in the x direction	1.0 mm
Strip height	0.7 mm
Tube temperature	313 K
Inlet air temperature	303 K
Inlet frontal velocity	0.5–5 m/s

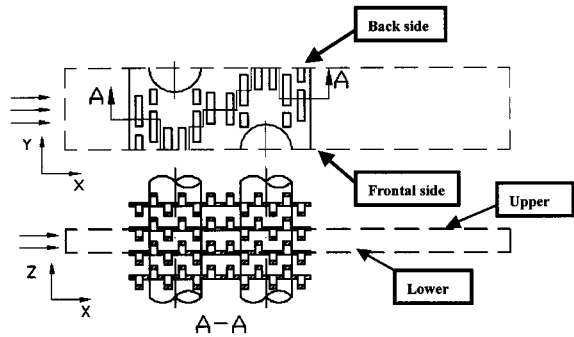


Fig. 7 Computational domain of strip fin geometry in the present study

the thermal resistance provided by the heat conduction in the fin, which depends on the fin geometry and thermal conductivity, hence is independent of the frontal velocity. The second one is the convective resistance from fin surface to the air, which strongly depends on the frontal velocity. In the low frontal velocity region, the convective thermal resistance prevails and the slotted surfaces have a better convective heat transfer, resulting a larger heat transfer rate under the same temperature difference between the tube wall and the air. Thus the fin efficiency of the slotted cases is a bit larger than that of the plain fin. With the increase in frontal velocity, however, the convective thermal resistance reduces significantly while the conduction thermal resistance remains the same, hence the latter soon prevails. The existence of the slit in the fin

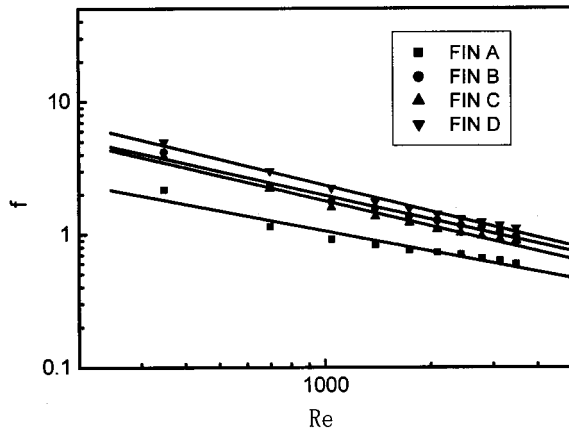


Fig. 8 Computational results of friction factor

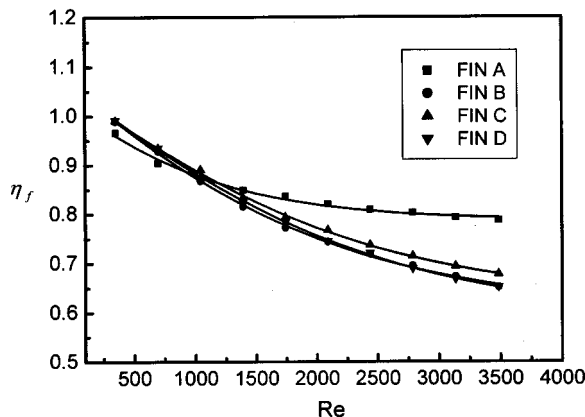


Fig. 9 Fin efficiency

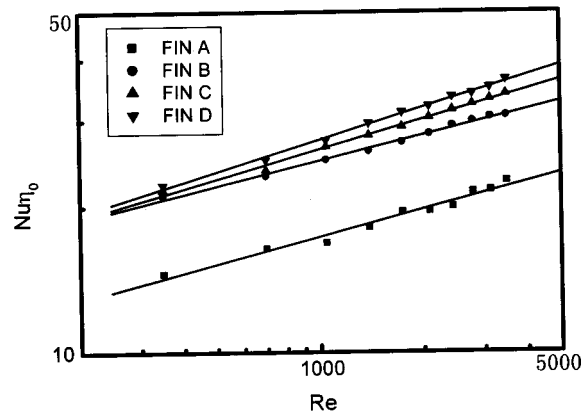


Fig. 10 Heat transfer results

surface leads to the increase of the conduction thermal resistance of the fin, leading to a lower heat transfer rate when the frontal velocity is relatively high. And the higher the frontal velocity is, the more prominent this fin efficiency difference. From the above discussion, it is obvious that case D has the lowest fin efficiency in the relative high frontal velocity region. Figure 9 shows that the fin efficiency of case B is almost the same as fin D. This means that case B has a worse convective heat transfer rate since its conduction thermal resistance should be less than that of case D. The fin efficiency of case C is higher than that of case B and D, indicating a better convective heat transfer compared with case B. The discussion made here will be directly demonstrated by heat transfer results.

3.2.3 Heat Transfer. Figure 10 shows the comparison results of heat transfer performance of the four fin types at different Re number. It is noted that the ordinate is the product of Nusselt number and the fin efficiency, which is proportional to the actual heat transfer rate. The variation ranges of Re number and the frontal velocity are the same as indicated before. The Nu number of fin D is far higher than the whole plain fin (fin A), and the values of fin B and fin C is lower than that of fin D. It is very interesting to note that fin C with strips mainly located in the down stream part of the fin surface provides more heat transfer rate than fin B with strips mainly located in the upstream part of the fin surface. For example, the values of $Nu\eta_0$ of fin C is 1.08 times of that of fin B at the frontal velocity of 2 m/s. The above numerical findings are consistent with the test results reported by Kang and Kim, [9], where scale-up models for the four type arrangement patterns were tested qualitatively. The above results provide important information for the design of fin geometries: since the flow resistance of fin C is lower than fin B, while fin C has higher heat transfer coefficient than fin B, the strips should be mainly located in the downstream part of the fin surface. It is also revealed that fin D has the best heat transfer rate, but its friction factor is much higher than that of fin B or C. This may restrict its usage when the pressure drop is a special care. Our main aim is to compare fin B and fin C and to analyze where the difference in their performance comes from. In the following, such an analysis is conducted from the view point of field synergy principle.

4 Discussion on Heat Transfer Enhancement Essence

As indicated above, from the traditional viewpoint, strips in the fin can enhance convective heat transfer because it can interrupt the flow boundary layer to reduce its thickness by repeatedly recreation of new thermal boundary layers, or can increase the disturbance in the flow field. A relatively thinner boundary layer serves positively to enhance heat transfer. But this concept can not explain why fin C has a better heat transfer performance than fin B even if they have the same number of strips. It is probably diffi-

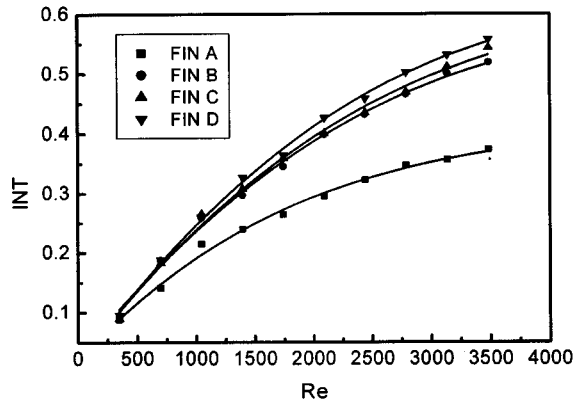


Fig. 11 Variation of dot product integration with Re

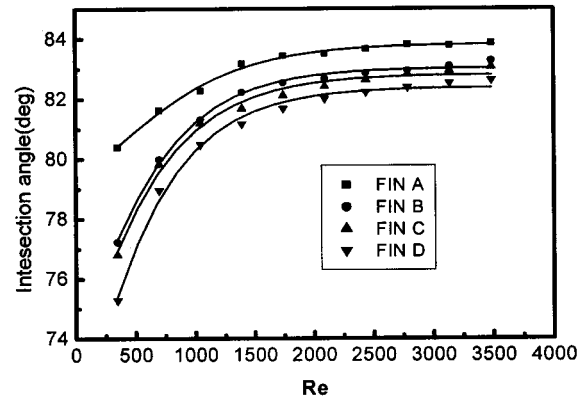


Fig. 13 Domain averaged intersection angle

cult to reveal the reason from the traditional viewpoint of heat transfer enhancement. This phenomenon can be easily explained by applying the field synergy principle proposed by Guo et al. [25,26] and later extended in [27–29]. According to the analysis provided in the above references, the convective heat transfer rate is proportional to $\rho c_p \int_{\Omega} (\vec{U} \cdot \vec{\nabla} T) d\Omega$, where Ω is the domain studied. The above integration was calculated from the numerical data and the results are presented in Fig. 11, where the symbol INT represents the integration over the entire domain for fluid control volume. Since we adopted the staggered grid system in the calculation of INT, the velocity has to be linearly interpolated to the main grid point from the interface as depicted in Fig. 12 for two dimensional case. The vector of velocity and temperature gradient for point P in three dimensional Cartesian coordinates are expressed as:

$$\vec{U} = u\vec{i} + v\vec{j} + w\vec{k} \quad (13)$$

$$\vec{\nabla} T = \frac{\partial T}{\partial x}\vec{i} + \frac{\partial T}{\partial y}\vec{j} + \frac{\partial T}{\partial z}\vec{k} \quad (14)$$

Then the term INT can be expressed as follows:

$$\text{INT} = \rho c_p \sum_{i,j,k} \left(u \frac{\partial T}{\partial x} + v \frac{\partial T}{\partial y} + w \frac{\partial T}{\partial z} \right) \quad (15)$$

This term is actually the convective term of a three dimensional energy equation. Under the given modules of velocity vector and temperature gradient, the dot product increases with the decrease

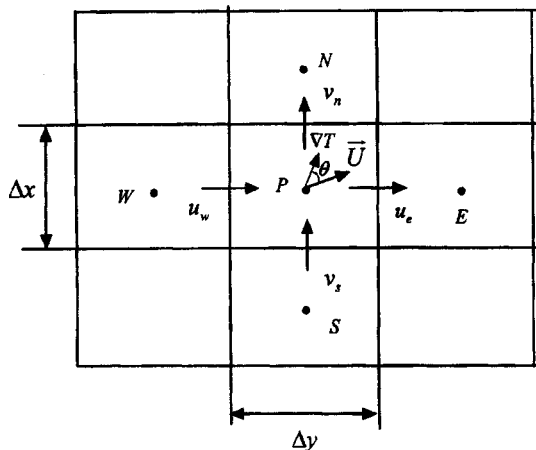


Fig. 12 The Calculation diagram for vector of velocity and temperature gradient

in their intersection angle. The basic idea of the field synergy principle then can be stated as follows: to enhance convective heat transfer the most fundamental mechanism is to reduce the intersection angle between velocity and the temperature gradient. For the four kinds of strip arrangement at the same inlet velocity, the mean intersection angle between the velocity and the temperature gradient of the whole computational domain was determined as follows.

The local intersection angle at a grid point is

$$\theta = \cos^{-1} \left(\frac{\vec{U} \cdot \vec{\nabla} T}{|\vec{U}| |\vec{\nabla} T|} \right) = \cos^{-1} \left(\frac{u \frac{\partial T}{\partial x} + v \frac{\partial T}{\partial y} + w \frac{\partial T}{\partial z}}{|\vec{U}| |\vec{\nabla} T|} \right) \quad (16)$$

The domain average intersection angle is defined as the volume averaged mean angle in the fluid region, i.e.,

$$\theta_{av} = \frac{\sum_{i,j,k} \theta_{i,j,k} \Delta x_i \Delta y_j \Delta z_k}{\sum_{i,j,k} \Delta x_i \Delta y_j \Delta z_k} \quad (17)$$

where the subscripts i, j, k only refer to the control volume of fluid.

The numerical results for the average intersection angle are plotted in Fig. 13. From the figure following features may be noted. First, the results show that the mean intersection angle increases with the increasing in Re number for the four fin types, indicating that the synergy between the velocity and temperature gradient becomes worse with the increase in the Reynolds number; Second, at the same Reynolds number, the intersection angle of fin D is the smallest, while that of fin A is the largest, with a difference about 5 to 2 deg. Third, it is especially interesting to note that the averaged intersection angle of fin C is always less than that of fin B. And this is the most fundamental reason why fin C has a better heat transfer performance than fin B: the synergy between the velocity and the temperature gradient of fin C is better.

Our numerical results not only once again show the correctness of the field synergy principle, but also provide more information on where we should locate the strips in order to have effective enhancement of heat transfer with mild increase in pressure drop. For this end, it is to be reminded that according to the field synergy principle, the dot product of the velocity vector and the temperature gradient, $|\vec{U} \cdot \vec{\nabla} T|$, will have the maximum result if the intersection angle between the velocity and the temperature gradient equals to zero when we have the full synergy and no any enhancement techniques are needed. Only when the intersection angle increases from zero degree enhancement techniques are re-

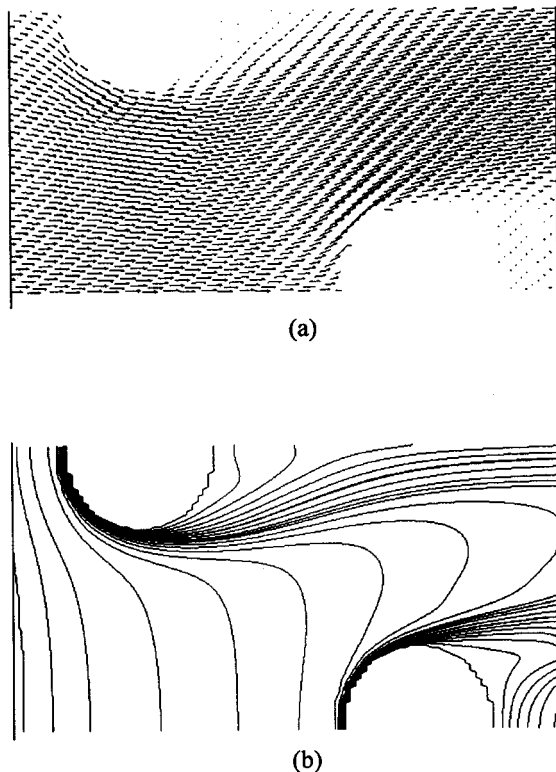


Fig. 14 Velocity vector and temperature contours for fin A: (a) flow field of the center section in the z-direction; and (b) temperature field of the center section in the z-direction.

quired in order to improve the synergy between the velocity and the temperature gradient. To have deeper understanding of this point of view, we examined some computational results of the velocity vector and isotherm distributions in the middle plan between the two adjacent fin surfaces for the plain plate fin situation. These results are presented in Fig. 14. It can be seen that in the upstream part of the fin, the temperature contours are almost perpendicular to the velocity vector, this implies that the fluid temperature gradient are almost in the same direction as the velocity, i.e., the synergy between velocity and temperature gradient is very good. Hence, in this part of the fin, there is no need to create the interruption within the fluid; however, in the downstream part of the fin, the temperature contours are almost parallel to the velocity vector in the major part of the region. It is this place that enhancement techniques are needed in order to improve the synergy between velocity and the temperature gradient. This is the further understanding why the heat transfer performance of fin C is better than that of fin B.

5 Performance Comparison of Four Types of Fin

A qualitative comparison for enhanced heat transfer surface is an important issue in evaluating the performance improvement by taking some enhancement technique. For such evaluation to be meaningful, it is necessary to specify the constants under which the comparison is being made. Depending on different comparison objectives, a lot of comparison constraints, or criteria, can be used, including the goodness factor of Shah [40], the constraint of identical pumping power, identical pressure drop [41]. A comprehensive review on this issue was made in [42]. In this paper the goodness factor is adopted simply because its simplicity and clearness in concept. In addition, the performance comparison in [9] was made under this criterion. In order that we can examine whether our comparison results are consistent with that of [9], the same criterion should be adopted. In the comparison, the heat

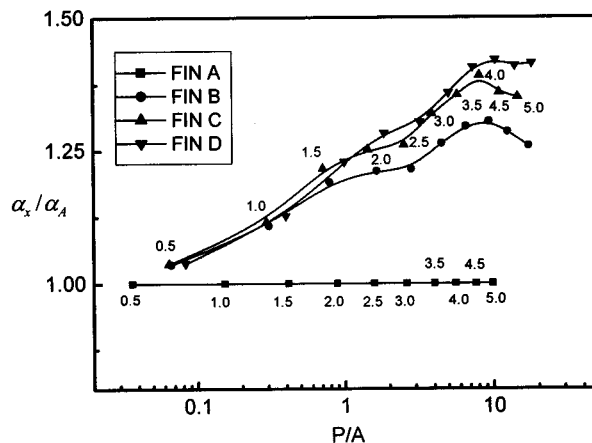


Fig. 15 Goodness factor comparison of four fin pattern

transfer and pressure drop characteristics of the plain plate fin is taken as a reference. The goodness factor, α , denotes the heat transfer rate per unit temperature difference between inlet and wall and per unit surface area. The values of this factor for different surfaces are compared with the value of P/A as a parameter, which stands for the fan power per unit heat transfer surface area. Namely, the parameters of α and P/A are defined as follows:

$$\alpha = Q/A(T_w - T_{in}) \quad (18)$$

$$P/A = VA_{fr}\Delta p/A \quad (19)$$

It is to be noted that Eq. (18) is very much like the definition of heat transfer coefficient, however, the α value is not the same as the heat transfer coefficient since here the thermal potential for the whole heat transfer process, $T_w - T_{in}$ is taken as the temperature difference. The goodness factor comparison results of the three slit fin surfaces are showed in Fig. 15, where the abscissa is P/A and the ordinate is the normalized value of the goodness factor, α_x/α_A , where the subscripts x and A stands for the slit fin of X -arrangement and the plain plate fin. In the Kang and Kim's research [9], the authors conducted a comparison with frontal velocity ranging about 0.25 m/s–0.85 m/s. Their main findings are as follows: (1) In the frontal velocity range of 0.5–0.8 m/s, fin C (plain-strip) has the best enhancement; (2) When frontal velocity is greater than 0.8 m/s, fin D (entire slit fin) tends to be the best, while fin C is still better than fin B (strip-plain fin); (3) Fin B, C, D all tend to be superior than fin A (plain plate) in the entire comparison range of P/A . By carefully examining Fig. 15, it can be observed that qualitatively the above findings can also be applied to the present situation. The only difference is the concrete value of P/A below or beyond which the ranking position changes. In the present study the frontal velocity of 2 m/s is a critical value, beyond which fin D has the best performance. Above analysis indicates two important issues: (1) In the conventional frontal velocity range, fin C has a better heat transfer performance than fin B, and can be comparable with fin D when the pumping power is taking into account; (2) Our numerical predictions lead to the same qualitative conclusions for the four types of fin studied in this paper which gives further support to our computational model.

6 Conclusions

In this paper, three-dimensional numerical simulation of the four types of strip arrangement are performed to reveal the location effects on the heat transfer and pressure drop characteristics. The major findings are summarized as follows:

1. The pressure drop of the whole strip fin (fin D) is the largest and that of the whole plain fin (fin A) is the smallest, the pressure

drops of half strip fins (fin B and C) are similar with the pressure drop of fin C (downstream part slotted) always lower than that of fin B (upstream part slotted).

2. For the same Reynolds number, the Nu number is increased in the order of A, B, C, and D. Fin C in which strip is located in the downstream part has better heat transfer performance than Fin B in which strip is located in the upstream part. This numerical finding is consistent with the test results reported in [9].

3. The domain averaged intersection angles of the four types of strip arrangement decreases in the order of A, B, C and D. The results once again demonstrate the correctness of the field synergy principle.

4. Detailed analysis on the velocity vector distribution and the temperature contours show that in the entry region of the plate fin and tube surface the synergy between velocity and temperature gradient is very good; while in the downstream part of the fin surface, synergy becomes worse and enhancement techniques are needed.

5. A comprehensive heat transfer performance comparisons are made by introducing the goodness factor and fan power consumption per unit heat transfer surface. The results show that among the three strip fin arrangements, fin C ranks first in conventional frontal velocity variation range (about $V < 2.0$ m/s), in the computation range of frontal velocity from 2.0 m/s to 4.0 m/s, fin C is always better than (and at least identical to) fin B, and is a little worse than fin D at higher frontal velocity region.

6. The numerical modeling presented in this paper again reveals that the basic mechanism function of enhancing heat transfer is to reduce the intersection angle between the velocity and the temperature gradient and, it may be suggested with great confidence that the heat transfer enhancement element should be positioned in the place where the synergy between the velocity and temperature gradient is worse.

Acknowledgments

This work was supported by the National Key Project of Fundamental R & D of China (Grant No. 2000026303), the National Natural Science Foundation of China (No. 50076034, 50276046), and KP0504200394.

Nomenclature

A	= heat transfer area, m^2
c_p	= specific heat at constant pressure, $\text{kJ} \cdot \text{kg}^{-1} \text{K}^{-1}$
D_e	= outer tube diameter, m
f	= friction factor
h	= heat transfer coefficient, $\text{W} \cdot \text{m}^{-2} \text{K}^{-1}$
L	= heat exchanger depth in air flow direction, m
p	= pressure, Pa
ΔP	= pressure drop, Pa
Re	= Reynolds number
η_f	= fin efficiency
η_0	= surface efficiency
Nu η_0	= Nu number multiplying surface efficiency
T	= temperature, K
u	= velocity vector, velocity in x -direction
v	= velocity in y -direction
w	= velocity in z -direction

Greek Symbols

ρ	= air density ($\text{kg} \cdot \text{s}^{-3}$)
μ	= dynamic viscosity ($\text{kg} \cdot \text{m}^{-1} \text{s}^{-1}$)
λ	= thermal conductivity ($\text{W} \cdot \text{m}^{-1} \text{K}^{-1}$)
Γ	= diffusion coefficient

Subscripts

in = inlet

m	= mean
max	= maximum
min	= minimum
out	= outlet
w	= wall

References

- [1] Incropera, F. P., and DeWitt, D. A., 1996, *Introduction to Heat Transfer*, Third ed., John Wiley & Sons, New York.
- [2] Kays, W. M., and London, M. E., 1980, *Convective Heat Transfer and Mass Transfer*, Second ed., McGraw-Hill Book Company, New York.
- [3] Yang, S. M., and Tao, W. Q., 1998, *Heat Transfer*, 3rd ed., Higher Education Press, Beijing.
- [4] Shah, R. K., Heikal, M. R., Thonon, B., and Tochon, P., 2000, "Progress in the Numerical Analysis of Compact Heat Exchanger Surfaces," in *Advances in Heat Transfer*, **34**, pp. 363–442.
- [5] Kang, H. J., Li, W., Li, H. J., Xin, R. C., and Tao, W. Q., 1994, "Experimental Study on Heat Transfer and Pressure Drop Characteristics of Four Types of Plate Fin-and-Tube Heat Exchanger Surfaces," *J. Thermal and Fluid Science*, **3**(1), pp. 34–42.
- [6] Kang, H. J., Li, W., Li, H. J., Xin, R. C., and Tao, W. Q., 1994, "Experiment Study on Heat Transfer and Pressure Drop for Plain Fin-and-Tube Heat Exchanger," *Journal of Xi'an JiaoTong University*, **28**(1), pp. 91–98.
- [7] Xin, R. C., Li, H. J., Kang, H. J., Li, W., and Tao, W. Q., 1994, "An Experiment Investigation on Heat Transfer and Pressure Drop Characteristics of Triangular Wavy Fin-and-Tube Heat Exchanger Surfaces," *Journal of Xi'an JiaoTong University*, **28**(2), pp. 77–83.
- [8] Horuz, I., Kurem, E., and Yamankaradeniz, R., 1998, "Experimental and Theoretical Performance Analysis of Air-Cooled Plate-Finned-Tube Evaporators," *Int. Commun. Heat Mass Transfer*, **25**(6), pp. 787–798.
- [9] Kang, H. C., and Kim, M. H., 1999, "Effect of Strip Location on the Air-Side Pressure Drop and Heat Transfer in Strip Fin-and-Tube Heat Exchanger," *Int. J. Refrig.*, **22**, pp. 302–312.
- [10] Kang, H. C., and Kim, M. H., 2001, "Performance of Material Saved Fin-Tube Heat Exchanger in Dehumidifying Conditions," *2001 Proceeding of the Third International Conference on Compact Heat Exchangers and Enhancement Technology for the Process Industries*, Davos, Switzerland, pp. 303–310.
- [11] Yun, J.-Y., and Lee, K.-S., 2000, "Influence of Design Parameters on the Heat Transfer and Flow Friction Characteristics of the Heat Exchanger With Slit Fins," *Int. J. Heat Mass Transfer*, **43**, pp. 2529–2539.
- [12] Yun, J.-Y., and Lee, K. S., 1999, "Investigation of Heat Transfer Exchangers With Interrupted Surfaces," *Int. J. Heat Mass Transfer*, **42**, pp. 2375–2385.
- [13] Wang, C. C., Lee, W. S., and Sheu, W. J., 2001, "A Comparative Study of Compact Enhanced Fin-and-Tube Heat Exchanger," *Int. J. Heat Mass Transfer*, **44**, pp. 3565–3573.
- [14] Wang, Chi-Chuan, Lo, Jerry, Lin, Yur-Tsai, and Wei, Chung-Szu, 2002, "Flow Visualization of Annual and Delta Winlet Vortex Generators in Fin-and-Tube Heat Exchanger Application," *Int. J. Heat Mass Transfer*, **45**, pp. 3803–3815.
- [15] Jacobi Anthony, M., and Shah Ramesh, K., 1998, "Air-Side Flow and Heat Transfer in Compact Heat Exchangers: A Discussion of Enhancement Mechanism," *Heat Transfer Eng.*, **19**(4), pp. 29–41.
- [16] Incropera, F. K., and DeWitt, D. P., 2002, *Fundamentals of Heat and Mass Transfer*, Fifth ed., John Wiley & Sons, New York, p. 410, 495–496.
- [17] Bejan, A., 1993, *Heat Transfer*, John Wiley & Sons, Inc., New York, pp. 265–266.
- [18] Xu, Wei, and Min, Jingchun, 2004, "Numerical Predictions of Fluid Flow and Heat Transfer in Corrugated Channels," *Proceedings of the 3rd International Symposium on Heat Transfer and Energy Conservation*, B. Hua, Z. Y. Guo, and C. F. Ma, eds., South China University of Technology Press, 1, pp. 714–721.
- [19] Jang, Jiin-Yuh, and Yang, Jyh-Yau, 1998, "Experimental and 3-D Numerical Analysis of the Thermal-Hydraulic Characteristics of Elliptic Finned-Tubes Heat Exchangers," *Heat Transfer Eng.*, **19**(4), pp. 55–67.
- [20] Ei-hawat, S. M., Heikal, M. R., and Sazhin, S. S., 2001, "An Improved Three-Dimensional Numerical Model of Flow and Heat Transfer Over Louver Fin Arrays," *Int. J. Heat Exchangers*, **11**, pp. 37–44.
- [21] Liu, J. S., Liu, M. S., Liaw, J. S., and Wang, J. S., 2001, "A Numerical Investigation Study of Louvered Fin-and-Tube Heat Exchangers Having Circular and Oval Tube Configuration," *Int. J. Heat Mass Transfer*, **44**, pp. 4235–4243.
- [22] Min, J. C., and Webb, R. L., 2001, "Numerical Prediction of Wavy Fin Coil Performance," *Enhanced Heat Transfer*, **8**, pp. 159–173.
- [23] Comini, G., and Groce, G., 2001, "Convective Heat and Mass Transfer in Tube-Fin Heat Exchangers Under Dehumidifying Conditions," *Numer. Heat Transfer, Part A*, **40**, pp. 5790–5799.
- [24] Hiroaki, K., Shinichi, I., Osamu, A., and Osao, K., 1989, "High-Efficiency Heat Exchanger," *National Technical Report*, **35**(6), pp. 653–661.
- [25] Guo, Z. Y., Li, D. Y., and Wang, B. X., 1998, "A Novel Concept for Convective Heat Transfer Enhancement," *Int. J. Heat Mass Transfer*, **41**, pp. 2221–2225.
- [26] Wang, S., Li, Z. X., and Guo, Z. Y., 1998, "Novel Concept and Devices of Heat Transfer Augmentation," *Proceedings of 11th International Conference of Heat Transfer*, Taylor & Francis, **5**, pp. 405–408.

- [27] Tao, W. Q., Guo, Z. Y., and Wang, B. X., 2002, "Field Synergy Principle for Enhancing Convective Heat Transfer—Its Extension and Numerical Verifications," *Int. J. Heat Mass Transfer*, **45**, pp. 3849–3856.
- [28] Tao, W. Q., He, Y. L., Wang, Q. W., Qu, Z. G., and Song, F. Q., 2002, "A Unified Analysis on Enhancing Convective Heat Transfer With Field Synergy Principle," *Int. J. Heat Mass Transfer*, **45**, pp. 4871–4879.
- [29] Tao, W. Q., and He, Y. L., 2002, "Field Synergy Principle and Its Applications in Enhancing Convective Heat Transfer and Improving Performance of Pulse Tube Refrigerators (Part 1)," *Journal of Xi'an Jiaotong University*, **36**(11), pp. 1101–1105.
- [30] He, Y. L., and Tao, W. Q., 2002, "Field Synergy Principle and Its Applications in Enhancing Convective Heat Transfer and Improving Performance of Pulse Tube Refrigerators (Part 2)," *Journal of Xi'an Jiaotong University*, **36**(11), pp. 1106–1110.
- [31] Tao, W. Q., 2001, *Numerical Heat Transfer*, 2nd ed. Xi'an Jiaotong University Press, Xi'an.
- [32] Patankar, S. V., 1980, *Numerical Heat Transfer and Fluid Flow*, McGraw-Hill, New York.
- [33] Tao, W. Q., 2000, *Recent Advances in Computational Heat Transfer*, Science Press, Beijing.
- [34] Orlanski, I., 1975, "A Simple Boundary Condition for Unbounded Hyperbolic Flows," *J. Comput. Phys.*, **21**, pp. 251–269.
- [35] Tsai, S. F., and Sheu, T. W. H., 1998, "Some Physical Insights Into a Two-Row Finned-Tube Heat Transfer," *Comput. Fluids*, **27**(1), pp. 29–46.
- [36] Tsai, S. F., Sheu, T. W. H., and Lee, S. M., 1999, "Heat Transfer in a Conjugate Heat Exchanger With a Wavy Fin Surface," *Int. J. Heat Mass Transfer*, **42**, pp. 1735–1745.
- [37] Li, P. W., and Tao, W. Q., 1994, "Effect of Outflow Boundary Condition on Convective Heat Transfer," *Warme-und-stoffubertragung*, **29**, pp. 463–470.
- [38] Tao, W. Q., Qu, Z. G., and He, Y. L., 2004, "A Novel Segregated Algorithm for Incompressible Fluid Flow and Heat Transfer Problems—Clear (Coupled and Linked Equations Algorithm Revised) Part I: Mathematical Formulation and Solution Procedure," *Numer. Heat Transfer, Part B*, **45**, pp. 1–17.
- [39] Tao, W. Q., Qu, Z. G., and He, Y. L., 2004, "A Novel Segregated Algorithm for Incompressible Fluid Flow and Heat Transfer Problems—Clear (Coupled and Linked Equations Algorithm Revised) Part II: Application Examples," *Numer. Heat Transfer, Part B*, **45**, pp. 19–48.
- [40] Shah, R. K., Afimiwala, K. A., and Mayne, R. W., 1978, "Heat Exchanger Optimization," *Proceedings of 6th Int. Heat Transfer Conference*, **4**, Hemisphere, pp. 185–191.
- [41] Huang, H. Z., and Tao, W. Q., 1993, "An Experimental Study on Heat/Mass Transfer and Pressure Drop Characteristics for Arrays of Non-Uniform Plate Length Positioned Obliquely to the Flow Direction," *ASME J. Heat Transfer*, **115**, pp. 568–575.
- [42] Webb, R. L., 1994, *Principles of Enhanced Heat Transfer*, John Wiley & Sons, New York, Chap. 3.

Second Law Based Optimization of Falling Film Single Tube Absorption Generator

S. Jani

M. H. Saidi

A. A. Mozaffari

Center of Excellence in Energy Conversion,
School of Mechanical Engineering,
Sharif University of Technology,
Tehran, Iran, P.O. Box. 11365-9567

The objective of this paper is to provide optimization of falling film LiBr solution on a horizontal single tube based on minimization of entropy generation. Flow regime is considered to be laminar. The effect of boiling has been ignored and wall temperature is constant. Velocity, temperature and concentration distributions are numerically determined and dimensionless correlations are obtained to predict the average heat transfer coefficient and average evaporation factor on the horizontal tube. Thermodynamic imperfection due to passing lithium bromide solution is attributed to nonisothermal heat transfer; fluid flow friction and mass transfer irreversibility. Scale analysis shows that the momentum and mass transfer irreversibilities can be ignored at the expense of heat transfer irreversibility. In the process of optimization, for a specified evaporation heat flux, the entropy generation accompanying the developed dimensionless heat and mass transfer correlations has been minimized and the optimal geometry and the optimum thermal hydraulic parameters are revealed. The investigation cited here indicates the promise of entropy generation minimization as an efficient design and optimization tool. [DOI: 10.1115/1.1795791]

Keywords: Absorption, Desorption, Film, Heat Transfer, Optimization, Second Law

Introduction

Falling film evaporation phenomenon which is used in the generators of absorption chillers has several advantages such as large heat transfer coefficient, low solution feed rate, small temperature difference and consequently usage of low-grade energy sources. Thermal hydraulic characteristics of this phenomenon have been investigated based on first law of thermodynamics by several researchers [1–4], but the state of the art is not well developed from the second law point of view, which is increasingly used the design and optimization of thermal systems in recent years. Entropy generation minimization technique emerged in engineering in the 1970s by Bejan [5] to optimize thermal hydraulic systems. Hirschfelder et al. [6] has derived a general formulation for the rate of irreversible production of entropy. Second law based optimization of a lithium bromide absorption chiller has been developed by Heydari et al. [7]. They have defined a second law energy efficiency for an absorption chiller and showed that the prevailing point of maximum performance coincides with the observed standard working states for the typical absorption chiller. Heydari and Jani [8] showed that based on entropy generation minimization method, a working condition for an automotive air conditioning system might be defined. Irreversible entropy generation for combined forced convection heat and mass transfer in a two dimensional channel was investigated by San et al. [9].

The aims of this paper are to model heat and mass transfer and to provide second law-based optimization of falling film LiBr solution on a horizontal tube commonly used in the generator of absorption chillers. The contribution of each process in total irreversibility of the system and optimal geometry and optimum thermal hydraulic parameters has been extracted.

Heat and Mass Transfer Modeling

A falling film impinging vertically on a horizontal smooth tube and moving symmetrically around the tube has been considered as

a model for investigation. Figure 1 shows the geometry of the proposed model. The following assumptions have been made in order to formulate the problem:

1. The fluid flow on the tube is laminar and hydro dynamically fully developed.
2. No shear stress exists at the vapor liquid interface.
3. Thermodynamic equilibrium achieves at the vapor liquid interface.
4. The heat transfer in the vapor phase can be neglected.
5. Tube wall is considered constant temperature.
6. The influence of mass diffusion on the temperature profile may be evaluated by two nondimensional groups as (π_1, π_2) [6]:

$$\pi_1 = \frac{M_2 D_{21} \Delta c}{\alpha \rho}; \quad (1)$$

$$\pi_2 = \frac{M_2 D_{21} \Delta c}{\alpha \rho} \left(\frac{T}{\Delta T} \right)$$

In general, for the case of coupled heat and mass transfer in the falling film LiBr solution, the two parameters in Eq. (1) become much less than unity and the mass diffusion has little effect on the temperature profile.

From the assumptions 1–6 mentioned above the velocity profile and thickness of falling film can be expressed as follows [3,4]:

$$u = \frac{\rho g}{2\mu} \sin(\theta) (2\delta y - y^2)$$

$$v = -\frac{g}{2\nu} y^2 \left[\frac{d\delta}{dx} \sin(\theta) + \frac{1}{r} \left(\delta - \frac{y}{3} \right) \cos(\theta) \right] \quad (2)$$

$$\delta = \left[\frac{3\nu\Gamma}{\rho g \sin(\theta)} \right]^{1/3}$$

The energy equation for the proposed model can be simplified to the following form:

Contributed by the Heat Transfer Division for publication in the JOURNAL OF HEAT TRANSFER. Manuscript received by the Heat Transfer Division September 11, 2002; revision received November 25, 2003. Associate Editor: V. P. Carey.

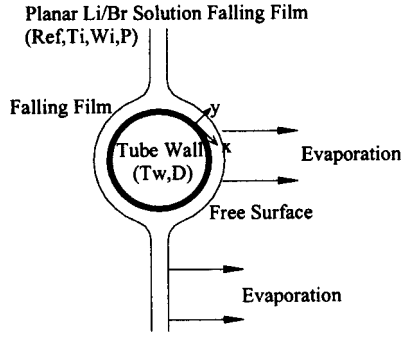


Fig. 1 Falling film thermal hydraulic parameters and geometry

$$u \frac{\partial T}{\partial x} + v \frac{\partial T}{\partial y} = \alpha \frac{\partial^2 T}{\partial y^2} \quad (3)$$

Similarly the mass transfer equation in terms of LiBr concentration is given by

$$u \frac{\partial w}{\partial x} + v \frac{\partial w}{\partial y} = D \frac{\partial^2 w}{\partial y^2} \quad (4)$$

The partial differential equations (3) and (4) is to be solved with the following boundary conditions:

$$\begin{aligned} T &= T_i, \quad w = w_i, \quad x = x_i, \quad 0 \leq y \leq \delta \\ T &= T_w, \quad \frac{dw}{dy} = 0, \quad x_i \leq x \leq x_o, \quad y = \delta \\ T_s &= f(p, w_s), \quad x_i \leq x \leq x_o, \quad y = \delta \\ M'' &= \frac{\rho D_{12}}{w_s} \frac{dw}{dy}, \quad x_i \leq x \leq x_o, \quad y = \delta \\ q_e'' &= k \frac{dT}{dy} = M'' h_{fg}, \quad x_i \leq x \leq x_o, \quad y = \delta \end{aligned} \quad (5)$$

In the above boundary conditions, temperature T_i is achievable from the saturation state at the entrance. Velocity, temperature and concentration distributions in the film having the governing equations (3) to (5) have been solved numerically and compared with the existing experimental data [4]. Based on the numerical results the following correlations for heat transfer coefficient and evaporation factor can be derived:

$$\begin{aligned} \frac{\bar{h} L_c}{k} &= a_1 \text{Re}_f^{a_2} \text{Pr}^{a_3} P^{a_4} \exp(a_5 w) (d/L_c)^{a_6} \\ EF &= b_1 \text{Re}_f^{b_2} \text{Pr}^{b_3} P^{b_4} \exp(b_5 \text{Re}_f) (d/L_c)^{b_6} (d_s/L_c)^{b_7} \end{aligned} \quad (6)$$

where

$$\begin{aligned} a_1 &= 0.7482, \quad a_2 = 0.17904, \quad a_3 = 0.26983, \quad a_4 = -0.02764, \\ a_5 &= 0.0032956, \quad a_6 = -0.43161 \\ b_1 &= 2.19445E-4, \quad b_2 = 0.59183, \quad b_3 = -0.81257, \\ b_4 &= 0.083305, \quad b_5 = -0.00706, \quad b_6 = 0.62828, \quad b_7 = 0.61664 \end{aligned}$$

It should be noted that thermodynamic properties are calculated at the mean value of saturation temperature of LiBr solution and wall temperature. The following are domains of applicability of the specified correlations

$$\begin{aligned} 7 &\leq \text{Pr} \leq 10 \\ 100 &\leq \text{Re}_f \leq 500 \\ 5 \text{ kPa} &\leq P \leq 10 \text{ kPa} \end{aligned} \quad (7)$$

$$50\% \leq w_i \leq 60\%$$

Deviation of heat transfer coefficient and evaporation factor in Eq. (6) from the numerical results is about 1.6 and 8%, respectively. The 8% deviation for the correlation of evaporation factor is due to nonlinear behavior of mass generation for the falling film mechanism.

Second Law Modeling

Stagnation and impingement zones are so called entrance region. Entropy generation at the entrance region can be neglected, as this region is so small compare to the overall domain of falling film. Entropy generation at the effective domain can be divided into three components, the first associates with the irreversibility due to nonisothermal heat transfer, the second is due to fluid friction and the third is due to mass transfer. The local entropy generation terms per unit volume in an incompressible Newtonian fluid have been derived [6]. The summary of entropy generation formulation is given as follows:

$$\dot{S}_g''' = \dot{S}_{g,h}''' + \dot{S}_{g,f}''' + \dot{S}_{g,m}''' \quad (8)$$

where

$$\begin{aligned} \dot{S}_{g,h}''' &= \frac{1}{T^2} \left[\left(\frac{\partial T}{\partial x} \right)^2 + \left(\frac{\partial T}{\partial y} \right)^2 \right] \\ \dot{S}_{g,f}''' &= \frac{\mu'}{T} \left\{ 2 \left[\left(\frac{\partial u}{\partial x} \right)^2 + \left(\frac{\partial v}{\partial y} \right)^2 \right] + \left[\left(\frac{\partial u}{\partial y} \right) + \left(\frac{\partial v}{\partial x} \right) \right]^2 \right\} \\ \dot{S}_{g,m}''' &= -\frac{1}{T} \left\{ \sum_{n=1}^2 j_{ni} \left[\left(\frac{\partial \mu_n}{\partial X_i} \right) + \bar{S}_n \left(\frac{\partial T}{\partial X_i} \right) - \frac{1}{M_n} B_i \right] \right\} \end{aligned} \quad (9)$$

where $\dot{S}_{g,h}'''$ is due to nonisothermal heat transfer, $\dot{S}_{g,f}'''$ is due to fluid friction and $\dot{S}_{g,m}'''$ is due to irreversibility associated with the simultaneous mass transfer and the coupling between heat and mass transfer.

The diffusion-thermo effect or ‘‘Dufour effect’’ and thermo-diffusion effect or ‘‘Soret effect’’ has been ignored in this research. Taking into consideration the fact that the chemical potential depends on the T , P , X_j and knowing that

$$\bar{S}_n = \left(\frac{\partial \mu_n}{\partial T} \right)_{P, X_j} \quad \text{and} \quad \bar{V}_n = \left(\frac{\partial \mu_n}{\partial p} \right)_{T, X_j} \quad (10)$$

Then the production of entropy associated with mass transfer diffusion in y -direction and coupling between heat and mass transfer is given as

$$\dot{S}_{g,m}''' = -\frac{1}{T} \left\{ \sum_{j \neq n}^2 j_{ny} \left[\frac{1}{M_n} \left(\frac{\partial \mu_n}{\partial X_j} \right) \left(\frac{\partial X_j}{\partial y} \right) + \frac{\bar{V}_n}{M_n} \left(\frac{\partial p}{\partial y} \right) - \frac{1}{M_n} B_y \right] \right\} \quad (11)$$

The diffusive contribution of LiBr concentration in the peripheral direction and the pressure difference across the thickness of falling film is negligible. Applying the Gibbs-Duhem relation, for a binary system Eq. (11) is reduced to

$$\dot{S}_{g,m}''' = -\frac{j_{2y}}{T} \frac{M}{M_1 M_2 (1 - X_2)} \frac{\partial \mu_2}{\partial X_2} \bigg|_{T,P} \frac{dX_2}{dy} \quad (12)$$

where j_{2y} is the mass flux of LiBr which is defined as

$$j_{2y} = -\frac{c^2}{\rho} M_1 M_2 D_{21} \frac{dX_2}{dy} \quad (13)$$

Substituting Eq. (13) into Eq. (12)

$$\dot{S}_{g,m}''' = \frac{c^2}{\rho} \frac{D_{21}}{T} \frac{M}{(1 - X_2)} \frac{\partial \mu_2}{\partial X_2} \bigg|_{T,P} \left(\frac{dX_2}{dy} \right)^2 \quad (14)$$

Based on the formulation of the chemical potential [10]

$$\mu_2 = 2\bar{R}T \times \ln\left(\frac{55.5\gamma X_2}{1-X_2}\right) + \mu_2^0 \quad (15)$$

Differentiating Eq. (15) with respect to X_2 , substituting into Eq. (12) and rearranging the result in terms of w_2 , we have

$$\dot{S}_{g,m}''' = \frac{2D_{21}\bar{R}}{M_2} \frac{1}{w_2(1-w_2)^2} \left(\frac{dw_2}{dy}\right)^2 \quad (16)$$

where M_2 being the molecular weight of LiBr is 86.86 kg/kmole.

The result is the rate of local entropy generation in a two-dimensional falling film flow over a horizontal tube with the LiBr diffusing in the y -direction which can be expressed as

$$\begin{aligned} \dot{S}_g''' = & \frac{1}{T^2} \left[\left(\frac{\partial T}{\partial x}\right)^2 + \left(\frac{\partial T}{\partial y}\right)^2 \right] + \frac{\mu'}{T} \left\{ 2 \left[\left(\frac{\partial u}{\partial x}\right)^2 + \left(\frac{\partial v}{\partial y}\right)^2 \right] \right. \\ & \left. + \left[\left(\frac{\partial u}{\partial y}\right) + \left(\frac{\partial v}{\partial x}\right) \right]^2 \right\} + \frac{2D_{21}\bar{R}\rho}{M_2 w_2 (1-w_2)^2} \left(\frac{dw_2}{dy}\right)^2 \quad (17) \end{aligned}$$

Scale Analysis

The following considerations can be derived from scale up analysis in the falling film domain of LiBr solution

$$x \approx s, \quad y \approx \delta, \quad u \approx U_{\max}, \quad \delta \ll s \quad (18)$$

where δ is the order of falling film thickness in the tube radial direction. The order of magnitude analysis of each term in entropy generation associated with fluid flow friction can be expressed as

$$\frac{\mu'}{T} \left[2 \left(\frac{U_{\max}}{s}\right)^2, 2 \left(\frac{v}{\delta}\right)^2, \left(\frac{U_{\max}}{\delta}\right)^2, \left(\frac{v}{s}\right)^2, 2 \left(\frac{U_{\max}}{\delta}\right) \left(\frac{v}{s}\right) \right] \quad (19)$$

From scale analysis of continuity equation it is revealed that

$$v \approx \frac{\delta}{s} U_{\max} \quad (20)$$

Substituting Eq. (20) into Eq. (19)

$$\frac{\mu'}{T} \left[2 \left(\frac{U_{\max}}{s}\right)^2, 2 \left(\frac{U_{\max}}{s}\right)^2, \left(\frac{U_{\max}}{\delta}\right)^2, \left(\frac{\delta U_{\max}}{s^2}\right)^2, 2 \left(\frac{U_{\max}}{\delta}\right) \left(\frac{v}{s}\right) \right] \quad (21)$$

In Eq. (21), at the expense of the third term, the rest of terms can be neglected. Invoking the same scaling methodology for entropy generation due to nonisothermal heat transfer, $(\partial T/\partial x)^2$ term can be neglected at the expense of the $(\partial T/\partial y)^2$.

Finally the local entropy generation Eq. (17) is reduced to

$$\dot{S}_g''' = \frac{1}{T^2} \left(\frac{\partial T}{\partial y}\right)^2 + \frac{\mu'}{T} \left(\frac{\partial u}{\partial y}\right) + \frac{2D_{21}\bar{R}\rho}{M_2 w_2 (1-w_2)^2} \left(\frac{dw_2}{dy}\right)^2 \quad (22)$$

Total Entropy Generation

Total entropy generation per unit length of the tube can be expressed as

$$\begin{aligned} \dot{S}_g' = & \int \int_{\sigma} \frac{1}{T^2} \left(\frac{\partial T}{\partial y}\right)^2 d\sigma + \int \int_{\sigma} \frac{\mu'}{T} \left(\frac{\partial u}{\partial y}\right) d\sigma \\ & + \int \int_{\sigma} \frac{2D_{21}\bar{R}\rho}{M_2 w_2 (1-w_2)^2} \left(\frac{dw_2}{dy}\right)^2 d\sigma \quad (23) \end{aligned}$$

which σ is the cross sectional area of the falling film perpendicular to tube wall. Considering that LiBr concentration profile penetrate only a short distance into the falling film [11], then the total entropy generation contributed to the mass transfer becomes small

in comparison with that associated with heat transfer. The relative magnitude of the three entropy generation terms in Eq. (23) is obtained by comparing the mass diffusion and the fluid flow effects on heat transfer. It can be verified that the fluid flow and the mass transfer total entropy generation can be neglected at the expense of the heat transfer, which will be shown later on in the results. Then the total entropy generation per unit length is reduced to

$$\dot{S}_g' = \int \int_{\sigma} \frac{1}{T^2} \left(\frac{\partial T}{\partial y}\right)^2 d\sigma \quad (24)$$

Applying vector calculus and divergence theorem [12], Eq. (24) can be expressed as

$$\dot{S}_g' = \int_0^{\pi R} \frac{-q_w''}{T_w} ds + \int_0^{\pi R} \frac{q_e''}{T_s} ds + \int_0^{\delta} \frac{ku}{\alpha} \ln\left(\frac{T_m}{T_i}\right) dy \quad (25)$$

The first two terms at RHS are associated with heat conduction and the last term is associated with heat convection entropy generation. Using the mean value of free surface temperature, T_{sav} , then

$$\dot{S}_g' = \frac{-q_w'}{T_w} + \frac{q_e'}{T_{s,av}} + \frac{Re_f Prk}{4} \ln\left(\frac{T_{o,av}}{T_i}\right) \quad (26)$$

Optimization

Heat and mass transfer and entropy generation are changed with the variations of the geometry and thermal hydraulic parameters such as film Reynolds number, inlet concentration, system pressure and temperature difference between wall surface and inlet solution. In the process of optimization the objective is to minimize the total entropy generation for a specified evaporation heat flux at free surface and to meet all side constraints of thermal and hydraulic parameters. The final constrained optimization formulation can be expressed as follows:

$$\begin{aligned} \dot{S}_g' = & \frac{-q_w'}{T_w} + \frac{q_e'}{T_{s,av}} + \frac{Re_f Prk}{4} \ln\left(\frac{T_{o,av}}{T_i}\right) \\ & q_w' = \bar{h} \pi R (T_w - T_i) \quad (27) \end{aligned}$$

whereas \dot{S}_g' should be minimized subject to

$$\begin{aligned} q_e' - q_{ep}' &= 0 \\ q_e' &= EF \times q_w' \\ 80 &\leq Re_f \leq 550 \\ \% 50 &\leq w_i \leq \% 60 \\ 5 \text{ kPa} &\leq P \leq 10 \text{ kPa} \\ 5 \text{ K} &\leq T_w - T_i \leq 30 \text{ K} \\ 10 \text{ mm} &< d < 50 \text{ mm} \end{aligned}$$

The augmented Lagrange multiplier method is used to solve the constrained optimization Eq. (27).

Results

The comparison of correlated heat transfer coefficient and evaporation factor with those of the numerical results has been shown in Figs. 2 and 3, respectively. The correlated heat and mass transfer coefficient and evaporation factor well satisfy the numerical data with reasonable RMS.

The three terms of local entropy generation at a cross sectional area perpendicular to tube wall is shown in Fig. 4. The entropy generation due to heat transfer and fluid flow friction decreases from wall to free surface while the entropy generation due to mass transfer increases.

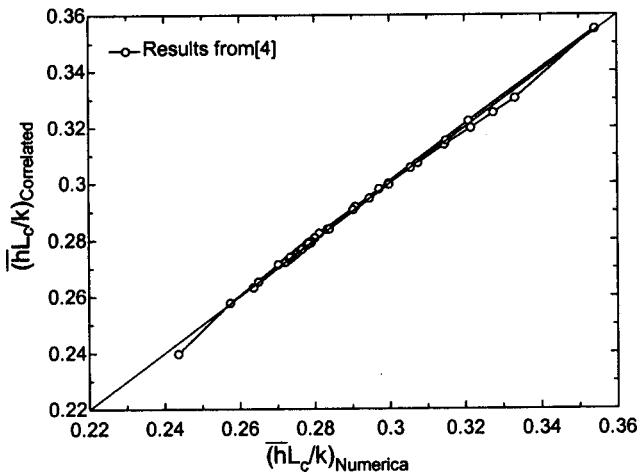


Fig. 2 Comparison of numerical and correlated average Nusselt number over a horizontal tube [4]

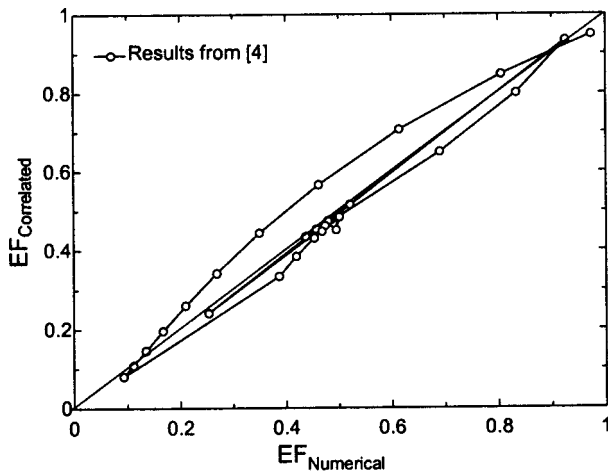


Fig. 3 Comparison of numerical and correlated average evaporation factor over a horizontal tube [4]

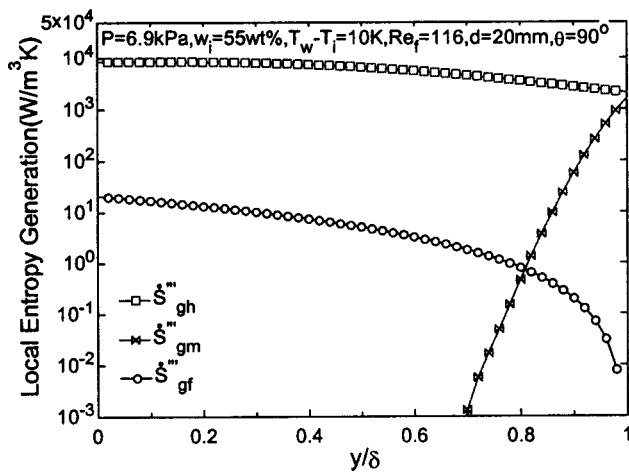


Fig. 4 Local entropy generation components at film cross section

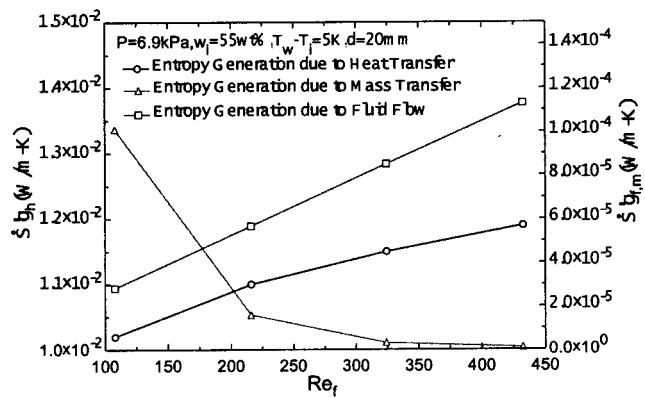


Fig. 5 Comparison of total entropy generation component as a function of film Reynolds number

Figure 5 represents the comparison between total entropy generation of nonisothermal heat transfer, fluid flow friction and mass transfer as a function of film Reynolds number. The nonisothermal contribution is much more than the two others. Although the local mass transfer irreversibility is the same as heat transfer contribution, but as the penetration of LiBr concentration into the falling film is relatively small, so that the heat transfer is dominant.

The results of optimization process are shown in Fig. 6. In the process of optimization for any fixed geometry and specified evaporation heat flux, the optimal thermal and hydraulic parameters are achievable based on entropy generation minimization.

Figure 6 shows the minimum entropy generation trends for specified evaporation heat fluxes as a function of tube diameter. In the range of low evaporation heat fluxes the minimum entropy generation increases with increasing the tube diameter whereas at high evaporation heat fluxes the minimum entropy generation decreases with increasing tube diameter. The minimum entropy generation has fluctuating behavior for a moderate evaporation heat flux. The optimum thermal hydraulic parameters as a function of evaporation heat flux are shown in Fig. 7. The optimum condition for degree of superheating temperature and inlet concentration increases with increasing evaporation heat flux where as the optimum film Reynolds number and system pressure decreases with increasing the evaporation heat flux.

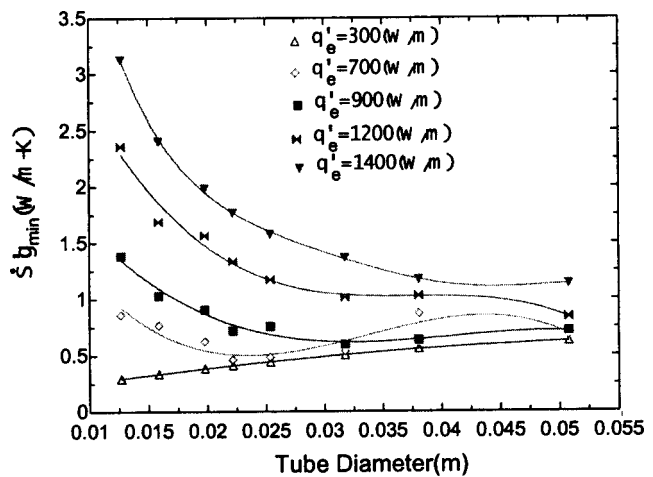


Fig. 6 Minimum entropy generation as a function of tube diameter

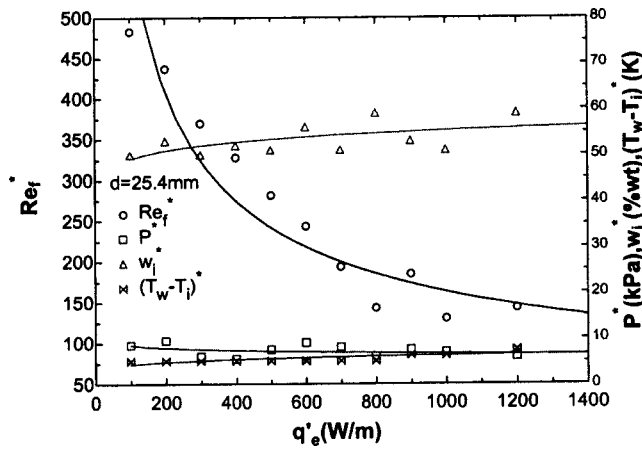


Fig. 7 Variation of optimum thermal hydraulic parameters as a function of free surface evaporation heat transfer

Conclusion

Second-law and thermal hydraulic modeling of planar, laminar falling film LiBr solution over a horizontal tube has been investigated in this research. The process of optimization is followed based on the entropy generation minimization for any specified evaporation heat flux and in the range of thermal hydraulic parameters. Scale analysis shows that irreversibility of nonisothermal heat transfer dominants in comparison with the fluid flow friction and mass transfer. Optimization shows that in the range of low-grade evaporation heat fluxes, using smaller tube diameter have more advantages and vice versa. However, in the range of low evaporation heat fluxes the film Reynolds number and system pressure must be as small as possible and the inlet concentration and inlet degree of superheating must be as high as possible and vice versa.

Nomenclature

- B = Body force [N/m^3]
- c = Molar concentration [$kmol/m^3$]
- D = Mass diffusivity [m^2/s]
- d = Tube diameter [m]
- d_s = Vertical tube spacing [m]
- EF = Evaporation factor [q''_g/q''_w]
- g = Gravity constant [m/s^2]
- h = Average heat transfer coefficient [W/m^2-K]
- h_{fg} = Latent heat of evaporation [kJ/kg]
- j = Mass flux [kg/m^2-s]
- k = Fluid thermal conductivity [$W/m-K$]
- L_c = Characteristics length [$(\nu^2/g)^{1/3}$] [m]
- LiBr = Lithium bromide
- M = Molecular weight [$kg/kmol$]
- M'' = Evaporative mass flux [kg/m^2-s]
- P = System pressure [kPa]
- Pr = Prandtl number
- q = Heat flow [W]
- R = Gas constant [$kJ/kmol-K$]
- r = Tube radius [m]
- Re_f = Film Reynolds number ($4\Gamma/\mu$)
- \dot{S}_g = Rate of entropy generation [$W/kg-K$]
- S = Entropy [$kJ/kg-K$]
- s = Half of tube perimeter [m]
- T = Temperature [K]
- u = Peripheral velocity [m/s]

- v = Normal velocity [m/s]
- V = Partial volume
- w = LiBr concentration [wt%]
- x = Peripheral coordinate [m]
- X = Mole fraction
- y = Normal coordinate [m]

Greek letter

- α = Thermal diffusivity [m^2/s]
- δ = Falling film thickness [m]
- γ = Chemical activity
- Γ = LiBr solution flow rate per unit length per one side of tube [$kg/m-s$]
- μ' = Fluid dynamic viscosity [$Pa-s$]
- μ = Chemical potential [$kJ/kmol$]
- ν = Fluid kinematics viscosity [m^2/s]
- θ = Angular position
- ρ = Density [kg/m^3]

Subscript

- av = Average value
- e = Evaporation
- f = Fluid flow friction
- h = Heat transfer
- i = Direction, Inlet condition
- $j, n, 1, 2,$ = Component $j, n, 1, 2, 3$
- m = Mass transfer
- w = Wall
- o = Outlet condition
- s = Saturation state

Superscript

- ' = Per unit length
- " = Per unit area
- ''' = Per unit volume
- = Per unit mole
- * = Optimum condition
- 0 = Reference state

References

- [1] Kocamustafaogullari, G., and Chen, I. Y., 1988, "Falling Film Heat Transfer Analysis on a Bank of Horizontal Tube Evaporator," *AICHE J.*, **34**(9), pp. 1539–1549.
- [2] Wang, C. Q., Lu, Z., Li, D. Q., Yu-CHI, B., and Sun, Y. G., 1995, "Heat and Mass Transfer in Falling Film Generator of LiBr Absorption Refrigeration Machine," *Proceeding of 19th International Congress of Refrigeration*, Vol. IIIa, pp. 209–214.
- [3] Kim, D. K., and Kim, M. H., 1999, "Heat Transfer Enhancement Characteristics for Falling Film Evaporation on Horizontal Enhanced Tubes With Aqueous LiBr Solution," *J. Enhanced Heat Transfer*, **16**(1), pp. 66–69.
- [4] Jani, S., Saidi, M. H., Mozafari, A., and Heydari, A., 2004, "Modeling of Heat and Mass Transfer in Falling Film Absorption Generators," *Scientia Iranica*, **11**(1&2), 81–91.
- [5] Bejan, A., 1995, *Entropy Generation Minimization*, CRC Press, p. 47.
- [6] Hirschfelder, J. O., Curtiss, F. C., and Bird, R. B., 1954, *Molecular Theory of Gases and Liquids*, Wiley, New York, p. 700.
- [7] Heydari, A., Babadi, F., Jani, S., and Bafkar, R., 2000, "Second Law Based Thermodynamics Analysis of a Lithium Bromide Absorption Chiller," *Proceeding of 4th International and 8th Annual Conference of Iranian Society of Mechanical Engineers*, **3**, pp. 403–408.
- [8] Heydari, A., and Jani, S., 2001, "Entropy-Minimized Optimization of an Automotive Air Conditioning and HVAC System," *SAE Technical Paper Series*, 2001-01-0592.
- [9] San, J. Y., Worek, W. M., and Lavan, Z., 1987, "Entropy Generation in Combined Heat and Mass Transfer," *Int. J. Heat Mass Transfer*, **30**(7), pp. 1359–1369.
- [10] Chandra, P. G., and Sharma, C. P., "Entropy Values of Lithium Bromide-Water Solution and Their Vapors," *ASHRAE Trans.*, **2404**, pp. 35–46.
- [11] Vanderplaats, G. N., 1987, *Numerical Optimization Techniques for Engineering Design*, McGraw-Hill, p. 140.
- [12] Marsden, J. E., and Tromba A. J., 1996, *Vector Calculus*, Freeman Company.

Free Surface Flow in High Speed Fiber Drawing With Large-Diameter Glass Preforms

Zhiyong Wei

e-mail: gte384w@prism.gatech.edu

Kok-Meng Lee*

e-mail: kokmeng.lee@me.gatech.edu

The George W. Woodruff School of Mechanical Engineering, Georgia Institute of Technology, Atlanta, GA 30332-0405

Serge W. Tchikanda

Sandia National Laboratories, MS 9161, 7011 East Ave, Livermore, CA 94550

Zhi Zhou

e-mail: zhizhou@ofsoptics.com

Siu-Ping Hong

e-mail: shong@ofsoptics.com

OFS, Norcross, GA 30071

This paper presents a complete two-dimensional (2D) thermo-fluid model for predicting the neck-down shape in the fiber drawing process. This model uses the controlled draw tension to calculate the Neumann boundary condition at the furnace exit; thus, it does not require specifying the speed (or diameter) of the fiber as most previous studies did. The model presented here can be applied to optimization of the high-speed draw process with large-diameter preforms. In this study, the radiative transfer equation is directly solved for the radiation fluxes using the discrete ordinate method coupled with the solution of the free surface flow, which does not assume that the glass is optically thick and does not neglect the glass absorption at the short-wavelength band. The artificial compressibility method is used to solve the Navier-Stokes equations. A staggered-grid computation scheme that is shown to be efficient and robust was used to reduce the computation load in solving the complete 2D model. The neck-down profile of a large preform (9 cm dia) drawn at a relatively high speed of 25 m/s was experimentally measured. The measured profile well matches that derived numerically. Results also show that the free surface calculated using the Dirichlet boundary condition deviates considerably from the measured profile, particularly near the furnace exit where the actual diameter (and, hence, the speed of the glass) is essentially unknown. Although the difference between the numerical results obtained from the full and semi-2D models was small, this difference could be significant if the location at which the glass converges to 125 μm dia is of interest, especially when the preform has a large diameter drawn at a high speed.

[DOI: 10.1115/1.1795237]

1 Introduction

A number of industrial processes, such as Czochralski crystal growth, VAD preform stretching, and optical fiber drawing, involve free surface flow coupled with complex radiative transfer in semitransparent materials. In manufacturing optical fibers, difficulties in making practical measurements in the furnace domain of the drawing process have motivated manufacturers to look for numerical tools to facilitate the design of new processes for drawing optical fibers at high speed from large-diameter preforms (glass rod). Significant efforts have been directed toward the modeling of a fiber-drawing process for the past three decades. Most of the existing models assume a Dirichlet boundary condition (DBC) at the furnace exit. This formulation is valid for drawing small-diameter preform as long as the glass fiber solidifies within the furnace. As larger preforms are drawn at higher speeds, the fiber diameter (or speed) at the furnace exit is essentially unknown because the glass often freezes into fiber well outside the furnace.

An accurate analytical prediction of the free surface being drawn is challenging in that the momentum and energy equations characterizing the drawing process are strongly coupled and nonlinear due to the highly temperature-dependent viscosity of the glass and the effects of the radiative heat transfer. During the late 1970s and the 1980s, various aspects of the optical fiber-draw problems were studied by a number of researchers, which include Paek and Runk [1], Homsy and Walker [2], Myers [3], and Vasiljev et al. [4]. These studies primarily focused on one-dimensional (1D) models for drawing fibers from small-diameter preforms at a relatively slow speed.

Radiative transfer is the dominant mode of heat transfer in the fiber-draw process. In [2], it was found that the Rosseland diffu-

sion (optically thick medium) assumption would fail at the surface—an assumption commonly used in many early studies due to its simplicity in solving the radiative transfer in the semi-transparent glass. Wei et al. [5] confirmed this finding in a study of radiative transfer modeling on a moving glass rod. They also numerically solved the radiative transfer equation (RTE) using the discrete ordinate method (DOM) to predict the temperature gradient built up during transient. In addition, their analysis showed that the glass absorption coefficient in the short-wavelength band cannot be neglected and proposed a modified band model that includes the glass absorption at short-wavelengths. However, only combined radiation and conduction with relatively simple geometry (concentric, uniform glass rods) were considered.

The desire to improve productivity has motivated researchers to develop a 2D model that is more accurate for drawing of large-diameter preforms at high speeds. Among these, Lee and Jaluria [6] and Choudhury and Jaluria [7] assumed a free-surface profile in the calculation to solve for the velocity and temperature field. Using intermediate free-surface profiles, Choudhury et al. [8] solved the 2D stream-vorticity governing equations, where a small-diameter preform of 1.2576 cm drawn at a relatively slow speed of 3 m/s was considered. Xiao and Kaminski [9] attempted to solve the 2D conjugate problem of glass and gas flow with free interface using the commercial finite-element code FIDAP. They found it difficult to obtain convergence (that was sensitive to the deformation mesh) as the number of radiative macrosurfaces increased. More recently, Yin and Jaluria [10] and Cheng and Jaluria [11] investigated the effects of process parameters on high-speed fiber drawing (up to 20 m/s).

For drawing large-diameter preforms at high speeds, it was found that the computed glass temperatures were well above the glass melting point at the furnace exit. This may imply that the glass cools to form a solid fiber after leaving the furnace and thus, the actual diameter and speed of the glass at the furnace exit are essentially unknown. In order to address some of the abovementioned

*Corresponding author.

Contributed by the Heat Transfer Division for publication in the JOURNAL OF HEAT TRANSFER. Manuscript received by the Heat Transfer Division September 23, 2003; revision received May 24, 2004. Associate Editor: C. P. Grigoropoulos.

tioned problems encountered in simulating the free-surface profile of melting glass in the furnace domain, we offer the following in this paper:

1. A complete 2D numerical model is presented for solving the neck-down shape of melting glass in the furnace domain, which does not require specifying a value to the glass speed. Instead, a Neumann boundary condition (NBC) at the furnace exit is assigned, where the velocity gradient can be more practically computed from the controlled draw tension. The model presented here can be applied to optimization of the high-speed draw process with large-diameter preforms.
2. This represents the first attempt to solve the RTE directly using DOM for the radiation intensities in the problem of predicting the neck-down shape of a fiber-draw process. The solution does not assume that the glass is optically thick and does not neglect the glass absorption at the short-wavelength band. More specifically, we extend our earlier work [5] to solve the full coupled 2D problem involving the combined radiation and conduction with viscous flow in the melting glass with an unknown free surface.
3. This paper introduces a robust and efficient computation scheme to solve for the free-surface flow in fiber-draw process based on the use of staggered grids. This staggered-grid scheme guarantees strict energy conservation and as a result, a much smaller grid number than those used in the previous studies is needed for a specified preform diameter. In addition, the explicit boundary condition of the pressure is not required at the free surface for this grid.
4. The numerical model presented here has been experimentally validated. Unlike previous studies [1] and [8], where comparisons were made against experimental data obtained for a small-diameter preform (1 cm) drawn at a slow speed (1 m/s), we compare our numerical prediction against an experimentally measured neck-down profile for a large preform of 9 cm in diameter drawn at a high speed of 25 m/s. As will be shown, both the numerical results and experimental data are in excellent agreement.

2 Analysis

Figure 1 shows the melting of a fused-silica glass rod (preform) with free surface inside the cylindrical furnace and the subsequent cooling inside a postchamber. The interest here is to solve for the geometry of the neck-down shape so that the glass radius at the furnace exit can be determined. For this purpose, a complete 2D model is developed for the furnace-draw process. The following assumptions are made in the formulation:

1. The system is axisymmetric and two-dimensional. Only the furnace domain is considered, where the furnace walls are gray and diffuse.
2. The glass flow is Newtonian and incompressible. The glass is semitransparent to radiation in the spectral range $0 < \lambda < 5 \mu\text{m}$ and is almost opaque beyond $5 \mu\text{m}$. The scattering of radiation can be neglected (Viskanta [12]). The glass refractive index is uniform and does not depend on temperature.
3. The inner and outer surfaces at the glass interface are treated as diffuse for the radiation reflection and transmission. This assumption is based on the fact that the surface of the melting preform may undergo wavy hydrodynamic instabilities with magnitude in the order-of-radiation wavelengths.

2.1 Fluid Dynamic Model. The 2D fluid dynamic governing equations for the glass flow, which include the continuity, Navier-Stokes, and energy equations, are given below in the cylindrical coordinates (r, z) system [13]:

$$\frac{1}{r} \frac{\partial}{\partial r} (r\rho u) + \frac{\partial}{\partial z} (\rho v) = 0 \quad (1)$$

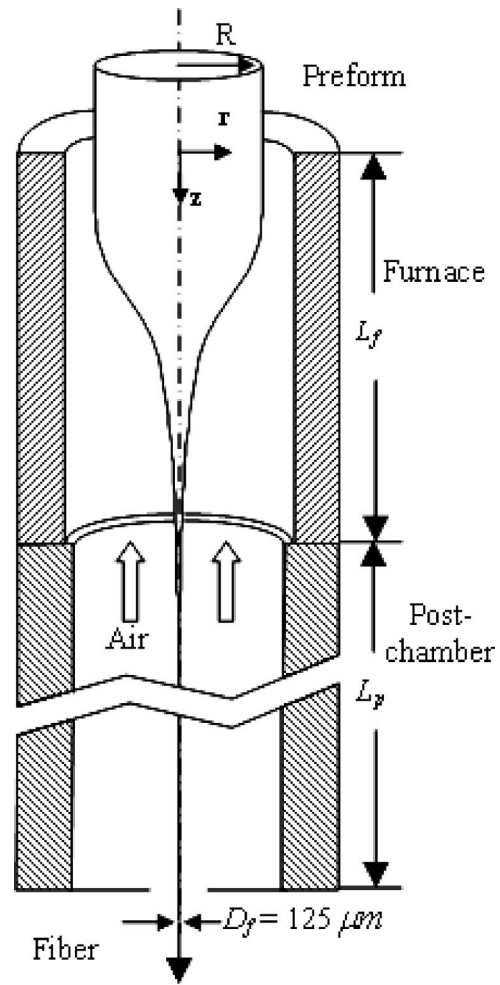


Fig. 1 Schematic of free-surface flow in the furnace and post-chamber

$$\rho \frac{\partial u}{\partial t} + \rho u \frac{\partial u}{\partial r} + \rho v \frac{\partial u}{\partial z} = -\frac{\partial p}{\partial r} + \frac{1}{r} \frac{\partial}{\partial r} \left(2\mu r \frac{\partial u}{\partial r} \right) - 2\mu \frac{u}{r^2} + \frac{\partial}{\partial z} \left[\mu \left(\frac{\partial u}{\partial z} + \frac{\partial v}{\partial r} \right) \right] \quad (2)$$

$$\rho \frac{\partial v}{\partial t} + \rho u \frac{\partial v}{\partial r} + \rho v \frac{\partial v}{\partial z} = -\frac{\partial p}{\partial z} + \frac{1}{r} \frac{\partial}{\partial r} \left[\mu r \left(\frac{\partial u}{\partial z} + \frac{\partial v}{\partial r} \right) \right] + \frac{\partial}{\partial z} \left(2\mu \frac{\partial v}{\partial z} \right) + \rho g \quad (3)$$

$$\rho C_p \left(\frac{\partial T}{\partial t} + u \frac{\partial T}{\partial r} + v \frac{\partial T}{\partial z} \right) = \frac{1}{r} \frac{\partial}{\partial r} \left(kr \frac{\partial T}{\partial r} \right) + \frac{\partial}{\partial z} \left(k \frac{\partial T}{\partial z} \right) - \nabla \cdot \mathbf{q}_R + \mu \Phi \quad (4)$$

where

$$\Phi = 2 \left[\left(\frac{\partial u}{\partial r} \right)^2 + \left(\frac{u}{r} \right)^2 + \left(\frac{\partial v}{\partial z} \right)^2 \right] + \left(\frac{\partial u}{\partial z} + \frac{\partial v}{\partial r} \right)^2$$

and \mathbf{q}_R is the radiation heat flux in the participating glass media, the solution of which will be described in Section 2.2. Other symbols in the above equations are defined in the Nomenclature.

The artificial compressibility method (ACM) [14] is used to solve the pressure-velocity coupled Navier-Stokes equations nu-

merically in the glass domain. An artificial time derivative of the pressure is added to the continuity equation as follows:

$$\frac{\partial p}{\partial \tilde{t}} + a \left[\frac{1}{r} \frac{\partial}{\partial r} (ru) + \frac{\partial v}{\partial z} \right] = 0 \quad (5)$$

where \tilde{t} is a fictitious time and a is the artificial compressibility factor.

The full 2D fluid dynamic model has five variables to solve; u , v , p , R , and T . The momentum and energy equations are strongly coupled because the viscosity of the glass changes by several orders of magnitude with temperature. Furthermore, the energy equation is highly nonlinear due to the radiative heat transfer between the furnace and the glass. The coupled equations (2)–(5) are solved numerically along with the following boundary conditions.

Since the system is axisymmetric, we have along the centerline or at

$$r=0, \quad u=0, \quad \frac{\partial v}{\partial r}=0, \quad \frac{\partial T}{\partial r}=0 \quad (6)$$

At the furnace inlet or at

$$z=0, \quad u=0, \quad v=v_{in}, \quad \frac{\partial^2 T}{\partial z^2}=0, \quad R=R_p \quad (7)$$

where v_{in} is the feed rate and R_p is the preform radius. The glass temperature is extrapolated at the furnace inlet since no significant differences were found in the simulations even when a more detailed temperature boundary condition was modeled.

The boundary conditions at the free surface are as follows:

$$\text{Normal force balance: } p_g - p_a + \zeta \kappa = 2\mu_g \left. \frac{\partial V_n}{\partial n} \right|_g - 2\mu_a \left. \frac{\partial V_n}{\partial n} \right|_a \quad (8)$$

$$\text{Tangential force balance: } \mu_g \left. \frac{\partial V_t}{\partial n} \right|_g = \mu_a \left. \frac{\partial V_t}{\partial n} \right|_a \approx 0 \quad (9)$$

$$\text{Net heat flux continuity: } -k_g \left. \frac{\partial T}{\partial n} \right|_g = q_{rad,opa} + q_{conv} \quad (10)$$

$$\text{Kinematic condition: } \frac{\partial R}{\partial t} + v \frac{\partial R}{\partial z} - u = 0 \quad (11)$$

where ζ is the surface tension and κ is the surface curvature; V_n and V_t are the normal and tangential components of the velocity at the interface; n is the magnitude of the normal vector; $q_{rad,opa}$ is the net radiation heat flux in the opaque band; q_{conv} is the natural convection heat flux from the air; the subscripts g and a denote the glass and air, respectively; and R is the radius of the glass, which is a function of z . In Eq. (8), the surface tension and the normal stress of the air can be neglected because they are several orders smaller than the other terms; p_a is set to 0 as a reference. Equations (8)–(11) can be used as the boundary conditions for variables u , v , T , and $R(z)$, respectively.

At the furnace exit, the glass temperature is extrapolated, as the downstream temperature of the glass outside the furnace does not have considerable effect on the upstream temperature of the glass

$$\text{at } z=L_f, \quad \frac{\partial u}{\partial z}=0, \quad \frac{\partial^2 T}{\partial z^2}=0 \quad (12)$$

In addition, we use the NBC for the axial velocity (instead of assuming an arbitrary value for the glass velocity at the furnace exit; often, the value of the specified fiber draw speed is used in published literature). The NBC can be obtained from the elongation model for the draw tension [1]:

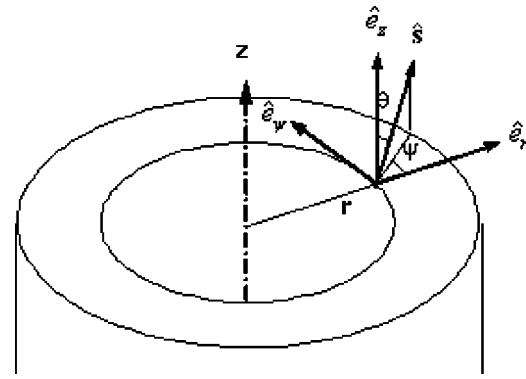


Fig. 2 Intensity orientation vector in the 2D axisymmetric cylindrical coordinates system

$$\text{at } z=L_f, \quad \frac{dv}{dz} = \frac{F_t}{3\mu\pi R_{L_f}^2} \quad (13)$$

where F_t is the specified draw tension on the fiber. It is worth noting that the glass may not reach the specified diameter at the furnace exit; thus, the glass velocity at the furnace exit is often an unknown. On the other hand, the value of the draw tension F_t can be measured and controlled immediately after the postchamber. Because the glass diameter is very small after it exits the furnace, its inertia and gravitational effects between the furnace exit and the tension measuring point are negligible in Eq. (13). The glass radius at the furnace exit R_{L_f} is known once the free surface is determined.

2.2 Radiation Model. The energy equation requires the divergence of the radiation heat flux \mathbf{q}_R that can be obtained by

$$\nabla \cdot \mathbf{q}_R = \int_0^\infty \left[4\pi\kappa_\lambda n_\lambda^2 I_{b\lambda}(T) - \kappa_\lambda \int_{\Omega=4\pi} I_\lambda(\mathbf{r}, \mathbf{s}) d\Omega \right] d\lambda \quad (14)$$

where the spectral radiative intensity $I_\lambda(\mathbf{r}, \mathbf{s})$ is a function of the position vector \mathbf{r} , orientation vector \mathbf{s} , and wavelength λ ; $I_{b\lambda}(T)$ is the spectral intensity of a blackbody radiation given by Planck's function; κ_λ is the spectral absorption coefficient. The radiative intensity is obtained by solving the RTE:

$$\frac{\alpha}{r} \frac{\partial (rI_\lambda)}{\partial r} - \frac{1}{r} \frac{\partial (\gamma I_\lambda)}{\partial \psi} + \beta \frac{\partial I_\lambda}{\partial z} = \kappa_\lambda [I_{b\lambda}(T) - I_\lambda] \quad (15)$$

where $(\alpha, \gamma, \beta) = (\sin \theta \cos \psi, \sin \theta \sin \psi, \cos \theta)$ describes the direction cosines of the orientation vector \mathbf{s} ; and θ and ψ are defined in Fig. 2.

Due to the arbitrary change of the free interface, Eq. (15) is cast into the fully conservative form in a general curvilinear coordinate system (η, ξ)

$$\begin{aligned} & \frac{\partial [rG(\alpha\eta_r + \beta\eta_z)I_\lambda]}{\partial \eta} + \frac{\partial [rG(\alpha\xi_r + \beta\xi_z)I_\lambda]}{\partial \xi} - G \frac{\partial (\gamma I_\lambda)}{\partial \psi} \\ & = \kappa_\lambda rG [n_\lambda^2 I_{b\lambda}(T) - I_\lambda] \end{aligned} \quad (16)$$

where (η_r, η_z) and (ξ_r, ξ_z) are the grid metrics; and G is the Jacobian of the transformation.

Equation (16) is solved numerically with the following boundary conditions. Along the axis of the cylinder or at

$$r=0 \quad I_\lambda = I'_\lambda \quad \text{for } \beta = \beta', \quad \alpha = -\alpha' \quad (17)$$

Because the temperatures of the preform and the ambient outside the furnace are much lower than that within the furnace, we can neglect the intensities from the outside of the furnace

$$\text{at } z=0, \quad I_\lambda \approx 0 \quad \text{for } \beta > 0 \quad (18)$$

and

$$\text{at } z=L_f, \quad I_\lambda \approx 0 \quad \text{for } \beta < 0 \quad (19)$$

For a diffuse interface, the radiation intensity at the inner glass surface pointing inward is given by

$$I_\lambda(\mathbf{r}, \mathbf{s}) = \frac{(1 - \rho_\lambda^+)H_\lambda + \rho_\lambda^-(q_{\lambda,r}^+ \mathbf{r} + q_{\lambda,z}^+ \mathbf{z}) \cdot \mathbf{n}}{\pi} \quad \mathbf{s} \cdot \mathbf{n} < 0 \quad (20)$$

where ρ_λ^+ and ρ_λ^- are the reflectivities at the outer and inner surfaces, respectively; $q_{\lambda,r}^+$, $q_{\lambda,z}^+$ are the one-way spectral fluxes in the glass in the positive r and z directions, respectively; \mathbf{n} is the unit normal vector at the free interface pointing outward; and H_λ is the irradiation on the outer surface.

In order to obtain the irradiation H_λ in Eq. (20), the radiosities of the furnace wall must be determined. For this, we consider the enclosure formed by the glass outer surface, the furnace wall, and the top and bottom disk openings. The radiosities on the glass outer surface are given by

$$J_\lambda = (1 - \rho_\lambda^-)(q_{\lambda,r}^+ \mathbf{r} + q_{\lambda,z}^+ \mathbf{z}) \cdot \mathbf{n} + \rho_\lambda^+ H_\lambda \quad 0 < \lambda < 5 \quad \mu\text{m} \quad (21)$$

$$J_\lambda = \varepsilon E_{b\lambda} + (1 - \varepsilon)H_\lambda \quad \lambda > 5 \quad \mu\text{m} \quad (22)$$

where ε is the emissivity of the surface, and $E_{b\lambda}$ is the blackbody emissive power. Since the furnace is opaque, its radiosities are also calculated from Eq. (22) in all the spectral range. The enclosure is divided into K small ring elements, and thus, the irradiations can be expressed as

$$H_{\lambda,i} = \sum_{j=1}^K J_{\lambda,j} F_{i-j} \quad (23)$$

where F_{i-j} is the diffuse view factor from surface element i to j . Substituting Eq. (23) into Eqs. (21) and (22) followed by applying the resulting equations on each surface element, a system of linear equations for the radiosities can be obtained. Once the radiosities are solved, the irradiations can be determined from Eq. (23). The formula derived by Myers [3] is used to calculate the view factors from the glass surface to the furnace wall. The view factor from one furnace element to another is obtained by numerical integration considering the block of the view by the preform.

In this study, the discrete ordinate method (DOM) is used to solve Eq. (16). A detailed procedure of the method and the absorption coefficient band model can be found in [5].

3 Numerical Method

The staggered grid [15] is used in solving for the free surface due to the following advantages:

1. The method guarantees the strict energy conservation in the finite volume discretization so that a smaller grid number can be used.
2. The fluctuations in the solution (especially at the free surface) due to the central differencing of the first derivative terms are avoided.
3. There is no need for the explicit boundary condition for pressure at the free surface.

The staggered grid scheme, though it requires tedious interpolations of variables, is robust and efficient.

Since the free interface has an arbitrary neck-down profile, the governing equations and boundary conditions are transformed into a curvilinear coordinates system (η, ξ) . Second-order accurate finite differencing is applied to discretize the equations. The linear equations are in semi-implicit form, as the source term is evaluated at every previous time step. In solving the Navier-Stokes equations, the pressure in Eq. (5) is updated explicitly by an artificial time-marching scheme at each real time step. The pressure derivative term vanishes when this iteration converges so that the continuity equation is satisfied.

Implementation of the Free Surface Boundary Conditions. Using the following definitions for the normal and tangential velocity components at the free surface, Eqs. (8) and (9) are implemented using the staggered grid; appropriate discretization and manipulation are required to ensure stable and robust convergence in the computation

$$V_n = \mathbf{v} \cdot \mathbf{n} = u \frac{\eta_r}{\sqrt{g^{11}}} + v \frac{\eta_z}{\sqrt{g^{11}}} \quad (24)$$

$$V_t = \mathbf{v} \cdot \mathbf{t} = -u \frac{\eta_z}{\sqrt{g^{11}}} + v \frac{\eta_r}{\sqrt{g^{11}}} \quad (25)$$

where $\mathbf{n} = (n_r, n_z)^T$ and $\mathbf{t} = (t_r, t_z)^T$ are the unit vectors in the normal and tangential directions at the free surface; and the grid metric tensor $g^{11} = \eta_r^2 + \eta_z^2$.

Substituting Eqs. (24) and (25) into Eqs. (8) and (9) and transforming them into the (η, ξ) coordinates, the following expressions can be derived:

$$\frac{2\mu}{\sqrt{g^{11}}} \left[g^{11} \frac{\partial}{\partial \eta} (n_r u + n_z v) + g^{12} \frac{\partial}{\partial \xi} (n_r u + n_z v) - B^n u - C^n v \right] = p_g + \zeta \kappa \quad (26)$$

$$g^{11} \frac{\partial}{\partial \eta} (-n_z u + n_r v) + g^{12} \frac{\partial}{\partial \xi} (-n_z u + n_r v) + G \frac{\partial}{\partial \xi} (n_r u + n_z v) - B^t u - C^t v = 0 \quad (27)$$

where

$$B^n = g^{11} \frac{\partial}{\partial \eta} (n_r) + g^{12} \frac{\partial}{\partial \xi} (n_r) \quad (28a)$$

$$C^n = g^{11} \frac{\partial}{\partial \eta} (n_z) + g^{12} \frac{\partial}{\partial \xi} (n_z) \quad (28b)$$

$$B^t = g^{11} \frac{\partial}{\partial \eta} (-n_z) + g^{12} \frac{\partial}{\partial \xi} (-n_z) + G \frac{\partial}{\partial \xi} (n_r) \quad (28c)$$

$$C^t = g^{11} \frac{\partial}{\partial \eta} (n_r) + g^{12} \frac{\partial}{\partial \xi} (n_r) + G \frac{\partial}{\partial \xi} (n_z) \quad (28d)$$

The grid metric tensor $g^{12} = \eta_r \xi_r + \eta_z \xi_z$ and the Jacobian $G = \eta_r \xi_z - \xi_r \eta_z$.

The first derivatives of the velocity components in Eqs. (26) and (27) must be evaluated along the free surface. We define u at the surface and v half a grid away from the boundary. In order to maintain the second-order accuracy in the differencing, the glass domain is extended outward by half a grid size, and a fictitious v component is defined on the new boundary as shown in Fig. 3 in dashed lines. The second-order accurate finite differencing can be implemented on the gray-colored control volume right on the free surface with the grid molecules shown in Fig. 3(a) as

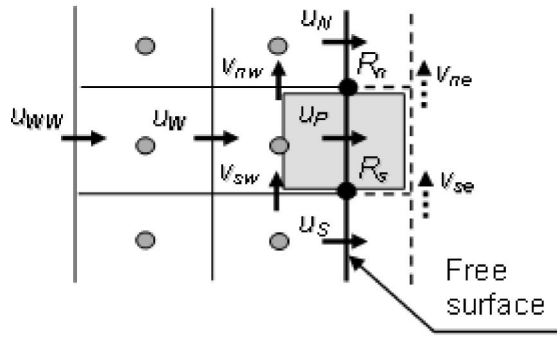
$$\frac{\partial u}{\partial \eta} = 1.5u_p - 2u_w + 0.5u_{ww} \quad (29a)$$

$$\frac{\partial u}{\partial \xi} = 0.5(u_s - u_N) \quad (29b)$$

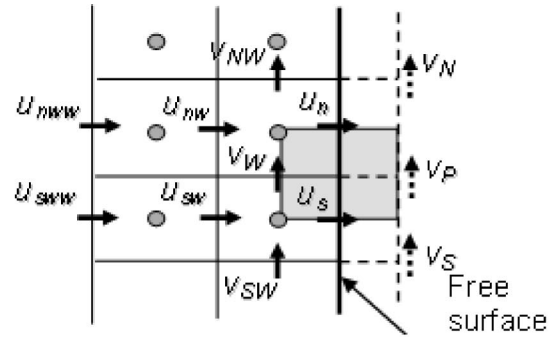
$$\frac{\partial v}{\partial \eta} = 0.5(v_{ne} + v_{se} - v_{nw} - v_{sw}) \quad (29c)$$

$$\frac{\partial v}{\partial \xi} = 0.5(v_{sw} + v_{se} - v_{nw} - v_{ne}) \quad (29d)$$

and with the grid molecules shown in Fig. 3(b) as



(a) control volume for u at the free surface



(b) control volume for v at the free surface

Fig. 3 Grid molecules for the staggered grid at the free surface a) control volume for u at the free surface b) control volume for v at the free surface

$$\frac{\partial v}{\partial \eta} = (v_p - v_w) \quad (30a)$$

$$\frac{\partial v}{\partial \xi} = 0.25(v_{sw} + v_s - v_{nw} - v_n) \quad (30b)$$

$$\frac{\partial u}{\partial \eta} = 0.5(1.5u_n - 2u_{nw} + u_{nww} + 1.5u_s - 2u_{sw} + u_{sww}) \quad (30c)$$

$$\frac{\partial u}{\partial \xi} = (u_s - u_n) \quad (30d)$$

Equations (29) and (30) are substituted into Eqs. (26) and (27), respectively, and the resulting linear equations are used as the boundary conditions for the velocity components u_p and v_p , respectively.

For the temperature boundary condition in Eq. (10), the radiation flux in the opaque band can be obtained, after the radiosities are solved in the enclosure analysis, and is simply given by $q_{rad,opa} = J_{opa} - H_{opa}$. The natural convection heat flux q_{conv} can be calculated numerically from the natural convection of the air in the open-ended channel. It is necessary to include the postchamber along with a detailed boundary condition at the entrance.

The axial derivative of the radius in Eq. (11) can be discretized as $\partial R / \partial z = (R_s - R_n) / dz$, where the nodes for R_s and R_n are located between every two adjacent u components as shown in Fig. 3(a). In this way, R_s and R_n are adjacent and the numerical fluctuations due to the central differencing using every other two nodes are avoided. The v component in Eq. (11) can be interpolated at the location of u_p using the adjacent four component values.

Computation Scheme. The free surface and the velocity and temperature fields are solved using the following procedures:

Step 1: Input the initial free surface profile and the values of the primitive variables (p, u, v, T).

Step 2: Temperature iteration (with a given free surface and the velocity field).

- Calculate the view factors.
- Solve Eq. (16) iteratively to solve for the intensities at the free interface.
- Then calculate $\nabla \cdot \mathbf{q}_R$ using Eq. (14).
- Solve the energy equation using implicit time marching scheme.
- Repeat Step 2a until a steady state is reached.

Step 3: Free surface inner iteration (the temperature field is fixed):

- Solve the Navier Stokes equations using ACM time marching scheme.
- Update free surface profile using kinematic condition, Eq. (11).
- Regenerate the curvilinear grid.
- Repeat Step 3a until a steady state has been reached.

Step 4: Free surface outer iteration

- Save the free surface profile obtained in Step 3.
- Compare it with the last result saved in Step 4.
- If the relative change between two consecutive computed free surface profiles is less than 10^{-5} , the final result is obtained; otherwise go back to Step 2.

As shown in the above procedures, the degrees of freedom (unknown variables) during the computation are effectively reduced by separating the temperature iteration and the free surface iteration. This results in a more robust and faster convergence in the computation.

4 Results and Discussions

A MATLAB program with C++ subroutines was written to simulate the free surface of a draw process. Numerical results were obtained for two geometries, where the values of the parameters are shown in Table 1. Case 1 was selected for validating the computational model. Case 2 was designed to study the effect of preform diameter on the computational model for a specified fiber diameter, draw speed, and tension on the fiber.

In both cases, the physical properties of the fused silica are taken from Fleming [16] and the three-band absorption coefficient model for the RTE can be found in [5]. Since the glass surface velocity is small and the air temperature is close to the glass temperature in the furnace domain, the convective heat flux is much smaller than the radiation flux. Hence the use of an approximate heat transfer coefficient h should not affect the accuracy of

Table 1 Parameters used in the simulation

Parameters	Case 1	Case 2
Specified fiber diameter, R_f (μm)	62.5	
Specified draw speed, v_f (m/s)	25	
Specified draw tension, F_f (grams)	110	
Preform radius, R_p (m)	0.045	0.09
Furnace peak temperature, $T_{f,max}$ (K)	2,400	2,460
Furnace minimum temperature, $T_{f,min}$ (K)	1,700	1,760
Furnace radius, R_{fur} (m)	0.06	0.12
Furnace length, L_{fur} (m)	0.45	0.7

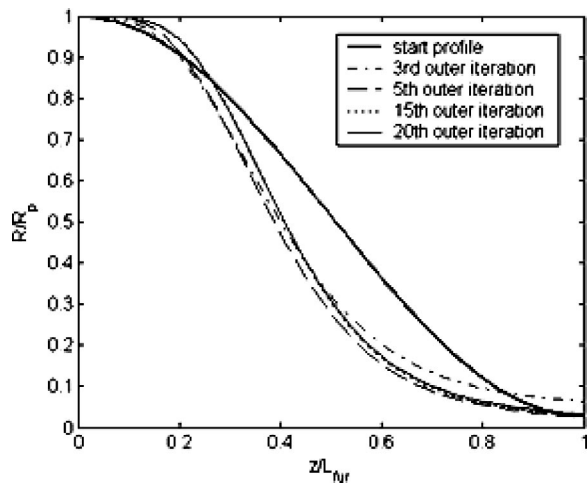


Fig. 4 Intermediate free-surface profiles during the outer iteration

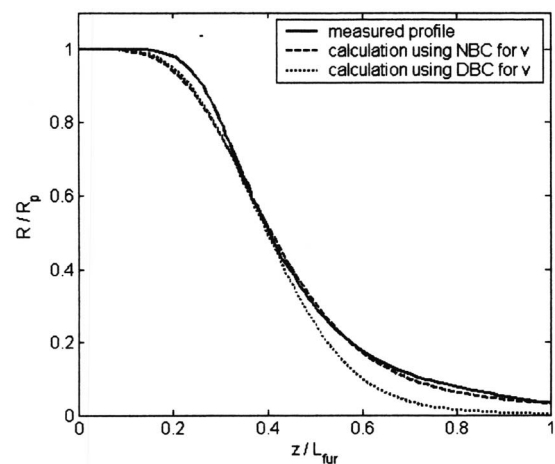
the solution significantly; however, the computation can be greatly reduced. A sinusoidal variation of h varying from $30 \text{ W/m}^2 \text{ K}$ at the furnace inlet to $50 \text{ W/m}^2 \text{ K}$ at the exit was used. This h was based on the combination of the experimental data in Paek [1] and simulation data from Yin and Jaluria [10]. The average air temperature inside the furnace was estimated to be 1900 K .

The numerical model developed here has the advantage of fast convergence. A nonuniform grid is used with a denser spacing near the interface. A grid-size study showed no noticeable changes in the results when the grid number is larger than 81×15 (in z and r directions, respectively). This is much smaller than 401×21 used by Choudhury et al. [8]. One of the reasons for the efficiency is that the staggered grid guarantees strict energy conservation in the finite volume discretization and reduces fluctuations in the solution. It usually takes about 300 outer iterations to arrive at the final results; this means 2.5 h of computation with a desktop PC (AMD1700 CPU with a 512M RAM). If a less strict convergent criterion is used (say, from 10^{-5} to 10^{-3}), it only takes 40 outer iterations (or 45 min). However, the temperature iteration usually converges within 150 steps (or the relative change between two steps is less than 10^{-5}). The inner free-surface iteration in Step 3 may take as much as 4000 steps to reach a relative error residual of 10^{-4} . Since the temperature data is only intermediate, a maximum iteration limit of 1500 steps can be set in the inner iteration to reduce computational time.

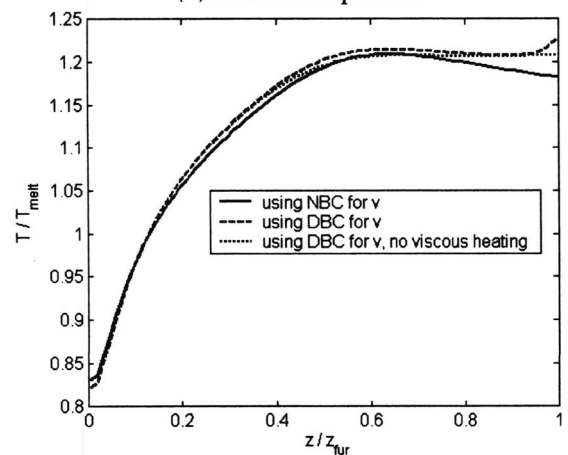
4.1 Simulation Case 1. The values for Case 1 were data provided by OFS so that models and numerical results can be validated experimentally. Thus, the temperature distribution of the furnace wall was experimentally measured [17] using a M90R single-color infrared thermometer (MIKRON, Inc.), which measures the radiositivities at $0.65 \mu\text{m}$ wavelength. This was followed by a radiation analysis on the enclosure to obtain the emission intensities and consequently, the temperature of the furnace wall. The temperature distribution is parabolic with the maximum at the middle and minimum at both ends.

Figure 4 shows some intermediate free surface profiles during the outer iteration. It is noticed that the free surface profile converges very fast. There is not noticeable change in most part of the neck-down region after the 15th iteration. The diameter of the glass at the exit may vary during the iteration due to the Neumann boundary condition used for v .

Model Validation. The steady-state surface profile of the glass rod was experimentally measured for the purpose of validating the model. The preform was moved out of the furnace in a very short time (less than 1 min) to prevent shape deformation due to the



(a) Neck-down profiles



(b) Centerline temperatures

Fig. 5 Comparison of results (Case 1) (a) Neck-down profiles (b) Centerline temperatures

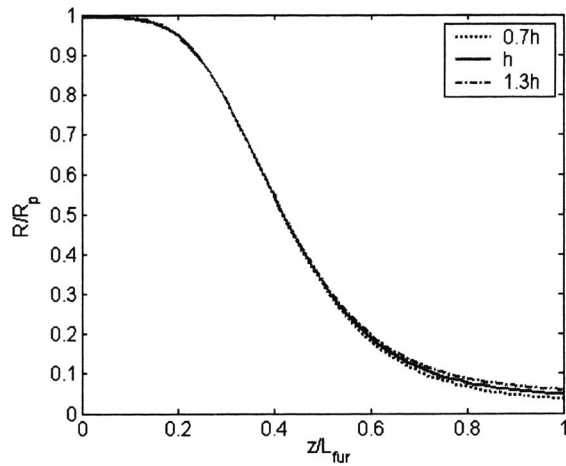
change of view factors. The handle of the preform was then held by a fixture and moved vertically at a constant speed while its diameter was measured by a laser scanner.

Figures 5(a) and 5(b) compare the free-surface profiles and the axial temperature distributions of the glass computed using two different boundary conditions at the furnace exit:

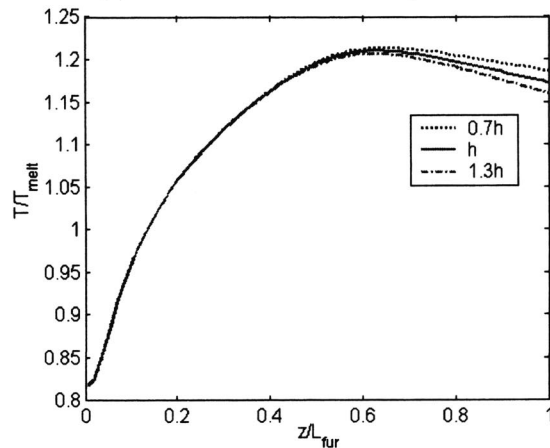
1. Neumann boundary condition (NBC) or Eq. (9), as proposed in this paper, which specifies the derivative of the glass exit velocity by computing it from the draw tension: $dv/dz = F_t / (3\mu\pi R_L^2)$.
2. Dirichlet boundary condition (DBC), commonly used, which assumes the draw speed as the glass velocity at the furnace exit: $v = v_f$.

The sensitivity of the free-surface profile and the axial temperature distributions to the changes of the heat transfer coefficient h ($\pm 30\%$) is illustrated in Figs. 6(a) and 6(b). The radial temperature distribution is given in Fig. 7.

Figure 5(a) compared the computed neck-down shape against the measured profile, where those predicted with NBC as suggested in this study is in excellent agreement with the experimental measurement. Those calculated using the DBC deviate significantly from the measurement, particularly near the furnace exit where the glass was assumed to move at the specified draw speed (or equivalently, the specified diameter at the exit). As compared in Fig. 5(b) where the temperature is normalized to the melting point of 1853 K , we note that the glass temperature increases



(a) Effect of h on neck-down profiles



(b) Effect of h on centerline temperatures

Fig. 6 Effects of heat transfer coefficient h (a) Effect of h on neck-down profiles (b) Effect of h on centerline temperatures

dramatically near the furnace exit in the case of DBC and as a matter of fact, reheating occurs and keeps it well above the glass melting point. The drastic increase in the glass temperature has been traced to the viscous heating induced by the unrealistic high-axial velocity gradient as the glass diameter converges rapidly to the assumed fiber diameter. This phenomenon is clearly in conflict with the assumption that the glass moving at the draw speed is a solid fiber having the desired (constant) diameter at the furnace

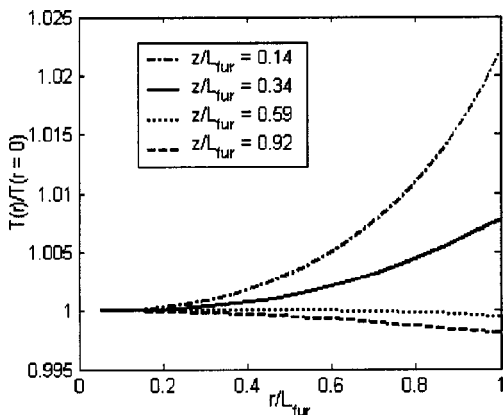


Fig. 7 Radial temperature distributions

exit. Hence, we conclude that the DBC is invalid for drawing large preforms at high speeds, where the fiber freezes well outside the furnace domain. Alternatively, draw tension can be utilized to obtain an appropriate NBC for specifying the derivative of the glass velocity in Eq. (13). NBC is thus used in the rest of the simulations.

As shown in Fig. 6, the solution is insensitive to the changes in h except near the furnace exit where the air convection becomes more pronounced. Figure 7 shows that the glass absorbs heat flux near the furnace inlet and dissipates heat flux at the furnace exit.

2-D Glass Flow. The glass flow of a large preform exhibits 2D characteristics that are not predicted with a 1D model. In order to provide a better understanding of the effects of the 2D velocity variation on the glass flow, a program utilizing the computed 2D velocity field was written.

Figure 8 shows the distributions of the radial and axial velocity components. Figure 8(a) shows an interesting radial variation of the glass axial velocity v . Near the furnace inlet, the glass melts from the surface due to the positive radial temperature gradient (Fig. 7) while it remains largely solid at the center. Hence, the surface velocity is higher than the centerline velocity. The glass completely melts in the neck-down region (at about $1/3 L_f$), the surface velocity becomes much slower than the centerline velocity. The radial variation of the axial velocity is small near the furnace exit where the molten glass is highly viscous and has a very small diameter. Figure 8(b) shows that the glass velocity increases exponentially in the neck-down region. Figure 8(c) shows that the radial velocity u is linear with r near the furnace exit, which is governed by the continuity equation with the almost 1D distribution of v . In the neck-down region, the distribution of u is nonlinear due to the radial variation of v .

The visualization program tracks a group of fictitious infinitesimal particles originally distributed at the same cross-section plane in the preform as they travel through the neck-down region. Snapshots of the particles can be graphed from the following integral:

$$\mathbf{r}(t) = \mathbf{r}(0) + \int_0^t \mathbf{V}[\mathbf{r}(s)] ds \quad (31)$$

where the location vector \mathbf{r} is obtained by integrating the velocity vector \mathbf{V} along a path in the r - z coordinate system; and s is a dummy integration variable representing time. Figure 9 shows how the particles travel through the neck-down region from the furnace inlet (or at $z=0$), where the dashed lines represent the interface between the core rod and the cladding tube. As predicted in Fig. 9(a), the particle distributions become dramatically distorted once they move past $1/3$ of the furnace length where the glass axial velocity is faster in the center than that near the surface. Although the radial variation of the axial velocity is small, it causes a distortion of the particle distribution due to the exponential increase in the axial velocity in the z direction as shown in Fig. 8(b). Simple 1D models are not able to capture this 2D particle flow pattern. This visualization could be used to track the change in the gap geometry, which occurs between two stacked cores in the glass preform. The study, however, requires extending the computation domain to the solidification of the fiber and is beyond the scope of this paper.

4.2 Simulation Case 2. The effects of a large-diameter preform on the computational model were studied using Case 2. Two numerical updating-schemes are compared, where the furnace temperature and geometry were modified appropriately to accommodate the large preform and to keep a reasonable furnace length.

1. Semi 2D solution using radially lumped 1D axial velocity and mass conservation [8].

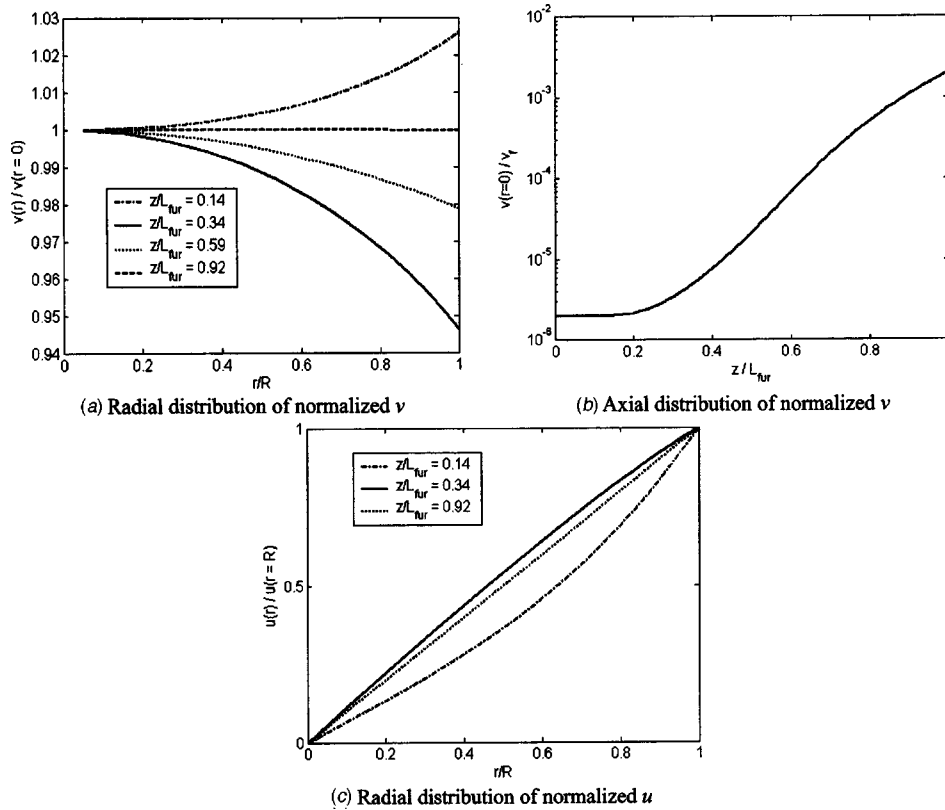


Fig. 8 Velocity distributions of the preform (a) Radial distribution of normalized v (b) Axial distribution of normalized v (c) Radial distribution of normalized u

2. Complete 2D solution using kinematic boundary condition in Eq. (11).

Comparisons are shown in Figs. 10(a) to 10(c). As shown in Fig. 10(a), the diameter of the preform in the neck-down region predicted by the semi-2D model is smaller than that from the 2D model. Consequently, the temperature in that region is higher due to the higher view factors to the hot spot of the furnace. At the bottom of the furnace, the diameter of the glass from the semi-2D model is larger than that in the full 2D model. As a consequence,

the velocity of the glass is smaller, as shown in Fig. 10(b), since the mass flow rate is conserved in the axial direction. The axial mass advection is weaker as the velocity is smaller, which results in a lower temperature near the exit in the semi-2D solution as shown in Fig. 10(c). It can be expected that the difference will be significant for the prediction of the location where the glass turns into fiber if the postchamber is included in the computation domain. This prediction is important for the industry to determine the necessary length of the postchamber.

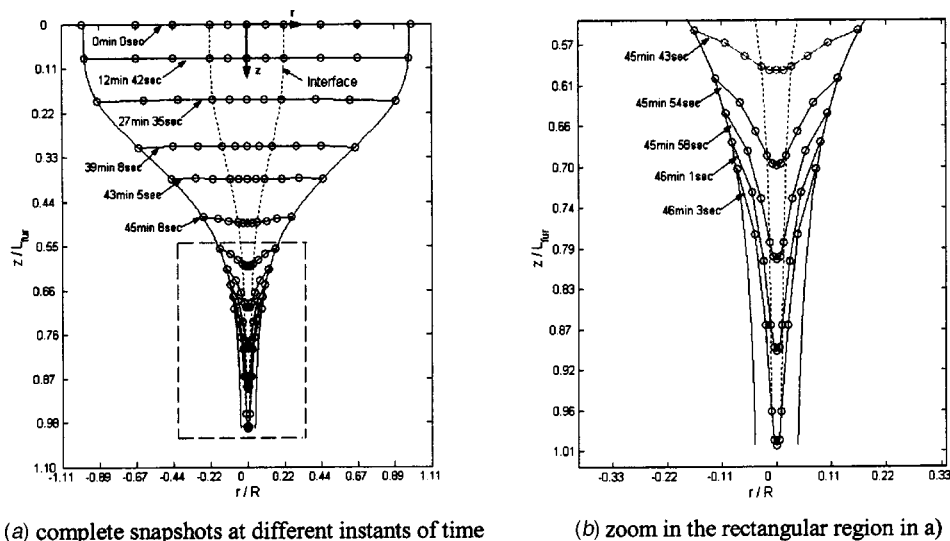


Fig. 9 Particle flow tracking a) complete snapshots at different instants of time b) zoom in the rectangular region in a)

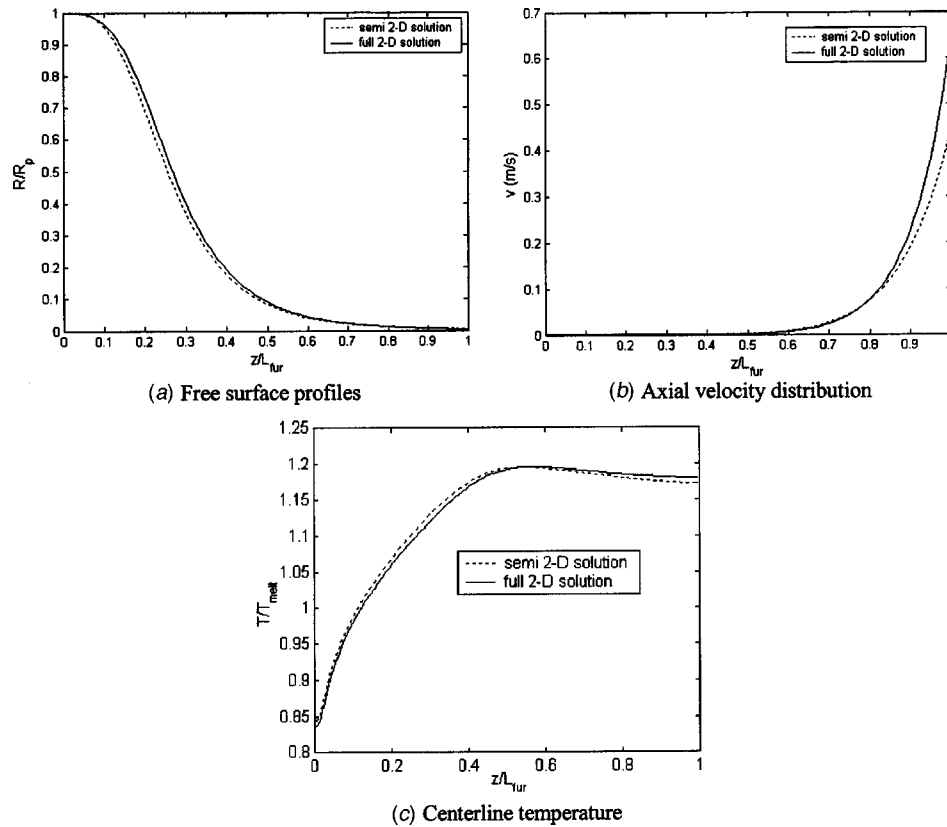


Fig. 10 Comparisons between semi-2D and full 2D models (a) Free surface profiles (b) Axial velocity distribution (c) Centerline temperature

5 Conclusions

A complete 2D numerical model for the high-speed fiber-drawing process in the furnace domain has been presented. This model uses the controlled draw tension to calculate the Neumann boundary condition at the furnace exit, and thus, it does not require specifying an assumed value to the glass speed as most previous studies did. The RTE has been directly solved for the radiation intensities using DOM, which is coupled with the solution of the free-surface flow. The computation scheme is shown to be efficient and robust. The required grid number is much smaller than that used in the previous study although the preform is larger and the furnace is longer.

The predicted free surface with NBC has been experimentally validated. The experimentally measured profile well agrees with that derived numerically. We have also noted that the free surface calculated using the DBC deviates significantly from the measured profile, particularly near the furnace exit. As the glass cools to form solid fiber after leaving the furnace, the actual diameter (and, hence, the speed) of the glass at the furnace exit is essentially unknown. This implies that assigning an arbitrary value to the glass speed at the furnace exit may not be valid for drawing large preforms at high speed.

The effects of the preform diameter on the free-surface calculation with a draw speed of 25 m/s have also been examined. Comparisons between the full and semi-2D models show that the difference is considerable when the preform has a large diameter. This difference is particularly significant if the interest is to predict the location where the glass converges to form the fiber of 125 μm in diameter. Our next step is to extend the computation domain to include the postchamber, and the conjugate problem of the glass flow and the natural convection of the air in the chamber will be solved.

Acknowledgments

This research has been funded by Lucent/OFS. The authors would like to thank Shunhe Xiong for his technical inputs.

Nomenclature

- C_p = Specific heat
- $E_{b\lambda}$ = blackbody emissive power
- F_{i-j} = diffuse view factor from element i to element j
- F_t = draw tension
- G = Jacobian of the grid transformation
- H_λ = irradiation
- I_λ = spectral radiative intensity
- $I_{b\lambda}$ = spectral blackbody intensity
- J_λ = spectral radiosity
- L_f = furnace length
- R = glass radius
- R_f = fiber radius
- R_{L_f} = glass radius at the furnace exit
- R_p = preform radius
- T = temperature
- V_n, V_t = normal and tangential components of the velocity at the free surface
- a = artificial compressibility factor
- g = gravitational acceleration
- g^{11}, g^{12} = grid metric tensors
- k = thermal conductivity
- n = magnitude of the normal vector
- \mathbf{n} = unit normal vector
- p = pressure
- \mathbf{q}_R = radiation heat flux

$q_{rad,opa}$ = net radiation heat flux in the opaque band
 q_{conv} = natural convection heat flux from the air
 $q_{\lambda,r}^+, q_{\lambda,z}^+$ = one-way spectral radiative fluxes in the positive r and z directions
 r = radial coordinate
 \mathbf{r} = position vector
 \mathbf{s} = orientation vector
 \tilde{t} = fictitious time
 u = radial component of velocity
 v = axial component of velocity
 v_{in} = preform feed rate
 v_f = fiber draw speed
 z = axial coordinate
 \mathbf{k}_λ = spectral absorption coefficient
 α, γ, β = direction cosines of the intensity orientation vector \mathbf{s}
 θ = local polar angle
 $\eta_r, \eta_z, \xi_r, \xi_z$ = grid metrics of the transformation
 $\rho_\lambda^+, \rho_\lambda^-$ = reflectivities at the outer and inner surfaces, respectively
 ε = emissivity
 ρ = density
 μ = dynamic viscosity
 Φ = dissipation function
 ζ = surface tension
 κ = surface curvature
 λ = wavelength
 η, ξ = general curvilinear coordinates
 ψ = local azimuthal angle

References

[1] Paek, U. C., and Runk, R. B., 1978, "Physical Behavior of the Neck-Down Region During Furnace Drawing of Silica Fibers," *J. Appl. Phys.*, **49**, pp. 4417–4422.

- [2] Homsy, G. M., and Walker, K., 1979, "Heat Transfer in Laser Drawing of Optical Fibers," *Glass Technol.*, **20**(1), pp. 20–26.
- [3] Myers, M. R., 1989, "A Model for Unsteady Analysis of Preform Drawing," *AIChE J.*, **35**(4), pp. 592–602.
- [4] Vasiljev, V. N., Dulnev, G. N., and Naumchic, V. D., 1989, "The Flow of a Highly Viscous Liquid With a Free Surface," *Glass Technol.*, **30**(2), pp. 83–90.
- [5] Wei, Z., and Lee, K. M., 2003, "Effects of Radiative Transfer Modeling on Transient Temperature Distribution in Semitransparent Glass Rod," *ASME J. Heat Transfer*, **125**, pp. 1–7.
- [6] Lee, S. H.-K., and Jaluria, Y., 1997, "Simulation of the Transport Processes in the Neck-Down Region of a Furnace Drawn Optical Fiber," *Int. J. Heat Mass Transfer*, **40**, pp. 843–856.
- [7] Choudhury, S. R., and Jaluria, Y., 1998, "Thermal Transport Due to Material and Gas Flow in a Furnace for Drawing an Optical Fiber," *J. Mater. Res.*, **13**(2), pp. 494–503.
- [8] Choudhury, S. R., Jaluria, Y., and Lee, S. H.-K., 1999, "A Computational Method for Generating the Free-Surface Neck-Down Profile for Glass Flow in Optical Fiber Drawing," *Numer. Heat Transfer, Part A*, **35**, pp. 1–24.
- [9] Xiao, Z., and Kaminski, D. A., 1997, "Flow, Heat Transfer, and Free Surface Shape During the Optical Fiber Drawing Process," *HTD Vol. 347, National Heat Transfer Conference*, ASME, New York, Vol. 9, pp. 219–229.
- [10] Yin, Z., and Jaluria, Y., 2000, "Neck Down and Thermally Induced Defects in High-Speed Optical Fiber Drawing," *ASME J. Heat Transfer*, **122**, pp. 351–362.
- [11] Cheng, X., and Jaluria, Y., 2002, "Effect of Draw Furnace Geometry on High-Speed Optical Fiber Manufacturing," *Numer. Heat Transfer, Part A*, **41**, pp. 757–781.
- [12] Viskanta, R., and Anderson, E. E., 1975, "Heat Transfer in Semitransparent Solids," *Adv. Heat Transfer*, **11**, pp. 317–441.
- [13] Schlichting, H., and Gersten, K., 1999, *Boundary Layer Theory*, Springer, Berlin.
- [14] Chorin, A. J., 1967, "A Numerical Method for Solving Incompressible Viscous Flow Problems," *J. Comput. Phys.*, **2**, pp. 12–26.
- [15] Patankar, S. V., 1980, *Numerical Heat Transfer and Fluid Flow*, Hemisphere Publishing, Washington, DC.
- [16] Fleming, J. D., 1964, "Fused Silica Manual," Final Report for the U.S. Atomic Energy Commission, Oak Ridge, Tennessee, Project No. B-153.
- [17] Garner, H., 2000, "An Experimental Procedure for Measuring Furnace Temperature Profiles in Optical Fiber Drawing," Lucent Technologies internal report.

Observation of Femtosecond Laser-Induced Ablation in Crystalline Silicon

Tae Y. Choi

Institute of Energy Technology,
Swiss Federal Institute of Technology Zurich,
Zurich, CH-8092 Switzerland
e-mail: choi@lnt.iet.mavt.ethz.ch

Costas P. Grigoropoulos

Department of Mechanical Engineering,
University of California, Berkeley,
Berkeley, CA 94720-1740
e-mail: cgrigoro@me.berkeley.edu

The ablation of crystalline silicon by ultrashort laser pulses is studied experimentally. A pump-and-probe experiment is implemented in a collinear arrangement, utilizing a time-delayed frequency-doubled probe beam for in situ reflectance measurement and ultrafast microscopy observation. Enhanced surface reflectivity in sub-picosecond time scale at the center of the irradiated spot indicates nonthermal liquid layer formation. A short-lived nonthermal liquid phase was detected at fluence of 1.5 J/cm². In addition to this observation, the reflected images for pump beam fluences ranging from 1.5 to 4.6 J/cm² provide evidence of plasma expansion above the irradiated target.

[DOI: 10.1115/1.1795224]

Keywords: Crystalline Silicon, Pump-and-probe, Ultrafast Microscopy, Plasma

I Introduction

Interactions of ultrashort pulsed laser radiation with solid matter have been investigated extensively [1–5]. Femtosecond laser pulses impart extremely high intensities, providing well-defined laser-ablation thresholds at substantially reduced laser energy densities. Precise control of the laser-beam coupling with the specimen reduces the extent of thermal penetration and enables high quality of machining reproducibility. Hence, high aspect ratio cuts, free of debris and less lateral damage are produced [6–8].

Femtosecond time-resolved optical experiments on ultrafast irradiation revealed the existence of a high-reflectivity phase for laser fluence exceeding a critical threshold [3,9,10]. These observations were attributed to a melt layer that is initiated at the surface and subsequently propagates into the underlying high-density electron hole plasma [10]. This ultrafast process accompanies so-called plasma annealing [5,11] with which the lattices are softened and disordered. Fundamental questions remain concerning the physical origin and evolution of the ultrafast ablative material removal process under the nonequilibrium conditions imposed by femtosecond laser irradiation.

Recent experiments applying X-ray diffraction with picosecond time resolution enabled detection of nonthermal melting of semiconductor materials [12–14]. The surface-mediated melting transformation via a distinct solid/liquid interface is contrasted with the homogeneous plasma annealing mechanism [11,15]. The latter is triggered by high-density electron hole plasma that inherently carries no normal molten phase. However, investigations utilizing femtosecond time-resolved reflectivity measurement [10,16] suggested existence of a molten layer whose properties and transient behavior differ from normal thermal melting. Experiments [2,4,17–19] and theoretical developments [5,20] showed distortion of the silicon diamond lattice structure that is related to lattice instability in the hundreds of femtoseconds time scale on ultrashort pulsed laser irradiation.

This paper presents an experimental study on the interaction of femtosecond laser pulses with crystalline silicon semiconductor wafers by utilizing a collinear optical arrangement (the heating beam and probe beam are at normal incidence to the sample). This does not need to consider polarization effect in the reflectivity measurement. Not only the reffectivity for sub-picosecond time scale, but also the plasma evolution at later times is considered

with higher fluences. The early stage of ultrafast phase change is explained via theoretical analysis as well as experimental observation.

II Theoretical Background

The electron density N in this study can be obtained by ignoring the contributions of recombination within a few picoseconds time scale. The impact ionization is also ignored due to the screening effect at high carrier density. The generated carriers by linear (one-photon absorption) and nonlinear absorption (two-photon absorption) are diffused and emitted from the surface. Hence, the one-dimensional conservation equation for ultrashort pulse-induced excitation of energy carriers can be written, excluding phase change as follows:

$$\frac{\partial N}{\partial t} + \frac{\partial}{\partial x} \cdot \left(-D \frac{\partial N}{\partial x} - J_e e^{-x/l} \right) = \frac{(1-R)\alpha I(x,t)}{h\nu} + \frac{(1-R)^2 \beta I^2(x,t)}{2h\nu} \quad (1)$$

where R is reflectivity, α is linear absorption coefficient, β is two-photon absorption coefficient [22], I is the laser intensity, D is ambipolar diffusion coefficient [22], $h\nu$ is the photon energy quantum, J_e is the electron current density due to thermionic electron emission at the surface, and l is the electron escape length (2.5 nm) [23]. Details of electron emission and simulation parameters are found in the literature [23–25]. The two-photon absorption is dominant because the linear absorption length is nearly 10 μm at wavelength of 800 nm. It should be noted that the reflectivity as well as the absorption coefficient change during the pulse due to the varying transient electron density distribution. The laser energy coupling with the material was calculated by employing the matrix method formulation in stratified media exhibiting gradients of the complex refractive index [21]. When the carrier density is high, the Drude model is sufficient to evaluate the complex refractive index n^c of the surface plasma layer [21]:

$$n^c = \left(\epsilon_{c-si} - \left(\frac{\omega_p}{\omega} \right)^2 \frac{1}{1 + i \frac{1}{\omega \tau_d}} \right)^{1/2} \quad (2)$$

where ω is angular frequency of the probe light, τ_d is damping time, ϵ_{c-si} is dielectric constant of crystalline silicon (30.87 + i4.31), and ω_p is plasma frequency expressed as $4\pi N e^2 / m^* m_e$

Contributed by the Heat Transfer Division for publication in the JOURNAL OF HEAT TRANSFER. Manuscript received by the Heat Transfer Division April 22, 2003; revision received February 27, 2004. Associate Editor: G. Chen.

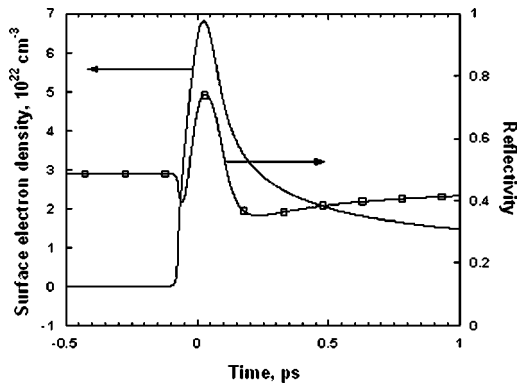


Fig. 1 Temporal evolution of calculated surface electron density and reflectivity at $\lambda = 400$ nm with no consideration of phase change. (Note the electron density at 0.5 ps is $2 \times 10^{22} \text{ cm}^{-3}$.) The laser fluence is 1.5 J/cm^2 . The critical density for lattice instability has been revealed theoretically at 10^{22} cm^{-3} (Ref. [5]).

where m_e is electron rest mass and m^* is ratio of electron effective mass to rest mass taken as 0.18. The damping time chosen is 1 fs, considering high carrier-carrier collision [1]. Since no detailed experimental data on the temperature dependence of the Drude parameters, we take constant effective mass and damping time for simplicity. In fact, at high temperature, high damping rate ($\omega\tau_d \gg 1$) was observed, which in turn the minimum reflectivity became that of the unperturbed solid. On the contrary, at low damping rate ($\omega\tau_d \ll 1$), the minimum reflectivity approaches zero [1]. Temperature-independent electron mass is also questionable, as hot electrons are situated far from the band edge. In this case, the effective mass should be averaged for all the occupied states, requiring detailed band-structure information.

The temporal evolution of the electron number densities is calculated by using a finite difference method and by taking into account many body effects [22] as indicated in Fig. 1 (laser fluence at 1.5 J/cm^2). Figure 1 also shows the reflectivity at the $\lambda = 400$ nm probing wavelength, predicted by considering a plasma layer of both temporally and spatially (i.e., in the depth direction) varying complex refractive index. The transmission matrix approach in stratified media [21] was employed to calculate the optical response of the structure. A sharp increase of reflection due to highly dense electron hole plasma was predicted at early times. In contrast, the reflectivity returns to the bare silicon reflectivity level at times far beyond the pulse length. This model identifies the highly reflecting phase existing only for a short time (a few hundred femtoseconds). As it will be shown later, this post-pulse reflectivity prediction is contrary to the experimental observation due to nonthermal liquid-layer formation launched by lattice instability.

III Experiment

A schematic of the experimental apparatus is shown in Fig. 2. A femtosecond mode-locked seed beam of 14 nm bandwidth, pulse energies in the nanojoule range, and repetition rate of 80 MHz is emitted from a Ti:sapphire oscillator pumped by a diode laser. A pulsed Nd:YLF operating at the repetition rate of 1 kHz pumps the seed beam through a regenerative amplifier. Using the chirped pulse amplification technique, ultrashort pulses are generated with a FWHM pulse width of about 83 fs, 800 nm wavelength, and 1 mJ maximum pulse energy. Fluctuations of the beam energy were measured to be within 1% of the mean value.

In the present experiment, single pulses of energy in the 0.04–0.36 mJ range are focused onto an approximately $100 \mu\text{m}$ -dia

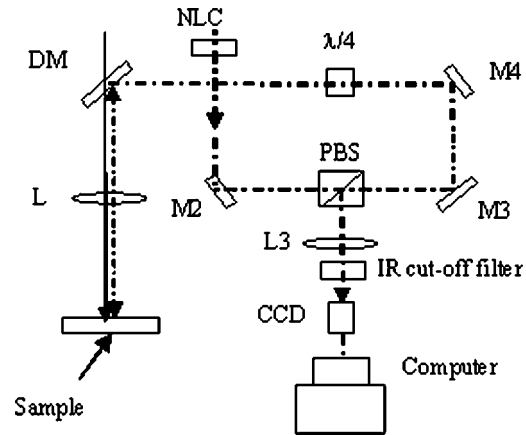


Fig. 2 Schematic diagram of experimental setup (DM: dichroic mirror; NLC: nonlinear crystal; $\lambda/4$: quarter wave plate; L: lens; M: Mirror). The pump beam (solid line) and probe beam (dotted line) are normally incident on the sample.

spot, yielding energy fluence of $0.4\text{--}4.6 \text{ J/cm}^2$. The position of the focal waist and the focal spot size of the pump beam were determined by a knife-edge technique [26].

The pump and probe beams are shown in the solid and dotted line, respectively. A 10% portion of the fundamental 800 nm beam (probe beam) served to generate a frequency-doubled ($\lambda = 400$ nm) beam through the nonlinear crystal (NLC). The remaining 90% of the original beam (pump beam) was utilized to process the sample. Errors introduced by misalignment of the two beams were thoroughly examined as suggested in the Ref. [27]. No shift of the probe beam intensity distribution was detected up to about 100 ps.

The reflected probe beam was directed through the $\lambda/4$ (quarter waveplate) so that its polarization was converted to S and after reflecting off the polarizing beamsplitter (PBS) formed an image of the heated target area at the focal plane of a 250 mm lens. The image was relayed via an interference filter centered at 400 nm, a $100\times$ microscope objective and a $10\times$ eyepiece to a CCD camera. The sample stage was translated in the X-Y directions by a precision microstage in order to acquire time-resolved images of fresh surface exposed to single-shot pulses. It is worth noting that both the pump and probe beams are normal to the sample, eliminating polarization dependence on reflectivity. Additionally, the entire image is taken at the same time in contrast to oblique-angle illumination.

IV Results and Discussion

The sequence of time-resolved surface images (Fig. 3) reveals a

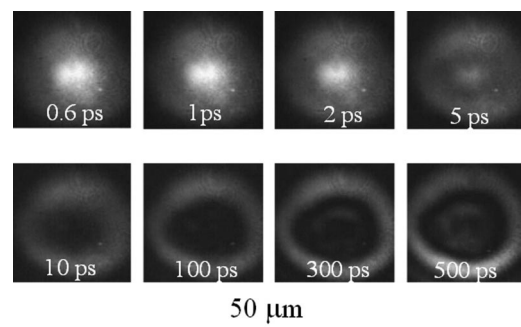


Fig. 3 Time-resolved surface images at fluence of 1.5 J/cm^2 . Highly reflecting phase is identified below 1 ps. The ablation starts at around 10 ps.

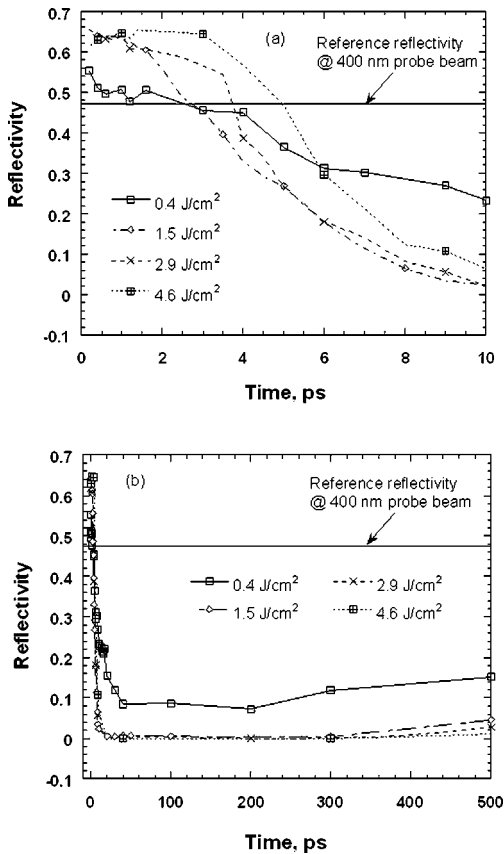


Fig. 4 (a) Short time scale and (b) longer time scale time-resolved surface reflectivity traces. Reflectivity at the early stage approaches that of liquid silicon.

variety of physical phenomena. The enhanced reflectivity recorded in the early stage of the heating process ($t < 2-3$ ps) indicates presence of dense electron-hole plasma and the evolution of a nonthermal liquid layer [11]. The absolute reflectivity data at the center of the irradiated spot displayed in Fig. 4 show that this mechanism is active up to 2 or 3 ps. Considering that the peak reflectivity for the fluence of $F = 0.4$ J/cm² stays substantially lower than the $R = 0.72$ reflectivity of bulk molten silicon at the 400 nm probe laser wavelength, no distinct signature of a liquid phase is detected. However, at higher fluences, the reflectivity increase within a couple of picoseconds, before the lattices are thermally relaxed (lattice-lattice relaxation time = 10 ps), implies the emergence of a transient, ultrafast liquid layer triggered by the destabilization of the crystal lattice [5] by a dense electron-hole plasma in ultrafast time scale.

The low reflectivity predicted by assuming electron-hole plasma layer beyond 500 fs does not allow a plausible explanation of the high reflection observed in the experiment. Figure 5 gives the reflectivity for a liquid layer of varying thickness having the complex refractive index of liquid silicon. Comparison with the reflectivity corresponding to different plasma densities confirms that the highly reflective phase observed in the early stage of ablation process is caused by the generation of the nonthermal liquid layer. For a 10 nm liquid layer, the reflectivity approaches 0.7 and is in agreement with the experimental results shown in Fig. 4. At higher fluences, the predicted surface electron density surpasses 10^{23} cm⁻³, driving the reflectivity past 0.75. Due to the transition to an ultrafast liquid phase, the surface reflectivity measurement does not yield such high values.

Based on the time-resolved images, it can be stated that material ablation starts at around 10 ps. Early part of ablation (~ 10 ps) can be explained by ejected electrons by electron emis-

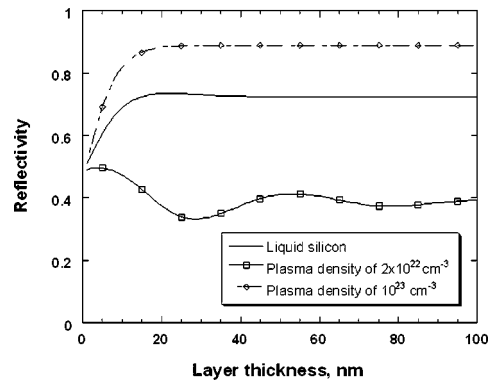


Fig. 5 Reflectivity as a function of layer thickness for liquid silicon and solid-state plasma. (The low plasma density, 2×10^{22} cm⁻³, is utilized for predicting the relectivity at 0.5 ps.)

sion as well as nonthermal ablation, generating strong absorbing plasma in the vicinity of the sample. The total electron yield reached 10^{20} cm⁻² by using a one-dimensional energy transport equation based on relaxation time approximation and considering electron emission [25]. At the later times ($t > 20-40$ ps) isentropic expansion into air can occur (phase explosion) leading to thermal ablation [28,29].

Figure 6 shows that the bright spot at the center of the irradiated zone persists longer as the laser fluence is increased. High-resolution, time-resolved shadowgraph images [25] show that the plasma front velocity is of the order of several thousands m/s. Consequently, the plasma layer formed at $t \sim 10$ ps is less than 1 μ m in thickness. Thus, the surface electron density exceeds 10^{23} cm⁻³. Gradual darkening of the central portion of the irradiated area was observed for longer elapsed times due to emergence of a plasma layer (a few micrometers thick) [25] in the proximity of the sample surface. Earlier study [3] explains the observation of a bright region at the center of the irradiated spot at a longer elapsed time (i.e., 500 ps) by assuming enhanced transmission of the probe laser beam toward the surface. They asserted that particles are first ejected in the form of nanometer-sized liquid droplets and are then atomized over the hot central region that remains in molten phase. The images displayed in Fig. 7 at fluences $F \geq 1.5$ J/cm² show that the central region at $t = 500$ ps is dark, due to strong attenuation of the probe laser beam by the high-density and opacity plasma formed above the surface. The peripheral dark ring corresponds to a rarefaction wave front pointing toward the substrate [25].

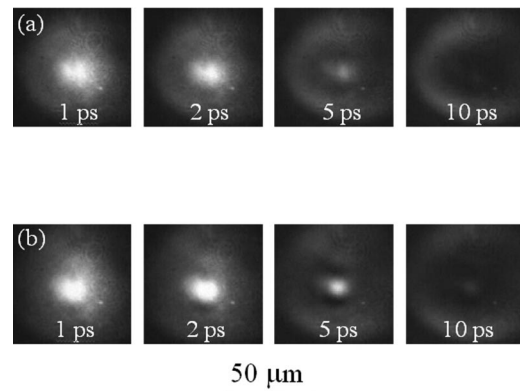


Fig. 6 Comparison of time-resolved image sequence (a) 2.9 and (b) 4.6 J/cm². The bright spot at the center of the irradiated zone persists longer at higher laser fluence.

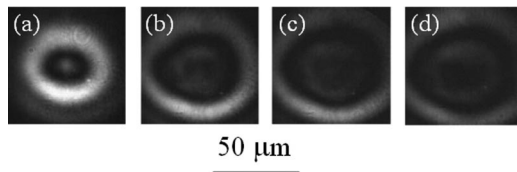


Fig. 7 Surface images taken at 500 ps for different energy densities for (a) 0.4, (b) 1.5, (c) 2.9, and (d) 4.6 J/cm². Peripheral dark rings at higher fluences correspond to rarefaction wave toward the sample surface.

V Conclusion

In conclusion, imaging with a time-delayed frequency-doubled probe beam, collinearly aligned with respect to the pump pulse has been performed. The results showed a highly reflecting phase, indicating creation of a dense plasma in conjunction with a non-thermal liquid phase of about 10 nm in thickness ($F = 1.5 \text{ J/cm}^2$) within 1 ps after the pump beam incidence on the sample surface. The early stage of ablation was shown to start at 10 ps. Darkening of the reflection image was explained by invoking the formation of a strongly absorbing plasma in the vicinity of the sample that is caused by electron emission.

Acknowledgment

Support of this work by the Department of Energy, Office of Basic Energy Sciences, Engineering Research Program, under Grant No. DE-FG03-95ER14562 is gratefully acknowledged.

Nomenclature

D	= ambipolar diffusion coefficient, m ² /sec
h	= Planck's constant, J·sec
i	= complex number ($i^2 = -1$)
I	= laser intensity, W/m ²
J	= current density, A/m ²
l	= electron escape length, m
m	= rest mass, kg
m^*	= ratio of effective mass to rest mass
n	= refractive index
N	= electron number density m ⁻³
R	= reflectivity
t	= time, sec
x	= space variable, m
α	= linear absorption coefficient, m ⁻¹
β	= two-photon absorption coefficient, m/W
ϵ	= dielectric constant
ν	= frequency, sec ⁻¹
τ	= damping time, sec
ω	= angular frequency, rad/sec

Subscripts and superscripts

c	= complex
c -Si	= crystalline silicon
d	= damping
e	= electron
p	= plasma

References

- [1] Sokolowski-Tinten, K., and von der Linde, D., 2000, "Generation of Dense Electron-Hole Plasmas in Silicon," *Phys. Rev. B*, **61**, pp. 2643–2650.
- [2] Tom, H. W. K., Aumiller, G. D., and Brito-Cruz, C. H., 1988, "Time-Resolved Study of Laser-Induced Disorder of Si Surfaces," *Phys. Rev. Lett.*, **60**, pp. 1438–1441.

- [3] Downer, M. C., Fork, R. L., and Shank, C. V., 1985, "Femtosecond Imaging of Melting and Evaporation at a Photoexcited Silicon Surface," *J. Opt. Soc. Am. B*, **2**, pp. 595–599.
- [4] Guidotti, D., Driscoll, T. A., and Gerritsen, H. J., 1983, "Second Harmonic Generation in Centro-Symmetric Semiconductors," *Solid State Commun.*, **46**, pp. 337–340.
- [5] Stampfli, P., and Bennemann, K. H., 1990, "Theory for the Instability of the Diamond Structure of Si, Ge, and C Induced by a Dense Electron-Hole Plasma," *Phys. Rev. B*, **42**, pp. 7163–7173.
- [6] Momma, C., Nolte, S., Kamlage, G., Von Alvensleben, F., and Tunnermann, A., 1998, "Beam Delivery of Femtosecond Laser Radiation by Diffractive Optical Elements," *Appl. Phys. A: Mater. Sci. Process.*, **67**, pp. 517–520.
- [7] Pronko, P. P., Dutta, S. K., Squier, J., Rudd, J. V., Du, D., and Mourou, G., 1995, "Machining of Sub-Micron Holes Using a Femtosecond Laser at 800 nm," *Opt. Commun.*, **114**, pp. 106–110.
- [8] Wu, M. C., 1997, "Micromachining for Optical and Optoelectronic Systems," *Proc. IEEE*, **85**, pp. 1833–1856.
- [9] Reitze, D. H., Wang, X., Ahn, H., and Downer, M. C., 1989, "Femtosecond Laser Melting of Graphite," *Phys. Rev. B*, **40**, pp. 11986–11989.
- [10] Shank, C., Yen, R., and Hirlimann, C., 1983, "Time-Resolved Reflectivity Measurements of Femtosecond-Optical-Pulse-Induced Phase Transitions in Silicon," *Phys. Rev. Lett.*, **50**, pp. 454–457.
- [11] Van Vechten, J., Tsu, R., and Saris, F., 1979, "Nonthermal Pulsed Laser Annealing of Si, Plasma Annealing," *Phys. Lett.*, **74A**, pp. 422–426.
- [12] Siders, C., Cavalleri, A., Sokolowski-Tinten, K., Toth, C., Guo, T., Kammler, M., von Hoegen, M., Wilson, K., von der Linde, D., and Barty, C., 1999, "Detection of Nonthermal Melting by Ultrafast X-Ray Diffraction," *Science*, **286**, pp. 1340–1342.
- [13] Rose-Petruck, C., Jimenez, R., Guo, T., Cavalleri, A., Siders, C., Raksi, F., Squier, J., Walker, B., Wilson, K., and Barty, C., 1999, "Picosecond-Milliångstrom Lattice Dynamics Measured by Ultrafast X-Ray Diffraction," *Nature (London)*, **398**, pp. 310–312.
- [14] Cavalleri, A., Siders, C., Brown, F., Leitner, D., Toth, C., Squier, J., Barty, C., and Wilson, K., 2000, "Anharmonic Lattice Dynamics in Germanium Measured With Ultrafast X-Ray Diffraction," *Phys. Rev. Lett.*, **85**, pp. 586–589.
- [15] Von der Linde, D., and Fabricius, N., 1982, "Observation of an Electronic Plasma in Picosecond Laser Annealing of Silicon," *Appl. Phys. Lett.*, **41**, pp. 991–3.
- [16] Sokolowski-Tinten, K., Solis, J., Bialkowski, J., Siegel, J., Afonso, C. N., and von der Linde, D., 1998, "Dynamics of Ultrafast Phase Changes in Amorphous GeSb Films," *Phys. Rev. Lett.*, **81**, pp. 3679–3682.
- [17] Govorkov, S. V., Schroder, Th., Shumay, I. L., and Heist, P., 1992, "Transient Gratings and Second-Harmonic Probing of the Phase Transformation of a GaAs Surface Under Femtosecond Laser Irradiation," *Phys. Rev. B*, **46**, pp. 6864–6868.
- [18] Sokolowski-Tinten, K., Bialkowski, J., and von der Linde, D., 1995, "Ultrafast Laser-Induced Order-Disorder Transitions in Semiconductors," *Phys. Rev. B*, **51**, pp. 14186–14198.
- [19] Shank, C. V., Yen, R., and Hirlimann, C., 1983, "Femtosecond-Time-Resolved Surface Structural Dynamics of Optically Excited Silicon," *Phys. Rev. Lett.*, **51**, pp. 900–902.
- [20] Silvestrelli, P. L., Alavi, A., Parrinello, M., and Frenkel, D., 1996, "Ab Initio Molecular Dynamics Simulation of Laser Melting of Silicon," *Phys. Rev. Lett.*, **77**, pp. 3149–3152.
- [21] Born, M., and Wolf, E., 1999, *Principles of Optics*, Cambridge University, Cambridge, England.
- [22] Young, J., and van Driel, H., 1982, "Ambipolar Diffusion of High-Density Electrons and Holes in Ge, Si, and GaAs: Many-Body Effects," *Phys. Rev. B*, **26**, pp. 2147–2158.
- [23] Ballarotto, V. W., Siegrist, K., Phaneuf, R. J., Williams, E. D., Yang, W. C., and Nemanich, R. J., 2001, "Photon Energy Dependence of Contrast in Photoelectron Emission Microscopy of Si Devices," *Appl. Phys. Lett.*, **78**, pp. 3547–3549.
- [24] Kittel, C., 1996, *Introduction to Solid State Physics*, Seventh Edition, Wiley, New York.
- [25] Choi, T. Y., and Grigoropoulos, C. P., 2002, "Plasma and Ablation Dynamics in Ultrafast Laser Processing of Crystalline Silicon," *J. Appl. Phys.*, **92**, pp. 4918–4925.
- [26] Duley, W. W., 1983, *Laser Processing and Analysis of Materials*, Plenum Press, New York.
- [27] Capinski, W. S., and Maris, H. J., 1996, "Improved Apparatus for Picosecond Pump-and Probe Optical Measurements," *Rev. Sci. Instrum.*, **67**, pp. 2720–2726.
- [28] Sokolowski-Tinten, K., Bialkowski, J., Cavalleri, A., von der Linde, D., Oparin, A., Meyer-ten-Vehn, J., and Anisimov, S., 1998, "Transient States of Matter During Laser Ablation," *Phys. Rev. Lett.*, **81**, pp. 224–227.
- [29] Cavalleri, A., Sokolowski-Tinten, K., Bialkowski, J., Schreiner, M., and von der Linde, D., 1999, "Femtosecond Melting and Ablation of Semiconductors Studied With Time of Flight Mass Spectroscopy," *J. Appl. Phys.*, **85**, pp. 3301–3309.

Molecular Dynamics Study of Phase Change Mechanisms During Femtosecond Laser Ablation

Xianfan Xu

e-mail: xxu@ecn.purdue.edu

Changrui Cheng

Ihtesham H. Chowdhury

School of Mechanical Engineering,
Purdue University

In this work, Molecular Dynamics (MD) simulation is employed to investigate femtosecond laser ablation of copper, with an emphasis on the understanding of the mechanism of phase change during laser ablation. Laser induced heat transfer, melting, surface evaporation, and material ablation are studied. Theoretically, it has been suggested that under intense femtosecond laser irradiation, the material undergoes a volumetric phase change process; its maximum temperature can be close to or even above the thermodynamic critical point. The MD simulations allow us to determine the transient temperature history of the irradiated material and to reveal the exact phase change process, which explains the mechanisms of femtosecond laser ablation. A finite difference calculation is also performed, which is used to compare results of heating and melting prior to a significant amount of material being ablated. [DOI: 10.1115/1.1797011]

Introduction

In recent years, commercial, turn-key femtosecond pulsed lasers have been rapidly developed and employed in materials processing. Due to the extremely short laser pulse duration, heat diffusion is confined, resulting in more precise machining compared with those obtained with longer laser pulses. On the other hand, femtosecond laser material interaction involves coupled, nonlinear, and non-equilibrium processes, inducing extremely high heating rate (10^{16} K/s) and high temperature gradient (10^{11} K/m) near the laser irradiated surface. The purpose of this work is to use numerical techniques to investigate the rapid phase change process during femtosecond laser ablation. Both finite difference (FD) and molecular dynamics (MD) calculations are carried out.

A large amount of work has been dedicated to the numerical study of laser material interactions. Several finite difference schemes have been reported in the literature. These works implement the two-temperature model first proposed by Anisimov et al. [1], which was later rigorously developed from the Boltzmann transport equation [2]. The two-temperature model considers electrons and the lattice as two sub-systems. The laser energy is first absorbed by electrons and subsequently coupled to the lattice over a time period of several picoseconds. Recently, this model has been extended to compute solid-liquid and liquid-vapor phase change induced by a femtosecond laser pulse [3]. For MD calculations, due to the limitation of computing power, most work has been restricted to systems with a small number of atoms. For example, MD calculations of laser ablation of a dielectric system consisting of 4851 atoms [4] and crystalline silicon containing approximately 23,000 atoms [5] have been reported. A metal system consisting of 160,000 atoms was simulated [6] using the Morse potential function [7]. Heat conduction by the electron gas in metal, which dominated the heat transfer process, could not be predicted by the Morse potential function. Rather, it was simulated using the finite difference method based on the thermal conductivity of electrons in metal. A larger argon crystal of about half a million atoms irradiated by a laser pulse was investigated [8]. Recently, Wang and Xu studied thermal and thermomechanical phenomena during picosecond laser ablation of an argon crystal of

a size of two million atoms [9,10]. Generation and propagation of the thermal stress, and the coupling between the temperature field and the stress field were discussed in detail.

In this work, MD simulations are conducted to study femtosecond laser ablation of copper. Over two million atoms are simulated using parallel computing techniques. Laser induced heat transfer, melting, surface evaporation, ablation (i.e., rapid removal of a significant amount of material, also referred to as a volumetric phase change process in this work) are studied. In addition, finite difference (FD) calculations are carried out and results of laser induced heating and melting are compared with those from MD calculations. The emphasis of this work is to investigate the mechanisms of laser ablation. Parameters relevant to laser ablation, such as the transient temperature history and superheating of the melted material are presented.

Theoretical Description of the Mechanisms of Femtosecond Laser Ablation

There are two processes of laser induced material removal: surface evaporation and volumetric liquid-vapor phase transformation [11]. Surface evaporation occurs at any melted surface. During pulse laser heating, however, surface evaporation normally accounts for a small fraction of the total material that is removed, since the high temperature state only lasts for a short period of time. Under high power, short pulse laser irradiation, another material removal mechanism, the volumetric phase transformation termed phase explosion becomes important [12,13]. Phase explosion can be illustrated using the p-v diagram as shown in Fig. 1(a). With rapid heating by a laser pulse, it is possible to raise the temperature above the boiling point "A". This is because the number of nucleation sites generated within the short heating duration is small. On the other hand, there is a boundary of thermodynamic phase stability, the spinode, which is marked as point "B" in Fig. 1(a). The spinodal temperature can be calculated from the derivatives of the Gibbs' thermodynamic potential using appropriate equation of state near the critical point. At the spinode, homogeneous (volumetric) nucleation, or phase explosion occurs. The liquid is turned into a mixture of liquid and vapor through an explosion (expansion) process as shown in Fig. 1(a) from state B to state C. Therefore, phase explosion is accompanied with melt

Contributed by the Heat Transfer Division for publication in the JOURNAL OF HEAT TRANSFER. Manuscript received by the Heat Transfer Division August 4, 2003; revision received June 3, 2004. Associate Editor: C. P. Grigoropoulos.

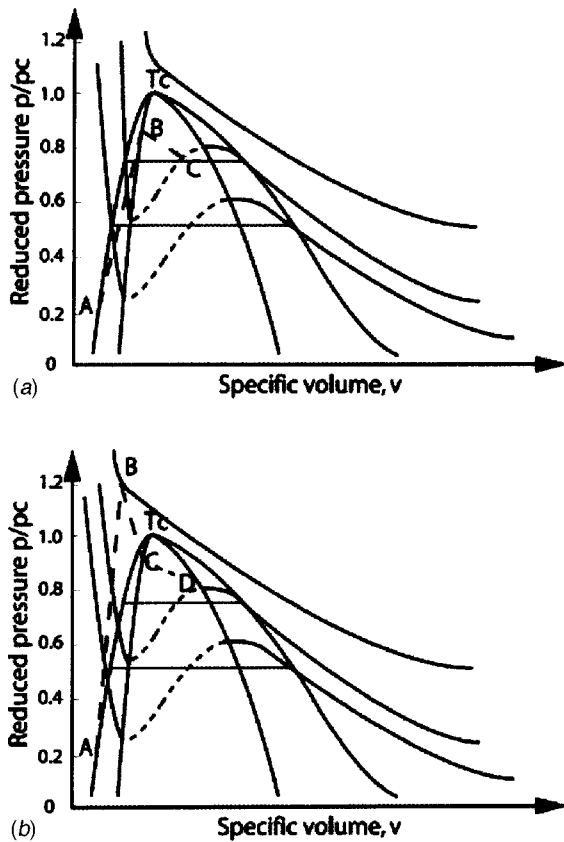


Fig. 1 (a) p - v diagram of phase explosion at spinode; and (b) p - v diagram of critical point phase separation

expulsion. Experimental work has shown that phase explosion occurs during nanosecond laser ablation of a metal [11,13].

The physical phenomena occurring in femtosecond laser ablation are much more complicated than those in nanosecond laser ablation. Due to the extremely short heating duration, the time required to transfer energy from the electron system to the lattice is longer than the laser pulse, leading to non-equilibrium between electrons and the lattice. Intense femtosecond laser pulses can cause electron emission. Because the mobility of electrons in dielectrics and semiconductors is low, a localized high ion density results which can exceed the lattice stability limit and cause Coulomb explosion—a type of nonthermal ablation [14,15]. Nonthermal Coulomb explosion is much more significant in dielectrics and semiconductors, while it plays a minor role in metal.

Femtosecond laser also causes an explosive type of material removal. An important factor that needs to be considered here is the time for vapor embryos to grow to nuclei prior to the volumetric phase change taking place. (Embryos smaller than a critical size will collapse, while those larger than the critical radius, called nuclei, will favor growing in order to reduce free energy.) The time for nucleation, or the time lag for phase explosion, has been estimated from the classical nucleation theory to be within 1 and 10 ns [16]. Experimental study showed that this time lag is about 5 ns during nanosecond laser ablation of a nickel target [17]. Since this time lag is longer than 1 ns, nucleation cannot occur during laser heating if the laser pulse is shorter than 1 ns. With the use of a femtosecond laser, heating above the spinodal temperature or even above the critical temperature becomes possible. A phase change process from the super-critical state to a two phase mixture is termed critical point phase separation [18]. The p - v diagram of critical point phase separation is shown in Fig. 1(b). Under an extreme heating rate, a material reaches a state above

the thermodynamic critical temperature “B”, followed by an expansion (relaxation) process during which the nucleation embryos continue to grow. When a sufficient number of nucleation sites are generated in this expansion process, a violent phase change process takes place (state “C” to “D”). The exact point when this phase change occurs (i.e., above or below the critical point) is not known, but is probably dependent on the peak temperature obtained during the process. In the past, such a phenomenon was only discussed in a theoretical context due to lack of means to achieve the required heating rate [18]. However, with femtosecond laser heating, it was suggested that the critical point phase separation could be responsible for ablation [19].

We have conducted many experimental and numerical researches on the phase change process during nanosecond laser ablation [11,13,17]. This work continues our efforts on the investigations of pulsed laser ablation, with the emphasis on the ablation induced by a femtosecond pulse. From the above discussion, information such as the transient temperature during the laser ablation process, the creation of the vapor phase inside the superheated liquid, and the time required to form a two-phase mixture are needed to describe the phase change phenomena induced by a femtosecond laser pulse. The MD calculations conducted in this work are intended to provide detailed descriptions of femtosecond laser ablation.

Numerical Approach

Molecular Dynamics simulation is a computational method to investigate the behavior of materials by computing the molecular or atomic motion governed by a given potential. For copper, a suitable potential is the Morse potential expressed as [7]

$$\Phi(r) = D[e^{-2b(r-r_e)} - 2e^{-b(r-r_e)}] \quad (1)$$

where D is the total dissociation energy and r_e is the equilibrium distance. The constant b in this equation determines the shape of the potential curve. When $r \rightarrow r_e$, the potential $\Phi \rightarrow -D$. At very large separation distance r , $\Phi \rightarrow 0$. Using the potential function, the force between two atoms is obtained as

$$F(r) = -\frac{\partial \Phi(r)}{\partial r} = 2Db[e^{-2b(r-r_e)} - e^{-b(r-r_e)}] \quad (2)$$

The Morse potential has been proven to be a good approximation to the interactions between atoms in fcc metals, and is capable of predicting many material properties [7]. It has been widely used in simulating laser ablation processes [6,20–23]. Although there are other potentials for copper used in literatures, such as the embedded atom method [24], we have chosen the Morse potential since it requires the least amount of computational time and also there is no evidence which potential provides better description for the laser ablation problem. MD simulations of picosecond laser ablation of metal using EAM yielded similar volumetric phase change phenomena as the one obtained in this work [25], although direct comparison is not possible because of the different laser parameters used in the two works (different pulsewidth, fluence, etc.).

The general approach of MD is to obtain atomic positions, velocities, etc. at time $t + \delta t$ based on positions, velocities, and other dynamic information at time t . The equations are solved on a step-by-step basis. Many different algorithms have been developed to solve Eqs. (1) and (2), of which the Verlet algorithm is widely used due to its numerical stability, convenience, and simplicity [26]. In this work, a modified Verlet algorithm is used [9].

In the calculation, most time is spent on calculating forces. However, it is not necessary to calculate forces between all atoms in a computational domain. When two atoms are far enough from each other, the force between them becomes very small (see Eq.

(2)). The distance beyond which the interaction force is negligible is called the cutoff distance (potential cutoff). In this work, r_c is taken as $2.4r_e$. At this distance r_c , the potential is about 0.9% of the equilibrium potential D .

Using the two-temperature model, the laser energy is considered absorbed by electrons in copper first, and is then transferred from electrons to the lattice. The governing equation for electrons and the electron-lattice coupling can be obtained from two-temperature model and is expressed as [27]

$$C_e \frac{\partial T_e}{\partial t} = \frac{\partial}{\partial x} \left(k_e \frac{\partial T_e}{\partial x} \right) - G(T_e - T_l) + S \quad (3)$$

The strength of energy coupling between electrons and the lattice is represented by G . The last term S represents absorption of energy by electrons from the laser. The laser source term S is expressed as the standard form for a laser pulse with a Gaussian temporal distribution:

$$S = 0.94 \frac{1-R}{t_p \delta} J \cdot \exp \left(-\frac{x}{\delta} - 2.77 \left(\frac{t-t_0}{t_p} \right)^2 \right) \quad (4)$$

The use of Eq. (3) for computing energy absorption and diffusion in the electron system is justified. This is because the time for electrons to absorb photon energy and reach thermal equilibrium (electron thermalization time) is short, on the order of 500 fs [28]. This time scale is less than the time for energy to transfer from electrons to the lattice (\sim ps) and the time of the subsequent phase change process (\sim 10 ps or longer), which is the main focus of this study. In other words, the detailed process of how the electrons reach equilibrium, which occurs much earlier than the lattice structural change, is not important for this work.

The TDMA (Tri-Diagonal Matrix Algorithm) method is used to solve Eq. (3). At each time step, the electron-lattice coupling term $G(T_e - T_l)$ is added to the lattice by scaling the velocities of all atoms in a structural layer by a factor $\sqrt{1 + G(T_e - T_l) \delta t / E_{k,t}}$, where $E_{k,t}$ is the total kinetic energy in the layer at the time t . This is equivalent to increasing the lattice energy as

$$C_l \frac{\partial T_l}{\partial t} = G(T_e - T_l) \quad (5)$$

Heat conduction in the lattice is always considered in the MD simulation, although it is insignificant compared with the electron conduction in a metal. The change of density due to thermal expansion or phase change is considered by scaling the thermal conductivity and specific heat of electrons in each cell by the ratio of the local density to the original density. Therefore, when expansion happens, the effective thermal conductivity and specific heat decreases, which is consistent with the electron properties of metals [29]. The total energy of the two systems is monitored and compared to the input laser energy at each time step. The procedure of handling heating of the lattice in a MD calculation has been described elsewhere [9].

A significant effect in femtosecond laser heating of metals is the ballistic motion of electrons [30,31]. This effect effectively leads to a greater absorption depth and hence lower surface temperatures [3]. However, no experimental data is available on the ballistic effect in copper, although it is expected to have some effect in all s/p-band metals [31]. As the main emphasis in this work is on identifying the material removal mechanisms rather than comparison with experimental data, inclusion of the ballistic effect is not strictly necessary as it would simply lead to a modification of the optical penetration depth and hence increase the threshold fluences for phase change.

The computational domain consists of 30 fcc (face-centered cubic) unit cells in y and z -directions, and 600 fcc unit cells in the

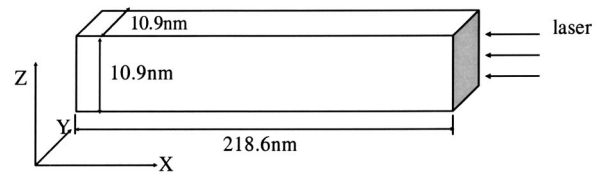


Fig. 2 Schematic of the computational domain

x -direction, which is shown in Fig. 2. The total number of atoms is 2,160,000. The whole computational domain before laser heating is $10.97 \text{ nm} \times 10.97 \text{ nm} \times 218.65 \text{ nm}$. This computational size is sufficient to track the propagation of the phase change interface in the direction normal to the laser irradiated surface (the x -direction), as well as to maintain a large number of atoms in the y - z cross-sectional area so that macroscopic properties such as temperature can be determined from statistical analysis [9]. Periodic boundary conditions are used in y and z -directions, and free boundary conditions in the x -direction.

The large number of atoms in the simulation necessitates the use of parallel computing platforms to accelerate computation. At the present time, a cluster of eight PCs is used, each with a 2.0 GHz AMD Athlon processor. The work across the processors is partitioned by dividing the whole domain into eight sub-domains so that the number of atoms for each processor is almost the same. Each processor computes forces and updates positions of all particles in the sub-domain. MPICH, a Message Passing Interface is used, which performs inter-processor communication for atoms close to inter-processor domain boundaries for both computing forces and reassigning atoms based on updated positions. Figure 3 shows the schematic of the domain division and calculation process. For simplicity, a four-node system is illustrated. Interfacial layers are designated in each sub-domain, where the information of the atom positions and velocities is identical in the neighboring sub-domains. During each time step, each subdomain is first calculated by its processor, and atom position and velocity updating and exchanging are carried out on the interfacial layers between sub-domains. In other words, each processor only computes one sub-domain; the interfacial layer does not need to be calculated by both processors as the information is passed from one sub-domain to the other as shown in Fig. 3. Therefore, no extra time is spent on force calculations which are the most time consuming part of the computation. This technique greatly reduces the storage space requirement, and more importantly, the information exchanging load between processors. Calculations show that the overall efficiency of the parallel program is excellent, about 90–92% on eight processors. This implies that the overhead associated with load imbalance and communication is small.

In addition to the MD calculations, finite difference calculations are also carried out. As will be shown later, the FD calculation does not provide correct results about the material removal since it

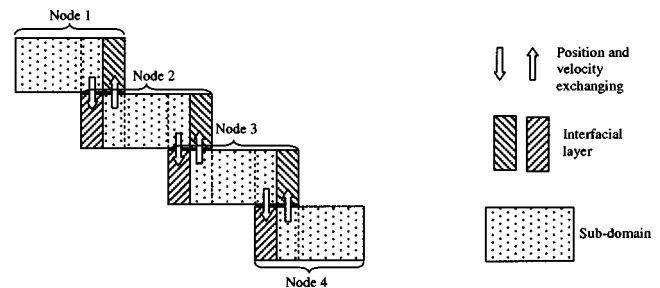


Fig. 3 Schematic of domain division and position and velocity exchange in parallel calculation

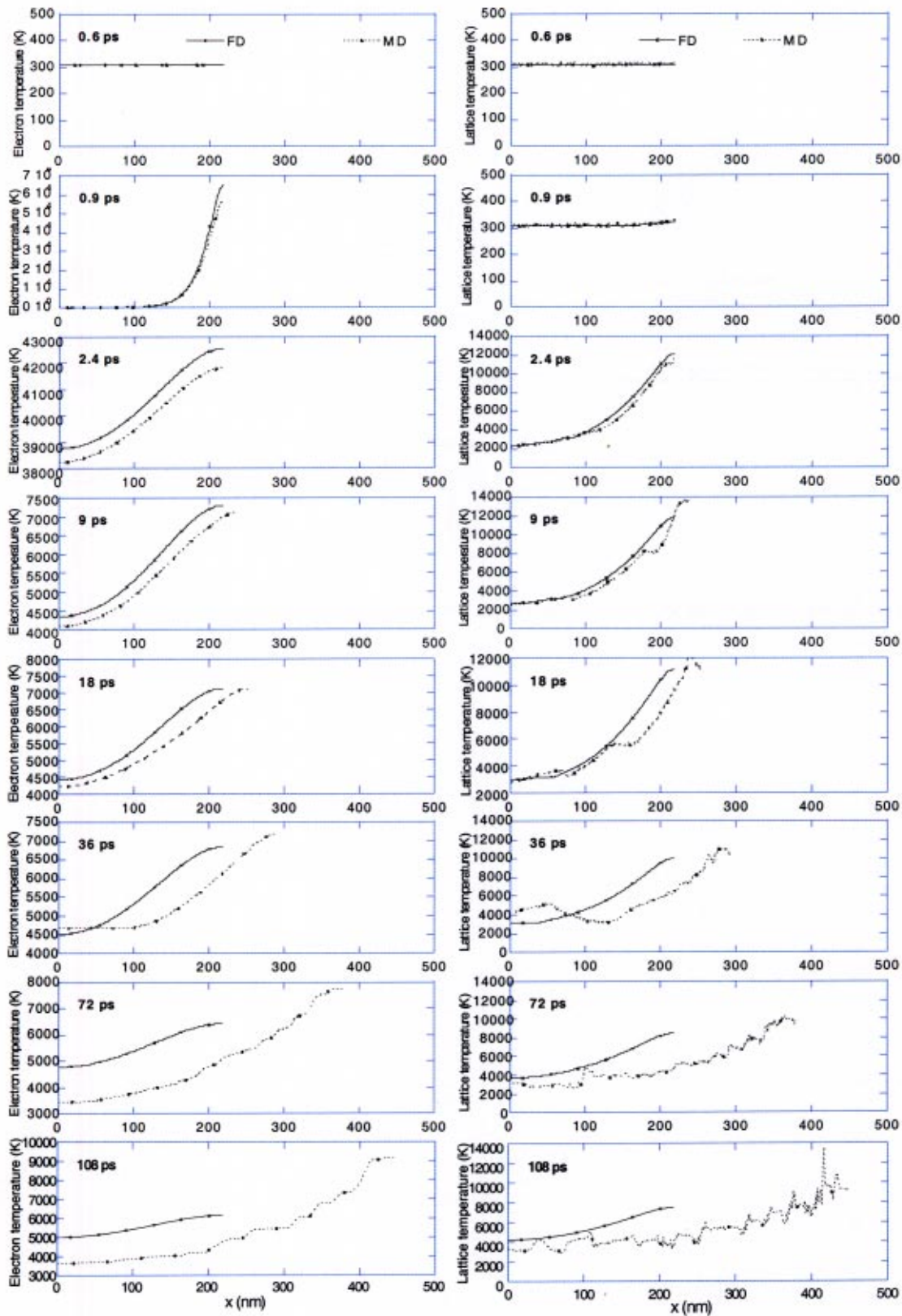


Fig. 4 Comparison of electron (left column) and lattice temperatures (right column) obtained from MD and FD calculations

does not account for the volumetric phase change described previously. The purpose here is to compare with the MD results before the volumetric phase change occurs. The FD calculation is based on the non-equilibrium hyperbolic two-step model [2]. For

the present simulation, the model is simplified to consider only one-dimensional heat conduction and the hyperbolic part is neglected to yield a simpler parabolic set of equations. These assumptions are justified as the laser spot size is large compared to

the heat penetration depth and the laser pulse width (100 fs) is long compared to the electron relaxation time [2]. The coupled equations of the model are:

$$C_e \frac{\partial T_e}{\partial t} = \frac{\partial}{\partial x} \left(\kappa_e \frac{\partial T_e}{\partial x} \right) - G(T_e - T_l) + S \quad (6a)$$

$$C_l \frac{\partial T_l}{\partial t} = \frac{\partial}{\partial x} \left(\kappa_l \frac{\partial T_l}{\partial x} \right) + G(T_e - T_l) \quad (6b)$$

It is seen that absorption of laser energy by electrons is modeled in the same way as in the MD calculation, while heat transfer in the lattice is modeled using the heat diffusion equation (Eq. 6(b)). The laser source term S is identical to what is shown in Eq. (4). The initial electron and lattice temperatures are taken to be equal to the room temperature and the top and bottom surfaces of the target are assumed to be insulated.

At high fluences and short pulse widths considered in this study, rapid solid-liquid phase changes are controlled by nucleation dynamics rather than by heat transfer at the phase change interface [32]. At the solid-liquid interface, the relation between the superheating/undercooling at the interface, $\Delta T = T_{sl} - T_m$, and the interface velocity V_{sl} is given by

$$V_{sl}(T_{sl}) = V_0 \left[1 - \exp \left(- \frac{L_{sl} \Delta T}{k_b T_{sl} T_m} \right) \right] \quad (7)$$

where T_{sl} is the temperature of the solid-liquid interface, T_m the equilibrium melting temperature, and L_{sl} the enthalpy of fusion per atom. V_0 is a velocity factor. The energy balance equation at the solid-liquid interface is

$$\kappa_s \left. \frac{\partial T_l}{\partial x} \right|_s - \kappa_{liq} \left. \frac{\partial T_l}{\partial x} \right|_{liq} = \rho_s V_{sl} L_{sl} \quad (8)$$

Procedures of solving Eqs. (5)–(7) have been described elsewhere [3].

In general, material removal by evaporation during femtosecond laser heating can be modeled using the Clausius-Clapeyron equation to provide for superheating at the liquid-vapor interface, the energy loss due to evaporation, and the amount of material evaporated [3,32]. However, it was noticed that evaporation contributes very little to the actual material removal process. It was seen that for femtosecond heating of gold, evaporation would contribute only about 0.1 nm of materials removal [3]. The energy lost due to evaporation is also negligible compared with the energy absorbed by the system. As such, in this calculation, the evaporation process was neglected and the material was allowed to stay liquid past the equilibrium evaporation temperature.

For both calculations, the laser beam is considered uniform in space, with a temporal Gaussian distribution (Eq. (4)) of 100 fs FWHM centered at 1 ps. The laser beam energy is absorbed exponentially in the target, with an absorption depth δ of 12.6 nm. Other parameters used in the calculations are: $C_e = 2.1 \times 10^4$ J/m³-K, $\kappa_e = 386$ W/m-K, $G = 4.8 \times 10^{16}$ W/m³-K, $C_l = 383.817$ J/kg-K, $\kappa_l = 0.01 \times \kappa_e$, $L_{sl} = 2.07 \times 10^5$ J/kg, $T_m = 1358.0$ K, $\rho_s = 8.96 \times 10^3$ kg/m³, $D = 0.3429$ eV, $b = 13.588$ nm⁻¹, and $r_g = 0.2866$ nm. The laser fluence (absorbed) is 0.4 J/cm². Properties used here are considered temperature-independent, since temperature dependent properties near the critical point are not available. However, the uncertainties in the properties will not affect this study since the focus is on the mechanisms of laser ablation, rather than obtaining the absolute thermodynamic parameters at the laser fluence used in the calculation.

Results and Discussion

Figure 4 shows electron and lattice temperature distributions in the target computed using the MD and FD methods. The surface is at the right edge, and laser pulse is incident on the surface from

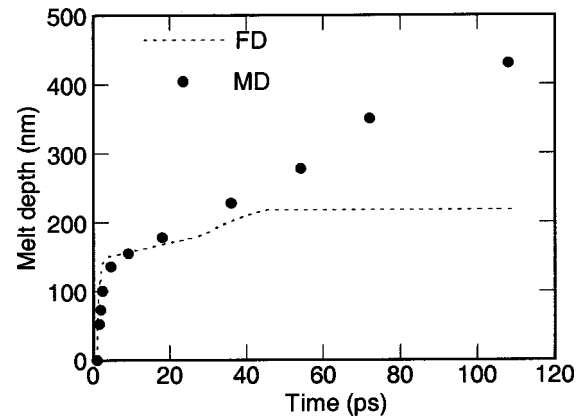


Fig. 5 Comparison of the melt depth obtained from MD and FD calculations

right to left. In the MD simulation, the temperature of the lattice at different locations is calculated as an ensemble average of a domain with a thickness of $2.4r_g$ in the x direction.

From Fig. 4, it is seen that the electron temperature on the surface increases from room temperature to a very high value (on the order of 10^5 K) within half a picosecond. However, at that time, the lattice temperature only increases tens of degrees. As electrons transfer energy to the lattice, the thermal expansion causes the length of the domain to increase. Note this lattice expansion is computed in the MD simulation only. It is observed from the figures that the results from the two calculations are comparable until about 9 ps. After that time, the results diverge as the FD calculation does not account for thermal expansion and the actual material removal caused by material breakup as observed in the MD calculation. For example, at 18 ps, the length of the MD calculation domain becomes more than 20 nm longer than the length of the FD calculation domain, which does not change with time. Further, at about 30 ps, the material starts break up (as will be seen in Figs. 6 and 7), which leads to a much longer total domain length. This type of volumetric phase change is not accounted for in the FD calculation. The temperature distributions from the FD and MD calculations diverge further after this volumetric phase change occurs.

A plot of the melt front position as a function of time shown in Fig. 5 also indicates that the two calculations yield similar results before liquid-vapor phase change begins. Before 20 ps, the melt depth calculated from MD is slightly larger than that from MD, which is caused by the thermal expansion as seen from the MD results in Fig. 4 and Fig. 6. After about 30 ps, the melt front positions calculated from the two methods start to differ significantly. This is because that the volumetric phase change is not considered in the FD calculation. In Fig. 5, the melt depth from the MD calculation is evaluated as the distance between the solid/liquid interface and the liquid surface, which includes gas bubbles formed inside the liquid (see Figs. 6 and 7) and therefore results in a much longer melt depth. The comparisons of the surface temperature and the melt depth indicate that the two methods provide similar results for heating and solid-liquid phase change prior to the beginning of the volumetric phase change.

The atomic number density at different times computed from the MD simulation is shown in Fig. 6. For solid, the value of number density at the location of a lattice layer is much higher than the average value, and the value at the location between lattice layers is almost zero. For liquid, the atomic number density is uniform due to the lack of periodic structures. For the gas state, the number density is very low compared with the liquid. Therefore, the atomic density shows clearly the state of matter at different locations in the computational domain. Figure 6 indicates that the lattice structure is intact within the first 1 ps or so, which

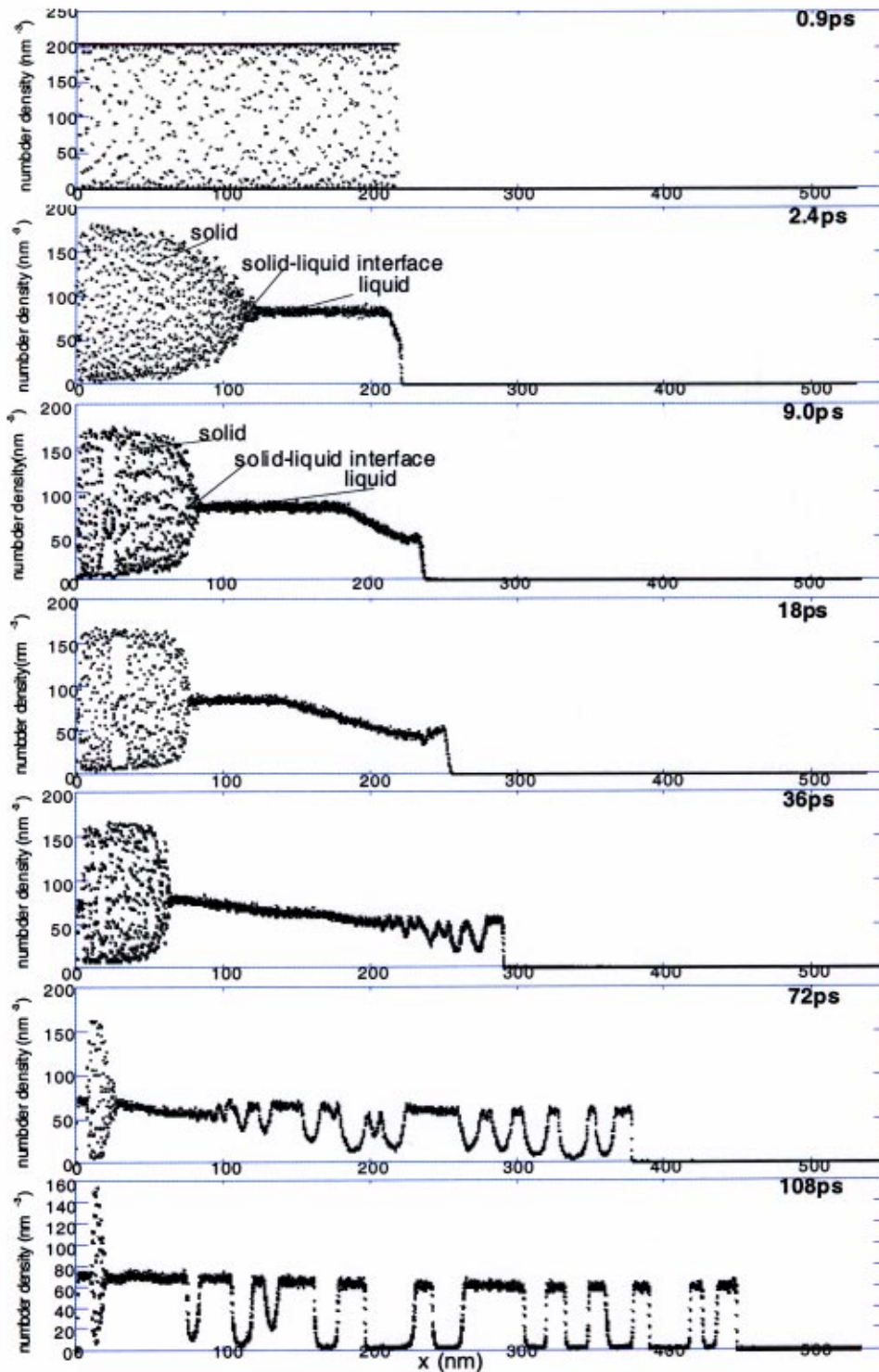


Fig. 6 Atomic number density at different time steps

is reflected by the oscillation of the atomic number density over the entire calculation domain. Melting has occurred at 2.4 ps but most of the target still has the lattice structure. On the surface, the number density drops from a uniform value to almost zero, showing evaporation occurs at the surface. At 9 ps, the melt propagates further into the target, and more atoms are evaporated. Fluctuation of the number density is seen near the surface at 36 ps, indicating bubbles are forming inside the liquid. This will be shown more

clearly in Fig. 7. At later times of 72 ps and 108 ps, more bubbles are generated and the sizes of the bubbles grow larger.

Figure 7 presents several snapshots of two-dimensional (z - x) projections of atomic positions. Because of the large number of atoms, the lattice structure, if it exists, cannot be seen clearly in Fig. 7. Rather, this figure provides another way to show the phase change process inside the melted layer. Bubbles are seen at 36 ps. As time progresses, more bubbles grow from inside the domain.

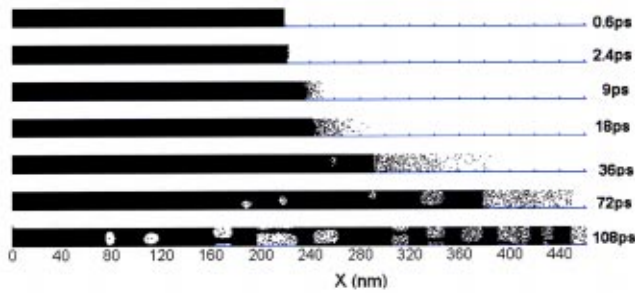


Fig. 7 Atomic positions at different time steps

At 108 ps, the liquid layer is broken into a number of pieces and has essentially ablated. It is found that the velocity of the ablated part near the surface is about 1960 m/s, while the inside part (at the location of 200 nm) is about 900 m/s.

Smaller bubbles may not be seen easily in Fig. 7. In order to observe the exact time when the bubble growth begins, atomic positions are re-plotted over 1/10th of the thickness in the y-direction (about 1 nm) at every time step. Bubbles can be seen as early as 18 ps, which is shown in Fig. 8. These bubbles are not observed in the 18 ps plot in Fig. 7 since they are obstructed by the atoms in front of and behind them along the y-direction.

A comparison between Fig. 4 and Fig. 6 provides more information on the relation between phase change and temperature distribution. In Fig. 4, the MD calculations show that there are two lattice temperature plateaus at 9 ps. One is at about 140 nm from the surface (86 nm measured from the bottom, or left). Figure 6 shows that at that time step, the solid-liquid interface is located at 86 nm. The other is at 185 nm, which is the evaporating surface as shown in Fig. 6. It is also seen that the lattice temperatures at these two locations are about 3200 K and 8200 K, respectively. For comparison, the equilibrium melting and boiling points of copper are 1358 K and 2835 K [33]. (The melting temperature of copper computed from the Morse potential is 2090 K [34].) Therefore, strong superheating at these interfaces is observed from the MD calculation.

To better illustrate the temperature history and to explain the ablation process, the transient lattice temperature at the surface is plotted in Fig. 9. It is seen that within a few picosecond, the surface temperature increases rapidly to its peak value of about 1.5×10^4 K. This temperature is above the critical temperature of copper, 7625 K [35]. After that, the temperature decreases due to the expansion of the high temperature material as shown in Figs. 6 and 7. The volumetric phase change does not occur until the expansion process continues for more than 10 ps. Since the volumetric phase change process occurs above the critical point, the critical point phase separation process described previously could have occurred. However, this may not be conclusive since the critical temperature used for comparison is not obtained from the MD calculation. Computations of the critical temperature are currently underway.

Comparing calculation results with experimental data is generally difficult because of the different criteria used in experiments to judge ablation. This is mainly due to the difficulty in distinguishing material removal from surface modification caused by

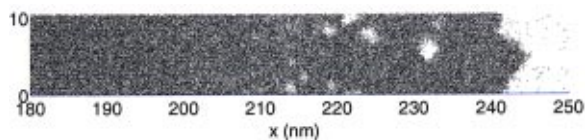


Fig. 8 Atomic position at 18 ps, showing a layer in the y-direction from $y=4$ nm to 5 nm

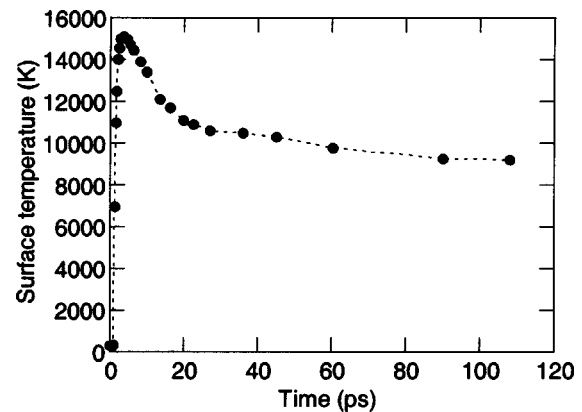


Fig. 9 Surface temperature history

melting and fluid flow. We conducted calculations of 248 nm, 0.5 ps KrF excimer laser ablation of copper, and found that the threshold for volumetric phase change is about 410 mJ/cm^2 (total fluence), while the threshold for melting is about 160 mJ/cm^2 . The ablation threshold reported in literature [36] is 170 mJ/cm^2 . It is difficult to assess whether the reported threshold value was actually the melting or surface damage threshold, or there was a discrepancy between calculation and experiments. Various factors can contribute to the discrepancy between calculations and experiments, including inaccurate potentials and properties used in the calculation, and oxidation of the surface in a normal experimental condition which leads to a much different absorptivity compared with that used in the calculation.

Conclusions

In summary, femtosecond laser material interaction is studied using numerical simulations. It is found that before the strong, volumetric material removal process takes place, heat transfer and the solid liquid phase change predicted using the FD approach agrees with the result of the MD simulation. At the solid-liquid and liquid-vapor interfaces, strong superheating is observed. The MD simulation predicts a volumetric type of phase change under the evaporating surface, which accounts for material removal during laser machining that is not computed by the FD method.

Acknowledgments

Support to this work by the National Science Foundation and the Office of Naval Research are gratefully acknowledged. The authors also thank Prof. A. Y. Grama of the Department of Computer Science, Purdue University for his help on parallel MD.

Nomenclature

- b = constant in Morse potential
- C_e = specific heat of electron
- C_l = specific heat of lattice
- D = total dissociation energy in Morse potential
- F = force between two atoms
- G = electron-lattice coupling factor
- J = laser fluence
- k_b = Boltzmann constant
- k_e = thermal conductivity of electron
- k_l = thermal conductivity of lattice
- k_{liq} = thermal conductivity of liquid
- k_s = thermal conductivity of solid
- L_{sl} = enthalpy of fusion per atom
- r = distance between two atoms
- R = reflectivity
- r_c = cutoff distance
- r_e = the equilibrium distance between two atoms

S = source term of laser heating
 t = time
 t_0 = center time of the laser pulse
 T_e = electron temperature
 T_l = lattice temperature
 T_m = equilibrium melting temperature
 t_p = laser pulse width
 T_{sl} = temperature of solid-liquid interface
 V_0 = factor to calculate solid-liquid interface velocity
 V_{sl} = velocity of solid-liquid interface
 x = coordinate in the direction of laser irradiation
 Φ = potential between two atoms
 δ = absorption depth
 ρ_s = density of solid

References

- [1] Anisimov, S. I., Kapeliovich, B. L., and Perel'man, T. L., 1974, "Electron Emission From Metal Surfaces Exposed to Ultra-Short Laser Pulses," *Sov. Phys. JETP*, **39**, pp. 375–377.
- [2] Qiu, T. Q., and Tien, C. L., 1993, "Heat Transfer Mechanisms During Short-Pulse Laser Heating of Metals," *ASME J. Heat Transfer*, **115**, pp. 835–841.
- [3] Chowdhury, I. H., and Xu, X., 2003, "Heat Transfer in Femtosecond Laser Processing of Metal," *Numer. Heat Transfer, Part A*, **44**, pp. 219–232.
- [4] Kotake, S., and Kuroki, M., 1993, "Molecular Dynamics Study of Solid Melting and Vaporization by Laser Irradiation," *Int. J. Heat Mass Transfer*, **36**, pp. 2061–2067.
- [5] Herrmann, R. F. W., and Campbell, E. E. B., 1998, "Ultrashort Pulse Laser Ablation of Silicon: an MD Simulation Study," *Appl. Phys. A: Solids Surf.*, **66**, pp. 35–42.
- [6] Ohmura, E., Fukumoto, I., and Miyamoto, I., 1999, "Modified Molecular Dynamics Simulation on Ultrafast Laser Ablation of Metal," *Proceedings of the International Congress on Applications of Lasers and Electro-Optics*, Laser Institute of America, Orlando, pp. 219–228.
- [7] Girifalco, L. A., and Weizer, V. G., 1959, "Application of the Morse Potential Function to Cubic Metals," *Phys. Rev.*, **114**, pp. 687–690.
- [8] Etcheverry, J. I., and Mesaros, M., 1999, "Molecular Dynamics Simulation of the Production of Acoustic Waves by Pulsed Laser Irradiation," *Phys. Rev. B*, **60**, pp. 9430–9434.
- [9] Wang, X., and Xu, X., 2002, "Molecular Dynamics Simulation of Heat Transfer and Phase Change During Laser Materials Interaction," *ASME J. Heat Transfer*, **124**, pp. 265–274.
- [10] Wang, X., and Xu, X., 2002, "Molecular Dynamics Simulation of Thermal and Thermomechanical Phenomena in Picosecond Laser Material Interaction," *Int. J. Heat Mass Transfer*, **46**, pp. 45–53.
- [11] Xu, X., 2001, "Heat Transfer and Phase Change in Pulsed Excimer Laser Ablation of Metal," *Annual Review of Heat Transfer*, **12**, C.-L. Tien, V. Prasad, and F. P. Incropera, eds., Bell House, New York, pp. 79–115.
- [12] Kelly, R., and Miotello, A., 1996, "Comments on Explosive Mechanisms of Laser Sputtering," *Appl. Surf. Sci.*, **96–98**, pp. 205–215.
- [13] Song, K. H., and Xu, X., 1998, "Explosive Phase Transformation in Pulsed Laser Ablation," *Appl. Surf. Sci.*, **127**, pp. 111–116.
- [14] Siders, C. W., Cavalier, A., Sokolowski-Tinten, K., Toth, Cs., Guo, T., Kammler, M., Horn von Hoegen, M., Wilson, K. R., von der Linde, D., and Barty, C. P. J., 1999, "Detection of Nonthermal Melting by Ultrafast X-Ray Diffraction," *Science*, **286**, pp. 1340–1342.
- [15] Henyk, M., Wolframm, D., and Reif, J., 2000, "Ultra Short Laser Pulse Induced Charged Particle Emission From Wide Bandgap Crystals," *Appl. Surf. Sci.*, **168**, pp. 263–266.
- [16] Skripov, V. P., 1974, *Metastable Liquids*, John Wiley & Sons, New York.
- [17] Xu, X., and Willis, D. A., 2002, "Non-Equilibrium Phase Change in Metal Induced by Nanosecond Pulsed Laser Irradiation," *ASME J. Heat Transfer*, **124**, pp. 293–298.
- [18] Skripov, V. P., and Skripov, A. V., 1979, "Spinodal Decomposition (Phase Transition via Unstable States)," *Soviet Physics Uspekhi*, **22**, pp. 389–410.
- [19] Vidal, F., Johnston, T. W., Laville, S., Barthelemy, O., Chaker, M., Le Drogoff, B., Margot, J., and Sabsabi, M., 2001, "Critical-Point Phase Separation in Laser Ablation of Conductors," *Phys. Rev. Lett.*, **86**, pp. 2573–2576.
- [20] Constantoudis, V., and Nicolaides, C. A., 2001, "Nonhyperbolic Escape and Changes in Phase-Space Stability Structures in Laser-Induced Multiphoton Dissociation of a Diatomic Molecule," *Phys. Rev. E*, **64**, p. 056211.
- [21] Ohmura, E., Fukumoto, I., and Miyamoto, I., 2000, "Molecular Dynamics Simulation of Ablation Process With Ultra-Short Pulsed Laser," *Proc. SPIE*, **4088**, pp. 84–89.
- [22] Nedialkov, N. N., Imamova, S. E., and Atanasov, P. A., 2004, "Ablation of Metals by Ultrashort Laser Pulses," *J. Phys. D*, **37**, pp. 638–643.
- [23] Atanasov, P. A., Nedialkov, N. N., Imamova, S. E., Ruf, A., Hügel, H., Dausinger, F., and Berger, P., 2002, "Laser Ablation of Ni by Ultrashort Pulses: Molecular Dynamics Simulation," *Appl. Surf. Sci.*, **186**, pp. 369–373.
- [24] Foiles, S. M., Baskes, M. I., and Daw, M. S., 1986, "Embedded-Atom-Method Functions for the fcc Metals Cu, Ag, Au, Ni, Pd, Pt, and Their Alloys," *Phys. Rev. B*, **33**, pp. 7983–7991.
- [25] Schäfer, C., Urbassek, M., and Zhigilei, L. V., 2002, "Metal Ablation by Picosecond Laser Pulses: A Hybrid Simulation," *Phys. Rev. B*, **66**, pp. 115404-1–115404-8.
- [26] Allen, M. P., and Tildesley, D. J., 1987, *Computer Simulation of Liquids*, Clarendon Press, Oxford.
- [27] Häkkinen, H., and Landman, U., 1993, "Superheating, Melting and Annealing of Copper Surfaces," *Phys. Rev. Lett.*, **71**, pp. 1023–1027.
- [28] Sun, C.-K., Vallée, F., Acioli, L. H., Ippen, E. P., and Fujimoto, J. G., 1994, "Femtosecond-Tunable Measurement of Electron Thermalization in Gold," *Phys. Rev. B*, **50**, pp. 15337–15347.
- [29] Berman, R., 1976, *Thermal Conduction in Solids*, Clarendon Press, Oxford.
- [30] Brorson, S. D., Fujimoto, J. G., and Ippen, E. P., 1987, "Femtosecond Electronic Heat-Transport Dynamics in Thin Gold Films," *Phys. Rev. Lett.*, **59**, pp. 1962–1965.
- [31] Hohlfeld, J., Wellershoff, S.-S., Gütde, J., Conrad, U., Jähnke, V., and Matthias, E., 2000, "Electron and Lattice Dynamics Following Optical Excitation of Metals," *Chem. Phys.*, **251**, pp. 237–258.
- [32] Xu, X., Chen, G., and Song, K. H., 1999, "Experimental and Numerical Investigation of Heat Transfer and Phase Change Phenomena During Excimer Laser Interaction With Nickel," *Int. J. Heat Mass Transfer*, **42**, pp. 1371–1382.
- [33] Lide, D. R., 2001, *CRC Handbook of Chemistry and Physics*, CRC Press, Boca Raton.
- [34] Wang, X., 2004, "Thermal and Thermomechanical Phenomena in Picosecond Laser Copper Interaction," *ASME J. Heat Transfer*, **126**, pp. 355–364.
- [35] Young, D. A., and Alder, B. J., 1971, "Critical Point of Metals From the van der Waals Model," *Phys. Rev. E*, **3**, pp. 364–371.
- [36] Preuss, S., Demchuk, A., and Stuke, M., 1995, "Sub-Picosecond UV Laser Ablation of Metals," *Appl. Phys. A: Solids Surf.*, **61**, pp. 33–37.

Modified Method of Characteristics for Simulating Microscale Energy Transport

Laurent Pilon*

e-mail: pilon@seas.ucla.edu

Kamal M. Katika

Mechanical and Aerospace Engineering
Department, Henri Samueli School of
Engineering and Applied Science,
University of California, Los Angeles
Los Angeles, CA 90095

This paper presents a new numerical scheme for simulating multidimensional transient and steady-state microscale energy transport. The new method is based on the method of characteristics that follows heat carriers along their pathline. Unlike traditional methods, it uses a fixed computational grid and follows the heat carriers backward in time. The method 1) is accurate, 2) is unconditionally stable, 3) can deal with complex geometries without a large increase in computational cost, and 4) can be used for solving coupled equations using other numerical schemes. First, the numerical scheme is described. Then, simulations for transient and steady-state phonon transport in dielectric thin films are discussed. Numerical results are compared with analytical and reported numerical solutions and good agreement is obtained. [DOI: 10.1115/1.1795233]

Keywords: Heat Conduction, Microscale, Nanoscale, Heat Transfer, Boltzmann Transport Equation

1 Introduction

During the last decade, heat transfer at microscale has been the object of intense studies [1,2]. The research effort has been driven by important applications in microelectronics, thin films, nanomaterials, and short-pulse laser heating. The conventional approach to heat conduction problems using macroscopic empirical laws such as Fourier's law or Joule's law of heat generation break down when the length scale of the system is comparable to the energy carrier mean free path or when the time scale of the physical process is smaller than the relaxation time of the heat carriers [2,3]. Then, transport of heat carriers must be treated in greater details.

Heat is transported by carriers comprising of electrons, phonons, and photons. Heat conduction is dominated by phonons in dielectric materials, predominantly by electrons in pure metals, and by both phonons and electrons in impure metals or alloys [4]. In all cases, transport of the heat carriers is governed by the Boltzmann transport equation (BTE). The density function of heat carriers can be described in a state space consisting not only of the physical space but also of an abstract wavevector space. In the physical space, the state vector coordinates consist of the spatial coordinates [e.g., (x, y, z) in Cartesian coordinates]. In the wavevector space, the system is characterized by its wavevector \vec{k} . Considering electron and phonon transport, the state vector \vec{S} can be expressed as $\vec{S} = [\vec{r}, \vec{k}, t]$. Let f_p be the distribution function of the energy carriers in the polarization state p . The distribution function $f_p(\vec{r}, \vec{k}, t)$ is assumed to be sufficiently smooth to allow differentiation with respect to any of its variables as many times as necessary [5]. Then, the BTE can be expressed as [6]

$$\frac{\partial f_p}{\partial t} + \vec{v} \cdot \nabla_x f_p + \frac{d\vec{k}}{dt} \cdot \nabla_k f_p = \left(\frac{\partial f_p}{\partial t} \right)_{sca} \quad (1)$$

where \vec{v} and \vec{k} are the group velocity vector (velocity of energy propagation) and wavevector of the heat carriers, respectively. The operators ∇_x and ∇_k are the gradient operators in the physical and wavevector space, respectively. The second term on the left-hand side of Eq. (1) represents the advection of the distribution,

while the third term corresponds to the change of momentum caused by external fields relating to the particle acceleration. Finally, the term $(\partial f_p / \partial t)_{sca}$ on the right-hand side of Eq. (1) represents the restoration of thermodynamic equilibrium due to scattering by electrons, holes, defects in the lattice, and phonons [7].

Different formulations of the BTE have been developed in recent years to solve engineering problems. The first alternative formulation to the BTE for phonon transport has been developed by Majumdar [3], who recognized that the flux of energy per unit time, per unit area, per unit solid angle in the direction \vec{s} , and per unit frequency interval around ω can be written as

$$I_\omega(\vec{r}, \vec{s}, \omega, t) = \frac{1}{4\pi} \sum_{p=1}^3 \hbar \omega v_{pf_p}(\vec{r}, \vec{s}, \omega, t) \mathcal{D}_p(\omega) \quad (2)$$

where \vec{s} is the unit vector in the direction of carrier propagation, $\hbar \omega$ is the heat carrier energy, while v_p and $\mathcal{D}_p(\omega)$ are the speed of sound and the phonon density of states per unit volume for each polarization, respectively. The summation is over the three phonon polarization states [3,4]. The resulting form of the BTE has been named the equation of phonon radiative transfer (EPRT) [3].

Another common approach used for electron transport consists of solving for one or several moments of the distribution function [6,7]. A partial differential equation for each moment can be derived from the BTE to assure conservation of charge, momentum, and energy resulting in the so-called hydrodynamic equations. They are the governing equations for the electron density n_e , momentum \vec{p}_e , and energy E_e and can be derived by integrating the BTE over all frequencies after multiplying it by 1, $p_e = m_e^* \vec{v}_e$, and $E_e = p_e^2 / 2m_e^*$, respectively. Hydrodynamic equations are often solved instead of the BTE. The moment method has the advantage of reducing computational times, a valuable feature in control and optimization [5]. However, the discrete formulation has major drawbacks that have been discussed extensively by Kumar and Ramkrishna [8,9]. In brief, the discrete formulation lacks of *internal consistency*, i.e., some of the moments of the particle density function f_p (or of the spectral intensity) cannot be predicted accurately. The calculation is designed for certain arbitrarily selected moments of the particle density function rather than for an estimate of the particle density function accurate enough for estimating *all* moments of the population [5]. For example, an important moment includes the energy flux due to electrons \vec{q}_e expressed as,

*Corresponding author.

Contributed by the Heat Transfer Division for publication in the JOURNAL OF HEAT TRANSFER. Manuscript received by the Heat Transfer Division June 11, 2003; revision received February 20, 2004. Associate Editor: C. P. Grigoropoulos.

$$\vec{q}_e(\vec{r}, t) = \int \epsilon \vec{v}_e f_e(\vec{r}, \epsilon, t) \mathcal{D}(\epsilon) d\epsilon \quad (3)$$

More recently, Chen [10] derived the ballistic-diffusion heat conduction equations by dividing the phonon distribution function into the carriers originating from the boundaries and the carriers originating from the medium. Governing equations and boundary conditions for each component (ballistic or diffuse) of the distribution have been derived from the BTE.

Even though the formulation of the thermal transport at microscale has long been established [4], experiments of heat transfer at subcontinuum scale poses great challenges, and numerical simulations have become critical to the fundamental understanding of the phenomena and to the engineering design of submicron electronic devices [11]. As recognized by different authors [1,3], the major difficulty lies in solving the BTE or the subsequent equations.

Due to the analogy between the radiative transfer equation (RTE) and the Boltzmann transport equation [3], the traditional numerical methods employed for solving the radiative transfer equation have been used to solve the EPRT [3,11–13]. For example, Joshi and Majumdar [12] used the Schuster-Schwarzchild two-flux approximation to solve the transient and steady-state heat conduction across a diamond thin film. In the case of steady-state heat conduction along a dielectric thin film with specular phonon reflection at the boundary, Klitsner et al. [14] solved the BTE using the Monte Carlo simulations while Majumdar [3] solved the EPRT using the discrete ordinate method of Kumar et al. [15]. In both cases, the dielectric thin film was assumed to be a gray medium. Traditional discrete ordinate methods have also been used by other researchers [13]. More recently, Murthy and Mathur [11] proposed the use of unstructured solution-adaptive finite volume methods. Each one of these methods has some advantages and drawbacks.

Finite difference or finite volume methods are widely used in engineering to solve partial differential equations. Numerical solutions of relatively simple problems are readily and efficiently found by using these techniques, particularly for steady states. However, major drawbacks include 1) false scattering due to inadequate spatial discretization of the transient BTE, which leads to smearing of the wavefront [16], 2) the numerical instability that may force one to reduce the time step or the finite volume dimensions, 3) the formulation and the computing requirements increase greatly for problems of complex geometry and anisotropic behavior of the medium [17], and 4) the ray effect due to angular discretization can cause “large errors in the prediction of the equivalent temperature unless fine angular discretizations are used, particularly at low acoustic thicknesses,” as recognized by Murthy and Mathur [18]. The authors combined a ray-tracing technique with the finite volume method to improve predictions of the method [18].

The discrete ordinate method (DOM) is another popular method for solving the RTE or the BTE for neutrons and phonons [3,17]. The equation is solved for an arbitrary set of discrete directions. The integrations over the solid angle are approximated by numerical quadrature. In multidimensional problems, spatial partial derivatives can be computed using finite volume methods. Then, the DOM has the same advantages and drawbacks as finite volume methods. Specific drawbacks of the DOM include 1) the “ray effect” that may be significant at low optical thickness and for transient simulations, as discussed in details by Murthy and Mathur [18], 2) the difficulty to deal with specularly reflecting boundaries since the reflected or transmitted beams might not coincide with the discrete ordinates, 3) the arbitrary choice of the quadrature that may result in significantly different numerical results [19], 4) the method does not assure conservation of radiative energy [20], and 5) false scattering.

Finally, solving transport equations by the Monte Carlo technique consists of tracing the history of a statistically meaningful random sample of particles from their point of birth to their point

of death. The advantages of the Monte Carlo method are its ability to handle complex problems in terms of geometry and spatial and directional dependency without significantly increasing the computing effort or the complexity of the formulation [17]. Major drawbacks include: 1) the higher computational cost than traditional methods for relatively simple problems, 2) the difficulty to couple the method to other methods such as finite difference, 3) the statistical error intrinsic to any statistical methods, and 4) the inefficiency to deal with problems considering the radiative intensity onto a small surface and/or a small range of solid angles. Modest [21] addressed the last issue by using backward Monte Carlo simulations.

The present study aims at presenting a new numerical scheme for solving thermal transport at submicron scales. We recognize that the BTE and subsequent equations fall in the framework of population balance theory, whose mathematical formalism has been recently reviewed by Ramkrishna [5]. The modified method of characteristics developed by Pilon and Viskanta [22] for solving multiphase particulate flows has been adapted to solve multidimensional transient and steady-state microscale heat conduction problems. First, the numerical method is described. Then, test problems are solved and the numerical solutions obtained are compared with analytical or numerical solutions already reported.

2 Governing Equations

The BTE applies to both electron and phonon transport. However, the present study is limited to phonon transport in dielectric materials. In order to compare the present numerical method with existing ones, the study focuses on the EPRT [3]. This section reviews the assumptions traditionally made to make the problem mathematically tractable. Then, the governing equation and the associated boundary conditions are derived.

2.1 Assumptions. The following assumptions are usually made for solving the EPRT for phonon transport at microscale in engineering applications dealing with dielectric materials such as diamond and silicon dioxide [3,6,7,10]:

1. Phonons are considered to be the only heat carriers.
2. Phonon transport is assumed to satisfy the Boltzmann transport equation. Regimes of heat conduction and conditions for validity of the BTE have been discussed by Tien and Chen [1].
3. The Debye model is assumed to be valid, thus [4]

- The phonon group velocity \vec{v}_p is considered to be constant (independent of frequency and time) with $\vec{v}_p = v_p \vec{s}$, where v_p is the speed of sound in the materials for polarization p in direction \vec{s} . The dispersion relation is given by $\omega_p = v_p k$ and the group velocity, being constant, leads to $dk/dt = 0$. Physically, phonons dominating the heat transport travel at the speed of sound which does not vary significantly over the dominating range of frequency for heat transfer [3].
- The phonon modes of frequency cannot be larger than the Debye frequency ω_D defined as [4],

$$\omega_D = \frac{k_B \theta_D}{\hbar} \quad (4)$$

where θ_D is the Debye temperature. Physically, it corresponds to the fact that phonons cannot assume wavelengths smaller than twice the atomic spacing [7].

- The number of energy levels per unit of energy range for each polarization, the so-called density of states, is assumed to be continuous, denoted $\mathcal{D}_p(\omega)$, and given by [4]

$$\mathcal{D}_p(\omega) = \frac{\omega^2}{2\pi^2 v_p^3} \quad \text{with} \quad 0 \leq \omega \leq \omega_D \quad (5)$$

4. The polarization effects are negligible and all polarizations are treated identically.

5. The single mode relaxation time approximation is used to express the scattering term of the BTE, i.e., [3,4],

$$\left(\frac{\partial I_\omega}{\partial t}\right)_{sca} = \frac{I_\omega^0 - I_\omega}{\tau_s(\omega)} = \frac{\frac{1}{2} \int_{-1}^1 I_\omega d\mu - I_\omega}{\tau_s(\omega)} \quad (6)$$

where θ is the polar angle, μ is the director cosine, i.e., $\mu = \cos \theta$, and I_ω^0 is the equilibrium phonon blackbody radiation intensity. The phonon scattering rate $1/\tau_s$ is assumed to be the sum of the scattering rates associated to 1) scattering on lattice imperfections $1/\tau_i$ and 2) three phonon inelastic Umklapp scattering $1/\tau_U$. Even though the normal (N) three phonon inelastic scattering processes indirectly influence energy transfer, they are neglected here for the sake of simplicity, and to permit comparison with previous studies [3,11] and validation of the method. Note that this assumption does not reduce the generality of the method since N processes can also be accounted for by using the relaxation time approximation [3].

6. The medium and the scattering processes are assumed to be isotropic, thus the relaxation time depends only on frequency $[\tau_s(\vec{r}, \vec{k}) = \tau_s(\omega)]$ [10].
 7. The contribution of the optical phonons to heat transfer is neglected due to their small velocity [7].
 8. The phase of the lattice waves is not considered, thus neglecting interferences.
 9. Thermal expansion is neglected [4].

Following the above assumptions, the equation of phonons radiative transfer (EPRT) can be derived from Eqs. (1), (2), and (6) as [3]

$$\frac{\partial I_\omega}{\partial t} + \vec{v} \cdot \nabla_x I_\omega = \frac{\frac{1}{2} \int_{-1}^1 I_\omega d\mu - I_\omega}{\tau_s(\omega)} \quad (7)$$

At temperatures much lower than the Debye temperature, the recovery of the temperature from the intensity $I_\omega(\vec{r}, \omega, t)$ can be performed by defining an equivalent equilibrium temperature from the following equation [3,11]:

$$\begin{aligned} \frac{\sigma [T(\vec{r}, t)]^4}{\pi} &= \frac{1}{4\pi} \int_0^{\omega_D} \int_0^{2\pi} \int_0^\pi I_\omega(\vec{r}, t) \sin \theta d\theta d\phi d\omega \\ &= \frac{1}{2} \int_0^{\omega_D} \int_{-1}^1 I_\omega(\vec{r}, t) d\mu d\omega \end{aligned} \quad (8)$$

where σ is the Stefan-Boltzman constant for phonons, given by

$$\sigma = \frac{\pi^2}{40} \frac{k_B^4}{\hbar^3 \nu} \quad (9)$$

Note that Eq. (8) can be used, at any temperature, for gray medium calculations which neglect the spectral dependence of the intensity [11].

2.2 Boundary Conditions. We limit our study to thermalizing boundaries and specularly reflecting boundaries.

Thermalizing Boundaries. At a thermalizing boundary, the temperature is prescribed. The interface absorbs all incident phonons [23] and emits blackbody phonon radiation assumed to be at equilibrium at the prescribed temperature T . Thus, the boundary conditions at the thermalizing boundaries yields the isotropic spectral radiation intensity according to

$$I_{b,\omega} = \frac{3\hbar^3 \omega^3}{8\pi^3 \nu^2 [e^{\hbar\omega/k_B T} - 1]} \quad (10)$$

For a gray medium, the thermalizing boundary condition for the total intensity becomes

$$I_b = \sigma T^4 / \pi \quad (11)$$

Specularly Reflecting Boundaries. A specularly reflecting boundary with an outward normal vector \vec{n} corresponds to an adiabatic interface at which [11]

$$I_\omega(\vec{r}_b, \vec{s}, t) = I_\omega(\vec{r}_b, \vec{s}_r, t) \quad (12)$$

with $\vec{s}_r = \vec{s} - 2(\vec{s} \cdot \vec{n})\vec{n}$ and \vec{r}_b is the spatial coordinates of the boundary. Specularly reflecting boundaries represent an ideal behavior achieved by acoustically smooth surfaces, i.e., the surface roughness is much smaller than the phonon wavelength.

3 Modified Method of Characteristics

The method of characteristics consists of transforming the partial differential BTE into an ordinary differential equation solved along the pathline of the heat carriers. The conventional implementation (or *direct marching method*) of the method of characteristics is based on the Lagrangian formulation: the heat carriers are identified and located at initial time $t=t_0$ and followed at subsequent time as they are transported. In 3D thermal transport, however, the deformation that the initial mesh undergoes as time progresses leads to deterioration of the numerical solution [24].

The modified method of characteristics (or *inverse marching method*) is an interpretation of the Lagrangian approach that overcomes the difficulties related to mesh deformation [24]. Unlike the direct marching method, the inverse marching method uses a fixed grid of arbitrary shape. In the remaining of the present study, we consider a Cartesian coordinate system for illustration purposes. However, the approach can be generalized to any system of coordinates. By definition, the total time derivative of $I_\omega = I_\omega(x, y, z, t)$ with respect to time t in the direction (θ, ϕ) can be written as

$$\frac{dI_\omega}{dt} = \frac{\partial I_\omega}{\partial t} + \frac{dx}{dt} \frac{\partial I_\omega}{\partial x} + \frac{dy}{dt} \frac{\partial I_\omega}{\partial y} + \frac{dz}{dt} \frac{\partial I_\omega}{\partial z} \quad (13)$$

We further define the characteristic curves in the physical space as

$$\frac{dx}{dt} = \nu \sin \theta \cos \phi \quad (14)$$

$$\frac{dy}{dt} = \nu \sin \theta \sin \phi \quad (15)$$

$$\frac{dz}{dt} = \nu \cos \theta \quad (16)$$

Then, along the characteristic curves in the (x, y, z, t) space, the BTE can be written as

$$\frac{DI_\omega}{Dt} = \frac{\frac{1}{2} \int_{-1}^1 I_\omega d\mu - I_\omega}{\tau_s(\omega)} \quad (17)$$

where DI_ω/Dt denotes the substantial derivative of I_ω , i.e., the total time derivative along the pathline of the energy carriers.

Figure 1 shows a 3D computational cell in Cartesian coordinates. The modified method of characteristics consists of determining the coordinates (x_n, y_n, z_n) of the point in space from where the particles located at the grid point (x_a, y_b, z_c) at time $t + \Delta t$ originated from at time t while traveling in the direction of polar angle θ_n and azimuthal angle ϕ_l . In other words, for each point of a specified grid, the pathline is projected rearward along the characteristic curve to the initial data surface to determine the initial data point. For example, in Fig. 1 the point (x_a, y_b, z_c) is the point $(x_{i+1}, y_{j+1}, z_{k+1})$. The solid line represents the section of the characteristic curve along which the particle traveled from location (x_n, y_n, z_n) to location (x_a, y_b, z_c) during the time interval between t and $t + \Delta t$.

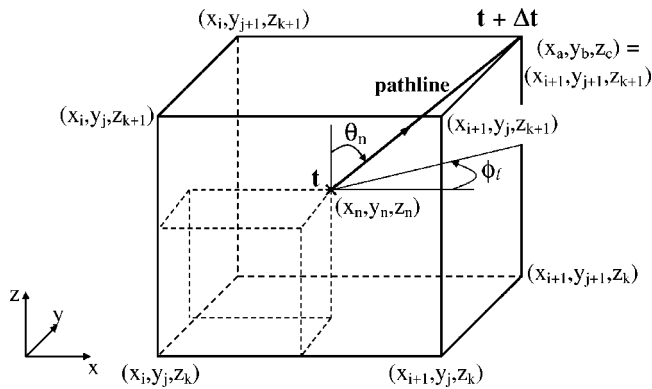


Fig. 1 Typical computational cell used for inverse marching method containing the pathline of the phonons

The general block diagram of the numerical procedure for solving the EPRT using the modified method of characteristics is shown in Fig. 2. First, temperature and spectral radiation intensity are set to their initial values across the computational domain. To avoid numerical instabilities, it is necessary to insure that the phonons do not leave the computational cell between the time t and $t + \Delta t$. In other words, each computational cell traveled by the phonons should contain at least one point on the characteristic

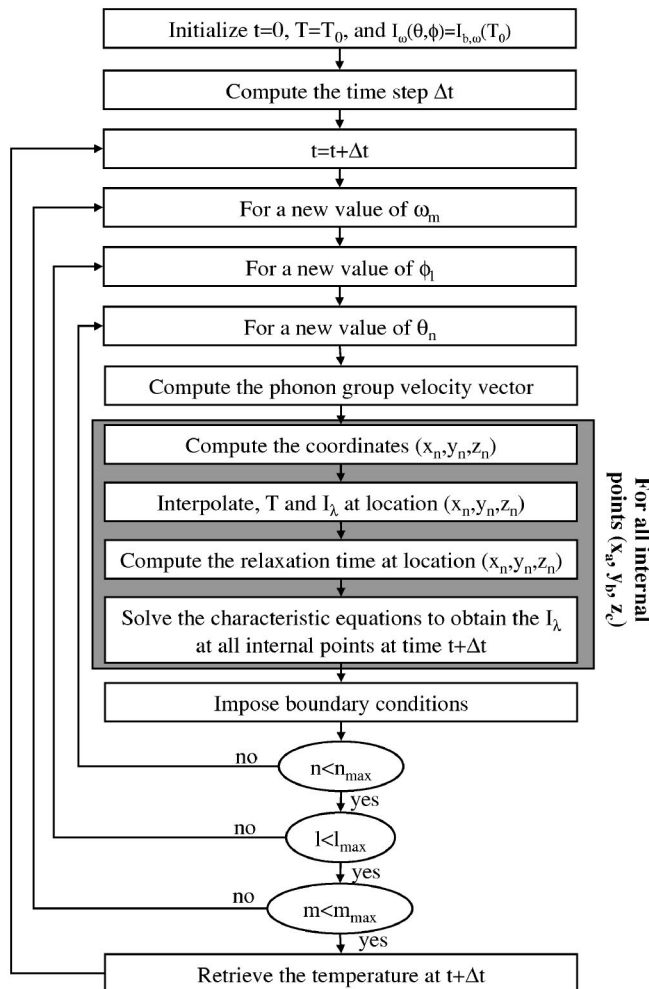


Fig. 2 Block diagram of the numerical procedure for solving the spectral EPRT by the modified method of characteristics

curve, i.e., the point (x_n, y_n, z_n) is always in a computational cell adjacent to (x_a, y_b, z_c) . Therefore, the time step Δt for the entire calculation is determined by the equation,

$$\Delta t = \min \left\{ \left| \frac{x_{i+1} - x_i}{v} \right|, \left| \frac{y_{j+1} - y_j}{v} \right|, \left| \frac{z_{k+1} - z_k}{v} \right| \right\} \quad (18)$$

For a given frequency ω_m , a polar angle θ_n , an azimuthal angle ϕ_l , and for all internal grid points (x_a, y_b, z_c) where phonons are located at time $t + \Delta t$, the phonon's position (x_n, y_n, z_n) at time t is calculated as

$$x_n = x_a - v \sin \theta_n \cos \phi_l \Delta t \quad (19)$$

$$y_n = y_b - v \sin \theta_n \sin \phi_l \Delta t \quad (20)$$

$$z_n = z_c - v \cos \theta_n \Delta t \quad (21)$$

The values of the variables T and I_ω at point (x_n, y_n, z_n) and time t are obtained by Lagrangian interpolation using their values at time t at the eight corners of the computational cell in which (x_n, y_n, z_n) is located. Then, the ordinary differential Eq. (17) is solved forward in time by the fourth-order Runge-Kutta method at location (x_a, y_b, z_c) and time $t + \Delta t$ at all interior points and outflow boundaries. The integrals appearing in Eqs. (8) and (17) are estimated by the 3/8 Simpson numerical integration method [25]. Finally, the boundary conditions are imposed in directions pointing toward the medium. The calculations are repeated for all the discretized values of frequency ω_m , polar angle θ_n , and azimuthal angle ϕ_l . The temperature at all grid points is recovered from Eq. (8) before the temperature and intensity fields are computed at the next time step.

The advantages and drawbacks of the modified method of characteristics over other methods are the following:

- Unlike finite-difference methods, in which the information propagates along coordinate lines, the method of characteristics propagates the information along the heat carriers' pathlines and thus matches the physics of the energy transport, resulting in extremely accurate numerical results.
- It does not require any outflow boundary conditions [26]. For this reason, the modified method of characteristics is recommended for hyperbolic equations such as the BTE, whose solution has a distinct domain of dependence and range of influence [25].
- The method can be used for solving coupled equations such as the BTE for electrons, the radiative transfer equation for photons, and/or the Maxwell's equations. Other numerical schemes such as finite-difference or finite element methods can also be used in combination with the present method.
- It can be used for both transient and steady-state calculations with great accuracy and without problems of numerical instability.
- Unlike finite-volume methods, there is no practical restriction on the aspect ratio of computational cells [27]. Here, on the contrary, the cell size is solely determined based on accuracy requirements, and any arbitrary set of points can be used as the computational grid.
- It may be more time consuming than other methods due to interpolations and numerical integrations. However, the computational time does not increase significantly as the geometry becomes more involved, or coupling with other heat carriers or fluid flow takes place.

4 Results and Discussion

For validation purposes, the results obtained by the modified method of characteristics for a set of test problems have been compared with analytical solutions or results reported in the literature using different numerical schemes. The cases considered are 1) transient and steady-state ballistic transport, 2) transient and

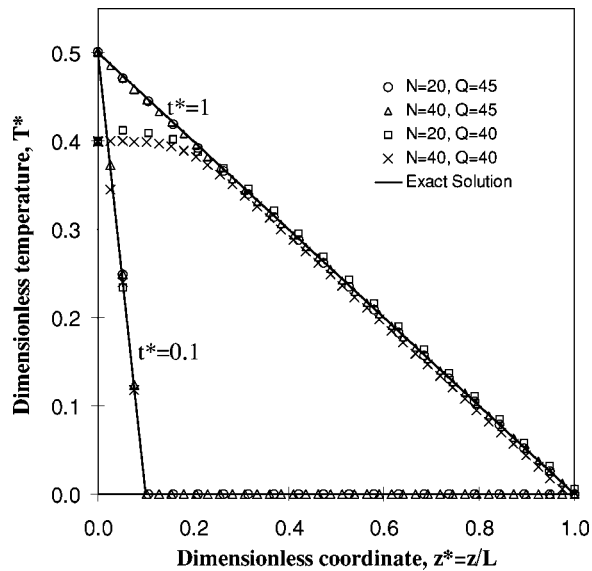


Fig. 3 Numerical solution for transient heat conduction in the ballistic limit for a 1 μm thick gray diamond type IIa thin film with black bounding surfaces using different grids and 30 directions

steady-state heat conduction across a diamond film, and 3) 2D steady-state heat conduction along a gray thin film with specularly reflecting boundaries.

4.1 Ballistic Transport. In order to validate the numerical method described previously, transient and steady-state heat conduction in dielectric thin films in the ballistic transport limit is considered, i.e., phonon scattering is neglected. We further assume that the spectral phonon intensity I_ω is independent of wavelength (gray behavior). Under these assumptions, the EPRT simplifies to [11]

$$\frac{\partial I}{\partial t} + \vec{v} \cdot \nabla I = 0 \quad (22)$$

where I is the total phonon intensity.

Transient Calculations. Two-dimensional numerical simulations were performed for a $10 \mu\text{m} \times 1 \mu\text{m}$ diamond type IIa polyhedral thin film initially at 300 K. At $t=0$, the bottom temperature $T(x, y, 0) = T_1$ is imposed to be 301 K while the top temperature T_2 is maintained at 300 K. The boundary conditions at the thermalizing boundaries in directions pointing toward the medium were $I(x, y, 0, t) = \sigma T_1^4 / \pi$ and $I(x, y, L, t) = \sigma T_2^4 / \pi$, respectively, while symmetry boundary conditions were imposed at the other surfaces. The width of the thin film is considered much larger than its thickness so that heat conduction can be treated as 1D. The temperature at each node was retrieved from the computed value of the total radiation intensity I based on the expression

$$T(x, y, z, t) = \left[\frac{\pi}{2\sigma} \int_{-1}^1 I(x, y, z, \mu, t) d\mu \right]^{1/4} \quad (23)$$

Furthermore, in order to simplify the presentation of the results, normalized temperature T^* , time t^* , and location z^* are defined, respectively, as

$$T^*(z^*) = \frac{T^4(z^*) - T_2^4}{T_1^4 - T_2^4}, \quad t^* = \frac{t}{L/\nu}, \quad \text{and} \quad z^* = z/L \quad (24)$$

The computational domain was discretized in a $10 \times N$ grid and Q discrete ordinate directions μ_i per quadrant with N and Q varying from 20 to 40 and from 8 to 50, respectively. Figure 3 shows the

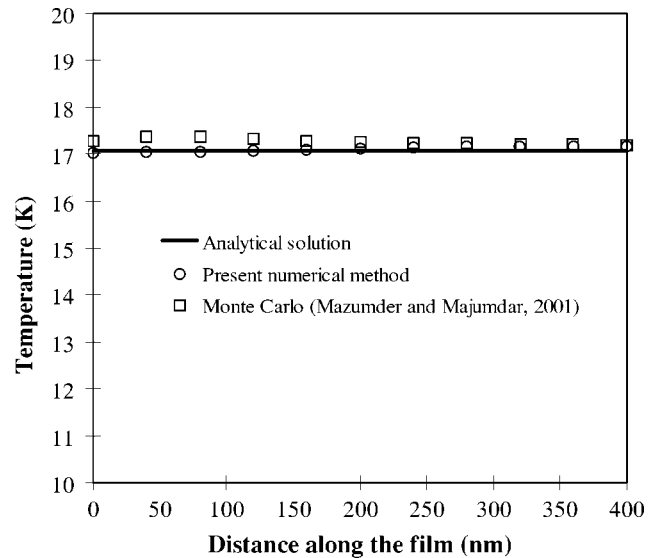


Fig. 4 Numerical solution for steady-state heat conduction in the ballistic limit for a 400 nm thick gray gallium arsenide thin film with black bounding surfaces

numerical results for the normalized temperature T^* as a function of the dimensionless location z^* for dimensionless times $t^* = 0.1$ and 1 for different spatial discretizations. The number of discretizations in the z direction does not affect the ability of the code to capture the propagating front while the number of directions influences the accuracy on the retrieved temperature. Furthermore, the number of grid points in the x and y directions had no effect, due to the symmetry of the problem, and 10 grid points were arbitrarily chosen. Good agreement with theoretical values is observed at both times for 20 cells in the z direction or finer grids and more than 45 directions per quadrant with time step $\Delta t = L/20\nu$. The large number of directions is due to the fact that the integral term is computed by numerical integration. As time increases, the temperature gradient across the film decreases and coarser grids can be used to capture the spatial change of temperature across the film. This must be compared with recent simulations by Murthy and Mathur [11,18] who reported 100 cells, $\Delta t = L/1000\nu$, and 8 discrete directions per quadrant. The authors used an unstructured finite volume scheme to solve the same test problem and recognized that “the problem is quite challenging from a numerical solution point of view,” and that “good spatial and temporal accuracy is required to minimize the numerical diffusion that tends to smear the step solution.” On the contrary, this study shows the advantages of the modified method of characteristics in that the method is unconditionally stable and both transient profile and wavefront are perfectly captured without any smeared front even with coarse grids.

Steady-State Calculations. Steady-state heat conduction across a 400 nm thick gallium arsenide film with black bounding surfaces in the ballistic limit is now considered. One face of the film is maintained at temperature $T(x, y, 0) = T_1 = 10$ K while the other face is maintained at $T(x, y, L) = T_2 = 20$ K. The exact solution to this problem is known to be uniform across the film and equal to $T(z) = [(T_1^4 + T_2^4)/2]^{1/4} = 17.075$ K with a discontinuity at the boundaries. The numerical results were obtained with a 10×11 grid and 45 directions per quadrant for a CPU time of less than 40 seconds on a 633 MHz Pentium III microprocessor. Figure 4 compares the numerical results with the analytical solution and those reported in the literature [28]. The maximum error between the two solutions is less than 0.6% compared to 2% obtained by Mazumder and Majumdar [28] using the Monte Carlo method. Note that an even better precision can be obtained by simulating a

Table 1 Physical properties of type IIa diamond 0.07% of ^{13}C isotope at room temperature [3]

Property	Value
Stefan-Boltzmann constant, σ	50.47 W/m ² K ⁴
Speed of sound, ν	12,288 m/s
Impurity density, η	$0.154 \times 10^{26}/\text{m}^3$
Radius of lattice imperfections, R	1.785 Å
Constant, A	163.94
Umklapp scattering constant, γ	1.58
Debye Temperature, θ_D	1860 K

longer time or by increasing the number of directions. On the contrary, the Monte Carlo method contains intrinsic statistical errors. Finally, the heat flux was computed and found to be constant and independent of location.

4.2 One-Dimensional Heat Conduction Across a Diamond Film. We now consider 1D heat conduction across a diamond type IIa thin film with 0.07% impurity concentration of ^{13}C . The film, of thickness L , is initially at $T = T_0$. At $t = 0$, a temperature difference $\Delta T = 1$ K is imposed across the film, while the cooler surface is maintained at temperature T_0 . Moreover, only scattering by lattice imperfections and Umklapp scattering are considered [3]. The relaxation time for imperfection scattering τ_i is expressed as [3]

$$\tau_i = \frac{1}{\alpha \varphi \eta \nu} \quad (25)$$

where α is a constant close to unity, η is the number of scatterings site per unit volume, and φ is the scattering cross section expressed as

$$\varphi = \pi R^2 \left(\frac{\chi^4}{\chi^4 + 1} \right) \quad \text{with} \quad \chi = \frac{\omega R}{\nu} \quad (26)$$

with R being the radius of the lattice imperfections. On the other hand, the relaxation time due to Umklapp scattering τ_U is expressed as [3]

$$\tau_U = A \frac{T}{\omega \theta_D} \exp\left(\frac{\theta_D}{\gamma T}\right) \quad (27)$$

where A and γ depend on the materials, while θ_D is the Debye temperature defined as $\theta_D = \hbar \omega_D / k_B$. The overall relaxation time is defined as $1/\tau_s = 1/\tau_i + 1/\tau_U$. Constants and properties required to compute the relaxation times for diamond type IIa with 0.07% impurity concentration of ^{13}C were taken from the literature [3] and are summarized in Table 1. A similar problem has been solved by Majumdar [3] using the discrete ordinate method proposed by Kumar et al. [15] with 8 discrete directions per quadrant. Moreover, the Stefan-Boltzmann constant for phonons is constant and Eq. (8) is valid only for low temperatures (less than 150 K for diamond type IIa). Therefore, in the present study the initial temperature T_0 has been arbitrarily set to 100 K.

Following Majumdar's work [3] and in order to cover the acoustically thin and thick regimes, three different film thicknesses ($L = 0.1 \mu\text{m}$, $1 \mu\text{m}$, and $10 \mu\text{m}$) have been considered for type IIa diamond. The calculations were performed on a spectral basis over the frequency range from 0 to ω_D . A converged solution was obtained for a 5×21 grid and 30 directions per quadrant, while the spectrum from 0 to ω_D was discretized into 90 different wavelengths. Figure 5 shows the transient evolution of the temperature profiles across a $1 \mu\text{m}$ thick diamond thin film. The results are plotted in terms of dimensionless temperature $T^+ = [T(z) - T_1] / [T_2 - T_1]$ and dimensionless time $\tau = vt/L$. Qualitatively, they compare well with results reported in the literature for $T_0 = 300$ K [12].

Figure 6 presents the steady-state temperature profiles across

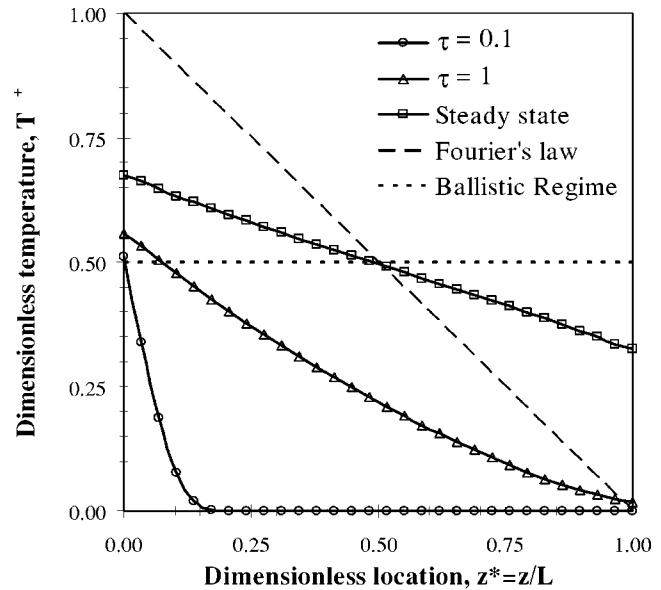


Fig. 5 Numerical solution for transient heat conduction across a $1 \mu\text{m}$ thick diamond type IIa thin film

diamond thin films having different thicknesses. One can see that the temperature gradient increases as the film thickness increases and that the numerical results fall between the acoustically thin (ballistic) and thick (Fourier's law) approximation limits. Similar results have been previously reported in the literature [3,11,12] for different temperatures and using other numerical schemes.

The present results confirm the good behavior of the numerical scheme for both transient and steady-state calculations, accounting for scattering on a spectral basis. Note that the actual time, and therefore the computational time, to reach steady-state increases with the film thickness.

4.3 Heat Conduction Along a Silicon Crystal Thin Film.

Phonon transport along a silicon crystal is considered in this section and schematically described in Fig. 7. The thin film is assumed to be a gray medium with a constant and uniform relax-

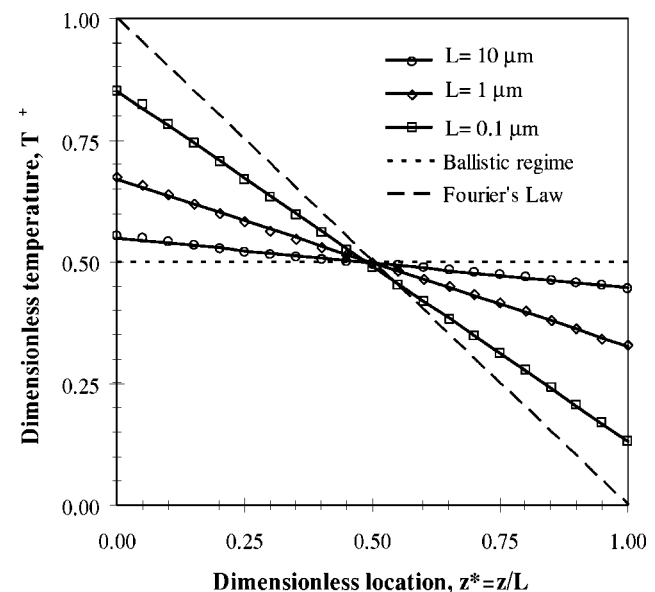


Fig. 6 Numerical solution for steady-state heat conduction across a diamond type IIa thin film of different thicknesses L

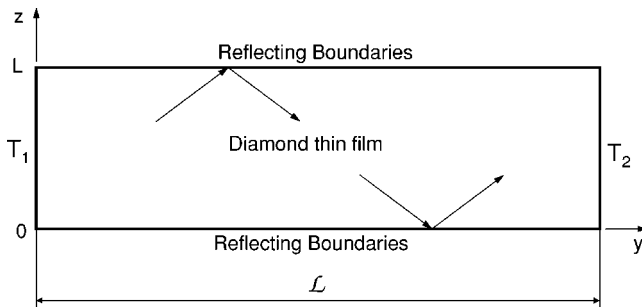
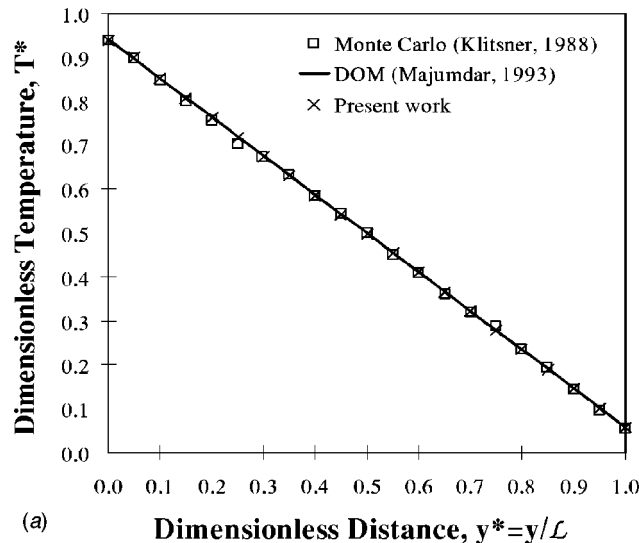


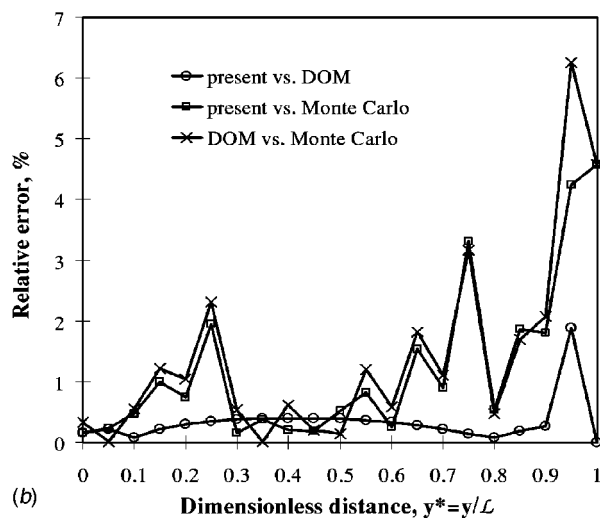
Fig. 7 Schematic for heat conduction problem along a silicon crystal thin film of length L

ation time defined as $\tau_s = \Lambda / \nu$, where Λ is the phonon mean free path that depends of the surface reflection [3,14] and the speed of sound in silicon ν is equal to 6400 m/s [29]. The lower ($z=0$) and upper ($z=L$) surfaces are specularly reflecting while the ends $y=0$ and $y=L$ are treated as black surfaces maintained at constant temperatures much below the silicon Debye temperature of 645 K.

Figure 8 compares the numerical results obtained by 1) the Monte Carlo method [14], 2) the discrete ordinate method [3,15],



(a)



(b)

Fig. 8 Comparison of numerical simulations of heat conduction along a $1 \mu\text{m}$ thick and $10 \mu\text{m}$ long silicon crystal thin-film.

and 3) the present method, for a silicon film with thickness $L=1 \mu\text{m}$ and length $\mathcal{L}=10 \mu\text{m}$. The results are given in dimensionless form with T^* given by Eq. (24) and $y^* = y/\mathcal{L}$. Figure 8 shows the relative difference between results obtained by the present method and those obtained by the Monte Carlo [14], and by the discrete ordinate methods [3] for specularly reflecting boundaries. The results compare very well with simulations reported in the literature [3,14]. The relative error between the present method and the DOM is less than 2%, while that with the Monte Carlo method is comparable to that between the DOM and the Monte Carlo method and stays below 6%. However, since no exact solution is available it is not possible to determine which method is the most accurate. Extension of the study to spectral diffuse surfaces and partially reflecting surfaces is straightforward. This test problem demonstrates the capability of the numerical scheme to deal with both 1D and 2D problems and with both black and specularly reflecting boundaries.

4.4 Discussion. The objective of the present paper is to demonstrate the capability of the modified method of characteristics to simulate microscale energy transport. Good agreement with reported results was shown. Similar or better stability and prediction capability than existing methods has been demonstrated. The numerical results have been obtained for 3D computational grids, and the program sequences, number of grid points, and directions have not been optimized. The scheme can be viewed as a hybrid method between the DOM and the ray tracing method. It is an alternative to that used by Coelho [30] for the radiative transfer equation. This section discusses trade-offs and compromises that can be made to achieve better numerical efficiencies.

First, the computational efficiency can be improved by approximating the integral present on the right-hand side of Eq. (17) by numerical quadrature. For example, given the symmetry of the above problems, the modified method of characteristics could have been used to solve the Schuster-Schwarzschild two-flux approximation by replacing the integral over all directions on the right-hand side of Eq. (7) by the sum of the positive and negative components [17]. In general, the computationally costly numerical integration over solid angle can be replaced by a weighted sum over an arbitrary number of discrete directions like in DOM. This procedure can significantly reduce the computational time, particularly for multidimensional and spectral calculations. It is recommended for optimization, real time transient calculations, and control of microscale devices. However, one will be faced with the same drawbacks inherent to the discrete ordinate method discussed in the Introduction. Similarly, the band approximation can be used for spectral calculations, as performed by Murthy and Mathur [11]. These approaches have not been retained here for the sake of accuracy, but they could easily be implemented for more complex problems or geometries.

Moreover, as discussed previously, the simulated boundary conditions were used in order to compare the results obtained by the present method with those reported in the literature. More realistic boundary conditions such as 1) diffusely reflecting opaque surfaces that are more appropriate for “acoustically rough” surfaces and 2) partially diffuse and specular reflecting boundaries as encountered in superlattices constitute an extension of the present work and can numerically be implemented with relative ease.

Finally, the present method is very well suited for parallel computing, since the intensity at each node at any time step depends explicitly and solely on the results obtained for the previous time step. The computing time can theoretically be divided by the number of grid points by using up to one CPU per grid point. Parallelization can significantly speed up the computation of the temperature field for real-time transient, multidimensional, and/or coupled problems, as well as for steady-state transport in optically thick media. In the diffusion approximation limit, when Fourier’s law prevails, the governing equation becomes parabolic for transient and elliptic for steady-state heat conduction problems [25]. Parabolic equations feature repeated characteristics also having a

distinct domain of dependence and range of influence, but the signal propagates at infinite speed, unlike hyperbolic equations such as the BTE or the EPRT [25]. Elliptic equations have no real characteristics and their solutions at any grid point depend on the solution at all the other grid points. For both parabolic and elliptic equations, other numerical methods appear to be more appropriate than the present method [25].

5 Conclusions

This paper has described in detail a new numerical method for solving multidimensional transient and steady-state thermal transport at subcontinuum scale with black or reflecting boundaries on a gray or spectral basis. The modified method of characteristics is unconditionally stable, accurate, and compatible with other numerical schemes and can be used for coupled problems employing the same prespecified grid. The numerical solutions obtained for 1D and 2D heat conduction in dielectric thin films have been compared with the analytical solution and, when possible, with reported numerical results. Good agreement has been found confirming the capability of the numerical procedure and the associated computer program.

The numerical scheme developed in the present study could easily be extended to complex 3D geometry. The advantage of the proposed method is that even the most complicated problem can be solved with relative ease. As the problem becomes more realistic (in terms of geometry and coupling with electron or photon transport), the complexity of the formulation and the computational effort increase much more rapidly for conventional approaches. Furthermore, the method could also be used for 1) solving the RTE for emitting, absorbing, and scattering materials and 2) the BTE for electrons and holes as well as coupled electron-phonon-photon transport problems. It can be used for solving energy transport in subcontinuum regions in thermal or electrical contact with continuum regions where traditional methods can be used. The method is particularly recommended for transient, multidimensional, and/or coupled problems.

Acknowledgments

The author is indebted to Professor Raymond Viskanta and Professor Gang Chen, and to Dr. David Sung for their valuable comments and discussions. The author would like to acknowledge the comments of anonymous referees on the model assumptions and their physical meaning, as well as on the implementation and discussion of the boundary conditions.

Nomenclature

A	= constant
D_p	= density of states for polarization p , $m^{-3} s$
f	= heat carriers distribution function
h	= Planck's constant
\hbar	= Planck's constant divided by 2π , $1.054 \times 10^{-34} J s/photon$
I_ω	= direction spectral phonon radiation intensity, $J m^{-2} sr$
\vec{k}	= wavevector, m^{-1}
k_B	= Boltzmann constant, $1.38 \times 10^{-23} J/K$ phonon
L	= thin-film thickness, m
\mathcal{L}	= thin-film length (see Fig. 7)
n	= total number of heat carriers
\vec{p}	= particle momentum, $kg m s^{-1}$
\vec{q}	= heat flux vector, $W m^{-2}$
R	= radius of impurities
\vec{r}	= vector location
\vec{s}	= unit vector
t	= time, s
t^*	= dimensionless time, $t^* = vt/L$
T	= temperature, K

T^*	= dimensionless temperature,
$T^*(z)$	$= (T(z)^4 + T_2^4)/(T_1^4 + T_2^4)$
\vec{v}	= heat carrier group velocity vector, m/s
x	= longitudinal location, m
y	= spanwise location, m
z	= vertical location, m

Greek Symbols

Λ	= mean free path of the heat carriers, m
ν	= speed of sounds, m/s
ϵ	= energy of an individual heat carrier, J
μ	= director cosine, $\mu = \cos(\theta)$
ω	= phonon angular frequency, rad/s
ω_D	= Debye frequency, rad/s
ϕ	= azimuthal angle
η	= number of scatterings site per unit volume
φ	= scattering cross section of an impurity
θ_D	= Debye temperature, K
θ	= polar angle
σ	= Stefan-Boltzmann constant for phonons, $W m^{-2} K^{-4}$
τ_i	= relaxation time for impurity scattering, s
τ_U	= relaxation time for Umklapp scattering, s
τ_s	= total relaxation time for scattering, s
τ^*	= acoustic thickness, $\tau^* = L/(\tau_s \nu)$

Subscripts

0	= refers to equilibrium
b	= refers to the boundary
e	= refers to electrons
i, j, k	= indices for the vector nodes of the computational grid
p	= polarization state

References

- Tien, C. L., and Chen, G., 1994, "Challenges in Microscale Conductive and Radiative Heat Transfer," *ASME J. Heat Transfer*, **116**, pp. 799–807.
- Tien, C. L., Majumdar, A., and Gerner, F. M. (eds.), 1997, *Microscale Energy Transport*, Taylor and Francis, London.
- Majumdar, A., 1993, "Microscale Heat Conduction in Dielectric Thin Films," *ASME J. Heat Transfer*, **115**, pp. 7–16.
- Kittel, C., 1996, *Introduction to Solid-state Physics*, Wiley, New York.
- Ramkrishna, D., 2000, *Population Balances*, Academic Press, San Diego.
- Goodson, K. E., Ju, Y. S., and Asheghi, M., 1997, "Thermal Phenomena in Semiconductor Devices and Interconnects," *Microscale Energy Transport*, Taylor and Francis, London, pp. 229–288.
- Majumdar, A., 1997, "Microscale Energy Transport in Solids," in *Microscale Energy Transport*, Taylor and Francis, pp. 3–93.
- Kumar, S., and Ramkrishna, D., 1996, "On the Solution of Population Balance Equation by Discretization—I a Fixed Pivot Technique," *Chem. Eng. Sci.*, **51**(8), pp. 1311–1332.
- Kumar, S., and Ramkrishna, D., 1997, "On the Solution of Population Balance Equation by Discretization—III Nucleation, Growth, and Aggregation of Particles," *Chem. Eng. Sci.*, **52**(4), pp. 4659–4679.
- Chen, G., 2001, "Ballistic-Diffusive Heat-Conduction Equations," *Phys. Rev. Lett.*, **86**(11), pp. 2297–2300.
- Murthy, J., and Mathur, S. R., 2002, "Computation of Sub-Micron Thermal Transport Using an Unstructured Finite Volume Method," *ASME J. Heat Transfer*, **124**, pp. 1176–1181.
- Joshi, A. A., and Majumdar, A., 1993, "Transient Ballistic and Diffusive Phonon Heat Transport in Thin Films," *J. Appl. Phys.*, **74**(1), pp. 31–39.
- Sverdrup, P. G., Ju, Y. S., and Goodson, K. E., 2001, "Sub-Continuum Simulations of Heat Conduction in Silicon-on-Insulator Transistors," *ASME J. Heat Transfer*, **123**, pp. 130–137.
- Klitsner, T., VanCleve, J. E., Fisher, H. E., and Pohl, R. O., 1988, "Phonon Radiative Heat Transfer and Surface Scattering," *Phys. Rev. B*, **38**(11), pp. 7576–7594.
- Kumar, S., Majumdar, A., and Tien, C. L., 1990, "The Differential-Discrete-Ordinate Method for Solving the General Equation of Radiative Transfer," *ASME J. Heat Transfer*, **112**, pp. 424–429.
- Chai, J. C., Lee, H. S., and Patankar, S. V., 1993, "Ray Effect and False Scattering in the Discrete Ordinates Method," *Numer. Heat Transfer, Part B*, **24**, pp. 373–389.
- Modest, M. F., 1993, *Radiative Heat Transfer*, McGraw-Hill, New York, NY.
- Murthy, J., and Mathur, S. R., 2003, "An Improved Computational Procedure for Sub-Micron Heat Conduction," *ASME J. Heat Transfer*, **125**, pp. 904–910.
- Truelove, J. S., 1987, "Discrete-Ordinate Solutions of the Radiative Transport Equation," *ASME J. Heat Transfer*, **109**, pp. 1048–1051.
- Raithby, G. D., 1994, "Discussion of the Finite-Volume Method for Radiation

- and its Application Using 3D Unstructured Meshes,” *Numer. Heat Transfer, Part B*, **35**, pp. 389–405.
- [21] Modest, M. F., 2003, “Backward Monte Carlo Simulations in Radiative Heat Transfer,” *ASME J. Heat Transfer*, **125**, pp. 57–62.
- [22] Pilon, L., and Viskanta, R., 2003, “Modified Method of Characteristics for Solving the Population Balance Equation,” *Int. J. Numer. Methods Fluids*, **42**, pp. 1211–1236.
- [23] Zeng, T., and Chen, G., 2001, “Phonon Heat Conduction in Thin Films: Impact of Thermal Boundary Resistance and Internal Heat Generation,” *ASME J. Heat Transfer*, **123**, pp. 340–347.
- [24] Allievi, A., and Bermejo, R., 2000, “Finite Element Modified Method of Characteristics for Navier-Stokes Equations,” *Int. J. Numer. Methods Fluids*, **32**, pp. 439–464.
- [25] Hoffman, J. D., 1998, *Numerical Methods for Engineers and Scientists*, McGraw-Hill, New York.
- [26] Marcum, D. L., 1985, *Calculation of three-dimensional inviscid flowfields*, PhD thesis, Purdue University.
- [27] Patankar, S., 1980, *Numerical Heat Transfer and Fluid Flow*, Hemisphere, Washington, DC.
- [28] Mazumder, S., and Majumdar, A., 2001, “Monte Carlo Study of Phonon Transport in Solid Thin Films Including Dispersion and Polarization,” *ASME J. Heat Transfer*, **123**, pp. 749–759.
- [29] Holland, M. G., 1964, “Analysis of Lattice Thermal Conductivity,” *Phys. Rev.*, **134**(2A), pp. A471–480.
- [30] Coelho, P. J., 2002, “Bounded skew high-order resolution schemes for the discrete ordinates method”, *J. Computational Physics*, **175**(2) pp. 412–437.

Thermal Characteristics of Microscale Fractal-Like Branching Channels

Ali Y. Alharbi

Department of Mechanical Power and Refrigeration, PAAET College of Technological Studies, P.O. Box 42325, Shuwaikh, Kuwait 70654
e-mail: aalharbi@paaetms.paaet.edu.kw

Deborah V. Pence*

Associate Professor
Department of Mechanical Engineering, Oregon State University, 204 Rogers Hall, Corvallis, OR 97331-6001
e-mail: pence@engr.orst.edu

Rebecca N. Cullion

Department of Mechanical Engineering, Oregon State University, 204 Rogers Hall, Corvallis, OR 97331-6001
e-mail: cullion@engr.orst.edu

Heat transfer through a fractal-like branching flow network is investigated using a three-dimensional computational fluid dynamics approach. Results are used for the purpose of assessing the validity of, and providing insight for improving, assumptions imposed in a previously developed one-dimensional model for predicting wall temperature distributions through fractal-like flow networks. As currently modeled, the one-dimensional code fairly well predicts the general wall temperature trend simulated by the three-dimensional model; hence, demonstrating its suitability as a tool for design of fractal-like flow networks. Due to the asymmetry in the branching flow network, wall temperature distributions for the proposed branching flow network are found to vary with flow path and between the various walls forming the channel network. Three-dimensional temperature distributions along the various walls in the branching channel network are compared to those along a straight channel. Surface temperature distributions on a heat sink with a branching flow network and a heat sink with a series of straight, parallel channels are also analyzed and compared. For the same observed maximum surface temperature on these two heat sinks, a lower temperature variation is noted for the fractal-like heat sink. [DOI: 10.1115/1.1795236]

Introduction

Societal demands have resulted in extremely compact yet powerful electronic devices, which require high watt-density cooling techniques. Heat sinks incorporating microscale channels are very effective in this endeavor by increasing both the convective heat transfer coefficient as well as the convective surface area per unit volume in the heat sink.

However, the improved heat transfer provided by a series of parallel microchannels is not without drawbacks. The small diameter of the channels produces large pressure drops, and nonuniform temperature distributions along the wall of the channel often occur. If used to cool an electronic component, a nonuniform temperature distribution, if significant enough, could result in uneven thermal expansion of the electronic device, possibly damaging it or affecting the electrical properties.

Tuckerman and Pease [1] first introduced the idea of microchannel heat sinks for cooling integrated circuits. Since that time, numerous investigations of single, straight microchannels and microchannel arrays in a heat sink have been conducted. Much of the experimental data prior to 2000, as noted in the review article by Sobhan and Garimella [2], are not well predicted by macroscale correlations. However, a recent study by Garimella and Singhal [3] demonstrates the validity of using conventional macroscale correlations for predicting laminar flow pressure drop and heat transfer through microscale geometries.

Bau [4] demonstrated, using a mathematical model, that a microchannel with a variable cross sectional area can be optimized to reduce temperature gradients along the channel length. Reduction in the maximum heated surface temperature can be achieved by tapering a channel in the direction of flow. However, a decrease in axial channel diameter can be accompanied by an increase in velocity and, hence, an increase in pumping power.

To improve the temperature uniformity while decreasing the pressure drop, Pence [5] proposed a fractal-like branching flow network, in which each new branch has a smaller diameter than

that from which it originated. The fractal-like flow network was designed using fixed diameter and length scale ratios between consecutive branching levels, as were proposed by West et al. [6] for transport systems optimized for metabolic processes. Using an optimization approach to minimize pumping power while adhering to a minimal volume constraint, Bejan [7] identified, on average, the same branching level ratios reported by West et al. [6].

Pence [8] developed a one-dimensional (1D) model, using macroscopic correlations, for predicting both the pressure distribution in, and wall surface temperature along, a fractal-like branching channel network. Results were compared to an array of straight channels having the same channel length and same convective surface area as the branching network. A lower maximum wall temperature along the fractal flow network was consistently noted for three different cases, which include identical pressure drop, identical flow rate, and identical total pumping power through both flow networks. The model of Pence [8] assumes that both hydrodynamic and thermal boundary layers redevelop at each wall following a bifurcation, but the model neglects the influence of branching angle on either pressure drop or wall temperature. Chen and Chang [9] also investigated pressure drop and the heat transfer capacity of fractal-like channel networks. In addition to neglecting the influence of branching angle, they also assumed fully developed flow, yet reached a similar conclusion regarding the advantage of branching flow networks. Wechsato et al. [10] recently investigated the optimal channel length distribution in a disk-shaped geometry similar to that proposed by Pence [5,8]. Length scale ratios that vary at each bifurcation level were deemed optimal in terms of minimizing flow resistance.

Method of Analysis

Based on the suggestion made by West et al. [6] for two-dimensional flow networks, Pence [5] developed a preliminary branching channel network in a disk-shaped heat sink using the following branching ratios,

$$\frac{d_{k+1}}{d_k} = n^{-1/3} \quad (1)$$

*Corresponding author.

Contributed by the Heat Transfer Division for publication in the JOURNAL OF HEAT TRANSFER. Manuscript received by the Heat Transfer Division September 4, 2003; revision received June 11, 2004. Associate Editor: S. P. Vanka.

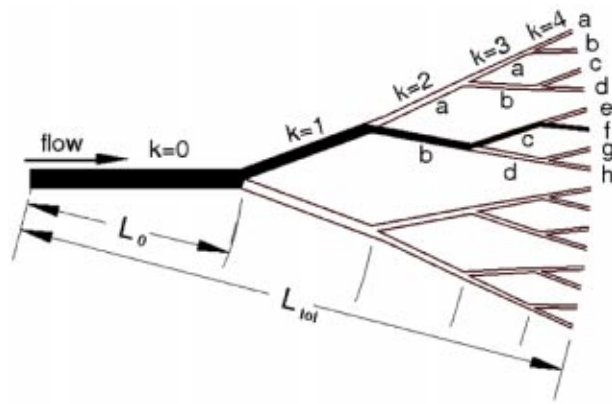


Fig. 1 Fractal-like branching channel network (Shaded path, known hereafter as path 1, includes branches $k=0$, $k=1$, $k=2b$, $k=3c$, $k=4f$)

$$\frac{L_{k+1}}{L_k} = n^{-1/2} \quad (2)$$

where d is the hydraulic diameter, L is the length of a channel segment, and n is the number of branches into which each channel splits. For the present analysis, $n=2$. Subscript k represents the lower-order branching level and subscript $k+1$ represents the higher-order branching level at a bifurcation. Note from Fig. 1, that the first branch emanating from the inlet flow plenum is the zeroth-order branch, i.e., $k=0$. The shaded region and the letters denoted in the figure are discussed later.

It is the objective of the present work to analyze, using a three-dimensional computational fluid dynamics (CFD) analysis, the wall temperature distribution in microscale fractal-like branching channel networks. Results from these analyses are used to assess the validity of assumptions imposed in the one-dimensional model of Pence [8]. The commercially available computational fluid dynamics package, Star-CD[®] (from Computational Dynamics Ltd.), was employed for this purpose. Dimensions of the flow network analyzed are provided in Table 1. Note that the total channel length reported for the fractal-like flow network is the radial distance from the entrance of the $k=0$ branch to the exit of the $k=4$ branch level. The length of each branch is defined by radial distances in Fig. 1. The original geometry proposed by Pence [5], which is shown in Fig. 1, has asymmetric branching, and branch segments $k=3a$ and $k=3d$ are tapered. The influence of these factors on the wall temperature distributions will be investigated.

One-Dimensional Predictive Model. In the one-dimensional model developed by Pence [8], the pressure distribution through and wall temperature distribution along rectangular cross-sectional ducts in a fractal-like branching flow network are predicted using empirical correlations for pressure drop and Nusselt number. The 1D model is restricted to laminar flow with the assumptions that: 1) both the thermal and hydrodynamic boundary layers redevelop following each channel bifurcation, 2) the influence of branching angle on temperature and pressure distributions

Table 1 Channel dimensions for fractal-like flow network ($\sum_{k=0}^4 L_k = L_{tot} = 16.3$ mm)

k	H_k (mm)	w_k (mm)	d_k (mm)	L_k (mm)
0	0.250	0.539	0.342	5.80
1	0.250	0.296	0.271	4.10
2	0.250	0.189	0.215	2.90
3	0.250	0.130	0.171	2.05
4	0.250	0.093	0.136	1.45

is negligible, and 3) the temperature dependence of the thermo-physical properties of the working fluid are negligible. It is the purpose of the present investigation to assess the validity of these three assumptions in order to determine the feasibility of using the model as a flow network design tool.

The pressure-drop correlation in White [11], which includes increased pressure drop due to developing flow conditions and the Nusselt number data for simultaneously developing thermal and hydrodynamic boundary layers (from Wibulswas [12]) and referred to in Shah and London [13], are employed in the one-dimensional model. Water is used as the working fluid, and a constant heat flux is applied to the infinitely thin walls of the ducts composing the 1D flow network.

Three-Dimensional Computational Model. Numerical simulations were performed using the finite-volume-based, CFD software Star-CD. Three-dimensional CFD simulations were performed for fractal-like flow networks and for heat sinks with embedded fractal-like flow networks. In flow network analyses, thermal energy is supplied to the walls forming the flow network. In heat sink analyses, a heat flux is imposed at the flat surface of a heat sink having fractal-like channels. Temperature distributions along the fractal-like flow network walls are compared to those forming a parallel channel array. In addition, the heated surface of a heat sink with an embedded fractal-like flow network is compared to that of a heat sink with a parallel network of flow paths.

The steady, incompressible form of the three-dimensional continuity, momentum, and energy equations governing the fluid transport in this investigation are, respectively,

$$\frac{\partial V_i}{\partial x_i} = 0 \quad (3)$$

$$\rho \left(\frac{\partial(V_i V_j)}{\partial x_i} \right) = \frac{\partial}{\partial x_i} \left(\mu \frac{\partial V_j}{\partial x_i} \right) - \frac{\partial p}{\partial x_i} \quad (4)$$

and

$$\rho \left(\frac{\partial(V_i c_p T)}{\partial x_i} \right) = \frac{\partial}{\partial x_i} \left(\lambda \frac{\partial T}{\partial x_i} \right) \quad (5)$$

Consistent for all analyses (flow networks and heat sinks) are the inlet and exit flow boundary conditions and no slip, impermeable conditions at all walls of the flow network. At the inlet, the bulk fluid temperature is fixed and a uniform velocity profile is assumed. The flow discharges to a water-filled reservoir assumed to be at atmospheric pressure at the point of discharge. For the flow network analyses, a uniform heat flux is applied at all walls of the channels.

For the heat sink analyses, the energy equation for the solid,

$$\frac{\partial}{\partial x_i} \left(\lambda \frac{\partial T}{\partial x_i} \right) = 0 \quad (6)$$

is also included. A uniform heat flux is applied to the bottom of the heat sink, whereas the top and edges of the heat sink are assumed to be insulated. In this configuration, fluid enters the heat sink from the top surface and flows radially outward.

The steady, incompressible 3D continuity, energy, and momentum equations are solved using a monotone advection and reconstruction scheme (MARS) for the advection terms. MARS is a two-step scheme of second-order accuracy which, of the available discretization schemes in Star-CD, is least sensitive to errors resulting from mesh structure and skewness. In the flow network analysis, 670,000 cells were used to model the flow field. Typical cell sizes were on the order of 15 μm with some cells as small as 5 μm . One million cells were employed in the heat sink analysis, with larger cells, up to 40 μm , used in the solid material away from the channel walls. The pressure-velocity coupling was accomplished using the SIMPLE method. Under-relaxation parameters of 0.2, 0.7, and 0.95 were employed for pressure, velocity,

Table 2 Geometric and flow conditions for flow network and heat sink analyses

		Fractal flow network	Straight channels
Both Analyses	L_{tot} (mm)	16.3	16.3
	w_i (mm)	0.930	0.136
	H (mm)	0.250	0.136
	d (mm)	0.136	0.136
Flow Network Analysis	N	12	77
	A_{conv} (mm ²)	685	686
	q'' (W/cm ²)	45	45
	Q (ml/s)	10.8	7.44
Heat Sink Analysis	N	12	212
	A_{conv} (mm ²)	685	1889
	A_{plate} (mm ²)	948	946
	q'' (W/cm ²)	50, 100	50, 100
	Q (ml/s)	10	10

and temperature, respectively. Convergence was achieved when a maximum residual tolerance of 10^{-6} was reached.

Results and Discussions

Three-dimensional computational results are sought that provide a means for assessing the previously mentioned assumptions imposed in the one-dimensional model by Pence [8] for predicting pressure and temperature distributions through fractal-like flow networks. To determine the validity of these assumptions, flow networks, rather than heat sinks, are analyzed. Heat sinks with fractal-like flow networks are subsequently analyzed.

One-Dimensional and Three-Dimensional Flow Network Analyses. Of particular interest from the 3D investigation are wall surface temperature distributions along various flow paths through the fractal-like branching flow networks. Due to asymmetry in the flow network, two separate flow paths are investigated. Using the branch labeling scheme in Fig. 1, path 1 is defined by segments $k=0, 1, 2b, 3c, 4f$, and path 2 is defined by segments $k=0, 1, 2a, 3a, 4a$. As a consequence of the 3D nature of the flow in the CFD analysis, temperature variations occur along the walls in a direction normal to the flow. Maximum temperatures are typically observed at the corners of the channels. Because the purpose of the 1D model is to serve as a tool in designing fractal-like flow networks, all wall temperatures from CFD results are taken along the middle of the wall and are compared with those predicted from the 1D model and with the wall surface temperatures along straight channel arrays.

Constant Property Analysis. The first comparison in the present analysis is of streamwise wall temperature distributions along a fractal-like flow network, as predicted from the 1D and 3D models. This comparison provides a means of assessing the validity of assumptions 1 and 2, which are 1) boundary layers redevelop at each wall following a bifurcation and 2) the angle of bifurcation has a negligible influence on the wall temperature distribution. In this part of the analyses, constant thermophysical properties are assumed and are evaluated at the average temperature between the inlet and exit bulk fluid temperatures. Wall temperature distributions along a fractal flow network and along a channel in an array of parallel channels are considered. Several geometric features and operating conditions are kept identical between the fractal-like and parallel flow networks. These include the total channel length, convective wall surface area, applied heat flux, and total pumping power. The channels in the parallel flow network are square in cross-section with a hydraulic diameter equal to that of the terminal branch of the fractal-like flow network. Values are noted in Table 2 under "flow network analysis."

Due to symmetry, the temperature distributions along all four walls of a straight channel from the parallel array are identical.

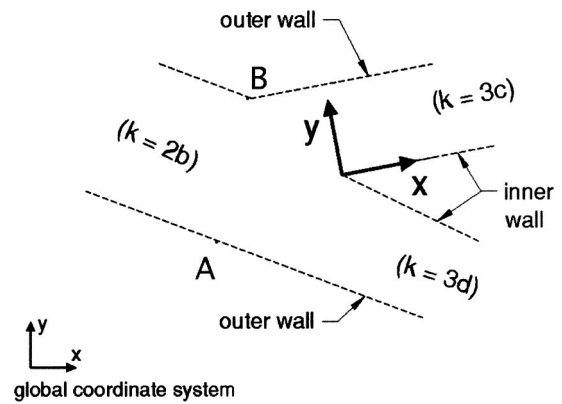


Fig. 2 Local coordinate system for the $k=3c$ branch. Note that z is always out of the page and that channel $k=3d$ is tapered.

However, the asymmetry of the 3D fractal-like flow network is anticipated to result in wall temperature distributions that vary along the various walls and along different flow paths. Figure 2 indicates the definition of inner and outer walls. The outer wall is that which is joined to a previously existing channel side wall. The inner wall is defined as that wall which is newly formed following the bifurcation. Obvious from this definition is that the inner and outer walls along path 1 alternate from side to side. For example, looking in the direction of flow in Fig. 1, the outer wall along path 1 is the left side wall of the $k=1$ and $k=3c$ branches and the right side wall of the $k=2b$ and $k=4f$ branches. Because of the symmetric nature of the first branching between $k=0$ and $k=1$, either the left or right side wall can be considered the inner wall of the $k=0$ branch. The result is a piecewise continuous curve, such as those designated as path 1 and path 2 in Fig. 3. Shown in Fig. 3 are three-dimensional CFD model simulations of wall temperature along a parallel flow network and the interior wall temperature along two different paths through the fractal-like flow network. Note that the abscissa x represents the streamwise distance from the inlet of the flow network to the exit.

Also provided in Fig. 3 are 1D temperature predictions for both fractal-like and parallel flow networks. The 1D model results will match the 3D model simulation of the straight channel, providing validation of the 3D model. The 3D microscale flow phenomenon in this fractal network was experimentally validated with pressure drop tests in Alharbi et al. [14]. The thermal capabilities of the CFD code at the microscale were previously validated by Pence et al. [15]. Application of the Navier-Stokes and energy equations

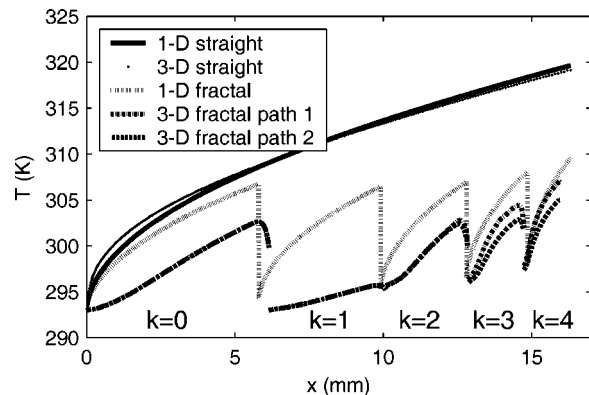


Fig. 3 One-dimensional and three-dimensional inner wall temperature distributions for fractal-like and straight-channel networks with constant properties

Table 3 Normalized mass flow and bulk fluid temperatures at inlet and exit branches

k	\dot{m}_e / \dot{m}_i	T_{bulk} (K)
0	1.0000	293.0
4a	0.0904	297.5
4b	0.0564	298.8
4c	0.0504	300.5
4d	0.0825	298.5
4e	0.0595	301.2
4f	0.0346	302.2
4g	0.0507	301.4
4h	0.0755	300.2

to microscale thermal and flow phenomena, as used in the present analysis, was experimentally shown to be valid by Garimella and Singhal [3].

Of the 3D simulations in Fig. 3, the maximum temperature along path 1 of the fractal-like network is approximately 12°C cooler than the maximum temperature predicted along a straight channel. The temperature variation or difference along the length of the fractal flow network, being lower than that across a straight channel array, is an attractive attribute of the fractal-like flow network. In addition, for the same pumping power and heat flux, the pressure drop is approximately 30% lower through the branching networks than through the parallel array, as was noted by Alharbi et al. [14].

In Fig. 3, with the exception of the $k=1$ branch, the 1D model well predicts the 3D inner-wall temperature trends for both paths through the fractal flow network; however, it does overpredict the magnitudes. The dramatic decrease in 1D wall temperature along a flow path in the fractal network is a result of the assumed reinitiation of the thermal boundary layer. The similarity of the 3D model trend to that predicted by the 1D model suggests that the boundary layer does, in fact, reinitiate at the inner wall following a bifurcation. This is expected as the inner wall is created only as a result of the bifurcation. The inner wall temperature distribution along the $k=1$ branch is distinctly different from the predicted values. It is also different from that of the other branching levels. The boundary layer development along this branch segment must be influenced by secondary flow phenomena. Secondary flow fields are considered later in the paper.

Also evident from Fig. 3 is that the inner wall temperature at the exit of path 1 is higher than that of path 2. The cause of this is due, in part, to the larger bifurcation angles and longer total flow length for path 1 in comparison with those of path 2. To highlight the influence of branching angle and path length on the thermal and flow conditions through the fractal flow network, exit mass flow values, normalized by the inlet mass flow \dot{m}_e / \dot{m}_i and the exiting bulk fluid temperatures T_{bulk} are tabulated in Table 3. Table 3 shows that path 2, exiting through $k=4a$, has the larger mass flow rate. The flow rate through this path is approximately three times larger than that through path 1, which exits through $k=4f$. Path 2 also has the lowest exiting bulk fluid temperature, as would be expected due to the higher flow rate.

Figure 4 shows, in addition to the inner wall temperature, the bottom and outer wall temperatures along path 1 of the fractal-like flow network along with the temperature distribution predicted by the 1D model for comparison. Due to symmetry about the z plane, the top wall temperatures are identical to those of the bottom wall. With the exception of the $k=1$ branch and the temperature spikes between branching levels, the temperature trends along the outer wall are quite similar to the 1D predicted results and to the inner wall temperatures. This occurs even though reinitiation of the thermal boundary layer is not anticipated at the outer wall or at the top and bottom walls following a bifurcation.

The outer-wall temperature distributions shown in Fig. 4 indicate an obvious discontinuity. For example, the outer wall temperature at the exit of the $k=2b$ branch is higher than the outer

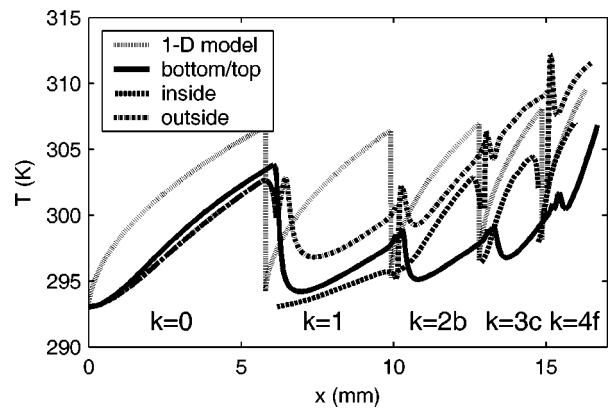


Fig. 4 Wall surface temperatures along path 1

wall temperature at the inlet of the $k=3c$ branch. Recall from Fig. 2, which shows a schematic representation of this bifurcation, that the outer wall of the $k=2b$ branch terminates at point A and the outer wall of the $k=3c$ branch originates at point B. Middepth temperature contours at this bifurcation are shown in Fig. 5. Clearly evident from Fig. 5 is a low temperature region at point B. The low outer wall temperature is due to flow accelerating around this point. However, immediately downstream of point B, the outer wall temperature increases significantly as a result of flow separation, which causes a zone of recirculating fluid, as was documented by Alharbi et al. [14]. This region is represented in Fig. 4 by a temperature spike near $x=13$ mm, which is followed by a downstream decrease in temperature.

In Fig. 4, with the exception of the $k=0$ branch, along which thermal boundary layers develop at each wall, the trends in the bottom wall temperatures are not well predicted by the 1D model. Rather, the temperature distribution along the bottom wall looks very similar to the trend observed for all walls of the $k=1$ branch. Also, for $k>1$, the bottom wall temperature is lower than the inner wall temperature for most of each branch segment. Because the boundary layer redevelopment is anticipated at the inner wall, but not along the bottom wall, the observed trend in temperature suggests a secondary flow phenomenon that disrupts the thermal boundary layer development. An investigation of secondary flow phenomena is presented later. Temperature spikes are also noted along the bottom wall near the bifurcations in Fig. 4. The primary cause for these temperature spikes is flow deceleration near the bifurcation, the result of a 26% increase in flow area. Note where the centerlines of the bottom walls of branches $k=2b$ and $k=3c$ intersect, which results in the continuous nature of this wall's streamwise temperature distribution.

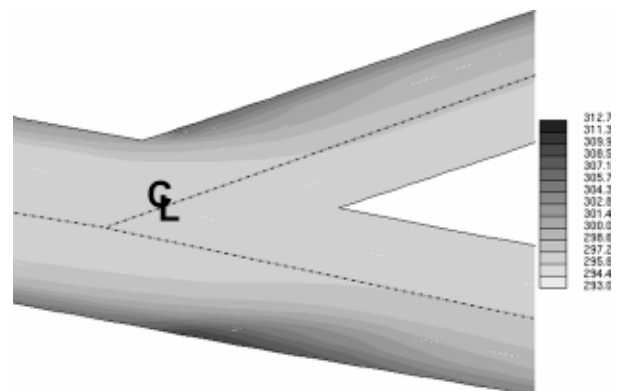


Fig. 5 Temperature contours in x - y plane at intersection of $k=2b$ and $k=3c$ branches

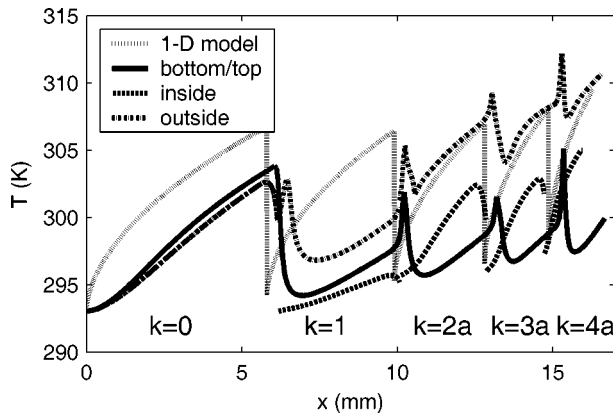


Fig. 6 Wall surface temperatures along path 2

Figure 6 shows the inner, outer and bottom wall temperature distributions along path 2 of the fractal network. Trends appear to be very similar to those in Fig. 4, but the wall temperatures at the flow network exit are lower than those along path 1. Again, this is because of the mass flow values reported in Table 3. The most notable difference between Figs. 4 and 6 is that the bottom wall temperature spikes along path 2 in Fig. 6 are larger than those along path 1 in Fig. 4, the reasons for which are addressed later.

In summary, yet to be explained are 1) the temperature trends at all walls for $k=1, 2$) why the bottom wall is cooler than the inner wall for $k>1$ along both paths, and 3) the difference in magnitude of the temperature spikes along the bottom walls of the two paths. To help explain the causes of the observations, an investigation of the spanwise and transverse temperature profiles is undertaken. Because the axial flow direction changes through each branch, a separate coordinate system is established for each branch segment in each level. The origin of the coordinate system is the apex of the inner wall, as noted in Fig. 2. Coordinate x represents the axial flow direction, y represents the transverse direction from the origin at the inner wall to the outer wall, and z is measured from the bottom of the channel to the top of the channel. Because z is always measured from the bottom of the channel, the right-hand rule is violated for the following branches: $k=2b, k=3b, k=3d, k=4b, k=4d, k=4f$, and $k=4h$. It is also relevant to note that the beginning of the outer wall of a branch is not necessarily aligned with the origin, but may correspond to a negative value of x relative to the local coordinate system, as is the case for the $k=3c$ segment, which originates at point B in Fig. 2.

Spanwise data are normalized by the channel width w of each branching level, which decreases for increasing values of k . Values of y' equal to 0 and 1, respectively, represent the inner and outer walls. Transverse temperature profiles are normalized by the channel depth and reported using the variable z' . The variable x' is introduced to represent the axial distance along the inner wall normalized by the inner wall length. Shown in Fig. 7 are the spanwise temperature profiles at the inlet, $x'=0$, of each branching level along path 1, taken from the x - y midplane at $z=0.5$. There is a distinct asymmetry in the temperature profiles. The fluid from the center of the preceding branch is just making contact with the origin of the inner wall, causing an initiation of the thermal boundary layer at $x'=0$ and $y'=0$. Note an increase in the fluid temperature near $y'=0$ as k increases beyond unity. On the other hand, the thermal boundary layer along the outer wall, $y'=1$, does not reinitiate at $x'=0$, but rather continues to change from branch to branch. Spanwise temperature profiles at the exit, $x'=1$, of each segment along path 1 are shown in Fig. 8. In contrast with Fig. 7, development of the thermal boundary layer along the inner wall, where $y'=0$, is observed for all branching levels except for $k=1$.

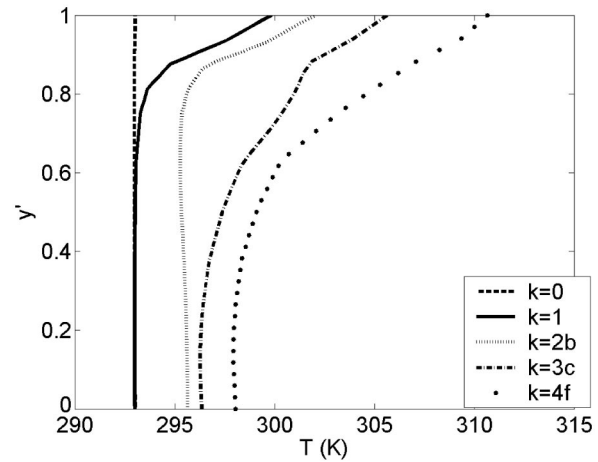


Fig. 7 Spanwise temperature profiles at $x'=0$ and $z'=0.5$ for all branches along path 1

A closer look at the inlet of the $k=1$ branch is provided in Fig. 9 in the form of a contour plot of temperature in the x - z plane midway between the inner and outer walls. It is evident that a high-temperature region, which originates at the channel inlet and penetrates into the channel, exists at both the top and bottom walls. This high-temperature region quickly diminishes in thickness shortly downstream of the inlet. Obvious from Figs. 7–9 is that a secondary flow must be influencing the thermal boundary layer development.

Shown in Fig. 10 are velocity vectors of the span-wise and transverse, y and z , components of the velocity field, as defined by the local coordinate system. In Fig. 10(a) are the secondary flow

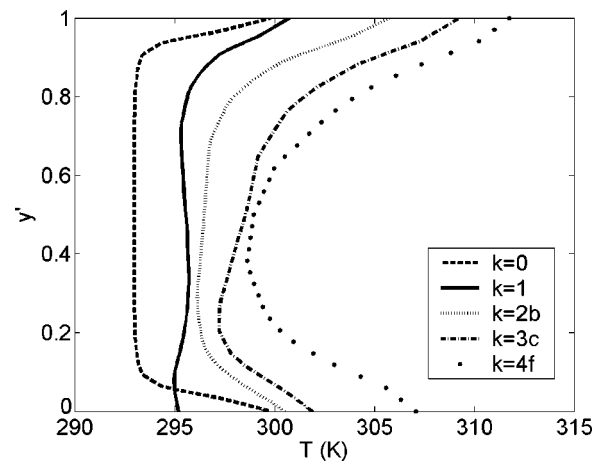


Fig. 8 Spanwise temperature profiles at $x'=1$ and $z'=0.5$ for all branches along path 1

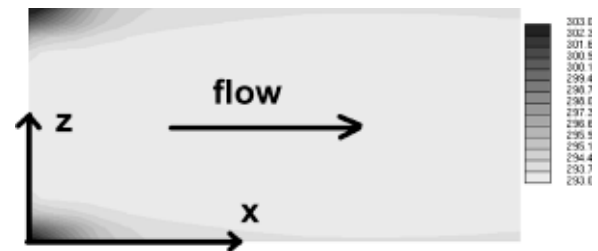


Fig. 9 Temperature contours in x - z plane at inlet of $k=1$ branch

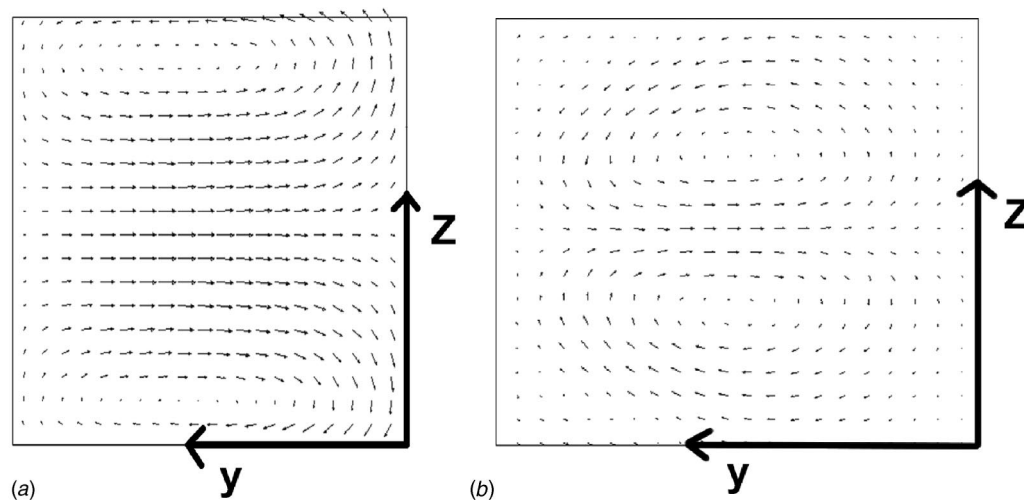


Fig. 10 Spanwise and transverse component velocity vectors at a) inlet and b) midstream location of $k=1$ branch

structures at the inlet of the $k=1$ segment, whereas Fig. 10(b) shows the secondary flow structures midstream through the $k=1$ branch. Note that velocity magnitude is proportional to vector length. Observed from Fig. 10(a) is a strong spanwise velocity component, with a maximum velocity of 3 m/s near the channel center, which is approximately 50% of the streamwise velocity component. This secondary flow brings cooler fluid from the center of the channel toward the inner wall. In addition, swirl patterns are observed near the top and bottom walls, which direct cooler fluid from the center of the channel toward these two walls. Both phenomena ultimately influence the thermal penetration near the wall, and thereby influence the cross-stream temperature profiles and the axial temperature distributions. Midstream down the $k=1$ branch, shown in Fig. 10(b), the cross-stream velocity component diminishes, but a region of swirl is still observed near the top and bottom walls. The maximum velocity in the swirl region is about 1 m/s, yet still represents a strong presence, approximately 15%, relative to the average streamwise velocity.

For all branch segments, the relative magnitude of the cross-stream velocity, which brings cooler fluid to the inner wall, diminishes along x from a maximum at the channel inlet. As the cross-stream contribution to the secondary flow diminishes, the swirl component, which delivers cooler fluid to the top and bottom walls, dominates. This tends to keep the top and bottom walls cooler than the inner walls. This flow phenomena is clearly evidenced in Figs. 11(a) and 11(b), which represent cross-stream velocity components, v and w , at the inlet and midstream locations of branch $k=2b$, respectively. The average streamwise velocity is 4.2 m/s through this branch.

It was shown that the bottom wall temperature spikes are larger along path 2 (Fig. 6) than path 1 (Fig. 4). This is attributed to the angle at which the branching occurs, which influences the magnitude of swirl. A cooler bottom wall temperature is anticipated for a stronger swirl than for a weaker swirl, as more cooler fluid is swept to this wall from the center of the channel. Also, the stronger the swirl, the less relative influence of decelerated flow. Along path 1, the branch segments $k=1, 2b, 3c, 4f$ split from their lower level branch at angle of 20.36 deg, 30.89 deg, 28.95 deg, 24.15 deg, respectively. Along path 2, the branch segments $k=1, 2a, 3a, 4a$ split from their lower level branch at angles of 20.36 deg, 5.17 deg, 0.38 deg, 1.42 deg, respectively. The maximum swirl velocity at the inlet of a branch that bifurcates with a shallow branching angle, as is the case for the last three branching levels along path 2, is weaker in magnitude relative to the stream-wise velocity, approximately 30%, than that observed for segments experiencing a sharper branching angle, approximately 50%. The lower the

swirl the less cool fluid moves to the top and bottom walls, hence, a higher wall surface temperature. This then accounts for the higher temperature spikes at the bottom wall observed along path 2 compared with path 1.

In summary, the branching angle, which was shown by Alharbi et al. [14] to influence the pressure distribution, also influences the bottom and outer wall temperatures and, under strong spanwise flow conditions, also influences the inner wall temperatures. The 1D code well predicts the maximum wall temperature, with the exceptions of the temperature spikes near the inlets of the bifurcations. To incorporate such effects in the model would be cumbersome. Therefore, the angle of bifurcation should be considered, in addition to the model results, in the design of a fractal-like flow network in order to minimize locations of flow separation. Inclusion of the redeveloping thermal boundary layer assumption allows the 1D code to fairly well predict the trend of the inner-wall temperature distribution and the maximum wall temperature at the channel exit. Because the primary purpose of the 1D model is to provide a simple and useful design tool, no changes to the boundary layer development assumption are recommended.

Variable Property Analysis. To assess the third and final assumption imposed in the 1D model, which is constant thermophysical properties, 3D CFD results with and without temperature dependence of properties is considered. Alharbi et al. [14] show a significant error in pressure drop for the straight channel array, on the order of 17%, when assuming constant viscosity evaluated at the mean temperature between the inlet and exit bulk fluid temperatures. Over the temperature range from 273 to 373 K, thermal conductivity and molecular viscosity of water vary by as much as 20% and 84%, respectively. Assuming these properties to remain constant in the 1D model could result in significant uncertainty in the predictions. To assess the degree of uncertainty, the 3D model was run with and without constant property limitations. Because the specific heat of water changes by only 1.6% over this same temperature range, it is held constant in both constant and variable property analyses.

Inner wall temperature distributions from the 3D CFD model through the straight channel and fractal-like branching channel networks with and without variable properties are presented in Fig. 12. Relative to the variable property analysis, assuming constant thermophysical properties results in a 2.5 K error for the straight channel and less than 1 K for the fractal-like flow network. For the straight and fractal-like networks, these account for 10% and 5% errors, respectively, in the temperature difference

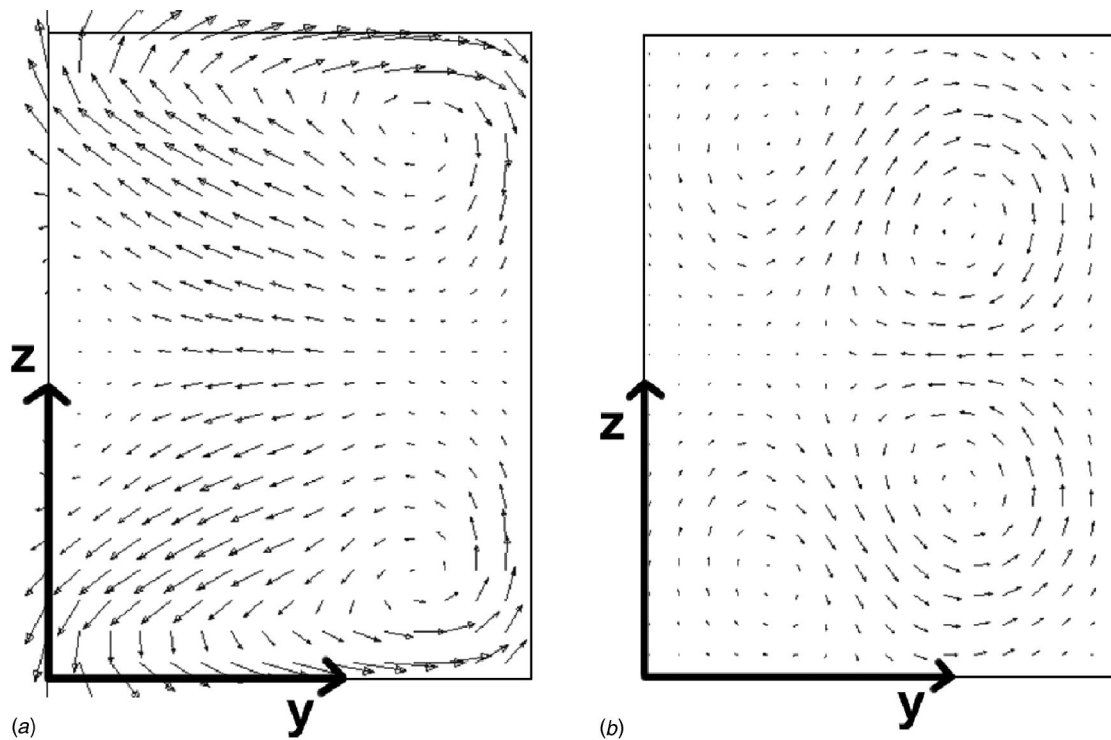


Fig. 11 Spanwise and transverse component velocity vectors at a) inlet and b) midstream location of $k=2b$ branch

between the inlet and exit. Such errors are acceptable for a 1D model used to design fractal-like flow networks in a heat sink. Because this error is expected to increase if the temperature range of fluid properties increases, it is recommended that the temperature dependence of thermal conductivity, in addition to the temperature dependence of viscosity as recommended by Alharbi et al. [14], be incorporated in the 1D model for high heat flux cases.

Three-Dimensional Heat Sink Analyses. Surface temperature contours on a heat sink with a fractal-like flow network are shown in Fig. 13. The material in which the fractal-like flow network is embedded is 2 mm thick copper. Although fluid properties are allowed to vary with temperature, those of the solid material are assumed fixed due to their slight variation, approximately 2%, over a temperature range from 273 to 373 K.

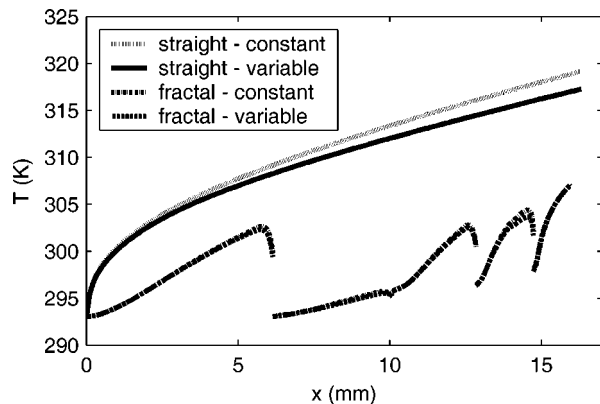


Fig. 12 Three-dimensional CFD stream-wise temperature distributions along inner wall of path 1 with constant and variable fluid properties

The heat sink consists of twelve branching networks, identical to the single network shown in Fig. 1. These twelve networks are arranged to share a single inlet plenum forming a circular heat sink. Due to the symmetric nature of the heat sink, 1/12 of the circular disk is studied in the present analysis. The surface shown in Fig. 13 has energy supplied at a rate of 100 W/cm^2 . The heat sink is cooled with water supplied at a total flow rate of 10 ml/s, which corresponds to 0.8333 ml/s supplied to the portion under investigation. Note that the location at which the surface is hottest, about 340.5 K, occurs along the edge of the heat sink section considered and corresponds to a radial distance of approximately $r/R=0.40$.

Surface temperature distributions along the fractal-like heat sink and the parallel channel heat sink are provided as a function of heat flux in Fig. 14. The temperature distribution for the fractal-like heat sink is along the edge of the section under consideration that would represent a symmetry plane. The temperature distribution for the parallel channel heat sink is at the heated surface midway between two channels where the surface temperature

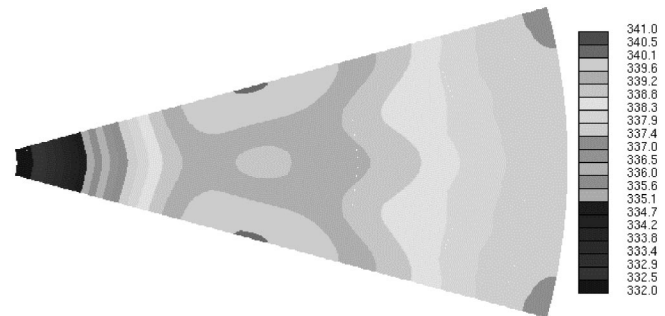


Fig. 13 Surface temperature distribution on heated surface of heat sink with fractal-like flow network; localized hot spots at symmetry plane near $r/R=0.4$

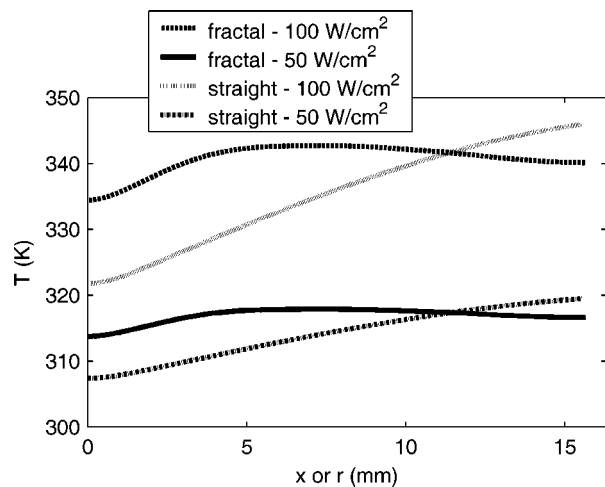


Fig. 14 Radial and axial heat surface temperatures along the symmetry plane of heat sinks with fractal-like and straight, parallel channel arrays, respectively

would be highest. The two heat sinks have the same heat sink thickness (2 mm), heat sink material (copper), total channel length, plate surface area, heat flux, and total flow rate. As in the case of the flow network analysis, the hydraulic diameter of the parallel channels is identical to that of the terminal branching of the fractal-like network. The values are noted in Table 2.

The center-to-center spacing of the channels in the parallel channel heat sink, based on anticipated fabrication constraints, is equal to twice the channel width. Note from Table 2 that the convective surface area in the heat sink with a parallel channel array is almost three times higher than for the heat sink with the fractal-like flow network. Although the channels in the branching channel heat sink in this particular design are not as closely spaced as they could be, it is obvious that a substantial benefit of the parallel channel heat sink is the higher convective area per plate surface area.

In Fig. 14, the temperature distributions are provided as a function of heat flux. Both heat sinks are supplied with heat fluxes of 50 and 100 W/cm² and a total flow rate of 10.0 ml/s. Note that the difference in maximum temperatures of the heat sinks with fractal-like and parallel flow networks is only a degree or two. It would appear that there exists little incentive to use heat sinks with fractal-like flow compared to parallel channel heat sinks given the same flow rate. It should be noted that the flow network, as proposed, is not optimized. However, there are several distinct advantages to using fractal-like flow networks. For example, the temperature variation along the fractal-like heat sink with 100 W/cm² is only 6 K, as opposed to a 24 K variation along the straight channel heat sink with the same applied heat flux. Also, a heat sink with a fractal-like flow network requires less convective area than a parallel channel array to achieve similar maximum surface temperatures given the same flow rate and applied heat flux. Unfortunately, for the same flow rate, the pressure drop through the fractal-like network is 63 kPa in comparison to 58 kPa through the straight channel array. There is a slight pressure-drop penalty. However, now that the 1D model has been validated for design purposes, a more optimal fractal-like flow network for use in a heat sink can be found such that the ratio of the thermal transport to the pumping power is maximized.

Numerical Uncertainty. Uncertainty in data reported from the 3D CFD analysis is limited to errors caused by mesh spacing, irregularity, nonorthogonality, and the choice of the differencing scheme used for the convective term. Error estimates in temperature for the variable property flow network analyses are on the

order of 10⁻⁵ K for 97% of the cells, and 0.2 K for 2% of the cells. Less than 30 localized cells out of 670,000 near the wall in the recirculation region and the point at which the inner walls originate yield errors as high as 0.8 K. Errors in velocity magnitude are on the order of 0.002 m/s for 90% of the cells, and 0.15 m/s for 9+% with a few localized errors on the order of 0.5 m/s. Errors introduced due to constant property assumptions have been previously reported and influence both 3D and 1D model predictions.

Due to memory limitations of the computer, refinement beyond 1M cells for the fractal-like branching channel heat sink model was not possible. For 80% of the fluid cells, the error is less than 0.1 K, but there are localized errors on the order of a few degrees for the fluid cells near the walls. To assess the propagation of these errors to the heated surface, the straight-channel heat sink model was modeled with a similar grid size on either side of the liquid/solid interface, then considerably refined. No significant change in the plate surface temperature distribution was noted, even though the fluid temperature errors were decreased to those found in the flow network analysis. For this reason, the temperature distributions presented for both heat sinks are considered qualitatively good and quantitatively acceptable. Errors in surface temperature distributions are anticipated to be less than 3 K.

Conclusions and Recommendations

In the present investigation, heat transfer through straight and fractal-like branching flow networks was investigated using a 3D CFD approach. Results of temperature distributions through a 3D flow network were compared to those predicted using a 1D model in order to assess the validity of assumptions imposed in the 1D model. These assumptions include 1) developing flow conditions following each bifurcation, 2) a negligible influence of branching angle on temperature distribution, and 3) constant thermophysical fluid properties.

Results indicate that the first assumption is acceptable with no further modifications needed, even though the thermal boundary does not truly redevelop at each of the channel's walls following a bifurcation. Due to the complex nature of secondary flow patterns in a 3D flow network, as influenced by branching angle, no modifications to the 1D model are proposed. Rather, branching angles need to be considered independently of the model during the design stage of a fractal-like flow network. Inclusion of temperature dependent properties is recommended for higher heat flux applications.

Heat sinks with fractal-like networks, versus those with parallel, straight channel arrays, were investigated. For an applied heat flux of 100 W/cm² and a flow rate of 10 ml/s, the maximum temperature at the surface to which energy is supplied is approximately the same between the two types of heat sinks. However, there is a 75% lower temperature variation along the fractal-like flow network with a 10% pressure-drop penalty in the fractal-like heat sink in comparison with the straight channel heat sink for the given geometric and flow conditions. Future work requires network optimization now that the model has been validated and improved.

Nomenclature

- A = area, m²
- c_p = specific heat, J/kg K
- d = hydraulic diameter, mm
- H = channel height, mm
- k = branch level
- L = channel length, mm
- \dot{m} = mass flow rate, kg/s
- N = number of channels emanating from inlet plenum
- n = number of bifurcating channels per segment

p = pressure, Pa
 Q = flow rate, L/s
 q'' = heat flux, W/m²
 R = total radius of fractal-like heat sink, mm
 r = radial distance along heat sink axis of symmetry of fractal-like heat sink, mm
 T = temperature, K
 V = total velocity, m/s
 w = channel width, mm
 x = axial direction
 y = spanwise direction
 z = transverse direction
 x' = dimensionless axial direction (x/L_{inner})
 y' = dimensionless span-wise direction (y/w)
 λ = thermal conductivity, W/m K
 μ = molecular viscosity, N s/m²
 ρ = density, kg/m³

Subscripts

$bulk$ = bulk
 $conv$ = convective
 k = branching level
 $plate$ = plate/heat sink
 i, j = coordinate indices
 i, e = inlet, and exit, respectively
 $inner$ = inner wall
 t = terminal
 tot = total

References

- [1] Tuckerman, D. B., and Pease, R. F. W., 1981, "High-Performance Heat Sinking for VLSI," *IEEE Electron Device Lett.*, **EDL-2**(5), pp. 126–277.
- [2] Sohban, B. S., and Garimella, S. V., 2001, "A Comparative Analysis of Studies on Heat Transfer and Fluid Flow in Microchannels," *Microscale Thermophys. Eng.*, **5**, pp. 293–311.
- [3] Garimella, S. V., and Singhal, V., 2003, "Single-Phase Flow and Heat Transport in Microchannel Heat Sinks," *Proc. of First International Conference on Microchannels and Minichannels*, Rochester, NY, pp. 159–169.
- [4] Bau, H. H., 1998, "Optimization of Conduits' Shape in Micro Heat Exchangers," *Int. J. Heat Mass Transfer*, **41**, pp. 2717–2723.
- [5] Pence, D. V., 2000, "Improved Thermal Efficiency and Temperature Uniformity Using Fractal-Like Branching Channel Networks," *Proc. International Conference on Heat Transfer and Transport Phenomena in Microscale*, Banff, Canada, pp. 142–148.
- [6] West, G. B., Brown, J. H., and Enquist, B. J., 1997, "A General Model for the Origin of Allometric Scaling Laws in Biology," *Science*, **276**, pp. 122–126.
- [7] Bejan, A., 1997, "Constructal Tree Network for Fluid Flow Between a Finite-Size Volume and One Source or Sink," *Rev. Gen. Therm.*, **36**, pp. 592–604.
- [8] Pence, D. V., 2002, "Reduced Pumping Power and Wall Temperature in Microchannel Heat Sinks With Fractal-Like Branching Channel Networks," *Microscale Thermophys. Eng.*, **6**(4), pp. 319–330.
- [9] Chen, Y., and Cheng, P., 2002, "Heat Transfer and Pressure Drop in Fractal Tree-Like Microchannel Nets," *Int. J. Heat Mass Transfer*, **45**, pp. 2643–2648.
- [10] Wechsato, W., Lorente, S., and Bejan, A., 2002, "Optimal Tree-Shaped Networks for Fluid Flow in a Disc-Shaped Body," *Int. J. Heat Mass Transfer*, **45**, pp. 4911–4294.
- [11] White, F. M., 1991, *Viscous Fluid Flow*, McGraw-Hill, New York.
- [12] Wibulswas, P., 1966, "Laminar Flow Heat Transfer in Non-Circular Ducts," Ph.D. dissertation, University of London.
- [13] Shah, R. K., and London, A. L., 1978, "Laminar Flow Forced Convection in Ducts," *Adv. Heat Trans.*, Supplement 1, pp. 219–222.
- [14] Alharbi, A. Y., Pence, D. V., and Cullion, R. N., 2003, "Fluid Flow Through Microscale Fractal-Like Branching Channel Networks," *ASME J. Fluids Eng.*, **125**(6), pp. 1051–1057.
- [15] Pence, D. V., Bouschouten, B. P., and Liburdy, J. A., 2003, "Simulation of Micro-Scale Jet Impingement Heat Transfer," *ASME J. Heat Transfer*, **125**(3), pp. 447–453.

Stephen E. Turner
Naval Undersea Warfare Center,
1176 Howell St.,
Newport, RI 02841

Lok C. Lam

Mohammad Faghri

University of Rhode Island,
Department of Mechanical Engineering,
203 Wales Hall,
Kingston, RI 02881

Otto J. Gregory

University of Rhode Island,
Department of Chemical Engineering,
210 Crawford Hall,
Kingston, RI 02881

Experimental Investigation of Gas Flow in Microchannels

This paper presents an experimental investigation of laminar gas flow through microchannels. The independent variables: relative surface roughness, Knudsen number and Mach number were systematically varied to determine their influence on the friction factor. The microchannels were etched into silicon wafers, capped with glass, and have hydraulic diameters between 5 and 96 μm . The pressure was measured at seven locations along the channel length to determine local values of Knudsen number, Mach number and friction factor. All measurements were made in the laminar flow regime with Reynolds numbers ranging from 0.1 to 1000. The results show close agreement for the friction factor in the limiting case of low Ma and low Kn with the incompressible continuum flow theory. The effect of compressibility is observed to have a mild (8 percent) increase in the friction factor as the Mach number approaches 0.35. A 50 percent decrease in the friction factor was seen as the Knudsen number was increased to 0.15. Finally, the influence of surface roughness on the friction factor was shown to be insignificant for both continuum and slip flow regimes. [DOI: 10.1115/1.1797036]

Keywords: Channel Flow, Experimental, Heat Transfer, Microscale, Rarefied, Roughness

Introduction

As one of the basic elements of micro electro mechanical systems (MEMS), microchannels have been utilized in micro-heat sinks, ink-jet printer heads, micro-gas sensors, micro-refrigerators, and many other micro-fluidic systems. Flow and heat transfer through microchannels have been investigated during the last twenty years to determine if the small characteristic length causes deviation from continuum flow behavior. Early research by Tuckerman and Pease [1] showed that laminar flow of water through a microchannel heat exchanger could dissipate up to 790 W/cm², a heat flux that is generally achieved only with boiling liquids. After the realization of such high rates of heat transfer, additional investigations were conducted in both fluid flow and heat transfer in microchannels.

Peiyi and Little [2] measured the friction factor for gas flow through microchannels of rectangular cross-section. Channels were chemically etched in silicon and abrasively etched in glass with heights ranging from 28 to 65 μm . The surface roughness was not measured, but the glass channels were reported to be rougher than the silicon channels. The data for both the silicon and glass channels showed substantially higher friction factors than those predicted by the Moody's chart; 3 to 5 times higher for the glass channels.

Pfahler et al. [3] conducted flow experiments with liquid and gas through microchannels with rectangular and trapezoidal cross-sections. The channels had heights of 0.5–38.7 μm , widths of 55–110 μm , and typical surface roughness of 1 percent as measured by a surface profilometer. The friction factor was measured for isopropanol, silicone oil, nitrogen, and helium flows based on inlet and outlet pressure measurements. For the isopropanol and silicon oil flows $f Re$ was measured between 73 percent and 105 percent of the theoretical value based on incompressible flow; the higher values of $f Re$ were obtained in the larger channels. The nitrogen and helium gas flow experiments resulted in $f Re$ between 81 percent and 98 percent of the theoretical value, with $f Re$ generally increasing as Re was increased.

Harley et al. [4] conducted flow experiments with nitrogen, helium, and argon through microchannels with channel heights be-

tween 0.51 and 19.79 μm and lengths of 10–11 cm. The pressure and temperature were measured upstream of the microchannel inlet and downstream of the microchannel outlet. The flowrate was determined by measuring the time required for the gas to displace a known volume of liquid in a precision bore tube. The investigators compared their data with a theoretical Poiseuille number determined by an isothermal, locally fully developed model including slip velocity. The experimental Poiseuille number for all the data is within 8 percent of the theoretical Poiseuille number.

Choi et al. [5] performed experiments to measure the friction factor and Nusselt number for nitrogen gas flow through micro tubes. The tube diameters ranged from 3 to 81 μm and the relative surface roughness ranged from 0.0002 to 0.0116. The flow was assumed to be fully developed since the length to diameter ratio was between 640 and 8100. Using the Fanno flow equations, the average laminar friction factors were reported to be 20 percent lower than the theoretical value, and $f Re$ was found to increase as the Reynolds number increased.

Peng and Peterson [6] measured the friction factor for water flow through microchannels with a rectangular cross-sections and $0.133 < D_h < 0.343$ mm. The test sections consisted of four similar microchannels in parallel with a common inlet and outlet. Using pressure data from the microchannel inlet and outlet, they found the friction factor for laminar flow to follow the curve $f Re^{1.98} = \text{Constant}$ rather than $f Re = \text{Constant}$ expected for laminar flow. The channel surface roughness was not reported in this investigation.

Pong et al. [7] fabricated a microchannel of rectangular cross-section (40×1.2 μm) equipped with thirteen pressure sensors built into the test section. Local pressure measurement was used to show that the axial pressure distribution is non-linear for gas flow. Shih et al. [8] conducted flow tests with nitrogen and helium through the same microchannel. An effective tangential momentum accommodation coefficient was determined such that the measured pressure distribution closely matches the theoretical pressure distribution for helium flow. For nitrogen flow, the measured pressure along the channel length was found to be greater than the predicted pressure.

Pfund et al. [9] conducted experiments with water flowing through rectangular microchannels with heights between 100 and 500 μm , width of 1 cm and length of 10 cm. To understand the influence of surface roughness on the friction factor, the lower

Contributed by the Heat Transfer Division for publication in the JOURNAL OF HEAT TRANSFER. Manuscript received by the Heat Transfer Division August 4, 2003; revision received June 8, 2004. Associate Editor: K. D. Kihm.

surface of the channel was roughened by using base plates made of polyimide, Lexan, and brass. The upper surface of the channel was a Lexan cover plate. The base plate surface roughness was measured to be 0.13, 0.19, and 0.45 μm for the polyimide, Lexan, and brass, respectively. Although the relative roughness was less than 10^{-3} , flow over the brass base plate was found to have a higher friction factor than flow over the Polyimide base plate.

Takuto et al. [10] conducted gas flow experiments through one microchannel with a triangular cross-section and two with trapezoidal cross-sections. The ratio of the measured friction factor to incompressible theoretical friction factor (normalized) was presented for channels with hydraulic diameters between 3 to 10 μm . For tests conducted with both nitrogen and helium the triangle cross-section channel exhibited a normalized friction factor between 1.0 and 1.2. The trapezoid channels exhibited a normalized friction factor between 0.8 and 1.0.

In a recent review of single phase flow and heat transfer data at the microscale, Guo and Li [11] discuss the influence of gas rarefaction, the combined influence of channel size and “predominant factors”, and surface roughness. A primary conclusion of their review is that the small characteristic length of microchannels enables large variations of flow properties (pressure, density, velocity), even in the absence of rarefaction. The viscous dominated flows make it necessary to evaluate gas flow/heat transfer data using a compressible equation of state. They recognized that there can be significant differences between inlet and exit Mach numbers and that flow compressibility is likely to influence the friction factor and Nusselt number. Surface effects like friction induced compressibility, surface roughness, viscous forces and axial heat conduction were attributed to the large surface area to volume ratio of microchannels, compared to conventional ducts. Finally, it was acknowledged that deviation between experimental results and theoretical values could be a result of entrance effects and measurement error rather than novel phenomena at microscale.

Two recent experimental investigations have focused on determination of the tangential momentum accommodation coefficient (TMAC). Arkilic, Breuer, and Schmidt [12] have conducted gas flow experiments through a microchannel of 1.33 μm height, 52.3 μm width, and 7490 μm length. Ar, N_2 , and CO gases were tested through the channels which have polished Si surfaces with a thin native oxide layer. The surface roughness of the microchannel is reported to be less than $0.65\text{E}-3 \mu\text{m}$. They report values of TMAC between 0.75 and 0.85 for $\text{Kn} > 0.1$. For $\text{Kn} < 0.1$, there is significant scatter in the reported data. Maurer, Tabeling, and Wilmaire [13] conducted gas flow tests through a microchannel of 1.14 μm height, 200 μm width and 1 cm length with a surface roughness reported to be 20 nm. Their microchannel had one silicon surface and one glass surface. Experiments were conducted with helium and nitrogen with the averaged Kn in the range 0.002 to 0.8. From the flow data TMAC was calculated to be 0.9 with significant scatter in the data at lower Kn . The experiments conducted by Arkilic et al. [12] and Maurer et al. [13] measure the pressure at the entrance and the exit. Both neglect entrance and exit effects. The variation of TMAC at low Kn , raises questions about verification of the experimental data in the limiting case of small Kn (in continuum flow range). Such verification of the experimental measurements without the influence of rarefaction would lend more credibility to measurements with the presence of rarefaction.

A local pressure measurement technique was reported by Turner et al. [14] to directly measure the axial pressure profile for compressible gas flow through microchannels of rectangular cross-section. Three microchannels were tested with nitrogen and helium having D_h between 9.7 and 46.6 μm . Laminar flows were tested for Reynolds numbers, $0.1 < \text{Re} < 1000$. By measuring the pressure along the length of the channel, the average friction factor was calculated between the internal pressure transducers. For each of the microchannels, the product of friction factor and Rey-

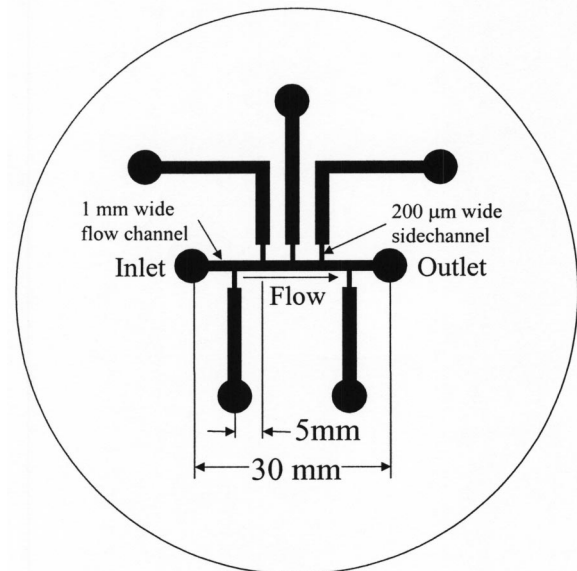


Fig. 1 Top view of microchannel with local pressure measurement

nolds number, $f \text{Re}$, was found to be within 63 to 66 percent of the theoretical value based on incompressible flow. For the range of Re tested, $f \text{Re}$ was constant. Subsequently, a calibration error was found in the measurement of channel depth, which accounts for the deviation between measured and theoretical friction factor.

In an effort to investigate surface roughness, Turner et al. [15] described fabrication of microchannels with corrugated periodic surface features. A pattern of lines perpendicular to the flow direction was fabricated on the silicon surface with a nominal line-width of 12 μm , a spacing of 12 μm and a height of 0.4 μm . Comparison of $f \text{Re}$ for smooth and corrugated channels of the same depth shows no apparent effect on the friction factor. The friction factors reported in this paper were also lower than the theoretical value because of the calibration error mentioned above.

The measurement equipment was calibrated and additional microchannels were fabricated and tested. The resulting flow data was reported in Turner et al. [16] and showed close agreement in the limiting case of low Ma and low Kn with the incompressible continuum flow theory. In this paper, a new method was reported for fabricating microchannels with uniformly rough surfaces. For the range of Knudsen numbers tested, $0.001 < \text{Kn} < 0.04$, the surface roughness exhibited no effect on the friction factor.

As can be seen from the review of the literature, there is a lack of consistency in the previously reported microchannel flow data. Some data, even our preliminary data, suggests that the friction factor for the micro-scale is lower than that predicted by continuum theory. Other reported data indicated that the friction factor is higher. Additionally, within the laminar flow regime, the friction factor has been found to increase as the Reynolds number increased. The deviation between experimental data and theory has been attributed to surface roughness and to microscale effects. The purpose of this present research is to systematically show the effects of rarefaction, compressibility and surface roughness on the laminar friction factor for gas flow through microchannels.

Experiment

Flow Geometry. The test section was designed with a main flow channel and five side channels equally spaced between the inlet and outlet. Figure 1 shows a top view of the flow channel and the five side channels that lead to pressure transducers. The nominal channel length and width were fixed at 30 mm and 1 mm

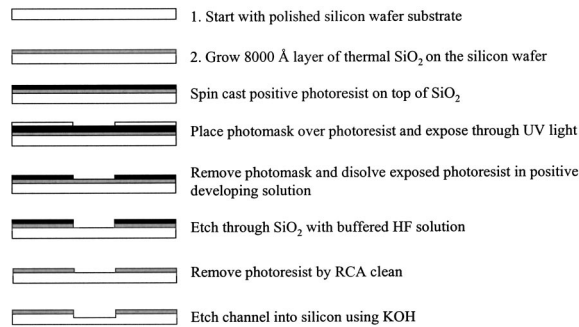


Fig. 2 Process steps to fabricate microchannels into a silicon wafer

while the channel height was varied between $2.3\ \mu\text{m}$ and $50\ \mu\text{m}$. The ratio of height to width (aspect ratio) was maintained below $1/20$ so that the effects of angled sidewalls can be neglected. The side channels, which lead to the pressure transducers, enter the main channel through the side wall. The width is $200\ \mu\text{m}$ and the depth is equal to the microchannel depth. The side channel width was made to be 20 percent of the flow channel width to minimize flow disturbance. A short distance away from the flow channel, the width of side channels is increased to 1 mm to reduce the time required to build up static pressure at the pressure transducers.

Test Section Fabrication. The microchannels were etched into 100 mm diameter polished silicon wafers using photolithography and wet etching. Bare silicon wafers were oxidized in a furnace to grow an $0.75\ \mu\text{m}$ thick layer of SiO_2 . Positive photoresist (Clariant AZ 4400) was spin coated onto the oxidized silicon surface and a broad spectrum UV light source was used to expose the photoresist through a photomask having the microchannel pattern as shown in Fig. 1. After developing (removing) the exposed photoresist, the uncovered SiO_2 layer was etched down to bare silicon in buffered hydrofluoric acid. The etch rate of SiO_2 in hydrofluoric acid is over 100 times faster than the etch rate of silicon in hydrofluoric acid, so the silicon surface was considered an etch stop surface. The remaining photoresist was removed with acetone leaving an SiO_2 mask covering the entire wafer surface except for the intended microchannel pattern. The exposed silicon was then etched with a potassium hydroxide (KOH) solution. KOH is a directional etchant that etches the (100) plane of silicon at a much faster rate than the (111) plane or the SiO_2 mask. The angle between the (111) and (100) planes is 54.7° . So, as the KOH etches the silicon normal to the wafer surface, the (111) plane becomes the sidewall, so that the channel cross-section has a trapezoidal shape. The aspect ratio of the microchannels was purposely made high so that the angled sidewalls can be neglected. The process steps are shown in Fig. 2.

After etching the silicon to form the microchannel and measuring the channel dimensions, the channel was enclosed by bonding a glass disk to the surface of the silicon wafer. Anodic bonding was selected as the preferred bonding method since there is direct contact between the glass and the wafer, and since it makes a permanent hermetic seal. Additionally, the anodic bonding process does not cause any change in channel dimensions and there is no intermediate adhesive layer to account for. The anodic bonding process is described by Mirza and Ayon [17] and requires only a hot plate and a high voltage DC power supply. The wafer and glass were aligned as desired and set on the hot plate with the positive electrode connected to the silicon and the negative electrode connected to the glass as shown in Fig. 3. The hot plate temperature was set to 450°C and the power supply was set between 2000–3000 VDC. Positive sodium ions (Na^+) in the glass become mobile and migrate toward the negative electrode, leaving

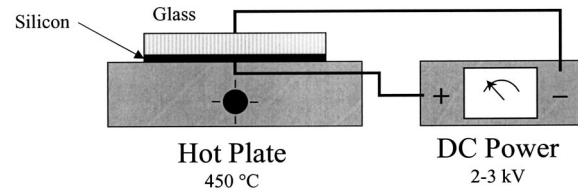


Fig. 3 Schematic of anodic bonding apparatus

a space charge at the silicon/glass interface. Then oxygen in the glass combines with silicon at the interface to form SiO_2 and a permanent bond.

Microchannel Characterization. The microchannel width, height, and surface roughness were measured with a Sloan Dektak IIA surface profilometer. Ten cross-section scans were made along the length of each microchannel. The data from each scan was processed to calculate the average width, height, and surface roughness. The channel width was measured between the sidewalls at half the channel height. The surface roughness, ϵ , was determined from multiple $80\ \mu\text{m}$ segments of each cross-section scan. A linear curve fit was applied to the data in each segment and the average deviation from that curve was calculated. The peak to peak surface roughness, ϵ , is two times the average deviation. The width, height, and surface roughness measurements for the ten scans were averaged to give a final width, height, and surface roughness. An optical microscope with a micrometer stage was used to verify the 5 mm spacing between the side channels. It was also used to measure the minimum distance from the inlet and outlet holes through the glass to the nearest side channel.

Surface Roughness. To assess the influence of surface roughness on the friction factor, the relative surface roughness, ϵ/H , was varied. Three pairs of test sections were fabricated for direct comparison of smooth and rough surfaces with channel heights of 5, 10, and $50\ \mu\text{m}$. The smooth microchannel surfaces were obtained by etching (100) silicon wafers in 30 percent KOH solution (by weight) at 80°C . The surface roughness of the smooth channels was measured to be in the range $0.002 < \epsilon < 0.06\ \mu\text{m}$.

The challenge associated with fabrication of a rough microchannel surface was to produce a channel of uniform depth and uniform roughness along both the channel length and width. Following the work of Sato et al. [18] and Kang et al. [19] the rough channels were etched into polished (110) wafers with 37 percent KOH solution at 70°C . This method was used to fabricate three microchannels with heights of 5.2, 9.9, and $50.2\ \mu\text{m}$ with surface roughness measured to be $\epsilon = 0.33, 0.18, \text{ and } 1.6\ \mu\text{m}$, respectively. To show the difference between the smooth and rough microchannels, images were taken of each microchannel through a microscope. A representative cross-section scan for each microchannel used in this investigation is shown in Figs. 4(a–h). The top surface of both the smooth and rough microchannels was a smooth glass disk. The surface roughness of the glass was measured to be in the range $0.0014 < \epsilon < 0.003\ \mu\text{m}$. Since the width of the microchannels is much larger than the height, the test conditions closely approximate flow between parallel plates in which both plates are smooth, or one plate is rough and the other is smooth.

Test Stand/Instrumentation. Fluid flow tests were conducted using two test stand configurations. The test stand shown in Fig. 5(a) was used when the gas pressure was greater than atmospheric pressure. The compressed gas pressure was reduced to about 900 kPa with a single stage pressure regulator and then reduced again through a two-stage pressure regulator to provide a stable pressure at the microchannel inlet. The test stand was re-configured as shown in Fig. 5(b) when flow tests were conducted at pressures below atmospheric pressure. Upstream of the manifold, the gas passed through a desiccant and a $0.8\ \mu\text{m}$ filter to

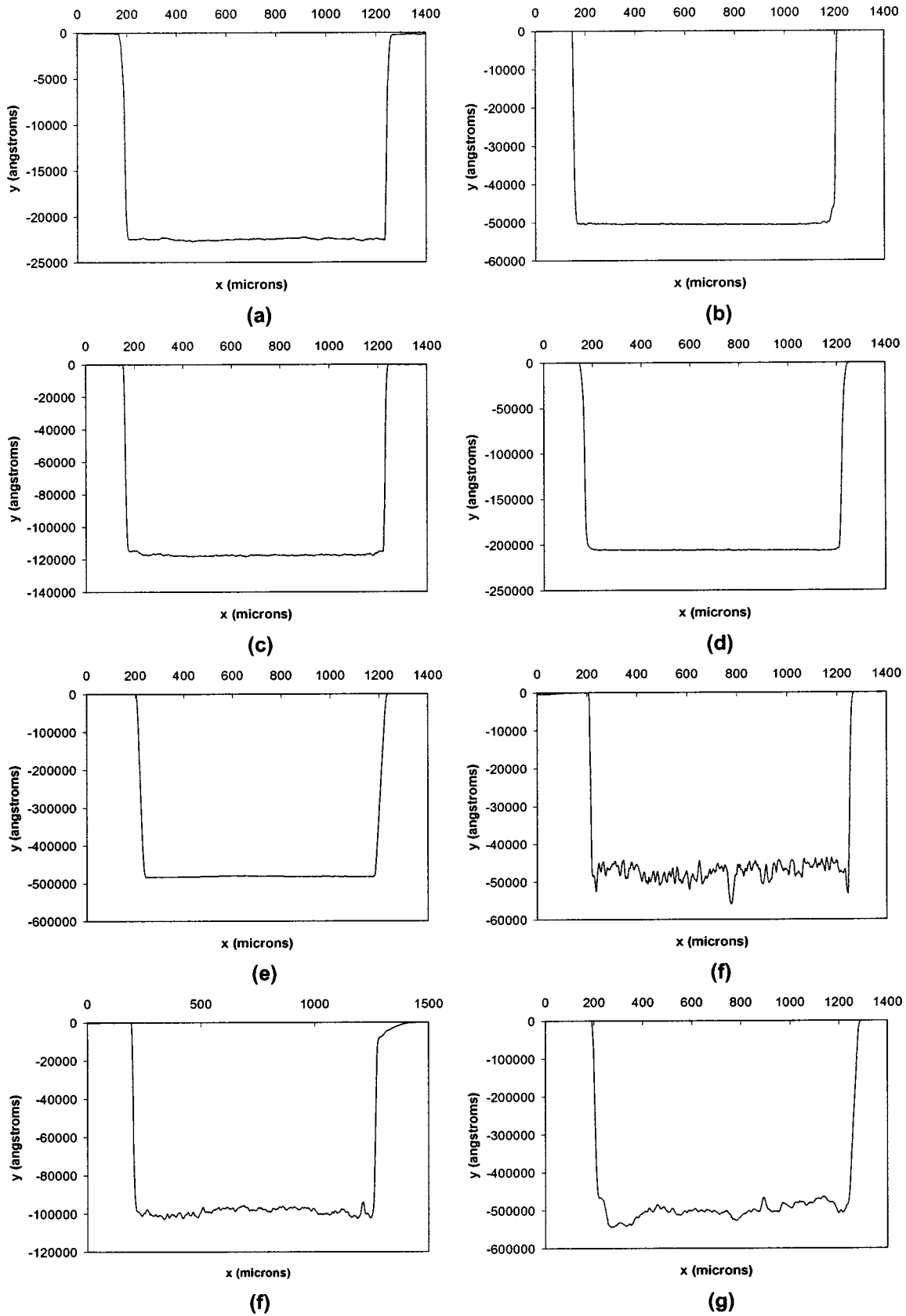


Fig. 4 Cross-section scans for microchannels: (a) 031; (b) 072; (c) 024; (d) 186; (e) 319; (f) 110g; (g) 110d; and (h) 110b

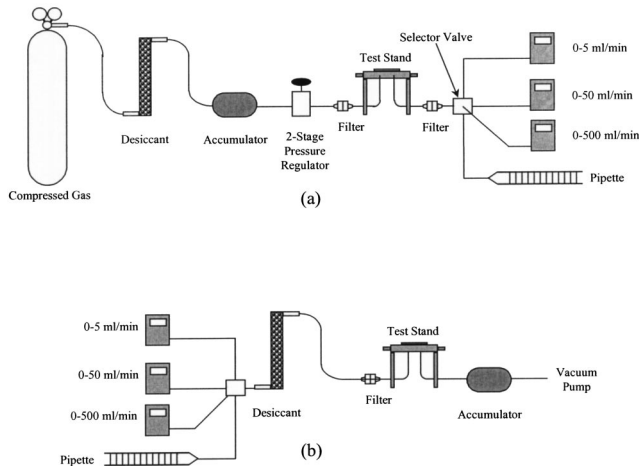


Fig. 5 Microchannel test stand (a) $P_{inlet} > 1$ atm and (b) $P_{inlet} < 1$ atm

ensure it was dry and free of solid particles. Omega PX811 and PX212 series pressure transducers were used for pressure measurement. The volumetric gas flow rate was measured where the gas was at atmospheric pressure. Three Cole-Parmer differential pressure flowmeters were used for flow ranges of 1–5, 5–50, and 50–500 mL/min. For very low flow rates, a graduated pipette was used. A few drops of water were injected into the horizontal pipette. The time for the water meniscus to travel through a fixed volume was measured to calculate the volumetric flow rate through the microchannel.

The interface between the test stand and the test section is the manifold shown in Fig. 6. The inlet and outlet ports each have a miniature type-T thermocouple positioned in the gas flow and a pressure transducer to measure the static pressure. The other five ports in the manifold lead to pressure transducers to measure static pressure along the microchannel length. The manifold permits interchange of the pressure transducers to match the pressure range of the test. The holes in each test section mate up to the ports and are sealed by soft, 50 durometer O-rings. A retaining ring fits over eight threaded studs (not shown in the figure) to seat the test section against the O-rings. After installing a test section in the manifold, a leak test was performed between the manifold inlet and the outlet of the flowmeters. A valve, located between the two stage regulator and the filter (but not shown in Fig. 5(a)) was closed. Another valve was connected downstream of the flowmeter. The microchannel was charged with nitrogen up to 10 psig and then the downstream valve was closed. After the pressure equalized through all the side channels, the system was required to maintain the equalized pressure without loss for one hour.

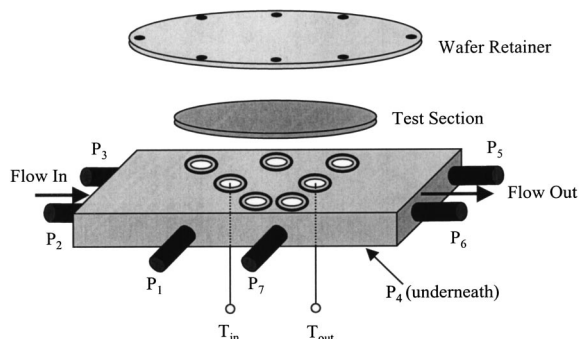


Fig. 6 Test section manifold and instrumentation

Table 1 Microchannel dimensions

Channel	W (μm)	H (μm)	L (μm)	D_h (μm)	ε (μm)	ε/H
031	1053	2.349	26.80	4.688	0.0082	0.004
072	1056	5.213	26.69	10.375	0.0096	0.002
024	1061	12.285	26.82	24.289	0.052	0.004
186	1059	21.430	26.59	42.010	0.031	0.002
319	994	50.097	26.87	95.384	0.054	0.001
110g	1051	5.178	26.75	10.305	0.33	0.06
110d	1100	9.916	25.12	19.655	0.18	0.02
110b	1056	50.201	25.20	95.846	1.62	0.03

Experimental Methodology. The objective of the experiments was to systematically determine the influence of rarefaction, compressibility and surface roughness on the friction factor for gas flow through microchannels. The relevant dimensionless parameters are the Knudsen number, Kn , which describes the degree of rarefaction, the Mach number, Ma , for compressibility, and ε/H for surface roughness. The Knudsen number is defined as $Kn = \lambda/H$, where λ is the mean free path of the test gas and H is the microchannel height. To determine the influence of rarefaction on the friction factor, smooth channels with small ε/H were tested at low velocities such that Ma was small. Kn was increased by independently increasing λ and decreasing H . λ was increased by changing the working fluid from nitrogen to helium. For a given pressure and temperature, the smaller molecule will have a greater mean free path ($\lambda_{\text{helium}} \approx 3\lambda_{\text{nitrogen}}$). Additionally, the pressure was reduced below atmospheric conditions to further increase the intermolecular spacing.

The influence of compressibility on the friction factor was determined by increasing Ma , while maintaining continuum flow ($Kn < 0.001$) through a smooth microchannel (small ε/H). Since the velocity and Ma increase along the channel length, the local pressure measurements were used to evaluate the local friction factor.

The effect of surface roughness was determined by direct comparison of the friction factor for channels of the same height, but different surface roughness. Channels etched into (100) silicon wafers result in quite smooth surfaces $0.002 < \varepsilon < 0.06 \mu\text{m}$ which is comparable to the glass which caps the channels ($0.0014 < \varepsilon < 0.003 \mu\text{m}$). Microchannels etched into (110) silicon wafers resulted in a uniform surface roughness in the range $0.18 < \varepsilon < 1.6 \mu\text{m}$ depending on the etch depth. The comparison of f between smooth and rough channels was carried out for the three cases of continuum, rarefied and compressible flow.

Experimental Results and Discussion

Eight microchannel test sections were fabricated using the processes described above. Five smooth channels were etched into (100) silicon and had hydraulic diameters in the range $4.7 < D_h < 95 \mu\text{m}$. The three channels with rough surfaces were etched into (110) silicon with $10 < D_h < 96 \mu\text{m}$. The dimensions of the eight channels are listed in Table 1. The number that is used to identify each channel is either part of the wafer serial number or the wafer crystal orientation.

Flow tests were conducted through each microchannel with the inlet above atmospheric pressure and the outlet at atmospheric pressure. The tests were conducted with nitrogen and helium gas for each microchannel except the smallest, 031, which could deplete the compressed gas cylinder before reaching steady conditions. An air compressor was used to provide steady pressure to the inlet of microchannel 031. Baseline tests were also conducted through microchannel 319 with air to verify the data obtained using microchannel 031. The friction factor was calculated from experimental data using the following equation.

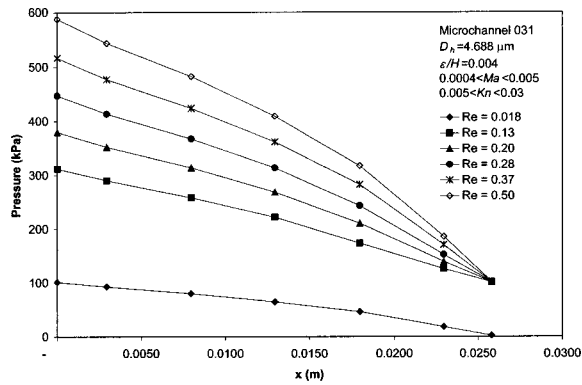


Fig. 7 Axial pressure distribution for air flow through microchannel 031

$$f = \frac{D_h}{L} \left[\frac{P_1^2 - P_2^2}{RTG^2} - 2 \ln \left(\frac{P_1}{P_2} \right) \right] \quad (1)$$

Equation (1) was derived from one-dimensional conservation of mass and momentum equations assuming compressible, isothermal gas flow with no-slip boundary conditions. Details of the derivation can be found in Choquette et al. [20]. To facilitate presentation of data, the experimental friction factor was normalized by the theoretical friction factor for fully developed flow through a rectangular cross-section having an aspect ratio, $\alpha = H/W$.

$$f Re = 96(1 - 1.3553\alpha + 1.9467\alpha^2 - 1.7012\alpha^3 + 0.9564\alpha^4 - 0.2537\alpha^5) \quad (2)$$

Equation (2) is an empirical equation reported by Shah and London [21] which approximates the two-dimensional exact solution for the fully developed friction factor within 0.05 percent.

Axial Pressure Distribution. During each flow test, the pressure was measured at the inlet, outlet, and five equally spaced locations along the microchannel length. The static pressure is plotted against the distance from the inlet in Fig. 7 for air flow through microchannel 031 ($D_h = 4.688 \mu\text{m}$). The curve on the bottom of the graph shows the pressure data for a low Reynolds number test conducted at sub-atmospheric pressure. The other five curves show the axial pressure distribution for inlet pressures between 300 and 600 kPa; the outlet pressure was maintained at about 101.3 kPa. When the ratio of inlet to outlet pressure is small, the change in gas density and velocity along the channel length is small and the pressure profile appears linear. As the pressure ratio is increased (by increasing the inlet pressure) the pressure profile becomes increasingly nonlinear. The range of Kn reported in Fig. 7 extends into the slip flow regime. However, to confirm that the non-linear pressure distribution is not an effect of rarefaction, but rather an effect of the compressible fluid, the pressure profile for continuum flow is presented in Fig. 8. This figure reports the pressure profile for air flow through microchannel 319 ($D_h = 95.384 \mu\text{m}$) in which $\text{Kn} < 0.001$. The inlet pressure was varied between 150 and 325 kPa and the resulting Re were between 152 and 978. For isothermal gas flow through a channel of constant area cross-section, the conservation of mass requires that the product of density and average velocity is constant. Consequently, Re remains a constant from inlet to outlet. Again, the pressure profile becomes increasingly nonlinear as the ratio of inlet to outlet pressure increases. Gas flow through microchannels represents a unique case of compressible flow in which Re and Ma can be small while changes in pressure and density from the inlet to the outlet are significant. As the gas flows through the channel, the pressure and density decrease, causing the gas to

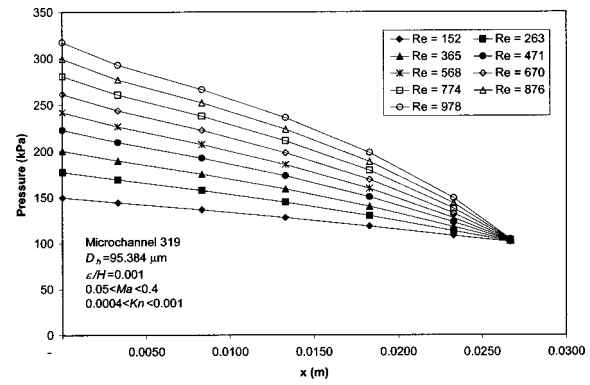


Fig. 8 Axial pressure distribution for air flow through microchannel 319

accelerate. The shear stress at the wall is proportional to the velocity gradient normal to the wall, so the pressure gradient increases along the channel.

Local Knudsen Number. The local pressure data is used to calculate Kn along the channel length. The mean free path of the gas is inversely proportional to pressure [22], so Kn increases along the length as the pressure decreases. A plot of Kn against x , the distance from the inlet, is shown in Fig. 9 for air flow through channel 319. The plot shows that all the Kn profiles approach a constant value at the outlet since the pressure is atmospheric. It is clear that along the channel length, Kn is significantly lower than the outlet value. Consequently, in the present investigation the local Kn is used to show the dependence of f on Kn. The figure also shows the influence that pressure has on Kn. In subsequent tests, Kn was driven into the slip flow regime by lowering the pressure below atmospheric pressure.

Continuum Friction Factor and Entrance Length. The experimental method was validated by conducting flow tests through large smooth microchannels. Experiments conducted with nitrogen in microchannel 319 resulted in $\text{Kn} < 0.001$, which indicates continuum flow. Figure 10 is a semi-log plot of the local product $f Re$ plotted against the dimensionless distance from the inlet, X^* , for $131 < \text{Re} < 1010$. For this microchannel, $f Re = 89.9$ is the fully developed value based on incompressible theory. For each Re tested, the value of X^* was calculated using x at the mid point between pressure measurements. The values of X^* calculated between the entrance and the first side channel are $0.017 < X^* < 0.13$, with $X^* = 0.017$ corresponding to $\text{Re} = 1010$. Between the first and second side channels, $0.06 < X^* < 0.46$, indicating that for large Re, the entrance region extends past the first side channel.

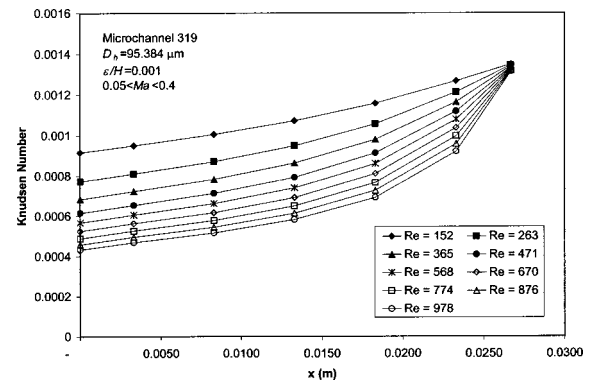


Fig. 9 Local Knudsen number for air flow through microchannel 319

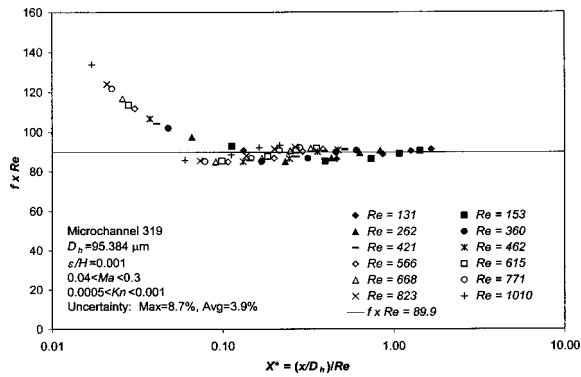


Fig. 10 Local friction factor for nitrogen flow through microchannel 319

The data in Fig. 10 shows that $f Re = 134$ for the smallest value of X^* . As X^* increases, $f Re$ decreases, approaching 89.9. This trend is observed in the data between the entrance and the first side channel. However, between the first and second side channels, even for $X^* = 0.06$, $f Re \approx 85 - 86$. Between the entrance and the first side channel, the friction factor is affected by both developing flow and entrance geometry effects (sharp-edged, rounded, . . .), while the friction factor between the first and second side channels is only affected by developing flow. It is clear that the entrance geometry has a dominant influence on f . Past the first side channel, the flow technically remains in the developing region since the velocity never becomes constant. The average $f Re$ between the first and last side channels is $88 < f Re < 90$ (very close to the theoretical value), while the local values of $f Re$ past the first side channel begin at 85, increase mildly to 91. For the larger Re , the local values of $f Re$ near the exit are observed to increase above 91, since they are also influenced by local Mach number (this effect is treated independently in a later section). The primary conclusion drawn from Fig. 10 is that the entrance geometry has a significant influence on friction factor measurements. It explains why some researchers have observed f to increase with Re in the laminar flow range when only inlet and outlet pressure is measured. Subsequent reporting of f in this paper exclude data from the entrance region.

After validating the experimental setup, flow tests were conducted at higher Kn through smooth microchannels with smaller hydraulic diameters. The inlet pressure was varied between 101 and 700 kPa and the outlet was maintained at atmospheric pressure. The average value of f/f_{theory} along the channel length is plotted against Re for nitrogen flow in Fig. 11. As Re increases from 1.8 to 2.8 for microchannel 072, a 5 percent decrease in f is observed. The flowrate for the lower Re data was measured with

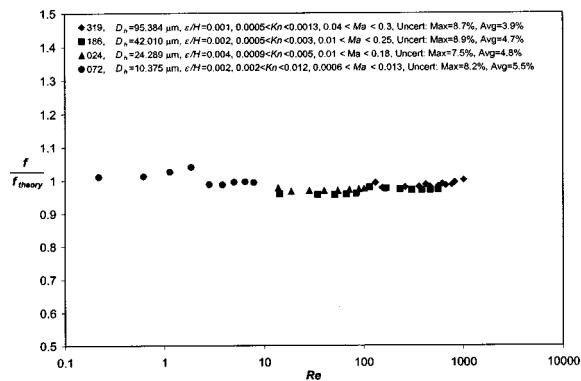


Fig. 11 Average friction factor for nitrogen flow plotted against Reynolds number

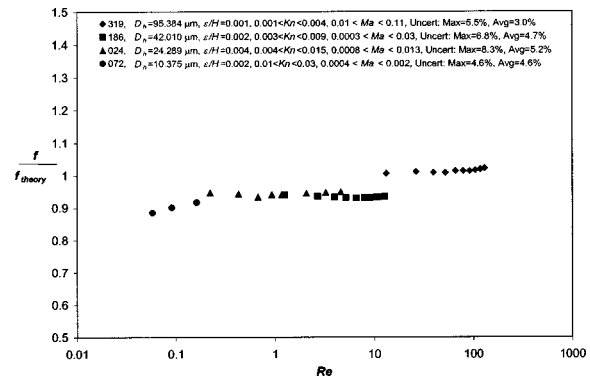


Fig. 12 Average friction factor for helium flow plotted against Reynolds number

the pipette method while a calibrated differential pressure flowmeter was used for the remaining data. Even though the pipette is not calibrated for flowrate measurement, the deviation is small and is considered sufficiently accurate for low flowrate measurement. This figure shows close agreement between the experimental friction factor and that predicted by incompressible theory for a broad range of laminar Reynolds numbers in the continuum flow regime. Additional experiments were conducted with helium through the same smooth microchannels. The molecular weight of helium is 1/7 of nitrogen, so the resulting Reynolds number is much lower. Additionally, the mean free path of helium is 3 times greater than nitrogen, so Kn is increased by a factor of 3. The average friction factor for the helium test cases is plotted against the Reynolds number in Fig. 12. For the largest microchannel (319), the experimental friction factor agrees with the theoretical value. As D_h is reduced, the friction factor tends to decrease. This is most notable with microchannel 072 in which $Kn > 0.01$ for the entire length of the channel.

Rarefaction Effects. The effect of rarefaction was isolated from the influence of compressibility and surface roughness by conducting low Re , low Ma flow tests through smooth microchannels. For a given microchannel, Kn was varied by testing gases with different mean free paths ($\lambda_{He} \approx 3\lambda_{air}$) and by decreasing the pressure to below atmospheric conditions. Microchannels with different heights were also tested to expand the range of Kn . Additionally, since Kn increases along the channel length (as the pressure decreases), the local pressure measurements were used to determine the friction factor for four different values of average Kn along the channel. The experimental f was normalized by the incompressible f_{theory} from Eq. (2) and is plotted against Kn in Fig. 13. The figure shows close agreement between f and f_{theory} for

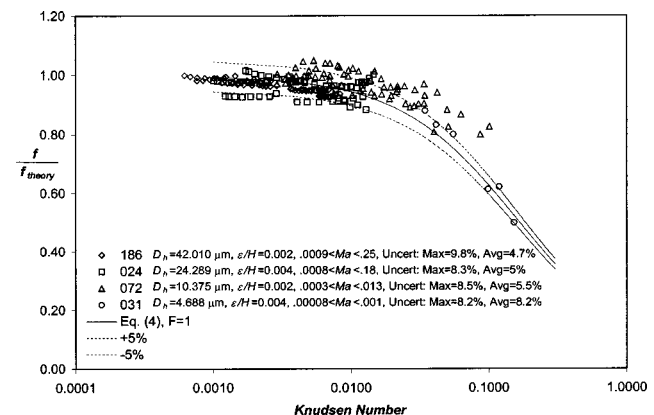


Fig. 13 Influence of rarefaction on the local friction factor

$Kn < 0.01$, (continuum flow regime). As Kn was increased above 0.01, f was found to decrease significantly. In fact, f decreased to 50 percent of the continuum value when Kn reached 0.15. This is considered the slip flow regime which exhibits a non-zero tangential velocity at the boundary: $u(y = \pm H/2) \neq 0$.

From the kinetic theory of gases, the slip velocity boundary condition for flow between parallel flat plates is (see Arkilic et al. [12], Choquette et al. [20], Ebert and Sparrow [23]):

$$u_w = \lambda \left(\frac{2-F}{F} \right) \frac{du}{dy} \Big|_w \quad (3)$$

In Eq. (3), F is the fraction of molecules that strike the wall of the microchannel and reflect at a random angle (diffuse reflection), also called the Tangential Momentum Accommodation Coefficient (TMAC). At the molecular level, surfaces are generally rough and behave as diffuse reflectors ($F = 1$). Application of Eq. (3) to the momentum equation and solving for the friction factor yields the following expression, in which f_{theory} is the continuum value of f for $Kn = 0$.

$$\frac{f}{f_{\text{theory}}} = \frac{1}{1 + 6 \left(\frac{2-F}{F} \right) Kn} \quad (4)$$

As a point of reference, F was set equal to unity (all molecules reflecting diffusely at the microchannel walls) and Eq. (4) was plotted in Fig. 13. Two additional lines at ± 5 percent with respect to Eq. (4) were also plotted in Fig. 13 to show the degree of agreement between the experiment and the slip flow theory. It is acknowledged that some of the data from microchannel 072 is outside the 5 percent bands on Eq. (4). However, both the experiments and Eq. (4) show that as Kn increases above 0.01, the friction factor decreases relative to the continuum value. The data does not support determination of a TMAC or $F < 1$.

Compressibility Effects. Experiments were conducted with air through microchannel 319 ($D_h = 95.384 \mu\text{m}$) to determine the effect of compressibility on the friction factor. The relative surface roughness is small ($\epsilon/H = 0.001$) and $Kn < 0.001$, so the experiments are effectively isolated from the influence of surface roughness and rarefaction. The Mach number was calculated from the local pressure and is plotted against x/L in Fig. 14 for several different Re . As Re increases, the gradient of Ma between the last side channel and the outlet increases. To eliminate both the ambiguity of Ma just before the outlet and the entrance/exit effects, the local friction factor is reported for flow between the five interior side channels. Additionally, data from several of the flow tests was not reported because Ma at the exit approached unity, resulting in choked flow rather than friction controlled flow. The local friction factor is plotted against Ma in Fig. 15 for air flow through micro-

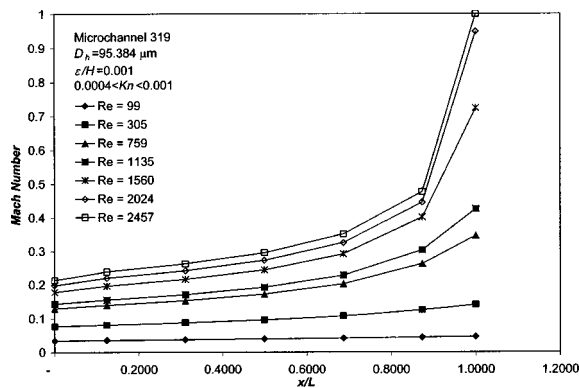


Fig. 14 Local Mach number for air flow through microchannel 319

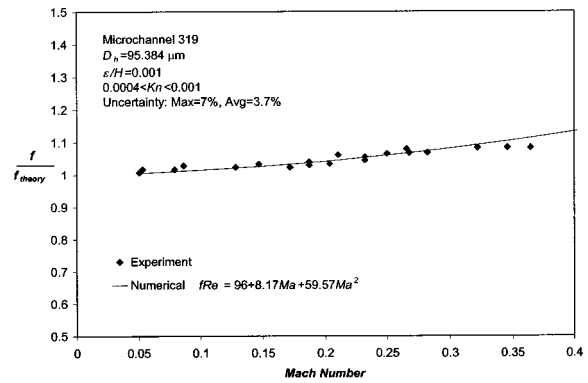


Fig. 15 Effect of compressibility on local friction factor for air flow through microchannel 319

channel 319. The local friction factor is calculated between adjacent pairs of side channels and is plotted against the average value of Ma between the two side channels. The experimental f increases about 8 percent above the theoretical f as Ma increases to 0.35. Asako et al. [24] has conducted a complementary numerical investigation of the effect of compressibility on the friction factor. A curve that shows f as a function of Ma for air flow through parallel flat plates with $H = 50 \mu\text{m}$ and $L = 5 \text{mm}$ is shown in Fig. 15 for comparison with the experimental data. There is good agreement between the experimental data and the numerical analysis.

Surface Roughness. Three microchannels with nominal heights of $H = 5, 10$ and $50 \mu\text{m}$ were fabricated with rough surfaces for direct comparison with the three smooth microchannels of the same height (see Table 1). Each pair of microchannels was tested under the same flow conditions with helium and nitrogen. The average f , normalized by f_{theory} , is plotted against Re for a channel height of $H = 50 \mu\text{m}$ in Fig. 16. The rough channel, (110)b, has a relative surface roughness 30 times that of the smooth channel, 319. The helium data ($Re < 130$) shows that for both the smooth and rough channels, f is within 2 percent of f_{theory} . For the helium data, f is lower for the rough channel than for the smooth channel, but still within 2 percent of each other. The nitrogen test data shows a larger difference in f between the smooth and rough channels. At low Re , f for the smooth channel is about 2 percent lower than f_{theory} , while f for the rough channel is about 3 percent higher than f_{theory} . As Re increases, f increases by 2–3 percent for both the smooth and rough microchannels. This mild increase in f is assumed to be an effect of compressibility since Ma increases with Re . Considering that the average un-

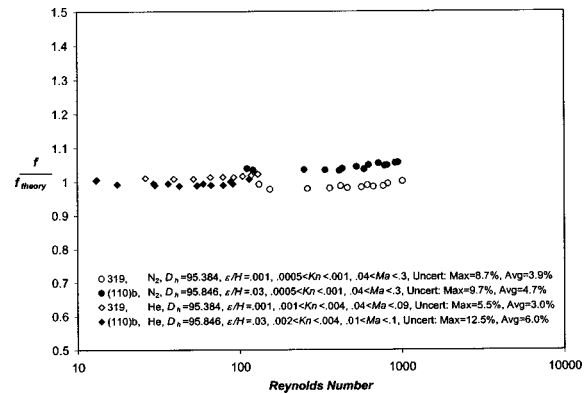


Fig. 16 Effect of surface roughness on $H = 50 \mu\text{m}$ microchannel

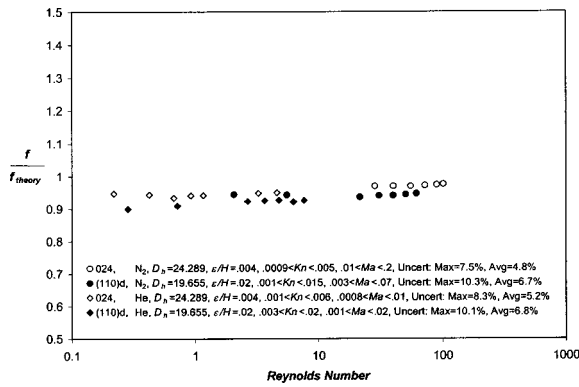


Fig. 17 Effect of surface roughness on $H=10\ \mu\text{m}$ microchannel

certainty of the experimental f is 3–6 percent, the 3 percent difference in f observed for the smooth and rough microchannels of $H=50\ \mu\text{m}$ is statistically insignificant. The second pair of microchannels have $H=10\ \mu\text{m}$ and relative surface roughness of 0.004 and 0.02, respectively. In this case the relative roughness of the rough channel is only 5 times that of the smooth channel. The average f is plotted against Re for the $H=10\ \mu\text{m}$ channels in Fig. 17. In this figure, the difference between f for the smooth and rough channels is generally less than 3 percent. Both the smooth and rough channels exhibit a mild decrease in f , attributed to the influence of rarefaction as Re decreases (and Kn increases to 0.02). The smallest smooth/rough pair of microchannels has $H=5\ \mu\text{m}$; and relative surface roughness of $\varepsilon/H=0.002$ and 0.06 for the smooth and rough channels, respectively. The friction factor for the $H=5\ \mu\text{m}$ channels is plotted against Re in Fig. 18. The relative surface roughness of the rough channel is 30 times greater than the smooth channel, yet the difference in f is relatively small. In this figure Kn increases to 0.04 as the inlet pressure and Re are reduced. The effect of rarefaction is observed as a decrease in the average f as Re decreases.

To further investigate the effect of surface roughness on rarefied gas flow, the smooth and rough channels of $H=5$ and $10\ \mu\text{m}$ were tested with air and helium at below atmospheric pressure. The test conditions resulted in a Knudsen number range of $0.006 < Kn < 0.11$. f was normalized by $f_{\text{theory}} (Kn=0)$ and is plotted against Kn in Fig. 19. Also, Eq. (4) is plotted, with $F=1$, for comparison with the experimental results. In the slip flow regime ($0.01 < Kn < 0.1$) there is no clear difference in f for the smooth and rough microchannels.

Experiments were also conducted with $H=50\ \mu\text{m}$ microchannels to determine if surface roughness has an effect on f as Ma increases. The rough microchannel, (110)b was tested with nitrogen in the Mach number range $0.045 < Ma < 0.28$. The smooth

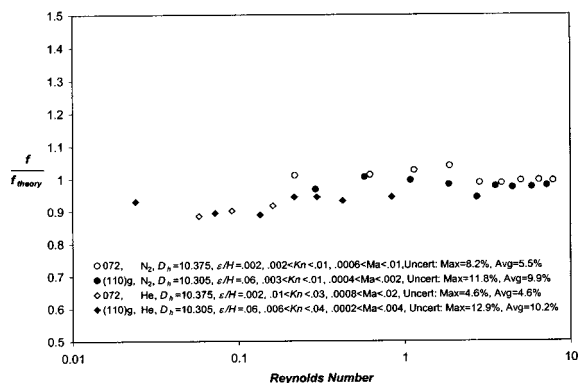


Fig. 18 Effect of surface roughness on $H=5\ \mu\text{m}$ microchannel

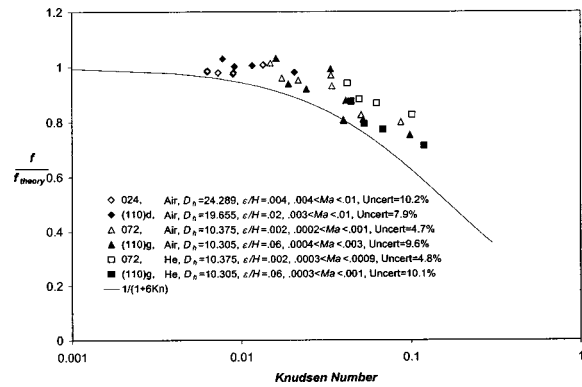


Fig. 19 Effect of surface roughness on rarefied flow

microchannel, 319, was tested with nitrogen and air resulting in a Mach number range of $0.04 < Ma < 0.38$. Using the local pressure measurement, the normalized f is plotted against Ma in Fig. 20. The fluid flow conditions were laminar and continuous in which $Re < 2024$ and $Kn < 0.0013$. As Ma increases, f increases for both the smooth and rough microchannels. However, the increase in f with Ma is slightly larger for the rough microchannel than for the smooth microchannel. At low Ma , $f=f_{\text{theory}}$ for the smooth microchannel while f is 4–5 percent greater than f_{theory} for the rough microchannel. As Ma increases to 0.28, f increases by 4 percent for the smooth channel and by 8 percent for the rough microchannel. Also shown in the figure is the friction factor determined for air flow through microchannel 319, in which f is consistently about 2 percent higher than for nitrogen flow through the same microchannel.

Overall, the influence of the relative surface roughness on the friction factor appears to be quite small (within 2–6 percent). The experiments show that f for smooth microchannels is within 3 percent of f for the rough microchannels, which is also within the experimental uncertainty. Accordingly, no claim can be made about the influence of surface roughness on the friction factor. Considering the rough channels have a larger uncertainty associated with the friction factor, there is no statistical difference between the smooth and rough channels. The friction factor is strongly dependent on the measurement of channel height. Consequently, as the standard deviation of the channel height measurements increases (as is expected and desired for rough surfaces), the uncertainty of the friction factor is increased. To accommodate for this inherent uncertainty, great care was taken to produce microchannels with uniform channel depth and surface roughness along both the channel width and length.

Uncertainty Analysis. Experimental measurements are used to calculate values like Reynolds number and friction factor. The

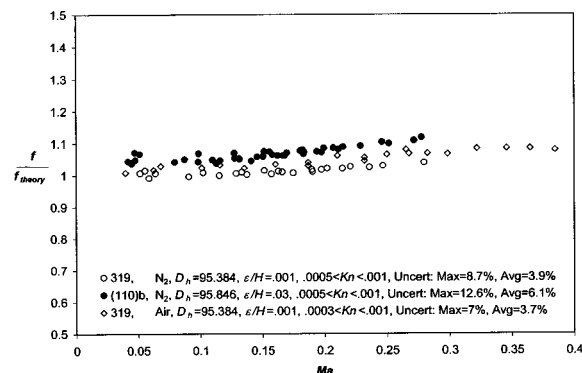


Fig. 20 Effect of surface roughness on compressible flow

Table 2 Measurement uncertainty

Measurement	Uncertainty
P1	±1.72 kPa (0.25 psi)
P2	±0.69 kPa (0.1 psi)
P3	±0.69 kPa (0.1 psi)
P4	±1.03 kPa (0.15 psi)
P5	±1.03 kPa (0.15 psi)
P6	±0.52 kPa (0.075 psi)
P7	±0.26 kPa (0.0375 psi)
P1 (vacuum tests)	±0.69 kPa (0.1 psi)
P2 (vacuum tests)	±0.69 kPa (0.1 psi)
P3 (vacuum tests)	±0.26 kPa (0.0375 psi)
P4 (vacuum tests)	±0.26 kPa (0.0375 psi)
P5 (vacuum tests)	±0.26 kPa (0.0375 psi)
P6 (vacuum tests)	±0.26 kPa (0.0375 psi)
P7 (vacuum tests)	±0.26 kPa (0.0375 psi)
T1	±1.0°C
T2	±1.0°C
0–5 ml/min flow meter	±0.1 ml/min
0–50 ml/min flow meter	±1 ml/min
0–500 ml/min flow meter	±5 ml/min
Pipette volume (1 ml)	0.02 ml

uncertainty of these values is based on the individual uncertainties of each measured quantity used in the calculation. For a given calculated value, y , the uncertainty, δy , is determined by the root-sum-square expression shown in Eq. (4), (Abernathy et al. [25]):

$$y = f(x_1, \dots, x_N) \quad (5)$$

$$\delta y = \left[\left(\frac{\partial f}{\partial x_1} \delta x_1 \right)^2 + \dots + \left(\frac{\partial f}{\partial x_N} \delta x_N \right)^2 \right]^{1/2}$$

For example, to calculate the uncertainty of the friction factor, Eq. (5) was applied to Eq. (1) and is shown in Eq. (6). The partial derivative of f is taken with respect to the six variables and then multiplied by the uncertainty, δ , of each variable. For variables like pressure and temperature, the uncertainty was determined from the standard deviation of the measurement set and the manufacturers specifications. D_h and G are variables which are calculated from one or more measured quantities (i.e., D_h depends on W and H), so δD_h and δG are first determined from Eq. (5) and then used in Eq. (6).

$$f = f(D_h, L, P_1, P_2, T, G) \quad (5)$$

$$\delta f = \left[\left(\frac{\partial f}{\partial D_h} \delta D_h \right)^2 + \left(\frac{\partial f}{\partial L} \delta L \right)^2 + \left(\frac{\partial f}{\partial P_1} \delta P_1 \right)^2 + \left(\frac{\partial f}{\partial P_2} \delta P_2 \right)^2 + \left(\frac{\partial f}{\partial T} \delta T \right)^2 + \left(\frac{\partial f}{\partial G} \delta G \right)^2 \right]^{1/2}$$

The uncertainty for each measurement device is listed in Table 2. The standard deviation of the microchannel height and width measurements is not listed, but was accounted for in the uncertainty analysis. The primary contributor to the uncertainty was the flowrate measurement which is a percentage of full scale reading. Consequently, flowrates measured at the lower end of a given range have a higher uncertainty associated with them. Conversely, the flowrate uncertainty with the pipette method decreased as the flowrate decreased because it took a longer time for the liquid to travel along the pipette.

Conclusions

For the first time, local pressure measurement has been used in microchannel flow to investigate the influence of (1) entrance region; (2) rarefaction; and (3) compressibility on the friction factor. Additionally, smooth and rough microchannels were fabricated to determine the influence of surface roughness on the friction factor for rarefied, continuum and compressible flow. A systematic investigation was conducted with microchannels having hydraulic diameters between 5 and 96 μm . A nonlinear pressure distribution

was measured for gas flow in both the rarefied and continuum flow regimes. This pressure distribution was used to determine Knudsen number and Mach number profiles along the length of the microchannel.

The results show close agreement between the experimental and theoretical friction factor in the limiting case of the continuum flow regime. The Knudsen number was varied to determine the influence of rarefaction on the friction factor while ε/H and Ma were kept small. The data shows that for $Kn < 0.01$, the measured friction factor is accurately predicted by the incompressible value. As Kn was increased above 0.01, the friction factor was seen to decrease; up to a 50 percent reduction in f was observed as Kn approached 0.15. The experimental friction factor showed agreement within 5 percent with the first order slip velocity model given in Eq. (4) with $F = 1$.

The influence of compressibility was assessed by varying the Mach number in the range $0 < Ma < 0.38$ while keeping Kn and ε/H small. Friction factor data was reported only if $Ma < 1$ at the exit, to ensure the flowrate was controlled only by viscous forces. The data from this investigation shows a mild increase in the friction factor (8 percent) as Ma approaches 0.38. This effect was also verified independently by numerical analysis for the same conditions as the experiment.

The effect of relative surface roughness was investigated for continuum, rarefied, and compressible flow. The range of relative surface roughness tested was $0.001 < \varepsilon/H < 0.06$, yet there was no significant effect on the friction factor for laminar gas flow. This is the expected result for continuum flow since Moody's chart indicates that the laminar friction factor is independent of surface roughness. However, it is a significant finding for microscale flow since surface roughness is often credited for deviation of experimental results from theory. For rarefied gas flow, the friction factor is independent of surface roughness in the range $0.001 < \varepsilon/H < 0.06$. For the range of surface roughnesses tested it is appropriate to assume diffuse reflection ($F = 1$ in Eq. (4)). For ultra smooth channel surfaces, the molecules tend to maintain velocity in the tangential direction upon collision with the microchannel wall, resulting in specular reflection ($F < 1$). The range of relative roughness in this investigation was chosen to be of practical use in MEMS designs in which flow over thin film sensors and other surface structures is expected. The surface roughness also had very minor influence on the friction factor in the compressible flow range. The data shows that as Ma increases, f increases more for the rough channel than for the smooth channel. However, it is believed that Ma has the dominant influence on f while the differences due to surface roughness are likely masked by uncertainty.

Nomenclature

- D_h = Hydraulic diameter = $4 * \text{Area} / \text{Perimeter} = 2 * (W * H) / (W + H)$
- f = Friction factor
- F = Maxwell's reflection coefficient
- G = Mass flux
- H = Microchannel height
- Kn = Knudsen number
- L = Microchannel length
- Ma = Mach number
- P = Pressure
- R = Gas constant
- Re = Reynolds number = $\rho U D_h / \mu$
- T = Temperature
- W = Microchannel width
- x = Axial distance from microchannel entrance
- X^* = Dimensionless distance from entrance = $(x / D_h) / Re$

Greek

- α = Ratio of height to width (H/W)
- ε = Height of surface roughness features = $2 * Ra$
- λ = Mean free path of gas

References

- [1] Tuckerman, D. B., and Pease, R. F. W., 1981, "High-Performance Heat Sinking for VLSI," *IEEE Electron Device Lett.*, **EDL-2**(5), pp. 126–129.
- [2] Peiyi, W., and Little, W. A., 1983, "Measurement of Friction Factors for the Flow of Gases in Very Fine Channels Used for Microminiature Joule-Thomson Refrigerators," *Cryogenics*, **23**(5), pp. 273–277.
- [3] Pfahler, J., Harley, J., Bau, H., and Zemel, J. N., 1991, "Gas and Liquid Flow in Small Channels," *Proceedings of ASME Winter Annual Meeting, Micro Mechanical Sensors, Actuators, and Systems*, DSC-Vol. 32, ASME, New York, pp. 49–60.
- [4] Harley, J. C., Huand, Y., Bau, H., and Zemel, J. N., 1995, "Gas Flow in Micro Channels," *J. Fluid Mech.*, **284**, pp. 257–274.
- [5] Choi, S. B., Barron, R. F., and Warrington, R. O., 1991, "Fluid Flow and Heat Transfer in Micro Tubes," *Micro Mechanical Sensors, Actuators, and Systems*, ASME DSC-Vol. 32, pp. 123–134.
- [6] Peng, X. F., and Peterson, G. P., 1996, "Convective Heat Transfer and Flow Friction for Water Flow in Microchannel Structures," *Int. J. Heat Mass Transfer*, **39**(12), pp. 2599–2608.
- [7] Pong, K., Ho, C., Liu, J., and Tai, Y., 1994, "Non-Linear Pressure Distribution in Uniform Micro Channels," *Proceedings of the ASME Winter Annual Meeting*, ASME, New York, pp. 47–52.
- [8] Shih, J. C., Ho, C. M., Liu, J., and Tai, Y. C., 1996, "Monatomic And Polyatomic Gas Flow Through Uniform Microchannels," *ASME Microelectromechanical Systems (MEMS)*, DSC-Vol. 59, pp. 197–203.
- [9] Pfund, D., Shekarriz, A., Popescu, A., and Welty, J., 1998, "Pressure Drop Measurements in a Microchannel," *ASME, Micro-Electro-Mechanical Systems (MEMS)*, DSC-Vol. 66, pp. 193–198.
- [10] Takuto, A., Soo, K. M., Hiroshi, I., and Kenjiro, S., 2000, "An Experimental Investigation of Gaseous Flow Characteristics in Microchannels," *Proceedings of the International Conference in Heat Transfer and Transport Phenomenon in Microscale*, Bannff, Canada, Oct. 15–20.
- [11] Guo, Z. Y., and Li, Z. X., 2003, "Size Effect on Single-Phase Channel Flow and Heat Transfer at Microscale," *Int. J. Heat Mass Transfer*, **24**, pp. 284–298.
- [12] Arkilic, E. B., Breuer, K. S., and Schmidt, M. A., 2001, "Mass Flow and Tangential Momentum Accomodation in Silicon Micromachined Channels," *J. Fluid Mech.*, **437**, pp. 29–43.
- [13] Maurer, J., Tabeling, P. J., and Willaime, H., 2003, "Second-Order Slip Laws in Microchannels for Helium and Nitrogen," *Phys. Fluids*, **15**(9), pp. 2613–2621.
- [14] Turner, S. E., Sun, H., Faghri, M., and Gregory, O. J., 1999, "Local Pressure Measurement of Gaseous Flow Through Microchannels," *ASME-Publications-HTD*, **364**(3), pp. 71–80.
- [15] Turner, S. E., Sun, H., Faghri, M., and Gregory, O. J., 2000, "Effect of Surface Roughness on Gaseous Flow Through Microchannels," *ASME-Publications-HTD*, **366**(2), pp. 291–298.
- [16] Turner, S. E., Sun, H., Faghri, M., and Gregory, O. J., 2001, "Compressible Gas Flow Through Smooth and Rough Microchannels," *ASME International Mechanical Engineering Congress and Exposition*, HTD-24145, ASME, New York.
- [17] Mirza, A. R., and Ayon, A. A., 1998, "Silicon Wafer Bonding: Key to MEMS High-Volume Manufacturing," *Sensors*, **15**(12), pp. 24–33.
- [18] Sato, K., Shikida, M., Yamashiro, T., Tsunekawa, M., and Ito, S., 1998, "Characterization of Anisotropic Etching Properties of Single Crystal Silicon: Surface Roughening as a Function of Crystallographic Orientation," *Proc. of IEEE MEMS Workshop* (Heidelberg, 25–29 Jan., 1998), IEEE, Piscataway, NJ., pp. 201–206.
- [19] Kang, S. W., Chen, J. S., and Hung, J. Y., 1998, "Surface Roughness of (110) Orientation Silicon Based Micro Heat Exchanger Channel," *Int. J. Mach. Tools Manuf.*, **38**(5–6), pp. 663–668.
- [20] Choquette, S. F., Faghri, M., Kenyon, E. J., and Sunden, B., 1996, "Compressible Fluid Flow in Micron Sized Channels," *HTD-Vol. 327*, National Heat Transfer Conference, ASME, New York, pp. 25–32.
- [21] Shah, R. K., and London, A. L., 1978, "Laminar Flow Forced Convection in Ducts," *Advances in Heat Transfer*, Academic Press, New York, p. 199.
- [22] *CRC Handbook of Chemistry and Physics*, 1997, CRC Press, UK, pp. 6–52.
- [23] Ebert, W. A., and Sparrow, E. M., 1965, "Slip Flow in Rectangular and Annular Ducts," *ASME J. Basic Eng.*, **87**, pp. 1018–1024.
- [24] Asako, Y., Pi, T., Turner, S. E., and Faghri, M., 2003, "Effect of Compressibility on Gaseous Flows in Microchannels," *Int. J. Heat Mass Transfer*, **46**, pp. 3041–3050.
- [25] Abernethy, R. B., Benedict, R. P., and Dowdell, R. B., 1985, "ASME Measurement Uncertainty," *ASME J. Fluids Eng.*, **107**, pp. 161–164.

Numerical Study of Mixed Convection Flow in an Impinging Jet CVD Reactor for Atmospheric Pressure Deposition of Thin Films

S. P. Vanka

Gang Luo

Nick G. Glumac

Department of Mechanical and Industrial
Engineering,
University of Illinois at Urbana-Champaign,
1206 West Green Street, Urbana, IL 61801

A systematic numerical study has been conducted of the mixed convection flow in a novel impinging jet chemical vapor deposition (CVD) reactor for deposition of thin films at atmospheric pressure. The geometry resembles that of a pancake reactor but the inflow gases enter through a small nozzle to provide high inlet momentum. A finite-volume-based computational procedure is used to integrate the governing flow, energy, and scalar transport equations with high accuracy. The effects of the temperature dependent properties are fully accounted for. The effects of operating pressure, wafer rotation rate, and inlet flow rate of the carrier gas are investigated. The main benefit of the new geometry is the suppression of the buoyancy-driven flow even at atmospheric pressures due to the lower mixed convection parameter. We show that the new geometry can produce thin films of high radial uniformity and also with high growth rate. Comparisons are also made with a conventional stagnation flow reactor for which it is shown that beyond a moderate pressure (~ 0.1 atm), the flow is dominated by natural convection, and the reactor is unsuitable for practical use. [DOI: 10.1115/1.1795232]

1 Introduction

A variety of thin films used in micro- and opto-electronic industries are today grown by chemical vapor deposition (CVD). In a chemical vapor deposition reactor, a mixture of a precursor and a carrier gas is supplied to a heated substrate. Bulk and surface reactions take place adjacent to and on the heated substrate, resulting in slow deposition of a thin film. Among the many types of CVD reactors are horizontal reactors [1–3], barrel reactors [4], and stagnation flow reactors [5–7]. The horizontal channel flow reactor has high throughput. However, it is difficult to achieve a highly uniform deposition over the entire susceptor. The vertical stagnation flow reactor is commonly used in microelectronic industry in which a thin film is deposited on a single wafer of large diameter. It has several important advantages. When it is operated at low pressures, it offers excellent uniformity. The stagnation flow generates a highly uniform species concentration distribution at the substrate, leading to uniform deposition rate. It also offers benefits such as a simplified design, safer operation, and easier modeling of the process.

The flow in CVD reactors usually is laminar and of mixed convection type with a forced convection due to the inlet flow and free convection due to the temperature difference between the substrate and inlet gases. The nonlinear interactions between forced and free convection can give rise to many complex flow phenomena that may affect the quality of the thin film [8]. The important design and operating parameters are the shape of the reactor, the operating pressure, the inlet velocity, the rotation rate of the substrate, and the wall boundary conditions. Choice of these operating and design parameters affects the growth rate and the film uniformity [9]. In particular, buoyancy-induced flow generated by the temperature difference can have an adverse effect on thin-film quality. Buoyancy-induced flows can create a recirculating eddy on top of the substrate and transport (as well as trap) reactants away from the substrate. These buoyant flows not only lead to slow rates of growth but can also produce very nonuniform

films that may be of no practical use. In addition, it is often necessary to deposit multiple layers of different materials with as abrupt an interface as possible [10,11]. Recirculating eddies are undesirable for obtaining such interface abruptness. Therefore, it becomes necessary to wait until all previous reactants trapped inside the recirculating eddies are removed out of reactor chamber by diffusion, before starting the supply of new reacting gases.

Our interests focus on the vertical stagnation flow reactor. The reactor consists of a rotating or stationary heated disk inside a cylindrical chamber. A carrier gas (typically Ar, N₂, He, or H₂), which is introduced at the top of the vertical chamber, transports very dilute precursors (often <1%) to the high-temperature substrate. The effluent gas is removed at the bottom of the growth chamber. Usually, the carrier and the precursor gases are forced through a screen or “showerhead” to create a uniform (plug) flow. The susceptor is heated to a temperature of 500–1500 K, whereas the reactor walls are cooled to minimize deposition on them. A scaling analysis of governing equations gives a set of nondimensional parameters Re , Re_w , Ga , Gr , Pr , and height to diameter ratio H/d , where Re is a characteristic Reynolds number, Re_w is the rotation Reynolds number, Ga is the Gay-Lusac number, Gr is the Grashof number, and Pr is Prandtl number. The ratio of natural to forced convection varies as Gr/Re^2 . Because the value of Gr increases with the square of the pressure ratio for a constant Reynolds number, reducing operating pressures will mitigate buoyancy effects. Alternately, for a fixed Grashof number, increasing the inlet velocity can reduce the relative effects of buoyancy.

A viscous pumping effect caused by substrate rotation enhances the stagnation flow. The ratio of rotation Reynolds number to the flow Reynolds number Re_w/Re is a measure of the strength of this centrifugally driven suction effect. An optimum Re_w/Re can improve the uniformity of growth rate across the wafer. The distance between the inlet and the substrate, H , influences the flow structure. When H is much greater than d , the natural convection is governed by the dimension d , with the characteristic Grashof number based on d . However, when $H/d < 1$, the height H is more representative of the characteristic length scale, as it influences the

Contributed by the Heat Transfer Division for publication in the JOURNAL OF HEAT TRANSFER. Manuscript received by the Heat Transfer Division May 21, 2003; revision received January 13, 2004. Associate Editor: A. F. Emery.

structure of the flow. Since the Grashof number varies as the third power of the characteristic length, this dimension is very important to the control of the flow structure.

Because of the nonlinear coupling between the fluid mechanics, heat transport, and species transport, the scaling analysis can only provide a limited qualitative description. To achieve an in-depth understanding of the flows, numerical simulations are the only recourse. Multidimensional numerical solutions of the governing equations began in 1980s with early papers by Houtman, Graves, and Jensen [12] and Coltrin, Kee, and Miller [13]. Evans and Greif [14] investigated the flow and heat transfer in a rotating-disk CVD reactor with insulated sidewalls. The effects of buoyancy, variable properties, and finite geometry were included in their numerical model. Based on the same model and reactor, Evans and Greif [15] studied the effects of inlet velocity and thermal boundary conditions. It is seen that increasing the reactor inlet velocity can reduce the buoyancy effect and result in more uniform heat transfer. Compared to an adiabatic wall, the cooled isothermal wall boundary conditions allow a larger value of the Grashof number to be employed without recirculation. Wang et al. [10] performed growth experiments and finite-element calculations of steady-state momentum, heat, and mass balance to characterize a vertical rotating-disk metal organic CVD (MOCVD) reactor operating at reduced pressure (0.2 atm). Both experimental and numerical results showed that recirculation-free gas flow can be achieved without rotation at an operating pressure less than 0.2 atm. Susceptor rotation was found to be an effective way in establishing a uniform boundary layer and improving thickness uniformity of the film. Based on the same reactor as in Ref. [10], Patnaik, Brown, and Wang [16] investigated the relationship between the thin-film uniformity and control parameters such as carrier gas flow rate, pressure, rotation rate, and substrate temperature for a vertical rotating-disk reactor by detailed numerical calculations of gas flow and species transport. They demonstrated that the secondary flows caused by buoyancy effects, reactor shape, forced convection, and substrate rotation can be eliminated by appropriate choice of operating pressure, gas flow, and substrate rotation rate.

Fotiadis et al. [11] performed numerical and experimental studies of axisymmetric flow patterns in vertical MOCVD reactors and examined their effects on growth rate uniformity. The finite radius of the substrate and presence of the reactor wall was found to cause flow circulations and make it difficult to achieve a uniform deposition rate. The increase of the ratio of substrate to reactor diameter was seen to produce higher nonuniformity. To obtain a more uniform film, the reactor wall and inlet were designed to provide a steady, recirculation free, uniform flow to the deposition surface. In a later paper [9], Fotiadis, Kieda, and Jensen considered the effects of geometry. Their results show that the buoyancy effects can be reduced by inverting the reactor, shortening distance between inlet and susceptor, introducing baffles, and reshaping reactor wall.

Dilawari and Szekely [17] presented numerical results for a modified stagnation point flow reactor. The major difference between their modified reactor and classical vertical stagnation reactor is that the reactor is inverted and the distance between the inlet showerhead and wafer was reduced to low values. They found that the inverted reactor is helpful in minimizing thermal natural convection and the inlet-wafer distance is critical in obtaining good spatial uniformity of deposition rate in their design. The inlet to wafer distance of 10 mm was seen to provide good spatial uniformity for a diameter of the reactor tube of 200 mm. They argue that the small inlet-to-wafer distance reduces the ability of the carrier gases to entrain fluid from the surroundings thus preventing the formation of the secondary flows.

Cho, Choi, and Kim [18] studied the optimization of inlet concentration profile of the reactant gas on the uniformity of the growth rate. Their results showed that the film uniformity could be significantly improved by enforcing an optimum inlet concentra-

tion distribution. However, they noted that controlling the inlet concentration is not easy. To make the optimization procedure more practical, Cho, Choi, and Kim [7] also devised a procedure to find the optimum inlet velocity profile. These calculations showed that a properly arranged inlet velocity profile can suppress buoyancy-driven recirculation, thus improving the growth rate uniformity.

Axisymmetric designs are used in most vertical CVD reactors to ensure that the flow is also axisymmetric. However, at certain pressures, nonaxisymmetric mixed convection flows, transient flows, or even turbulence may be caused by large buoyancy effects [19,20]. These phenomena destroy the uniform deposition in the circumferential direction; thus they are unwanted. Symmetry breaking in a stagnation flow CVD reactor has been studied by van Santen, Kleijn, and van den Akker [21]. Their work shows that this unwanted phenomenon in practice can be avoided by selecting appropriate operating parameters. A sufficiently high inlet flow and rotation of the wafer guarantees a perfectly axisymmetric flow, and a decrease in distance between wafer and inlet can also suppress asymmetric flows. van Santen, Kleijn, and van den Akker also investigated the effect of turbulence in a vertical reactor using large eddy simulations (LES). It was found that buoyancy-induced turbulence can be important in cold-wall reactors operating at or near atmospheric pressure, when the forced inlet flow and rotation of the wafer are not strong enough. Although instantaneous uniformity of heat flux is poor due to the chaotic nature of buoyancy-induced turbulence, when averaged over time the heat flux on the wafer may be high and uniform. However, the authors mention that it is not clear whether turbulence can be beneficially exploited in CVD of thin films.

In a more recent study, van Santen, Kleijn, and van den Akker [22,23] also investigated the mixed convection between two circular disks with an impinging jet at the center. They showed that with no inflow, the free convection flow becomes three dimensional at low Grashoff numbers. However, a sufficiently large forced inflow through the central jet was observed to sweep away the natural convection cells and produce stable, axisymmetric flow.

Flow visualizations of the reactor flows have also been performed. Gadgil [24] used smoke flow experiments to optimize the design parameters of a stagnation point flow reactor. Among various reactor geometries he examined, the modified reactor with diffuser shape inlet section was found to result in a recirculation-free flow without substrate rotation or application of vacuum. It was found that modification of chamber geometry is the best way to achieve a vortex-free flow at high temperatures and pressures. Mathews and Peterson [25] used similar visualization techniques to investigate buoyancy-induced flows in a stagnation flow reactor under the transient conditions of rapid thermal chemical vapor deposition (RTCVD) for pressures up to 0.2 atm. They observed buoyancy-induced flows for all conditions, though the degree to which these flows affected the uniformity of the flow in the vicinity of the growth surface varied significantly with substrate temperature.

In order to guarantee high uniformity of the deposit, most CVD reactors operate at low pressures in the range of a few hundredths of an atmosphere. At these low pressures, the buoyant forces are relatively small, and the precursor and carrier gases directly reach the substrate without complex flow recirculation, producing a film of high radial uniformity. However, operation under vacuum conditions requires expensive facilities and careful process control. The reactor chambers cannot be very large, and the vessel walls must be of a material of sufficient thickness to withstand the pressure differentials. Operation of CVD reactors at atmospheric pressure is much easier and can be scaled easily to larger dimensions without the penalty of expensive vacuum equipment. In addition, atmospheric growth conditions may be required by reaction schemes, materials, or other practical constraints.

We have recently undertaken an extensive numerical study to

quantify the mixed-convection flow field in a novel impinging jet CVD reactor. This geometry holds potential to be operated at atmospheric pressure and to produce a film of nearly uniform thickness. The reactor is also a stagnation flow reactor with the substrate mounted on a pedestal with provision for rotation. The inlet gases enter the reactor from a narrow inlet at the top and counteract the buoyancy-induced flow generated by the substrate. The momentum of the inlet jet is made strong enough to sweep away the buoyancy-driven vortex, thereby producing a uniform concentration boundary layer. The distance between the substrate and the top wall is decreased such that the buoyant vortices are weakened. A number of systematic numerical simulations have been conducted to quantify the effects of inlet flow rate, substrate rotation rate, and the chamber pressure on the flow and temperature fields, the rates of growth of the film, and its uniformity. The present article discusses in detail the results of these numerical studies. We believe that after further optimization and experimental validation, the impinging jet geometry can be a viable candidate for uniform and high growth rate deposition of thin films at atmospheric pressure. Also, as an initial step, the current study has considered wafer sizes of only 5 cm in diameter. However, industrial sizes being larger, further scale-up is now being considered in a separate study.

2 Governing Equations and Numerical Procedure

2.1 Governing Equations. The velocities encountered in a typical CVD reactor are small. Hence the flow can be treated essentially as incompressible. However, the density variations in the fluid are significant to the extent that the Boussinesq approximation cannot be considered to be accurate. Hence, the local density variations must be accounted for in the convective terms, in addition to the gravitational term. We consider here the nondimensional equations obtained by using the scales d (diameter of the reactor), V (inlet velocity), $\rho_{\text{ref}}V^2$, $\Delta T_c (T_{\text{wafer}} - T_{\text{inlet}})$, Y_{inlet} , and d/V for length, velocity, pressure, temperature, concentration, and time, respectively. The governing equations for mass, momentum, energy, and species concentration can be stated as [21]

$$\frac{\partial \rho}{\partial t} + \nabla \cdot (\rho \mathbf{u}) = 0, \quad (1)$$

$$\begin{aligned} \frac{\partial \rho \mathbf{u}}{\partial t} + \nabla \cdot (\rho \mathbf{u} \mathbf{u}) = -\nabla p + \frac{1}{\text{Re}} \nabla \cdot \{ \mu [\nabla \mathbf{u} + (\nabla \mathbf{u})^T - \frac{2}{3} (\nabla \mathbf{u}) \cdot \mathbf{I}] \} \\ + \frac{\text{Gr}}{\text{Re}^2} \left[\frac{\Theta - \frac{1}{2}}{(\Theta - \frac{1}{2})\text{Ga} + 1} \right] \mathbf{e}_x, \end{aligned} \quad (2)$$

$$C_p \frac{\partial \rho \Theta}{\partial t} + C_p \nabla \cdot (\rho \mathbf{u} \Theta) = \frac{1}{\text{Re Pr}} \nabla \cdot (k \nabla \Theta), \quad (3)$$

$$\frac{\partial \rho Y}{\partial t} + \nabla \cdot (\rho \mathbf{u} Y) = \frac{1}{\text{Re Sc}} \nabla \cdot (\rho D_{AB} \nabla Y), \quad (4)$$

where \mathbf{u} is the velocity vector, \mathbf{I} is the unit tensor, \mathbf{e}_x is the unit vector with a component only in the x direction (the x positive direction points upwards), p is pressure, Θ is the temperature, Y is the mass fraction of precursor gas, and t is the time. The superscript T on $\nabla \mathbf{u}$ refers to the transpose of the tensor. All variables are nondimensional. The material properties, density ρ , dynamic viscosity μ , thermal conductivity k , heat capacity C_p , and the mass diffusivity D_{AB} are made dimensionless with their value at the reference temperature $T_{\text{ref}} = (T_{\text{wafer}} + T_{\text{inlet}})/2$. The Dufour and Soret diffusions are assumed to be small for the particular gases considered here and hence neglected. The Reynolds (Re), Prandtl (Pr), Schmidt (Sc), Grashof (Gr), and Gay-Lusac (Ga) numbers appearing in the above equations are defined as

$$\text{Re} = \rho_{\text{ref}} V d / \mu_{\text{ref}},$$

$$\text{Pr} = \mu_{\text{ref}} C_p / k_{\text{ref}},$$

$$\text{Sc} = \mu_{\text{ref}} / (\rho_{\text{ref}} D_{\text{ref}}), \quad (5)$$

$$\text{Gr} = g \rho_{\text{ref}}^2 d^3 (T_{\text{wafer}} - T_{\text{inlet}}) / (\mu_{\text{ref}}^2 T_{\text{ref}}),$$

$$\text{Ga} = (T_{\text{wafer}} - T_{\text{inlet}}) / T_{\text{ref}},$$

where g is the acceleration due to gravity, and T_{wafer} and T_{inlet} represent dimensional temperatures at the wafer and at the inlet. Reference values denoted by the subscript ref are taken at reference temperature. Expansion effects caused by density changes with heating of the gas phase are modeled by the ideal gas law. This gives the following dimensionless relation:

$$\rho = [(\Theta - \frac{1}{2})\text{Ga} + 1]^{-1}. \quad (6)$$

The current study assumed axisymmetric flow because of the computational simplicity provided, and the large number of parametric computations that were planned. However, natural convection flows do become three dimensional in some parameter ranges. To validate the axisymmetric assumptions full three-dimensional calculations are needed. The spatial terms in the governing equations are discretized using a second-order finite-volume method on a nonstaggered cylindrical polar grid. The time integration is performed using a predictor-corrector method similar to that used by Najm, Wyckoff, and Knio [26] and Boersma [27].

2.2 Boundary Conditions. At the top surface the velocities and concentration values corresponding to the inflow gases are prescribed as Dirichlet conditions. At the wafer, the temperature is fixed at 900 K, and the nondimensional concentration is prescribed to be zero. The normal and radial velocities are also prescribed to be zero at the wafer surface with the tangential velocity prescribed by the rotation rate. At the outlet of the reactor, zero-derivative conditions are prescribed on all variables. The temperature at the outer wall is an important aspect for the operation of the reactor. It is necessary to select this in such a way that there is no deposit on the outer wall, but at the same time the buoyancy forces due to the cold outer walls are mitigated. In this study we considered two different boundary conditions to understand the effect of outer wall thermal boundary condition on the flow inside the reactor. The first condition considered was an adiabatic outer wall. The second condition was an isothermal wall, implying some form of external cooling to maintain the walls at the temperature of the inlet gases. This second condition was used in most of the calculations reported in this paper. On the pedestal side wall, a linear temperature difference from the wafer surface temperature to the ambient of 300 K was prescribed. We believe this condition will not affect the deposition patterns on the wafer; hence other conditions appropriate to an industrial setting may also be considered.

2.3 Properties and Deposition Parameters. The present simulations have been performed with argon and acetone as the carrier and precursor gases, respectively. The dynamic viscosity, specific heat, and conductivity of the carrier gas are obtained from database of National Institute of Standards and Technology (NIST) [28]. Binary diffusion coefficients are calculated from the Chapman-Enskog theory. For details, see Ref. [29]. For the present study, the rate of deposition is assumed to be limited by the rate of mass transfer, implying fast chemical kinetics. Thus the growth rate is taken to be proportional to the gradient of the concentration normal to the wafer surface (growth rate $\propto \text{Sh} = -\partial Y / \partial x|_{\text{wafer}}$, where Sh is the Sherwood number). Here the growth rate is derived in a nondimensional sense, as the inlet concentration is fixed at a non-dimensional value of unity. The growth rate is given by the product of the local density, diffusion coefficient and the concentration gradient. In our study, the variations of density and diffusion coefficients are small because of the dilute concentrations of the precursor and uniform wafer tempera-

ture. When the deposition rate is limited by the kinetics of the reaction, it is necessary to include the specific kinetic mechanisms before actual film deposition rates are estimated. By appropriately specifying a value to the inlet concentration, a dimensional value can be then obtained. Hence the units for current growth rates are arbitrary. Two different nonuniformities and usage are defined as the following. The simple nonuniformity is

$$\text{Nonuniformity (1)} = \frac{|\text{Sh}_{\text{wafer center}} - \text{Sh}_{\text{wafer edge}}|}{\text{Sh}_{\text{wafer center}}} \quad (7)$$

The root mean square (rms) nonuniformity is

$$\text{Nonuniformity (2)} = \left\{ \int_{A_{\text{wafer}}} (\text{Sh} - \bar{\text{Sh}})^2 dA / \bar{\text{Sh}}^2 A_{\text{wafer}} \right\}^{1/2}, \quad (8)$$

where $\bar{\text{Sh}} = \int_{A_{\text{wafer}}} \text{Sh} dA / A_{\text{wafer}}$ is the average growth rate and A_{wafer} is the area of the wafer. The usage is

$$\text{Usage} = \frac{\int_{A_{\text{wafer}}} \rho D_{AB} (\partial Y / \partial x)_{\text{wafer}} dA}{\int_{A_{\text{inlet}}} \rho V Y_{\text{inlet}} dA} \quad (9)$$

3 Results

As indicated above, increasing the reactor pressure increases the Grashof number and therefore the mixed-convection parameter Gr/Re^2 . The key to a successful atmospheric pressure CVD reactor is the control of this mixed-convection parameter. To lower its value, two strategies can be employed. The height of the chamber can be made significantly smaller than the chamber diameter as the Grashof number will then be based on the reactor height and will decrease as the third power of the height. This strategy is followed in pancake reactors. However, in common pancake reactors, the carrier gases enter uniformly from the top surface. This may not completely suppress the natural convection. Alternately, or in addition to the reduction in height, the inflow gases can be admitted with a high momentum through a narrow central pipe, thus providing a high inlet Reynolds number. This strategy was used by Snyder, Sides, and Ko [30] in their version of the impinging jet reactor. However, for the parameters chosen in the geometry of Snyder, Sides, and Ko [30], the film thickness varied significantly with position on the wafer. In the geometry of

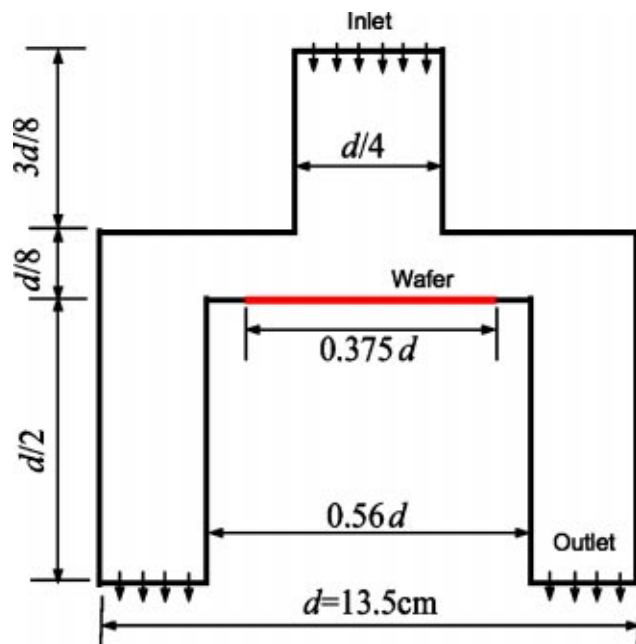


Fig. 1 Schematic of a modified impinging jet CVD reactor

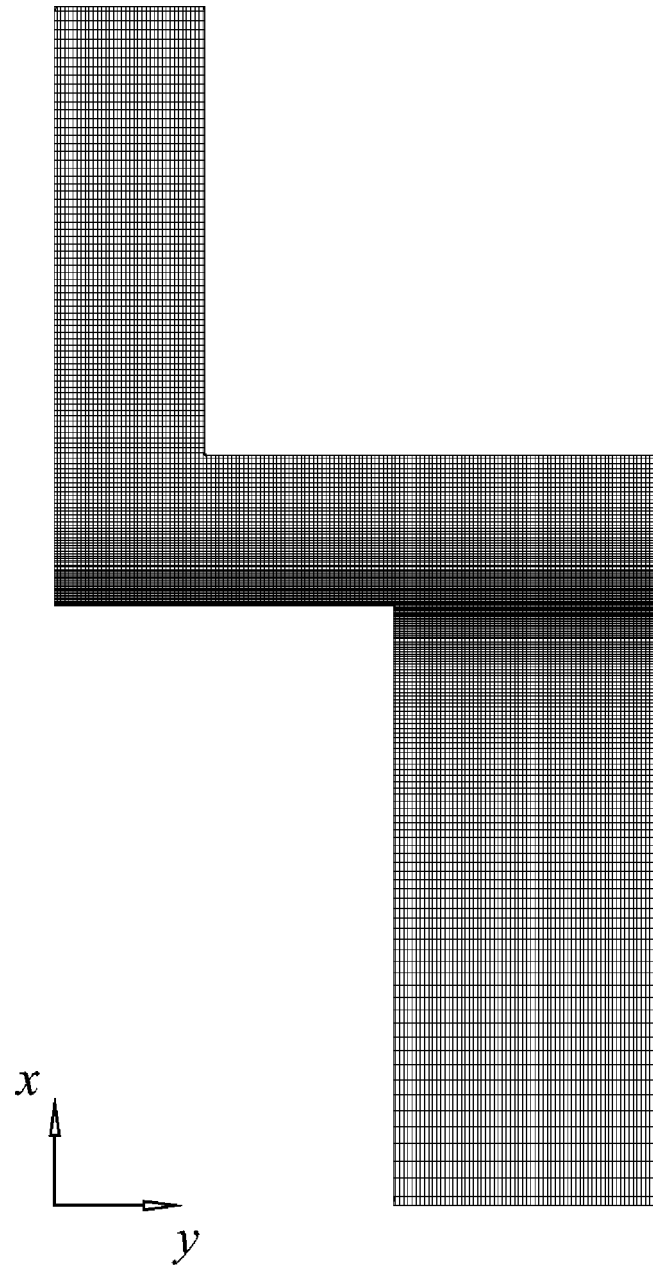


Fig. 2 Finite volume grid used for the calculations

Snyder, Sides, and Ko, the height of the top wall was of the same order as the chamber diameter. Hence the natural convection was still significantly large.

Figure 1 shows the new geometry of the impinging jet reactor considered in this study, which combines the height reduction with the increased inlet momentum. This reactor has a low height with inflow from the top through a central nozzle. For the current configuration, the carrier gases enter from a nozzle of diameter $d/4$ (d is the chamber diameter). The height of the top surface is $d/8$ from the substrate. The substrate is mounted on a pedestal and rotated if necessary. The gases leave the reactor through an annulus between the substrate and the outer wall. The reduced height provides a reduction in Grashof number by a factor of 512 from a value based on the chamber diameter. The decrease in the diameter of inlet stream provides a fourfold increase in the characteristic Reynolds number. Together, the mixed convection parameter

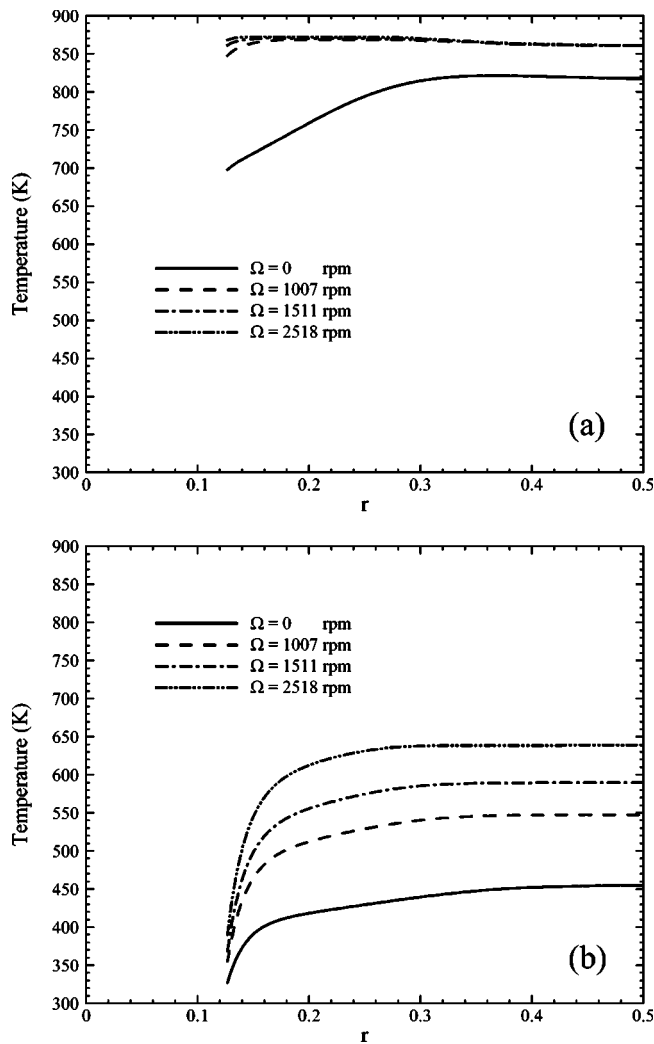


Fig. 3 Temperature distribution on the top wall as a function of radial position for different substrate rotation rates for pressure=0.5 atm, and adiabatic sidewall: (a) inlet flow rate=1 SLM and (b) inlet flow rate=10 SLM

is reduced by a factor of 8192 from a value appropriate to a traditional stagnation flow reactor with uniform inflow and large height (typically of the order of d).

We have performed a number of calculations in this impinging jet geometry by systematically varying the pressure, inlet flow rate, and substrate rotation. Three different values of pressure are explored increasing all the way up to 1 atm. A finite volume grid, which is shown in Fig. 2, containing 18,142 cells was used to discretize the governing equations. The grid spacing was uniform in the y direction, but a nonuniform spacing, symmetrically expanding from the substrate towards the inlet and outlet boundary, was employed in the x direction. A finer grid calculation with four times this number of control volumes was also performed for the

most sensitive parameter set, and it was observed that the results differed by less than 0.5%. Hence all calculations were made with the 18,142 cell grid. The flow is assumed to be axisymmetric and two dimensional. The time step was chosen as a value that guaranteed the maximum Courant number at all control volumes to be less than 0.8. The steady-state solution was considered to be reached when the sum of the temporal derivatives of density of all control volumes over the entire domain became less than 10^{-7} .

3.1 Effect of the Outer Wall Thermal Boundary Condition

Figure 3a shows the temperature distribution along the top wall with inlet flow rate of 1 SLM for four calculations at a pressure of 0.5 atm and three rotation rates in the case of an adiabatic boundary. The resulting temperature differences are observed to be small between the outer wall and the substrate but are large between the inlet gases and the substrate. The temperature reaches a high value, around 850 K, at $\Omega=2518$ rpm. Such high temperatures can cause deposition on the hot top wall, reducing the overall usage of the precursor gases. When the flow rate is increased to 10 SLM, the temperature of the top wall drops to 640 K (Fig. 3b), but it is still large for the deposition reaction to occur at the surface. Hence, the adiabatic wall boundary condition is not an appropriate condition for the current design of the impinging jet reactor. For all the calculations presented below, the reactor walls have been considered to be isothermal at 300 K. This temperature can be easily maintained by water cooling.

3.2 Results for the 1 SLM Flow Rate.

Table 1 shows the parameters for the set of calculations performed in the present geometry. The pressure was varied from 0.5 to 1.0 atm in order to test the performance of this geometry at near atmospheric pressures. Table 1 also provides values of the corresponding Grashof, Reynolds, and mixed-convection parameters. For the imposed temperature of 900 K for the substrate and a chamber pressure of 0.5 atm, the Grashof number based on the diameter of the outer housing is about 2.6×10^6 . However, for an upper wall height of $d/8$, the Grashof number based on this dimension is only about 5096. The inlet Reynolds number ($V_{\text{inlet}}d/\nu$) is 13.08 for 1 SLM flow rate, giving a value of about 30 for the mixed convection parameter. Since this is much greater than 1, it is to be expected that the natural convection effects will be significant at this flow rate.

Figures 4 and 5 show the velocity vectors, temperature, and scalar distributions and streamlines for four calculations at 0.5 atm and 1 SLM flow rate. At zero rotation (Fig. 4) there is a large recirculation eddy on the top of the substrate. This eddy lifts off the flow from the substrate and lowers the transport of the precursors to the substrate. The result is a nonuniform rate of deposition, as shown in Fig. 6. For the case of zero rotation, the deposition is low in the center and high at the outer edge. Figure 5 shows the effects of substrate rotation on the velocity fields, temperature, and concentration distributions. The viscous pumping induced by the substrate rotation increases the velocity in the center and the local concentration gradient. Thus, rotation in fact increased the rate of deposition in the center and the nonuniformity of the substrate deposition. From these results, it is clear that a flow rate of 1 SLM is inadequate to neutralize the buoyancy effects at 0.5 atm pressure, even in this modified impinging jet reactor geometry. As

Table 1 Details of calculation parameters

Pressure (atm)	Grashof number based on $d/8$	Volumetric flow rate (SLM)	Inlet Reynolds number based on $d/4$	V_{inlet} (cm/s)	Gr/Re^2
0.5	5,096.07	1	13.08	3.7	29.787
0.5	5,096.07	10	130.8	37.2	0.298
0.75	11,466.21	10	130.8	24.8	0.670
1.0	20,384.77	10	130.8	18.6	1.191

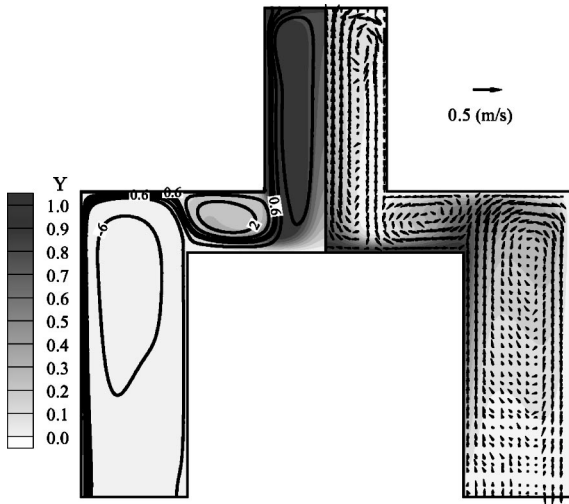


Fig. 4 Streamlines, concentration (left) and temperature (right) contours, and vector plot for pressure=0.5 atm, inlet flow rate=1 SLM, $\Omega=0$ rpm, and isothermal sidewall

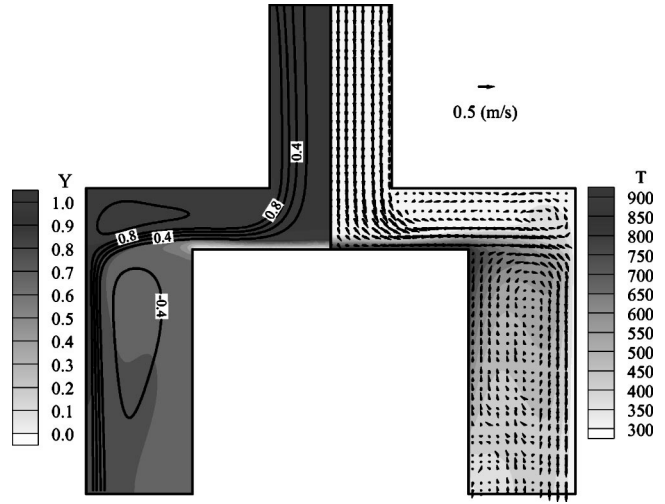


Fig. 7 Streamlines, concentration (left) and temperature (right) contours, and velocity vectors for pressure=0.5 atm, inlet flow rate=10 SLM, $\Omega=0$ rpm, and isothermal sidewall

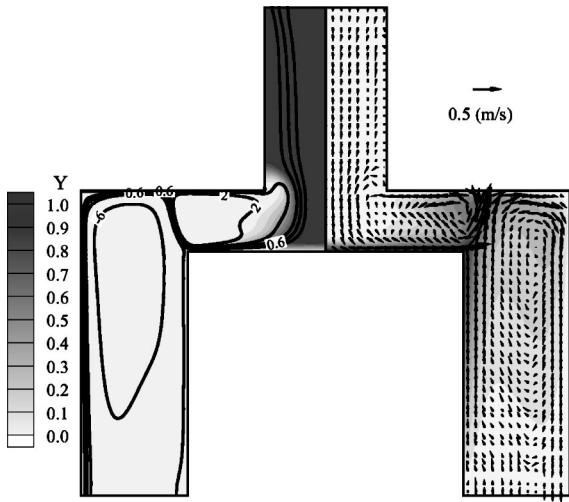


Fig. 5 Streamlines, concentration (left) and temperature (right) contours, and vector plot for pressure=0.5 atm, inlet flow rate=1 SLM, $\Omega=1007$ rpm, and isothermal sidewall

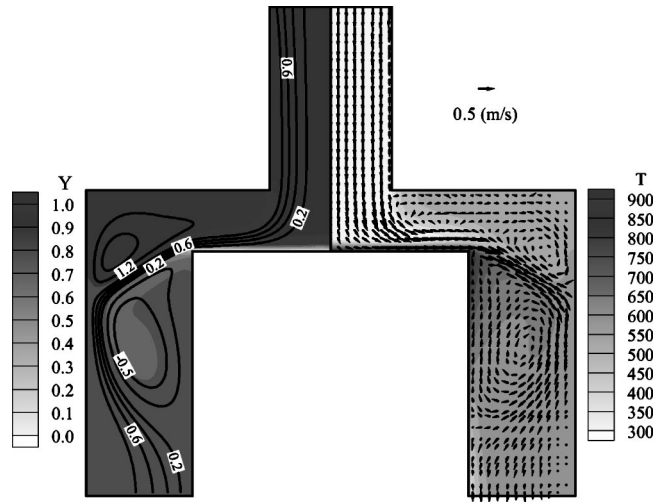


Fig. 8 Streamlines, concentration (left) and temperature (right) contours, and velocity vectors for pressure=0.5 atm, inlet flow rate=10 SLM, $\Omega=1007$ rpm, and isothermal sidewall

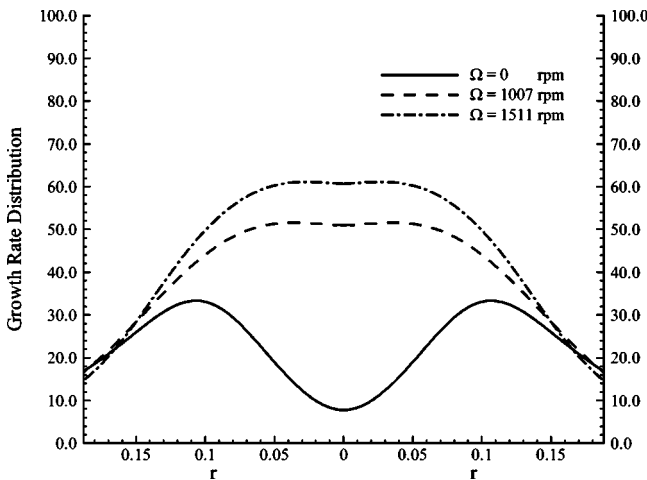


Fig. 6 Growth rates along the wafer for different substrate rotation rates for pressure=0.5 atm, inlet flow rate=1 SLM, and isothermal sidewall

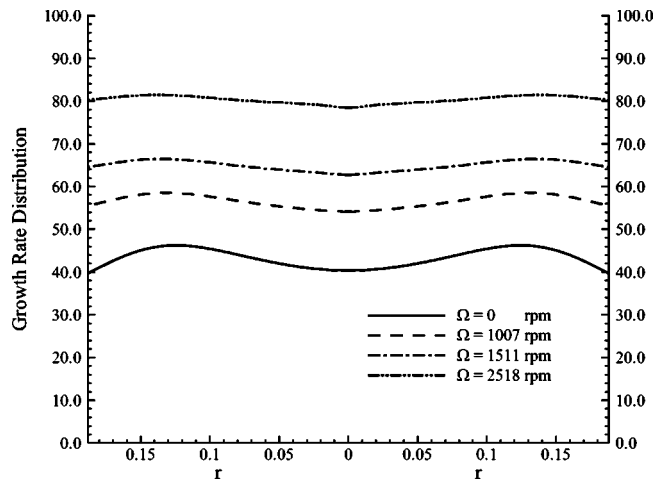


Fig. 9 Growth rates along the wafer for different substrate rotation rates for pressure=0.5 atm, inlet flow rate=10 SLM, and isothermal sidewall

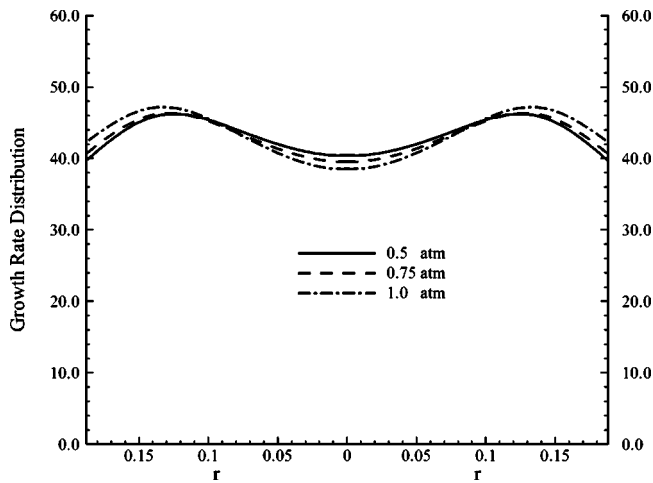


Fig. 10 Growth rates along the wafer for different pressures for inlet flow rate=10 SLM and isothermal sidewall

the natural convection will become stronger at higher pressures, we did not make calculations at pressures higher than 0.5 atm with 1 SLM flow rate.

3.3 Results for the 10 SLM Flow Rate. An increase in the flow rate increases the inlet velocity and the inlet Reynolds number. Although it is not clear what the appropriate length scale is for the definition of the Reynolds number in the vicinity of the substrate, we have used the inlet diameter ($d/4$) as the appropriate length scale. For an SLM flow rate of 10, the Reynolds number is 130.8. At a pressure of 0.5 atm, the corresponding mixed convection parameter (Gr/Re^2) now reduces by a factor of 100 to about 0.3, a value less than unity. Thus a forced convection dominated flow is produced. For the flow rate of 10 SLM, we have computed the flow fields and concentration distributions for pressures of 0.5, 0.75, and 1.0 atm. At 1 atm pressure, the mixed convection parameter is small, around 1.2. Therefore, at a flow rate of 10 SLM, there is a potential for uniform deposition rates.

Figures 7 and 8 show the flow, temperature, and concentration fields for 0.5 atm pressure at two rotation rates. The corresponding growth rates are shown in Fig. 9. With a 10 SLM flow rate, the recirculation eddy on the top of the substrate is eliminated by the strong inflow stream. The flow field is much different than that at

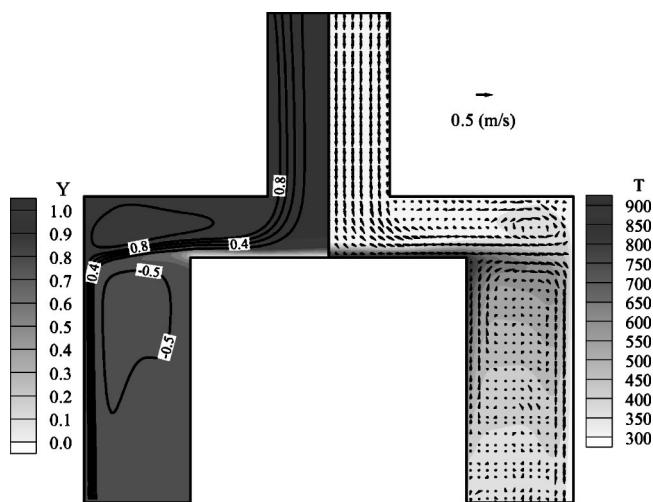


Fig. 11 Streamlines, concentration (left) and temperature (right) contours, and velocity vectors for pressure=1.0 atm, inlet flow rate=10 SLM, $\Omega=0$ rpm, and isothermal sidewall

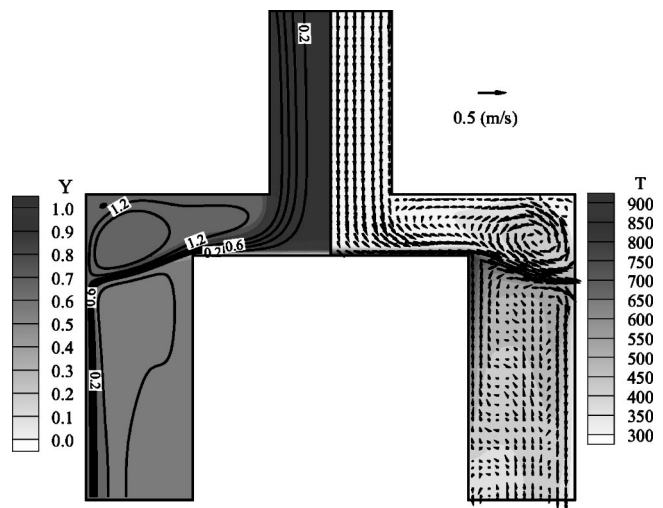


Fig. 12 Streamlines, concentration (left) and temperature (right) contours, and velocity vectors for pressure=1.0 atm, inlet flow rate=10 SLM, $\Omega=1007$ rpm, and isothermal sidewall

1 SLM. The inflow gases move directly down in the inlet section, then move horizontally along the substrate, and form a uniform boundary layer above the substrate. A recirculation eddy forms near the top corner because of the impingement on the wall jet on the side wall. However, it is located outer to the deposition surface, and its effects are confined to the corner. Figure 9 clearly indicates that the uniformity of the film can be quite good if the rate of deposition is solely limited by the mass transfer to the substrate. It can be seen that the uniformity of deposition has significantly improved when the flow rate is increased from 1 to 10 SLM. Lower flow rates such as 5 or 7.5 SLM may also be adequate to give good deposition uniformity with a higher usage of the precursor gases.

The effect of the chamber pressure is to increase the natural convection, and thereby modify the flow pattern. This in turn can change the deposition uniformity by altering the concentration boundary layer. Figure 10 shows the growth rates for the three pressures. It is seen that when the forced convection is dominant, pressure does not influence much the rate of growth as well as the uniformity of the deposit. The deposit is nonuniform with a smaller thickness in the center. Figure 11 shows the flow fields at

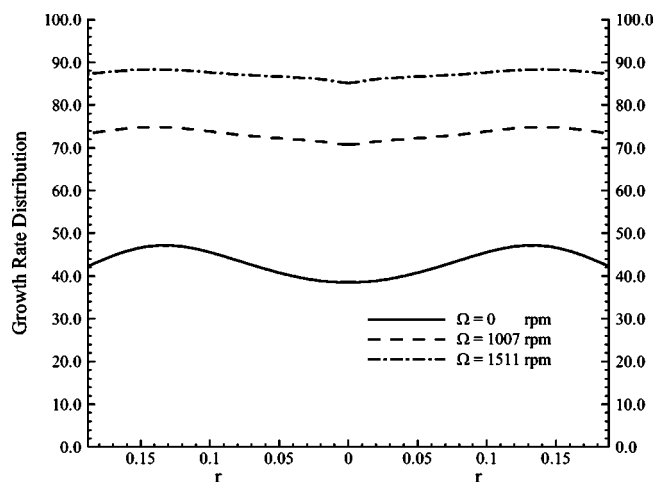


Fig. 13 Growth rates along the wafer for different substrate rotation rates for pressure=1.0 atm, inlet flow rate=10 SLM, and isothermal sidewall

Table 2 Growth rates and nonuniformity for the impinging jet CVD reactor

Pressure (atm)	Inlet flow rate (SLM)	Rotation speed (rpm)	Rotation Reynolds number	Growth rate			Uniformity (%)		Usage (%)
				Average	Center	Edge	a	b	
0.5	1	0	0	25.26	7.79	16.79	115.58	24.23	53.36
		1007	20,000	34.24	51.04	16.57	67.54	33.85	72.56
		1511	30,000	36.89	60.73	14.62	75.94	41.84	78.06
		2518	50,000	c	c	c	c	c	c
0.5	10	0	0	43.82	40.41	39.66	1.84	4.59	9.65
		1007	20,000	57.13	54.13	55.46	2.45	2.00	12.43
		1511	30,000	65.44	62.76	64.52	2.79	1.32	14.19
		2518	50,000	80.73	78.41	80.25	2.34	0.76	17.45
0.75	10	0	0	44.00	39.56	40.64	2.73	4.42	9.69
		1007	30,000	65.65	62.65	64.86	3.54	1.43	14.24
		1511	45,000	77.21	74.67	76.70	2.72	0.90	16.70
		2518	75,000	97.03	94.80	96.83	2.14	0.48	20.93
1.0	10	0	0	44.73	38.53	42.27	9.72	4.91	9.85
		1007	40,000	73.87	70.80	73.31	3.54	1.21	15.99
		1511	60,000	87.67	85.20	87.31	2.48	0.67	18.93
		2518	100,000	c	c	c	c	c	c

^aSimple nonuniformity.
^brms nonuniformity.
^cFlow is unsteady.

1.0 atm at zero substrate rotation and 10 SLM flow rate. The flow fields at 1 atm are similar to those at 0.5 and 0.75 atm, reflecting the point that the growth rate is not significantly affected by pressure when the substrate is not rotated.

The lower deposition rate in the central region can be increased by increasing the concentration gradient in that region. This can be accomplished by rotating the substrate. Rotation induces additional suction forces in the central region, accelerating the flow. The effect of rotation on the flow field at 1 atm is shown in Fig. 12 for 1007 rpm. This corresponds to a rotation Reynolds number of 40,000. Figure 12 shows that the central jet has now become stronger with rotation, as expected, but the corner vortex has also increased in size and strength. This is to be expected because of the stronger radial wall jet impacting the side casing. However, the uniformity of the growth rate has not been impacted at the edges by this vortex. As expected, the increased velocities in the central region have increased the concentration gradients in that

region and have made the film more uniform than that at no rotation. It is seen that at 1 atm pressure, the deviation from uniformity is about 2.5%, a considerably low value. Figure 13 shows the growth rates for 0, 1007, and 1511 rpm rotation rates. In addition, the growth rates have increased in value because of the thinning of the concentration boundary layers due to rotation. We observe that the growth rate is nearly doubled by rotating the substrate at 1511 rpm. We believe that such rotation rates are feasible in practice. Hence the computed uniformity and high growth rates can be achieved in industrial reactors.

For any given pressure, the growth rate increases monotonically with the rotation of the substrate. At a pressure of 0.75 atm, the averaged growth rate increased from 44.0 to 97.03 with the rotation increasing from 0 to 2518 rpm. At 1517 rpm and 1.0 atm, the percentage uniformity is 2.48. Also, as the substrate is rotated, increase in pressure at the same rotation rate increases the growth rate because of the large centrifugal force (due to density increase) at higher pressure. Thus, rotation is relatively more advantageous at higher pressures. Table 2 gives the growth rates and nonuniformities for the various cases studied. In most cases the trends are monotonic, i.e., rotation brings more uniformity. However, in some cases, rotation can overshoot the profiles from being uniform and can increase nonuniformity. This is seen, for example, at 0.75 atm for 10 SLM and 1007 rpm.

3.4 Comparisons With the Conventional Stagnation Flow Reactor. Figure 14 shows the conventional stagnation flow reactor. In this configuration, the mixture of gases enters the reactor uniformly over the entire cross section instead as a narrow jet through the central region. The height of the reactor is usually

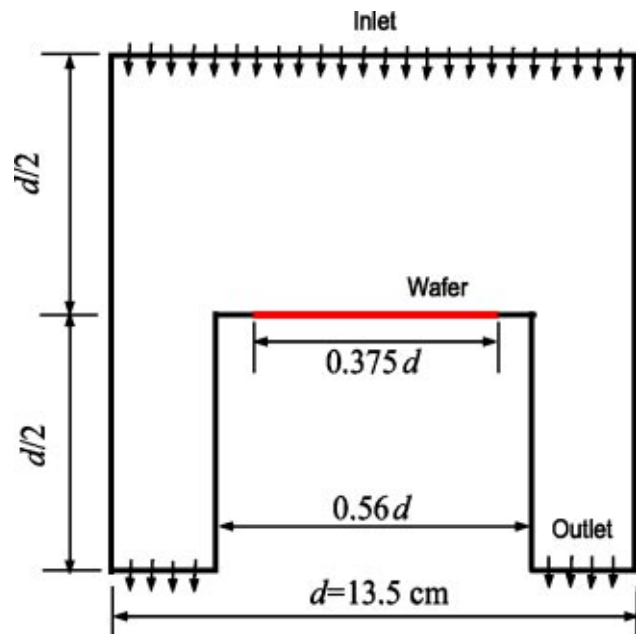


Fig. 14 Schematic of a prototypical stagnation flow CVD reactor

Table 3 Details of calculation parameters for the conventional stagnation flow reactor

Pressure (atm)	Grashof number based on $d/2$	Volumetric flow rate (SLM)	Inlet Reynolds number based on d	V_{inlet} (cm/s)	Gr/Re^2
0.01	130.375	1	3.27	11.6	12.20
		10	32.7	116.0	0.1220
0.1	13,037.5	1	3.27	1.16	1220.05
		10	32.7	11.6	12.20
0.5	325,937.5	1	3.27	0.23	30,501.4
		10	32.7	2.3	305.014

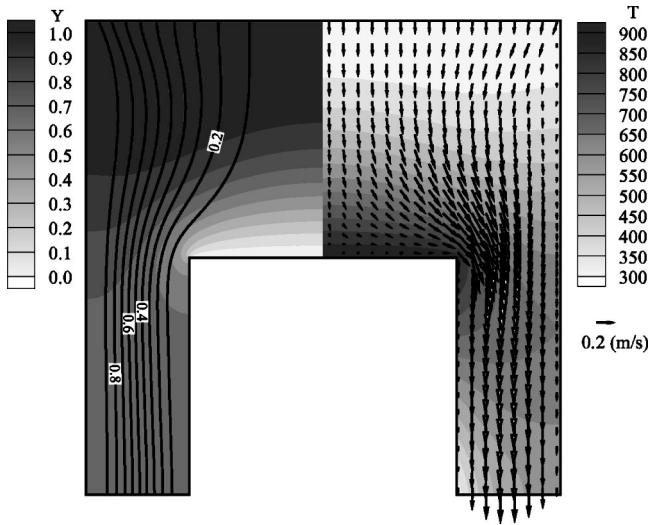


Fig. 15 Streamlines, concentration (left) and temperature (right) contours, and velocity vectors for pressure=0.01 atm, inlet flow rate=1 SLM, and $\Omega=0$ rpm

much larger ($d/2$) than the impinging jet reactor shown previously ($d/8$). This geometry has been built in our laboratory and has been used to grow thin films at low pressures. Because of the large buoyancy forces, such reactors usually operate at very low pressures, of the order of a few hundredths of an atmosphere. To illustrate the relative advantages of the impinging jet reactor over the conventional stagnation flow reactor, we performed another set of systematic calculations for pressures of 0.01, 0.1, and 0.5 atm and various rates of rotation and flow rates of 1.0 and 10.0 SLM. In addition, two sets of inlet conditions for the precursor gas were also considered. The carrier gases entered the reactor through the full reactor opening, but the precursor gases came in either at the full opening or through a partial opening of diameter $d/2$. The results from these calculations are fully documented by Luo [29]. Here only a few calculations are presented to compare with the results of the impinging jet reactor.

Table 3 shows the Grashof and Reynolds numbers and the mixed-convection parameters for the various cases. It can be seen that the mixed-convection parameter is small at 0.01 atm, but increases significantly when the pressure is increased to 0.5 atm.

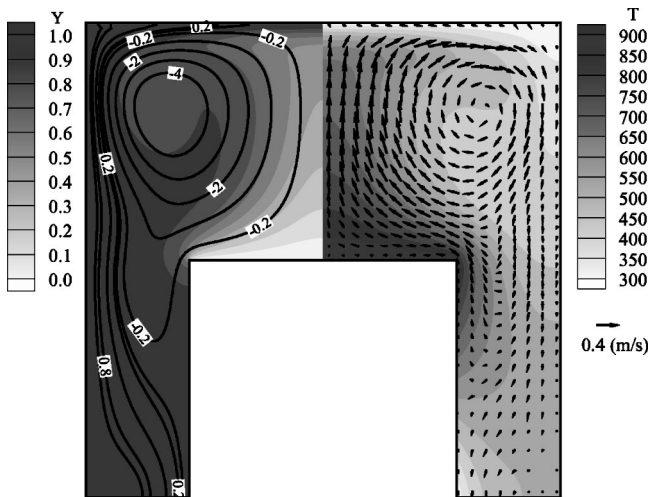


Fig. 16 Streamlines, concentration (left) and temperature (right) contours, and velocity vectors for pressure=0.1 atm, inlet flow rate=1 SLM, and $\Omega=0$ rpm

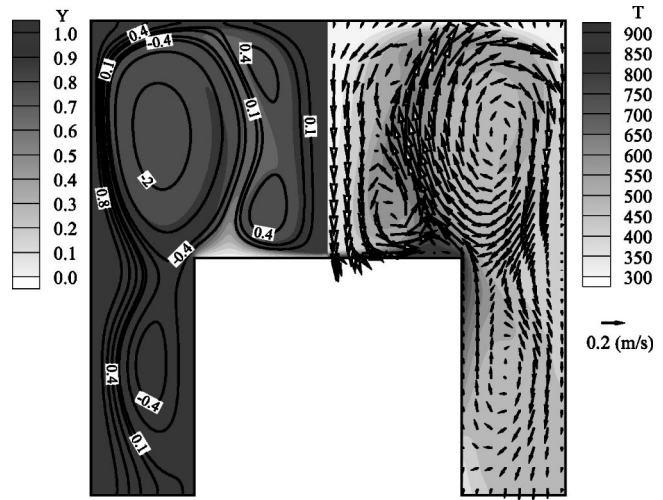


Fig. 17 Streamlines, concentration (left) and temperature (right) contours, and velocity vectors for pressure=0.5 atm, inlet flow rate=10 SLM, and $\Omega=0$ rpm

Figure 15 illustrates the flow field, temperature, and concentration distributions for a pressure of 0.01 atm and a flow rate of 1 SLM. The substrate is not rotated. It can be seen that the flow is primarily unidirectional, leading to a uniform deposit. However, as the pressure is increased to 0.1 atm, we see a vortex forming on the top of the substrate (Fig. 16). This vortex is clockwise and the inlet gases flow through the periphery instead of the central region. When the pressure was further increased to 0.5 atm, the flow became unsteady and was not considered suitable for practical use.

Increasing the inlet flow rate to 10 SLM reduces the mixed convection parameter hundredfold, but it is still not enough to bring it below unity. Here the value is of the order of 300 for pressure of 0.5 atm, and 12.2 for a pressure of 0.1 atm. However, for 0.1 atm pressure, and no substrate rotation, no steady solution was found at 1 SLM flow rate. Figure 17 shows the flow field for 0.5 atm pressure, 10 SLM flow rate, and zero rotation rate. For this case the flow is highly complex (but steady) with multiple recirculation eddies on top of the substrate. The effect of these eddies is a very nonuniform film growth, as seen in Fig. 18. For a flow rate of 10 SLM and 0.5 atm, the deposition rate has a peak of about 80 units in the center and about 12 in the outer region.

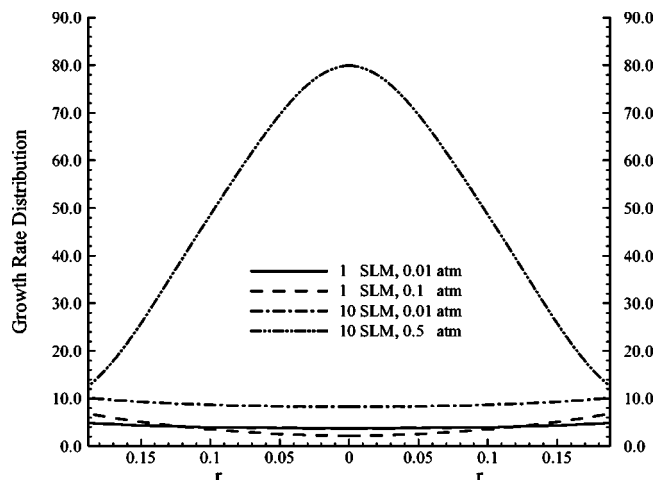


Fig. 18 Growth rates along the wafer for different cases

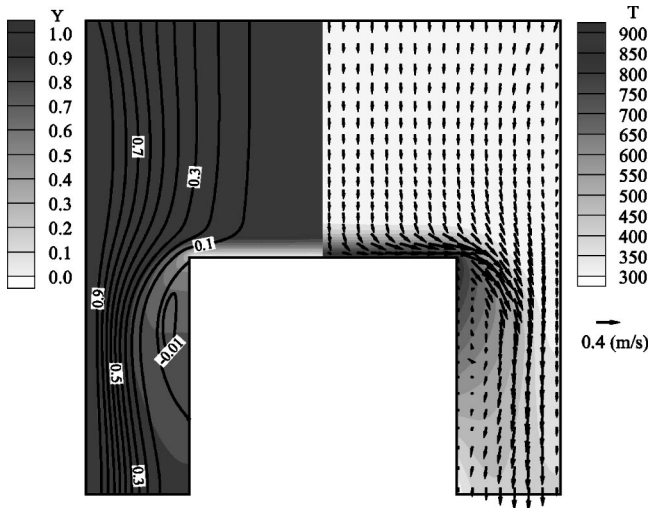


Fig. 19 Streamlines, concentration (left) and temperature (right) contours, and velocity vectors for pressure=0.1 atm, inlet flow rate=10 SLM, and $\Omega=1007$ rpm

Figure 18 also shows the growth profile for 1 SLM and 0.1 atm. It is less nonuniform, but the average growth rate is small.

The effects of a representative rotation speed on the flow and temperature fields and the film nonuniformity at 0.1 atm and 10 SLM flow rate are shown in Fig. 19. Three rotation rates of 1007, 1511, and 2518 rpm, as considered previously, were computed. The rotation of the substrate has now made the flow steady with a strong down flow at the center. The suction force provided by the substrate rotation now pulls the reactants towards the substrate, creating a nearly uniform concentration layer near the substrate (Fig. 20). This manifests in a film of uniform thickness, considering that the reaction is mass transfer limited. Substrate rotation also increases the rate of deposition because of the thinner concentration boundary layer, from a value around 22 (nondimensional units) at 1007 rpm to 34 at 2518 rpm. No steady solutions were found for the pressure of 0.5 atm, 10 SLM, and nonzero rotation. Thus, the conventional stagnation flow reactor geometry considered here cannot be beneficially used at pressures substantially higher than 0.1 atm. In comparison, we see that the impinging jet reactor with a modified geometry can be operated fruitfully at pressures all the way to one atmosphere.

Tables 4 and 5 list the growth rates and nonuniformity factors at 0.01 and 0.1 atm pressures. Significant variations in growth rate and nonuniformity can be produced when the parameters are varied. The least nonuniformity at 0.01 atm is about 0.2%, whereas at 0.1 atm, a nonuniformity of 1.4% can be obtained. Rotation of the substrate in principle improves uniformity, but in some cases, the

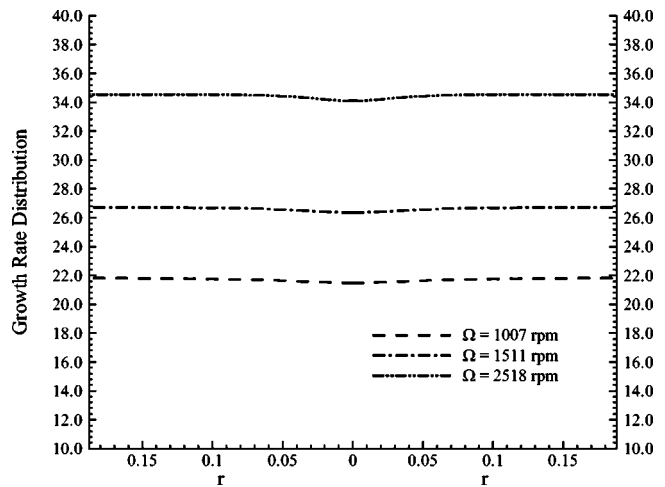


Fig. 20 Growth rates along the wafer for various substrate rotation rates for pressure=0.1 atm and inlet flow rate=10 SLM

uniformity can be degraded if used in excess as the growth rate in the central region can become larger. Data for 0.5 atm are not given, as only a few solutions were steady.

4 Conclusions

A systematic computational study has been conducted to study the mixed convection phenomena and deposition patterns in an impinging jet stagnation flow CVD reactor. The reactor geometry is such that the momentum of the inflow gases counteracts the buoyancy-induced vortices and sweeps them out of the reactor without the detrimental effects on film uniformity. Calculations have been performed for a wide range of parameters including pressure, substrate rotation, flow rates, and precursor supply area. It is seen that the impinging jet reactor can be operated at atmospheric pressure at a moderate inflow rate without the adverse effects of the buoyancy-induced flow. By tailoring the flow rates and the rotation speed as well as the inlet area for the precursor gases, we have been able to reduce the nonuniformity to about 3% at an operating pressure of 1 atm. Simultaneously, the growth rate has also been increased significantly from the value at 0.01 atm. The impinging jet geometry can therefore be used for the deposition of many thin solid films without the penalty of a vacuum system and associated equipment costs. A systematic study in conventional stagnation flow geometry was also conducted to compare the performance of the two systems. It is seen that the conventional reactor has significant natural convection at modest pressures and such buoyancy flows cannot be easily controlled by increasing the flow rate and rotation of the substrate. These results need to be verified in the future through physical experiments.

Table 4 Growth rates and nonuniformity at 0.01 atm pressure for the conventional reactor

Inlet flow rate (SLM)	Rotation speed (rpm)	Rotation Reynolds number	Growth rate			Uniformity (%)		Usage (%)
			Average	Center	Edge	a	b	
1	0	0	4.23	3.76	4.82	28.10	7.39	10.66
	1007	400	5.93	5.99	5.98	0.22	0.48	14.39
	1511	600	7.50	7.84	7.21	8.11	2.58	17.68
	2518	1000	10.16	10.56	9.65	8.56	2.72	22.96
10	0	0	9.10	8.28	10.05	21.46	5.82	2.16
	1007	400	9.62	8.93	10.45	16.98	4.69	2.27
	1511	600	10.20	9.63	10.90	13.21	3.70	2.39
	2518	1000	11.67	11.30	12.12	7.25	2.06	2.70

^aSimple nonuniformity.

^brms nonuniformity.

Table 5 Growth rates and nonuniformity at 0.1 atm pressure for the conventional reactor

Inlet flow rate (SLM)	Rotation speed (rpm)	Rotation Reynolds number	Growth rate			Uniformity (%)		Usage (%)
			Average	Center	Edge	a	b	
1	0	0	4.46	2.21	6.60	199.00	28.76	8.56
	1007	4000	19.67	23.32	17.19	26.27	8.94	35.85
	1511	6000	22.15	25.72	19.54	24.03	8.10	38.38
	2518	10,000	26.69	28.75	24.40	15.14	5.15	39.65
10	0	0	c	c	c	c	c	c
	1007	4000	21.75	21.50	21.80	1.39	0.29	4.76
	1511	6000	26.68	26.36	26.72	1.33	0.24	5.77
	2518	10,000	34.52	34.11	34.56	1.32	0.20	7.39

^aSimple nonuniformity.

^brms nonuniformity.

^cFlow is unsteady.

Acknowledgment

This work was partly supported by the National Science Foundation under Grant No. DMI-0099748.

Nomenclature

A	= Area
C_p	= Dimensionless specific heat of the carrier gas
D_{AB}	= Dimensionless mass diffusivity
d	= Diameter of the reactor
e_x	= Unit vector with component in the x direction
g	= Gravitational acceleration
Ga	= Gay-Lusac number
Gr	= Grashof number
\mathbf{I}	= Unit tensor
k	= Thermal conductivity
Sh	= Sherwood number
SLM	= standard liters per minute
p	= Pressure
Pr	= Prandtl number
r	= Radial coordinate
Re	= Reynolds number
Re_w	= Rotation Reynolds number ($Re_w = \rho_{ref} \Omega d^2 / \mu_{ref}$)
Sc	= Schmidt number
T	= Temperature
T_{inlet}	= Temperature at inlet (300 K)
T_{wafer}	= Temperature at wafer (900 K)
t	= Nondimensional time
\mathbf{u}	= Velocity vector
V	= Inlet velocity
x	= Nondimensional vertical coordinate
Y	= Nondimensional concentration of precursor gas

Greek Symbols

μ	= Dynamic viscosity
Θ	= Non dimensional temperature
ρ	= Density
Ω	= Rotation speed

Subscripts

inlet	= At inlet
ref	= At reference temperature
wafer	= At wafer

References

- [1] Salinger, A. G., Shadid, J. N., Hutchinson, S. A., Hennigan, G. L., Devine, K. D., and Moffat, H. K., 1999, "Analysis of Gallium Arsenide Deposition in a Horizontal Chemical Vapor Deposition Reactor Using Massively Parallel Computations," *J. Cryst. Growth*, **203**, pp. 516–533.
- [2] Ern, A., Giovangigli, V., and Smooke, M. D., 1997, "Detailed Modeling of Three-Dimensional Chemical Vapor Deposition," *J. Cryst. Growth*, **180**, pp. 670–679.
- [3] Cho, W. K., and Choi, D. H., 2000, "Optimization of a Horizontal MOCVD

- Reactor for Uniform Epitaxial Layer Growth," *Int. J. Heat Mass Transfer*, **43**, pp. 1851–1858.
- [4] De Paola, E., and Duverneuil, P., 1998, "Simulation of Silicon Deposition From SiHCl_3 in a CVD Barrel Reactor at Atmospheric Pressure," *Comput. Chem. Eng.*, **22**, (Suppl)(May), pp. S683–S686.
- [5] Theodoropoulos, C., Mountziaris, T. J., Moffat, H. K., and Han, J., 2000, "Design of Gas Inlets for the Growth of Gallium Nitride by Metalorganic Vapor Phase Epitaxy," *J. Cryst. Growth*, **217**, pp. 65–81.
- [6] Pawlowski, R. P., Theodoropoulos, C., Salinger, A. G., Mountziaris, T. J., Moffat, H. K., Shadid, J. N., and Thrush, E. J., 2000, "Fundamental Models of the Metalorganic Vapor-Phase Epitaxy of Gallium Nitride and Their use in Reactor Design," *J. Cryst. Growth*, **221**, pp. 622–628.
- [7] Cho, W. K., Choi, D. H., and Kim, M.-U., 1999, "Optimization of the Inlet Velocity Profile for Uniform Epitaxial Growth in a Vertical Metalorganic Chemical Vapor Deposition Reactor," *Int. J. Heat Mass Transfer*, **42**, pp. 4143–4152.
- [8] Jensen, K. F., Einset, E. O., and Fotiadis, D. I., 1991, "Flow Phenomena in Chemical Vapor Deposition of Thin Films," *Annu. Rev. Fluid Mech.*, **23**, pp. 197–232.
- [9] Fotiadis, D. I., Kieda, S., and Jensen, K. F., 1990, "Transport Phenomena in Vertical Reactors for Metalorganic Vapor Phase Epitaxy," *J. Cryst. Growth*, **102**, pp. 441–470.
- [10] Wang, C. A., Patnaik, S., Caunt, J. W., and Brown, R. A., 1988, "Growth Characteristics of a Vertical Rotating-Disk OMVPE Reactor," *J. Cryst. Growth*, **93**, pp. 228–234.
- [11] Fotiadis, D. I., Kremer, A. M., McKenna, D. R., and Jensen, K. F., 1987, "Complex Flow Phenomena in Vertical MOVCD Reactors: Effects on Deposition Uniformity and Interface Abruptness," *J. Cryst. Growth*, **85**, pp. 154–164.
- [12] Houtman, C., Graves, D. B., and Jensen, K. F., 1987, "CVD in Stagnation Point Flow," *J. Electrochem. Soc.*, **133**, pp. 963–975.
- [13] Coltrin, M. E., Kee, R. J., and Miller, J. A., 1987, "A Mathematical Model of Silicon Chemical Vapor Deposition," *J. Electrochem. Soc.*, **133**, p. 1206.
- [14] Evans, G. H., and Greif, R., 1987, "A Numerical Model of the Flow and Heat Transfer in a Rotating Disk Chemical Vapor Deposition Reactor," *Trans. ASME, Ser. C: J. Heat Transfer*, **109**, pp. 928–935.
- [15] Evans, G. H., and Greif, R., 1987, "Effects of Boundary Conditions on the Flow and Heat Transfer in a Rotating Disk Chemical Vapor Deposition Reactor," *Numer. Heat Transfer*, **12**, pp. 243–252.
- [16] Patnaik, S., Brown, R. A., and Wang, C. A., 1989, "Hydrodynamic Dispersion in Rotating-Disk OMVPE Reactors: Numerical Simulation and Experimental Measurements," *J. Cryst. Growth*, **96**, pp. 153–174.
- [17] Dilawari, A. H., and Szekely, J., 1991, "A Mathematical Representation of a Modified Stagnation Flow Reactor for MOCVD Applications," *J. Cryst. Growth*, **108**, pp. 491–498.
- [18] Cho, W. K., Choi, D. H., and Kim, M.-U., 1999, "Optimization of the Inlet Concentration Profile for Uniform Deposition in a Cylindrical Chemical Vapor Deposition Chamber," *Int. J. Heat Mass Transfer*, **42**, pp. 1141–1146.
- [19] van Santen, H., Kleijn, C. R., and van den Akker, H. E. A., 2001, "On Multiple Stability of Mixed-Convection Flows in a Chemical Vapor Deposition Reactor," *Int. J. Heat Mass Transfer*, **44**, pp. 659–672.
- [20] van Santen, H., Kleijn, C. R., and van den Akker, H. E. A., 2000, "On Turbulent Flows in Cold-Wall CVD Reactors," *J. Cryst. Growth*, **212**, pp. 299–310.
- [21] van Santen, H., Kleijn, C. R., and van den Akker, H. E. A., 2000, "Symmetry Breaking in a Stagnation-Flow CVD Reactor," *J. Cryst. Growth*, **212**, pp. 311–323.
- [22] van Santen, H., Kleijn, C. R., and van den Akker, H. E. A., 2000, "Mixed Convection in Radial Flow Between Horizontal Plates—I. Numerical Simulations," *Int. J. Heat Mass Transfer*, **43**, pp. 1523–1535.
- [23] van Santen, H., Kleijn, C. R., and van den Akker, H. E. A., 2000, "Mixed Convection in Radial Flow Between Horizontal Plates—II. Experiments," *Int. J. Heat Mass Transfer*, **43**, pp. 1537–1546.
- [24] Gadgil, P. N., 1993, "Optimization of a Stagnation Point Flow Reactor Design

- for Metalorganic Chemical Vapor Deposition by Flow Visualization,” *J. Cryst. Growth*, **134**, pp. 302–312.
- [25] Mathews, A. G., and Peterson, J. E., 2000, “Flow Visualizations and Transient Temperature Measurements in an Axisymmetric Impinging Jet Rapid Thermal Chemical Vapor Deposition Reactor,” *Trans. ASME, Ser. C: J. Heat Transfer*, **124**, pp. 564–570.
- [26] Najm, H. N., Wyckoff, P. S., and Knio, O. M., 1998, “A Semi-Implicit Numerical Scheme for Reacting Flow. I. Stiff Chemistry,” *J. Comput. Phys.*, **143**, pp. 381–402.
- [27] Boersma, B. J., 1998, “Direct Simulation of a Jet Diffusion Flame,” *Annual Research Briefs, Center for Turbulence Research, Stanford, CA*, pp. 47–56.
- [28] Database of the Thermophysical Properties of Gases Used in the Semiconductor Industry, retrieved June 7th, 2002 from <http://properties.nist.gov/SemiProp/Gases/Index.html>.
- [29] Luo, G., 2003, “Study of Buoyancy-Induced Flows in a Prototypical CVD Reactor,” Ph.D. thesis, University of Illinois, Urbana-Champaign, IL.
- [30] Snyder, D. W., Sides, P. J., and Ko, E. I., 1992, “On the Rate and Uniformity of CdTe Deposition in an Impinging Jet Reactor: Numerical Simulations,” *J. Cryst. Growth*, **121**, pp. 631–642.

Shuangbiao Liu
e-mail: liusb@northwestern.edu
Department of Mechanical Engineering,
Northwestern University,
Evanston, IL 60208

Sylvie Lannou
Département de Mécanique,
Ecole Polytechnique,
F-91128 Palaiseau, France

Qian Wang

Leon Keer

Department of Mechanical Engineering,
Northwestern University,
Evanston, IL 60208

Solutions for Temperature Rise in Stationary/Moving Bodies Caused by Surface Heating With Surface Convection

Determining the temperature rise of contact interfaces subject to surface heating is essential to controlling thermally induced failures in manufacturing processes and tribology. This paper provides a summary of solutions to problems of a stationary/moving half-space or half-plane without/with surface convection. In the first two sections, basic formulations for bodies with negligible surface convection are grouped as explicitly and completely as possible in terms of the Green's function, the influence coefficients, and the frequency response function. In the final section, the influence coefficients are applied to solve surface-heating problems with surface convection. The time required to reach approximately steady state is found for bodies subject to a unit heat flux. The effect of convection is found to be dependent on the Péclet number and location. [DOI: 10.1115/1.1795234]

Introduction

Surface heating is a common phenomenon in manufacturing processes [1] and tribology [2]. For example, the frictional loss between two meshing gear teeth is converted into surface heat flux. More importantly, surface heating is one of the culprits of gear scuffing [3]. Modeling the temperature rise due to surface heating, especially the surface temperature rise known as the flash temperature [4], is essential to the failure study of cutting tools and contact components. Temperature effects on metallurgical microstructure, thermal shrinkage, thermal cracking, residual stresses, and chemical modifications of materials are collectively studied as surface integrity problems, which are significant to the performance and reliability analyses of mechanical components. The modeling of temperature rise could date back to the beginning of last century [5].

Surface-heating problems of a stationary or moving half-space and half-plane are complicated due to time dependency, component motion, heat source distribution [6,7], and boundary conditions. This paper summarizes known results, while exploring a more complete set of solutions to surface-heating problems without surface convection that are presented by Carslaw and Jaeger [5]. These results can be applied to develop solutions to problems with surface convection. In the first two sections, basic formulations are grouped into three categories, with an adiabatic boundary in the nonheating surface: Green's functions (Beck et al. [8] discussed the Green's functions in great depth), influence coefficients, and frequency response functions in order to facilitate analytical and numerical modeling. These formulations are applied to solve surface-heating problems with a surface convection boundary in the final section. Three cases are discussed according to the time variation of the heat source: a) an instantaneous case (TI) with a varying heat source, where "T" indicates the transient characteristics; b) a continuous case (TC) with a constant heat source; and c) a steady state case (SS), which is a special TC case with infinite time. Table 1 summarizes the available fundamental formulas in a closed form, i.e., the formulas are free of integrals but may contain special mathematical functions such as the error function, the complementary error function, the exponential inte-

gral, and the Bessel functions. Two new items presented in this paper are identified by "#" in Table 1. Note that in all cases, the Péclet numbers are not a function of spatial coordinates. In addition, the motion is time independent in the TC and SS cases, while it could be a function of time in the TI cases.

The time required to reach approximately steady state is derived for bodies subject to a unit heat flux. For a half-plane, a reference point [9] is required for TC and SS cases. It is found that a half-plane requires less time than a half-space to achieve steady state, where a reference point is located one unit away from the origin. If the surface heat-transfer coefficient is not negligible, results in Section 3 show that under a small Péclet number (less than three), all temperature values are reduced; while under larger Péclet numbers, the temperature values are significantly reduced at locations on the leading side of the surface-heating region.

1 Surface Heating of a Half-Space

An irregularly distributed heat source \bar{q} per unit time per unit area is applied on the surface of a half-space [Fig. 1(a)] with uniform initial temperature. A nondimensional coordinate system, $x_j = \bar{x}_j/l$, where l is a characteristic length, is fixed to the heat source. All barred variables are dimensional. The half-space is stationary or moving relative to the heat source (and the coordinate system) with speeds, \bar{V}_1 and \bar{V}_2 ($\bar{V}_3 = 0$), which can vary with time, but not with position. One could combine two speeds into a single speed and adjust the x_1 coordinate to be in the speed direction. Material properties of the half-space are diffusivity κ and thermal conductivity K . The nondimensional heat source ($q = \bar{q}/q_0$) will cause a nondimensional temperature rise, $T = \bar{T}K/(lq_0)$, governed by the heat-conduction equation,

$$T_{,ii} = \frac{\partial T}{\partial t} + \text{Pe}_1 T_{,1} + \text{Pe}_2 T_{,2} \quad (1.1)$$

where t is nondimensional time, $t = \kappa \bar{t}/l^2$; Pe_j is the Péclet number in the x_j direction, $\text{Pe}_j = \bar{V}_j l/\kappa$. In the surface-heated region S , a boundary condition is specified as

$$-T_{,3} = q \quad (1.2)$$

Outside S , an adiabatic boundary condition is applied. Alternatively, a convection boundary condition could be applied (see Sec. 3).

Contributed by the Heat Transfer Division for publication in the JOURNAL OF HEAT TRANSFER. Manuscript received by the Heat Transfer Division August 7, 2003; revision received June 11, 2004. Associate Editor: G. S. Dulikravich.

Table 1 Equation number of fundamental solutions in a closed form

Body	Case	Green's Functions		Influence Coefficients		Frequency Response
		Stationary	Moving	Stationary	Moving	Functions
Half-space	TI	1.4	1.5		1.17	1.24a
	TC	1.10	1.7 [#]		NA	1.24b
	SS		1.12	1.21a [#]	Large Pe [11]	1.24c
Half-plane	TI		2.3		2.9	2.21a
	TC	2.4	NA	2.11a in the surface	NA	2.21b
	SS	2.6	2.5	2.20	2.13 in the surface	2.21c

1.1. Green's Functions

1.1.1 Instantaneous Case. One can find the following solution with the Green's function [5] for the *stationary* half-space:

$$T(x_1, x_2, x_3, t) = \int_0^t \int_{-\infty}^{+\infty} \int_{-\infty}^{+\infty} G^{TI}(x_1 - x'_1, x_2 - x'_2, x_3, t - t') q(x'_1, x'_2, t') dx'_1 dx'_2 dt' \quad (1.3)$$

$$G^{TI}(x_1, x_2, x_3, t) = \frac{\exp[-R^2/(4t)]}{4(\pi t)^{3/2}} \quad (1.4)$$

where $R^2 = x_1^2 + x_2^2 + x_3^2$. Note that in the denominator, four is used rather than eight ([5], p. 256) because half-space, not infinite space, problems are studied. The Green's function in Eq. (1.4) can be extended to the *moving* half-space with time-dependent Péclet numbers,

$$G^{TI}(x_1, x_2, x_3, \Delta t) = \frac{\exp[-R'^2/(4\Delta t)]}{4(\pi\Delta t)^{3/2}} \quad (1.5)$$

where $\Delta t = t - t'$ and $R'^2 = (x_1 - \int_{t'}^t Pe_1 d\tau)^2 + (x_2 - \int_{t'}^t Pe_2 d\tau)^2 + x_3^2$. The general expression of the temperature rise consists of four integrals: one in R' and the remaining three in Eq. (1.3), which are costly for numerical computation and require analytical simplification if possible.

1.1.2 Continuous Case. When the heat source is constantly applied from time 0 to t and the half-space has only a time-invariant Péclet number in the x_1 direction ($Pe_2 = 0$), then the temperature rise at time t is

$$T(x_1, x_2, x_3, t) = \int_{-\infty}^{+\infty} \int_{-\infty}^{+\infty} G^{TC}(x_1 - x'_1, x_2 - x'_2, x_3, t) q(x'_1, x'_2) dx'_1 dx'_2 \quad (1.6)$$

$$\begin{aligned} G^{TC}(x_1, x_2, x_3, t) &= \int_0^t G^{TI}(x_1, x_2, x_3, t - t') dt' \\ &= \frac{1}{4\pi R} \exp\left[\frac{-Pe_1(R - x_1)}{2}\right] \left[2 - \operatorname{erfc}\left(\frac{Pe_1\sqrt{t}}{2} - \frac{R}{2\sqrt{t}}\right) \right. \\ &\quad \left. + \exp(RPe_1) \operatorname{erfc}\left(\frac{Pe_1\sqrt{t}}{2} + \frac{R}{2\sqrt{t}}\right) \right] \end{aligned} \quad (1.7)$$

where the integration with respect to time has been carried out. The above Green's function is probably novel since reported results are not explicitly integrated. For example, Hou and Komanduri [7] recently presented the following integral, rewritten in current nondimensional form with the speed pointing in the positive x_1 direction, as

$$\begin{aligned} G^{TC}(x_1, x_2, x_3, t) &= \frac{Pe_1}{8\pi^{3/2}} \exp\left(\frac{Pe_1 x_1}{2}\right) \int_0^{Pe_1^2 t/4} \\ &\quad \times \left(-\xi - \frac{R^2 Pe_1^2}{16\xi}\right) \frac{d\xi}{\xi^{3/2}} \end{aligned} \quad (1.8)$$

Equation (1.7) can be obtained from Eq. (1.8) by using the following integral

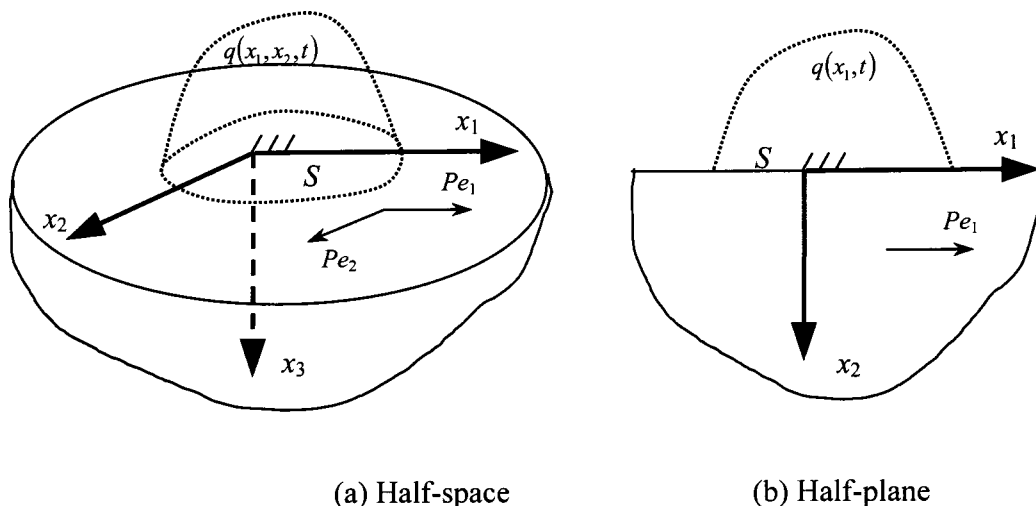


Fig. 1 Bodies subject to the surface heat source

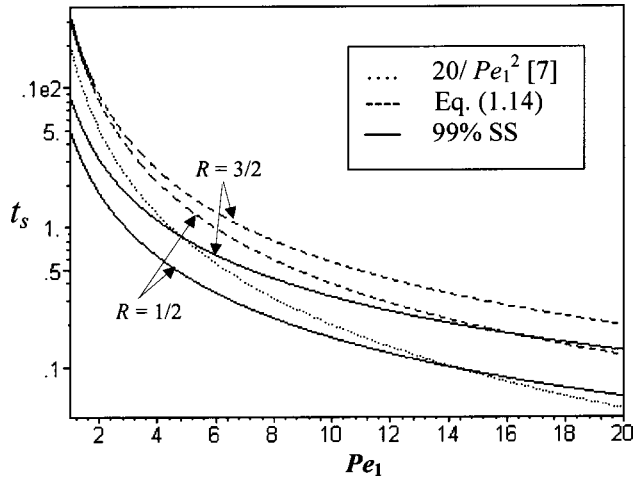


Fig. 2 Effect of the Péclet number on the time required to reach approximately steady state

$$\int \exp\left(-C^2\xi - \frac{D^2}{\xi}\right) \frac{d\xi}{\xi^{3/2}}$$

$$= -\sqrt{\pi}[\exp(-2CD)\operatorname{erfc}(C\sqrt{\xi} - D/\sqrt{\xi}) - \exp(2CD)\operatorname{erfc}(D/\sqrt{\xi} + C\sqrt{\xi})]/(2D) \quad (1.9)$$

where C and D are independent of ξ .

For the *stationary* half-space, Eq. (1.7) becomes the known solution (p. 261 [5]),

$$G^{TC}(x_1, x_2, x_3, t) = \frac{1}{2\pi R} \operatorname{erfc}\left(\frac{R}{2\sqrt{t}}\right), \quad \text{Pe}_1 = 0 \quad (1.10)$$

1.1.3 Steady-State Case. The SS solution for the half-space can be found simply by letting time approach infinity in Eq. (1.7) (alternatively, see p. 267 [5])

$$T(x_1, x_2, x_3) = \int_{-\infty}^{+\infty} \int_{-\infty}^{+\infty} G^{SS}(x_1 - x'_1, x_2 - x'_2, x_3) \times q(x'_1, x'_2) dx'_1 dx'_2 \quad (1.11)$$

$$G^{SS}(x_1, x_2, x_3) = \frac{1}{2\pi R} \exp\left[\frac{-\text{Pe}_1(R - x_1)}{2}\right] \quad (1.12)$$

It is interesting to determine time t_s when the steady state is approximately reached. Hou and Komanduri argued that the contribution to the integration beyond five is negligible in Eq. (1.8), so that the upper limit of the integration could be set approximately as five. Therefore, it was concluded in their work that the steady state could have been established at approximately $t_s = 20/\text{Pe}_1^2$, which corresponds to dimensional time of $20\kappa/\bar{V}^2$. From Eqs. (1.7)–(8), t_s should be a function of the Péclet number (Pe_1) and the radius (R). The ratio of the TC result to the SS result gives a quantitative criterion to evaluate the degree to which the steady state is reached. Given this ratio, the location, and the Péclet number, one can accurately find t_s by substituting Eq. (1.7) into the ratio expression. When this ratio is set as 0.99 at $R=0.5$ or 1.5, the corresponding time is depicted in Fig. 2 (solid line) with respect to the Péclet number. Figure 2 shows that the Hou and Komanduri result (dotted line) overestimates the time for low Péclet number and underestimates the time for high Péclet number.

The Green's function of TC cases involves the complementary error function, which decays to zero faster than the exponential function. It is reasonable to claim that the steady state is approximately reached when the following condition is fulfilled,

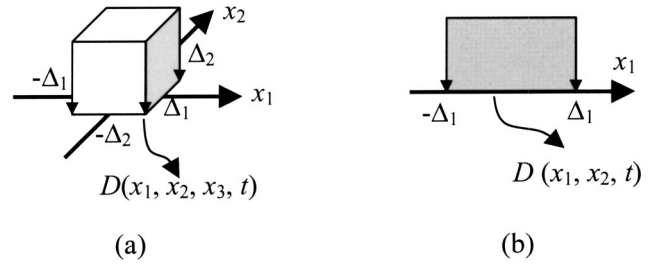


Fig. 3 Schematics of influence coefficients

$$\frac{\text{Pe}_1\sqrt{t_s}}{2} - \frac{R}{2\sqrt{t_s}} = n \quad (1.13)$$

where n is 3 or larger since $\operatorname{erfc}(3)$ is $O(10^{-5})$. After rewriting, one can find t_s

$$t_s = [(n + \sqrt{n^2 + R\text{Pe}_1})/\text{Pe}_1]^2 \quad (1.14)$$

which has a square root term and thus differs from Hou and Komanduri [7] ($t_s \sim \text{Pe}_1^{-2}$). Figure 2 also depicts results obtained from Eq. (1.14) with $n=3$, where the curve trends reveal that the smaller the Péclet number, the longer the time to reach the steady state. From Eq. (1.14), it is seen that locations far from the origin require a longer time to reach the steady state.

Equation (1.14) is not applicable for zero Péclet number (the *stationary* half-space); instead the term, $\operatorname{erfc}[R/(2\sqrt{t_s})]$, in Eq. (1.10) should go toward one as time increases. If the ratio of the TC result to the SS result is denoted as $1 - e$, then t_s can be found as follows:

$$t_s \approx R^2/(e^2\pi) \quad (1.15)$$

For example, set e to 0.01 so that the ratio is 0.99. If the half-space is *moving* with $\text{Pe}_1 = 1$, t_s is approximately 5 at $R = \frac{1}{2}$. However, t_s should be around 800 for the same location in the *stationary* half-space. From the comparison between Eq. (1.14) and Eq. (1.15), it is seen that the location has greater effect on t_s in *stationary* bodies than in *moving* ones. It should be pointed out that these equations for t_s are valid for locations inside the half-space as well. However, since the equations for t_s are obtained from Green's functions, they are only accurate in the case of a unit heat source. For problems with arbitrary heat sources, these equations are applicable to locations far away from the heat source.

1.2 Influence Coefficients. Influence coefficients are responses to a constant heat distribution on the surface over the rectangular patch $x_1 \in [-\Delta_1, \Delta_1]$ and $x_2 \in [-\Delta_2, \Delta_2]$ [Fig. 3(a)]. Since an arbitrary heat source can be discretized into a set of uniformly distributed heat sources, influence coefficients are widely used in numerical simulation. The influence coefficients for a half-space are generally written as the following double integrals:

$$D(x_1, x_2, x_3, t) = \int_{-\Delta_1}^{\Delta_1} \int_{-\Delta_2}^{\Delta_2} G(x_1 - x'_1, x_2 - x'_2, x_3, t) dx'_1 dx'_2 \quad (1.16)$$

For the steady state, the variable t in Eq. (1.16) should be absent.

1.2.1 Instantaneous Case. Integrating the Green's function for the *stationary* half-space leads to

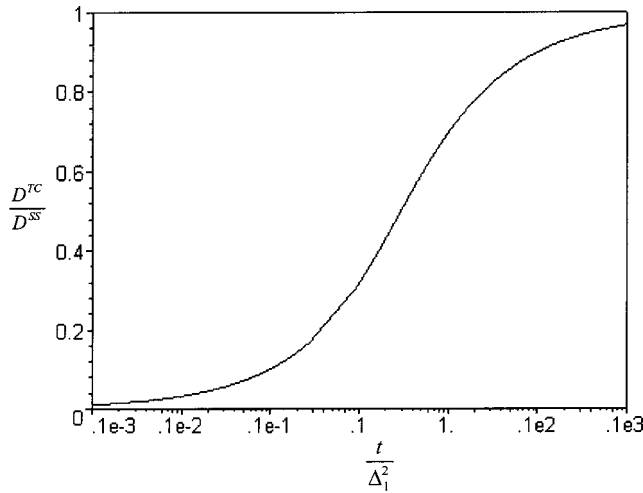


Fig. 4 Evolution of the influence coefficient at the origin with time

$$D^{TC}(x_1, x_2, x_3, t) = \frac{\exp[-x_3^2/(4t)]}{4\sqrt{\pi t}} \left[\operatorname{erf}\left(\frac{x_1 + \Delta_1}{2\sqrt{t}}\right) - \operatorname{erf}\left(\frac{x_1 - \Delta_1}{2\sqrt{t}}\right) \right] \left[\operatorname{erf}\left(\frac{x_2 + \Delta_2}{2\sqrt{t}}\right) - \operatorname{erf}\left(\frac{x_2 - \Delta_2}{2\sqrt{t}}\right) \right] \quad (1.17)$$

For the *moving* half-space, t and x_i in the above equation should be replaced by $t - t'$ and $x_i - \int_{t'}^t \operatorname{Pe}_i d\tau$, respectively.

1.2.2 Continuous Case. An attempt by the authors to express the influence coefficients in a closed form was unsuccessful. However, instead of double integrals (Eq. 1.16) the influence coefficients for the *stationary* half-space could be written as a single integral with respect to time based on Eq. (1.17) as follows:

$$D^{TC}(x_1, x_2, x_3, t) = \int_0^{\sqrt{t}} \frac{\exp[-x_3^2/(4\tau^2)]}{2\sqrt{\pi}} \left[\operatorname{erf}\left(\frac{x_1 + \Delta_1}{2\tau}\right) - \operatorname{erf}\left(\frac{x_1 - \Delta_1}{2\tau}\right) \right] \left[\operatorname{erf}\left(\frac{x_2 + \Delta_2}{2\tau}\right) - \operatorname{erf}\left(\frac{x_2 - \Delta_2}{2\tau}\right) \right] d\tau \quad (1.18a)$$

where $\tau = \sqrt{t - t'}$ is used. The maximum value is at the origin and can be obtained numerically by evaluating

$$D^{TC}(0,0,0,t) = \frac{2}{\sqrt{\pi}} \int_0^{\sqrt{t}} \operatorname{erf}\left(\frac{\Delta_1}{2\tau}\right) \operatorname{erf}\left(\frac{\Delta_2}{2\tau}\right) d\tau \quad (1.18b)$$

For the *moving* half-space, x_i in Eq. (1.18a) should be replaced by $x_i - \int_{t-\tau}^t \operatorname{Pe}_i du$. From the computational point of view, a single integration can be handled more efficiently than double integration. Figure 4 shows the evolution of the influence coefficients with $\Delta_1 = \Delta_2$ at the origin normalized by the SS result of Eq. (1.21b), which is discussed in Sec. 1.2.3. Since the horizontal axis in Fig. 4 is time divided by Δ_1^2 , the value of t_s at the origin strongly depends on the size of the heated region and is roughly 100 to 1000 times Δ_1^2 .

1.2.3 Steady-State Case. For the *stationary* half-space, the Green's function has a kernel of the Newtonian potential, $G^{SS}(x_1, x_2, x_3) = 1/2\pi R$. From [10], the following integration can be found,

$$F(x_1, x_2, x_3) = \int \int \frac{1}{R} dx_1 dx_2 = \frac{x_1}{2} \ln\left(\frac{R+x_2}{R-x_2}\right) + \frac{x_2}{2} \ln\left(\frac{R+x_1}{R-x_1}\right) - x_3 \arctan\left(\frac{x_1 x_2}{x_3 R}\right) \quad (1.19)$$

$$\text{and } F(x_1, x_2, 0) = x_1 \ln(\sqrt{x_1^2 + x_2^2} + x_2) + x_2 \ln(\sqrt{x_1^2 + x_2^2} + x_1) \quad (1.20)$$

Therefore, the influence coefficients with $\operatorname{Pe}_1 = 0$ can be expressed as,

$$D^{SS}(x_1, x_2, x_3) = [F(x_1 + \Delta_1, x_2 + \Delta_2, x_3) - F(x_1 - \Delta_1, x_2 + \Delta_2, x_3) - F(x_1 + \Delta_1, x_2 - \Delta_2, x_3) + F(x_1 - \Delta_1, x_2 - \Delta_2, x_3)] / (2\pi) \quad (1.21a)$$

The maximum value is at the origin and expressed as

$$D^{SS}(0,0,0) = \frac{2}{\pi} \left[\Delta_1 \ln \frac{\sqrt{s^2 + 1} + 1}{s} + \Delta_2 \ln(\sqrt{s^2 + 1} + s) \right] \quad (1.21b)$$

where $s = \Delta_1/\Delta_2$ is the ratio of the heated region. If the patch is square (i.e., $s = 1$), $D^{SS}(0,0,0) = (4/\pi) \Delta_1 \ln(1 + \sqrt{2})$, which is approximately $2\Delta_1/\sqrt{\pi}$ as obtained in [9].

When the half-space is *moving*, the influence coefficients may not be expressed in a closed form and numerical integration is used to obtain numerical values. However, Tichy [11] derived the temperature rise in the fast *moving* half-space under a uniform rectangular heat flux, which is, in fact, the influence coefficients for a very large Péclet number.

1.3 Frequency Response Functions. The general form of temperature rise in a mixed time and frequency domain can be expressed as [12],

$$\tilde{\tilde{T}}(\omega_1, \omega_2, x_3, t) = \int_0^t \frac{\tilde{\tilde{q}}(\omega_1, \omega_2, t')}{\sqrt{\pi} \Delta t \exp[\Delta t \omega^2 + x_3^2/(4\Delta t)]} dt' \quad (1.22)$$

where $\Delta t = t - t'$, $\omega^2 = \omega_1^2 + \omega_2^2 + i(\omega_1 \int_{t'}^t \operatorname{Pe}_1 d\tau + \omega_2 \int_{t'}^t \operatorname{Pe}_2 d\tau)/\Delta t$, and a double tilde ($\tilde{\tilde{\quad}}$) denotes a two-dimensional Fourier transform with respect to x_1 and x_2 . The mixed domain involves the frequency domain with respect to x_1 and x_2 , the space domain of x_3 and the time domain.

If the Péclet number varies with time, numerical integration must be used to evaluate the time integrals. However, temperature in Eq. (1.22) is simplified below for problems with time-invariant Péclet numbers with the notation

$$w = \sqrt{\omega_1^2 + \omega_2^2 + i\omega_1 \operatorname{Pe}_1 + i\omega_2 \operatorname{Pe}_2} \quad (1.23)$$

For the *instantaneous case*, the integral in Eq. (1.22) is a convolution and the Fourier transform with respect to time changes the convolution to multiplication,

$$\frac{\tilde{\tilde{\tilde{T}}}(\omega_1, \omega_2, x_3, \omega_t)}{\tilde{\tilde{\tilde{q}}}(\omega_1, \omega_2, \omega_t)} = \frac{\exp(-x_3 \sqrt{w^2 + i\omega_t})}{\sqrt{w^2 + i\omega_t}} \quad (1.24a)$$

where ω_t is the frequency domain counterpart of time. A triple tilde ($\tilde{\tilde{\tilde{\quad}}}$) denotes a three-dimensional Fourier transform with respect to x_1 and x_2 and time. For the *continuous case* and *steady-state case*, one can find the frequency response functions as follows, respectively:

$$\frac{\tilde{T}(\omega_1, \omega_2, x_3, t)}{\tilde{q}(\omega_1, \omega_2)} = \frac{1}{2w} \left[\exp(-x_3 w) \operatorname{erfc} \left(\frac{x_3}{2\sqrt{t}} - w\sqrt{t} \right) - \exp(x_3 w) \operatorname{erfc} \left(\frac{x_3}{2\sqrt{t}} + w\sqrt{t} \right) \right] \quad (1.24b)$$

$$\frac{\tilde{T}(\omega_1, \omega_2, x_3)}{\tilde{q}(\omega_1, \omega_2)} = \frac{\exp(-x_3 w)}{w} \quad (1.24c)$$

2 Surface Heating of a Half-Plane

An irregularly distributed heat source per unit time per unit length is applied on the surface of a half-plane [Fig. 1(b)] with uniform initial temperature. All quantities in this section are identical to those in Sec. 1 except that the x_2 coordinate is directed into the half-plane and the x_3 coordinate is absent. The temperature rise is governed by

$$T_{,ii} = \frac{\partial T}{\partial t} + \operatorname{Pe}_1 T_{,1} \quad (2.1)$$

In the surface-heated region S , a boundary condition is specified as

$$-T_{,2} = q \quad (2.2)$$

Outside S , an adiabatic boundary condition is applied. Solutions involving a convection boundary condition are presented in Sec. 3.

2.1 Green's Functions. The Green's functions for the half-plane can be found by integration of the half-space result. Carslaw and Jaeger [5] presented these Green's functions for the following cases:

- a. *Instantaneous case* with $\operatorname{Pe}_1 = 0$:

$$G^{TI}(x_1, x_2, t) = \frac{1}{2\sqrt{\pi t}} \exp\left(-\frac{R^2}{4t}\right) \quad (2.3)$$

where $R = \sqrt{x_1^2 + x_2^2}$. If the half-space is *moving*, t and x_1 in Eq. (2.3) should be replaced by $t - t'$ and $x_1 - \int_{t'}^t \operatorname{Pe}_1 d\tau$, respectively.

- b. *Continuous case* with $\operatorname{Pe}_1 = 0$:

$$G^{TC}(x_1, x_2, t) = \int_0^t G^{TI}(x_1, x_2, t - t') dt' = \frac{-1}{2\pi} \operatorname{Ei}\left(-\frac{R^2}{4t}\right) \quad (2.4)$$

The Green's function of the *moving* half-plane for continuous cases is not available in a closed form.

- c. *Steady-state case*:

$$G^{SS}(x_1, x_2) = \frac{1}{\pi} \exp\left[\frac{\operatorname{Pe}_1 x_1}{2}\right] K_0\left[\frac{R \operatorname{Pe}_1}{2}\right] \quad (2.5)$$

The Green's functions in Eq. (2.4) for TC cases and Eq. (2.5) for SS cases are singular at the origin. Furthermore, Eq. (2.5) is everywhere infinity. The asymptotic behavior of modified Bessel functions can be shown to be $\lim_{x \rightarrow 0} K_0(cx) = -\ln c - \ln x + \ln 2 - \gamma$, where γ is the Euler's constant (0.5772). By ignoring a bulk value (the logarithmic infinity and constant terms), the Green's function with an appropriate reference point for the *stationary* half-plane is

$$G^{SS}(x_1, x_2) = -\frac{1}{\pi} \ln R \quad (2.6)$$

Recall that t_s is the time when the steady state is approximately

reached and the exponential integral for any small x can be written as $\operatorname{Ei}(-x) = \gamma + \ln x - x + O(x^2)$. If the ratio between the TC and SS results is given as $1 - e$, one can approximate t_s for the *stationary* half-plane by the following expression with the reference point at R_0 ,

$$t_s = \frac{R^2 - R_0^2}{8e(\ln R - \ln R_0)} \quad (2.7)$$

which is dependent on R_0 . The relationship between t_s and R here is different from that of the *stationary* half-space in Eq. (1.15). t_s is about 13.5 at $R = \frac{1}{2}$ with $e = 0.01$ and $R_0 = 1$. For the *moving* half-plane, t_s could be found numerically, and is about 3.1 at $R = \frac{1}{2}$ with $\operatorname{Pe}_1 = 1$, $e = 0.01$, and $R_0 = 1$. For this specific R_0 , the t_s of the half-plane is less than that of the half-space so in the neighborhood of $R = 1$, the half-plane reaches the steady state more rapidly than the half-space.

2.2 Influence Coefficients. Similar to half-space problems, the influence coefficients for the half-plane can be written as

$$D(x_1, x_2, t) = \int_{-\Delta_1}^{\Delta_1} G(x_1 - x'_1, x_2, t) dx'_1 \quad (2.8)$$

with a uniformly distributed heat source over $x_1 \in [-\Delta_1, \Delta_1]$ [Fig. 3(b)]. For the steady-state case, time should not be included in this expression.

2.2.1 Instantaneous Case. By integrating the Green's function of Eq. (2.3), one can obtain,

$$D^{TI}(x_1, x_2, t) = \frac{1}{2\sqrt{\pi t}} \exp[-x_2^2/(4t)] \left[\operatorname{erf}\left(\frac{x_1 + \Delta_1}{2\sqrt{t}}\right) - \operatorname{erf}\left(\frac{x_1 - \Delta_1}{2\sqrt{t}}\right) \right] \quad (2.9)$$

If the half-plane is *moving*, t and x_1 in Eq. (2.9) should be replaced by $t - t'$ and $x_1 - \int_{t'}^t \operatorname{Pe}_1 d\tau$, respectively.

2.2.2 Continuous Case. It is convenient to write the influence coefficients in a time-integral form as following,

$$D^{TC}(x_1, x_2, t) = \frac{1}{\sqrt{\pi}} \int_0^{\sqrt{t}} \exp[-x_2^2/(4\tau^2)] \left[\operatorname{erf}\left(\frac{x_1 + \Delta_1}{2\tau}\right) - \operatorname{erf}\left(\frac{x_1 - \Delta_1}{2\tau}\right) \right] d\tau \quad (2.10)$$

If the half-plane is *moving*, x_1 in Eq. (2.10) should be replaced by $x_1 - \int_{t-\tau}^t \operatorname{Pe}_1 du$. In the surface of the *stationary* half-plane, Eq. (2.10) can be simplified due to the indefinite integral, $\int \operatorname{erf}(c/\tau) d\tau = \tau \operatorname{erf}(c/\tau) - c \operatorname{Ei}(-c^2/\tau^2)/\sqrt{\pi}$,

$$D^{TC}(x_1, 0, t) = \sqrt{\frac{t}{\pi}} \left[\operatorname{erf}\left(\frac{x_1 + \Delta_1}{2\sqrt{t}}\right) - \operatorname{erf}\left(\frac{x_1 - \Delta_1}{2\sqrt{t}}\right) \right] - \frac{x_1 + \Delta_1}{2\pi} \operatorname{Ei}\left[-\frac{(x_1 + \Delta_1)^2}{4t}\right] + \frac{x_1 - \Delta_1}{2\pi} \operatorname{Ei}\left[-\frac{(x_1 - \Delta_1)^2}{4t}\right] \quad (2.11a)$$

(see also p. 264 [5]). The maximum value is at the origin and can be expressed as

$$D^{TC}(0, 0, t) = 2\sqrt{\frac{t}{\pi}} \operatorname{erf}\left(\frac{\Delta_1}{2\sqrt{t}}\right) - \frac{\Delta_1}{\pi} \operatorname{Ei}\left(-\frac{\Delta_1^2}{4t}\right) \quad (2.11b)$$

2.2.3 Steady-State Case

2.2.3.1 *Surface temperature rise.* In the surface, one can calculate the influence coefficients by using the following integration (p. 269 [5]),

$$\int_0^a \exp(\pm u) K_0(u) du = a \exp(\pm a) \{K_0(a) \pm K_1(a)\} \mp 1 \quad (2.12)$$

where K_1 is the modified Bessel function of the second kind of order one. The influence coefficients can be written as

$$D^{SS}(x_1, 0) = \frac{1}{\pi} \begin{cases} \frac{(x_1 + \Delta_1) \exp(P_+) [K_0(-P_+) - K_1(-P_+)] + (\Delta_1 - x_1) \exp(P_-) [K_0(-P_-) - K_1(-P_-)]}{(x_1 + \Delta_1) \exp(P_+) [K_0(P_+) + K_1(P_+)]}, & x_1 \leq -\Delta_1 \\ \frac{(\Delta_1 - x_1) \exp(P_-) [K_0(-P_-) - K_1(-P_-)]}{(x_1 + \Delta_1) \exp(P_+) [K_0(P_+) + K_1(P_+)]} + \frac{(x_1 + \Delta_1) \exp(P_+) [K_0(P_+) + K_1(P_+)]}{(x_1 + \Delta_1) \exp(P_+) [K_0(P_+) + K_1(P_+)]}, & -\Delta_1 \leq x_1 \leq \Delta_1 \\ \frac{(x_1 + \Delta_1) \exp(P_+) [K_0(P_+) + K_1(P_+)]}{(x_1 + \Delta_1) \exp(P_+) [K_0(P_+) + K_1(P_+)]} - \frac{(x_1 - \Delta_1) \exp(P_-) [K_0(P_-) + K_1(P_-)]}{(x_1 + \Delta_1) \exp(P_+) [K_0(P_+) + K_1(P_+)]}, & \Delta_1 \leq x_1 \end{cases} \quad (2.13)$$

where $P_{\pm} = Pe_1(x_1 \pm \Delta_1)/2$. The location of the maximum value is found between 0 and Γ_1 and is governed by

$$\exp(P_+) K_0(P_+) - \exp(P_-) K_0(P_-) = 0 \quad (2.14)$$

The numerical solution of x_1 for Eq. (2.14) with $\Gamma_1 = 1$ is plotted against the Péclet number in Fig. 5. The location of the maximum temperature apparently approaches the leading side of the heat source when the Péclet number increases. The maximum value can be determined by the middle expression in Eq. (2.13) with the numerical value of x_1 in Fig. 5. In Fig. 6, the influence coefficients with $\Gamma_1 = 1$ are shown for different Péclet numbers with Eq. (2.13) (solid lines without symbols). For a large Péclet number and thus a large P_{\pm} , it is convenient to use the following asymptotic behavior of the modified Bessel functions,

$$K_n(u) \approx \sqrt{\frac{\pi}{2u}} \exp(-u) \quad (2.15)$$

where u is large and n is an integer. By using this approximation, one can find the influence coefficients for large Pe_1

$$D^{SS}(x_1, 0) = \frac{2}{\sqrt{\pi Pe_1}} \begin{cases} 0, & x_1 < -\Delta_1 \\ \sqrt{x_1 + \Delta_1}, & -\Delta_1 \leq x_1 \leq \Delta_1 \\ \sqrt{x_1 + \Delta_1} - \sqrt{x_1 - \Delta_1}, & \Delta_1 < x_1 \end{cases} \quad (2.16)$$

which is identical to the results obtained by Ling et al. [9]. At the origin, it is obvious that $D^{SS}(0, 0) = 2\sqrt{\Delta_1}/(Pe_1\pi)$. The maximum value is at the leading edge of the heated region and equals $2\sqrt{2\Delta_1}/(Pe_1\pi)$.

For the *stationary* half-plane, the influence coefficients in Eq. (2.13) are infinite; however, these can be expressed in relative to the value at the origin, as

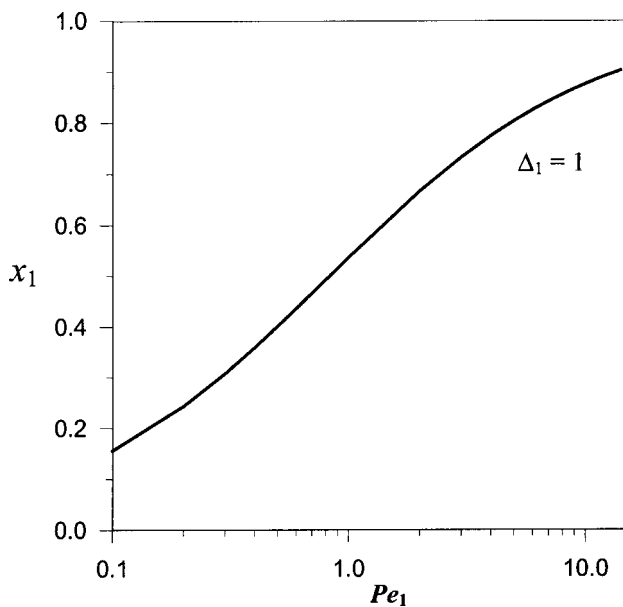


Fig. 5 Location of maximum temperature with the Péclet number

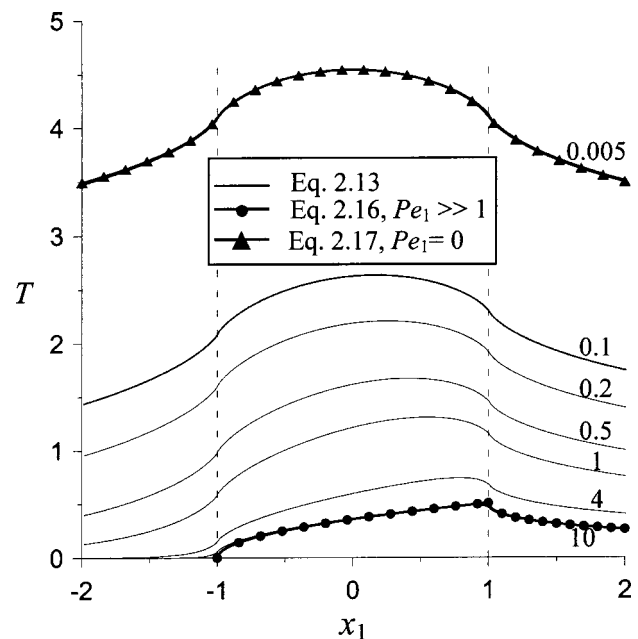


Fig. 6 SS surface temperature of the half-plane for various Péclet numbers. Those values around curves are Péclet number for Eq. (2.13).

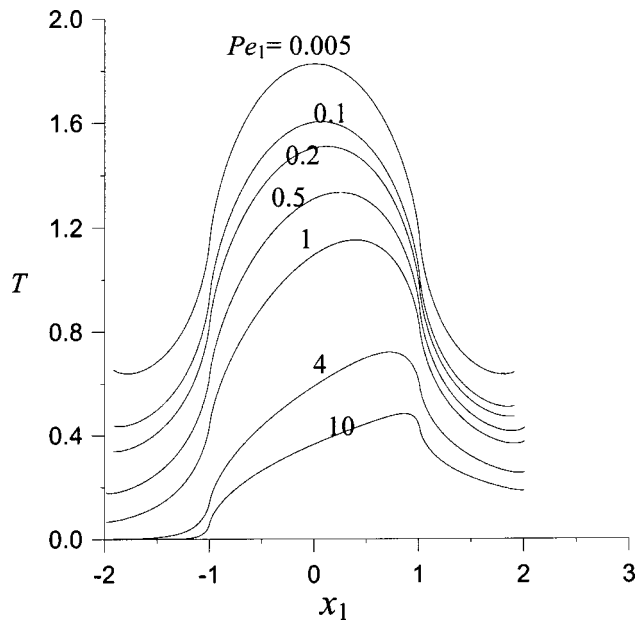


Fig. 7 SS surface temperature of the half-plane for different Peclet numbers ($h=1$)

$$D^{SS}(x_1, 0) - D^{SS}(0, 0) = \frac{1}{\pi} \left[\ln \left(\frac{|x_1 - \Delta_1|^{x_1 - \Delta_1}}{|x_1 + \Delta_1|^{x_1 + \Delta_1}} \right) + 2\Delta_1 \ln \Delta_1 \right], \quad (Pe_1 = 0) \quad (2.17)$$

where the asymptotic behaviors of the modified Bessel functions

$$\lim_{x \rightarrow 0} K_0(cx) = -\ln c - \ln x + \ln 2 - \gamma \quad \text{and} \quad \lim_{x \rightarrow 0} K_1(cx) = 1/(cx) \quad (2.18)$$

are used. In addition to the solid lines without symbols, obtained by Eq. (2.13), Fig. 6 shows the two limiting results evaluated by Eqs. (2.16) and (2.17) with dots and triangles, respectively. In general, the result at the origin required in Eq. (2.17) should be infinite, which is artificially set by the value at the origin evaluated from Eq. (2.13) with $Pe_1 = 0.005$ for comparison in Fig. 6. One can see that the result with $Pe_1 = 0.005$ has almost the same shape as that with $Pe_1 = 0$, and the result with $Pe_1 = 10$ is very close to that with $Pe_1 = \infty$.

2.2.3.2 Subsurface temperature rise. Inside the half-plane, the integration of Eq. (2.8) with Eq. (2.5) is not analytically available. Thus the influence coefficient for the *moving* half-plane can be expressed only in an integral form and numerically evaluated. But for the *stationary* half-plane, it is found that

$$g(x_1, x_2) = \int \ln R dx_1 = x_1 \ln R - x_1 + x_2 \tan^{-1}(x_1/x_2), \quad R = \sqrt{x_1^2 + x_2^2} \quad (2.19)$$

$$D^{SS}(x_1, x_2) - D^{SS}(0, x_2) = [g(x_1 - \Delta_1, x_2) - g(x_1 + \Delta_1, x_2) + 2g(\Delta_1, x_2)]/\pi \quad (2.20)$$

It is easy to verify that Eq. (2.17) is a special case of Eq. (2.20) with $x_2 = 0$.

2.3 Frequency Response Functions. Noticing that the x_2 coordinate points inside the half-plane in Fig. 1(b), one can obtain the frequency response function for the half-plane from those for the half-space by setting $\omega_2 = 0$ and changing x_3 into x_2 . Thus,

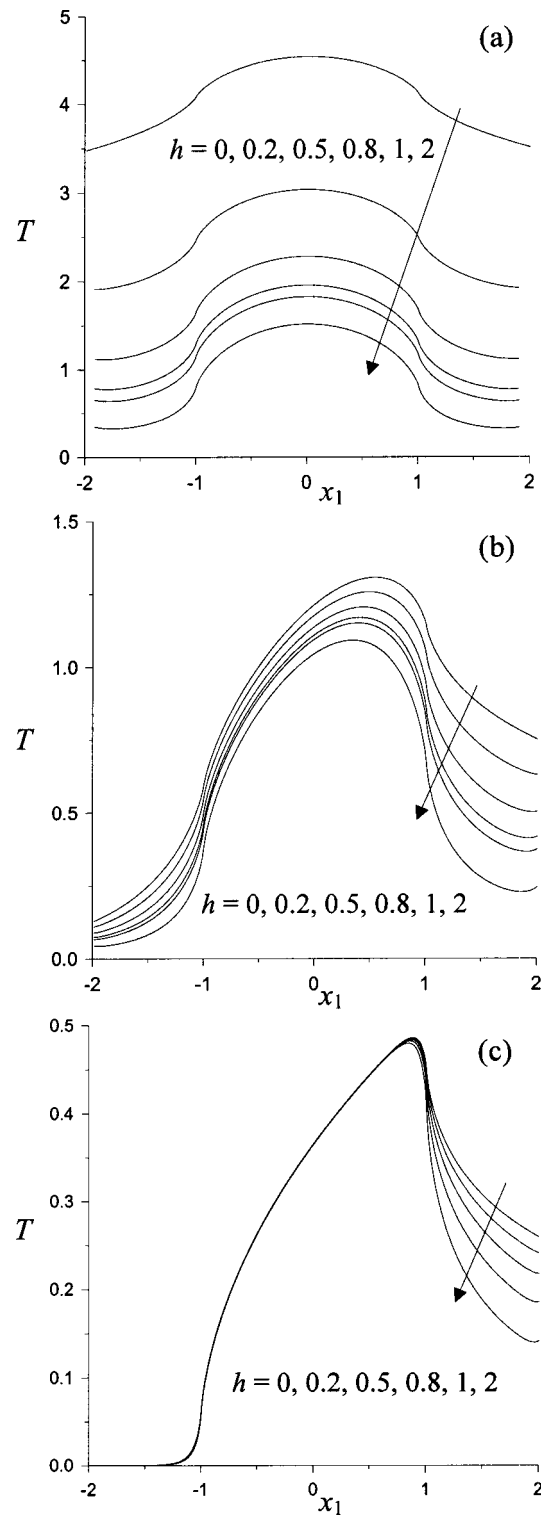


Fig. 8 Surface temperature with different h (half-plane) a) $Pe_1 = 0.005$; b) $Pe_1 = 1$; c) $Pe_1 = 10$

with the new notation, the radius in the frequency domain is defined as $w^2 = \sqrt{\omega_1^2 + i\omega_1 Pe_1}$. For completeness, the frequency response function for each case is listed below,

$$\frac{\tilde{T}(\omega_1, x_2, \omega_t)}{\tilde{q}(\omega_1, \omega_t)} = \frac{\exp(-x_2 \sqrt{w^2 + i\omega_t})}{\sqrt{w^2 + i\omega_t}} \quad (\text{Instantaneous}) \quad (2.21a)$$

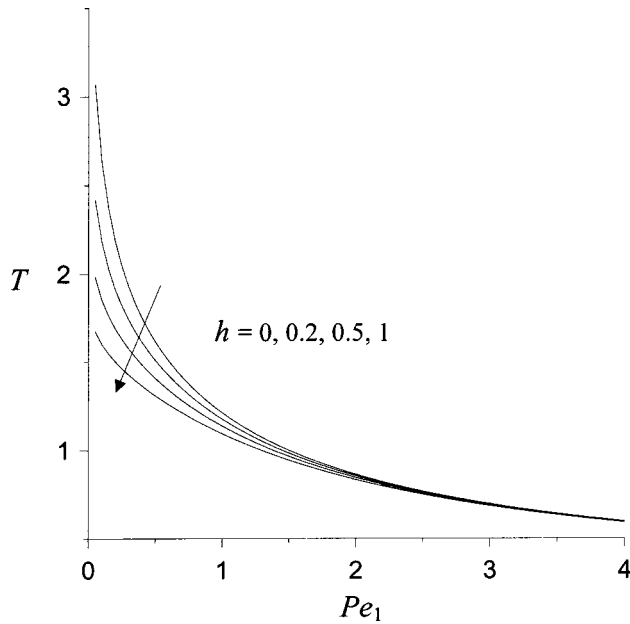


Fig. 9 Variation of temperature at the origin with Péclet number and h (half-plane)

$$\frac{\tilde{T}(\omega_1, x_2, t)}{\bar{q}(\omega_1)} = \frac{1}{2w} \left[\exp(-x_2 w) \operatorname{erfc} \left(\frac{x_2}{2\sqrt{t}} - w\sqrt{t} \right) - \exp(x_2 w) \operatorname{erfc} \left(\frac{x_2}{2\sqrt{t}} + w\sqrt{t} \right) \right] \quad (\text{Continuous}) \quad (2.21b)$$

$$\frac{\tilde{T}(\omega_1, x_2)}{\bar{q}(\omega_1)} = \frac{\exp(-x_2 w)}{w} \quad (\text{Steady state}) \quad (2.21c)$$

3 Effect of the Convection Boundary Condition

In previous sections, the adiabatic boundary is assumed outside the surface-heated region S . The effect of the convection boundary condition on the temperature distribution due to surface heating is of interest, since the adiabatic boundary condition may not be reasonable for certain applications. Using the half-space as an example, the convective boundary condition is specified as follows ([5] p. 19):

$$T_{,3} = hT \quad \text{for } (x_1, x_2) \in S \quad (3.1)$$

where h is the dimensionless surface heat-transfer coefficient ($h = \bar{h}l/K$), which is assumed to be constant.

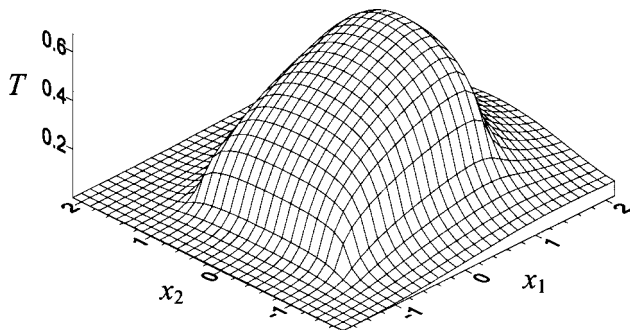


Fig. 10 Surface temperature distribution with $Pe_1=4$ and $h=1$ (half-space)

In this section, the heat source q is assumed to be uniform over $x_i \in [-1, 1]$, $i=1$ or 2. From the point of view of numerical simulation, complicated heat sources can be solved by the same code as that used for the uniform one. Only the SS surface temperature is considered since it contains the maximum temperature. Fischer et al. [13] found an analytical solution for large Péclet numbers. By introducing a general heat source,

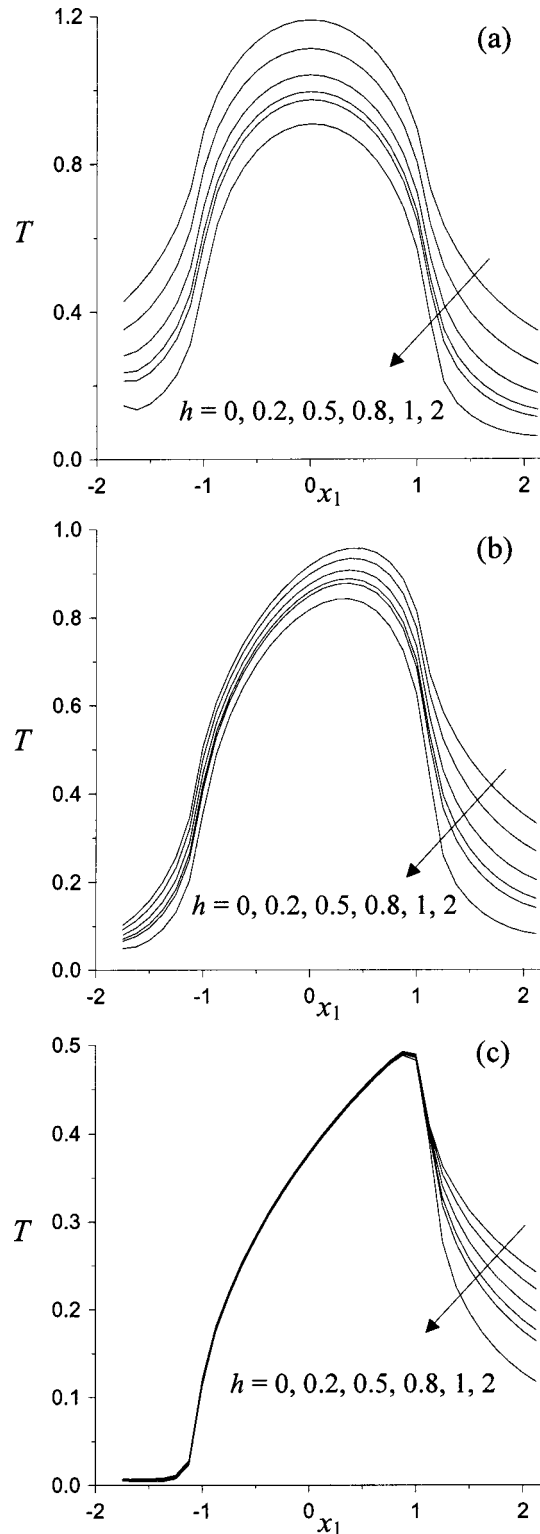


Fig. 11 Surface temperature in x_1 direction with $x_2=0$ and different h (half-space) a) $Pe_1=0$; b) $Pe_1=1$; c) $Pe_1=10$

$$q^*(x_1, x_2) = \begin{cases} q, & (x_1, x_2) \in S \\ -hT, & (x_1, x_2) \notin S \end{cases} \quad (3.2)$$

those formulations with q replaced by q^* presented in Sections 1 and 2 are readily applicable to the problems here. Therefore, the SS temperature rise can be expressed by the following integral:

$$T(x_1, x_2, x_3) = \int_{-\infty}^{+\infty} \int_{-\infty}^{+\infty} G^{SS}(x_1 - x'_1, x_2 - x'_2, x_3) q^*(x'_1, x'_2) dx'_1 dx'_2 \quad (3.3)$$

The integral involves the unknown temperature, because q^* depends on temperature. The grid number N is used for discretization. Define $x_j^i = \Delta_j(i - (N/2) - 1)$, $j = 1$ or 2 and $i = 1 \dots N$, and $f(x_1^i, x_2^j, x_3)$ is denoted by $f^{ij}(x_3)$. By using the influence coefficients, one can express the temperature on each grid point as

$$T^{nm} = \sum_{k=1}^N \sum_{j=1}^N (q^*)^{kj} D^{SS}(x_1^n - x_1^k, x_2^m - x_2^j, x_3) \quad (3.4)$$

It should be pointed out that truncation is involved in the rewriting of Eq. (3.3) as Eq. (3.4). This truncation will cause significant error along the border of the computational domain. Equation (3.4) can be rewritten into a linear equation of the temperature field

$$T^{nm} + \sum_{(k,j) \notin S} \sum h T^{kj} D^{(n-k)(m-j)} = \sum_{(k,j) \in S} \sum q^{kj} D^{(n-k)(m-j)} \quad (3.5)$$

This equation is in the form of $AT=b$, where A is a matrix $N^2 \times N^2$, and b and T are vectors with N^2 members. This linear equation is solved using the LU decomposition. One should use the analytical expressions of the influence coefficients for the half-plane and the *stationary* or *fast moving* half-space summarized in Sections 1 and 2. If the half-space is *moving* with a moderate Péclet number, the influence coefficients can be obtained numerically from the frequency response functions. An accurate and efficient method to determine the influence coefficients can be found in [14], which uses the fast Fourier technique and is more efficient than the numerical double integration of the Green's function.

3.1 Half-Plane Results. For the half-plane with convection boundary conditions, the linear equation of temperature rise is expressed as follows:

$$T^n + \sum_{k \in S} h T^k D^{(n-k)} = \sum_{k \in S} q D^{(n-k)} \quad (3.6)$$

The temperature distribution along the x_1 axis is shown in Fig. 7 with $h=1$ and different Péclet numbers. By comparing Figs. 6 and 7, one can see that surface convection reduces temperature values significantly with small Péclet number (<1). When the half-plane is moving very slowly, the maximum value is dramatically reduced. Figs. 8(a)–8(c) further show the surface temperature distributions for three specific Péclet numbers (0.005, 1, and 10), respectively. In each plot of Fig. 8, results are shown for six different values of h (0, 0.2, 0.5, 0.8, 1, and 2). For small Péclet numbers [Figs. 8(a) and 8(b)] the whole temperature distribution is substantially reduced by convection. Figure 8(c) shows that when the half-plane is moving from left to right with a large Péclet number, the effect of convection varies based on location. The convection has little effect on the temperature at points in the left-hand side of the plot or inside the surface-heating region, but significantly reduces the temperature at all other points. Figure 9 shows the temperature at the origin as a function of the Péclet number and h . One can conclude that for $Pe_1 > 3$ convection slightly reduces the temperature at the origin, but for small Péclet numbers, convection has a significant effect on the temperature.

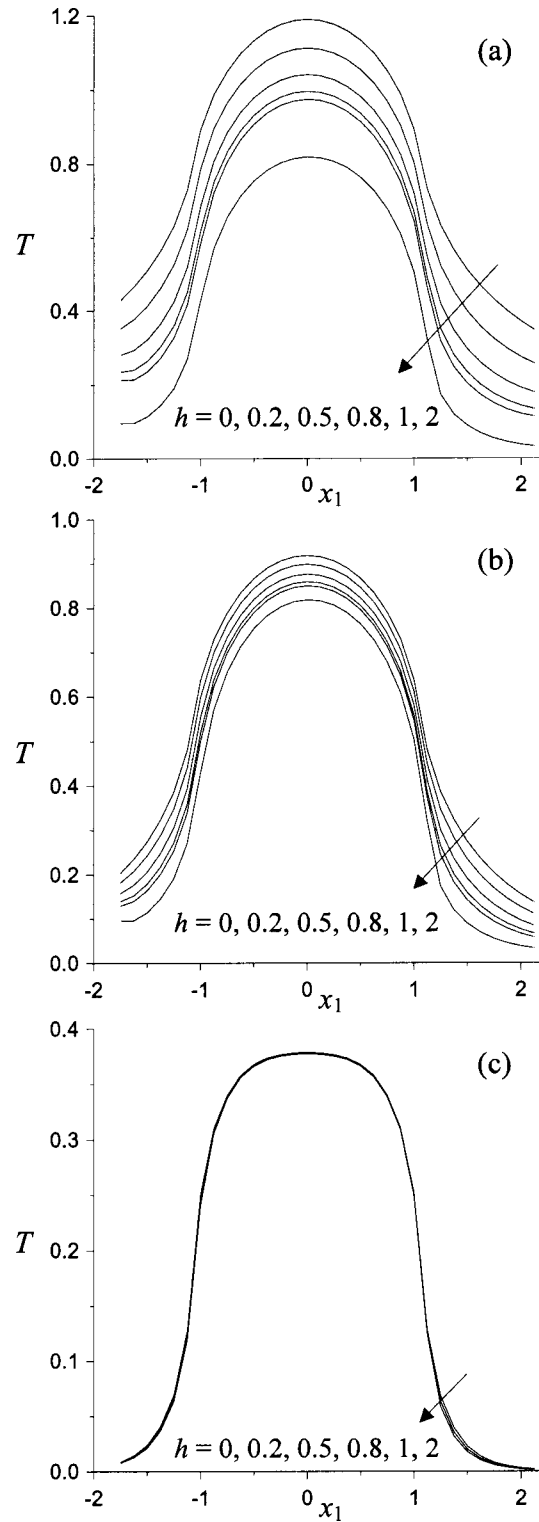


Fig. 12 Surface temperature in x_2 direction with $x_1=0$ and different h (half-space) a) $Pe_1=0$; b) $Pe_1=1$; c) $Pe_1=10$

3.2 Half-Space Results. Since the linear equation of Eq. (3.5) has N^2 unknowns, N is limited by computer memory. The following results are obtained with $N=64$. Figure 10 illustrates the three-dimensional temperature distribution with $Pe_1=4$ and $h=1$, which is typical for the moving half-space. Figures 11(a)–11(c) and 12(a)–12(c) show cross sections in the x_1 directions ($x_2=0$) and in the x_2 directions ($x_1=0$), respectively, with dif-

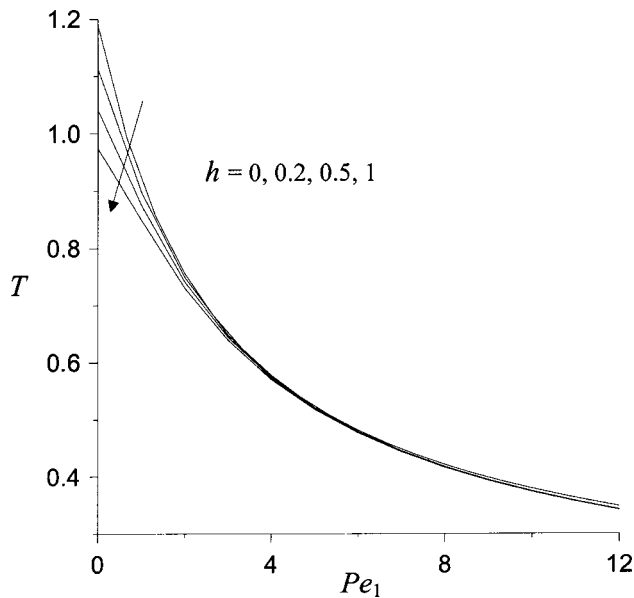


Fig. 13 Variation of temperature at the origin with Péclet number and h (half-space)

ferent values of h under three Péclet numbers (0, 1, and 10). The effect of convection on surface temperature in the half-space is similar to that in the half-plane. For small Péclet numbers the entire computation region is significantly affected by the convection. For large Péclet numbers, the convection hardly affects the temperature rise of points located at $x_1 < 1$ and $\forall x_2$, but significantly affects other points located at $x_1 > 1$. The temperature rise at the origin is obtained for different values of h and shown in Fig. 13 as a function of the Péclet number. It is found that the temperature at the origin is substantially reduced with increasing h when the Péclet number is less than three.

Conclusion

The Green's functions, influence coefficients, and frequency response functions for temperature rise due to surface heating are investigated and summarized. These formulations, which deal with time dependency and component motion, are applicable to half-space and half-plane problems with or without surface convection outside the surface-heated region. The time required to reach approximately steady state is found for moving/stationary half-spaces or stationary half-planes subject to a unit heat flux. It is revealed that a half-plane needs less time than a half-space to achieve a steady state with a reference point located one unit away from the origin. Results also show that with a Péclet number less than three, the convection reduces surface temperature everywhere, while with larger Péclet numbers, the convection significantly reduced the temperature only on the leading side of the surface-heating region.

Nomenclature

$Ei(x)$ = exponential integral
 $\text{erf}(x)$ = error function, $(2/\sqrt{\pi}) \int_0^x \exp(-\tau^2) d\tau$
 $\text{erfc}(x)$ = complementary error function,
 $(2/\sqrt{\pi}) \int_x^\infty \exp(-\tau^2) d\tau$

$\bar{h}; h$ = surface heat-transfer coefficient,
 $J/(\text{m}^2 \text{K s})$; $h = \bar{h}l/K$
 i = pure imaginary, $\sqrt{-1}$
 K = conductivity, $J/(\text{m K s})$ or $\text{W}/(\text{m K})$
 $K_0(x)$ = modified Bessel function of the second kind of order zero
 $K_1(x)$ = modified Bessel function of the second kind of order one
 l = characteristic length, m
 Pe_j = Péclet number, $\bar{V}_j l / \kappa$
 $\bar{q}; q$ = heat source, W/m^2 (half-space) and W/m (half-plane); $q = \bar{q}/q_0$
 $R = \sqrt{x_1^2 + x_2^2 + x_3^2}$ (half-space) and $R = \sqrt{x_1^2 + x_2^2}$ (half-plane).
 S = surface-heating region
 $\bar{T}; T$ = temperature rise, K; $T = \bar{T}K/(lq_0)$
 $\bar{t}; t$ = time, s; $t = \kappa \bar{t}/l^2$
 \bar{V}_j = velocity in the x_j direction, m/s
 $\bar{x}_j; x_j$ = coordinate, m; $x_j = \bar{x}_j/l$
 γ = Euler's constant
 κ = thermal diffusivity, m^2/s
 ω_1, ω_2 = frequency domain counterparts of x_1, x_2 , respectively
 ω_t = counterpart of time in the frequency domain
 $_j$ = subscript, partial derivative with respect to x_j coordinate
 \sim = Fourier Transform, e.g., with respect to x_1 ,
 $\int_{-\infty}^{\infty} f(x_1) e^{-i\omega_1 x_1} dx_1$

References

- [1] Komanduri, R., and Hou, Z. B., 2001, "Thermal Modeling of the Metal Cutting Process, Part II—Temperature Rise Distribution Due to Frictional Heat Source at the Tool-Chip Interface," *Int. J. Mech. Sci.*, **43**, pp. 57–88.
- [2] Cowan, R. S., and Winer, W. O., 1992, "Frictional Heating Calculations," *ASM Handbook*, Vol. 18: Friction, Lubrication, and Wear Technology, ASM International, pp. 39–44.
- [3] Kennedy, F. E., 1984, "Thermal and Thermomechanical Effects in Dry Sliding," *Wear*, **100**, pp. 453–476.
- [4] Blok, H., 1937, "Theoretical Study of Temperature Rise at Surfaces of Actual Contact Under Oiliness Lubricating Conditions," *Proc. General Discussion on Lubrication and Lubricants*, Institute of Mechanical Engineers, London, pp. 222–235.
- [5] Carslaw, H. S., and Jaeger, J. C., 1959, *Conduction of Heat in Solids*, Oxford University Press, London.
- [6] Muzychka, Y. S., and Yovanovich, M. M., 2001, "Thermal Resistance Models for Non-Circular Moving Heat Sources on a Half Space," *ASME J. Heat Transfer*, **123**, pp. 624–632.
- [7] Hou, Z. B., and Komanduri, R., 2000, "General Solutions for Stationary/Moving Plane Heat Source Problems in Manufacturing and Tribology," *Int. J. Heat Mass Transfer*, **43**, pp. 1679–1698.
- [8] Beck, J. V., Cole, K., Haji-Sheikh, A., and Litkouhi, B., 1992, *Heat Conduction Using Green's Functions*, Hemisphere, Washington, DC.
- [9] Ling, F. F., Lai, W. M., and Lucca, D. A., 2002, *Fundamentals of Surface Mechanics, With Applications*, Springer-Verlag, New York.
- [10] Campbell, G. A., and Foster, R. M., 1931, *Fourier Integrals for Practical Applications*, Bell Telephone Laboratories, New York.
- [11] Tichy, J., 1991, "Closed-Form Expression for Temperature in a Semi-Infinite Solid Due to a Fast Moving Surface Heat Source," *ASME J. Tribol.*, **113**, pp. 828–831.
- [12] Liu, S., Wang, Q., Rodgers, M., Keer, L., and Cheng, H. S., 2002, "Temperature Distributions and Thermoelastic Displacements in Moving Bodies," *Comput. Model. Eng. Sci.*, **3**(4), pp. 465–482.
- [13] Fischer, F. D., Werner, E., and Knothe, K., 2000, "The Surface Temperature of Half-Plane Subjected to Rolling/Sliding Contact with Convection," *ASME J. Tribol.*, **122**, pp. 864–866.
- [14] Liu, S. B., Wang, Q., and Liu, G., 2000, "A Versatile Method of Discrete Convolution and FFT (DC-FFT) for Contact Analyses," *Wear*, **243**, pp. 101–110.

Effects of Periodic Structures on the Coherence Properties of Blackbody Radiation

L. Hu

A. Schmidt

A. Narayanaswamy

G. Chen*

e-mail: gchen2@mit.edu

Mechanical Engineering Department,
Massachusetts Institute of Technology,
Cambridge, MA 02139

Radiative properties have been studied for one-dimensional dielectric multilayer structures subjected to blackbody radiation sources. The total hemispherical transmittances are calculated for periodic structures and structures with random variation in layer thickness, using wave-optics and ray-tracing methods. Simulation results show that for periodic structures, the transmittance calculated using wave optics approaches a nonzero constant value with an increasing number of layers, while the transmittance obtained using the ray-tracing method asymptotically approaches zero. For random structures, the transmittance given by wave optics drops to zero at different rates depending on the order of random variations in layer thickness. It is found that the wave interference effect always plays a role when dealing with multilayer structures. The results are explained based on extended and localized waves. [DOI: 10.1115/1.1795241]

Keywords: Radiative Properties, Wave Optics, Ray Tracing, Multilayer, Disordered Media, Localization

1 Introduction

The coherence theory of light deals with the correlation of electromagnetic fields at two space/time points. To measure the correlation, the coherence length of waves was introduced and has been used extensively as a scale for observation of interference phenomena [1]. The coherence length is often employed as an indication of whether the transport falls into the wave regime or the particle regime. In the particle regime, the ray-tracing method (i.e., energy method) can be used and the intensity of the electromagnetic fields is directly superposed. On the other hand, in the wave regime, it is the fields that need to be superposed, where the phase and amplitude of the electromagnetic waves are obtained by solving Maxwell's equations. Optical coherence theory has been employed to analyze radiative properties of single-layer and multilayer thin films with a small number of layers (up to three layers) [2–5]. These studies found that, in general, the wave-method results approach the ray-tracing results when the films are much thicker than the coherence length of the radiation field, which for blackbody radiation is of the order of the wavelength given by Wien's displacement law [6–10]. Based on these studies, it is generally assumed that ray-tracing methods can be applied to study the optical properties of single and multilayer thin dielectric films when the layer thickness is larger than the coherence length of the radiation field.

The above conclusion, however, has not been tested for structures with a larger number of layers. In recent years, studies on the phonon transport, which shares many similarities to photon transport in periodic structures, suggest that this may not be the case. It was observed that the phonon transmissivities in superlattices calculated from the wave-optics method and from the ray-tracing method do not approach each other, but the cause of this phenomenon was not elaborated [11]. The similarity between phonon and photon transport leads us to believe that similar behavior will occur for the thermal radiative properties of multilayer structures and prompts us to reexamine the coherence of blackbody radiation in multilayer structures. In the present work, we study the total hemispherical transmittance of alternating multilayer thin film

structures, using both the wave method and the ray-tracing method, for periodic structures and structures with random thickness variations. The simulation results show that for perfectly periodic structures, wave optics yields a transmittance that soon approaches a nonzero plateau for a large number of layers. The ray-tracing result asymptotically approaches zero as the inverse of the number of layers. The transmittance given by wave optics drops to zero at different rates depending on the order of random variations of thickness added to the perfectly periodic structures. These behaviors are observed for both thin and thick layers, as compared to the coherence length of the blackbody radiation. These results imply that for one-dimensional multilayer thin film structures with perfectly aligned interfaces, there may not be an incoherence regime in which the ray-tracing method can be applied.

The phenomenon, although surprising from the coherence-length point of view, may be explained by localization theory, which addresses the problem of wave propagation in disordered media. The localization theory was proposed by Anderson in his classic paper to study the quantum transport of electrons in crystal lattices [12]. He found that the absence of diffusion (i.e., localization) occurs with the introduction of randomness to the lattice potential. Researchers soon discovered that almost all classic wave equations have localized solutions when solved for a random medium [13,14]. The localization of electromagnetic wave has been experimentally observed [15]. A proper scaling theory for the exponential decay of the localized modes has also been developed [16]. It was found that all the states in one- (1D) or two-dimensional (2D) systems can be localized in the presence of infinitesimal disorder, while in three-dimensional (3D) systems, the picture is not very clear because some modes may not be localized even with a high degree of disorder [17–19].

Although our current study is mainly focused on fundamental understanding, the 1D multilayer structures may find potential applications in thermophotovoltaic devices for radiation spectral control [20]. Compared to 2D or 3D photonic crystal structures [21,22], the geometries of 1D structures are much simpler and are more easily fabricated. Better understanding of radiation transport in multilayer structures is also critical in rapid thermal processing [5].

*Corresponding author.

Contributed by the Heat Transfer Division for publication in the JOURNAL OF HEAT TRANSFER. Manuscript received by the Heat Transfer Division December 5, 2003; revision received March 18, 2004. Associate Editor: S. Thynell.

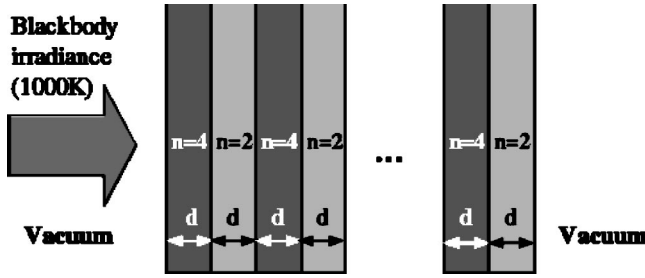


Fig. 1 Schematic of the multilayer structure. The “unit cell” consists of two nonabsorbing materials which have refractive indices of 4 and 2, respectively. The thickness of individual layer is d .

2 Physical Models and Formulation

A model structure is shown in Fig. 1. It consists of multiple layers of thin films. In the current model, two nonabsorbing materials with refractive indices of 4 and 2, respectively, are considered. These refractive indices are chosen arbitrarily, although they are close to those of some common materials. Absorption is not included because the focus is on the fundamental behavior of electromagnetic (EM) waves in periodic structures. Absorption can create artificial damping of waves that masks the phenomenon to be addressed in this paper. A pair of layers forms the “unit cell” of the multilayer structure. The multilayer structure is in vacuum, and blackbody radiation is incident on one side of it. The spectral distribution is of the form (Planck distribution),

$$I_{b,\lambda}(\lambda, T) = \frac{2hc_0^2}{\lambda^5 [\exp(hc_0/\lambda k_b T) - 1]} \quad (1)$$

where h and k_b are the Planck and Boltzmann constants, respectively, λ is the wavelength in vacuum, T is the absolute temperature of the blackbody, c_0 is the speed of light in vacuum, and subscript b denotes blackbody radiation. In the present work, only temporal coherence of the blackbody radiation is considered. The coherence length of a blackbody radiation field is given by [10]

$$l_c = 0.15 \frac{hc}{k_b T} \quad (2a)$$

and in vacuum, it can be rewritten as

$$l_c T = 2167.8 \mu\text{m} \cdot \text{K} \quad (2b)$$

where c is the speed of light and the other symbols have the same definitions as in Eq. (1). The expression in Eq. (2b) is very similar to Wien’s displacement law [19]

$$\lambda_{\max} T = 2897.8 \mu\text{m} \cdot \text{K} \quad (3)$$

where λ_{\max} is the wavelength corresponding to the peak blackbody radiation at a given temperature T . In this sense, in a homogeneous medium, the coherence length relates to the effective wavelength of the blackbody radiation. According to Eq. (2a), the coherence lengths at 1000 K in $n=2$ and $n=4$ are $1.08 \mu\text{m}$ and $0.54 \mu\text{m}$, respectively. For simplicity, the smaller value is taken as the coherence length l_c in the following text.

In our models, the multilayer structures are assumed to be one-dimensional. Surface roughness and nonparallelism are not considered. The disorder is introduced by varying the film thicknesses (i.e., adding a uniform random distribution to the nominal layer thickness). Wave optics and ray-tracing methods were used to predict the overall transmittance of the structures. We further ignore the spatial coherence properties of the blackbody radiation source. At each angle of incidence, the incoming blackbody radiation is approximated by a plane wave.

2.1 Wave Optics. The transfer matrix method is used to calculate the transmittance and reflectance for the multilayer structure [1]. These are standard methods for thin film structures and will not be explained in detail here. The transmittance of a multilayer structure containing m layers can be calculated from

$$T_m = 1 - R_m = 1 - \frac{\left| (m_{11} + m_{12} p_{m+1}) p_0 - (m_{21} + m_{22} p_{m+1}) \right|^2}{\left| (m_{11} + m_{12} p_{m+1}) p_0 + (m_{21} + m_{22} p_{m+1}) \right|^2} \quad (4)$$

where 0 and $m+1$ denote the materials adjacent to the first layer and the last layer, respectively, and m_{ij} is the element of the 2×2 overall transfer matrix M of the multilayer structure, which is the product of the transfer matrix of individual layers,

$$M = \prod_{j=1}^m M_j = \begin{bmatrix} m_{11} & m_{12} \\ m_{21} & m_{22} \end{bmatrix} \quad (5)$$

where

$$M_j = \begin{bmatrix} \cos \varphi_j & -\frac{i}{p_j} \sin \varphi_j \\ -i p_j \sin \varphi_j & \cos \varphi_j \end{bmatrix} \quad (6)$$

The elements in M_j are given by

$$\varphi_j = \frac{\omega n_j d_j \cos \theta_j}{c_0} \quad (7a)$$

$$p_{j,TM} = \sqrt{\frac{\mu_j}{\varepsilon_j}} \cos \theta_j \quad (7b)$$

$$p_{j,TE} = \sqrt{\frac{\varepsilon_j}{\mu_j}} \cos \theta_j \quad (7c)$$

where j denotes the j th layer, counting from the side of incident radiation, ω is the frequency of the incident EM waves, n is the refractive index of the corresponding layer, d represents the layer thickness, θ is the angle that the propagation direction of the wave makes with the normal to the layer interface, and ε and μ are the electric permittivity and magnetic permeability of the corresponding layer, respectively. The acronyms TM and TE represent transverse magnetic polarization and transverse electric polarization, respectively. It is assumed here that $\mu = \mu_0$ (permeability in vacuum) for all the layers, which is true for most materials in the infrared wavelength range.

2.2 Ray Tracing. Ray tracing is extensively employed in designing optical instruments, analyzing radiation heat exchange through windows, etc. When the wavelength is far less than the feature size of the medium, Maxwell’s equations reduce to the eikonal equation, which is the basis of geometric optics [1], or the ray-tracing method. The ray-tracing method tracks the trajectories of light rays and applies the laws of reflection and refraction successively. This method determines the paths of light rays based on simple geometric rules and excludes any possible interference effects.

For multilayer structures, the following recursive formulas have been developed for calculating the reflectance and transmittance of multilayer films [23].

$$R_m = R_{m-1} + \frac{\rho_{m,m+1} T_{m-1}^2}{1 - \rho_{m,m+1} R_{m-1}} \quad (8a)$$

$$T_m = 1 - R_m \quad (8b)$$

where the results are for a structure with m layers, $\rho_{m,m+1}$ is the reflectivity (TE or TM) at the interface between layer m and outside medium ($m+1$), which can be calculated from,

$$\rho_{m,m+1(TM)} = \left(\frac{n_m \cos \theta_{m+1} - n_{m+1} \cos \theta_m}{n_m \cos \theta_{m+1} + n_{m+1} \cos \theta_m} \right)^2 \quad (9a)$$

$$\rho_{m,m+1(TE)} = \left(\frac{n_m \cos \theta_m - n_{m+1} \cos \theta_{m+1}}{n_m \cos \theta_m + n_{m+1} \cos \theta_{m+1}} \right)^2 \quad (9b)$$

2.3 Total hemispherical transmittance. The transmittance given in the above is the spectral directional value. Blackbody irradiance is isotropic, but each monochromatic component at a specific incident angle can be viewed as a plane wave. Integration over all angles and wavelengths is needed to calculate the total hemispherical transmittance of the multilayer structure. The spectral hemispherical transmittance for *TE* or *TM* waves is obtained by integrating over the hemisphere:

$$T_{\lambda,p} = \frac{\int_{\varphi=0}^{2\pi} \int_{\theta=0}^{\pi/2} T(\lambda, \theta) I_{b,\lambda} \cos \theta \sin \theta d\theta d\varphi}{\int_{\varphi=0}^{2\pi} \int_{\theta=0}^{\pi/2} I_{b,\lambda} \cos \theta \sin \theta d\theta d\varphi} = 2 \int_{\theta=0}^{\pi/2} T(\lambda, \theta) \cos \theta \sin \theta d\theta \quad (10)$$

where p denotes the polarization status *TE* or *TM*, $T(\lambda, \theta)$ is given by Eq. (4) or (8b) depending on wave or ray tracing approach, and $I_{b,\lambda}$ is the Planck distribution given by Eq. (1). The polarized total hemispherical transmittance can be calculated based on the spectral hemispherical transmittance in Eq. (10) as follows:

$$T_p = \frac{\pi \int_0^{\infty} T_{\lambda,p} \cdot I_{b,\lambda} d\lambda}{\sigma T^4} \quad (11)$$

where $\sigma = 5.67 \times 10^{-8} \text{ W/m}^2 \cdot \text{K}^4$ is the Stefan-Boltzmann constant. Blackbody radiation is unpolarized. The electric field has no definite orientation and can be resolved into equal *TE* and *TM* components. Then the unpolarized total hemispherical transmittance is the average of T_{TE} and T_{TM} :

$$T = (T_{TE} + T_{TM})/2 \quad (12a)$$

Similarly, the unpolarized spectral hemispherical transmittance is given by

$$T_{\lambda} = (T_{\lambda,TE} + T_{\lambda,TM})/2 \quad (12b)$$

2.4 Scaling of localization. Localization is a result of wave interference. Destructive interference of reflected and scattered waves effectively cancels the waves (in the case of an external incident wave) or confines the wave in a finite region (in the case of a source inside the medium). The localization length is often used as a measure of the attenuation of waves in random media. The definition of the localization length in one-dimensional systems is given by [24,25],

$$l = - \frac{2L}{\langle \ln T \rangle} \quad (13)$$

where L is the total thickness of the medium and $\langle \ln T \rangle$ is the ensemble average of the logarithmic transmittance. Equation (13) is a simple scaling rule that depicts the exponential decay behavior of localized waves. In our model, the individual layers have the same base thickness, we express the localization length in terms of the number of layers. The localization length is determined by the randomness of the system as well as the frequency of the incoming waves. For a given frequency, the intensity of localized waves decays exponentially along the propagation direction, where the decay rate depends on the disorder of the medium. As an example, we calculated the spectral directional transmittance for normal incident waves. With random variation in the layer thickness being on the order of $4l_c$, the localization lengths

for $1 \mu\text{m}$ and $2.898 \mu\text{m}$ waves are 5 layers and 10 layers, respectively. The latter wavelength is corresponding to the maximum intensity given by Eq. (3).

Rigorously, this definition is only valid when L is infinitely long. However, in computer simulations or experiments, only systems with finite dimensions can be dealt with. The localization length is thus being used as a comparison scale. For $l < L$, the waves will almost decay to zero at the boundary. In this sense, the system is effectively infinite to the waves with localizations lengths less than L and these waves exhibit exponential decay. For waves with a localization length l larger than the system length L , the transmittance may not obey exponential decay [24].

3 Results and Discussion

Numerical methods were used to calculate transmittance, integrated over both wavelength and angle. For a temperature of 1000 K, 99% of blackbody radiation emissive power is concentrated between $0.1 \mu\text{m}$ and $30 \mu\text{m}$, which were selected as the integration upper and lower limits, respectively. The evaluation of transmittance based on ray tracing is straightforward. However, in the case of wave optics, due to interference effects the corresponding transmittance value is very sensitive to frequency change. It exhibits highly oscillatory behavior and needs special treatment for numerical integration. There exist some standard methods for integrating highly oscillatory triangular functions [26], but in general there is no preferred method for an irregularly oscillatory integrand, such as Eq. (4). We found that Simpson's method [27], with twice as many grid points, is generally more effective than other more advanced integration techniques, such as the Gaussian-quadrature family which is ideal for smooth functions, considering both computational time and accuracy. For integration over the incident angle, fewer grid points were used because the transmittance-angle function is smooth. Typically 40 grid points can yield satisfactory accuracy.

3.1 Periodic structures. In the present paper, periodic structures are defined as systems consisting of layers with identical thickness. As shown in Fig. 1, the multilayer structure is formed by alternating nonabsorbing layers of the same thickness but different indices of refraction. For a system containing an even number of layers, the "unit cell" consists of two layers that have refractive indices of 4 and 2, sequentially. For a system containing an odd number of layers, the first layer has a refractive index of 4 and the rest of the system can be viewed as constructed with a unit cell that still consists of double layers, but with switched positions (i.e., 2 and 4), sequentially. The results for the odd and the even number of layers differ slightly, but the trends are similar in all cases. For convenience, we will only present results for systems containing an even number of layers, while all the conclusions also hold true for odd-layer systems.

If the individual layer thickness is less than the coherence length, interference effects are expected. Figure 2 shows the transmittance value with respect to the number of total layers for layer thickness smaller than the coherence length. The transmittance curves vary according to the layer thickness, which suggests strong wave interference in the systems. The result obtained using the ray-tracing method is also plotted in the same figure for comparison. As expected, the ray-tracing result does not agree with those obtained using wave optics because interference exists.

Detailed analysis for the thickness dependence of transmittance is shown in Fig. 3 for structures with few numbers of layers. It reveals that for thick layers, the ray-tracing approach is a good approximation for up to three layers; a result also shown in previous research [2–5]. For a large number of layers, however, even when the layer thickness exceeds the coherence length, wave optics still does not give the same predictions as the ray-tracing method, as shown in Fig. 4. The transmittances calculated using the wave-optics method for different thicknesses overlap and approach a nonzero value, while those calculated using the ray-tracing method asymptotically approach zero. This implies that

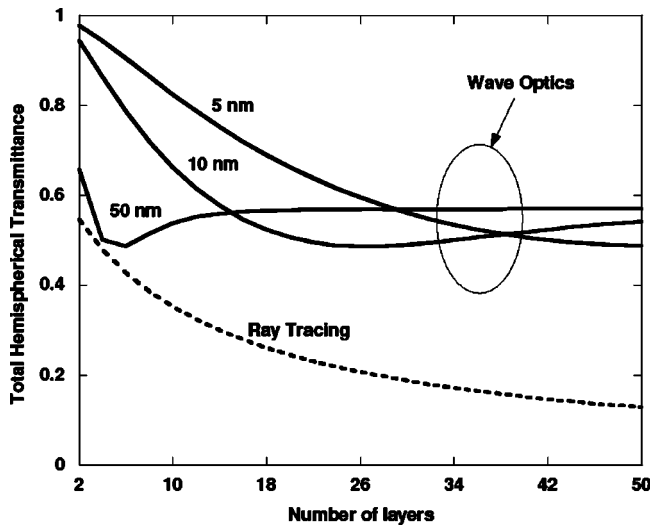


Fig. 2 The total hemispherical transmittance of three periodic structures as a function of the number of total layers. The individual layer thicknesses of the structures are 5 nm, 10 nm and 50 nm, respectively, which are much less than the coherence length. The thickness dependence of the transmittance is due to interference effects.

interference effects still need to be considered in periodic structures even if every single layer is thicker than the blackbody coherence length. The ray-tracing method fails to accurately predict the transmittance because it neglects phase information. It is interesting to note that varying the nominal layer thickness does not affect the simulation results at a given temperature; the number of layers is the only determinant variable when the layer thickness exceeds the coherence length of the blackbody radiation.

A frequency analysis can provide more insight into the problem. Figure 5(a) shows the frequency dependence of the directional transmittance at normal incidence and Fig. 5(b), the unpolarized spectral hemispherical transmittance for a 100-layer periodic structure. The thickness of the individual layers is $8 \mu\text{m}$, larger than the coherence length. Figure 5(a) clearly shows the stop-band behavior. In the transmission bands, the transmittance approaches one, indicating that the waves are extended throughout the whole structure. In the stop band, the transmittance is zero due to the destructive interference effect. This is analogous to the band structure of electrons and phonons in periodic structures, which

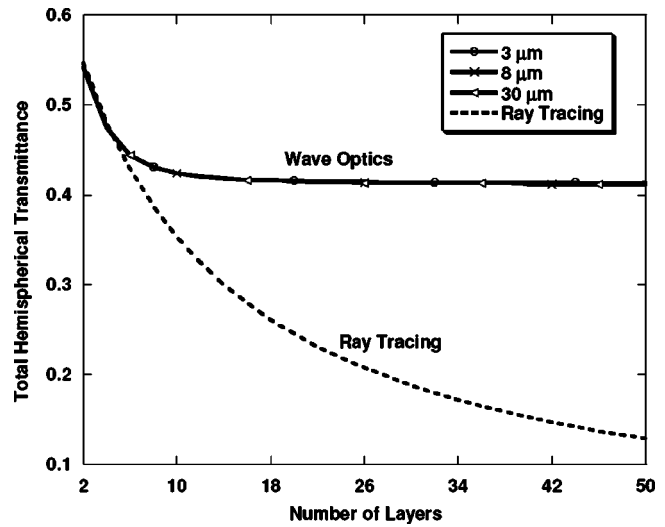


Fig. 4 The total hemispherical transmittance of three periodic structures as a function of the number of total layers. The individual layer thicknesses of the structures are $3 \mu\text{m}$, $8 \mu\text{m}$ and $30 \mu\text{m}$, respectively, which are larger than the coherence length. The transmittances calculated using the wave optics method for different thicknesses overlap and approach a non-zero value, while that calculated using the ray tracing method asymptotically approaches zero.

can also be obtained by applying Bloch periodic boundary conditions to Maxwell's equations [19]. Figure 5(b) is simply an average of the band structure along different directions. This shows that waves in periodic structures are either extended through the whole structure (in the pass bands) or are completely destroyed due to destructive interference (in the stop bands). The average of the extended waves leads to the finite transmittance in Fig. 4. The fact that the transmittance does not change above 10–20 layers suggests that these are the numbers of layers needed to form the nearly complete destructive and constructive interference required for the formation of the stop and pass bands. As the layer thickness increases, the pass bands and stop bands become narrower but more bands form. The average of the spectral transmittance gives the same results, which are the thickness- and layer-independent transmittances shown in Fig. 4.

In comparison, the ray-tracing method leads to a transmittance, which continuously decays as the number of layers increases. Fig-

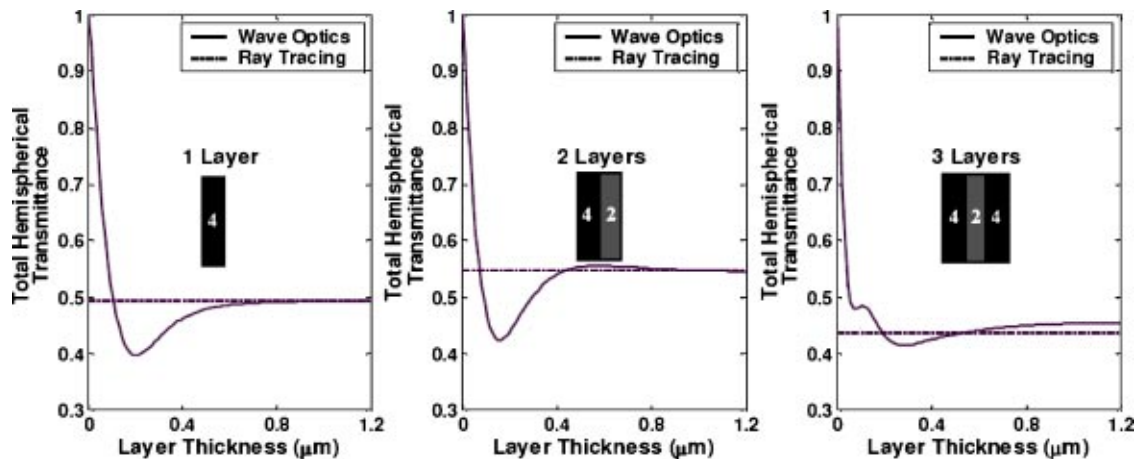


Fig. 3 The thickness dependence of the total hemispherical transmittance for up to three layers. The refractive index of each layer is given in the illustration. In the thick film region, the transmittance values of all three structures approach constants, which are close to the values predicted by ray tracing method.

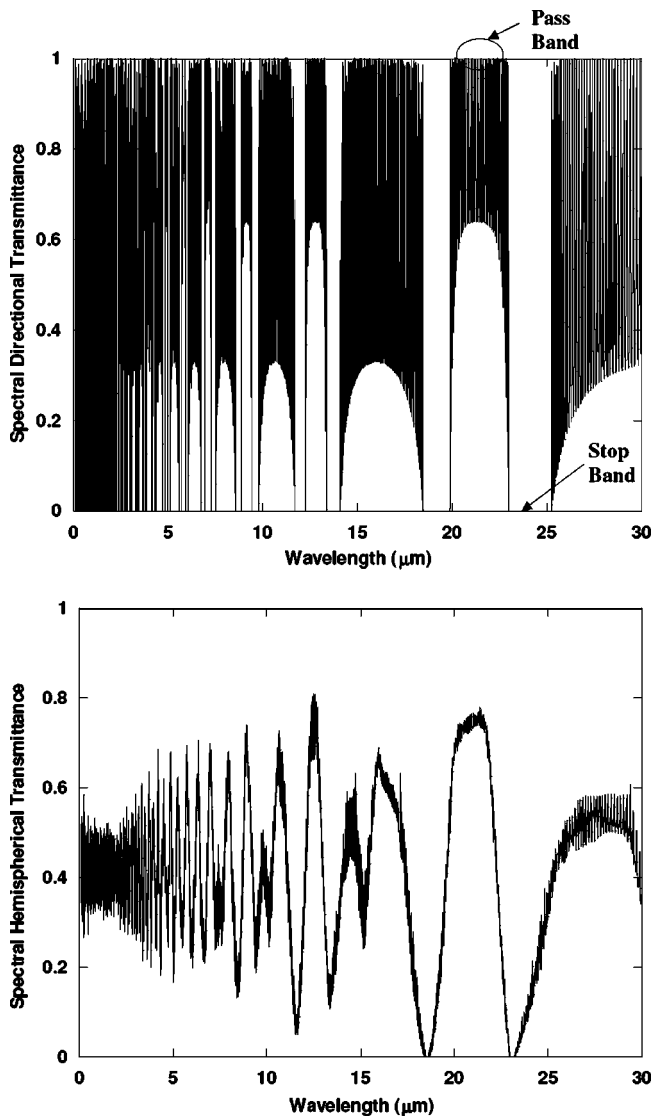


Fig. 5 (a) The spectral directional transmittance of a 100-layer periodic structure for normal incident waves. The thickness of individual layers is $8 \mu\text{m}$. Stop band and pass band are shown in the figure, (b) The spectral hemispherical transmittance for the same structure.

ure 4 shows that for ray tracing, the transmittance decreases inversely with the number of layers. This is because under the ray-tracing picture, each layer adds an additional reflection to the radiation transmitted through previous layers.

Although the above results indicate that the coherence length is not a proper criterion for justifying the ray-tracing method for multilayer structures, the fact that the transmittance is independent of the individual layer thickness as the layers become thicker than the coherence length still suggests its usefulness. If the layer thickness is smaller than the coherence length, the average values of radiative properties over the spectrum width of the incoming radiation depend on the layer thickness, as is seen from Fig. 3. In the other limit, the average properties are independent of the individual layer thickness, as is clear from Fig. 4. However, due to the persistence of the wave effects (i.e., the formation of pass and stop bands for periodic structures), the characteristics of the electromagnetic waves in the structure are very different from those required by the ray-tracing method, and the two methods never agree with each other. The existence of wave effects in large sys-

tems is not surprising in solids. Extended electron waves in crystals lead to different materials: metals, insulators, and semiconductors.

3.2 Structures with randomness. The above discussions are focused on perfectly periodic structures. Real physical structures may have thickness variation, interface roughness, and non-parallel interfaces. The question is then whether these disorders can lead to the agreement between the wave and the ray-tracing results. As a first step to investigate the effects of disorder, the variation of individual layer thickness is considered as the only form of disorder in the present structures. The variation is introduced by adding a random distribution onto the layer thickness,

$$d_j = \bar{d} + \delta \cdot \sigma \quad (14)$$

where d_j is the thickness of the j th layer, \bar{d} is the base thickness of the layers, δ represents a uniform distribution on $[0, 1]$, and σ is the order of randomness, which is in length units.

Figure 6(a) shows the dependence of the transmittance on the randomness for structures with individual layer thickness larger than l_c , where l_c is the coherence length. We did calculations based on three different base thickness, $5 \mu\text{m}$, $8 \mu\text{m}$ and $10 \mu\text{m}$, respectively. It was found that the transmittance does not depend on the base thickness if the thickness is larger than the coherence length. Also shown in Fig. 6(a) is the result obtained using the ray-tracing method. The transmittances are the ensemble average values over large sets of random numbers. Figure 6(b) shows both the nonaveraged results and the ensemble average results. Every point in the ensemble average curves represents the result of averaging over 100 configurations. As shown in the figure, the ensemble averaging smooths the transmittance curve. In general, the fluctuations are not significant even without averaging, especially in the presence of higher randomness where the localization effects dominate. For all the cases shown in the figure, the thickness of every layer is larger than the blackbody coherence length at 1000 K. For small numbers of layers, the transmittance is nearly independent of the randomness and overlap with ray-tracing results. However, for structures with more layers, the two methods do not lead to the same results for either periodic or random structures. According to the figure, larger randomness leads to more rapid decay. The transmittance exhibits exponential decay in the regime of higher randomness and large number of layers, which is more rapid than the inverse N (number of layers) decay predicted by the ray-tracing method. Figure 6(c) is plotted in semi-log scale to show the exponential decay. In the presence of slight or moderate randomness, the transmittance decays at slower rate. It is interesting to notice in the figure that with certain randomness ($\sigma = 0.6l_c$) the wave-optics result follows a similar decay trend as the ray-tracing result. We believe that this is just a coincidence, and the two results will eventually diverge as the number of layers increases. More information can be provided through frequency analysis because the decay of intensity is an integral effect of all wavelengths in the blackbody spectrum.

Figure 7 presents the wavelength dependence of transmittance for a 100-layer random structure, of which the base thickness is $8 \mu\text{m}$. The figure clearly shows that the transmittance in the $0.5\text{--}10 \mu\text{m}$ range falls virtually to zero (i.e., waves are localized) when the magnitude of randomness is on the order of the coherence length. The localization of EM waves is frequency dependent as shown in Fig. 7. The simulation results demonstrate that higher frequency waves are more prone to be localized, which agrees with the previous findings [17]. In contrast, long wavelength components are more difficult to be localized because they are not capable of resolving small amounts of randomness. Consequently, the low-randomness cases shown in Fig. 7 tend to overlap with the periodic case in the long wavelength regime. With slight or moderate randomness, a non-negligible fraction of energy is not localized such that the overall transmittance decays at a slower rate than exponential. As a very special case, with moderate random-

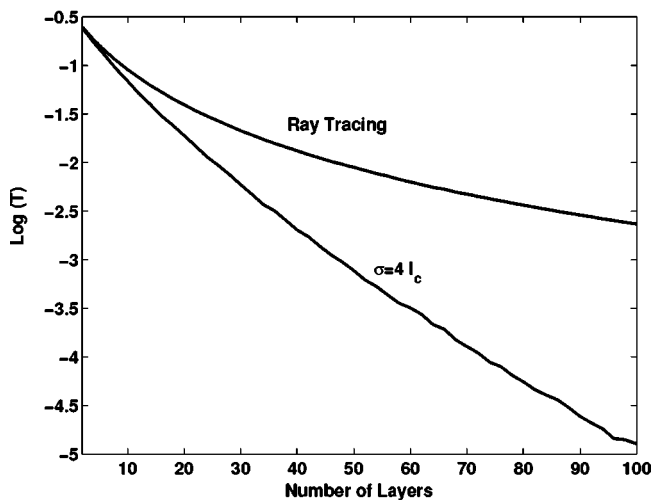
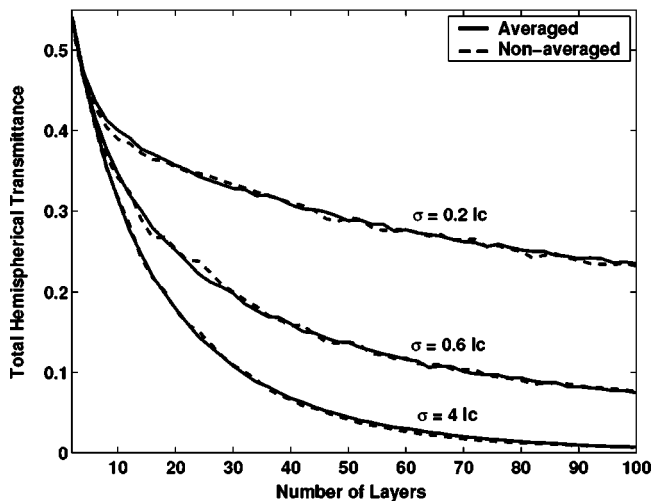
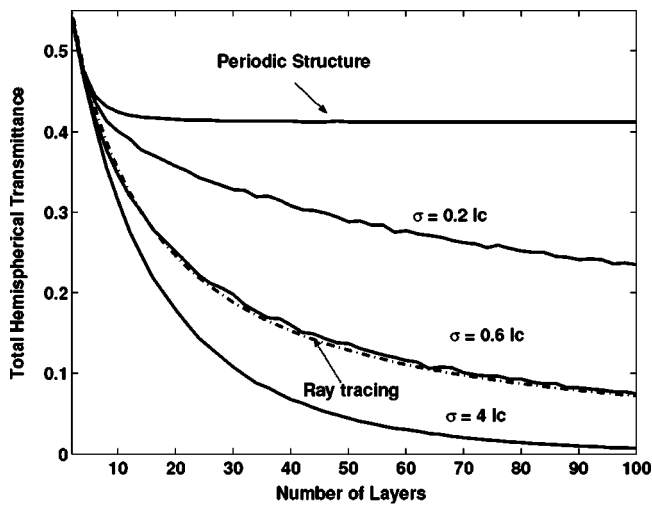


Fig. 6 (a) The total hemispherical transmittance as a function of the number of layers, where σ is the order of randomness and l_c is the localization length. The base thickness of individual layers is larger than the coherence length. (b) The averaged and non-averaged transmittance. (c) The y axis is $\text{Log}(T)$. In the presence of high order of randomness ($\sigma=4 l_c$) and large number of layers, the transmittance decays exponentially.

ness ($\sigma=0.6l_c$), the ray-tracing method could give similar results as the wave-optics method, as shown in Fig. 6(a). As the ran-

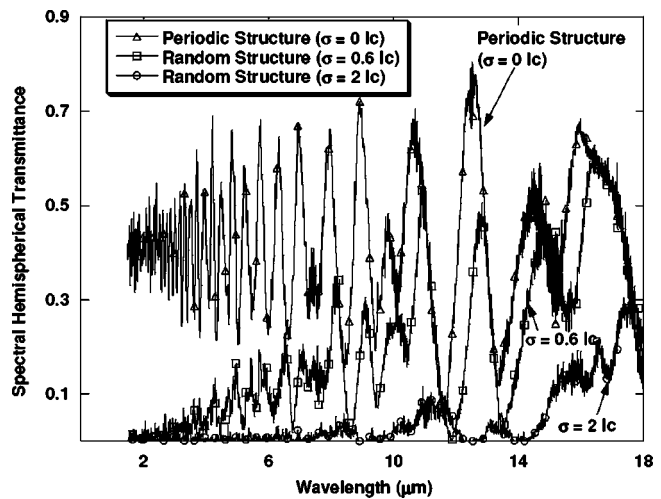


Fig. 7 The spectral hemispherical transmittances of different random systems, where σ is the order of randomness and l_c is the localization length. High frequency (short wavelength) components are localized relatively more easily.

domness increases, the lower-frequency components are localized. When the randomness is larger than the coherence length, most energy is localized and the average transmittance follows exponential decay.

It should be pointed out that zero transmittance in the stop band is not caused by absorption because the materials are nonabsorbing. The exponential decay shown in the figures is caused by the localization of the EM waves in the disordered multilayer structures, which does not incur any energy dissipation in the media. The localization is due to the destructive interference of EM wave packets, which leads to the eventual vanishing of the waves inside the medium and total reflection of the incident waves. The concept of localization differs from the conventional image that the wave propagation in random structures is a series of independent scattering events where the phase is destroyed everywhere in the medium [28]. More detailed analysis regarding field distributions in disordered systems can be found in [29,30].

4 Conclusions

The total hemispherical transmittance of multilayer structures for blackbody incident radiation is numerically studied in both periodic and random one-dimensional systems, using both the wave-optics method and the ray-tracing method. It is found that the two methods usually lead to different results even when the individual layer thickness is much larger than the coherence length of the blackbody radiation source. This result, although surprising from the coherence-length point of view, can be well explained by localization theory. This study suggests that for multilayer structures with large number of layers, for most cases ray tracing is invalid and wave effects need to be taken into account. It should be pointed out that the present work does not consider disorder introduced by surface roughness, internal scattering, or nonparallel interfaces, which are essentially three-dimensional systems. Some modes may not be localized in such three-dimensional disordered systems where the diffusion process may dominate instead of localization.

Acknowledgments

We acknowledge J.J. Sáenz and J.-J. Greffet for stimulating discussion. This work was supported by DoD/ONR MURI on electromagnetic Metamaterials through UCLA (ONR Grant No. N00014-01-1-0803).

Nomenclature

I = intensity of light [$W/(m^2 \cdot sr \cdot \mu m)$]
 L = thickness of the medium (μm)
 M = characteristic matrix
 R = reflectance
 T = temperature (K); transmittance
 c_0 = speed of light in vacuum (m/s)
 d = layer thickness (μm)
 h = Planck constant (J·s)
 k_b = Boltzmann constant (J/K)
 l = localization length (μm)
 l_c = coherence length (μm)
 m_{ij} = element of the characteristic matrix
 n = refractive index
 p = parameter in the characteristic matrix

Greek Symbols

δ = order of randomness (μm)
 ϵ = electric permittivity (F/m)
 θ = angle of incidence, refraction or reflection (rad)
 λ = wavelength (μm)
 μ = magnetic permeability (H/m)
 ρ = reflectivity
 σ = random distribution
 φ = parameter in the characteristic matrix
 ω = frequency (rad/s)

Subscripts

b = blackbody radiation
 c = coherence
 i = in the i th layer
 i, j = at the medium i side of the $i-j$ interface
 j = in the j th layer
 m = system with m layers
 $m+1$ = the environment adjacent to the m th layer
 $m, m+1$ = from layer m to layer $m+1$ at interface m
max = maximum
 p = polarized
 TE = transverse electric polarized
 TM = transverse magnetic polarized
 λ = at given wavelength
0 = the environment adjacent to the first layer

References

- [1] Born, M., and Wolf, E., 1989, *Principles of Optics*, Sixth Corrected ed., Pergamon, Oxford.
- [2] Chen, G., and Tien, C. L., 1992, "Partial Coherence Theory of Thin Film Radiative Properties," *ASME J. Heat Transfer*, **114**, pp. 636–643.
- [3] Richter, K., Chen, G., and Tien, C. L., 1993, "Partial Coherence Theory of Multilayer Thin-Film Optical Properties," *Opt. Eng. (Bellingham)*, **32**, pp. 1897–1903.
- [4] Zhang, Z. M., 1994, "Optical Properties of Layered Structures for Partially Coherent Radiation," *Heat Transfer 1994—Proc. of 10th International Heat Transfer Conference*, Brighton, UK, G. F. Hewitt, ed., Institute of Chemical Engineers, Rugby, Warwickshire, UK, **2**, pp. 177–182.
- [5] Wong, P. Y., Hess, C. K., and Miaoulis, I. N., 1992, "Thermal Radiation

- Modeling in Multilayer Thin Film Structures," *Int. J. Heat Mass Transfer*, **35**(12), pp. 3313–3321.
- [6] Mehta, C. L., and Wolf, E., 1964, "Coherence Properties of Blackbody Radiation I: Correlation Tensors of the Classic Field," *Phys. Rev.*, **134**(5A), pp. A1143–A1149.
 - [7] Mehta, C. L., and Wolf, E., 1964, "Coherence Properties of Blackbody Radiation II: Correlation Tensors of the Quantized Field," *Phys. Rev.*, **134**(5A), pp. A1149–A1153.
 - [8] Mehta, C. L., and Wolf, E., 1967, "Coherence Properties of Blackbody Radiation, III: Cross-Spectral Tensors," *Phys. Rev.*, **161**(5), pp. 1328–1334.
 - [9] Kano, Y., and Wolf, E., 1962, "Temporal Coherence of Blackbody Radiation," *Proc. Phys. Soc. London*, **80**, pp. 1273–1276.
 - [10] Mehta, C. L., 1963, "Coherence-Time and Effective Bandwidth of Blackbody Radiation," *Nuovo Cimento*, **XXVIII**(2), pp. 401–408.
 - [11] Chen, G., 1999, "Phonon Wave Heat Conduction in Thin Films and Superlattices," *ASME J. Heat Transfer*, **121**, pp. 945–953.
 - [12] Anderson, P. W., 1958, "Absence of Diffusion in Certain Random Lattices," *Phys. Rev. Lett.*, **109**(5), pp. 1492–1505.
 - [13] Kotulski, Z., 1993, "Wave Propagation in Randomly Stratified Media and Anderson Localization," *Proc. of Euromech Colloquim: Chaos and Noise in Dynamical Systems*, Spala, Poland, T. Kapitaniak, and J. Brindley, eds., World Scientific Publishing, River Edge, NJ, **308**, pp. 138–146.
 - [14] John, S., 1990, "The Localization of Waves in Disordered Media," *Scattering and Localization of Classical Waves in Random Media*, P. Sheng, ed., World Scientific, Singapore.
 - [15] Albada, M. P., Mark, M. P. and Lagendijk, A., 1990, "Experiments on Weak Localization of Light and Their Interpretation," *Scattering and Localization of Classical Waves in Random Media*, P. Sheng, (ed.), World Scientific, Singapore.
 - [16] Sheng, P., 1995, *Introduction to Wave Scattering, Localization, and Mesoscopic Phenomena*, Academic Press, New York.
 - [17] Sheng, P., White, B., Zhang, Z. Q., and Papanicolaou, G., 1986, "Minimum Wave-Localization Length in a One-Dimensional Random Medium," *Phys. Rev. B*, **34**(7), pp. 4757–4761.
 - [18] Gredeksul, S. A., and Freilikher, V. D., 1990, "Localization and Wave Propagation in Randomly Layered Media," *Sov. Phys. Usp.*, **33**(2), pp. 134–146.
 - [19] Figotin, A., and Klein, A., 1998, "Localization of Light in Lossless Inhomogeneous Dielectrics," *J. Opt. Soc. Am. A*, **15**(5), pp. 1423–1435.
 - [20] Chubb, D. L., and Lowe, R. A., 1993, "Thin-Film Selective Emitter," *J. Appl. Phys.*, **74**(9), pp. 5687–5698.
 - [21] Sakoda, K., Sasada, M., Fukushima, T., Yamanaka, A., Kawai, N., and Inoue, K., 1999, "Detailed Analysis of Transmission Spectra and Bragg-Reflection Spectra of a Two-Dimensional Photonic Crystal with a Lattice Constant of 1.15 μm ," *J. Opt. Soc. Am. B*, **16**(3), pp. 361–365.
 - [22] Fleming, J. G., Lin, S. Y., El-Kady, I., Biswas, R., and Ho, K. M., 2002, "All-Metallic Three-Dimensional Photonic Crystals with a Large Infrared Bandgap," *Nature (London)*, **417**, pp. 52–55.
 - [23] Siegel, R., and Howell, J., 1992, *Thermal Radiation Heat Transfer*, Third Edition, Hemisphere, Washington, p. 928.
 - [24] Ziegler, K., 2003, "Localization of Electromagnetic Waves in Random Media," *J. Quant. Spectrosc. Radiat. Transf.*, **79–80**, pp. 1189–1198.
 - [25] Siglas, M. M., Soukoulis, C. M., Chan, C.-T., and Turner, D., 1996, "Localization of Electromagnetic Waves in Two-Dimensional Disordered Systems," *Phys. Rev. B*, **53**(13), pp. 8340–8348.
 - [26] Evans, G. A., and Webster, J. R., 1999, "A Comparison of Some Methods for the Evaluation of Highly Oscillatory Integrals," *J. Comput. Appl. Math.*, **112**, pp. 55–69.
 - [27] Hoffman, J. D., 1992, *Numerical Methods for Engineers and Scientists*, McGraw-Hill, New York.
 - [28] Escande, D. F., and Souillard, B., 1984, "Localization of Waves in a Fluctuating Plasma," *Phys. Rev. Lett.*, **52**(15), pp. 1296–1299.
 - [29] Garcia-Martin, A., and Sáenz, J. J., 2000, "Spatial Field Distributions in the Transition from Ballistic to Diffusive Transport in Randomly Corrugated Waveguides," *Phys. Rev. Lett.*, **84**(16), pp. 3578–3581.
 - [30] Froufe-Pérez, L. S., García-Mochales, P., Serena, P. A., Mello, P. A., and Sáenz, J. J., 2002, "Conductance Distributions in Quasi-One-Dimensional Disordered Wires," *Phys. Rev. Lett.*, **89**(24), pp. 246403(1–4).

Mie Scattering Theory for Phonon Transport in Particulate Media

Ravi S. Prasher¹

Assembly Technology Development,
CH5-157,
Intel Corporation,
5000 W. Chandler Blvd.,
Chandler, AZ 85226-3699
e-mail: ravi.s.prasher@intel.com

Scattering theory for the scattering of phonons by particulate scatterers is developed in this paper. Recently the author introduced the generalized equation of phonon radiative transport (GEPRT) in particulate media, which included a phase function to account for the anisotropic scattering of phonons by particulate scatterer. Solution of the GEPRT showed that scattering cross section is different from the thermal transport cross-section. In this paper formulations for the scattering and transport cross section for horizontally shear (SH) wave phonon or transverse wave phonon without mode conversion is developed. The development of the theory of scattering and the transport cross section is exactly analogous to the Mie scattering theory for photon transport in particulate media. Results show that transport cross section is very different from the scattering cross section. The theory of phonon scattering developed in this paper will be useful for the predictive modeling of thermal conductivity of practical systems, such as nanocomposites, nano-micro-particle-laden systems, etc. [DOI: 10.1115/1.1795243]

Introduction

Recently the author modified the equation of phonon radiative transport (EPRT) [1] by including a phase function in the EPRT and called it the generalized equation of phonon radiative transport (GEPRT) [2,3]. GEPRT is given as

$$\mu \frac{\partial I_\omega}{\partial x} = K_u(I_\omega^0 - I_\omega) - K_p I_\omega + \frac{K_p}{4\pi} \int_{4\pi} \Phi(\Omega_i - \Omega) I_\omega(\Omega_i) d\Omega_i \quad (1)$$

where μ is the direction cosine, I the intensity, I^0 the equilibrium intensity, ω the frequency, K_u and K_p are the scattering coefficient for Umklapp (or an inelastic scattering process) and particle scattering respectively (elastic process), and Φ the phase function for the scattered wave from solid angle Ω_i to Ω . ω in the subscript indicates that I is a function of ω . K_u and K_p are given by $K_p = 1/l_p$, $K_u = 1/l_u$ where l_p and l_u are the mfp due particle and Umklapp scattering respectively. Phase function was introduced for phonons to take care of the anisotropic nature of scattering of phonons by particles, which is analogous to the scattering of photons by particles.

GEPRT does not include the normal phonon scattering terms (N process). There are various reasons for not including N process into GEPRT, which was not mentioned in earlier publications [2,3]. The N process conserves momentum and, therefore, does not pose any resistance to heat flow [1]. If only the N process were to exist, a solid will have infinite thermal conductivity. Therefore, typically it is neglected [1]. Although posing no direct resistance by themselves, N processes do play a role in resistance to heat flow. Since the frequency of the incident phonon is changed in inelastic scattering, N processes are responsible for distributing the phonon energy over different frequencies. Because other scattering process are frequency dependent, they feel the effect of phonons scattered by N processes. Therefore the N process indirectly affects the resistance to heat flow. Although N processes have been shown to influence thermal conductivity [4], neglecting N processes may not be totally inaccurate in some temperature ranges [1]. At very low temperatures, boundary scattering is dominant. As the temperature increases, the scattering due to the particles in the medium becomes important. Further increase in tem-

perature makes Umklapp scattering more dominant, and N processes are negligible. It is in the intermediate range between the boundary scattering and the Umklapp scattering where N processes play a role [5]. Inclusion of the N process in the GEPRT is possible in the form of an effective relaxation time following the work of Callaway [4]. However, considering the dominance of other scattering processes, the N process has been ignored in the GEPRT, but we emphasize that it is possible to include it in GEPRT. It is to be noted that Majumdar [1] also ignored the N process due to the reasons cited above in this EPRT.

It is to be noted that GEPRT is valid for a particulate media only if the energy transport inside the particles fall in the wave regime [2,3], i.e. the mfp of phonon is much larger than the characteristic dimension of the particle. Phase function is derived solely based on matching the boundary conditions at the particle and medium interface assuming wave behavior. The implicit assumption inside the particle is that energy transport can still be treated like waves. If the particle diameter is much larger than the energy carrier mfp, then GEPRT is not valid for the particulate media as a whole. In that situation GEPRT has to be applied separately in the particle and the medium, and the boundary conditions have to be matched at the particle and medium interface. Note that as long as the waves are coherent within the particle (i.e. particle size is much larger than the phonon mfp, GEPRT is valid and the phase function approach is valid irrespective of the condition at the interface (i.e., whether the scattering of the phonons is specular or diffuse). If the particle is large but smaller than the mfp so that wave transport is coherent in the particle, then it is possible that interface between the particle and the medium might be rough, leading to diffuse scattering of phonons rather than specular scattering. The degree of specular versus diffuse scattering will dependent on the ratio of the roughness at the interface and the wavelength of the phonons. Since the dominant wavelength of the phonon is inversely proportional to temperature [1], specular scattering is expected to be dominant at low temperatures as the wavelength of the phonons might be larger than the interface roughness. At higher temperature if the wave transport is still coherent in the particle, then the scattering might be diffuse if the dominant wavelength becomes comparable to or smaller than the interface roughness. However, as the temperature increases the Umklapp scattering dominates the phonon transport [1] and, therefore, even though the scattering may be diffuse it might not be important as compared to the Umklapp scattering. In the diffuse situation, one will have to derive the phase function for the diffuse scattering of phonons, however, in this paper phase function will be derived for the specular scattering of phonons by particles.

¹Adjunct Professor, Department of Mechanical and Aerospace Engineering, Arizona State University.

Contributed by the Heat Transfer Division for publication in the JOURNAL OF HEAT TRANSFER. Manuscript received by the Heat Transfer Division December 17, 2003; revision received July 8, 2004. Associate Editor: C. P. Grigoropoulos.

So far the emphasis of the microscale heat transfer community has been on understanding the size effects on the thermal conductivity of a pure material due to reduced dimensions, such as that in a thin film or thin-film superlattice [1,6,7]. For a pure material with atomistic impurity, isotropic assumption has worked quite well and the mfp of phonons is extracted by applying the kinetic theory [1]. To understand the size effects on thermal conductivity the bulk, mfp is fed into the EPRT assuming isotropic scattering [1]. Strictly speaking, this type of modeling is not predictive, as the author [2,3] has shown that mfp can be size dependent. Due to the advent of nanotechnology, now it is possible to mix nanoparticles in a bulk medium, such as nano- and microporous silicon [8], nanofluids [9], and nanowires in a matrix [10] for various applications. Scattering by particles can be highly anisotropic depending on the acoustic and elastic properties of the host medium and the particles [2,3]. Considering that scattering by particles is highly anisotropic and the need to develop predictive modeling capability [11] for better design of materials, it is important to compute the phase function and the scattering and transport cross section for phonons by particles. This paper develops the theory of phonon scattering by particles. The development of the scattering theory for phonons given in this paper is exactly analogous to the Mie scattering theory of photons by particles [12,13] and, hence, the title of the paper is "Mie Scattering Theory for Phonon Transport in Particulate Media." Note that Mie scattering only deals with specular reflection of waves. As it was pointed out earlier, depending on the roughness of the particle surface, it is possible that the scattering of phonons might be totally diffuse or partially diffuse and partially specular. For photons, phase function for the diffuse reflection is available in the literature [14] for a completely absorbing particle. This formulation cannot be applied to phonons because for phonons, the particles are lossless. Therefore, for the diffuse scattering of phonons in the coherent regime, the phase function will have to be derived from first principles, however, this paper only deals with derivation of phase function for specular scattering of phonons by spherical particles.

Although the scattering of elastic waves has been thoroughly covered in the literature [15,16], it is discussed in detail in this paper because the intermediate steps, which have been omitted in most of the literature [15–17], are very important for deriving the phase function. Another difference between the derivation in earlier literature and derivation presented in this paper is that we use the wave zone analysis [17] for the far field scattered wave, which is analogous to the analysis for photons. By employing the wave zone analysis, it is easy to derive the form of the scattering and the phase functions. Furthermore, the wave zone analysis is compared with the detailed analysis to show that they lead to the same result. The wave zone analysis simplifies the analysis of longitudinal and *SV* phonon scattering quite a bit, as they are more complex due to mode conversion. Wave zone analysis has been used to derive the phase function of the longitudinal and *SV* phonon scattering [18,19] by the author. In the wave zone analysis, the scattered field is derived from the asymptotic relation for the scattered wave [17]. The scattering of elastic waves in the literature has only dealt with calculation of the scattering cross section, whereas in this paper we calculate the thermal transport cross section, phonon phase function, and also the scattering cross section. We also show the connection between the transport cross section derived on the basis of geometric acoustics and the detailed calculations based on the Mie scattering theory developed in this paper and resolve some known contradictions. Finally, this paper provides the link between the phonon thermal transport based on GEPRT and the wave transport at the interface between the particle and the medium, which has not been done for *phonon* transport, but is well established for *photon* transport.

The paper is divided into five sections. Section 1 introduces some of the basic definitions and concepts. Section 2 deals with acoustic wave propagation in an elastic medium. Mie scattering theory for phonon scattering is developed in Sec. 3. The unknown

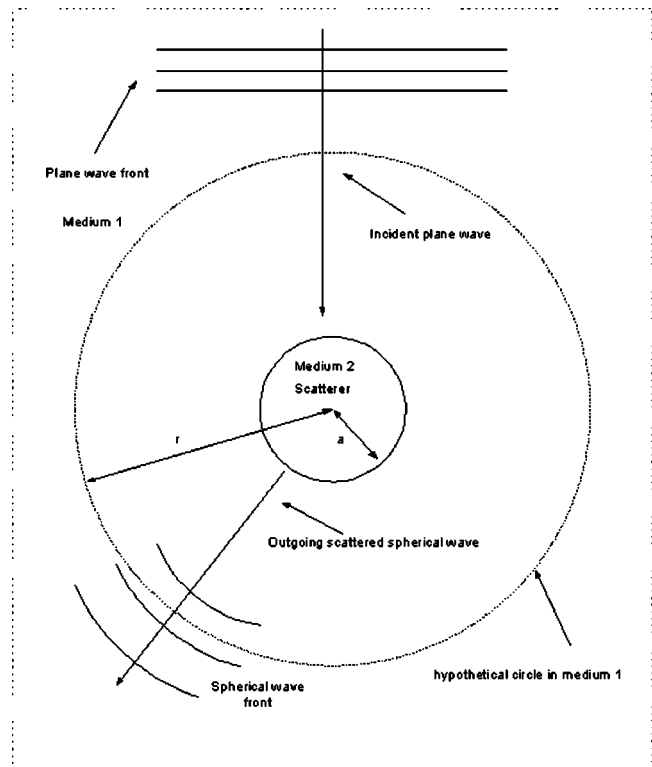


Fig. 1 Scattering a plane elastic wave by spherical scatterer

coefficient in the scattered wave is calculated in Sec. 4. Section 5 cover calculations for elastic, rigid, and cavity scatterers.

1 Basic Definitions and Limitations

Before the full development of the theory is given, the limitations imposed on the development of the theory in this paper are stated below:

1. Only independent scattering is considered. The net effect is that intensities scattered by the various particles must be added.
2. Effect of multiple scattering will be neglected.
3. Theory will be developed for spherical particles although some of the physics and equations are equally valid for particles of any shape.

As electromagnetic (EM) waves are the wave counterpart of photons, elastic waves are the wave counterpart of phonons in a solid medium. Just like an EM wave, the scattered elastic wave at any point in the distant field has the character of a spherical wave [13], i.e., a plane wave after scattering by particle converts into a spherical wave in the distant field. This phenomenon has been schematically illustrated in Fig. 1. Let I_i be the intensity of the incident elastic wave, I_s the intensity of the scattered wave in a point at a large distance r from the particle as shown in Fig. 1, and k_1 the wave number in the elastic medium 1. Since I must be proportional to I_s [13] and r^{-2} (due to the spherical wave nature), we may write [13]

$$\frac{I_s}{I_i} = \frac{F(\theta, \phi)}{k_1^2 r^2} \quad (2)$$

where $F(\theta, \phi)$ is dimensionless function of the direction θ and ϕ but not of r . Note that the theory has been developed in the spherical polar coordinate where θ is the polar angle and ϕ is the azimuthal angle. F is also called scattering function. Let the total energy scattered in all directions be equal to the energy of the incident wave falling on the area C'_{sca} , where C'_{sca} is the scatter-

ing cross section of the scatterer. C'_{sca} can be calculated by integrating Eq. (2) over the surface area of an imaginary sphere of radius r as shown in Fig. 1. This leads to

$$C'_{sca} = \int_0^\pi \int_0^{2\pi} \frac{F(\theta, \phi)}{k_1^2 r^2} r^2 \sin \theta d\theta d\phi$$

$$= \int_0^\pi \int_0^{2\pi} \frac{F(\theta, \phi)}{k_1^2} \sin \theta d\theta d\phi \quad (3)$$

The phase function in Eq. (1) is related to F by [2,3]

$$\Phi(\theta, \phi) = \frac{4\pi}{k_1^2} \frac{F(\theta, \phi)}{C'_{sca}} = 4\pi \frac{F(\theta, \phi)}{\int_0^\pi \int_0^{2\pi} F(\theta, \phi) \sin \theta d\theta d\phi} \quad (4)$$

To solve GEPRT an asymmetry factor $\langle \Phi \rangle$ was defined by the author [2,3]. $\langle \Phi \rangle$ is given by

$$\langle \Phi \rangle = \frac{\int_0^\pi \int_0^{2\pi} \frac{F(\theta, \phi)}{k_1^2} \cos \theta \sin \theta d\theta d\phi}{C'_{sca}}$$

$$= \frac{\int_0^\pi \int_0^{2\pi} F(\theta, \phi) \cos \theta \sin \theta d\theta d\phi}{\int_0^\pi \int_0^{2\pi} F(\theta, \phi) \sin \theta d\theta d\phi} \quad (5)$$

The author showed [2,3] that the thermal transport cross section ($C'_{T sca}$) is related to C'_{sca} by the following equation:

$$C'_{T sca} = C'_{sca}(1 - g) \quad (6)$$

where $g = \langle \Phi \rangle$ in the diffusive or acoustically thick regime, and g is different for the acoustically thin regime. Although the theory developed in this paper is general, $C'_{T sca}$ will only be derived for the diffusive regime. The implication of difference between $C'_{T sca}$ and C'_{sca} is that the true mfp (l) is different from the isotropic scattering mfp (l_{iso}) and is given by [3]

$$\frac{l}{l_{iso}} = \frac{1}{1 - g} \quad (7)$$

Two more quantities are defined below that will be computed in this paper

$$C = \frac{C'_{sca}}{\pi a^2} \quad (8)$$

where C is the scattering efficiency and a is the radius of the spherical scatterer and

$$C_T = \frac{C'_{T sca}}{\pi a^2} \quad (9)$$

where C_T is the transport efficiency of the scatterer. Note that the host medium is denoted as 1 and the scattering medium is denoted as 2 as shown in Fig. 1.

2 Wave Propagation in an Elastic Medium

The elastic wave equation for an isotropic lossless media is given as [15]

$$(\lambda + \mu)\nabla\nabla\cdot\vec{U} + \mu\nabla^2\vec{U} = \rho\frac{\partial^2\vec{U}}{\partial t^2} \quad (10)$$

where λ and μ are the two Lamé constants, ρ is the density, and \vec{U} is the displacement. Considering a simple harmonic wave, \vec{U} is

$$\vec{U} = \vec{u}e^{i\omega t} \quad (11)$$

where ω is the frequency, t the time, and i denotes the imaginary number. Substitution of \vec{U} in Eq. (10) gives

$$\frac{1}{k_L^2}\nabla\nabla\cdot\vec{u} + \frac{1}{k_T^2}(\nabla^2\vec{u} - \nabla\nabla\cdot\vec{u}) + \vec{u} = 0 \quad (12)$$

where

$$k_L = \omega\left(\frac{\lambda + 2\mu}{\rho}\right)^{-1/2} \quad (13)$$

$$k_T = \omega\left(\frac{\mu}{\rho}\right)^{-1/2} \quad (14)$$

where k_L and k_T are the wave numbers for longitudinal and transverse waves, respectively, in the elastic medium. Equations (13) and (14) give

$$v_L = \left(\frac{\lambda + 2\mu}{\rho}\right)^{1/2} \quad (15)$$

and

$$v_T = \left(\frac{\mu}{\rho}\right)^{1/2} \quad (16)$$

where v_L and v_T are the wave speed for longitudinal and transverse waves, respectively, in the elastic medium. Figure 2 shows the difference between the longitudinal and the transverse waves. In the longitudinal wave, the displacement and the wave propagation direction are same. Longitudinal waves are also called P waves. In the transverse wave the displacement and the wave propagation direction are at an angle of 90° . There are two types of transverse wave. One is called the horizontally polarized shear (SH or T_1) wave, and the other one is called vertically polarized (SV or T_2) wave. Figure 2(a) shows the propagation and scattering of SH wave with a plane medium. Plane medium has been chosen just to schematically explain the propagation and scattering of these 3 different waves. Figure 2(a) shows that a SH wave is propagating in the x - y plane. The displacement vector (not shown) of the elastic medium is in z direction (i.e., perpendicular to the plane of incidence). For the SV wave the displacement vector is perpendicular to the direction of incidence, but is in the plane of incidence as shown in Fig. 2(b). Figure 2(c) shows that for longitudinal wave, the displacement vector is in the same direction as the direction of wave propagation. The solution of the time-independent wave equation [Eq. (12)] can be obtained by writing

$$\vec{u} = \vec{u}_L + \vec{u}_T \quad (17)$$

where \vec{u}_L is the displacement due to the longitudinal wave and \vec{u}_T is the displacement due to transverse wave. \vec{u}_L and \vec{u}_T satisfy the following condition [16]:

$$\nabla \times \vec{u}_L = 0 \quad (18)$$

$$\nabla \cdot \vec{u}_T = 0 \quad (19)$$

By using Eqs. (12) and (17)–(19), it can be shown that [16]

$$(\nabla^2 + k_L^2)\nabla\cdot\vec{u}_L = 0 \quad (20)$$

$$(\nabla^2 + k_T^2)\vec{u}_T = 0 \quad (21)$$

In this paper the theory is developed only for the SH wave scattering, but the theoretical framework is equally applicable to the scattering of SV wave or longitudinal wave. The reason for only considering SH wave scattering is that it does not go through mode conversion at the interface as shown in Fig. 2(a), where as both SV and longitudinal waves give rise to mode conversion at the interface as shown in Figs. 2(b) and 2(c). Mode conversion gives rise to four new waves at the interface where, without mode conversion, there are only two new waves at the interface. This leads to a big simplification in computing the scattering cross

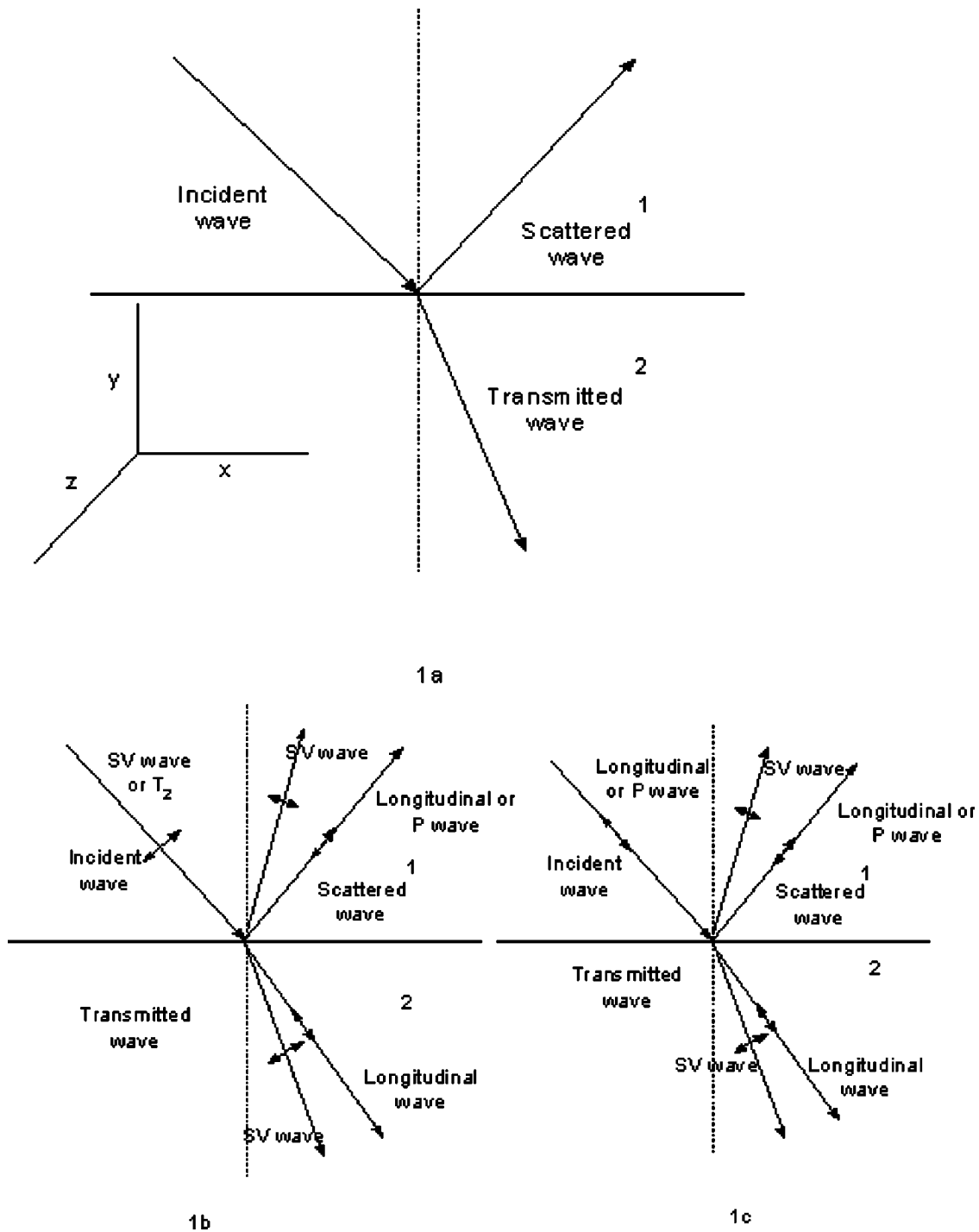


Fig. 2 Definition and scattering of various waves a) SH wave or T_1 wave b) SV or T_2 wave and c) Longitudinal or P wave

section. The scattering of longitudinal and SV phonon scattering will be published somewhere else [18,19]. Although the no-mode conversion case is much more simplified than the mode conversion case, it is still very tedious and cumbersome. Equation (21) is the vector wave equation. It will be converted into a scalar wave equation to obtain the solution. Following the methodology for EM wave theory \vec{u}_T can be written as [12]

$$\vec{u}_T = \nabla \times (\vec{H} \psi_{SH}) \quad (22)$$

where \vec{H} is an arbitrary constant vector and ψ_{SH} is as scalar function. Note the subscript SH indicates that this solution of \vec{u}_T gives rise to SH waves.

It is to be remembered that EM waves are transverse waves, and therefore, the methodology and physics of the scattering of transverse elastic waves is the same as EM waves with a few differences that will be pointed out in the paper. Using the vector identities [12]

$$\nabla \times (\vec{A} \times \vec{B}) = A(\nabla \cdot \vec{B}) - \vec{B}(\nabla \cdot \vec{A}) + (\vec{B} \cdot \nabla)\vec{A} - (\vec{A} \cdot \nabla)\vec{B} \quad (23)$$

$$\nabla \vec{A} \cdot \vec{B} = \vec{A} \times (\nabla \times \vec{B}) + \vec{B} \times (\nabla \times \vec{A}) + (\vec{B} \cdot \nabla)\vec{A} + (\vec{A} \cdot \nabla)\vec{B} \quad (24)$$

and Eq. (22), Eq. (21) can be reduced to

$$(\nabla^2 + k_T^2)\vec{u}_T = \nabla \times [\vec{H} \cdot (\nabla^2 \psi_{SH} + k_T^2 \psi_{SH})] \quad (25)$$

Therefore, \vec{u}_T satisfies the vector wave Eq. (25) only if ψ_{SH} is the solution of the scalar wave equation, i.e.,

$$(\nabla^2 + k_T^2)\psi_{SH} = 0 \quad (26)$$

This is the scalar wave equation. Another solution to the vector transverse wave equation can be obtained by writing

$$\vec{u}_{SV} = \frac{\nabla \times \nabla \times (\vec{H} \psi_{SV})}{k} \quad (27)$$

This solution of \vec{u}_T gives rise to an *SV* wave. It is important to point out that Eq. (27) is a little different for the EM wave. Equations (22) and (27) show that there is no coupling between the *SH* and *SV* waves because ψ_{SV} and ψ_{SH} are different, whereas for EM waves, $\psi_{SV} = \psi_{SH}$ [12]. As mentioned, earlier *SH* waves do not go through mode conversion at the interface between two mediums and *SV* waves go through mode conversion at the interface (Fig. 2); whereas for EM waves, both *SH* and *SV* modes do not go through mode conversion at the interface [12]. Since the methodology given in this paper is the same as that for EM waves, one might be tempted to think that one can directly use the EM wave equations and replace the various terms in the EM wave equations with their elastic wave counterparts. However, this is not true for the following reasons: 1) For EM waves, $\psi_{SV} = \psi_{SH}$, whereas this is not the case for elastic waves. This leads to cross coupling between the *SV* and *SH* wave terms in the calculation of transport cross section for EM wave scattering [12], whereas for elastic waves this is not the case as *SV* and *SH* waves are not coupled. 2) For EM waves, the refractive index is same as the ratio of the speed of EM waves between two mediums [12], whereas this is not the case for elastic waves. Due to this, the unknown term in the scattered wave has a different form, for the elastic wave, than the EM wave, which will be shown later. Subscript *T* will be dropped from the wave vector, and it will be simply written as *k*. Since scattering by sphere is being considered in this paper, \vec{H} can be chosen as the radius vector [12] \vec{r} . Therefore, Eqs. (22) and (27) can be written as

$$\vec{u}_{SH} = \nabla \times (\vec{r} \psi_{SH}) \quad (28)$$

$$\vec{u}_{SV} = \frac{1}{k} \nabla \times \nabla \times (\vec{r} \psi_{SV}) \quad (29)$$

The discussions in this section so far provide a good description of the physics of elastic waves of all three polarizations, but the scattering problem has been only solved for the *SH* wave, as it is the simplest of all the three polarizations. However, the theoretical framework developed in this paper can be easily extended to tackle the scattering of other polarizations. Because only *SH* wave scattering is being considered, ψ_{SH} will be simply written as ψ . Using Eq. (28) and by applying elementary vector algebra it can be shown that

$$\vec{u} = \frac{1}{r \sin \theta} \partial_\phi (r \psi) \hat{\theta} - \frac{1}{r} \partial_\theta (r \psi) \hat{\phi} \quad (30)$$

i.e.,

$$u_r = 0 \quad (31a)$$

$$u_\theta = \frac{1}{r \sin \theta} \partial_\phi (r \psi) \quad (31b)$$

$$u_\phi = -\frac{1}{r} \partial_\theta (r \psi) \quad (31c)$$

The stress components are related to the displacement and are given as [16]

$$\sigma_{rr} = \lambda \nabla \cdot \vec{u} + 2\mu \partial_r u_r = 0 \quad (32a)$$

$$\sigma_{r\theta} = \mu \left(\partial_r u_\theta - \frac{u_\theta}{r} + \frac{1}{r} \partial_\theta u_r \right) = \mu \left(\partial_r u_\theta - \frac{u_\theta}{r} \right) \quad (32b)$$

$$\sigma_{r\phi} = \mu \left(\partial_r u_\phi - \frac{u_\phi}{r} + \frac{1}{r \sin \theta} \partial_\theta u_r \right) = \mu \left(\partial_r u_\phi - \frac{u_\phi}{r} \right) \quad (32c)$$

where σ denotes the stress.

3 Development of Theory Scattering of Phonons by Particles

To solve the scattering problem in the spherical polar coordinates, the incident and transmitted plane waves need to be expanded in vector spherical harmonics [12,13]. Taking the expressions from EM wave-scattering theory [13], the incident *i* can be written as

$$\psi^i = \sin \phi \sum_{n=1}^{\infty} (-i)^n \left(\frac{2n+1}{n(n+1)} \right) p_n^1(\cos \theta) j_n(k_1 r) \quad (33)$$

where j_n is the spherical Bessel function of first kind [20] and p_n^1 is the associated Legendre function of order 1 [20]. The transmitted *t* wave can be written as

$$\psi^t = \sin \phi \sum_{n=1}^{\infty} (-i)^n b_n \left(\frac{2n+1}{n(n+1)} \right) p_n^1(\cos \theta) j_n(k_2 r) \quad (34)$$

where the coefficient b_n will be determined by applying the appropriate boundary conditions at the interface of medium 1 and 2. Since the scattered (*s*) wave has to have the spherical wave form as mentioned earlier (Fig. 1), it can be written as

$$\psi^s = \sin \phi \sum_{n=1}^{\infty} (-i)^n a_n \left(\frac{2n+1}{n(n+1)} \right) p_n^1(\cos \theta) h_n^2(k_1 r) \quad (35)$$

where the coefficient a_n will be determined applying the proper boundary conditions and h_n^2 is the spherical Henkel function [20] of second kind. The reason for choosing h_n^2 is that [13]

$$h_n^2(x) = \frac{i^{n+1}}{x} e^{-ix} \text{ for } x \rightarrow \infty \quad (36)$$

If $x = kr$, then Eq. (36) combined with the factor $e^{i\omega t}$ represents an outgoing spherical wave as is required for the scattered wave. Note that a_n and b_n in Eqs. (34) and (35) can be complex. $h_n^2(x)$ is given by [20]

$$h_n^2(x) = j_n(x) - i \eta_n(x) \quad (37)$$

where η_n is the spherical Bessel function of second kind. Two other functions are defined below:

$$z_n(x) = x j_n(x) \quad (38)$$

$$\varepsilon_n(x) = x h_n^2(x) \quad (39)$$

Using these functions and Eqs. (33)–(35) can be written as

$$r \psi^i = \frac{\sin \phi}{k_1} \sum_{n=1}^{\infty} (-i)^n \left(\frac{2n+1}{n(n+1)} \right) p_n^1(\cos \theta) z_n(k_1 r) \quad (40)$$

$$r \psi^s = \frac{\sin \phi}{k_1} \sum_{n=1}^{\infty} (-i)^n a_n \left(\frac{2n+1}{n(n+1)} \right) p_n^1(\cos \theta) \varepsilon_n(k_1 r) \quad (41)$$

$$r\psi' = \frac{\sin \phi}{k_1} \sum_{n=1}^{\infty} (-i)^n b_n \left(\frac{2n+1}{n(n+1)} \right) p_n^1(\cos \theta) z_n(k_2 r) \quad (42)$$

Two other functions are defined

$$\pi_n(\cos \theta) = \frac{1}{\sin \theta} p_n^1(\cos \theta) \quad (43)$$

$$\tau_n(\cos \theta) = \frac{d}{d\theta} p_n^1(\cos \theta) \quad (44)$$

Using Eqs. (31), (41), (43), and (44), displacement for the scattered wave can be written as

$$u_\theta = \frac{\cos \phi}{rk_1} \sum_{n=1}^{\infty} a_n (-i)^n \left(\frac{2n+1}{n(n+1)} \right) \pi_n \varepsilon_n(k_1 r) \quad (45a)$$

$$u_\phi = -\frac{\sin \phi}{rk_1} \sum_{n=1}^{\infty} a_n (-i)^n \left(\frac{2n+1}{n(n+1)} \right) \tau_n \varepsilon_n(k_1 r) \quad (45b)$$

and the complex conjugate of u_θ and u_ϕ are given as

$$\bar{u}_\theta = \frac{\cos \phi}{rk_1} \sum_{n=1}^{\infty} \bar{a}_n (i)^n \left(\frac{2n+1}{n(n+1)} \right) \pi_n \bar{\varepsilon}_n(k_1 r) \quad (46a)$$

$$\bar{u}_\phi = -\frac{\sin \phi}{rk_1} \sum_{n=1}^{\infty} \bar{a}_n (i)^n \left(\frac{2n+1}{n(n+1)} \right) \tau_n \bar{\varepsilon}_n(k_1 r) \quad (46b)$$

Similarly using Eqs. (32) and (45), the stress components for the scattered wave can be written as

$$\sigma_{r\theta} = \mu_1 \cos \phi \sum_{n=1}^{\infty} a_n (-i)^n \left(\frac{2n+1}{n(n+1)} \right) \pi_n \left(\frac{\varepsilon'_n}{r} - \frac{2\varepsilon_n}{r^2 k_1} \right) \quad (47a)$$

where

$$\varepsilon'_n = \frac{d\varepsilon_n(k_1 r)}{d(k_1 r)}$$

$$\bar{\sigma}_{r\theta} = \mu_1 \cos \phi \sum_{n=1}^{\infty} \bar{a}_n (i)^n \left(\frac{2n+1}{n(n+1)} \right) \pi_n \left(\frac{\bar{\varepsilon}'_n}{r} - \frac{2\bar{\varepsilon}_n}{r^2 k_1} \right) \quad (47b)$$

$$\sigma_{r\phi} = \mu_1 \sin \phi \sum_{n=1}^{\infty} a_n (-i)^n \left(\frac{2n+1}{n(n+1)} \right) \tau_n \left(\frac{2\varepsilon_n}{r^2 k_1} - \frac{\varepsilon'_n}{r} \right) \quad (48a)$$

$$\bar{\sigma}_{r\phi} = \mu_1 \sin \phi \sum_{n=1}^{\infty} \bar{a}_n (i)^n \left(\frac{2n+1}{n(n+1)} \right) \tau_n \left(\frac{2\bar{\varepsilon}_n}{r^2 k_1} - \frac{\bar{\varepsilon}'_n}{r} \right) \quad (48b)$$

Intensity I for elastic wave is given by [12]

$$I = \frac{i\omega}{2} \left[(\sigma_{rr} \bar{u}_r + \sigma_{r\theta} \bar{u}_\theta + \sigma_{r\phi} \bar{u}_\phi) - (\bar{\sigma}_{rr} u_r + \bar{\sigma}_{r\theta} u_\theta + \bar{\sigma}_{r\phi} u_\phi) \right] \\ = \frac{i\omega}{2} \left[(\sigma_{r\theta} \bar{u}_\theta + \rho_r \bar{u}_\phi) - (\bar{\sigma}_{r\theta} u_\theta + \bar{\sigma}_{r\phi} u_\phi) \right] \quad (49)$$

Since both u and σ involve summations, the multiplication of u and σ cannot have the same index n . Index n is used for σ and m for u , which gives

$$\sigma_{r\theta} \bar{u}_\theta = \frac{\mu_1 \cos^2 \phi}{rk_1} \sum_{n=1}^{\infty} \sum_{m=1}^{\infty} a_n \bar{a}_m (-i)^n (i)^m \\ \times \frac{2n+1}{n(n+1)} \frac{2m+1}{m(m+1)} \pi_n \pi_m \left(\frac{\varepsilon'_n}{r} - \frac{2\varepsilon_n}{r^2 k_1} \right) \bar{\varepsilon}_m \quad (50a)$$

For $\bar{\sigma}_{r\theta} u_\theta$, index m is used for σ and n for u as this leads to the cancellation couple of terms in Eq. (49). This gives

$$\bar{\sigma}_{r\theta} u_\theta = \frac{\mu_1 \cos^2 \phi}{rk_1} \sum_{n=1}^{\infty} \sum_{m=1}^{\infty} a_n \bar{a}_m (-i)^n (i)^m \\ \times \frac{2n+1}{n(n+1)} \frac{2m+1}{m(m+1)} \pi_n \pi_m \left(\frac{\bar{\varepsilon}'_m}{r} - \frac{2\bar{\varepsilon}_m}{r^2 k_1} \right) \varepsilon_n \quad (50b)$$

Therefore,

$$\sigma_{r\theta} \bar{u}_\theta - \bar{\sigma}_{r\theta} u_\theta = \frac{\mu_1 \cos^2 \phi}{rk_1} \sum_{n=1}^{\infty} \sum_{m=1}^{\infty} a_n \bar{a}_m (-i)^n (i)^m \\ \times \frac{2n+1}{n(n+1)} \frac{2m+1}{m(m+1)} \pi_n \pi_m \left[\left(\frac{\varepsilon'_n}{r} - \frac{2\varepsilon_n}{r^2 k_1} \right) \bar{\varepsilon}_m \right. \\ \left. - \left(\frac{\bar{\varepsilon}'_m}{r} - \frac{2\bar{\varepsilon}_m}{r^2 k_1} \right) \varepsilon_n \right] \quad (51a)$$

Similarly,

$$\sigma_{r\phi} \bar{u}_\phi - \bar{\sigma}_{r\phi} u_\phi = \frac{\mu_1 \sin^2 \phi}{rk_1} \sum_{n=1}^{\infty} \sum_{m=1}^{\infty} a_n \bar{a}_m (-i)^n (i)^m \\ \times \frac{2n+1}{n(n+1)} \frac{2m+1}{m(m+1)} \\ \times \tau_n \tau_m \left[\left(\frac{\varepsilon'_n}{r} - \frac{2\varepsilon_n}{r^2 k_1} \right) \bar{\varepsilon}_m - \left(\frac{\bar{\varepsilon}'_m}{r} - \frac{2\bar{\varepsilon}_m}{r^2 k_1} \right) \varepsilon_n \right] \quad (51b)$$

Therefore,

$$(\sigma_{r\theta} \bar{u}_\theta - \bar{\sigma}_{r\theta} u_\theta) + (\sigma_{r\phi} \bar{u}_\phi - \bar{\sigma}_{r\phi} u_\phi) \\ = \frac{\mu_1}{r^2 k_1} \sum_{n=1}^{\infty} \sum_{m=1}^{\infty} \frac{2n+1}{n(n+1)} \frac{2m+1}{m(m+1)} a_n \bar{a}_m (-i)^n (i)^m [\varepsilon'_n \bar{\varepsilon}_m \\ - \bar{\varepsilon}'_m \varepsilon_n] [\tau_n \tau_m \sin^2 \phi + \pi_n \pi_m \cos^2 \phi] \quad (52)$$

Intensity of the incident wave I_i is given as [13]

$$I_i = \frac{\rho_1 \omega^3}{2k_1} \quad (53)$$

Therefore, using Eqs. (49) and (52)–(53)

$$\frac{I_s}{I_i} = \frac{i}{r^2 k_1^2} \sum_{n=1}^{\infty} \sum_{m=1}^{\infty} A_{n,m} [\tau_n \tau_m \sin^2 \phi + \pi_n \pi_m \cos^2 \phi] \quad (54)$$

where

$$A_{n,m} = \frac{2n+1}{n(n+1)} \frac{2m+1}{m(m+1)} a_n \bar{a}_m (-i)^n (i)^m [\varepsilon'_n \bar{\varepsilon}_m - \bar{\varepsilon}'_m \varepsilon_n] \quad (55)$$

Equations (2) and (54) give

$$F(\theta, \phi) = i \sum_{n=1}^{\infty} \sum_{m=1}^{\infty} A_{n,m} [\tau_n \tau_m \sin^2 \phi + \pi_n \pi_m \cos^2 \phi] \quad (56)$$

Using Eq. (3), the scattering cross section is given by

$$C'_{sca} = \frac{i}{k_1^2} \int_0^\pi \int_0^{2\pi} \sum_{n=1}^{\infty} \sum_{m=1}^{\infty} A_{n,m} [\tau_n \tau_m \sin^2 \phi \\ + \pi_n \pi_m \cos^2 \phi] \sin \theta d\theta d\phi \quad (57)$$

where

$$\int_0^{2\pi} \cos^2 \phi d\phi = \int_0^{2\pi} \sin^2 \phi d\phi = \pi \quad (58)$$

i.e.,

$$C'_{sca} = \frac{\pi i}{k_1^2} \int_0^{2\pi} \int_0^{2\pi} \sum_{n=1}^{\infty} \sum_{m=1}^{\infty} A_{n,m} [\tau_n \tau_m + \pi_n \pi_m] \sin \theta d\theta \quad (59)$$

and [12]

$$\int_0^{\pi} (\pi_n \pi_m + \tau_n \tau_m) \sin \theta d\theta = \delta_{nm} \frac{2n^2(n+1)^2}{2n+1} \quad (60)$$

where δ_{nm} is the Kroncker delta function.

Therefore,

$$C'_{sca} = \frac{2\pi i}{k_1^2} \sum_{n=1}^{\infty} (2n+1) a_n \bar{a}_n [\varepsilon'_n \bar{\varepsilon}_n - \bar{\varepsilon}'_n \varepsilon_n] \quad (61)$$

or using the definition of C from Eq. (8)

$$C = \frac{2i}{a^2 k_1^2} \sum_{n=1}^{\infty} (2n+1) a_n \bar{a}_n [\varepsilon'_n \bar{\varepsilon}_n - \bar{\varepsilon}'_n \varepsilon_n] \quad (62)$$

Using Eqs. (39), it can be shown that

$$\varepsilon_n(x) = z_n(x) + i\chi_n(x) \quad (63)$$

where

$$\chi_n(x) = -x\eta_n(x) \quad (64)$$

which gives

$$[\varepsilon'_n \bar{\varepsilon}_n - \bar{\varepsilon}'_n \varepsilon_n] = 2i[z_n \chi'_n - \chi_n z'_n] \quad (65)$$

Using the identity [20]

$$j_n(x)n'_n(x) - j'_n(x)n_n(x) = \frac{1}{x^2} \quad (66)$$

and definition of z_n [Eq. (38)] and χ_n [Eq. (64)]

$$z_n(x)\chi'_n(x) - z'_n(x)\chi_n(x) = -1 \quad (67)$$

Therefore, Eq. (65) becomes

$$[\varepsilon'_n \bar{\varepsilon}_n - \bar{\varepsilon}'_n \varepsilon_n] = -2i \quad (68)$$

Substituting Eq. (68) in Eq. (67) gives

$$C = \frac{4}{x_1^2} \sum_{n=1}^{\infty} (2n+1) a_n \bar{a}_n \quad (69)$$

where $x_1 = k_1 a$. It is to be noted that expression of C for phonons has the same form as that for photons [12]. In the following paragraphs, C will be reduced to Eq. (69) using an alternate method, which will be also used to derive C_T .

Noting that [13]

$$\varepsilon_n(x) = i^{n+1} e^{-ix} \quad \text{for } x \rightarrow \infty \quad (70)$$

where

$$x = kr$$

and using Eq. (A-2)

$$\varepsilon'_n = \frac{n\varepsilon_{n-1} - (n+1)\varepsilon_{n+1}}{2n+1} = i^n e^{-ikr} \quad (71)$$

Combining Eqs. (70) and (71) gives

$$[\varepsilon'_n \bar{\varepsilon}_n - \bar{\varepsilon}'_n \varepsilon_n] = -2i \quad (72)$$

This is the same as Eq. (68). Using Eqs. (70) and (71), it can be shown that

$$\varepsilon'_n \bar{\varepsilon}_m - \bar{\varepsilon}'_m \varepsilon_n = [-2i](i)^n (-i)^m \quad (73)$$

Substituting Eq. (73) in Eq. (56)

$$F(\theta, \phi) = 2 \sum_{n=1}^{\infty} \sum_{m=1}^{\infty} \frac{2n+1}{n(n+1)} \frac{2m+1}{m(m+1)} a_n \bar{a}_m [\tau_n \tau_m \sin^2 \phi + \pi_n \pi_m \cos^2 \phi] \quad (74)$$

$F(\theta, \phi)$ in radiative transport is normally expressed as $F(\theta)$ [12,13]. This analysis is also called the wave zone analysis [17]. Following the same representation for phonon transport, $F(\theta)$ is given as

$$F(\theta) = \frac{1}{2\pi} \int_0^{2\pi} F(\theta, \phi) d\phi \quad (75)$$

or

$$F(\theta) = \sum_{n=1}^{\infty} \sum_{m=1}^{\infty} \frac{2n+1}{n(n+1)} \frac{2m+1}{m(m+1)} a_n \bar{a}_m [\tau_n \tau_m + \pi_n \pi_m] \quad (76)$$

Using Eq. (76) and (4), $\Phi(\theta)$ is

$$\Phi(\theta) = \frac{\sum_{n=1}^{\infty} \sum_{m=1}^{\infty} \frac{2n+1}{n(n+1)} \frac{2m+1}{m(m+1)} a_n \bar{a}_m [\tau_n \tau_m + \pi_n \pi_m]}{\sum_{n=1}^{\infty} (2n+1) a_n \bar{a}_n} \quad (77)$$

It can be shown using Eq. (5) that $\langle \Phi \rangle$ can be written as

$$\langle \Phi \rangle = \frac{1}{2} \int_0^{\pi} \Phi(\theta) \cos \theta \sin \theta d\theta \quad (78)$$

To evaluate $\langle \Phi \rangle$ in Eq. (78), the integral $\int_0^{\pi} (\tau_n \tau_m + \pi_n \pi_m) \sin \theta \cos \theta d\theta$ needs to be evaluated. This integral is [12]

$$\int_0^{\pi} (\tau_n \tau_m + \pi_n \pi_m) \sin \theta \cos \theta d\theta = \frac{2n^2(n+1)(n+2)^3}{(2n+1)(2n+3)} \quad \text{for } m = n+1 \quad (79a)$$

$$\int_0^{\pi} (\tau_n \tau_m + \pi_n \pi_m) \sin \theta \cos \theta d\theta = \frac{2n(n+1)^2(n-1)^2}{(2n-1)(2n+1)} \quad \text{for } m = n-1 \quad (79b)$$

$$\int_0^{\pi} (\tau_n \tau_m + \pi_n \pi_m) \sin \theta \cos \theta d\theta = 0 \quad \text{for } m \neq n \pm 1 \quad (79c)$$

Substituting Eq. (79) in Eq. (78), $\langle \Phi \rangle$ is given as

$$\langle \Phi \rangle = \frac{2 \sum_{n=1}^{\infty} \left(\frac{n(n+2)}{n+1} \right) \text{Re}(a_n \bar{a}_{n+1})}{\sum_{n=1}^{\infty} (2n+1) a_n \bar{a}_n} \quad (80)$$

Note that Eq. (80) is a little different for EM waves [12] due to cross coupling between SV and SH waves as mentioned earlier. Therefore, C_T in the diffusive regime is given as

$$C_T = C(1-g) = C(1-\langle \Phi \rangle) \quad (81)$$

In this section, the expression for C and C_T was derived. The expression for a_n is derived in Sec. 4.

4 Calculation of a_n

At the interface the displacement and the stress are continuous. Using Eq. (45) and the application of displacement continuity

$$u_{\theta}^i + u_{\theta}^s = u_{\theta}^t \quad (82)$$

gives

$$\frac{z_n(x_1)}{x_1} + a_n \frac{\varepsilon_n(x_1)}{x_1} = b_n \frac{z_n(x_2)}{x_2} \quad (83)$$

$$\begin{aligned} & \mu_1 \left(\frac{z'_n(x_1)}{a} - \frac{2z_n(x_1)}{ax_1} \right) + a_n \mu_1 \left(\frac{\varepsilon'_n(x_1)}{a} - \frac{2\varepsilon_n(x_1)}{ax_1} \right) \\ & = b_n \mu_2 \left(\frac{z'_n(x_2)}{a} - \frac{2z_n(x_2)}{ax_1} \right) \end{aligned} \quad (85)$$

Similarly using Eq. (47) and the application of stress continuity,

$$\sigma_{r\theta}^i + \sigma_{r\theta}^s = \sigma_{r\theta}^t \quad (84)$$

where

$$f'(x) = \left(\frac{df(x)}{dx} \right)_{r=a}$$

gives

$x_1 = k_1 a$ and $x_2 = k_2 a$ where a is the radius of the scatterer. Solving Eqs. (83) and (85) provides

$$a_n = - \frac{\mu_2 z_n(x_1) [x_2 z'_n(x_2) - 2z_n(x_2)] - \mu_1 z_n(x_2) [x_1 z'_n(x_1) - 2z_n(x_1)]}{\mu_2 \varepsilon_n(x_1) [x_2 z'_n(x_2) - 2z_n(x_2)] - \mu_1 z_n(x_2) [x_1 \varepsilon'_n(x_1) - 2\varepsilon_n(x_1)]} \quad (86)$$

For EM waves Eq. (86) is a little different due to the fact that the refractive index is the same as the ratio of speed of EM waves in the medium and the particle, as mentioned earlier. Noting that

$$z'_n(x) = j_n(x) + x j'_n(x) \quad (87a)$$

$$\varepsilon'_n(x) = h_n(x) + x h'_n(x) \quad (87b)$$

a_n from Eq. (86) can be written as

$$a_n = - \frac{\mu_2 j_n(x_1) [x_2 j'_n(x_2) - j_n(x_2)] - \mu_1 j_n(x_2) [x_1 j'_n(x_1) - j_n(x_1)]}{\mu_2 h_n(x_1) [x_2 j'_n(x_2) - j_n(x_2)] - \mu_1 j_n(x_2) [x_1 h'_n(x_1) - h_n(x_1)]} \quad (88)$$

The denominator of Eq. (88) can be written as

$$\begin{aligned} & \mu_2 j_n(x_1) [x_2 j'_n(x_2) - j_n(x_2)] - \mu_1 j_n(x_2) [x_1 j'_n(x_1) - j_n(x_1)] \\ & - i [\mu_2 \eta_n(x_1) [x_2 j'_n(x_2) - j_n(x_2)] \\ & - \mu_1 j_n(x_2) [x_1 \eta'_n(x_1) - \eta_n(x_1)]] \end{aligned} \quad (89)$$

Using Eqs. (A-2) and (A-3) and Eq. (88), a_n can be written as

$$a_n = \frac{-c_n}{c_n - i d_n} \quad (90)$$

where

$$\begin{aligned} c_n = & j_{n-1}(x_2) \left[(n-1) \left\{ \frac{\mu_2}{\mu_1} j_{n+1}(x_1) + \frac{\mu_2 - \mu_1}{\mu_1} j_{n-1}(x_1) \right\} \right. \\ & \left. + (n+2) j_{n+1}(x_1) \right] - j_{n+1}(x_2) \left[(n+2) \left\{ \frac{\mu_2}{\mu_1} j_{n-1}(x_1) \right. \right. \\ & \left. \left. + \frac{\mu_2 - \mu_1}{\mu_1} j_{n+1}(x_1) \right\} + (n-1) j_{n-1}(x_1) \right] \end{aligned} \quad (91a)$$

$$\begin{aligned} d_n = & j_{n-1}(x_2) \left[(n-1) \left\{ \frac{\mu_2}{\mu_1} \eta_{n+1}(x_1) + \frac{\mu_2 - \mu_1}{\mu_1} \eta_{n-1}(x_1) \right\} \right. \\ & \left. + (n+2) \eta_{n+1}(x_1) \right] - j_{n+1}(x_2) \left[(n+2) \left\{ \frac{\mu_2}{\mu_1} \eta_{n-1}(x_1) \right. \right. \\ & \left. \left. + \frac{\mu_2 - \mu_1}{\mu_1} \eta_{n+1}(x_1) \right\} + (n-1) \eta_{n-1}(x_1) \right] \end{aligned} \quad (91b)$$

It is to be noted that every term in Eq. (91) is known in terms of x_1 as $x_2 = v_1/v_2 x_1$ where v_1 and v_2 are the speed of SH wave in medium 1 and 2, respectively. Equation (90) gives

$$a_n \bar{a}_n = \frac{c_n^2}{c_n^2 + d_n^2} \quad (92)$$

which will be used to calculate C and

$$\text{Re}(a_n a_{n+1}) = \frac{c_n c_{n+1} [c_n c_{n+1} + d_n d_{n+1}]}{(c_n^2 + d_n^2)(c_{n+1}^2 + d_{n+1}^2)} \quad (93)$$

which will be used to calculate $\langle \Phi \rangle$ and C_T from Eqs. (80) and (81).

Two special cases of a spherical cavity and a rigid body are treated separately to calculate a_n . For a rigid body scatterer, the displacement at the boundary is zero which by using Eq. (83) leads to

$$c_n = j_n(x_1) \quad (94a)$$

and

$$d_n = \eta_n(x_1) \quad (94b)$$

For a cavity the stress at the boundary vanishes, which by using Eq. (85), leads to

$$c_n = (n-1) j_{n-1}(x_1) - (n+2) j_{n+1}(x_1) \quad (95a)$$

and

$$d_n = (n-1) \eta_{n-1}(x_1) - (n+2) \eta_{n+1}(x_1) \quad (95b)$$

5 Results

C , C_T , and g have been calculated for rigid, cavity, and elastic scatterers for different values of x_1 . Figures 3 and 4 show the calculations of C and C_T for rigid and cavity scatterers. Figures 3 and 4 show that C approaches 2 and C_T approaches 1 for large values of x_1 where $x_1 = k_1 a$ for both rigid and cavity scatterers. Large values of x_1 means that the scattering falls in the geometrical scattering regime. In the geometrical scattering regime calcu-

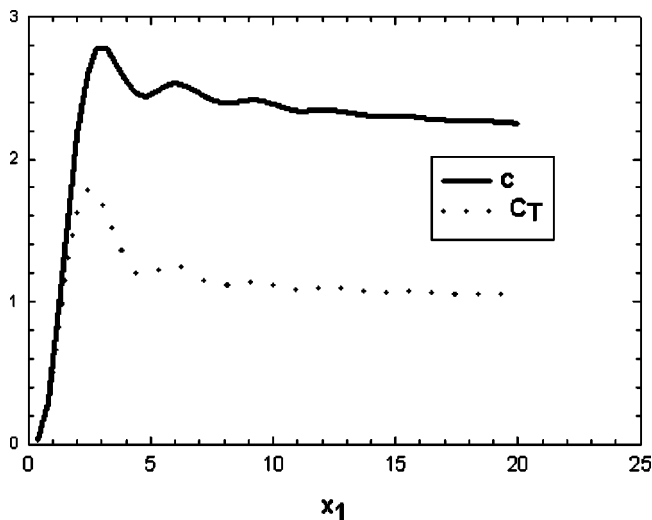


Fig. 3 Scattering and transport efficiency of a rigid scatterer

lation of C by geometrical acoustic leads to $C=1$, i.e., scattering cross section, is the same as the geometric cross section (πa^2) where calculation based on the theory developed in this paper shows that C approaches 2. This is totally consistent with the scattering of EM waves, where $C=2$ based on the Mie theory is called scattering paradox [12]. The reason for $C=2$ based on Mie scattering theory is that Mie scattering theory also takes care of the diffraction of waves, where geometrical scattering calculations only include the reflection and refraction of waves. However, Figs. 3 and 4 show that for cavity and rigid scatterers, C_T approaches 1 in the geometrical scattering regime, i.e., the thermal transport cross section is same as the geometrical cross section. Note that for the cavity and rigid scatterers, both C and C_T do not depend on the speed of sound and the density of the medium as seen from Eqs. (94) and (95). The number of terms used to calculate the summation in Eqs. (69) and (80) was two times the largest value of x_1 used in the calculation. For the calculation of C and C_T for the cavity, it was not possible to perform the calculations beyond $x_1=12$ because the summation became unstable due to the convergence problem. A lot of care needs to be taken in the evaluation of Eqs. (69) and (80) because it involves summation of spherical Bessel function of first and second kind. Bohren and Huffman [12] have provided a good discussion on the calculation of the scattering coefficient of EM waves, which also involves the

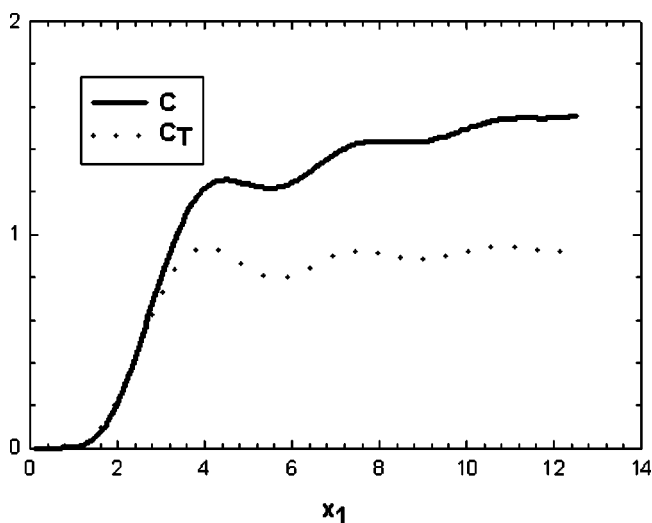


Fig. 4 Scattering and transport efficiency of a cavity

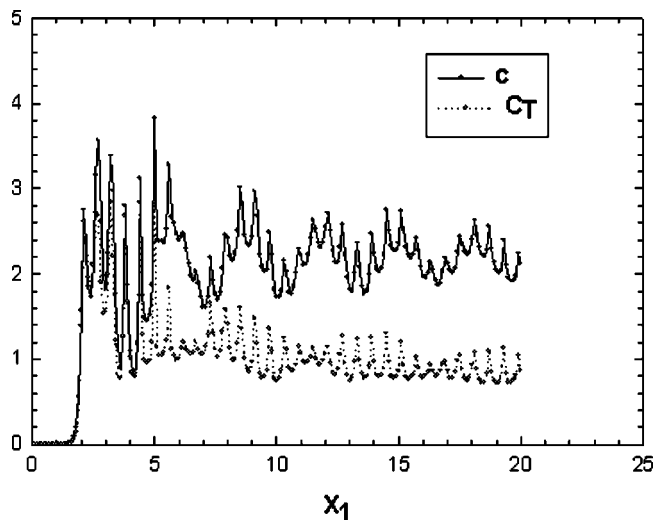


Fig. 5 Scattering and transport efficiency of an elastic scatterer with $v=0.5$ and $z=0.5$

summation of spherical Bessel function of first and second kind. After various trials, it was found out that number of terms needed for stable evaluation of summations in Eqs. (69) and (80) was two times the value of x_1 . If the number of terms were less than two times the value of x_1 , then both C and C_T continuously dropped with increasing value of x_1 , and if it was higher than 2 times x_1 , then, depending on the ratio speed of sound between the medium and the particle and the acoustic mismatch between the medium and the particle, the summation ran into convergence problems. For $x_1 < 1$, the number of terms was always kept at 4.

Figures 5–8 show the calculations of C and C_T for elastic scatterers for different values of v where $v=v_2/v_1$ and z where $z=\rho_2 v_2/\rho_1 v_1$ (z is also called the acoustic mismatch). μ_1 and μ_2 needed in Eq. (91) are calculated using Eq. (16). Figures 5–8 show that as x_1 becomes very large C approaches the value of 2, whereas C_T is approaching a value smaller than 1. Figures 5–8 show that even for x_1 as large as 20 both C and C_T show an oscillatory trend, i.e., scattering is still not strictly in the geometrical scattering regime. This type of oscillatory behavior of C and C_T is also consistent with the scattering of EM waves [12]. Figures 3–8 show that transport cross section can be very different from the scattering cross section, depending on the acoustic mis-

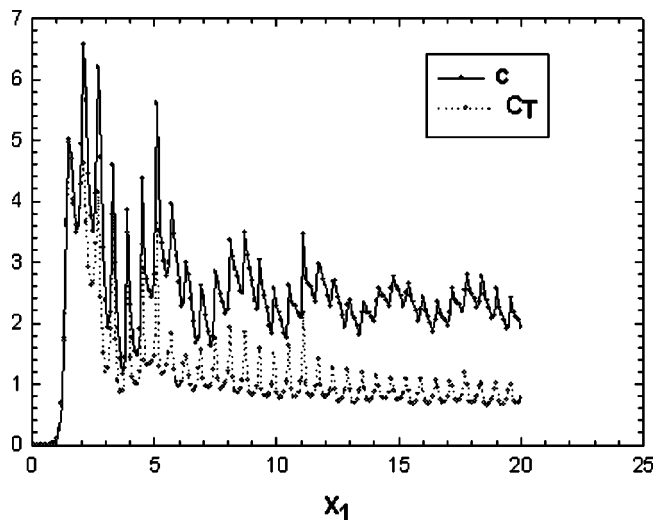


Fig. 6 Scattering and transport efficiency of an elastic scatterer with $v=0.5$ and $z=2$

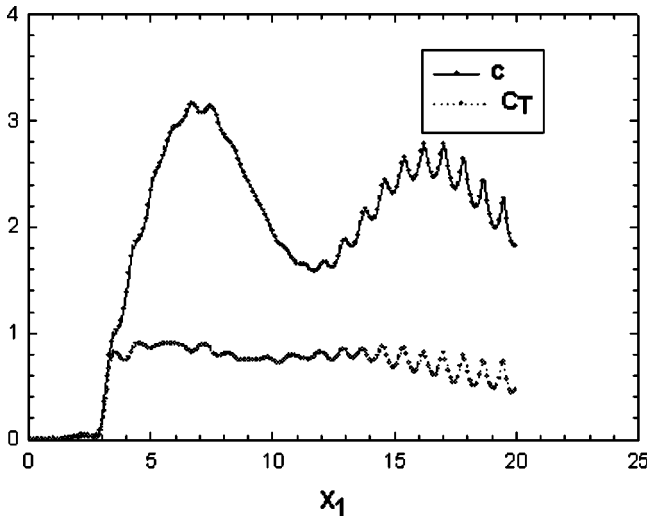


Fig. 7 Scattering and transport efficiency of an elastic scatterer with $\nu=0.75$ and $z=0.5$

match between the medium and the scatterer. Figures 9–13 show the calculations of g or $\langle \Phi \rangle$. Figure 9 shows that g approaches the value of 0.5 for rigid and cavity scatterer for large values of x_1 , whereas for elastic scatterers (Figs. 10–13) considered in this paper, g can be sometimes negative.

The author, in an earlier paper [3], presented a closed-form analytical solution for the calculation of g for SH waves in the geometrical scattering regime based on the phenomenon of multiple reflection and refraction of waves by a large sphere, as shown in Fig. 14. g calculated by this method is called G in this paper. G is given by [3]

$$G = \int_0^1 \frac{2R^2(1 - \cos 2\tau') + (1 - R)\cos(2\tau - 2\tau')}{1 - 2R \cos 2\tau' + R^2} d(\cos^2 \tau) \quad (96)$$

$$R(\tau) = \frac{4z \sin \tau \sqrt{1 - [\nu \cos \tau]^2}}{[\sin \tau + z \sqrt{1 - [\nu \cos \tau]^2}]^2} \quad (97)$$

The angles τ and τ' are related to each other by Snell's law as

$$\cos \tau' = \nu \cos \tau \quad (98)$$

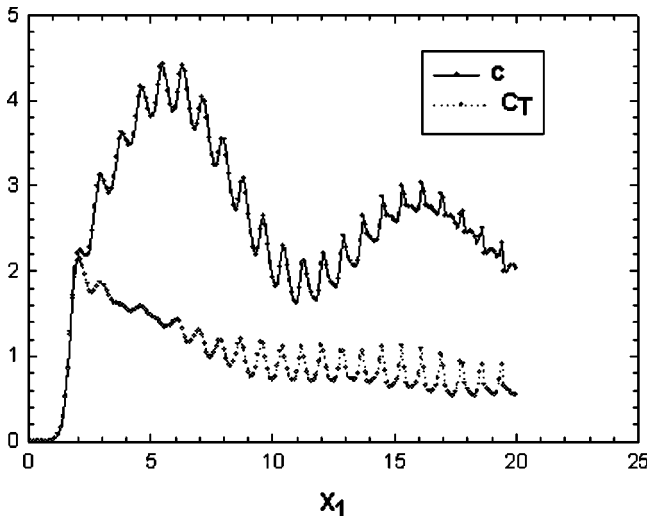


Fig. 8 Scattering and transport efficiency of an elastic scatterer with $\nu=0.75$ and $z=2$

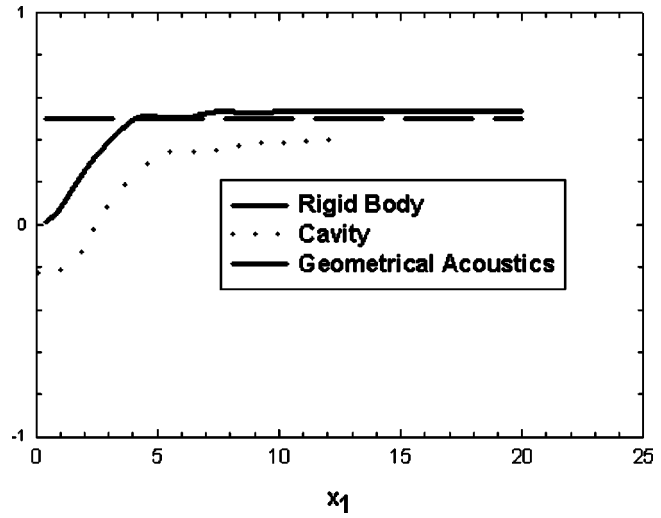


Fig. 9 Asymmetry factor g for rigid and cavity scatterer

The transport scattering efficiency based on geometric scattering theory is given as

$$C_{TG} = C_G(1 - G) \quad (99)$$

where C_G and C_{TG} are the scattering and transport efficiency, respectively, based on geometric scattering theory. The transport cross section from the Mie scattering theory developed in this paper and the geometrical scattering theory from the previous paper [3] has to be equal. Therefore,

$$C_{TG} = C_T \quad (100)$$

i.e.,

$$C_G(1 - G) = C(1 - g) \quad (101)$$

$C_G=1$ based on geometrical scattering theory and $C=2$ as mentioned earlier from Mie scattering theory. Therefore, Eq. (101) gives in the geometric scattering regime,

$$g = \frac{1}{2} + \frac{G}{2} \quad (102)$$

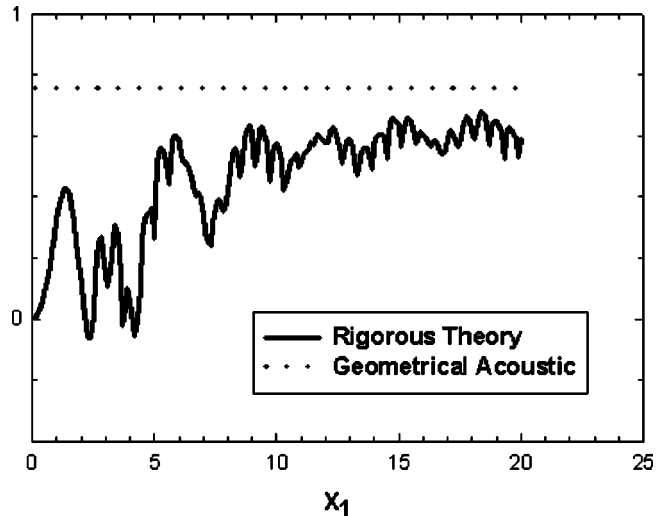


Fig. 10 Asymmetry factor g for an elastic scatterer ($\nu=0.5, z=0.5$)

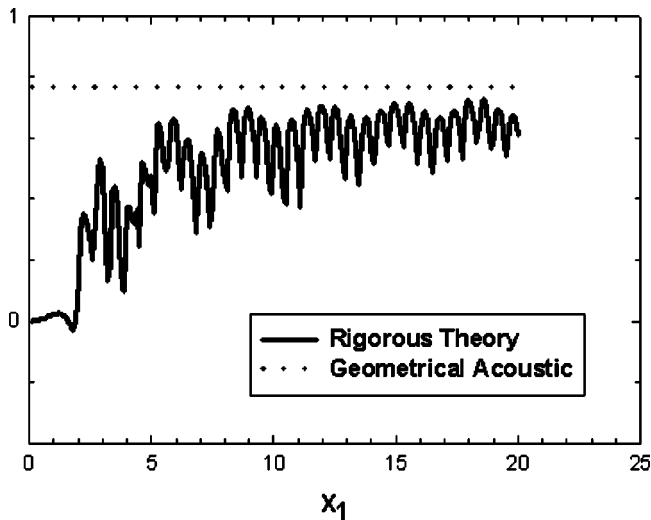


Fig. 11 Asymmetry factor g for an elastic scatterer ($\nu=0.5, z=2$)

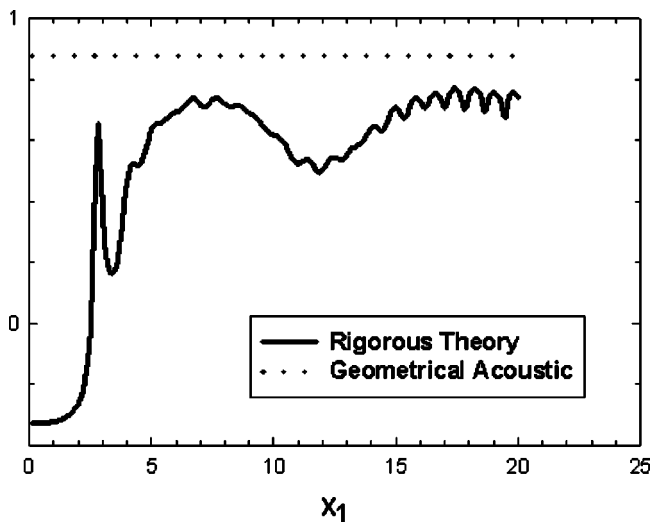


Fig. 12 Asymmetry factor g for an elastic scatterer ($\nu=0.75, z=0.5$)

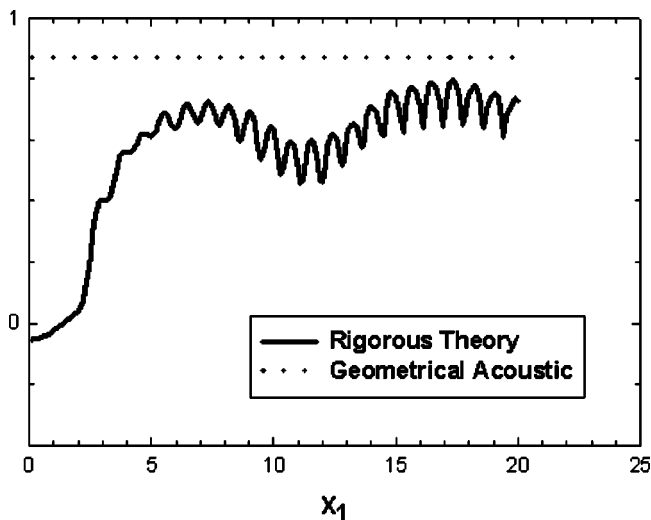


Fig. 13 Asymmetry factor g for an elastic scatterer ($\nu=0.75, z=2$)

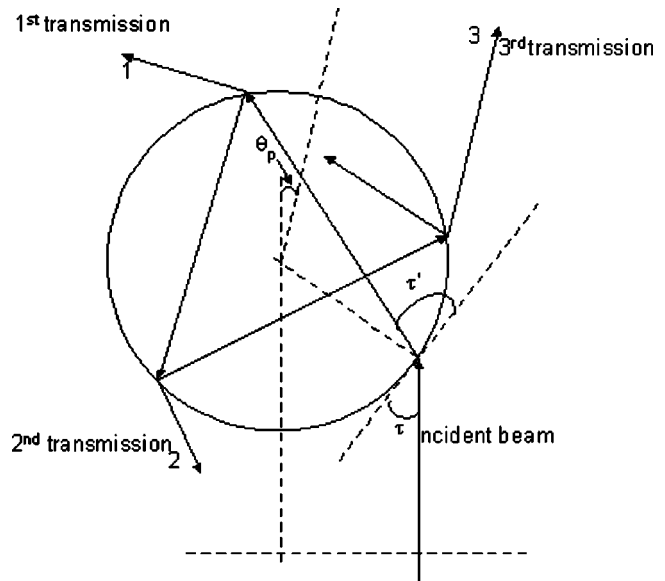


Fig. 14 Schematic of the multiple reflection and refraction of acoustic waves by a large sphere

Figures 9–13 show the value of g calculated by Eq. (102). For the rigid body and cavity, R in Eq. (96) is 1, i.e., $G=0$. Therefore, $g=0.5$ from Eq. (102), and Fig. 9 shows that the rigorous theory developed in this paper matches this result for large values of x_1 . Figures 10–13 show that g approaches the value of g calculated by Eq. (102) for different elastic scatterer considered in this paper.

Conclusions

This paper developed the rigorous Mie scattering theory for the scattering of SH wave phonons, i.e., no-mode conversion case by spherical scatterer. Most of the physics and methodology given in this paper can be extended to the scattering of SV and longitudinal phonon, i.e., for the mode conversion case. Calculations based on the theory developed in this paper show that the thermal transport cross section can be very different from the scattering cross section.

Nomenclature

- \vec{U} = displacement vector
- \vec{u} = amplitude of displacement vector
- C'_{sca} = scattering cross section (m^2)
- C'_{Tscg} = transport cross section (m^2)
- \vec{A} = vector
- \vec{B} = vector
- \vec{H} = vector in Eq. (22)
- a = radius of the scatterer (m)
- a_n = scattering coefficient
- b_n = transmission coefficient
- c = defined in Eq. (92)
- C = scattering efficiency
- C_G = scattering cross section using geometric scattering theory (m^2)
- C_T = transport efficiency
- C_{TG} = transport cross section using geometric scattering theory (m^2)
- d = defined in Eq. (92)
- F = scattering function
- G = asymmetry factor in diffusive regime calculate by using geometric
- g = asymmetry factor in diffusive regime
- h = spherical Hankel function of second kind
- I = phonon or photon Intensity ($Wm^{-2}sr^{-1}s$)

j = spherical Bessel function of first kind
 k = wave vector (m^{-1})
 K_p = scattering coefficient due to particle scattering (m^{-1})
 K_u = scattering coefficient due to Umklapp scattering (m^{-1})
 l = mean free path (m)
mfp = mean free path
 r = radius (m)
 R = reflectivity of acoustic waves
 $?$ = scattering theory
 v = speed of elastic wave (m s^{-1})
 x = size parameter (ka)
 z = function in Eq. (38)

Greek

λ = Lamé's constant
 η = spherical Bessel function of second kind
 $\langle \Phi \rangle$ = asymmetry factor
 X = function in Eq. (64)
 Φ = phase function
 Ω = solid angle (sr)
 ε = function in Eq. (39)
 ϕ = azimuthal angle
 μ = direction cosine
 μ = Lamé's constant
 π = function in Eq. (44)
 θ = polar angle
 ρ = density (kg m^{-3})
 σ = stress
 τ = angle of incidence and function in Eq. (44)
 τ' = angle of reflection
 ω = angular frequency (s^{-1})
 ψ = scalar function in Eq. (22)

Subscript

1 = medium 1 (host medium)
2 = medium 2 (scatterer)
 i = incident wave
iso = isotropic
 L = longitudinal
 m = index
 n = index
 s = scattered wave
SH = horizontally polarized transverse wave
SV = vertically polarized transverse wave
 t = transmitted wave
 T = Transverse

Appendix

$$f_{n-1}(x) + f_{n+1}(x) = \frac{2n+1}{x} f_n(x) \quad (\text{A-1})$$

$$n f_{n-1}(x) - (n+1) f_{n+1}(x) = (2n+1) f'_n(x) \quad (\text{A-2})$$

$$\frac{n+1}{x} f_n(x) + f'_n(x) = f_{n-1}(x) \quad (\text{A-3})$$

$$\frac{n}{x} f_n(x) - f'_n(x) = f_{n+1}(x) \quad (\text{A-4})$$

where $f_n(x)$ can be $h_n(x)$, $j_n(x)$, $\eta_n(x)$, $z_n(x)$, $\chi_n(x)$, and $\varepsilon_n(x)$.

References

- [1] Majumdar, A., 1993, "Microscale Heat Conduction in Dielectric Thin Films," ASME J. Heat Transfer, **115**, pp. 7–16.
- [2] Prasher, R. S., 2003, "Generalized Equation of Phonon Radiative Transport," Appl. Phys. Lett., **83**(1), pp. 48–50.
- [3] Prasher, R. S., 2003, "Phonon Transport in Anisotropic Scattering Particulate Media," ASME J. Heat Transfer, **125**, pp. 1156–1162.
- [4] Callaway, J., 1959, "Model of Lattice Thermal Conductivity at Low Temperatures," Phys. Rev., **113**(4), pp. 1046–1051.
- [5] Ziman, J. M., 1996, *Electrons and Phonons*, Oxford Press, London.
- [6] Sverdrup, P. G., Ju, Y. S., and Goodson, K. E., 2001, "Sub-Continuum Simulations of Heat Conduction in Silicon-on-Insulator Transistors" ASME Journal of Heat Transfer, **123**, pp. 130–137.
- [7] Chen, G., 1997, "Size and Interface Effects on Thermal Conductivity of Superlattices and Periodic Thin-Film Structures," ASME J. Heat Transfer, **119**, pp. 220–229.
- [8] Song, D., and Chen, G., 2004, "Thermal Conductivity of Periodically Microporous Silicon Films," Appl. Phys. Lett., **84**, pp. 1883–1885.
- [9] Keblishki, P., Phillpot, S. R., Choi, S. U. S., and Eastman, J. A., 2002, "Mechanisms of Heat Flow in Suspensions of Nano-Sized Particles (Nanofluids)," Int. J. Heat Mass Transfer, **45**, pp. 855–863.
- [10] Dresselhaus, G., Dresselhaus, M. S., Sun, X., Zhang, Z., and Chen, G., 1998, "Modeling Thermoelectric Behavior in Bi Nano-Wires," Proceedings of 17th International Conference on Thermoelectrics, Nagoya, Japan, pp. 43–46.
- [11] Cahill, D. G., Ford, W. K., Goodson, K. E., Mahan, G. D., Majumdar, A., Maris, H. J., Merlin, R., and Phillpot, S. R., 2003, "Nanoscale Thermal Transport," J. Appl. Phys., **93**(2), pp. 793–818.
- [12] Bohren, C. F., and Huffman, D. R., 1983, *Absorption and Scattering of Light by Small Particles*, Wiley, New York.
- [13] Van De Hulst, H. C., 1981, *Light Scattering by Small Particles*, Dover Publication, New York.
- [14] Modest, M. F., 1993, *Radiative Heat Transfer*, McGraw Hill, Inc., New York.
- [15] Ying, C. F., and Truell, R., 1956, "Scattering of a Plane Longitudinal Wave by a Spherical Obstacle in an Isotropically Elastic Solid," J. Appl. Phys., **27**(9), pp. 1086–1097.
- [16] Hinders, M. K., 1991, "Plane-Elastic-Wave Scattering From an Elastic Sphere," Nuovo Cimento B, **106**(7), pp. 799–818.
- [17] Morozhnik, V. S., 1983, "The Scattering of Elastic S-Waves on a Low-Contrast Spherical Inclusion," Izv. Earth Phys., **19**(6), pp. 460–465.
- [18] Prasher, R. S., 2004, "Thermal Transport Due to Transverse Phonons in Nano and Micro Particulate Media," J. of Applied Physics (submitted).
- [19] Prasher, R. S., 2004, "Thermal Transport Cross Section and Phase Function of Longitudinal Phonons for Scattering by Nano and Micro Particles," J. of Applied Physics, **96** (submitted).
- [20] Arfken, G. B., and Weber, H. J., 1995, *Mathematical Methods for Physicists*, Academic Press, San Diego.

Vladimir V. Kulish
 Mem. ASME
 e-mail: mvvkulish@ntu.edu.sg
 School of Mechanical & Production
 Engineering,
 Nanyang Technological University,
 50 Nanyang Ave., Singapore 639798

Vasily B. Novozhilov
 Assoc. Mem. ASME
 Faculty of Engineering,
 University of Ulster,
 Shore Rd., Newtownabbey,
 Co. Antrim, BT37 0QB, United Kingdom

An Integral Equation for the Dual-Lag Model of Heat Transfer

An integral relation is obtained between local temperature and local temperature gradient for the dual-lag model of heat transport, which substitutes classical Fourier law at short time scales. Both the heat flux lag and the temperature gradient lag are considered, however, it is shown that only difference between the two affects temperature profile. Being applied at exposed surface of material, the integral equation predicts surface temperature variation for any form of imposed heat flux. The solution is tested considering solid heating by a picosecond laser impulse. Results are compared with the classical solution of the parabolic heat transfer equation and available experimental data. [DOI: 10.1115/1.1797034]

Keywords: Analytical, Heat Transfer, Laser, Thin Films

Introduction

Heat transport at small scales receives increasing attention due to application in modern electronics [1], [2], and [3]. Many commonly used devices, such as personal computers or cellular phones, operate already on nanosecond time scale, and the spatial scales for the energy transport are of the order of a single atom.

It has become established that the heat transport equation is different from the classical one at such time scales [4]. In particular, one has to modify the Fourier law, which relates heat flux and the temperature gradient. According to Fourier law, heat flux adjusts immediately to the imposed temperature gradient, i.e., there is no relaxation time for the heat flux. At those scales where the Fourier hypothesis fails, one has to take into account the lag between the heat flux and the temperature gradient. In the most consistent way, such model for micro-scale heat transport has been proposed by Tzou [5], who introduced the two lags, namely the heat flux time lag and the temperature gradient time lag. Such a model represents a new type of constitutive relation between the heat flux and the temperature gradient, which supercedes the Fourier law at small scales. Being combined with the energy conservation law, such relationship leads to the energy transport equation, which is different from the classical parabolic one.

Numerical solution of the modified heat transport equation has been attempted in [5], using phase lags as small parameters and obtaining Taylor expansion of the constitutive relationship.

The present study generalizes analysis of the one-dimensional homogeneous energy transport equation with the dual phase lag. The integral form of the solution is obtained for the most general form of the constitutive relationship. It is shown that the general formulation, which does not involve approximate Taylor series, in fact leads to quite simple heat transfer equation and integral relationship for the solution.

Analysis is restricted to a one-dimensional semi-infinite domain with constant material thermal properties. Note that materials behave as thermally thick in most microheating applications. Further, in many typical cases (such as the one considered below) the temperature rise is very small; therefore the constant material properties assumption is an excellent approximation.

The energy transport equation is reduced to the form, closely reminiscent of the classical heat transfer equation, but with the time lag. Integral equation, which relates local values of the temperature and its gradient at any point inside the domain, is

obtained. This equation is then applied for prediction of the surface temperature under heating conditions, and the results are compared with the available experimental data.

Mathematical Model and Preliminary Analysis

Consider an infinite solid, $-\infty < x < +\infty$. According to the dual-phase-lag model proposed by Tzou [5], for any $-\infty < x < +\infty$, $-\infty < t < +\infty$ there is a lag between the local temperature gradient, $\partial T / \partial x$, and the local heat flux, q'' ,

$$q''(x, t + \tau_q) = -k \cdot \frac{\partial T}{\partial x}(x, t + \tau_T);$$

$$-\infty < x < +\infty, \quad -\infty < t < +\infty \quad (1)$$

Here τ_q is the phase lag of the heat flux, τ_T is the temperature gradient phase lag, and k is the thermal conductivity of the material. This is in contrast to Fourier's law, where heat flux adjusts immediately to the imposed temperature gradient

$$q''(x, t) = -k \cdot \frac{\partial T}{\partial x}(x, t); \quad -\infty < x < +\infty, \quad -\infty < t < +\infty \quad (2)$$

Constitutive relation (1) results in the new form of energy conservation equation, which in general form is written as

$$\frac{\partial T}{\partial t}(x, t) = -\frac{1}{\rho c_p} \cdot \frac{\partial q''(x, t)}{\partial x}; \quad -\infty < x < +\infty, \quad -\infty < t < +\infty \quad (3)$$

The nature of the modified equation can be established if one expands the left and right hand sides of Eq. (1) to get

$$q'' + \tau_q \frac{\partial q''}{\partial t} + o(\tau_q) = -k \left[\frac{\partial T}{\partial x} + \tau_T \frac{\partial^2 T}{\partial x \partial t} \right] + o(\tau_T);$$

$$-\infty < x < +\infty, \quad -\infty < t < +\infty \quad (4)$$

Upon substitution into the conservation law (3), the following heat transport equation is obtained [2]

$$\frac{\tau_q}{\alpha} \frac{\partial^2 T}{\partial t^2} + \frac{1}{\alpha} \frac{\partial T}{\partial t} = \frac{\partial^2 T}{\partial x^2} + \tau_T \frac{\partial^3 T}{\partial x^2 \partial t} + o(\tau_q) + o(\tau_T);$$

$$-\infty < x < +\infty, \quad -\infty < t < +\infty \quad (5)$$

for the temperature field, $T(x, t)$, in the domain.

It is clear from Eq. (5) that the lagging behavior should be taken into account for the processes whose characteristic time scales are comparable to τ_q , τ_T .

Contributed by the Heat Transfer Division for publication in the JOURNAL OF HEAT TRANSFER. Manuscript received by the Heat Transfer Division October 22, 2002; revision received June 3, 2004. Associate Editor: G. S. Dulikravich.

Different approaches may be taken to solve the heat transport equation with the lags numerically. Tzou [5], for instance, considers the truncated Eq. (5) and then obtains a solution of this equation in the Laplace space. The solution thus obtained cannot be inverted. Therefore, approximate methods, such as partial expansions and the Riemann–Sum approximation, have to be applied. Although the numerical results agree quite satisfactory with most of the experimental results, the exact solution is believed hard—if at all possible—to obtain.

In fact, truncation of the constitutive relation (1) is not necessary. Even involving conventional finite volume methods, one can easily solve the conservation equation (3) with the general constitutive relation (1).

Moreover, in the next section we demonstrate that a simple integral equation can be obtained involving the constitutive relation (1). Therefore, the problem is considered here in the most general form, involving the both lags and untruncated constitutive relation.

Note that Eq. (1) can be written in equivalent form as

$$q''(x,t) = -k \cdot \frac{\partial T}{\partial x}(x,t - (\tau_q - \tau_T));$$

$$-\infty < x < +\infty, \quad -\infty < t < +\infty \quad (6)$$

Substitution of (6) into the conservation equation (3) yields

$$\frac{\partial T}{\partial t}(x,t) = \alpha \frac{\partial^2 T}{\partial x^2}(x,t - (\tau_q - \tau_T));$$

$$-\infty < x < +\infty, \quad -\infty < t < +\infty \quad (7)$$

Equation (7) has the same form as the classical heat transfer equation, but with the lag $\tau_q - \tau_T$ in the diffusion term.

An immediate and important conclusion from Eq. (7) is that solution in the dual-lag model does not depend on τ_q and τ_T separately, but on the difference $\tau_q - \tau_T$ only.

Integral Equation

Consider now the problem for semi-infinite solid

$$\frac{\partial \vartheta}{\partial t}(x,t) = \alpha \frac{\partial^2 \vartheta}{\partial x^2}(x,t - \Delta\tau); \quad t \in [\Delta\tau, \infty]; x \in [0, \infty[\quad (8)$$

This domain is initially in thermal equilibrium. Therefore, the initial and boundary conditions are written as

$$\vartheta(x,0) = 0, \quad \frac{\partial \vartheta}{\partial x}(0,t - \Delta\tau) = -\frac{1}{k} q''(0,t), \quad \vartheta(\infty,t) = 0 \quad (9)$$

The condition at $x=0$ depends on particular specified rate of solid heating given by the flux $q''(0,t)$, and is a direct consequence of constitutive relation (6).

Here the excess temperature is introduced as $\vartheta = T - T_0$, and $\Delta\tau = \tau_q - \tau_T$ is the difference between the lags.

Differential equations with lag are readily handled by Laplace transform.

Taking transform of Eq. (8) with respect to t , $L(\vartheta(x,t)) = \Theta(x,s)$, and involving initial condition, one gets the ODE

$$\frac{d^2 \Theta}{dx^2} - \frac{s}{\alpha} \cdot \exp(\Delta\tau \cdot s) \cdot \Theta = 0 \quad (10)$$

with the general solution

$$\Theta(x,s) = C_1(s) e^{-\sqrt{s/\alpha} \exp(\Delta\tau \cdot s) \cdot x} + C_2(s) e^{\sqrt{s/\alpha} \exp(\Delta\tau \cdot s) \cdot x} \quad (11)$$

The latter must be bounded at $x \rightarrow \infty$, therefore, $C_2(s) \equiv 0$, and the solution is written as

$$\Theta(x,s) = C_1(s) e^{-\sqrt{s/\alpha} \exp(\Delta\tau \cdot s) \cdot x} \quad (12)$$

It is obvious now that the temperature and its gradient are related locally. Taking the derivative of Eq. (12)

$$\frac{d\Theta(x,s)}{dx} = -C_1(s) \cdot \sqrt{\frac{s}{\alpha}} \cdot \exp(\Delta\tau \cdot s) \cdot e^{-\sqrt{s/\alpha} \exp(\Delta\tau \cdot s) \cdot x} \quad (13)$$

and comparing to Eq. (12) itself,

$$\Theta(x,s) = -\sqrt{\frac{\alpha}{s}} \cdot \exp\left(-\frac{\Delta\tau}{2} \cdot s\right) \cdot \frac{d\Theta(x,s)}{dx} \quad (14)$$

The inverse Laplace transform of Eq. (14) can be found involving the table transform [6]

$$L^{-1}\left(\sqrt{\frac{\alpha}{s}} \cdot \exp\left(-\frac{\Delta\tau}{2} \cdot s\right)\right) = \sqrt{\frac{\alpha}{\pi}} \cdot \frac{u\left(t - \frac{\Delta\tau}{2}\right)}{\sqrt{t - \frac{\Delta\tau}{2}}} \quad (15)$$

where $u(t)$ is the unit step-function, and applying the convolution theorem [6]. This results in the following integral equation:

$$-\sqrt{\frac{\alpha}{\pi}} \cdot \int_0^t u\left(t^* - \frac{\Delta\tau}{2}\right) \cdot \frac{\partial \vartheta}{\partial x}(x,t - t^*) dt^* = \vartheta(x,t) \quad (16)$$

or, after simple re-arrangement, $t - t^* = \zeta$,

$$T(x,t) = T_0 - \sqrt{\frac{\alpha}{\pi}} \cdot \int_0^{t - \Delta\tau/2} \frac{\frac{\partial T}{\partial x}(x,\zeta)}{\sqrt{t^* - \frac{\Delta\tau}{2} - \zeta}} \cdot d\zeta \quad (17)$$

Integral equation (17) relates values of temperature and its gradient at the same point, and holds everywhere inside the domain.

In terms of the heat flux, Eq. (17) can be written as

$$T(x,t) = T_0 + \frac{1}{\sqrt{\pi k \rho c_p}} \cdot \int_0^{t - \Delta\tau/2} \frac{q''(x,\zeta + \Delta\tau)}{\sqrt{t^* - \frac{\Delta\tau}{2} - \zeta}} \cdot d\zeta \quad (18)$$

Being applied at the surface ($x=0$), Eq. (18) provides the means to predict behavior of the surface temperature of the material, $T_s(t) = T(0,t)$, based on the imposed flux $q_s''(t) = q''(t,0)$,

$$T_s(t) = T_0 + \frac{1}{\sqrt{\pi k \rho c_p}} \cdot \int_0^{t - \Delta\tau/2} \frac{q_s''(\zeta + \Delta\tau)}{\sqrt{t^* - \frac{\Delta\tau}{2} - \zeta}} \cdot d\zeta \quad (19)$$

Surface temperature is the most important parameter in micro-scale heat transfer applications.

For the case $\tau_q = \tau_T = 0$, the above equation reduces to integral relation obtained for the classical heat transfer equation by Kulish and Lage [7].

Model Validation

A test solution is obtained by integrating Eq. (19), in order to predict surface temperature of the material, subjected to prescribed heat flux. The heat flux applied at the boundary imitates laser impulse according to Gaussian distribution in time, namely

$$q_s''(t) = q_{s,\max}'' \exp\left[-\left(\frac{t-b}{\sigma}\right)^2\right]; \quad t \geq 0 \quad (20)$$

with $b = 10$ ps and $\sigma = 5.0$ ps (Fig. 1). Characteristic time of the considered heating process is, therefore, of the order of picoseconds. In the course of computations, the maximum value of the surface heat flux, $q_{s,\max}''$, was 10^3 W/m².

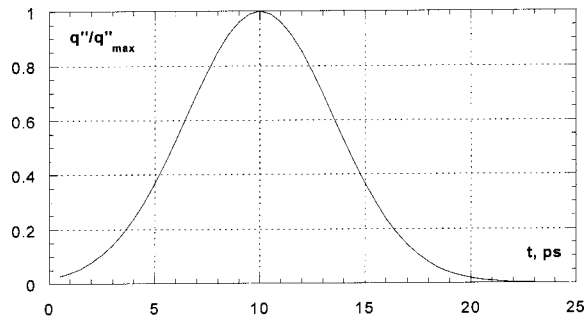


Fig. 1 Laser impulse for the test case

Material properties are taken as those of gold (Au), i.e., $k = 315 \text{ W/(m K)}$, $\alpha = 1.2495 \times 10^{-4} \text{ m}^2/\text{s}$, $\tau_q = 0.7438 \text{ ps}$ and $\tau_T = 89.286 \text{ ps}$ [5]. The time lags cited in [5] have been determined experimentally.

For a given heat flux history, integration of Eq. (19) is straightforward, and is carried out by explicit time advancement using trapezoidal rule for integration. In order to handle singularity, analytical integration is performed in the vicinity of the upper limit. The time step is chosen in such a way that the relative error of the solution does not exceed $\varepsilon = 10^{-6}$. Upon achieving this criterion, the solution also becomes independent of further reduction in time step.

The evolution of the normalized surface temperature, $\theta = (T_s - T_0)/(T_m - T_0)$, is shown in Fig. 2. Also shown in this plot is the profile for the classical heat transfer equation ($\tau_q = \tau_T = 0$).

It is obvious from Fig. 2 that the classical solution deviates significantly from solution of Eq. (19) at time scales comparable with τ_q , τ_T , and, therefore, cannot be used at such scales. In particular, the maximum surface temperature is predicted at later time by the classical equation, and the shape of the temperature profile is quite different from the solution of Eq. (19).

An interesting mathematical exception is the case $\tau_q = \tau_T$, where the solution of Eq. (19) coincides with that of the classical equation. However, such a case is unlikely for real materials, since the lags seem to differ significantly (see above example of gold).

Note also that for real materials $\tau_T > \tau_q$ so that the upper limit in the integral (Eqs. (17)–(19)) is always positive.

The lags τ_q , τ_T are material properties, which are known, however, with limited accuracy. It is worthwhile, therefore, to investigate sensitivity of the solution to these parameters. Plotted in Fig. 3 is a family of solutions that are obtained for different values of $\Delta\tau$, which deviate $\pm 10\%$ from the base values given in [7]. The sensitivity is small, compared with difference between the classical and dual-lag solutions.

From Fig. 3, one can see that the less value of the lag is, the closer the solution is to the classical model (no lag).

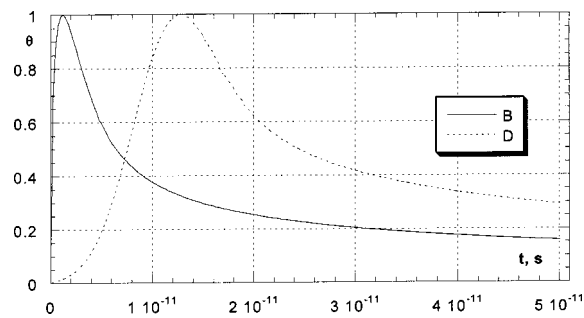


Fig. 2 Normalized surface temperature obtained for a bulk sample of gold (Au) in the case of the dual (B) phase lag, and classical energy equation (D)

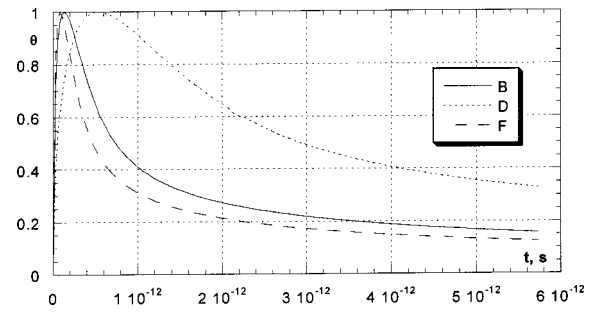


Fig. 3 Time evolution of the surface temperature for different values of the phase lags: (B) $\Delta\tau = -88.5422 \text{ ps}$ ($\tau_q = 0.7438 \text{ ps}$, $\tau_T = 89.286 \text{ ps}$)—base case; (F) $\Delta\tau = -97.3964 \text{ ps}$; (D) $\Delta\tau = -79.6880 \text{ ps}$

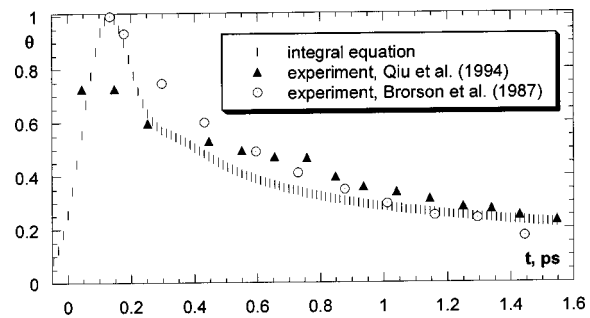


Fig. 4 Comparison between the numerical solution and experimental data

Finally, Fig. 4 shows the numerical solution of Eq. (19) compared with the available experimental data by Brorson et al. [8] and Qiu et al. [9]. Direct comparison of the maximum temperature with the measurements was not possible, since experimental data [8] and [9] are presented in normalized way. The maximum excess temperature obtained in the present calculations was $\Delta T_{\text{max}} \approx 0.06 \text{ K}$.

Conclusions

The heat transport equation with the dual-phase lag constitutive relation is considered. In contrast to previous studies, general formulation of the constitutive relationship is retained in the analysis. It is shown that such a general formulation results, in fact, in much simpler solution of the problem. Heat transfer equation with the dual lag is reduced to the form, similar to the classical parabolic equation. The solution of such equation depends only on the difference between the two lags. Therefore, the lagging behavior of the particular material is, in fact, described by the single parameter.

The method of Laplace transform has been used to obtain relationship between the local temperature and the local heat flux for the considered model. Such a relationship is written in the form of a simple integral equation.

Being applied at the surface, the integral equation provides a convenient way to predict maximum (surface) temperature during heating. The integral equation has been tested for the case of material heating by a picosecond laser impulse. The result has been compared with the solution of the classical (parabolic) heat transfer equation and with the experimental data available in literature.

In case of zero lags (or for time scales much longer than time lags), the proposed integral equation reduces to the previously established integral relation [3] and [7], applicable to problems, described by classical Fourier law.

Nomenclature

b = mean of normal distribution, s
 c_p = specific heat of solid material
 k = thermal conductivity, $\text{W m}^{-1} \text{K}^{-1}$
 L = Laplace transform operator
 q'' = local heat flux, W m^{-2}
 q_s'' = surface heat flux (at $x=0$), W m^{-2}
 s = Laplace transform variable
 t = time, s
 t^* = dummy time variable, s
 T = absolute temperature, K
 T_0 = initial temperature (at $t \leq 0$), K
 T_s = surface temperature (at $x=0$), K
 T_m = maximum temperature during heating, K
 $u(t)$ = unit step-function
 x = co-ordinate normal to material surface, m

Greek Symbols

α = thermal diffusivity, $\text{m}^2 \text{s}^{-1}$
 ϑ = excess temperature, $= T - T_0$, K
 Θ = Laplace transform of θ
 θ = normalized non-dimensional temperature,
 $= (T_s - T_0)/(T_m - T_0)$
 σ = variance of normal distribution, s
 ρ = density, kg m^{-3}
 τ_q = phase lag of heat flux, s

τ_T = temperature gradient phase lag, s
 $\Delta\tau$ = difference between lags, $= \tau_q - \tau_T$, s

References

- [1] Brorson, S. D., Kazeroonian, A., Moodera, J. S., Face, D. W., Cheng, T. K., Ippen, E. P., Dresselhaus, M. S., and Dresselhaus, G., 1990, "Femtosecond Room Temperature Measurement of the Electron-Proton Coupling Constant in Metallic Superconductors," *Phys. Rev. Lett.*, **64**, pp. 2172–2175.
- [2] Qiu, T. Q., and Tien, C. L., 1994, "Femtosecond Laser Heating of Multilayered Metals—I. Analysis," *ASME J. Heat Transfer*, **37**, pp. 2789–2797.
- [3] Kulish, V. V., Lage, J. L., Komarov, P. L., and Raad, P. E., 2001, "Fractional-Diffusion Theory for Calculating Thermal Properties of Thin Films From Surface Transient Thermoreflectance Measurements," *ASME J. Heat Transfer*, **123**(6), pp. 1133–1138.
- [4] Cattaneo, C., 1958, "A Form of Heat Conduction Equation Which Eliminates the Paradox of Instantaneous Propagation," *Compte Rendus*, **247**, pp. 431–433.
- [5] Tzou, D. Y., 1997, *Macro to Microscale Heat Transfer: The Lagging Behavior*, Taylor & Francis.
- [6] Abramowicz, M., and Stegun, I. A., 1964, *Handbook of Mathematical Functions: With Formulas, Graphs, and Mathematical Tables*, Dover, New York.
- [7] Kulish, V. V., and Lage, J. L., 2000, "Fractional-Diffusion Solutions for Transient Local Temperature and Heat Flux," *ASME J. Heat Transfer*, **122**, pp. 372–376.
- [8] Brorson, S. D., Fujimoto, J. G., and Ippen, E. P., 1987, "Femtosecond Electron Heat-Transport Dynamics in Thin Gold Film," *Phys. Rev. Lett.*, **59**, pp. 1962–1965.
- [9] Qiu, T. Q., Juhasz, T., Suarez, C., Bron, W. E., and Tien, C. L., 1994, "Femtosecond Laser Heating of Multilayered Metals—II. Experiments," *Int. J. Heat Mass Transfer*, **37**, pp. 2799–2808.

Estimating Parameters and Refining Thermal Models by Using the Extended Kalman Filter Approach

Ashley F. Emery

e-mail: emery@u.washington.edu
 Department of Mechanical Engineering,
 University of Washington,
 Seattle, WA 98195-2600

Parameter estimation is based upon a comparison of predicted deterministic model responses to data. The models are often numerical, e.g., finite volume, with intrinsic inaccuracies. In addition, the models typically assume a full knowledge of the physical processes. By using the concept of state variables and employing the extended Kalman filter approach it is possible to include additional effects in the model to achieve better agreement between the model and the data. This paper describes such an approach to the estimation of thermal conductivity in a transiently heated and cooled one-dimensional system and shows that it leads to a resolution of questions about the time behavior of the residuals previously observed in an estimation based upon the least squares analysis. [DOI: 10.1115/1.1795811]

Keywords: Models, Parameter Estimation, Correlated Data, Uncertainty, Kalman Filter

Introduction

Consider estimating the thermal conductivity by measuring temperatures as a function of time and position, $T = F(x, t, k)$. The usual approach is to minimize the weighted sum of the errors squared

$$S = \sum_{i=1}^N w_i \epsilon_i^2 = \sum_{i=1}^N w_i (T_i - F_i(x, t, k))^2 \quad (1)$$

where T_i are the measured temperatures, w_i are the weights, and $F_i(x, t, k)$ is the modeled response. Eq. (1) can be expressed as

$$S = \{T_i - F_i(x, t, k)\}^T \Sigma^{-1} \{T_i - F_i(x, t, k)\} \quad (2)$$

where Σ , the covariance matrix of the errors, is typically taken as a diagonal matrix whose elements are σ_i^2 which is equivalent to setting $w_i = 1/\sigma_i^2$ [1]. If the errors are correlated then Σ is a fully populated matrix.

Since minimizing S may be quite difficult for complex functions it is usual to expand F in a Taylor series about an initial guess k_0 , keeping only the first term

$$\{T_i\} = \{F_i(x, t, k_0)\} + H^T(k - k_0) \quad (3)$$

where $\{T\}$ is the column vector of measured temperatures, and $H = \{\partial F / \partial k|_{k_0}\}$ is the sensitivity of the model to k . Minimization is achieved by choosing a sequence of values of k producing values of $F_i(x, t, k)$ that converge to the minimum point. The converged value, \hat{k} , is taken to be the best estimate of the true value of k . It can be shown [2,3] that if the model is exact but that the measured temperatures have errors (noise) that are of zero mean and normally distributed then \hat{k} has a normal distribution with a mean of μ and a standard deviation of $\sigma(\hat{k})$ where

$$\mu = k_0 + \sigma^{-2}(\hat{k}) H^T \Sigma^{-1} \{T_i - F_i(k_0)\} \quad (4a)$$

$$\sigma^{-2}(\hat{k}) = H^T \Sigma^{-1} H \quad (4b)$$

If the errors are independent and identically distributed, i.e., $\sigma_i = \sigma(T)$, then the uncertainty in the estimate of \hat{k} given in terms of the standard deviation is simply

$$\sigma(\hat{k}) = \frac{\sigma(T)}{\sqrt{\sum_{i=1}^N \left(\frac{\partial T}{\partial k} \Big|_{t_i} \right)^2}} \quad (5)$$

This is an optimistic estimate of the precision of the estimate and frequently the precision actually achieved is less. The optimal experiment will have been designed to achieve the maximum precision, but more often than not, the experiment is run first and the data analyzed later to determine the precision. Given the data, the questions arise about how much of the data should be used, how the errors may be interrelated, and particularly how the conductivity should be deduced from the data.

When the data streams in at a high rate, as in communications or radar positioning, it is often desirable to estimate the properties on-line. For this recursive least squares fitting [4] (sometimes called sequential least squares) and Kalman filtering [5,6,7] are often used. It is not likely that the temperature measurements used to estimate conductivity will be observed at such high rates or that one would desire to estimate k on the fly. However, Kalman filtering and the concept of state variables can often prove to be helpful in understanding the experimental results, particularly when the usual approach reveals inconsistencies. In this paper we describe an experiment for which the estimation of thermal conductivity based on Eq. (3) displayed an unusual behavior of the residuals, leading to questions about the resulting values. The Kalman filter approach was then utilized with different models to ascertain what may have caused this behavior, i.e., temperature dependent conductivity, sensor position error, or unmeasured heat transfer. By augmenting the model to include additional internodal heat transfer the anomalies are eliminated.

The Experiment. Blackwell et al. [8] estimated the conductivity of stainless steel by measuring the temperatures in a thin hollow tube of length $2L$. Full details are given in [8] but a brief description is given here. Figure 1 is a schematic of the system. The outer surface of the tube was covered by and the hollow interior filled with space insulation to minimize losses from the

Contributed by the Heat Transfer Division for publication in the JOURNAL OF HEAT TRANSFER. Manuscript received by the Heat Transfer Division February 10, 2003; revision received June 30, 2004. Associate Editor: G. S. Dulikravich.

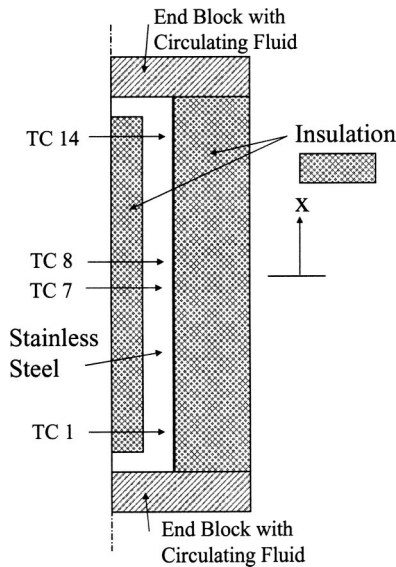


Fig. 1 Schematic of the experiment

surfaces and to create a one dimensional temperature field. The ends of the tube were heated by a fluid which flowed through serpentine channels in copper end blocks. In principle the temperature was symmetric with respect to the length of the tube. Temperatures were measured at 14 equally spaced axial locations each with 4 thermocouples spaced equally about the circumference. The estimation of the thermal conductivity from the experiment requires a knowledge of the heat flux history.

Because of the unknown thermal characteristics of the copper end blocks and the contact resistance between the end blocks and the steel tube, it is not possible to precisely specify the boundary conditions and the inverse problem then involves estimating both the conductivity and the time history of the end heat fluxes. Because the time history of the fluxes is difficult to obtain, as demonstrated in many papers [9,10] the time varying temperatures measured at the ends, $x = \pm L$ were taken to be the prescribed end boundary conditions and the temperature histories computed using a finite volume code. The measured transient temperatures were fitted to the numerically computed temperatures as a function of k , x , and t and the conductivity estimated using the usual least squares equations under the assumptions of unit weight and independent errors of zero mean

$$\hat{k} = \sum_{i=1}^N \frac{\left(\frac{\partial T}{\partial k} \right)_{t_i} (T_i - F_i(k, x, t))}{\sum_{i=1}^N \left(\frac{\partial T}{\partial k} \right)_{t_i}^2} \quad (6)$$

There are a total of 48 thermocouple histories with measurements taken every 1.5 seconds. Figure 2 shows the first 750 seconds of the temperature history. The temperatures histories of the symmetrically placed thermocouples match so well that they cannot be differentiated on the figure. If the errors of the measured temperatures are correlated, then the information gained is less than the sum of the information from all sensors and the standard deviation is greater than would be predicted using Eq. (5) under the assumption of independence. Emery et al. [11] have shown that the signals depicted on Fig. 2 were correlated to such a degree that no new information was gained from the 4 circumferentially spaced thermocouples over one at each axial location and from the thermocouples 8–13 over those at 2–7. Thus the standard deviation is that computed from only 1/8th of the sensors, namely sensors 2 through 7 and $\sigma(\hat{k})$ is increased by a factor of $\sqrt{8}$ from that

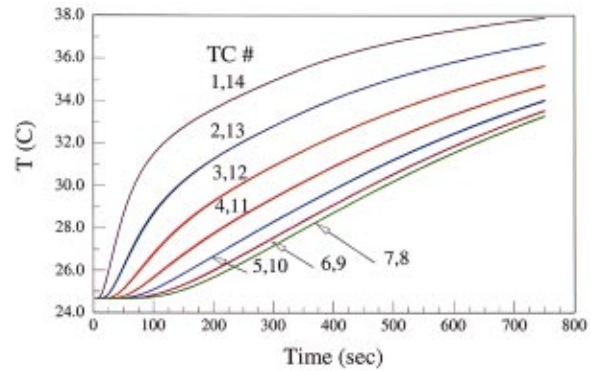


Fig. 2 Measured temperatures at the indicated thermocouples with TC 1 and 14 located at $x = \pm L$ and 7 and 8 located adjacent to the centerline, $x = 0$: (a) estimated conductivity; and (b) estimated standard deviation.

based upon Eq. (5) using all the measured data. Computing the conductivity using each sensor individually and using the data from thermocouples 2–13 during the heating phase and assuming no error in density or specific heat gives the results shown in Table 1.¹

If the noise in the measured temperatures is independent and of constant standard deviation, we see from Eq. (5) that as more data is gathered the standard deviation will diminish. Figure 3 illustrates how the estimated conductivity and its standard deviation vary as the experiment time increases for conductivities estimated from single thermocouples and from all of the data.

Because the sensitivities are functions of thermocouple position and time, the standard deviations associated with the individual sensors vary considerably. Combining all the data reduces $\sigma(\hat{k})$ to the apparently very acceptable level of 0.0049 W/mK or less than 0.03%. However, estimating the standard deviations of k using the residuals typically yields a minimum value which is rarely achieved.

In fact, the noise associated with the different thermocouples is correlated. Emery et al. [11] have shown that this correlation and that associated with thermocouples 1 and 14 which are used as the boundary conditions for the model result in an increase in the

¹The results differ slightly, 0.14%, from those presented in [8] since a different numerical simulation code was used.

Table 1 Estimated conductivity and standard deviation using Eq. (5) with a value of $\sigma(T) = 0.08$ C

Sensor	\hat{k}	$\sigma(\hat{k})$
2 only	14.9235	0.0431
3	14.6862	0.0240
4	14.6291	0.0180
5	14.5367	0.0152
6	14.6090	0.0139
7	14.5894	0.0133
8	14.5307	0.0132
9	14.5048	0.0138
10	14.5328	0.0152
11	14.3825	0.0177
12	14.3178	0.0233
13	14.3155	0.0410
all 12 sensors	14.5420	0.0049
accounting for spatial correlation [11]		0.0071
accounting for correlation in time [11]		0.0389
using the values of \hat{k} from sensors 2–13		
Extended Kalman Filter at minimum $\sigma(k)$	14.5465	0.1676
all 12 sensors	14.5488	0.0638

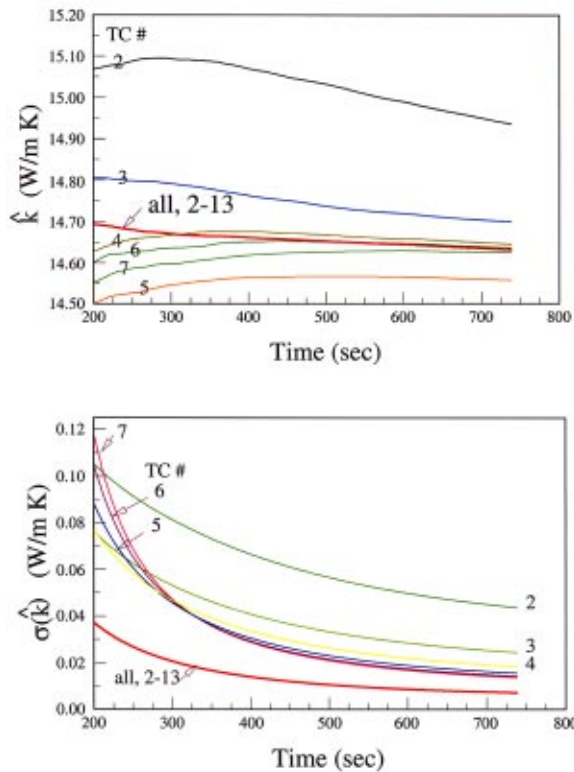


Fig. 3 Sequential least squares fitting during heating showing individual results from thermocouples 2–7 and that from averaging values from thermocouples 2–13

standard deviation by a factor of ≈ 5 , leading to the value of 0.0389 shown in the table. A more realistic estimate of the standard deviation is obtained by using the values of \hat{k} obtained from each of the sensors, giving $\sigma(\hat{k}) = 0.1676$ or slightly more than 1%. This value of $\sigma(\hat{k})$ is approximately four times greater than that estimated from the least squares fit when including the effects of spatial and temporal correlation and raises the question of why.

In estimating a property using the least squares approach, it is instructive to examine the residuals [12]. Ideally these residuals when weighted by the sensitivities, as indicated in Eq. (6) should average to zero and be distributed about zero with a normal distribution if the errors are normally distributed. If one examines the residual for each thermocouple history taken individually this does occur. But when using the value of k based upon all the data, the residuals behave rather strangely. Figure 4 illustrates the residuals for thermocouples 2–13 computed using the value of $\hat{k} = 14.542$ based on all 12 thermocouples (Table 1).

There are a number of possible reasons for this behavior of the residuals: (a) the use of a one term Taylor series in Eq. 3 in which the effect of conductivity is presumed to be linear is not sufficient; (b) the positions of the sensors may be uncertain; (c) the use of the temperatures at thermocouples 1 and 14 as boundary conditions may not accurately reflect the true behavior; (d) the noise in the temperatures used for the boundary conditions may affect the results; and (e) there may be small axial heat transfer along the tube or losses through the enclosing insulation which are not included in the model.

When the response is linear in k , for a reasonable number of readings, typically more than 20, the residuals for each sensor are known to have a mean of zero and to be normally distributed about zero [2,3]. Highly nonlinear dependency can show up as residuals which do not average to zero, as in Fig. 4, and which lead to a biased estimate of the conductivity. In a recent paper, Emery and Bardot [13] have analyzed the nonlinear dependence

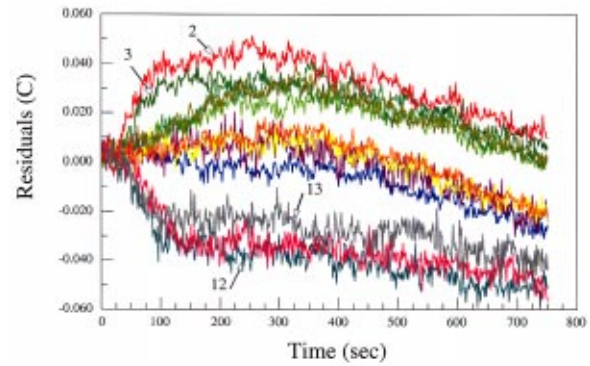


Fig. 4 Residuals for thermocouples 2–13 (the curves for TC 4–11 are not identified)

of $T(x,t)$ upon k and shown that the nonlinear effects were negligible, that the individual residuals should have zero means, and that the expected bias in the estimated value of k is less than 0.01%.

This leaves (b)–(e) as possible explanations for the unusual behavior. Blackwell et al. [8] have discussed the effect of inaccuracies in the thermocouple positions (which also may reflect that the thermocouple senses the temperature in the vicinity but not at the exact point in the model) and concluded that there was a maximum uncertainty in position of 0.44 mm, leading to $\sigma(T) = 0.13$ C. Effects (c) and (d), discussed in the following section entitled “Consideration of Other Effects,” were found to be negligible.

The most likely deficiency in the model is that there may be minor amounts of axial heat transfer by conduction or by radiation via the encapsulating insulation or losses through the insulation. Estimating these effects cannot be done with any precision. At best one can use a model with control volumes centered at the thermocouple locations and develop an approximate energy balance. This means that there can be at most 14 nodes (including the two boundary nodes) and the resulting estimates will be only approximate. Figure 5 compares these minor heat flows to the energy flowing in through the two boundary nodes, thermocouples 1 and 14. The time averaged minor heat fluxes summed over all internal nodes is approximately 2 W/m^2 with a time averaged standard deviation of approximately 101 W/m^2 as compared to the energy flowing in through each of the boundaries of approximately 7500 W/m^2 at the peak. From this point of view, these minor effects are insignificant and should not contribute to the wide variation in the estimated values of the conductivity or to the

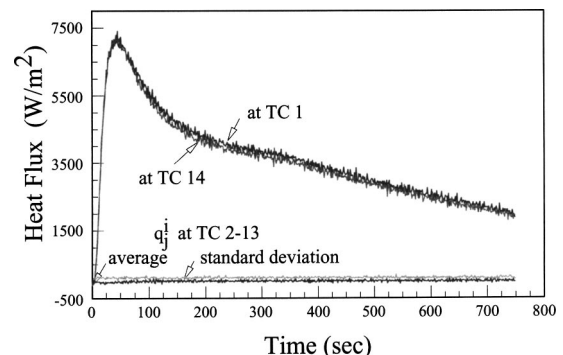


Fig. 5 Comparison of estimated axial heat transfer averaged over nodes 2–13 to the flux at the boundaries, TC 1, and 14

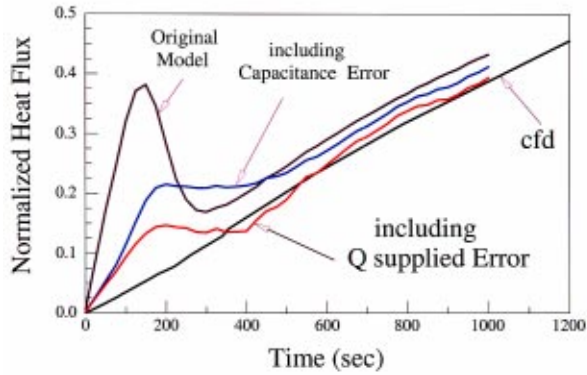


Fig. 6 Estimated surface heat flux for free convection from a cylinder showing the effect of inaccuracies in the heat supplied and stored

behavior of the residuals. Furthermore, including these in the usual parameter estimation model as time varying quantities would be very difficult.

A recent paper [14] described an experiment in which a horizontal hollow cylinder was fitted with an internal electrical heater and transiently heated while it convected and radiated to quiescent ambient air. The convective heat transfer coefficient was based on the surface flux, the difference between the energy produced by the heater and that stored in the cylinder, and the temperature difference between the cylinder surface and the ambient air. The resulting free convective heat transfer coefficient was found to differ substantially from that predicted by a conjugate cfd calculation. While some of the difference could be attributed to small local air currents which were highly correlated in time, these effects were minor and could not explain the discrepancy. An analysis was done using the principles of the Kalman filter by introducing new state variables to account for a thermal resistance between the heater and the cylinder, for a time varying amount of energy stored in the heater itself, and for losses through the insulated end caps of the heater to the ambient air. Figure 6 compares the estimated surface heat flux based upon the original solution and that including these effects. We note how much better the fluxes agree when the model includes an unknown parameter to represent the heater endcap losses, suggesting that the heat supplied to the cylinder was in error especially at early times. Based upon these results, the experiment was modified to minimize the thermal contact resistance between the heater and the cylinder and to reduce endcap heat losses. As a result, the free convection heat transfer estimated from the experiment was found to be in much better agreement with the simulation.

Following this example, let us use the Kalman filter approach to investigate the cause of the behavior shown in Fig. 4.

Kalman Filter Analysis. The idea behind the Kalman filter is to estimate a value of the parameter at time t_i based upon all of the data up to and including that at time t_i . The Kalman filter is an extension of recursive least squares approach based upon state variables which has been found in its usual formulation to successfully handle slowly varying parameters [5]. The Kalman filter approach has been successfully used in analyzing heat exchangers [15,16] and in inverse linear conduction problems [17,18]. Moultanovsky [19,20] has used this method (referred to in his papers as Adaptive Iterative Filter) to determine the temperature dependent properties in materials and to both estimate heat transfer coefficients and appropriately control HVAC systems. Details of the method are given in a number of excellent texts [5,6] and in [19,20]. The method can also be used to estimate constant properties by treating them as slowly varying. If the system response is a non-linear function of the parameter sought, the

method is termed the Extended Kalman Filter (EKF) approach. In our case, we will treat the conductivity as a slowly varying parameter. Of course, k does not vary with time. What the EKF approach does is to modify the value of \hat{k} as data are accumulated in such a way that the variance of \hat{k} is minimized. In this sense it is no different than watching how \hat{k} changes when using sequential least squares with an ever increasing amount of data.

Let \mathbf{y}_i be the n component state vector characterizing the system at time t_i . $\{\mathbf{y}_i\}^T = \langle T_1^i, T_2^i, \dots, T_{13}^i, T_{14}^i, p_1, p_2, \dots, p_m \rangle$ where T_j^i are the nodal temperatures and p_1, \dots, p_m are the parameters of the model.

The time evolution of the system, \mathbf{y}_i , and the measurements, \mathbf{z}_i , are described by

$$\mathbf{y}_{i+1} = \mathbf{f}_i(\mathbf{y}_i) + \xi_i \quad (7a)$$

$$\mathbf{z}_i = \mathbf{D}_i(\mathbf{y}_i) + \eta_i \quad (7b)$$

where \mathbf{f} is a vector valued function of \mathbf{y} , ξ is the system noise, \mathbf{z} are the measured temperatures, and η is the measurement noise. Both ξ and η are zero mean, Gaussian distributed random values with covariance matrices of \mathbf{S} and \mathbf{R} , respectively. Because only the nodal temperatures are measured, but the parameters are not, \mathbf{D} is a matrix with elements diagonal elements = 1 for rows corresponding to the measured temperatures and with all other elements being zero. In these calculations the experimental system was assumed not to be affected by extraneous external influences and $\mathbf{S} = 0$. One might argue when considering the effects of noise in the boundary conditions that a non-zero \mathbf{S} should be used, but since in this case the boundary temperature will be taken as one of the parameters of the model, its associated noise will be incorporated directly into the conditional covariance \mathbf{P} .

Using a model based upon finite difference discretization

$$\rho c \frac{(T_j^{i+1} - T_j^i)}{\Delta t} = k \frac{(T_{j-1}^i - 2T_j^i + T_{j+1}^i)}{\Delta x^2} + q_j^i \quad (8)$$

the j^{th} component of the vector function \mathbf{f}_i is given by an expression of the form

$$f_i = T_j^i + k(b_{j-1}T_{j-1}^i + b_jT_j^i + b_{j+1}T_{j+1}^i) + q_j^i \frac{\Delta t}{\rho c} \quad (9)$$

where the conductivity, k , is explicitly stated since it is a component of the state vector. Because of the products, kT_j^i , $\mathbf{f}(\mathbf{y})$ is a nonlinear function of the state variables and the usual Kalman filter approach based on linearity cannot be used. Instead, \mathbf{f} is expanded in a one term Taylor series

$$\mathbf{f}_i(\mathbf{y}_i) \approx \mathbf{f}_i(\hat{\mathbf{y}}_i) + \mathbf{A}_i(\mathbf{y}_i - \hat{\mathbf{y}}_i) \quad (10)$$

where \mathbf{A}_i is a matrix with elements $A_i(k, l)$ given by differentiating the k^{th} component of \mathbf{f}_i with respect to the l^{th} component of \mathbf{y}_i and evaluated at $\hat{\mathbf{y}}_i$.

Let $\hat{\mathbf{y}}_{i|i-1}$ represent our estimate of the system state at time i based upon measurements up to time $i-1$. The procedure consists of the following steps [5]: (a) a prediction of the response $\hat{\mathbf{y}}_{i|i-1}$ based upon $\hat{\mathbf{y}}_{i-1|i-1}$

$$\hat{\mathbf{y}}_{i|i-1} = \mathbf{f}_{i-1}(\hat{\mathbf{y}}_{i-1}) \quad (11a)$$

and (b) a correction

$$\hat{\mathbf{y}}_{i|i} = \hat{\mathbf{y}}_{i|i-1} + \mathbf{G}_i(\mathbf{z}_i - \mathbf{D}_i\hat{\mathbf{y}}_{i|i-1}) \quad (11b)$$

The Kalman gain matrix, \mathbf{G}_i is chosen to minimize the mean square errors of the state variables and is recursively computed from

$$\begin{aligned} \mathbf{P}_{i|i-1} &= \mathbf{A}_{i-1}\mathbf{P}_{i-1|i-1}\mathbf{A}_{i-1}^T + \mathbf{S}_{i-1} \\ \mathbf{G}_i &= \mathbf{P}_{i|i-1}\mathbf{D}_i^T(\mathbf{D}_i\mathbf{P}_{i|i-1}\mathbf{D}_i^T + \mathbf{R}_i)^{-1} \\ \mathbf{P}_{i|i} &= (\mathbf{I} - \mathbf{G}_i\mathbf{D}_i)\mathbf{P}_{i|i-1} \end{aligned} \quad (11c)$$

where $\mathbf{P}_{i|i}$ is the conditional covariance matrix of the error in the estimated state variable

$$\mathbf{P}_{i|i} = E(\{\mathbf{y}_i - \hat{\mathbf{y}}_{i|i}\}\{\mathbf{y}_i - \hat{\mathbf{y}}_{i|i}\}^T) \quad (12)$$

The process is begun by assuming maximal ignorance about \mathbf{P} , i.e., setting $\mathbf{P}_{0|0} = \sigma_0 \mathbf{I}$ where σ_0 is a large number relative to the observed noise and \mathbf{I} is the identity matrix. \mathbf{P} will very quickly converge to the correct value. The process described by Eqs. (11,12) is termed the Extended Kalman Filter, **EKF**. Although it would appear from Fig. 4 that the sensors have different variances, it is not critical to the success of the filtering approach to use precise values in \mathbf{R} . One must only be careful to use values that are at least as large or larger than actually occur. Using values that are too small slows the convergence of the estimation. The calculations reported herein used $\sigma_0 = 0.1$ C, T_j^0 equal to the initial temperature, and an initial values of k from 5 to 20, although the range from [21] is from 14 to 15 W/mK. The effect of choosing the initial value of k vanished very quickly and had no effect, less than 0.05%, on the values of k estimated after 300 seconds. The results reported herein are for an initial value of 14.5 (Table 1).

Estimation of k Only. Let us take the measured values of T_i and T_{14} to be the known boundary conditions of the model, i.e., not to be included in \mathbf{y} , and estimate only one parameter $p_1 = k$. The state vector \mathbf{y} has 13 components, the 12 estimates of the nodal temperatures and the temporally slowly varying, but spatially constant, conductivity k , i.e., $n = 13$. In this case we assume that $q_j^i = 0$ and that the model is exact, that is the covariance matrix \mathbf{S} is zero. $R(13,13)$ is set equal to σ_1^2 , an estimate of $\sigma^2(k)$. Again we must note that we cannot set $\sigma_1^2 = 0$, otherwise k_i will remain constant [5]. However, the process is quite insensitive to the value of σ_1 assumed. Even very large values of σ_1 do not seem to affect the estimation. Applying this approach with $\sigma_1 = 0.5$ W/mK gives the time history of the estimated conductivity and the residuals as shown in Fig. 7.

In addition to predicting $\hat{\mathbf{y}}_{i|i}$, the method also provides an estimate of $\sigma(\hat{k})$ and $\sigma(T)$. When using the ordinary or sequential least squares approach, estimating σ_T requires a considerable effort [8,11]. Here one obtains the values automatically as part of the computation. Looking at the residuals, Fig. 4, and recognizing that for a normal distribution that 99.9% of the values are found within $\pm 3\sigma$, gives an estimate of $\sigma_T \approx 0.002$ C. This agrees well with the value of 0.0025 C computed using the EKF method.

Note that the estimated value of k found from all sensors is consistent with that found by the sequential least squares approach, Fig. 7, but that the estimated value of $\sigma(\hat{k})$ is in much better accord with the value found using the values estimated by individual sensors, Table 1, than is the standard deviation computed from Eq. (5). The agreement results from the ability of the Kalman filter approach to build into its process the effects of both the autocorrelation in time and the cross correlation between the signals. It is also important to note that the maximum precision was achieved very early in the experiment, at approximately 75 seconds, and that later temperatures, which occurred as steady state is approached and whose errors became more correlated, actually diminished the precision.

Figure 8 shows the cross-correlation between TC 2 and the remaining thermocouples. As shown in Ref. [11], the information provided by correlated measurements is reduced by the factor $(1 - \rho)/(1 + \rho)$ when compared to the information from uncorrelated measurements. A reasonable upper limit for useful measurements is $\rho = 0.7$ at which point the new information has less than 20% value. From the figure ρ exceeds 0.7 very quickly and little additional information is obtained about k as steady state is approached. In fact, because of the different temporal variation of the sensitivity with respect to position, the precision actually diminishes, i.e., $\sigma(\hat{k})$ increases as steady state is approached.

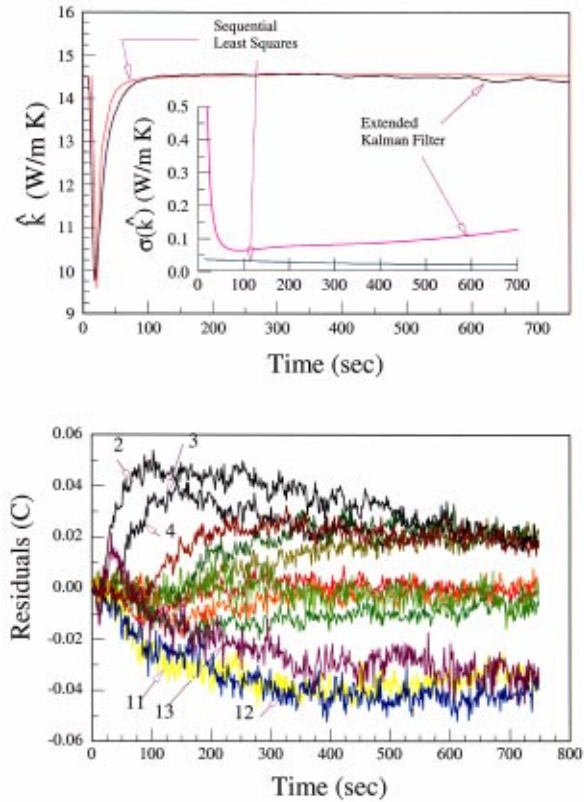


Fig. 7 (a) Estimated \hat{k} computed using the extended Kalman filter; and (b) the residuals computed using the extended Kalman filter

Consideration of Other Effects

The values of \hat{k} and residuals shown in Fig. 7 agree very well with those computed using the sequential least squares approach in which the noise is assumed to be independent and constant in time. Questions still remain: (a) what is the cause of the unusual behavior of the residuals and (b) why do the errors in the different thermocouples appear to be correlated, Fig. 8. Since the residuals and the estimation of correlation are dependent upon the model response, is it possible that the model is deficient in describing the observed experimental response? Let us now investigate the effect of other uncertainties in the model to see if these questions can be resolved.

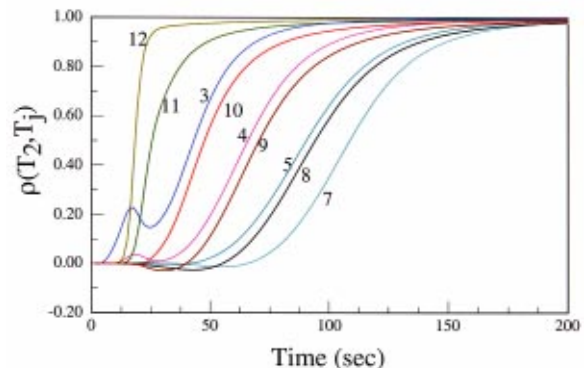


Fig. 8 Correlation between T_2 and the other sensors

Boundary Conditions. The state variables include the measured temperatures at thermocouples 1 and 14 which are used to specify the boundary conditions. These measurements are noisy and the EKF method includes this uncertainty either by including the noise in \mathbf{R} or in \mathbf{S} . This is only possible since the noise is assumed to be of zero mean. The results were essentially identical to those shown in Fig. 7.

Uncertain Thermocouple Position. Here the state variable was augmented by identifying the parameters p_1, \dots, p_{12} with the thermocouple locations x_1, \dots, x_{12} and p_{13} with the conductivity, k . In this application of the EKF method, the thermocouple positions do not change with time, but our estimate of the positions may, based upon the data. The thermocouples are nominally 9.51 mm apart. The predicted values of \hat{k} are unchanged from those shown in Fig. 7 and the maximum re-assignment of a thermocouple's position was less than 0.5 mm. This estimate agrees well with Blackwell's estimate of an uncertainty in thermocouple location of 0.44 mm.

Uncertain Local Thermal Conductivity. Assigning a different conductivity to each node and including this in the state vector gave results comparable to the values of \hat{k} shown in Fig. 3 which were based upon individual thermocouple measurements. Again, there was no substantive change in the time history of the residuals.

Axial Heat Transfer/Losses. Even though the tube was carefully insulated, there is the possibility that heat was transferred axially by conduction in the insulation or by radiation between the tube and the insulation. In addition, some heat may have been lost to the environment through the insulation. Letting the terms q_j^i in Eq. (8) be taken as additional state variables, giving $\mathbf{y}_i = \langle T_2^i, \dots, T_{13}^i, q_2^i, \dots, q_{13}^i, k \rangle^T$, produced the results shown in Fig. 9. It must be realized that although it might appear that q_j^i could be considered as system noise, i.e., ξ , and not as state variables, they cannot since they are not of zero mean with respect to time. Note that: (a) the estimated conductivity and standard deviation are essentially unchanged and (b) but the residuals after 200 seconds are now centered about 0 and superimposed on each other—just what we were hoping for, although the behavior at early times has not changed.

The predicted values of q_j^i are shown on Fig. 10. The average over nodes 2 through 13 is close to zero, Fig. 10(b), reflecting satisfaction of the overall energy balance, and the standard deviation is only about 1% of the flux at the boundaries. Effects of this magnitude are almost negligible and could normally be ignored. However, by considering them, we are able to achieve residuals which behave as we expected. In addition, the correlation between thermocouples is eliminated, Fig. 12(b), over most of the time period.

Early Time Behavior. By considering q_j^i as a state variable we have resolved most of our problems. However, we still need to understand what is happening at the early time when the estimated conductivity shows a substantial reduction and then recovery. The actual experiment involved heating to approximately steady state and then cooling. Figure 11 shows the sensitivities. At the onset of heating, the sensitivities are zero until approximately 20 seconds when the thermal pulse first reaches TC 2. Thermocouples 7 and 8 are affected at 100 seconds.

During this initial period, the estimated conductivity is substantially in error and has unusually high values of $\sigma(\hat{k})$ because of the very small values of $\partial T/\partial k$ used in Eqs. (5) and (6). By 100 seconds, the sensitivities are sufficient so that \hat{k} has become essentially constant, as seen on Figs. 7(a) and 9(a). However, the residuals shown in Fig. 9(b) remain large and spread out until approximately 250 seconds. Estimating the conductivity over the entire duration of the experiment, which involves both heating and cooling, gives the results shown in Figs. 12 and 13 and we see

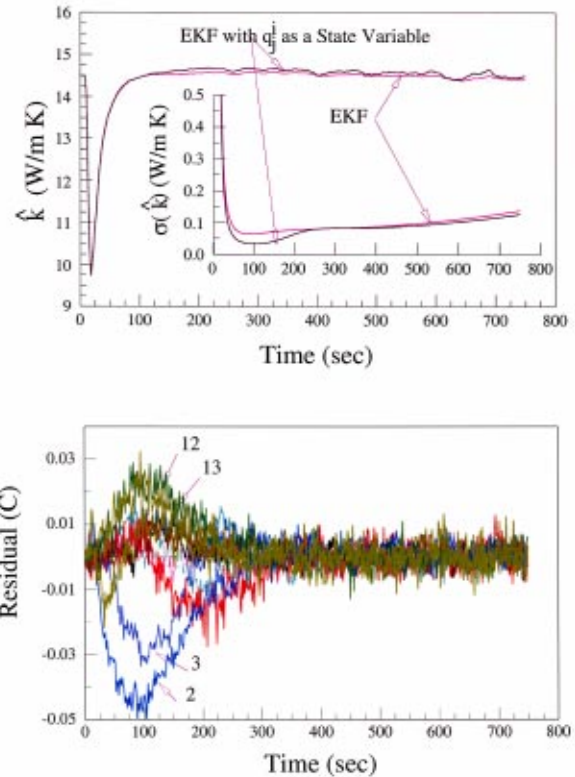


Fig. 9 (a) The effect of considering q_j^i on the estimated \hat{k} ; and (b) the effect of considering q_j^i on the residuals

similar behavior at both the onset of heating and cooling. The behavior at the onset of cooling was not expected at that time since the sensitivities are substantial and remain reasonably high until approximately 1000 seconds.

The residuals have the same patterns as before with the consideration of q_j^i as state variables reducing the residuals to small values over most of the experiment, Fig. 13. As before, this model eliminates the cross-correlation between the measured temperatures, Fig. 12(b). The estimated values of q_j^i during the cooling period are approximately the negative of those during the heating period with an average value of about 5 W/m^2 and the same magnitude and temporal behavior of the standard deviation as shown in Fig. 10.

The value of \hat{k} when considering losses shows a large jump at the onset of cooling and only at the end of the experiment does it drop and match the value obtained when losses are not included in the model. Apparently something occurs at the onset of cooling. If we ignore the first 100 seconds of the heating and cooling phases: (a) the EKF method gives the same results as including them; and (b) but when considering losses, the cooling phase predictions do not show the sudden increase at the onset of cooling and match the EKF values throughout the cooling period as shown on Fig. 11(a).

In both approaches $\sigma(\hat{k})$ increases substantially during the cooling phase, eventually reaching a value tripling that at the end of the heating phase because of the reduced sensitivity at long times. From the temperature shown on Fig. 11 and the trace of $\sigma(\hat{k})$ on Fig. 12 it appears that the estimation of k should not rely on data taken after 1500 seconds and that the cooling phase is of less value in estimating k than is the heating phase.

It appears that an unexplained and unanticipated effect exists at the onset of heating and cooling. To check this, we created an artificial data set by adding a zero mean, normally distributed

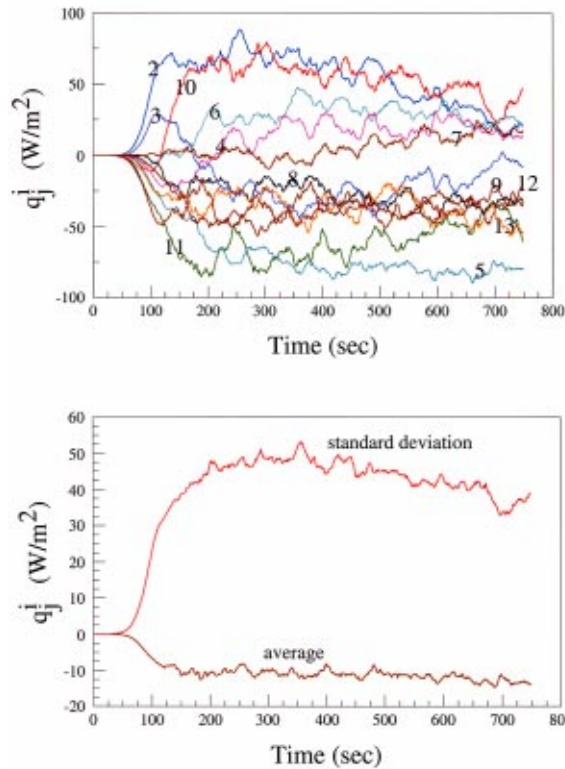


Fig. 10 (a) Values of q_j^i at each node; and (b) average of q_j^i over nodes 2-13

noise with $\sigma(T)=0.002$ C to the computed temperatures based upon $k=14.542$. This set was then analyzed and the results are shown on Fig. 14.

Because of the small sensitivity at early times, the artificial data exhibits the same behavior during heating as does the experimental data but \hat{k} becomes relatively constant after 30 seconds while \hat{k} estimated from the real data takes until 100 seconds. When cooling begins, as a result of the relatively high sensitivity, \hat{k} predicted from the artificial data remains constant, but that predicted from the real data exhibits a marked reduction. Behavior similar to that of the artificial data is reported in [5], Sec. 8.4 and appears to be a consequence of the EKF method basing the estimates of the parameters on relatively crude estimates of the system response at

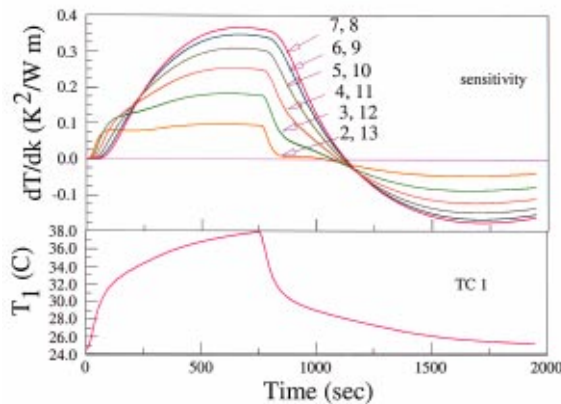


Fig. 11 Estimated conductivity using an artificial set of measured temperatures as compared to the real data

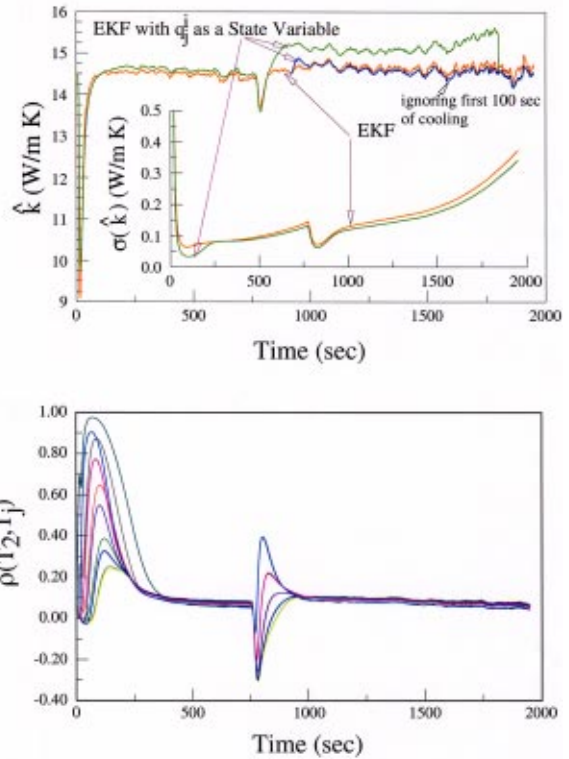


Fig. 12 (a) Estimated k over the combined heating and cooling periods; and (b) cross correlation when considering q_j^i over the combined heating and cooling periods

early times. As illustrated in Fig. 14, the effect is relatively small and quickly disappears. The cause of this effect at the onset of cooling is not understood. Similar results have been found for the free convective heat transfer from the horizontal cylinder [14] whenever the level of heating was changed and Dowding [22] has reported similar results.

Conclusions

When estimating parameters it is important to determine the precision of the estimate, $\sigma(\hat{k})$. In the least squares approach, whether sequential or treating all the data, it is usual to assume that the errors in the measured data are independent and of zero mean. $\sigma(\hat{k})$ is determined using Eq. (5) with $\sigma(T)$ estimated from the residuals [23]. The resulting value of $\sigma(\hat{k})$ is typically overly

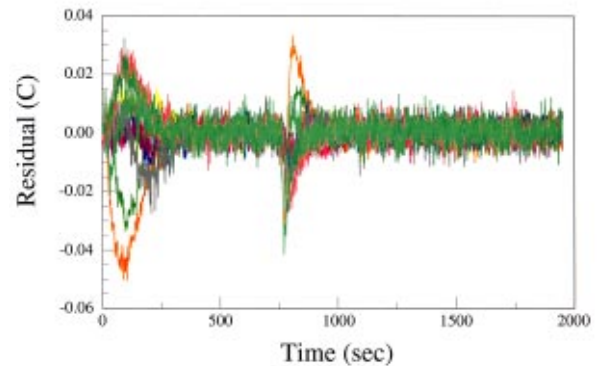


Fig. 13 Residuals over the combined heating and cooling periods when considering q_j^i as state variables

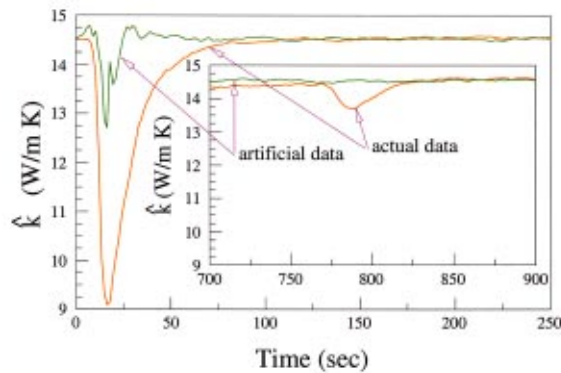


Fig. 14 Estimated conductivity using an artificial set of measured temperatures as compared to the real data (the lower curve is the time history of the boundary temperature)

optimistic, as illustrated in this example. The EKF approach gives a more reasonable value while predicting the same value of \hat{k} and residuals. The gradual increase in $\sigma(\hat{k})$ as shown in Fig. 7 suggests that the data gathered at long times is of lesser value and that the best estimates of k are those estimated at conditions associated with the minimum standard deviation. Because the usual least squares approach ignores correlations between the measured temperatures, it substantially overestimates the precision of the estimated conductivity, in this case by an order of magnitude. The Kalman filter approach detects the substantial cross correlation between the measurements from the different sensors and incorporates these effects into the final estimates. It also revealed the existence of the cross correlation which was unexpected.

The consideration of q_j^i as state variables resolved these effects. While these values summed to zero, indicating conservation of energy of the entire system, the individual nodal values showed a persistence over the duration of the experiment. Although we termed these effects as axial heat transfer/losses, their physical nature is unknown. They simply reflect the inability of the model to represent what is happening on a local level. They can represent numerical inaccuracies, radiation heat transfer between nodes or through the insulation, an inaccurate accounting for transient storage, or even the effect of the thermocouples measuring a temperature which is more representative of the average at a point other than the thermocouple location when the temperature spatial gradients are high. Their magnitudes are small, of the order of 1%, and they have no substantive effect on the estimated \hat{k} .

The analysis suggests that something unusual happens at the onset of heating or cooling. The very low sensitivities that exist at the start of the experiment preclude any understanding of this. However, an analysis of the behavior at cooling in which the state variable including losses was augmented by including uncertain thermocouple positions showed a reduction in the residuals of about 1/2 and indicated that the gradients near the boundaries, $x = \pm L$, were being incorrectly estimated because of the higher spatial gradients in temperature.

One apparent solution is to ignore the very early time behavior. Now the estimation is based upon comparing the predicted and measured temperatures and to do this the initial conditions must be well defined. When starting from a uniform initial temperature, the numerical accuracy of the model can be refined as much as desired by increasing the number of nodes without any problem. However, when starting from an initial profile, as in the cooling case, that is defined by a small number of thermocouples, the initial profile can only be approximated. Interpolating for the number of nodes in the model introduces an error which may be sufficient to affect the results.

Finally we must give a word of caution. The application of the EKF is very straightforward and does not entail higher computa-

tional costs and markedly improves our ability to judge the value of the measurements in terms of the standard deviations of the estimated parameters. However, the EKF method with an augmented state variable is not a universal panacea for the ill conditioned problems usually associated with parameter estimation. EKF estimates \mathbf{y}_i in terms of \mathbf{y}_{i-1} and the data at time t_i and then minimizes the variance by modifying both the model and the predicted state, \mathbf{y}_i . As the state variable increases in size, either by increasing the number of nodes or by adding additional terms such as losses, while holding the number of measurements fixed, the amplification matrix, G , becomes singular and the method becomes unstable. It is a case of the tail (the very few sensors) wagging the dog, the very large state variable. However, when used with care the augmented EKF offers a way to understand both the system behavior and the results of the least squares estimation and gives some guidance towards improving the model of the system.

Acknowledgments

This work was supported by the Sandia National Laboratory, Albuquerque, NM, under the technical direction of Dr. S. Kempka. Discussions with Dr. B. Blackwell and Dr. K. Dowding are gratefully recognized.

Nomenclature

c	=	specific heat
f	=	state model
$E(x)$	=	expected value of x
F	=	predicted temperature model
H	=	sensitivity
k	=	thermal conductivity
\hat{k}	=	estimate of k
m	=	number of parameters
n	=	size of state vector
N	=	number of data points
p	=	parameter
q_j^i	=	source term in Eq. (9)
\mathbf{R}	=	noise covariance matrix
\mathbf{S}	=	system covariance matrix
t	=	time
T	=	temperature
x	=	position
\mathbf{y}	=	state vector
$\hat{\mathbf{y}}$	=	estimated state vector
w_i	=	weight
\mathbf{z}	=	measurement vector
ϵ	=	error
ρ	=	correlation coefficient
ρc	=	product of density and specific heat
Σ	=	covariance matrix of ϵ
$\sigma(x)$	=	standard deviation of x
$\{\}$	=	column vector
$\langle \rangle$	=	row vector
$\{\}^T, \langle \rangle^T$	=	transpose

References

- [1] Gans, P., 1992, *Data Fitting in the Chemical Sciences*, J. Wiley and Sons, New York, NY.
- [2] Sorenson H. W., 1980, *Parameter Estimation: Principles and Problems*, Marcel Dekker, Inc., New York, NY.
- [3] Cowan, G., 1998, *Statistical Data Analysis*, Oxford Press, Oxford, England.
- [4] Young, P., 1984, *Recursive Estimation and Time Series Analysis*, Springer Verlag, New York, NY.
- [5] Chui, C. K., and Chen, G., 1999, *Kalman Filtering with Real Time Applications*, Springer Publ., New York, NY.
- [6] Anderson, B. D. O., and Moore, J. B., 1979, *Optimal Filtering*, Prentice-Hall Publ. New York, NY.
- [7] Ghanem, R., and Shinozuka, M., 1995, "Structural-System Identification I: Theory," *J. Eng. Mech.*, **121**, pp. 255–264.

- [8] Blackwell, B. F., Gill, W., Dowding, K. J., and Easterling, R. G., 2000, "Uncertainty Estimation in the Determination of Thermal Conductivity of 304 Stainless Steel," *Proc. IMECE 2000*, ASME, New York, NY.
- [9] Beck, J. V., and Arnold, K. J., 1977, *Parameter Estimation in Engineering and Science*, J. Wiley and Sons, New York, NY.
- [10] Beck, J. V., Blackwell, B., and Haji-Sheikh, A., 1996, "Comparison of Some Inverse Heat Conduction Methods using Experimental Data," *Int. J. Heat Mass Transfer*, **39**, pp. 3649–3657.
- [11] Emery, A. F., Blackwell, B., and Dowding, K. J., 2002, "The Relationship between Information, Sampling Rates, and Parameter Estimation Models," *ASME J. Heat Transfer*, **124**(6), pp. 1192–1199.
- [12] Pope, A. J., 1976, "The Statistics of Residuals and the Detection of Outliers," NOAA Tech. Rept. NOS 65 NGS 1.
- [13] Emery, A. F., and Bardot, D., 2003, "Parameter Estimation for Highly Non-linear Models with Noisy Data," Paper HT2003-40193, presented at the ASME Summer Heat Transfer Conference, Las Vegas, NV.
- [14] Emery, A. F., 2002, "Transient and Steady State Free Convection from a Horizontal Cylinder," *Proc. 4th International Conference on Inverse Problems in Engineering*, Rio de Janeiro, Brazil.
- [15] Jonsson, G., and Palsson, O. P., 1994, "An Application of Extended Kalman Filtering to Heat Exchanger Models," *ASME J. Dyn. Syst., Meas., Control*, **116**, pp. 257–264.
- [16] Al-Haik, M. S., and Haik, Y. S., 1999, "System Identification of a Lumped Heat Exchanger Using the Extended Information Filter," *SPIE Conf. Sensor Fusion and Decentralized Control in Robotic Systems II*, pp. 9–20.
- [17] Scarpa, F., and Milano, G., 1995, "Kalman Smoothing Technique Applied to the Inverse Heat Conduction Problem," *Numer. Heat Transfer, Part B*, **28**, pp. 79–96.
- [18] Al-Khalidy, N., 1998, "Application of Stochastic Method for Solving Inverse Heat Conduction Problems," *Numer. Heat Transfer, Part A*, **34**, pp. 331–342.
- [19] Moultanovsky, A. V., and Rekada, M., 2002, "Inverse Heat Conduction Problem Approach to Identify the Thermal Characteristics of Super-Hard Synthetic Materials," *Inverse Probl. Eng.*, **10**(1), pp. 19–39.
- [20] Moultanovsky, A. V., 2002, "Mobile HVAC System Evaporator Optimization and Cooling Capacity Estimation by Means of Inverse Problem Solution," *Inverse Probl. Eng.*, **10**(1), pp. 1–18.
- [21] Incropera, F. P., and DeWitt, D. P., 2002, *Introduction to Heat Transfer*, J. Wiley and Sons, New York, NY.
- [22] Dowding, K. J., 2003, personal communication.
- [23] Johnston, J., 1972, *Econometric Methods*, McGraw-Hill, New York, NY.

Thermal Analysis of Laser-Densified Dental Porcelain Bodies: Modeling and Experiments

K. Dai
X. Li
L. Shaw

Department of Metallurgy and Materials Engineering,
Institute of Materials Science,
University of Connecticut,
Storrs, CT 06269, USA

Thermal analysis of laser densification of a dental porcelain powder bed has been investigated using a three-dimensional thermal finite element model, which encompasses (i) the incoming laser beam power with a Gaussian distribution, (ii) optical pyrometer simulation in addition to the closed-loop temperature control, (iii) powder-to-solid transition, (iv) temperature-dependent thermal convection, and (v) temperature and porosity-dependent thermal conduction and radiation. The simulation results are compared with the experiments. It is found that the predicted temperature distribution in the porcelain body matches the experiments very well. Further, the maximum discrepancy between experimental and simulated pyrometer temperatures is less than 8 percent. The simulation predicts that in order to achieve the desired microstructure of a dense dental porcelain body, the maximum local temperature during laser densification should be below 1573 K or the nominal surface temperature should be below 1273 K. Otherwise, the undesired microstructure (i.e., a leucite-free glass phase) forms. [DOI: 10.1115/1.1795812]

Keywords: Dental Restoration, Laser Processing, Finite Element Modeling, Thermal Analyses, Powder Melting and Solidification

1 Introduction

The dominant procedure currently used for permanent fixed prosthodontics is porcelain-fused-to-metal (PFM) restoration in which a dental restoration is cast from a metallic alloy and then covered with dental porcelains by several furnace firing processes [1]. PFM restoration is a very time consuming and labor intensive work because PFM restoration requires a multi-stage process using multiple materials (both ceramics and metals) and each stage involves multiple processing steps. As such, labor costs account for about 90 percent of the final cost to the patient, while dental materials only account for less than 5 percent of the final cost [1]. Therefore, there is a critical need for new dental restoration methods to reduce costs and provide faster and better service to dental patients.

Solid freeform fabrication (SFF) is an automated manufacturing process that builds three-dimensional complex-shaped structures layer-by-layer directly from CAD data [2]. The recent advancement of SFF has led to a multi-material laser densification (MMLD) process for dental restoration [3–5]. In the MMLD process, dental alloy and porcelain powders are delivered line by line because both dental alloy and porcelain have to be present even on one single plane for most of the planes to be fabricated. As a result of the presence of multiple materials which have different densification temperatures, localized densification methods (e.g., laser-assisted densification) are needed to convert the delivered powder lines and planes into a dense body. Dental restorations such as three-unit bridges made of the metal substructure and porcelain crown can then be fabricated via the repetition of dental powder delivery followed by laser densification layer by layer. Through this approach artificial teeth are expected to be fabricated from a computer model without part-specific tooling and human intervention, thereby offering the potential to reduce the labor cost and increase the restoration rate.

As the densification of dental porcelain and alloy powders is accomplished via a laser beam, an understanding of the temperature distribution in the laser-assisted densification process is necessary. The understanding developed will provide the guideline to optimize the laser processing condition so that the microstructure and thus the mechanical properties of the laser-densified bodies are similar to those obtained via the traditional PFM furnace firing process. This is especially important for dental porcelains because dental porcelains rely on the presence of crystalline leucite particles in the feldspar glass matrix to raise the coefficient of thermal expansion (CTE) of the dental porcelains to match that of dental alloys [6–9]. Without the match in CTE between the dental porcelain and alloy, cracking would occur in the porcelain section [6–9]. Thus, this study investigates the temperature distribution in the dental porcelain body during laser densification in order to understand the phase transformation and microstructural evolution of the dental porcelain during laser densification. The approach of finite element modeling (FEM) has been taken in this study, which is necessary because the relative density of the workpiece changes continuously with time during laser densification until it reaches near full density. As a result, the thermal conductivity of the workpiece also changes continuously. Thus, the transient temperature field of the workpiece is too complex to calculate using analytical methods, and numerical simulation becomes necessary.

Many numerical modeling efforts have been carried out to investigate the temperature field in various SFF processes [10–32]. However, they are not suitable for the laser-assisted dental restoration process which requires the numerical models to encompass at least the effects of the powder-to-solid transition, laser power density, closed-loop temperature control, temperature-dependent thermal convection, and temperature- and porosity-dependent thermal conduction and radiation. Most of the existing SFF models (e.g., [10–32]) are not so sophisticated. Therefore, in this study we have developed a model that includes (i) the incoming laser beam power with a Gaussian distribution, (ii) optical pyrometer simulation in addition to the closed-loop temperature control, (iii) powder-to-solid transition, (iv) temperature-dependent thermal convection, and (v) temperature- and porosity-dependent thermal conduction and radiation. The results from the numerical

Contributed by the Heat Transfer Division for publication in the JOURNAL OF HEAT TRANSFER. Manuscript received by the Heat Transfer Division September 23, 2003; revision received June 30, 2004. Associate Editor: C. Amon.

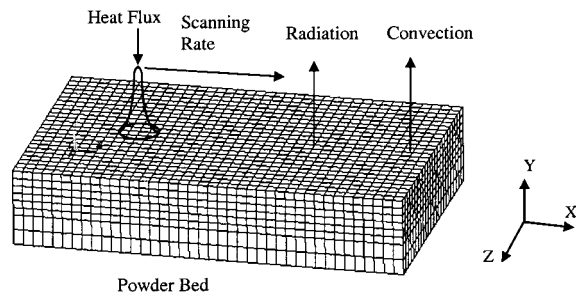


Fig. 1 Finite element model developed to simulate the temperature field during laser densification of the dental porcelain body

simulation have been compared with experiments and found to match the experimental measurements quite well.

2 Model Description

The model developed is shown in Fig. 1 and consists of a dental porcelain powder compact with a dimension of 10 mm length, 6 mm width, and 2 mm height before laser densification. In simulation the laser beam is modeled as a heat flux, q , with a Gaussian power distribution as an incoming heat source, which moves at a constant rate (240 $\mu\text{m/s}$) along the X -axis as shown in Fig. 1. The heat losses from the six surfaces of the model are assumed to result from natural convection and radiation. However, in some cases the effect of the substrate pre-heating is considered. For these cases, the nodal temperature of the bottom face of the model is increased to the pre-heating temperature before laser scanning and kept at that temperature throughout the entire laser fabrication process. The bonding between the porcelain and the substrate is not considered in the model because the substrate here is to provide a surface on which the porcelain can rest and in some cases to control the cooling condition during laser densification. In experiments, a right material (such as SiC in this study) has to be chosen as the substrate so that the porcelain will not stick to the substrate and can be easily separated from the substrate after laser densification. The dental porcelain powder investigated is composed of 63.40% SiO_2 , 16.70% Al_2O_3 , 1.50% CaO , 0.80% MgO , 3.41% Na_2O , and 14.19% K_2O (wt %). The thermal properties for the dense solid porcelain used in the model are summarized in Table 1. The dental porcelain is assumed to be at a molten state above 1073 K (100 K higher than the lower temperature of the forming temperature range of the porcelain). Furthermore, there is no heat of fusion involved when the porcelain changes from solid to liquid or vice versa, because the porcelain is a glass.

The modeling is carried out using the ANSYS commercial finite element package. The thermal element (Solid70), which has eight nodes with a single degree of freedom (i.e., temperature) at each node and has a three-dimensional thermal-conduction capability, is used to simulate the temperature field [38]. Each

element near the surface has a size of 0.25 mm length, 0.25 mm width and 0.2 mm height. The model is first used to calculate the temperature distribution in the powder bed within a small time step resulting from the heating of a laser beam moving at a constant rate along the laser scanning direction (i.e., the X -axis in Fig. 1). The powder elements convert to dense molten elements if their temperatures are higher than 1073 K according to the calculated temperature field. The temperature distribution in the powder bed within the next small time step is then calculated using the updated material properties. This simulation loop continues until the total amount of the small time steps, which is decided by the laser scanning rate, is reached, and then the laser beam moves stepwise by one element to carry out the next simulation loop.

The thermal properties of the powder bed are a strong function of the porosity of the powder bed. It is assumed that the porosity of the powder bed is temperature independent before the powder becomes liquid. This is a reasonable assumption because the reduction in porosity due to solid-state sintering is minimal under the present laser densification condition which brings the local temperature of the area irradiated by the laser beam to above the forming temperature of the porcelain in less than 6 seconds. For the region outside the irradiated area, the time for the region to expose to high temperatures is also relatively short (less than 100 seconds) because of the scanning rate used. Furthermore, the temperature at the region outside the irradiated area is also relatively low because of the low thermal conductivity of the powder compact. As such, the porosity of material has been simplified in two levels, that is, the initial porosity φ_0 before the powder converts to liquid, and zero porosity (fully dense) after the powder has converted to liquid and subsequently to a fully dense solid once the liquid is cooled below 1073 K. The thermal properties of the powder bed, therefore, are treated as a function of temperature and the initial porosity φ_0 which is assumed to be 0.4 in this study. In contrast, the thermal properties of the densified liquid and solid are treated as a function of temperature only because the liquid and solid are fully dense.

The volume shrinkage due to the densification caused by conversion of the powder compact to the dense liquid is neglected in order to simplify the model. The error introduced by this approximation is relatively small for the following reasons. First, the volume shrinkage will not change the temperature distribution profile, i.e., the center of the laser-densified body always has higher temperatures than the edge, whether there is volume shrinkage or not. Second, the values of temperature near the center of the laser-densified body will not be affected by the volume shrinkage because the temperature distribution right at the center (i.e., the surface area irradiated by the laser beam) is constant or nearly constant due to the closed-loop temperature control in the experiment as well as in the simulation. As such, the simulated temperature distribution near the center of the laser beam would be close to the real profile because of the closed-loop temperature control implemented in the experiment and the simulation.

The thermal conductivity and thermal radiation of the powder bed and the thermal convection around the powder bed as a func-

Table 1 Summary of thermal properties of dental porcelain [33–37]*

T (K)	300	520	631	700	830	960	1173	1373	1540	1726	1730	1800
k (W/m-K)	1.11	1.37	1.55	1.67	1.93	2.23	2.82	2.82	2.82	2.82	2.82	2.82
C_p (J/kg-K)	742	1025	1125	1178	1266	1341	1444	1474	1474	1474	1474	1474
α (10^{-6} /K)	2.80	3.36	3.87	4.27	5.25	6.54	9.43	9.43	9.43	9.43	9.43	9.43
E (GPa)	70	55.6	48.4	43.9	35.4	26.9	—	—	—	—	—	—
ϵ							0.7					
ρ (kg/m^3)							2520					
T_m (K)							1573					
T_f (K)							973 to 1273					
ν							0.2					

* T —Temperature, k —Thermal Conductivity, C_p —Specific Heat, α —Thermal Expansion Coefficient, E —Elastic Modulus, ϵ —Emissivity, ρ —Density, T_m —Melting Temperature, T_f —Forming Temperature, ν —Poisson's Ratio.

tion of the powder bed porosity have been detailed in a recent paper [30]. The model containing a moving Gaussian distribution laser beam, pyrometer temperature simulation, and closed-loop temperature control of the laser power has also been developed recently [29]. These functions and thermal boundary conditions are summarized as follows.

2.1 Thermal Conductivity of the Powder Bed. Effective thermal conductivity of the powder bed, K , is estimated by [39]

$$\frac{K}{K_f} = (1 - \sqrt{1 - \phi}) \left(1 + \frac{\phi K_r}{K_f} \right) + \sqrt{1 - \phi} \left[(1 - \phi) \times \left(\frac{2}{1 - \frac{BK_f}{K_s}} \left(\frac{B}{\left(1 - \frac{BK_f}{K_s} \right)^2} \left(1 - \frac{K_f}{K_s} \right) \ln \left(\frac{K_s}{BK_f} \right) - \frac{B+1}{2} - \frac{B-1}{1 - \frac{BK_f}{K_s}} \right) + \frac{K_r}{K_f} \right) + \phi \frac{K_s}{K_f} \right] \quad (1)$$

where ϕ is the fractional porosity of the powder bed, K_f is the thermal conductivity of the fluid surrounding the powder particles (which is air in this study), K_s is the thermal conductivity of the solid, ϕ is the flattened surface fraction of a particle in contact with another particle, B is the deformation parameter of the particle, and K_r is the thermal conductivity portion of the powder bed due to radiation among particles. K_r is equal to [39,40]

$$K_r = 4F\sigma T_p^3 D_p \quad (2)$$

where σ is the Stefan-Boltzmann constant, D_p is the average diameter of the powder particles, T_p the temperature of powder particles, and F is a view factor which is approximately taken as 1/3 [40].

Assuming that the particles are spheres ($B=1$) and there is no flattening of contact surfaces ($\phi=0$), equation (1), the effective thermal conductivity of the powder bed, can then be simplified to [39]

$$\frac{K}{K_f} = (1 - \sqrt{1 - \phi}) \left(1 + \frac{\phi K_r}{K_f} \right) + \sqrt{1 - \phi} \left(\frac{2}{1 - \frac{K_f}{K_s}} \left(\frac{1}{1 - \frac{K_f}{K_s}} \ln \left(\frac{K_s}{K_f} \right) - 1 \right) + \frac{K_r}{K_f} \right) \quad (3)$$

According to the simplification discussed previously, the porosity of the powder bed, ϕ , in equation (3) is assumed to be equal to the initial porosity, ϕ_0 , before melting.

2.2 Thermal Radiation of the Powder Bed. Heat loss q_r due to radiation of the powder bed is described by [41]

$$q_r = \sigma \varepsilon (T^4 - T_{amb}^4) \quad (4)$$

where T is the surface temperature of the powder bed, T_{amb} is the ambient temperature, ε is the emissivity of the powder bed, and σ is the Stefan-Boltzmann constant as defined before. ε is expected to be higher than the emissivity of the corresponding solid, and follows the expression [42]

$$\varepsilon = A_h \varepsilon_h + (1 - A_h) \varepsilon_s \quad (5)$$

where A_h is the area fraction of the surface that is occupied by the radiation-emitting holes, ε_s is the emissivity of the solid particle, and ε_h is the emissivity of the hole. For a powder bed composed of randomly packed, single-sized spheres [42]

$$A_h = \frac{0.908 \phi^2}{1.908 \phi^2 - 2\phi + 1} \quad (6)$$

and

$$\varepsilon_h = \frac{\varepsilon_s \left[2 + 3.082 \left(\frac{1 - \phi}{\phi} \right)^2 \right]}{\varepsilon_s \left[1 + 3.082 \left(\frac{1 - \phi}{\phi} \right)^2 \right] + 1} \quad (7)$$

Similar to Section 2.1, the porosity of the powder bed, ϕ , in Eq. (7) is assumed to be equal to the initial porosity, ϕ_0 , before melting.

2.3 Thermal Convection Around the Powder Bed. Heat loss q_c due to natural convection of the fluid around the powder bed is described by [41]

$$q_c = h_c (T - T_{amb}) \quad (8)$$

where h_c is the heat transfer coefficient. h_c is temperature and size dependent and is equal to [41]

$$h_c = \frac{\text{Nu} K_f}{L} \quad (9)$$

where L is the characteristic length of the specimen, Nu is the Nusselt number, and K_f is the thermal conductivity of the ambient air as defined before. Nu is given by [43]

$$\sqrt{\text{Nu}} = \sqrt{\text{Nu}_0} + \left[\frac{\text{GrPr}/300}{(1 + (0.5/\text{Pr})^{9/16})^{16/9}} \right]^{1/6} \quad (10)$$

when $10^{-4} \leq \text{GrPr} \leq 4 \times 10^{14}$, $0.022 \leq \text{Pr} \leq 7640$, and $\text{Nu}_0 = 0.67$ for a plate [42]. Gr and Pr in Eq. (10) are Grashof and Prandtl numbers, respectively, [41] and

$$\text{Gr} = g \frac{L^3 \rho_f^2 \beta_f (T - T_{amb})}{\eta_f^2} \quad (11)$$

and

$$\text{Pr} = \frac{C_p \eta_f}{k_f} \quad (12)$$

where g is the gravitational acceleration, ρ_f is the density of the ambient air, β_f is the thermal volumetric expansivity and $\beta_f = 1/T_f$ for idea gases, η_f is the viscosity of the air, C_p is the specific heat capacity of the air. The effect of the variation of air properties with temperature is evaluated at $T_f = 0.5(T + T_{amb})$ [41].

2.4 Thermal Boundary Conditions for Powder, Liquid, and Solid. The workpiece being built is assumed to be in contact with air and the heat loss through air is approximated through the natural thermal convection and thermal radiation between the workpiece and the ambient air. Since the model includes three kinds of material status (i.e., powder, liquid and solid), the thermal boundary conditions are very complicated and vary with porosity, phase status and surface temperature. Under the assumption of little convection of liquid within the molten pool due to its small size (~ 2 mm), liquid and solid have been assumed to have the same thermal convection boundary as the powder bed, i.e., thermal convection around the surface of liquid pool and solid is determined by the temperatures of the ambient air and the liquid and solid under consideration (see Eqs. (8–12)). Heat loss q_r due to radiation of solid and liquid is described by [41]

$$q_r = \sigma \varepsilon_s (T^4 - T_{amb}^4) \quad (13)$$

where T is the surface temperature of solid and liquid, and ε_s is the emissivity of the dense porcelain, T_{amb} is the ambient temperature, and σ is the Stefan-Boltzmann constant.

2.5 Heat Input. The incident heat flux of the Gaussian-distribution laser beam, q , is related to the incident laser power, Q_I , through the following relation [44]:

$$q = \frac{2Q_I\alpha_a}{\pi R_l^2} e^{-2R^2/R_l^2} \quad (14)$$

where α_a is the absorptance of the workpiece, R_l is the radius of the laser beam at which the heat flux value is e^{-2} times of that of the laser beam center, and R is the distance of a point on the surface of the powder bed measured from the laser beam center. When the center of the laser beam scans the surface of the powder bed from the starting point (X_0, Y_0, Z_0) to (X, Y_0, Z_0) point along the positive X -direction with a constant velocity v for a period time t , R is given by

$$R^2 = (X - X_0 - vt)^2 + (Z - Z_0)^2 \quad (15)$$

In the present study, the radius of the incident laser beam, R_l , is 0.5 mm, the laser scanning velocity, v , is 0.24 mm/s. However, the absorptance of the workpiece, α_a , is unknown before the simulation. To address this issue, the absorbed power by the porcelain, Q_a , defined as

$$Q_a = Q_I\alpha_a \quad (16)$$

is varied in the simulation to achieve the desired nominal surface temperature. Note that Q_I here is the incident laser power defined in Eq. (14) and can be measured experimentally.

2.6 Pyrometer Simulation. In laser-densification experiments, an optical pyrometer continually monitors the temperature distribution at the surface of the powder bed during laser densification. This pyrometer temperature is used as the feedback signal in a closed-loop control program to adjust the incident laser power as needed to achieve a desired constant laser spot temperature. In the simulation, the pyrometer temperature measurement and the closed-loop control process are modeled as follows.

The power, Q_r , of the thermal radiation emitted by the laser-heated workpiece that reaches the pyrometer can be expressed by [45]

$$Q_r = \int I_b(\lambda, T) \Delta\lambda dA \quad (17)$$

where λ is the wavelength of the emitted radiation ($\lambda = 865$ nm), $\Delta\lambda$ is the wavelength band ($\Delta\lambda = 50$ nm) of the emitted radiation that is sampled by the pyrometer [46], T is the temperature at a very small area dA through which the radiation passes to reach the pyrometer, termed the pyrometer sampling area hereafter, and $I_b(\lambda, T)$ is the spectral distribution of blackbody emissive power and given by Planck's radiation law [41]:

$$I_b = \frac{2\pi hc^2}{\lambda^5 (e^{hc/\lambda kT} - 1)} \quad (18)$$

Here h is Planck's constant, c is the speed of light, and k is the Boltzmann constant. Because of the Gaussian heat input and movement of the laser beam, the surface temperature, T , within the pyrometer sampling area is not uniform, and neither is $I_b(\lambda, T)$. Thus, to carry out the integration of Eq. (17), approximations are made by dividing the entire sampling area into n small areas and assuming that T and I_b are constant within each small area. With these assumptions, Eq. (17) is reduced to [29]

$$Q_r = \Delta\lambda \Delta A \sum_{i=1}^n I_b(\lambda, T_i) \quad (19)$$

where n is the number of the small areas of equal size, ΔA , within the pyrometer sampling area which is 2 mm in diameter and T_i is the surface temperature of each small area ΔA .

To relate the thermal radiation power collected by the pyrometer to the pyrometer temperature reading, an effective temperature, T_{eff} (the simulated temperature equivalent to the measured radiance temperature), is introduced as

$$Q_r = \Delta\lambda \Delta A n I_b(\lambda, T_{\text{eff}}) \quad (20)$$

Combining Eqs. (18)–(20), one has

$$T_{\text{eff}} = \frac{hc}{\lambda k \ln \left(1 + n \sum_{i=1}^n (e^{hc/\lambda k T_i} - 1)^{-1} \right)} \quad (21)$$

2.7 Closed-Loop Temperature Control. T_{eff} in Eq. (21) is the effective (nominal) surface temperature of the workpiece as measured by the pyrometer for a given incident laser power. If T_{eff} differs from the user-defined (nominal) surface temperature, T_{nor} , then the absorbed laser power, Q_a , in Eq. (16) and thus q in Eq. (14) are adjusted accordingly to simulate the closed-loop temperature control in the experiment. This is achieved by adjusting the absorbed laser power from one simulation step to the next using the following equation:

$$Q_a^{i+1} = Q_a^i \frac{T_{\text{nor}}}{T_{\text{eff}}} \quad (22)$$

where Q_a^i and Q_a^{i+1} are the absorbed laser power by the powder bed in the simulation steps i and $i+1$, respectively. It is found that this equation allows the surface temperature of the workpiece, T_{eff} , to approach the user-defined surface temperature quickly, reproducing in the simulation the closed-loop temperature control process used in the experiments.

3 Experimental Procedure

To validate the model developed, laser densification of a dental porcelain powder bed has been carried out. The laser densification conditions are (i) a 50W CO₂ laser beam of 1 mm in diameter, (ii) the scanning rate 0.24 mm/s, (iii) the chamber pressure 700 torr, and (iv) the user-defined surface temperature (i.e., nominal surface temperature) 1073–1373 K with an equivalent laser output power of about 3–20 watts. The powder bed of 2–5 mm thick is resting on a SiC substrate and is scanned by the laser beam along a single line. Four different nominal surface temperatures, 1373 K, 1273 K, 1173 K, and 1223 K, have been investigated and termed hereafter as Cases I, II, III, and IV, respectively. Furthermore, the substrate in Case I is preheated to 673 K before laser densification, whereas no pre-heating is performed for Cases II, III and IV.

The laser-densified porcelain bodies are mounted using an epoxy resin and then cut in such an orientation to reveal the cross section perpendicular to the laser scanning direction. To determine the microstructure of the densified body, the cut samples are grinded and polished down to 1 μm diamond suspension and then etched using 1 percent hydrofluoric (HF) acid for 20 seconds. An environmental scanning electron microscope (PHILIPS ESEM 2020) is used to examine the microstructure of all the samples at as-polished and etched conditions after being carbon sputter-coated.

4 Comparison Between Simulation and Experimental Results

One of the criteria for validating the model is to check whether the model can simulate the closed-loop temperature control process, i.e., achieving a constant surface temperature in the area sampled by the pyrometer through continuously adjusting the absorbed laser power. Figure 2 shows the comparison between the experimental and simulated pyrometer temperatures as a function of the location of the scanning laser beam with a nominal surface

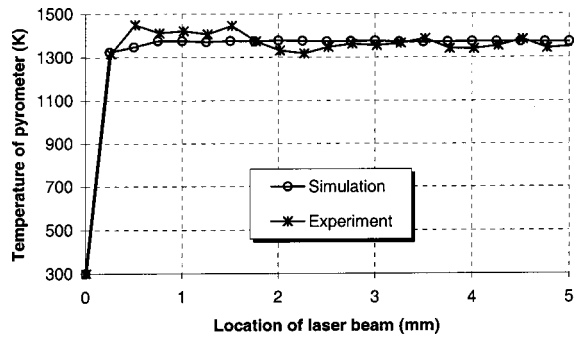


Fig. 2 Comparison between the experimental and simulated values of the pyrometer temperature as a function of the location of the scanning laser beam with a nominal surface temperature of 1373 K and substrate preheating to 673 K (Case I)

temperature of 1373 K and substrate preheating to 673 K, i.e., Case I mentioned in section 3. It can be seen that the temperature discrepancies between the simulated pyrometer temperature and the desired pyrometer temperature are less than 4 percent for the entire laser densification process. In fact, the comparisons between the experimental and simulated pyrometer temperatures for the other three cases (Cases II, III and IV) also exhibit the similar small discrepancy. If all the four cases are considered, the maximum discrepancy between experimental and simulated pyrometer temperatures is less than 8 percent. These results indicate that Eq. (22), although simple, can adequately describe the closed-loop temperature control process in experiments. Furthermore, these results also indicate that Eqs. (17) to (21) are adequate in describing the pyrometer temperature measurement because the effective temperature in Eq. (22) is obtained through Eqs. (17) to (21).

The second criterion that can be used to check the model is to compare the experimentally measured incident laser power with the simulated incident laser power under the constraint of a constant nominal surface temperature. However, as mentioned before, the direct outcome from the simulation is the absorbed laser power, Q_a , as a function of the process time, since the absorptance of the workpiece is unknown before the simulation. Thus, to compare the simulated absorbed laser power with the measured incident laser power, an effective absorptance of the workpiece, α_a , which includes the effects of the curved surface, volume shrinkage, temperature change during the transient stage, and variation of the state of matter from powder to liquid, has to be chosen. It is found that if α_a is chosen to be 0.41 for laser densification with a nominal surface temperature of 1273 K, the simulated incident laser power, $Q'_l = Q_a / \alpha_a$, as a function of the processing time would fit the experimental incident laser power Q_l quite well, as shown in Fig. 3. This result lends further credence to

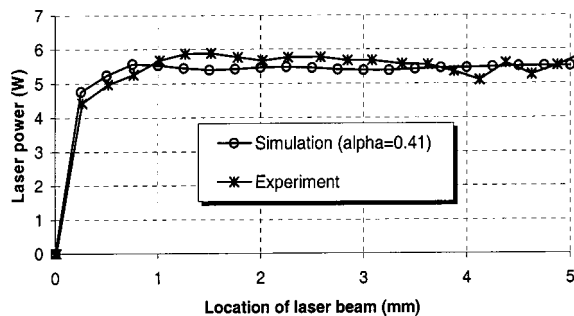


Fig. 3 Comparison between the experimental and simulated incident laser power as a function of the location of the scanning laser beam with a nominal surface temperature of 1273 K and $\alpha_a=0.41$ (Case II)

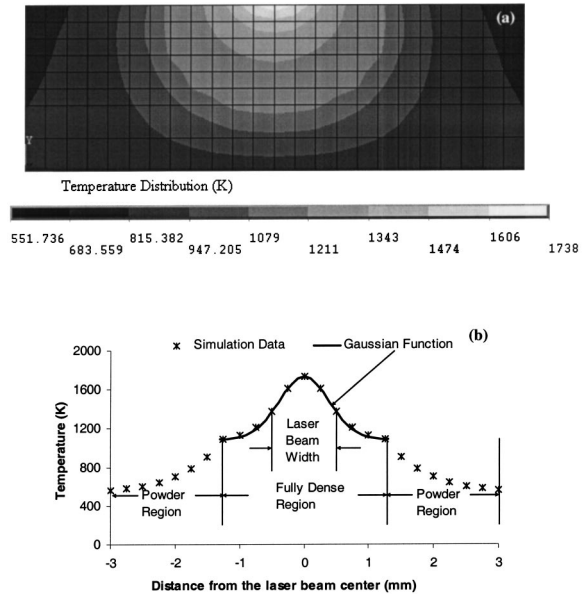


Fig. 4 (a) The simulated temperature distribution in the powder bed at the cross section of $X=6.75$ mm when the laser beam scans to this location with a nominal surface temperature of 1373 K and substrate preheating to 673 K (Case I), and (b) the simulated temperature distribution on the surface of the porcelain body at the cross section of $X=6.75$ mm and the matched Gaussian function

the model because the match between the simulated and measured incident laser powers under the constraint of a constant nominal surface temperature (i.e., a closed-loop temperature control in the experiment) requires a good match between the simulated and experimental cooling and heating conditions.

The third check of the model would be to compare the simulated temperature field in the porcelain body during laser densification with that measured experimentally. Figure 4 shows the simulated temperature field for Case I. It is quite clear that the temperature distribution obtained is consistent with the expectation that the highest temperature is located at the center of the laser beam and the temperature gradually decreases as the location moves away from the center in all directions within the porcelain body. More importantly, when compared with the experimental result (Fig. 5), it is found that the predicted temperature distribution pattern and temperature range match the measurement quite well. The experimental temperature field (Fig. 5) is established

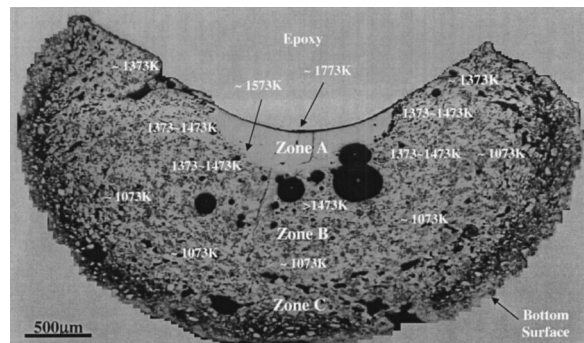


Fig. 5 The temperature distribution and microstructure measured experimentally at the cross section of a porcelain body perpendicular to the laser scan direction during laser densification with a nominal surface temperature of 1373 K and substrate preheating to 673 K (Case I)

based on a comprehensive examination of the dental porcelain microstructure as a function of (i) the location with respect to the center of the laser beam and (ii) the relationship between the dental porcelain microstructure and the furnace firing temperature. The detail of this experimental investigation has been described in a forthcoming paper [47].

It is noted that the predicted surface temperature in the laser-densified region follows a Gaussian distribution (Fig. 4(b)). This is not a surprise since several previous studies have shown that the resulting temperature distribution on the surface of a solid irradiated by a Gaussian laser beam is also Gaussian [48–50]. The difference between the current and the previous studies is the presence of the powder bed which modifies the heat transfer behavior of the material under the laser beam. In spite of this modification, the surface temperature distribution in the densified region is still Gaussian, but with a larger standard deviation (50% larger) when compared with that of the Gaussian distribution in the heat flux of the laser beam.

Because of the Gaussian distribution of the surface temperature, the surface temperature at the center of the laser beam is much higher than the nominal surface temperature. It can be seen from the simulation result for Case I (Fig. 4) that the maximum central surface temperature reaches 1738 K, which is 365 K higher than the nominal surface temperature (1373 K). Systematic experiments [47] have shown that when the local temperature during laser densification exceeds 1573 K, the microstructure of the dental porcelain at that specific location will be substantially different from that produced from the traditional PFM furnace firing process. As shown in Fig. 5, the microstructure of the laser-densified porcelain can be divided into three regions, Zones A, B and C. Zone A is the region that only has a glassy phase and does not contain leucite precipitates, whereas Zone B possesses both the glassy matrix and leucite precipitates [3,5]. Zone C is the region where dental porcelain powder is only partially densified and thus there exists a large amount of porosity. Zone B has the same microstructure as that produced from the traditional PFM process and is the desired microstructure [3,5]. The presence of leucite precipitates is essential for the integrity of artificial teeth because leucite has a high coefficient of thermal expansion (CTE) and raises the inherently low CTE of the porcelain glass matrix to match that of the dental metallic alloy [7]. Therefore, the appearance of Zone A should be avoided during laser densification.

It can be seen from Fig. 5 that Zone A forms when the local temperature is higher than 1573 K, whereas Zone B forms when the local temperature is between 1073 to 1473 K. Zone C forms when the local temperature is lower than 1073 K. Thus, in an effort to provide guidelines for laser densification of the dental porcelain without the formation of Zone A, several additional simulations with different nominal surface temperatures without the substrate preheating (i.e., Cases II, III, and IV) have been performed. The results from these simulations are shown in Figs. 6, 7, and 8. The corresponding microstructures generated from experiments for Cases II and III are also included in Figs. 6 and 7 for comparison. It can be seen from Fig. 6 that the simulation predicts a maximum surface temperature of 1558 K at the center of the laser beam for a nominal surface temperature of 1273 K (Case II). The predicted maximum surface temperature of 1558 K is near the critical temperature of 1573 K above which Zone A appears [47]. Such a prediction is consistent with the experimental result. As shown in Fig. 6(b), a small Zone A appears at the central surface of the porcelain body laser-densified with a nominal surface temperature of 1273 K. Clearly, in order to avoid the formation of Zone A, laser densification of the dental porcelain should be conducted with a nominal surface temperature below 1273 K or with the maximum local temperature lower than 1573 K.

This critical nominal surface temperature (1273 K) is also confirmed by the simulations with lower nominal surface temperatures. Shown in Figure 7 is the predicted temperature field and the

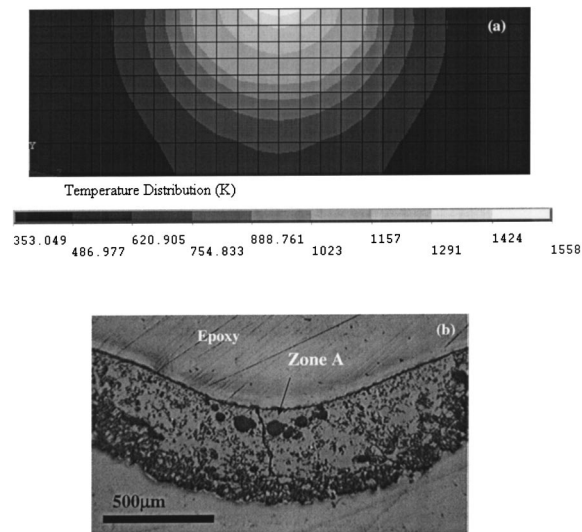


Fig. 6 (a) The simulated temperature distribution and (b) the microstructure determined experimentally at the cross section of a porcelain body perpendicular to the laser scan direction during laser densification with a nominal surface temperature of 1273 K (Case II)

microstructure of the porcelain body laser densified with a nominal surface temperature of 1173 K (Case III). It can be seen that the simulation predicts that the central surface temperature of the porcelain body (1379 K) is lower than the critical temperature for the formation of Zone A (1573 K). This prediction is confirmed by the experimental result (Fig. 7(b)) that reveals no formation of Zone A, but a 100 percent Zone B microstructure.

The simulation result for a nominal surface temperature of 1223 K (Case IV) is shown in Fig. 8. It suggests that the nominal surface temperature of 1223 K is also good enough to avoid the appearance of Zone A because the maximum temperature at the central region is 1472 K, lower than the critical temperature for the formation of Zone A (1573 K). Therefore, both the experimental and simulated results suggest that the nominal surface tempera-

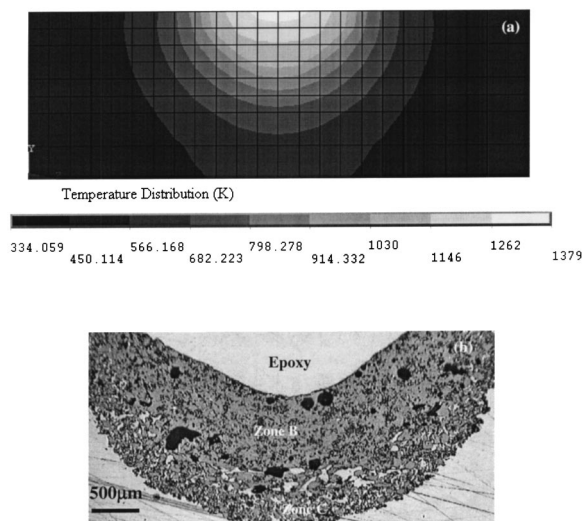


Fig. 7 (a) The simulated temperature distribution and (b) the microstructure determined experimentally at the cross section of a porcelain body perpendicular to the laser scan direction during laser densification with a nominal surface temperature of 1173 K (Case III)

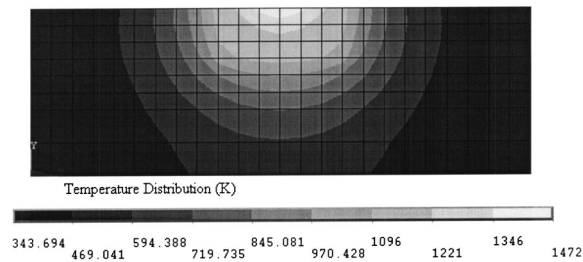


Fig. 8 The simulated temperature distribution at the cross section of a porcelain body perpendicular to the laser scan direction during laser densification with a nominal surface temperature of 1223 K (Case IV)

ture during laser densification of the dental porcelain powder should be lower than 1273 K or the maximum local temperature should be lower than 1573 K in order to achieve the desired microstructure of a dense porcelain body.

A comparison of Case I with Cases II, III and IV also suggests that whether Zone A forms or not during laser densification is determined by the nominal surface temperature, whereas substrate preheating has minimal effect on the Zone A formation. This is consistent with the expectation. Substrate preheating decreases the temperature gradient in the part being fabricated. However, it does not change the maximum temperature at the central surface region which is determined by the constant nominal surface temperature because of the closed-loop temperature control in both experiments and simulations. Therefore, substrate preheating does not affect whether Zone A forms or not, but it does decrease residual stresses, warping and the propensity for cracking.

Finally, it should be pointed out that there is room for improving the model developed in this study. First, the curved surface observed in the experiment (Fig. 5) and the volume shrinkage due to transformation from a powder compact to dense liquid are not included in the model. Although the non-inclusion of these two phenomena will not introduce large errors, an accurate prediction would require the inclusion of these two phenomena. Another important area that is not covered by the model is the laser-material interaction issue, which is handled in this study through an empirical approach by comparing the experimental incident laser power with the simulated absorbed laser power. The effective absorptance of the porcelain powder compact obtained through this empirical approach includes the effects of the curved surface, volume shrinkage, temperature change during the transient stage, and variation of the state of matter from powder to liquid. Although simulation of the absorptance as a function of these changes is a complex topic of research by itself, inclusion of such simulation would certainly enhance the prediction capability of the model.

5 Conclusions and Remarks

A three-dimensional finite element model that encompasses the effects of the powder-to-solid transition, laser power density, closed-loop temperature control, temperature- and porosity-dependent thermal conduction and radiation as well as the temperature-dependent natural thermal convection has been developed to carry out the thermal analysis of laser-densified dental porcelain bodies. The temperature distribution in the porcelain body during laser densification under different processing conditions has been simulated using the present model and is compared with the experiments. The results predicted by the model match the experiment quite well. The established model has been used to predict the temperature field during laser densification and the nominal surface temperature that should be adopted during experiments in order to achieve the desired microstructure. A critical maximum local temperature (1573 K) or a nominal surface tem-

perature in laser densification of the dental porcelain (1273 K) has been identified above which an undesired microstructure, Zone A, will appear. As a result of this critical nominal surface temperature, laser densification of the dental porcelain powder should be conducted below this critical nominal surface temperature.

The model developed in this study is the first comprehensive one that includes all key parameters in laser densification of a powder bed. It is expected that the model can be extended to simulate many other laser materials processing methods that require consideration of the phase transformation, closed-loop temperature control, and heat transfer.

Acknowledgment

The authors gratefully acknowledge financial support provided by the National Science Foundation under Grant Nos: DMI-9908249 and DMI-0218169.

Nomenclature

A	= area (m^2)
B	= deformation parameter of the particle
c	= speed of light (2.998×10^8 m/s)
C_p	= specific heat capacity (J/Kg-K)
D	= diameter (m)
F	= view factor
g	= gravitational acceleration (m/s^2)
Gr	= Grashof number
h	= heat transfer coefficient (W/m^2-K) (when subscripted), Planck constant (6.62618×10^{-34} J s/molecule)
I	= spectral distribution of blackbody emissive power (W/m^3)
k	= Boltzmann's constant (1.38×10^{-23} J/K)
K	= thermal conductivity ($W/m-K$)
L	= characteristic length (m)
Nu	= Nusselt number
Pr	= Prandtl number
Q	= power (W)
q	= heat flux (W/m^2)
R	= radius (m)
T	= temperature (K)
t	= time (s)
v	= velocity (m/s)
X, Y, Z	= spatial coordinates

Greek Symbols

α	= absorptivity
β	= thermal volumetric expansivity (1/K)
Δ	= interval
ε	= emissivity
ϕ	= flattened surface fraction of a particle in contact with another particle
η	= viscosity ($N s/m^2$)
φ	= porosity
λ	= wavelength (m)
ρ	= density (kg/m^3)
σ	= Stefan-Boltzmann constant (5.6703×10^{-8} W/m^2-K^4)

Subscripts

0	= initial time
a	= absorption
amb	= ambient
b	= blackbody
c	= convection
eff	= effective
f	= fluid
h	= hole
i	= small area number

l = laser
 n = total number of the small areas
 nor = nominal
 p = particle
 py = pyrometer
 r = radiation
 s = solid

Superscripts

i = simulation step number

References

- [1] Cameron, T. B., 2004, private communication, Dentsply Cermco, Burlington, NJ.
- [2] Beaman, J. J., Barlow, J. W., Bourell, D. L., Crawford, R. H., Marcus, H. L., and McAlea, K. P., 1997, *Solid Freeform Fabrication: A New Direction in Manufacturing*, Kluwer Academic Publishers, MA.
- [3] Shaw, L., Li, X.-X., Wang, J.-W., Marcus, H. L., Cameron, T. B., and Kennedy, C., 2002, "Dental Restoration Through Laser Densification of Dental Porcelain Powder," in *Rapid Prototyping of Materials*, F. D. S. Marquis and D. L. Bourell, eds., TMS, Warrendale, PA, pp. 107–118.
- [4] Wang, J.-W., Li, X.-X., Shaw, L., Marcus, H. L., Cameron, T. B., and Kennedy, C., 2002, "Studies on Slurry Extrusion for Dental Restoration," in the *Proceedings of the 13th Annual SFF Symposium*, D. L. Bourell, J. J. Beaman, R. H. Crawford, H. L. Marcus, and J. W. Barlow, eds., The University of Texas at Austin, pp. 83–91.
- [5] Li, X. X., Wang, J. W., Augustine, A., Shaw, J. L., Marcus, H. L., and Cameron, T. B., 2001, "Microstructure Evaluation for Multi-Materials Laser Densification of Dental Porcelains," in the *Proceedings of the 12th Annual SFF Symposium*, D. L. Bourell, J. J. Beaman, R. H. Crawford, H. L. Marcus, and J. W. Barlow, eds., The University of Texas at Austin, pp. 195–202.
- [6] Weinsin, M., Katz, S., and Weinstein, A. B., 1962, "Fused Porcelain-to-Metal Teeth," US Patent #: 3,052,982.
- [7] Mackert, Jr., J. R., and Williams, A. L., 1996, "Microcracks in Dental Porcelain and Their Behavior during Multiple Firing," *J. Dent. Res.*, **75**(7), pp. 1484–1490.
- [8] Mackert, Jr., J. R., and Evans, A. L., 1991, "Effect of Cooling Rate on Leucite Volume Fraction in Dental Porcelains," *J. Dent. Res.*, **70**, pp. 137–139.
- [9] Mackert, Jr., J. R., Rueggeberg, F. A., Lockwood, P. E., Evans, A. L., and Thompson, W. O., 1994, "Isothermal Anneal Effect on Microcrack Density around Leucite Particles in Dental Porcelain," *J. Dent. Res.*, **73**, pp. 1221–1227.
- [10] Kandis, M., and Bergman, T. L., 1997, "Observation, Prediction, and Correlation of Geometric Shape Evolution Induced by Non-Isothermal Sintering of Polymer Powder," *ASME J. Heat Transfer*, **119**, pp. 824–831.
- [11] Zhang, Y., and Faghri, A., 2000, "Thermal Modeling of Selective Area Laser Deposition of Titanium Nitride on a Finite Slab with Stationary and Moving Laser Beams," *Int. J. Heat Mass Transfer*, **43**(20), pp. 3835–3846.
- [12] Zhang, Y., and Faghri, A., Buckley, C. W., and Bergman, T. L., 2000, "Three-Dimensional Sintering of Two-Component Metal Powders with Stationary and Moving Laser Beams," *ASME J. Heat Transfer*, **122**(1), pp. 150–158.
- [13] Zhang, Y., and Faghri, A., 1999, "Melting of a Subcooled Mixed Powder Bed with Constant Heat Flux Heating," *Int. J. Heat Mass Transfer*, **42**(5), pp. 775–788.
- [14] Chin, R. K., Beuth, J. L., and Amon, C. H., 1996, "Thermomechanical Modeling of Molten Metal Droplet Solidification Applied to Layered Manufacturing," *Mech. Mater.*, **24**, pp. 257–271.
- [15] Amon, C. H., Beuth, J. L., Merz, R., Prinz, F. B., and Weiss, L. E., 1998, "Shape Deposition Manufacturing with Microcasting: Processing, Thermal and Mechanical Issues," *J. Manuf. Sci. Eng.*, **120**(3), pp. 656–665.
- [16] Chin, R. K., Beuth, J. L., and Amon, C. H., 2001, "Successive Deposition of Metals in Solid Freeform Fabrication Processes Part 1: Thermomechanical Models of Layers and Droplet Columns," *J. Manuf. Sci. Eng.*, **123**(4), pp. 623–631.
- [17] Chin, R. K., Beuth, J. L., and Amon, C. H., 2001, "Successive Deposition of Metals in Solid Freeform Fabrication Processes Part 2: Thermomechanical Models of Adjacent Droplets," *J. Manuf. Sci. Eng.*, **123**(4), pp. 632–638.
- [18] Ong, R., Beuth, J. L., and Weiss, L. E., 2000, "Residual Stress Control Issues for Thermal Deposition of Polymers in SFF Processes," in the *Proceedings of the 11th Annual SFF Symposium*, D. L. Bourell, J. J. Beaman, R. H. Crawford, H. L. Marcus, and J. W. Barlow, eds., The University of Texas at Austin, pp. 209–218.
- [19] Vasinonta, A., Beuth, J. L., and Griffith, M. L., 2001, "A Process Map for Consistent Build Conditions in the Solid Freeform Fabrication of Thin-Walled Structures," *J. Manuf. Sci. Eng.*, **123**(4), pp. 615–622.
- [20] Vasinonta, A., Beuth, J. L., and Ong, R., 2001, "Melt Pool Size Control in Thin-Walled and Bulky Parts via Process Maps," in the *Proceedings of the 12th Annual SFF Symposium*, D. L. Bourell, J. J. Beaman, R. H. Crawford, H. L. Marcus, and J. W. Barlow, eds., The University of Texas at Austin, pp. 432–440.
- [21] Nickel, A. H., Barnett, D. M., and Prinz, F. B., 2001, "Thermal Stresses and Deposition Patterns in Layered Manufacturing," *Mater. Sci. Eng., A*, **317**, pp. 59–64.
- [22] Shiomi, M., Matsumoto, M., Osakada, K., Abe, F., 2001, "Two-Dimensional Finite Element Simulation of Laser Rapid Prototyping, Simulation of Materials Processing: Theory, Methods and Applications," in *Proc. NUMIFORM 2001*, K. Mori, ed., Toyohashi, Japan, A. A. Balkema Publishers, pp. 1059–1064.
- [23] Matsumoto, M., Shiomi, M., Osakada, K., and Abe, F., 2002, "Finite Element Analysis of Single Layer Forming on Metallic Powder Bed in Rapid Prototyping by Selective Laser Processing," *Int. J. Mach. Tools Manuf.*, **42**, pp. 61–67.
- [24] Niebling, F., and Otto, A., 2001, "FE-Simulation of the Selective Laser Sintering Process of Metallic Powders," in the *Proceedings of 3rd International Conference on Laser Assisted Net Shaping* LANE 2001, M. Geiger and A. Otto, eds., Meisenbach Verlag, Germany, August 2001, pp. 371–382.
- [25] Dai, K., and Shaw, L., 2001, "Thermal and Stress Modeling of Multi-Material Laser Processing," *Acta Mater.*, **49**, pp. 4171–4181.
- [26] Dai, K., and Shaw, L., 2003, "The Size Effect on Stresses and Distortion of Laser Processed Multi-Material Components," *Metall. Mater. Trans. A*, **34A**, pp. 1133–1145.
- [27] Dai, K., and Shaw, L., 2002, "Distortion Minimization of Laser-Processed Components through Control of Laser Scanning Patterns," *Rapid Prototyping J.*, **8**(5), pp. 270–276.
- [28] Dai, K., and Shaw, L., 2003, "Finite Element Modeling for Laser-Assisted Dental Restoration Process," in *Proc. of the 2003 NSF Design, Service and Manufacturing Grantees and Research Conference*, R. G. Reddy, eds., Birmingham, AL, pp. 2292–2300.
- [29] Dai, K., Crocker, J., Shaw, L., and Marcus, H., 2003, "Modeling of Selective Area Laser Deposition (SALD) and SALD Vapor Infiltration of Silicon Carbide," *Rapid Prototyping J.*, **9**(4), pp. 231–239.
- [30] Dai, K., and Shaw, L., 2004, "Thermal and Mechanical Finite Element Modeling of Laser Forming from Metal and Ceramic Powders," *Acta Mater.*, **52**(1), pp. 69–80.
- [31] Dai, K., and Shaw, L., 2002, "Preheating Effects on Multiple Materials Laser Densification," in the *Proceedings of the 13th Annual SFF Symposium*, D. L. Bourell, J. J. Beaman, R. H. Crawford, H. L. Marcus, and J. W. Barlow, eds., The University of Texas at Austin, pp. 392–399.
- [32] Dai, K., and Shaw, L., 2002, "Finite Element Analysis of Distortion Minimization in Layer-by-Layer Laser-Processed Components," in *Rapid Prototyping of Materials*, F. D. S. Marquis, and D. L. Bourell, eds., TMS (the Minerals, Metals & Materials Society), Warrendale, PA, pp. 29–39.
- [33] Mackert, J. R., Butts, M. B., Morena, R., and Fairhurst, C. W., 1986, "Phase Changes in a Leucite-Containing Dental Porcelain Frit," *J. Am. Ceram. Soc.*, **69**(4), pp. C-69–C-72.
- [34] Touloukian, Y. S., and DeWitt, D. P., 1972, *Thermophysical Properties of Matter, Volume 8, THERMAL RADIATIVE PROPERTIES: Nonmetallic Solids*, IFI/Plenum, New York, NY.
- [35] Touloukian, Y. S., Powell, R. W., Ho, C. Y., and Klemens, P. G., 1970, *Thermophysical Properties of Matter, Volume 2, THERMAL CONDUCTIVITY: Nonmetallic Solids*, IFI/Plenum, New York, NY.
- [36] Touloukian, Y. S., and Buycio, E. H., 1970, *Thermophysical Properties of Matter, Volume 5, SPECIFIC HEAT: Nonmetallic Solids*, IFI/Plenum, New York, NY.
- [37] Schneider, S. J., 1991, *Engineered Materials Handbook, Volume 4: Ceramics and Glasses*, ASM International, Metals Park, OH.
- [38] ANSYS Inc., 2002, *ANSYS On-Line Reference Manuals: The ANSYS Elements Reference*, Release 6.1, ANSYS Inc., Canonsburg, PA.
- [39] Sih, S. S., and Barlow, J. W., 1995, "The Prediction of the Thermal Conductivity of Powders," in the *Proceedings of the 6th Annual SFF Symposium*, H. Marcus, J. Beaman, D. Bourell, J. Barlow, and R. Crawford, eds., The University of Texas at Austin, pp. 397–401.
- [40] Sih, S. S., and Barlow, J. W., 1994, "Measurement and Prediction of the Thermal Conductivity of Powders at High Temperature," in the *Proceedings of the 5th Annual SFF Symposium* H. Marcus, J. Beaman, J. Barlow, D. Bourell, and R. Crawford, eds., The University of Texas at Austin, pp. 321–329.
- [41] Poirier, D. R., and Geiger, G. H., 1994, *Transport Phenomena in Materials Processing*, The Minerals, Metals and Materials Society, Warrendale, PA.
- [42] Sih, S. S., and Barlow, J. W., 1995, "Emissivity of Powder Beds," in the *Proceedings of the 6th Annual SFF Symposium*, H. Marcus, J. Beaman, D. Bourell, J. Barlow, and R. Crawford, eds., The University of Texas at Austin, pp. 402–408.
- [43] E. U. Schlunder, (ed.), 1983, *Heat Exchanger Design Handbook*, Hemisphere Publishing Corporation, New York, NY.
- [44] Mazumder, J., and Kar, A., 1995, *Theory and Application of Laser Chemical Vapor Deposition*, Plenum Publishing Co., New York, NY.
- [45] <http://140.114.58.65/heat%20transfer/pdf/HTchap12.pdf>
- [46] The Pyrometer Instrument Co., Inc., 1996, *Pyrofiber Models 865 & 1550—Operation Manual*, Revision: 8.0, Northvale, NJ.
- [47] Li, X.-X., and Shaw, L., 2004, "Microstructure of Dental Porcelains in a Laser-Assisted Rapid Prototyping Process," *Dental Mater.*, in press.
- [48] Sanders, D. J., 1984, "Temperature Distributions Produced by Scanning Gaussian Laser Beams," *Appl. Opt.*, **23**(1), pp. 30–36.
- [49] Modest, M. F., and Abakians, H., 1986, "Evaporative Cutting of a Semi-Infinite Body with a Moving CW Laser," *ASME J. Heat Transfer*, **108**, pp. 602–607.
- [50] Roy, S., and Modest, M. F., 1993, "CW Laser Machining of Hard Ceramics; Effects of Three-Dimensional Conduction, Variable Properties and Various Laser Parameters," *Int. J. Heat Mass Transfer*, **36**(14), pp. 3515–3528.

Local Heat Transfer and Pressure Drop for Finned-Tube Heat Exchangers Using Oval Tubes and Vortex Generators

James E. O'Brien

Manohar S. Sohal

Philip C. Wallstedt

Idaho National Engineering and Environmental
Laboratory
Idaho Falls,
Idaho 83415

This paper presents the results of an experimental study of forced convection heat transfer in a narrow rectangular duct fitted with an elliptical tube and one or two delta-winglet pairs. The duct was designed to simulate a single passage in a fin-tube heat exchanger. Heat transfer measurements were obtained using a transient technique in which a heated airflow is suddenly introduced to the test section. High-resolution local fin-surface temperature distributions were obtained at several times after initiation of the transient using an imaging infrared camera. Corresponding local fin-surface heat transfer coefficients were then calculated from a locally applied one-dimensional semi-infinite inverse heat conduction model. Heat transfer results were obtained over a Reynolds number range based on duct height of 670–6300. Pressure-drop measurements have also been obtained for similar elliptical-tube and winglet geometries, using a separate single-channel, multiple-tube-row pressure-drop apparatus. The pressure-drop apparatus includes four tube rows in a staggered array. Comparisons of heat transfer and pressure-drop results for the elliptical tube versus a circular tube with and without winglets are provided. Mean heat transfer results indicated that the addition of the single winglet pair to the oval-tube geometry yielded significant heat transfer enhancement, averaging 38% higher than the oval-tube, no-winglet case. The corresponding increase in friction factor associated with the addition of the single winglet pair to the oval-tube geometry was very modest, less than 10% at $Re_{D_h} = 500$ and less than 5% at $Re_{D_h} = 5000$. [DOI: 10.1115/1.1795239]

Introduction

Air-cooled condensers used in binary-cycle geothermal power plants require the use of finned tubes in order to increase heat transfer surface area on the air side. Air is forced through several rows of long individually finned tubes by large fans. The condenser units can be very large, representing as much as 50% of the overall capital cost of these power plants. In addition, the power required to operate the fans represents a significant parasitic house load, reducing the net power production of the plant. The research presented in this paper and previous papers [1–3] has been undertaken with the aim of devising viable heat transfer enhancement strategies for application to geothermal air-cooled condensers and similar applications. An effective strategy can result in a reduction in condenser size (and plant capital cost) and/or parasitic power consumption. The specific objective of this paper is to determine whether improved air-side heat transfer can be achieved through the use of oval tubes in combination with fin-surface vortex generators (winglets), while maintaining low heat-exchanger pressure drop.

Longitudinal vortices are generated naturally in fin-tube heat exchanger passages by the interaction of the flow velocity profile with the heat exchanger tube. These naturally occurring vortices are called horseshoe vortices. Longitudinal vortices can also be created through the use of winglet vortex generators mounted or punched into the fin surfaces. Jacobi and Shah [4] provide an excellent review of heat transfer enhancement through the use of longitudinal vortices. Various winglet shapes have been studied. Fiebig et al. [5], using the unsteady liquid crystal thermography technique, found that delta winglets provided the highest local heat transfer enhancement. Results presented in the present paper

are restricted to delta winglets, deployed in conjunction with an elliptical tube. Fiebig et al. [6] have also examined local heat transfer and pressure drop in fin-tube heat exchanger geometries with winglet vortex generators using both round tubes and flat tubes. Their results indicated much stronger vortex-induced heat transfer enhancement for the staggered arrangement of flat tubes than with round tubes. Wang et al. [7] also studied banks of flat tubes, using four delta-winglet vortex generators per tube. Local heat/mass transfer results were obtained using the naphthalene sublimation technique. Mean heat transfer enhancement as high as 47.5% was observed over the no-winglet case. The specific winglet deployment geometries considered in this experimental study are based on configurations studied numerically for low Reynolds numbers by Chen et al. [8] for a single winglet pair and a staggered array of two winglet pairs located near the upstream end of an oval tube. A related numerical study of in-line arrays of winglets was presented by Chen et al. in [9]. Their numerical results predicted higher heat transfer for the staggered winglet array than for in-line arrays.

Baseline local heat transfer measurements for both circular and oval tubes without winglets were obtained previously by the present authors and are presented in [1]. Results presented in the present oval-tube-plus-winglets study will be compared to the baseline results.

Additional fundamental studies of heat transfer associated with longitudinal vortex generators are available in the literature. Heat transfer enhancement with double rows of longitudinal vortex-generators (delta-winglet pairs) in a channel flow without tubes has been evaluated experimentally by Tiggelbeck et al. [10]. Their results indicated heat transfer enhancement of up to 80% for aligned delta winglet double rows. An investigation of the mechanisms of heat transfer enhancement associated with delta-winglet vortex generators was performed by Torii et al. [11]. This study revealed details of the local velocity and turbulence fields associ-

Contributed by the Heat Transfer Division for publication in the JOURNAL OF HEAT TRANSFER. Manuscript received by the Heat Transfer Division November 7, 2003; revision received May 11, 2004. Associate Editor: K. S. Ball.

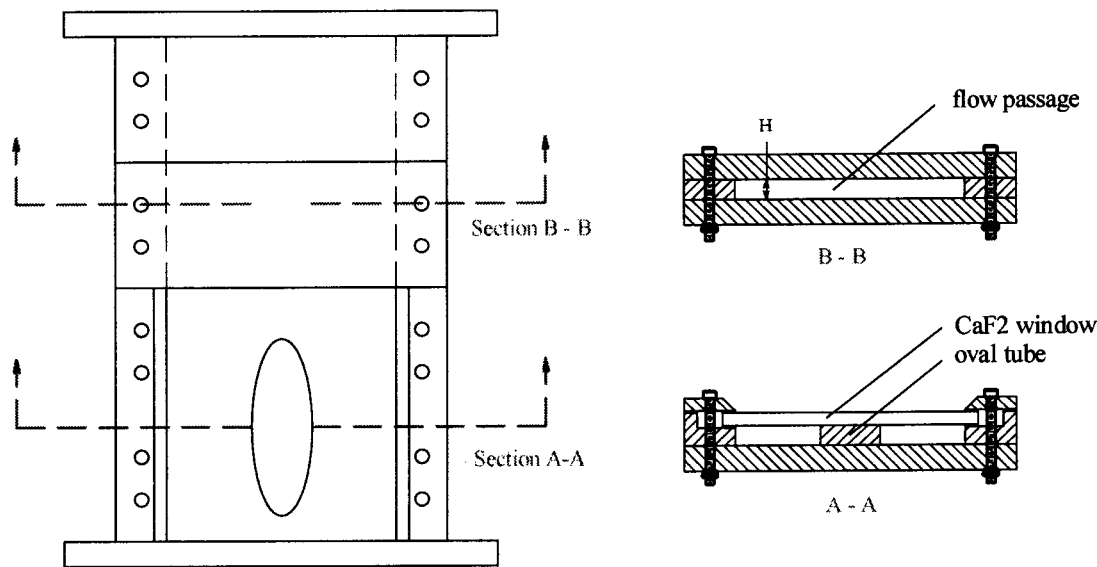


Fig. 1 Test section

ated with the longitudinal vortices downstream of delta winglet vortex generators. Lin and Jang [12] used an infrared imaging system to examine local heat transfer with embedded wave-type vortex generators in fin-tube heat exchangers. Their results indicated 18.5% enhancement in average heat transfer with the wave-type vortex generators.

In order to assess the heat transfer effectiveness of various combinations of tube and vortex-generator geometries, a heat transfer measurement technique that allows for high-resolution visualization and measurement of local heat transfer was chosen for this work. Results presented in this paper reveal visual and quantitative details of local fin-surface heat transfer in the vicinity of an elliptical tube, an elliptical tube with a single delta-winglet pair, and an elliptical tube with a staggered array of two delta-winglet pairs. Average heat transfer coefficients are also presented, along with a comparison to previously published results obtained with a circular tube and a circular tube with winglets. Pressure drop results are also presented for these geometries.

Apparatus

The heat transfer experiments were performed in a narrow rectangular duct designed to simulate a single passage of a fin-tube heat exchanger. A drawing of the test section is shown in Fig. 1. The duct height is 1.016 cm and the duct width-to-height ratio W/H is 11.25. The single elliptical tube had an aspect ratio of 3:1 and a major axis half-length a/H equal to 4.33. The triangular (delta) winglets had a 1:2 height/length aspect ratio and were oriented at a 30-deg angle to the flow. The height of the winglets h_w was 90% of the channel height.

The duct was fabricated primarily out of lexan polycarbonate. The test section length was 14.0 cm (5.50 in.), yielding $L/H = 13.7$. A flow-development section with $L/H = 30$ was located upstream of the test section. Consequently, depending on Reynolds number, the flow is approximately hydrodynamically fully developed as it enters the test section.

In order to enable thermal visualization of the test-section bottom surface (representing the fin surface), the top wall of the flow duct in the vicinity of the circular tube was formed by a calcium fluoride (CaF_2) window with dimensions: 12.7 cm \times 12.7 cm \times 6 mm (5 in. \times 5 in. \times 0.24 in.). The CaF_2 windows enabled viewing of the test-section bottom surface with an imaging infrared camera whose wavelength range of sensitivity was 3.6–5 μm .

The transmissivity of the CaF_2 window is very high ($>95\%$) in this wavelength range. The test section bottom surface (polycarbonate) was painted black using ultraflat black paint in order to achieve a surface emissivity very close to 1.0. This emissivity value was verified over a wide temperature range in separate camera-calibration tests by comparing camera-indicated temperatures with surface temperatures measured using a precision thin-foil flush-mounted thermocouple bonded to a black-painted polycarbonate test surface. Therefore, no emissivity corrections were required for the infrared temperature measurements.

A transient heat transfer measurement technique was employed for obtaining detailed local heat transfer measurements on the model fin surface. A schematic of the flow loop is shown in Fig. 2. Inlet air is heated to a desired setpoint temperature using an in-line, feedback-controlled, finned-element air heater (350 W). The heated air initially flows through a bypass line until the desired air temperature and flow rate is established. The air is then suddenly diverted through the test section by changing the position of a three-way valve. The apparatus was designed with a short axial distance, $L_i = 7.39$ cm, from the test section bypass line to the test section, such that $L_i/H = 18.5$. Using this technique, the room-temperature fin-tube model is suddenly exposed to a uniformly heated airflow, initiating a heat conduction transient in the lexan substrate. Local surface temperatures on the substrate increase at a rate that is dependent on the value of the local heat transfer coefficient. This transient localized heating is quantitatively recorded using an imaging infrared camera. Values of local heat transfer coefficients can then be determined from an inverse heat conduction analysis.

The bypass flow is diverted from the main flow duct through a circular hole (4.85 cm diam) cut into the bottom of the flow-development section. The center of the hole is located 8.25 cm (3.25 in.) upstream of the test-section entrance. The duct walls downstream of this location are not preheated during the flow-establishment period. Therefore, this distance represents a thermal entry length. When flow is suddenly initiated through the test section by changing the position of the three-way valve, the flow bypass hole in the bottom of the flow-development section is covered by sliding a flat lexan cover (sliding gate valve) over the hole. This procedure provides a continuous flat smooth flow surface, eliminating any concerns about a cavity-type flow disturbance associated with the hole.

Heater control is accomplished using a PID controller

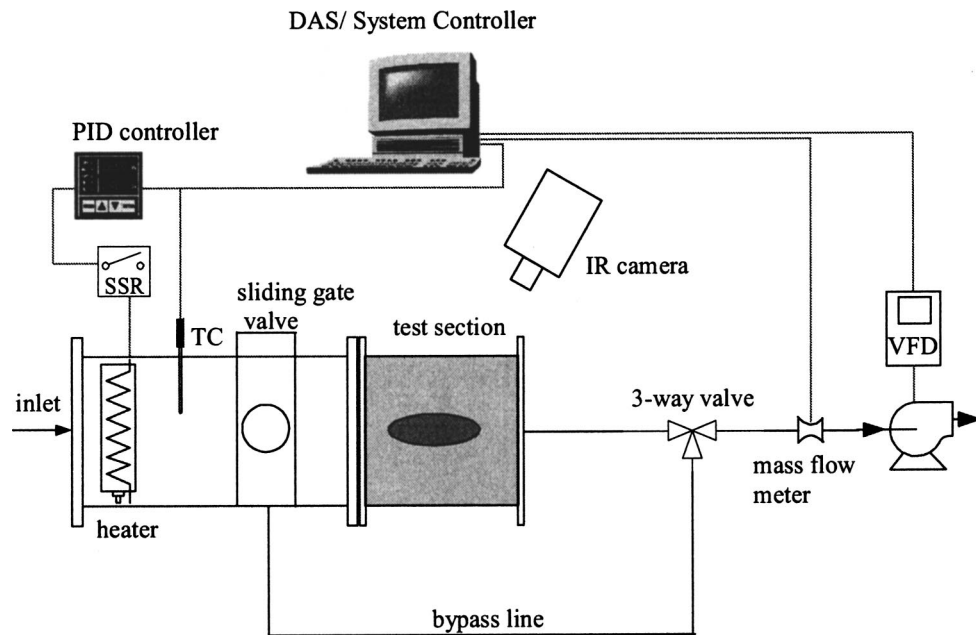


Fig. 2 Schematic of flow loop

(Yokogawa Model 514) coupled to a solid-state relay with a pulsed relay output. A thermocouple mounted inside the duct measures the process variable. The air temperature uniformity across the duct was verified via infrared imaging of the test surface during preliminary tests with no test cylinder in place. The airflow rate is monitored through the use of an in-line precision mass-flow meter (Kurz model 504FT) plumbed into the exhaust line. Test-section mass-average velocities and Reynolds numbers were calculated based on the SCM values obtained from the mass-flow meter. Air is drawn through the system by a centrifugal blower (1/3 HP, 240 V 3-phase) located at the flow exit. Blower speed is controlled by a sub-micro inverter variable-frequency drive (AC Tech model SF215), which in turn is controlled by a computer-generated 4–20 mA control signal. System flow rate varies linearly with blower speed over the range used in this study from about 1.51×10^{-3} to 14.0×10^{-3} kg/s. These flow rates correspond to a duct-height Reynolds number ($Re_H = \rho UH/\mu = \dot{m}/\mu W$) range of 670–6300 with a duct height of 1.016 cm and a duct width-to-height ratio W/H of 11.25. Geothermal air-cooled condensers typically operate within a Reynolds number range of $500 < Re_H < 1200$.

Two flush-mounted thin-foil thermocouples were bonded to the bottom surface of the test section near the test-section inlet. These thermocouples provide a continuous indication of surface temperature at two locations and are used to help determine the exact start time of each test, which occurs when the heated airflow is diverted through the test section.

Heat transfer results will be presented for three experimental configurations: elliptical tube, elliptical tube plus a single delta-winglet pair, and elliptical tube plus two delta winglet pairs in a staggered array. The geometric details of the elliptical tube, the winglets, and the winglet deployment locations are presented in Fig. 3. The winglets had a 1:2 height/length aspect ratio and were oriented at a 30-deg angle to the flow. The height of the winglets was 90% of the channel height. This height was chosen rather than the full channel height in order to avoid damage to the CaF_2 windows. The winglets were machined from lexan polycarbonate and were bonded to the test surface. The winglet deployment geometry for these tests was based on the geometry recommended in Ref. [8].

Quantitative thermal visualization images are obtained using a precision imaging infrared camera (FLIR PRISM DS). This cam-

era uses a fully calibrated 320×244 platinum-silicide IR CCD focal-plane array detector, which operates at a temperature of 77 K. The detector temperature is maintained by a mechanical split-Stirling-cycle helium cryocooler. In its base mode of operation, the camera can be used to measure infrared intensities corresponding to temperatures in the -10 – 250°C range, with extended ranges available through the use of filters up to 1500°C . The camera detector has a 12-bit digital dynamic range and a minimum discernible temperature difference (MDT) of 0.1°C at 30°C . It is equipped with a 25-mm standard lens, which provides a 17-deg \times 13-deg field of view. All radiometric information is stored in binary digital files on PCMCIA flash memory cards for subsequent analysis. Infrared thermography has several advantages over thermochromic liquid crystals for surface temperature mapping, including wide available temperature range, high spatial resolution, excellent thermal resolution, and full-field direct digital data acquisition and processing.

The thermal image binary data files created by the camera on-board processor are stored in a specialized 16-bit TIFF gray-scale format. These files include not only the image pixel values, but also a large amount of camera and test-specific information, such as camera and firmware identifiers, date and time of image acquisition, camera settings at image acquisition, and temperature/pixel calibration data points. This information is included in the TIFF file in the form of "private tags" [13]. Specific file-format information provided by FLIR was used in conjunction with general information about the TIFF standard found in Ref. [13] to fully decode the binary data files for subsequent thermal analysis using a Labview (National Instruments, Version 5.1) program created for this purpose.

A separate single-channel multiple-tube-row apparatus was fabricated for evaluating the pressure-drop performance of the various tube and winglet configurations studied in the heat transfer experiments. A drawing of the pressure-drop test section core is shown on the left side of Fig. 4 for the case of oval tubes with two pairs of winglets. The axial and spanwise tube spacing is shown in the figure. The circular tube arrays had the same spanwise and axial tube spacing, with a tube diameter of 2.54 cm. The oval and circular tubes were designed to have the same cross-sectional flow area. Dried and filtered shop air enters the flow channel from a slot located 24 cm upstream of the tube bundle. The flow channel dimensions are 0.254 cm high \times 22.86 cm wide. A row of six pres-

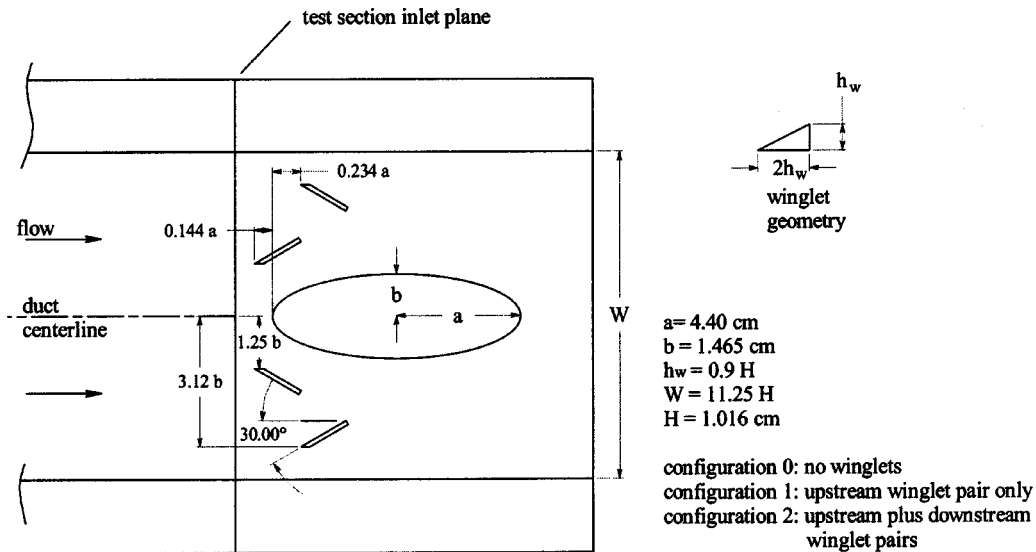


Fig. 3 Winglet locations and geometry

sure taps was drilled along the channel centerline upstream and downstream of a four-tube-row staggered array of either circular or elliptical tubes, with or without winglets. The tube array simulates a single passage in a plate-fin heat exchanger. The tubes and winglets were machined from a solid sheet of lexan using a CNC mill. A close-up photograph of the oval tubes and winglets is shown on the right side of Fig. 4. Pressure drop was measured using a precision differential pressure transducer (MKS Model 223BD, 1- and 10-Torr ranges). Air flow rates were obtained from a precision mass-flow meter (Hasting Model HFM, 500 and 300 slpm ranges).

Instrumentation signals from both the heat transfer and pressure-drop flow loops were fed into a modular multiplexing data-acquisition system (Hewlett Packard 3852A), which in turn was interfaced to a system-controller computer via an IEEE-488 bus. For this experiment, the data acquisition unit was configured with a 20-channel FET multiplexer with thermocouple compensation, a 5.5 digit integrating voltmeter, and a 4-channel voltage/current DAC. The DAC module was used to provide control signals (4–20 mA) to the variable-frequency drive for the blower. The mass-flow meter was configured to communicate directly with the computer using an RS-232 interface. Data-acquisition and instrument-control system programming was accomplished

using Labview software. The data files included time histories of the thermocouple mass-flow meter and pressure-transducer signals with updates at 0.7-s intervals.

Experimental Procedure

Heat Transfer Measurements. Details of the experimental procedure for the transient heat transfer tests will now be provided. After the IR camera is powered up and the detector array has reached its 77K operating temperature, the camera is positioned above the test section at an appropriate height for observing either the entire portion of the test section or a close-up view. In order to avoid IR reflections of the warm camera body off the CaF₂ windows, the camera is positioned at a small angle off the vertical. The camera gain and level adjustments are set such that the minimum observable temperature corresponds to the initial temperature with a temperature range of 10–15°C. The software clock on the camera is synchronized with the clock on the data acquisition computer to within ± 0.5 s. The three-way valve is set to the bypass position and the sliding gate valve is opened. Flow is initiated through the bypass line by adjusting the blower RPM until the desired flow rate is observed. The air temperature is established by adjusting the PID controller set-point value to the

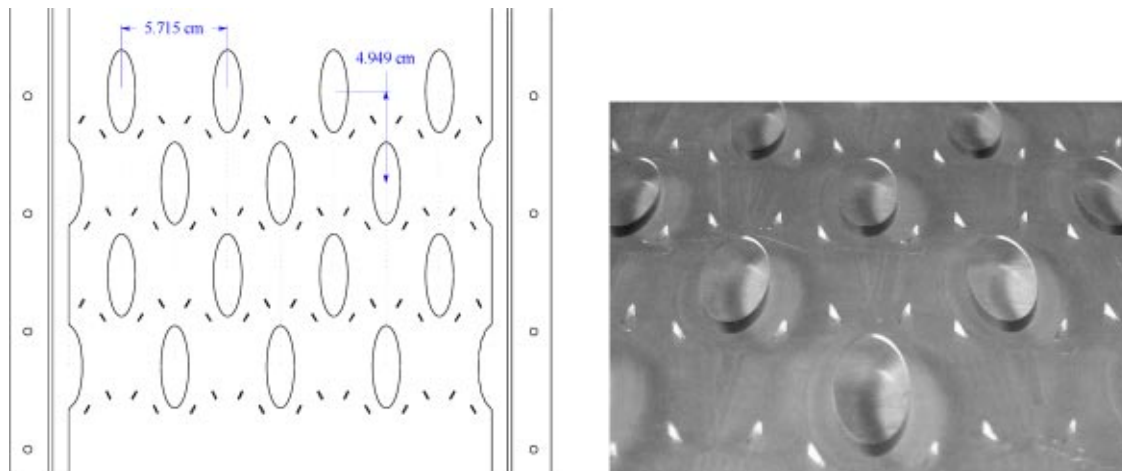


Fig. 4 Pressure-drop test section core

desired level, typically 45°C. Before diverting heated air through the test section, a pretest thermal image of the test section is acquired. At this time, the data acquisition system is set to begin writing data to disk. The three-way valve position is then changed, and the sliding gate valve is closed to divert the heated airflow through the test section, initiating the thermal transient. A number of thermal images of the test section (typically 5) are acquired during the first 5–60 s of the transient. These images are stored on PCMCIA flash memory cards and are transferred to the system controller computer after each test. The images selected for final presentation in this paper were typically acquired at 30–40 s after initiation of the transient. Heat transfer results were obtained over an airflow rate ranging from 1.51×10^{-3} to 14.0×10^{-3} kg/s, corresponding to a Reynolds number range based on duct height of 670–6300.

Pressure-Drop Measurements. Two techniques were used for the pressure-drop tests: steady-flow and blow-down. Steady-flow tests were performed by establishing a steady air flow using a flow-control valve, then acquiring a large number of averages of both flow rate and pressure drop at a fixed flow rate. Blow-down tests were performed by charging the air compressor storage tank to a predetermined pressure with no flow, then discharging the tank through the system while continuously monitoring instantaneous flow rate and pressure drop. The air compressor was disabled during the blow-down. Blow-down testing allowed pressure-drop measurements to be obtained over a much broader flow range (both higher and lower flows) than steady-flow tests. It also provided a complete pressure-drop versus flow-rate data set over the entire flow-rate range of interest in a single test. Results obtained with the steady-state and blow-down techniques were in excellent agreement.

Data Reduction

In order to obtain heat transfer coefficients from the surface temperatures measured during the transient heat-up of the test section, the bottom surface of the test section is assumed to behave locally as a one-dimensional semi-infinite solid undergoing a step change in surface convection heat transfer. For the 1.27 cm thickness of the lexan test surface, the semi-infinite assumption is valid for at least 88 s after initiation of the transient. The assumption of a step-change in convection heat transfer is not exactly correct because the mean air temperature at the test section actually increases slightly with time, due to heat transfer to the duct wall downstream of the flow diversion location [14]. This mean-temperature-depression effect is most serious at low Reynolds numbers and for small values of elapsed time at image acquisition. However, auxiliary calculations and examination of preliminary data indicated that, for the geometry and flow conditions of our tests and for the image acquisition times used, neglecting this effect would not have a significant impact on the heat transfer coefficient distribution results. The time-dependent surface temperature for a semi-infinite solid subjected to this boundary condition is given in [15]

$$\frac{T(0,t) - T_i}{T_\infty - T_i} = 1 - \exp\left(\frac{h^2 \alpha t}{k^2}\right) \operatorname{erfc}\left(\frac{h \sqrt{\alpha t}}{k}\right) \quad (1)$$

and if we let

$$\theta = \frac{T(0,t) - T_i}{T_\infty - T_i}; \quad \gamma = \frac{h \sqrt{\alpha t}}{k} = \frac{h \sqrt{t}}{\sqrt{\rho c k}} \quad (2)$$

the equation reduces to

$$\theta = 1 - \exp(\gamma^2) \operatorname{erfc}(\gamma) \quad (3)$$

This equation represents the relationship between heat transfer coefficient and surface temperature measured at a specific time

after the start of the test. It must be solved iteratively for γ . However, since the camera pixel array includes over 78,000 pixels, it is not practical to directly solve the equation at every pixel. Instead, a look-up-table approach was used in the data-reduction scheme. The measured temperature range for each thermal image is divided into 100 increments, and a value of heat transfer coefficient is obtained for each of these 100 temperatures by iteratively solving Eq. (4). Each actual pixel temperature is then converted to a heat transfer coefficient by linear interpolation among the 100 increments.

Local heat transfer results are presented in terms of heat transfer coefficient. Average heat transfer is presented in terms of Nusselt number based on channel height $Nu_H = hH/k$, parameterized by the Reynolds number based on channel height $Re_H = \rho UH/\mu = \dot{m}/\mu W$. Pressure-drop results are presented in terms of friction factor, defined as

$$f = \frac{\Delta P \rho}{G^2/2(4L/D_h)} \quad (4)$$

where G is the mass flux at the minimum flow area, ΔP is the pressure drop across the tube bundle, and L is the axial length of the tube bundle. The hydraulic diameter D_h is given by

$$D_h = \frac{4LA_{\min}}{A} \quad (5)$$

where A_{\min} is the minimum flow cross-sectional area, and A is the total heat transfer surface area. Friction factors are parameterized using the Reynolds number based on hydraulic diameter, $Re_{D_h} = GD_h/\mu$. Note that this friction factor definition does not include any entrance or exit effects. Only core friction is considered because the measured pressure drop only corresponds to core friction.

Experimental Uncertainty

Estimates of the experimental uncertainties of the Reynolds numbers, heat transfer coefficients, and friction factors presented in this paper have been obtained based on constant-odds, 95% confidence level [16]. For Reynolds numbers, the uncertainties associated with the mass-flow meters and the viscosity were considered. For the heat transfer coefficients, individual uncertainties in image-capture time, surface temperature, air temperature, and substrate thermal product ($\sqrt{\rho c k}$) were considered. For the friction factors, uncertainties in mass flow rate, pressure drop, and air density were considered. A plot indicating estimated uncertainties

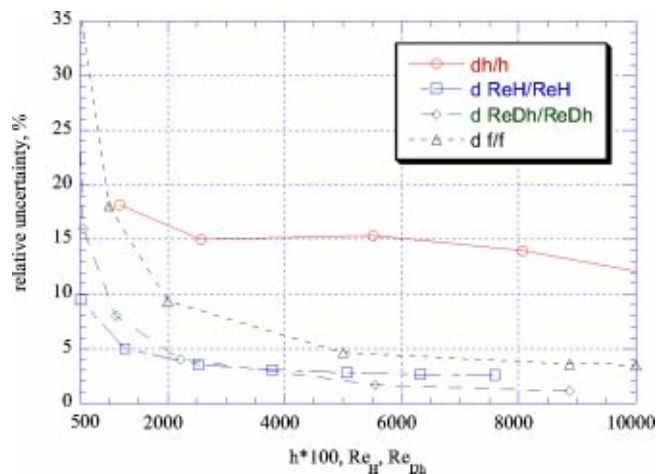


Fig. 5 Experimental uncertainties

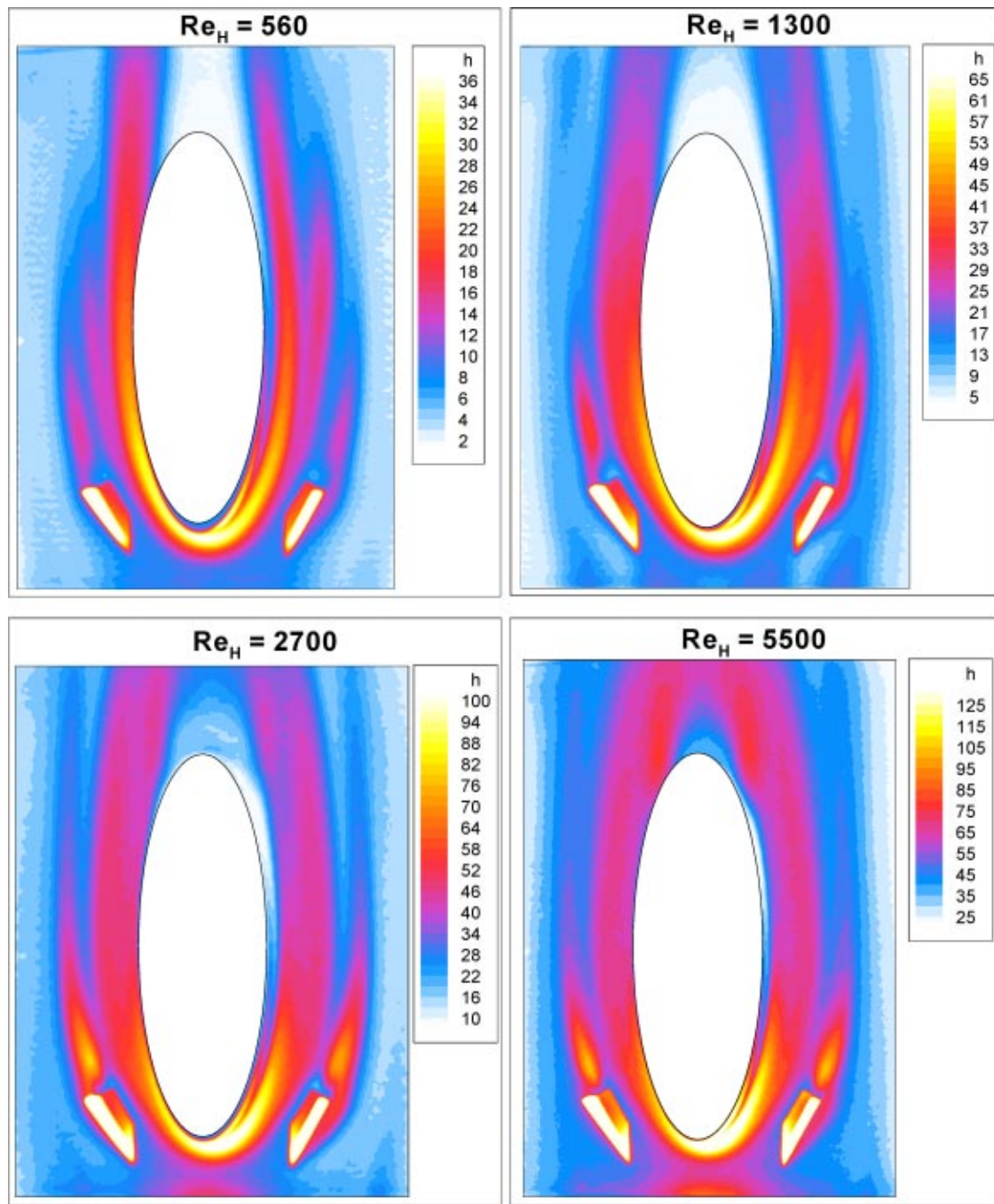


Fig. 6 Local fin surface heat transfer coefficients for an oval tube plus a single winglet pair

for these quantities is presented in Fig. 5. Heat transfer coefficient uncertainties are plotted against $h \cdot 100$. Therefore, if the heat transfer coefficient value is 30, $h \cdot 100 = 3000$ and the uncertainty in heat transfer coefficient is around 15%. Reynolds number uncertainties are plotted against the respective Reynolds number values. Friction factor uncertainties are plotted against Re_{D_h} . Reynolds number and friction factor uncertainties increase dramatically for very low flow rates, but are reasonable for Reynolds numbers greater than 500. Friction factor uncertainties include contributions from both the mass flow meter and the pressure transducer, both cited by the manufacturer as a percentage of full scale. Observed repeatability of the flow-rate and pressure-drop measurements were significantly better than the relative uncertainty values shown in Fig. 5.

Results

Local fin-surface heat transfer distributions for the baseline case of flow around an elliptical tube with no winglets were presented in reference [1]. Local fin-surface heat transfer distributions for flow around an elliptical tube with winglets are presented in Figs. 6 and 7 for four Reynolds numbers. Results for the case of a single winglet pair are presented in Fig. 6. Results for the case of two delta winglet pairs in a staggered array are presented in Fig. 7. In these figures, flow is from bottom to top. The winglets are visible in the figures near the upstream leading edge of the oval tubes. Apparent heat transfer coefficients on the winglets themselves are not valid because the winglets protrude into the flow and, therefore, do not behave as a semi-infinite solid. The slight

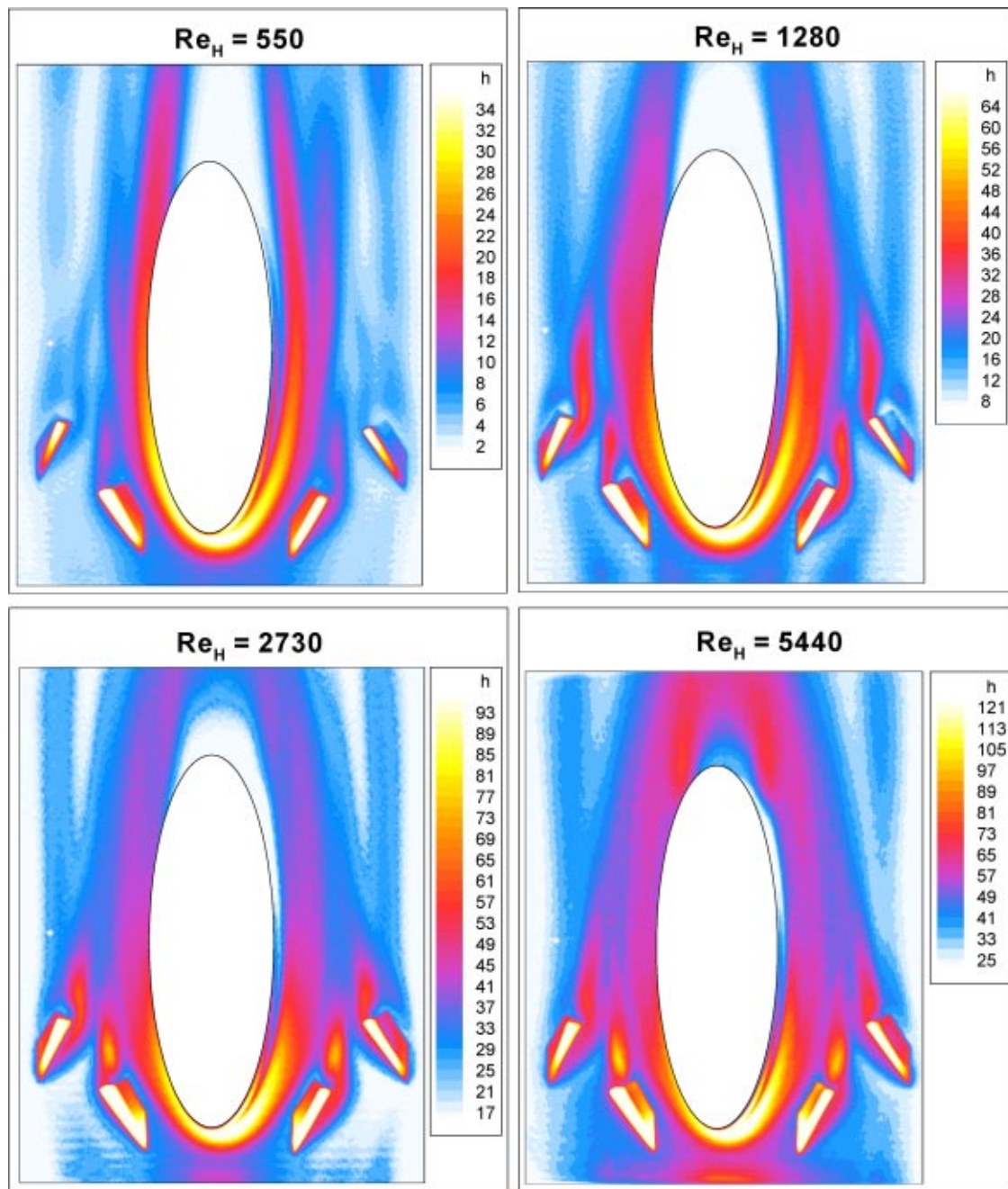


Fig. 7 Local fin-surface heat transfer distributions for flow around an elliptical tube with two pairs of delta winglets in a staggered configuration

asymmetry visible in the heat transfer images is due to the effect of the slightly off-vertical viewing angle of the IR camera

Results presented in Fig. 6 clearly indicate local areas of high fin-surface heat transfer in the stagnation region of the oval tube, along the side of the oval tube, and downstream of the winglets. Highest heat transfer coefficients are in the tube stagnation region. The very high heat transfer coefficients, which would normally be expected to occur at the fin leading edge in an actual finned tube, are absent because the test section is preceded by both a momentum and thermal entry length, as described in the Apparatus Section. The horseshoe vortex that forms in the tube stagnation region is swept downstream along the side of the tube as a longitudinal vortex, producing a streak of high fin-surface heat transfer that persists well downstream of the tube.

Each winglet produces two vortices: a primary vortex and a

corner, horseshoe-type vortex. The primary vortex, located directly downstream of the vortex generators, is formed by flow separation along the top edge of the winglets. The corner vortex, located outside of the main vortex, develops like a horseshoe vortex on the upstream-facing pressure side of the winglets. The fin-surface heat transfer enhancement associated with the primary vortex is visible in the images of Fig. 6 directly downstream of each winglet, starting about a half-winglet-length directly axially downstream of each winglet. The heat transfer enhancement associated with the corner vortex of each winglet is visible in the images as a streak that begins on the upstream side of each winglet and is swept to the outside and downstream. The heat transfer effects of all three of these vortices are most distinctly visible in the lowest Reynolds number case presented in Fig. 6. In this figure, moving outward spanwise from the side of the tube,

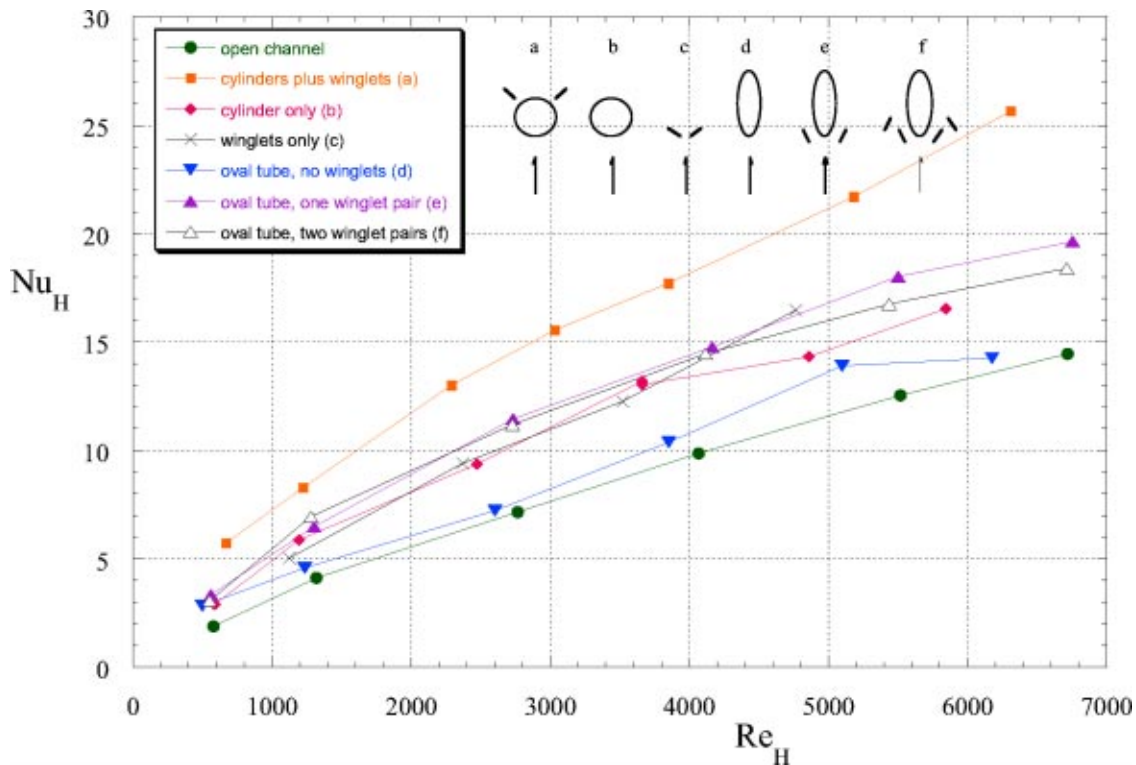


Fig. 8 Mean fin-surface Nusselt numbers for seven flow configurations, based on local heat transfer results

the tube horseshoe vortex, the primary winglet vortex, and the corner winglet vortex are all visible. At the higher Reynolds numbers, the effects of the three vortices are still visible, but they tend to merge together and become less distinct. At low Reynolds numbers, the wake region downstream of the oval tube represents a very low heat transfer region. However, at higher Reynolds numbers, this region “fills in” due to the transition to turbulent flow in the duct and in the boundary layers that form on the tube wall. The enhancement of overall heat transfer associated with the deployment of the winglets will be discussed later.

Local heat transfer results presented in Fig. 7 are similar to the results shown in Fig. 6, but with two winglet pairs deployed in the leading-edge region of the elliptical tube in a staggered configuration. Local regions of high heat transfer associated with the tube stagnation region, the tube horseshoe vortex, and the primary and corner vortices produced by each winglet are all visible in the images. Trends with increasing Reynolds number are also similar to the single-winglet-pair case.

Mean fin-surface heat transfer coefficients have been calculated based on the local heat transfer results for the seven flow configurations studied to date (two detailed in this paper plus five detailed in Refs. [1–2]). For these calculations, only the active fin area is considered. The areas covered by the tubes (circular or oval) or the winglets are not included. Results of these calculations are presented in Fig. 8 in the form of Nusselt number based on channel height Nu_H versus Reynolds number based on channel height Re_H . A small schematic of each flow configuration is shown in the top of Fig. 8. Highest heat transfer coefficients were observed for the case of a circular tube plus winglets with the winglets located on the downstream side of the cylinder, oriented at a 45-deg angle to the flow. The cases of oval tube plus one pair of winglets and oval tube plus two pairs of winglets yielded similar mean heat transfer results, with the single-winglet-pair configuration actually producing higher heat transfer at the highest Reynolds numbers. The addition of the single winglet pair to the oval-tube geometry yielded significant heat transfer enhancement, averaging 38% higher than the oval-tube, no-winglet case. Mean Nusselt numbers

for the cases of a circular tube without winglets and a single delta-winglet pair with no tube yielded similar results. Heat transfer results for the oval tube without winglets were quite low. Lowest heat transfer coefficients, as expected, were produced by the open-channel configuration.

In order to fully assess the performance of any of these flow configurations, the pressure-drop behavior must be also considered. Results of the pressure-drop measurements obtained with the single-channel, multiple-tube-row pressure drop apparatus are presented in Fig. 9 in terms of friction factor versus Reynolds number based on hydraulic diameter, as defined in Eqs. (4)–(5). Based on this definition, in the laminar regime, the highest friction factors were observed for the open channel, followed by the oval-tube cases and finally by the circular-tube cases. Actual pressure drop magnitudes are in the opposite order. The friction factor results reflect the fact that the minimum-area mass flux G is successively higher for the oval-tube cases and the circular-tube cases for a specified total mass flow rate (note that G^2 appears in the denominator of the friction-factor definition). Open-channel data agree well with the theoretical value of $24/Re_{D_h}$ for laminar flow in a parallel-plate channel. The friction factor data for all cases tend to converge at higher (turbulent) Reynolds numbers, approaching the Petukov [17] correlation for turbulent-flow friction factor. Friction factor results for cases with winglets are higher than their respective baseline cases since the only quantity that is different in calculating those friction factors is the magnitude of the pressure drop. No correction is made to the minimum-flow area for the winglet cases. It should be noted that because the mean heat transfer results were obtained from the single-tube heat transfer tests and the friction factor results were obtained from a multiple-tube-row configuration, the heat transfer and friction factor results do not correspond to identical flow situations. This is why the mean heat transfer results have not been converted to j -factors for presentation on the same graph as the friction factors, as is standard practice for presentation of heat exchanger results.

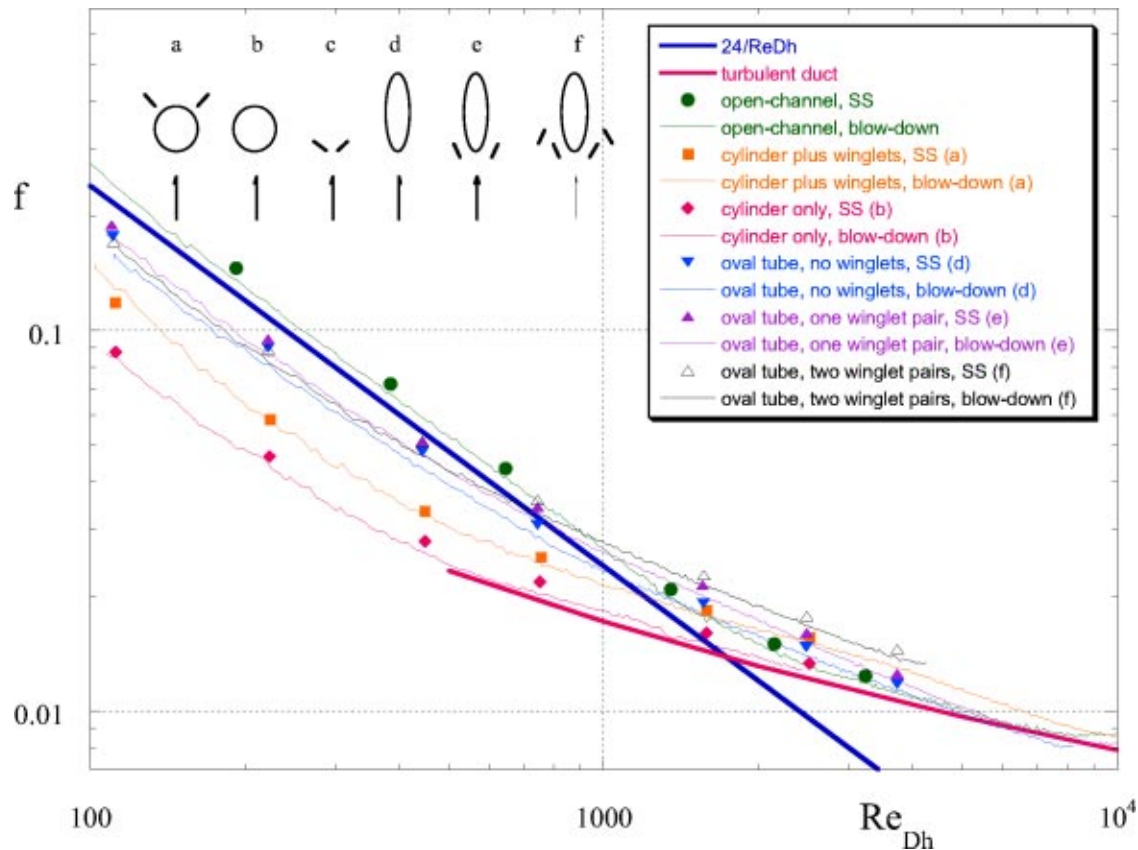


Fig. 9 Friction factors measured for six flow configurations, steady-state and blow-down results

We are in the process of developing a new apparatus that will provide both overall heat transfer and pressure-drop results for an entire tube bundle.

Conclusions

An experimental study of forced convection heat transfer in a narrow rectangular duct fitted with an elliptical tube and one or two delta-winglet pairs has been performed. The duct was designed to simulate a single passage in a fin-tube heat exchanger. Heat transfer measurements were obtained using a transient technique in which a heated airflow is suddenly introduced to the test section. High-resolution local fin-surface temperature distributions were obtained at several times after initiation of the transient using an imaging infrared camera. Corresponding local fin-surface heat transfer coefficients were then calculated from a locally applied one-dimensional semi-infinite inverse heat conduction model. Pressure-drop measurements have also been obtained for similar elliptical-tube and winglet geometries using a separate single-channel, multiple-tube-row pressure-drop apparatus. The pressure-drop apparatus includes four tube rows in a staggered array. Heat transfer and pressure-drop results were obtained over a Reynolds number range based on duct height of approximately 600–6500.

Local heat transfer results clearly indicate areas of high fin-surface heat transfer in the stagnation region of the oval tube, along the side of the oval tube, and downstream of the winglets. Highest heat transfer coefficients are in the tube stagnation region. The local heat transfer enhancement associated with both the primary vortex and the corner, horseshoe-type vortices produced by each winglet are visible in the heat transfer images. Evaluation of mean fin-surface heat transfer coefficients indicated that the addition of the single winglet pair to the oval-tube geometry yielded significant heat transfer enhancement, averaging 38% higher than

the oval-tube, no-winglet case. The corresponding increase in friction factor was very modest, less than 10% at $Re_{D_h}=500$ and less than 5% at $Re_{D_h}=5000$. Highest mean heat transfer coefficients were observed for the case of a circular tube plus winglets with the winglets located on the downstream side of the cylinder, oriented at a 45-deg angle to the flow.

Acknowledgments

This work was sponsored by the U.S. Department of Energy, Geothermal Program. The Idaho National Engineering and Environmental Laboratory is operated by Bechtel, Babcock and Wilcox Idaho, LLC under Contract No. DE-AC07-99ID13727. The authors would also like to acknowledge the support received from the Japanese New Energy and Industrial Technology Development Organization, under research Grant No. 99EF1.

Nomenclature

- a = elliptical tube major axis half length, cm
- A = tube bundle heat transfer surface area, m^2
- A_{\min} = minimum flow cross-sectional area, m^2
- b = elliptical tube minor axis half-length, cm
- c = specific heat, J/kg K
- D_h = duct hydraulic diameter, cm
- f = friction factor
- G = air flow mass flux, $kg/m^2 s$
- h = heat transfer coefficient, $W/m^2 K$
- h_w = winglet height, cm
- H = channel height, cm
- k = thermal conductivity, $W/m K$
- L = test section length, tube bundle length, cm
- \dot{m} = air mass flow rate, kg/s
- $Nu_H = hH/k$ = Nusselt number based on channel height

ΔP = pressure drop across tube bundle, Pa
 $Re_H = \rho UH/\mu$ = Reynolds number based on channel height
 $Re_{D_h} = GD_h/\mu$ = Reynolds number based on hydraulic diameter
 t = time, s
 T = temperature, K
 T_i = initial temperature, K
 T_∞ = flow mean temperature, K
 U = mean flow velocity, m/s
 W = channel width, cm
 α = lexan thermal diffusivity, m²/s
 ρ = density, kg/m³
 $\gamma = h\sqrt{t}/\sqrt{\rho ck}$ = nondimensional heat transfer coefficient
 $\theta = T(0,t) - T_i / T_\infty - T_i$ = nondimensional temperature difference
 μ = air absolute viscosity, N s/m²

References

- [1] O'Brien, J. E., and Sohal, M. S., 2000, "Local Heat Transfer for Finned-Tube Heat Exchangers Using Oval Tubes," *Proc. of 2000 ASME National Heat Transfer Conference*, Pittsburgh, Paper No. NHTC2000-12093, CD-ROM, ASME, New York.
- [2] O'Brien, J. E., and Sohal, M. S., 2000, "Heat Transfer Enhancement for Finned-tube Heat Exchangers with Winglets," *Proc. of 2000 ASME Int. Congress and Exposition*, Orlando, HTD-Vol. 365/PID-Vol. 4, ASME, New York, pp. 137–146.
- [3] Foust, T. D., O'Brien, J. E., and Sohal, M. S., 2001, "Numerical and Experimental Methods for Heat Transfer Enhancement for Finned-Tube Heat Exchangers with Oval Tubes," 2001 ASME National Heat Transfer Conference, Anaheim, Paper No. NHTC01-12363.
- [4] Jacobi, A. M., and Shah, R. K., 1995, "Heat Transfer Surface Enhancement Through the Use of Longitudinal Vortices: A Review of Recent Progress," *Exp. Therm. Fluid Sci.*, **11**, pp. 295–309.
- [5] Fiebig, M., Kallweit, P., and Mitra, N. K., 1986, "Wing Type Vortex Generators for Heat Transfer Enhancement," *Heat Transfer 1986*, Proc. of 8 Int. Heat Transfer Conf., Hemisphere, New York, Vol. 6, pp. 2903–2908.
- [6] Fiebig, M., Valencia, A., and Mitra, N. K., 1994, "Local Heat Transfer and Flow Losses in Fin-Tube Heat Exchanger with Vortex Generators: A Comparison of Round and Flat Tubes," *Exp. Therm. Fluid Sci.*, **8**(1), pp. 35–45.
- [7] Wang, L. B., Ke, F., Gao, S. D., and Mei, Y. G., 2002, "Local and Average Characteristics of Heat/Mass Transfer Over Flat Tube Bank Fin With Four Vortex Generators per Tube," *ASME J. Heat Transfer*, **124**, pp. 546–552.
- [8] Chen, Y., Fiebig, M., and Mitra, N. K., 2000, "Heat Transfer Enhancement of Finned Oval Tubes with Staggered Punched Longitudinal Vortex Generators," *Int. J. Heat Mass Transfer*, **43**, pp. 417–435.
- [9] Chen, Y., Fiebig, M., and Mitra, N. K., 1998, "Heat Transfer Enhancement of a Finned Oval Tube With Punched Longitudinal Vortex Generators In-line," *Int. J. Heat Mass Transfer*, **41**, pp. 4151–4166.
- [10] Tiggelbeck, S., Mitra, N. K., and Fiebig, M., 1993, "Experimental Investigations of Heat Transfer Enhancement and Flow Losses in a Channel with Double Rows of Longitudinal Vortex Generators," *Int. J. Heat Mass Transfer*, **36**(9), pp. 2327–2337.
- [11] Torii, K., Nishino, K., and Nakayama, K., 1994, "Mechanism of Heat Transfer Augmentation by Longitudinal Vortices in a Flat Plate Boundary Layer," *Proc. of 10 Int. Heat Transfer Conf.*, Hemisphere, New York, Vol. 6, pp. 123–128.
- [12] Lin, C. N., and Jang, J. Y., 2002, "Conjugate Heat Transfer and Fluid Flow Analysis in Fin-Tube Heat Exchangers with Wave-Type Vortex Generators," *J. Enhanced Heat Transfer*, **9**(3–4), pp. 123–136.
- [13] TIFF Revision 6.0, 1992, Adobe Developers Association, Adobe System Inc.
- [14] Ekkad, S. V., and Han, J. C., 1997, "Detailed Heat Transfer Distributions in Two-Pass Square Channels With Rib Turbulators," *Int. J. Heat Mass Transfer*, **40**(11), pp. 2525–2537.
- [15] Incropera, F. P., and DeWitt, D. P., 1990, *Fundamentals of Heat and Mass Transfer*, Third, edition, Wiley, New York.
- [16] Moffatt, R. J., 1988, "Describing the Uncertainties in Experimental Results," *Exp. Therm. Fluid Sci.*, **1**, pp. 3–17.
- [17] Petukhov, B. S., 1970, "Heat Transfer in Turbulent Pipe Flow With Variable Physical Properties," *Advances in Heat Transfer*, T. F. Irvine and J. P. Hartnett, eds., Academic Press, New York, Vol. 6, pp. 504–564.

Three-Dimensional Forced Convection in Plane Symmetric Sudden Expansion

J. H. Nie and B. F. Armaly*

Department of Mechanical and Aerospace Engineering,
and Engineering Mechanics, University of
Missouri–Rolla, Rolla, MO 65401

Simulations of three-dimensional laminar forced convection in a plane symmetric sudden expansion are presented for Reynolds numbers where the flow is steady and symmetric. A swirling “jet-like” flow develops near the sidewalls in the separating shear layer, and its impingement on the stepped wall is responsible for the maximum that develops in the Nusselt number adjacent to the sidewalls and for the reverse flow that develops in that region. The maximum Nusselt number on the stepped wall is located inside the primary recirculation flow region and its location does not coincide with the jetlike flow impingement region. The results reveal that the location where the streamwise component of wall shear stress is zero on the stepped walls does not coincide with the outer edge of the primary recirculation flow region near the sidewalls.
[DOI: 10.1115/1.1795242]

Introduction

Flow separation in internal flow and its subsequent reattachment, caused by sudden changes in geometry, occur in many engineering applications where heating or cooling is required. These applications appear in electronic cooling equipment, cooling of turbine blades, combustion chambers, and many other heat exchanging devices. The flow and the heat transfer in most of these applications exhibit three-dimensional (3D) behavior, but most of the published results have treated only two-dimensional (2D) problems [1–4]. Experimental and numerical studies [5–9] have shown that two-dimensional laminar flow in plane symmetric sudden expansion undergoes a bifurcation from symmetric to asymmetric equilibrium states at a critical Reynolds number. The flow symmetry breaks down when the Reynolds number is higher than the critical value, and recirculation flow regions of different size develop adjacent to the two symmetric stepped walls. Flow with Reynolds numbers below the critical value is steady and symmetric. Cherdron et al. [10] demonstrated experimentally that the critical Reynolds number increases with decreasing both the aspect ratio and the expansion ratio of the duct. They established that for a duct with expansion ratio ($ER=H/h$, where H and h are duct heights downstream and upstream from the step, respectively) of 2 and aspect ratio ($AR=W/H$, where W is width of duct) of 8, the flow is steady and symmetric for Reynolds number ($Re=2\rho u_0 h/\mu$, where ρ is density, u_0 is the average inlet velocity, and μ is the dynamic viscosity) equal to or smaller than 150. Chiang et al. [11] examined the effects of the aspect ratio on the developments of flow asymmetry and established that, for an expansion ratio of 3 and a Reynolds number of 160, the flow is steady and symmetric when the upstream aspect ratio is smaller than 3.5. All of the published work on the plane symmetric expansion geometry has been limited to examining the fluid flow behavior only, and none, to the authors' knowledge, has been published about the resulting convection heat transfer in this geom-

etry. This fact, along with the realization that such geometry appears regularly in many industrial heat transfer devices, motivated the present study.

Problem Statement and Solution Procedures

Three-dimensional laminar forced convection in plane symmetric sudden expansion is simulated, and a schematic of the computational domain is presented in Fig. 1. The duct's heights H and h downstream and upstream of the expansion respectively are 0.04 m and 0.02 m. The step height S and the duct's width W are maintained as 0.01 m and 0.08 m, respectively. This provided a configuration with an expansion ratio of 2 and an upstream aspect ratio of 4. The origin of the coordinate system is located at the bottom corner of the step where the sidewall, the backward-facing step, and the stepped-wall intersect, as shown in Fig. 1. The directions of the streamwise (x), spanwise (z), and transverse (y) coordinates are shown in that figure. The length of the computational domain is 0.5 m downstream and 0.02 m upstream of the step, respectively, i.e., $-2 \leq x/S \leq 50$. This choice was made to ensure that the flow at the inlet section of the duct ($x/S=-2$) is not affected by the sudden expansion in geometry at the step and the flow at the exit section of the duct ($x/S=50$) can be treated as fully developed. It was confirmed that the use of a longer computational domain did not change the flow behavior in the region downstream from the step ($x/S < 25$). The three-dimensional Navier-Stokes, energy, and continuity equations for laminar steady incompressible flow are solved numerically using the finite volume method. The physical properties are treated as constants and evaluated for air at the inlet temperature of $T_0=20^\circ\text{C}$ [i.e., density ρ is 1.205 kg/m^3 , specific heat C_p is $1005\text{ J/(kg}\cdot^\circ\text{C)}$, dynamic viscosity μ is $1.81 \times 10^{-5}\text{ kg/(m}\cdot\text{s)}$, and thermal conductivity k is equal to $0.0259\text{ W/(m}\cdot^\circ\text{C)}$]. Inlet flow ($x/S=-2$, $1 \leq y/S \leq 3$, for all z) is considered to be isothermal ($T_0=20^\circ\text{C}$), hydrodynamically steady and fully developed with a distribution for the streamwise velocity component u equal to the one described by Shah and London [12] for fully developed laminar flow in a rectangular duct. The other velocity components (v and w) are set to be equal to zero at that inlet section. No slip condition (zero velocities) is applied to all of the wall surfaces. Uniform and constant wall heat flux ($q_w=5\text{ W/m}^2$) is specified for the stepped wall ($y/S=0$ and 4 , $0 \leq x/S \leq 50$, for all z), while other walls are treated as adiabatic surfaces. At this low wall heat flux, the buoyancy effects are negligible and can be neglected in the simulation. Fully developed flow and thermal conditions are imposed at the exit section ($x/S=50$, for all y and z) of the calculation domain by equating the streamwise gradients of all quantities to zero at the exit. The governing equations are discretized using the finite volume method, and a line-by-line method combined with the alternating direction implicit (ADI) scheme is used to solve the resulting finite volume equations. The SIMPLE algorithm is utilized for the computation of pressure correction in the iteration procedure. Hexahedron volume elements and a non-uniform grid system are employed in the simulations. The grid is highly concentrated close to the step and near the step corners in order to ensure the accuracy of the numerical simulations. Comparisons of computed u -velocity profiles at different streamwise locations with the measurements of Fearn et al. [8] are presented in Fig. 2. Very good agreement between measured and predicted values can be seen in that figure, thus validating the current simulation code. Additional details about the numerical methods and code validation can be found in Ref. [13]. Results from several grid densities for a Reynolds number ($Re=150$) were used in developing a grid independent solution for this study. The velocity and temperature values at a selected point in the flow domain are presented in Table 1 for different computational grids. A grid of $190 \times 56 \times 56$ was selected for these simulations. Using a finer grid of $210 \times 76 \times 76$ resulted in less than 1% difference in the predicted results. The convergence criterion required that the maximum relative mass residual based on the inlet mass be less

*Corresponding author.

Contributed by the Heat Transfer Division for publication in the JOURNAL OF HEAT TRANSFER. Manuscript received by the Heat Transfer Division December 12, 2003; revision received April 21, 2004. Associate Editor: K. S. Ball.

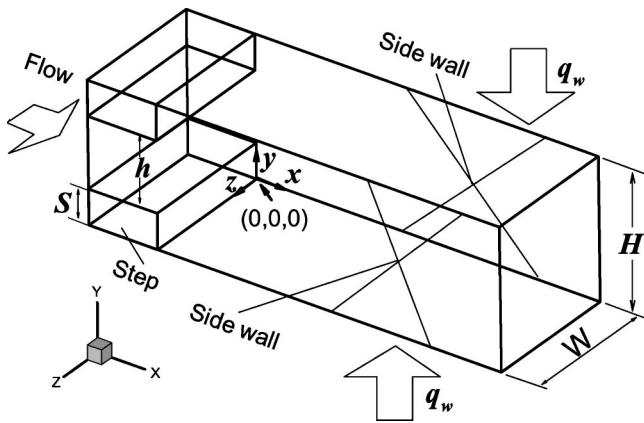


Fig. 1 Schematic of the computation domain

than 10^{-6} . All calculations were performed on Hewlett-Packard Visualize B1000 workstations. One iteration required approximately 168 s when the total number of grid points was about 5.8×10^5 .

Results and Discussions

Simulations of the flow and thermal fields were performed for the Reynolds numbers of 50, 100, and 150. These Reynolds numbers are smaller than the critical value for flow bifurcation in this geometry [6,9,10]. Simulated distributions of velocity components

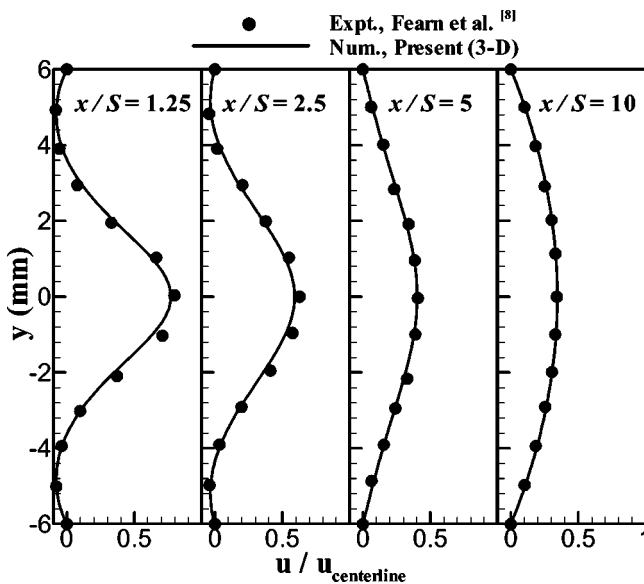


Fig. 2 Comparison with the measured results of Fearn et al. [8] (u -velocity distribution, at different streamwise locations on the plane of symmetry at $Re=26$)

Table 1 Velocities and temperatures at $x/S=10$, $y/S=1$, and $z/L=0.5$ for different computational grids ($Re=150$)

Grid	$x \times y \times z$ Grid size	u (m/s)	T ($^{\circ}C$)	x_u/S $z/L=1$ and $y/S=0.01$
1	$90 \times 20 \times 20$	0.0375781	20.8691	3.604308
2	$100 \times 26 \times 26$	0.0364984	20.9106	3.747488
3	$120 \times 36 \times 36$	0.0363543	20.9109	3.832524
4	$150 \times 46 \times 46$	0.0364438	20.9020	3.916536
5	$180 \times 56 \times 56$	0.0366213	20.8991	3.959706
6	$190 \times 56 \times 56$	0.0366294	20.8985	3.961865
7	$210 \times 76 \times 76$	0.0366651	20.8968	3.972831

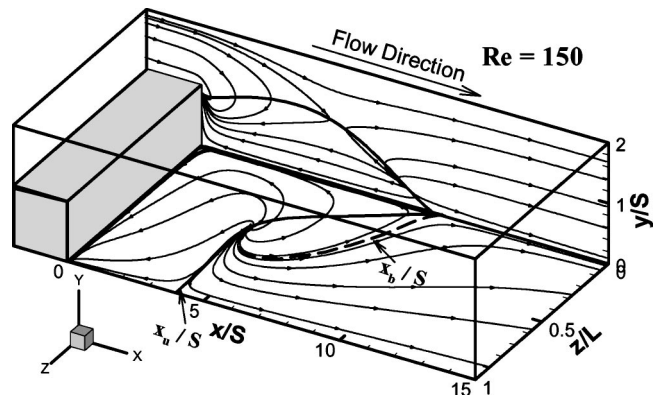


Fig. 3 Limiting streamlines on planes parallel to the stepped wall ($y/S=0.01$) and sidewall ($z/L=0.01$)

(u , v , and w) and temperature at selected planes downstream from the sudden expansion revealed that the flow and heat transfer is symmetric relative to the center planes of the duct [13].

The general flow features downstream from the sudden expansion were discussed in details in Ref. [13]; they consist of a downwash, which develops adjacent to the sidewall, that flows directly into the primary recirculation flow region in swirling motion while moving toward the center of the duct. A swirling "jetlike" flow also develops in the separating shear layer adjacent to the sidewall, and that flow impinges on the stepped wall at a distance of approximately $z/L=0.5$. A fraction of the impinging jetlike flow reverses its direction and moves upstream, both toward the sidewall and the center of the duct, into the primary recirculation flow region adjacent to the step and into the reverse flow region that develops adjacent to the sidewall. Limiting streamlines on a plane parallel to the stepped wall ($y/S=0.01$) and to the sidewall ($z/L=0.01$), which are shown in Fig. 3, illustrate some of this behavior. The limiting streamlines on a plane parallel to the stepped wall ($y/S=0.01$) are used to identify the outer boundary of the primary recirculation flow region (x_b line). This boundary line, (x_b line), is determined by the criterion that streamlines on both sides of this boundary line move in opposite directions: streamlines upstream from this line flow upstream toward the step, and streamlines downstream from this line flow downstream and away from the step. The "sourcelike" point that appears on the stepped wall ($y/S=0.01$) is the impingement location of the jetlike flow. At this singular point, both the streamwise component ($\mu \partial u / \partial y|_{y=0}$) and the spanwise component ($\mu \partial w / \partial y|_{y=0}$) of the wall shear stress are zero. Some of the rebounded streamlines, after the jetlike impingement, move first downstream and later reverse their direction upstream while moving toward the sidewall, and in that process a reverse flow region develops adjacent to the sidewall. The size (length in the streamwise direction) of the reverse flow region adjacent to both the sidewall and the stepped wall increases with increasing Reynolds numbers. Distribution of the x_u line [a line identifying the locations where the streamwise component of the wall shear stress ($\mu \partial u / \partial y|_{y=0} = 0$) is zero at the stepped wall] is presented also in this figure. This definition is commonly used to define reattachment length in 2D separated-reattached flow in this geometry. The spanwise distribution of that line is relatively uniform at the center region of the duct ($0.5 < z/L < 1.0$), and then it increases almost linearly to its maximum value at the sidewall. The outer boundary of the primary recirculation region (x_b line) is different from the x_u line, the bold solid line in Fig. 3 where the streamwise component of the wall shear stress is zero on the stepped wall for three-dimensional flow (especially near the sidewall), but they are identical to each other for two-dimensional flow (i.e., at the center of a duct with large aspect ratio).

The results in Fig. 4 map the distributions of various parameters

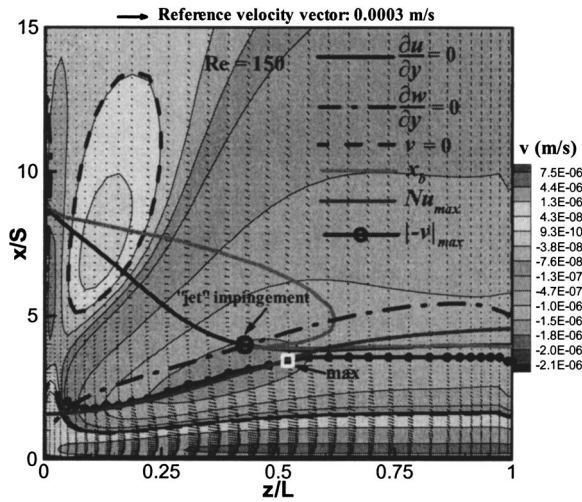


Fig. 4 Velocity field on a plane parallel to the stepped wall ($y/S=0.01$)

on a plane parallel to the stepped wall ($y/S=0.01$). The color in that figure designates the value of the mean transverse velocity component (v) on that plane. Regions with positive and negative mean transverse velocity components can be easily identified in that figure. Lines identifying the locations where a) the mean transverse velocity component is zero ($v=0$); b) the gradient of the mean streamwise velocity component is zero ($\partial u/\partial y|_{y=0}=0$, the x_u line); c) the gradient of the mean spanwise velocity component is zero ($\partial w/\partial y|_{y=0}=0$, the x_w line); d) the Nusselt number is a maximum; e) the negative transverse velocity $-v$ is a maximum; and f) the outer edge of the primary recirculation region (x_b line) are shown in this figure. A line identifying the locations where the wall shear stress is a minimum is also presented in this figure, but that line is almost identical to the x_u line because the magnitude of $(\partial w/\partial y)^2$ is much smaller than that of $(\partial u/\partial y)^2$ in that region. The location where the jetlike flow impinges on the stepped wall and the location where the Nusselt number is a maximum are also identified in this figure. The location of the maximum Nusselt number is upstream from the jetlike impingement location, inside the primary recirculation flow region. The significant spanwise flow that develops in the impingement region influences the wall heat transfer and causes the maximum Nusselt number to develop away from the jet impingement region. It is interesting to note that the line for the maximum transverse velocity on that plane is the closest one to the line locating the maximum Nusselt number. The significant spanwise flow inside the primary recirculation flow region can be seen clearly in that figure. The two lines that have been identified in this figure (the x_u line and the x_b line) do not identify the location of reattachment region near the sidewall for this three-dimensional flow. This conclusion is reached from the fact that a region in Fig. 4 near the sidewall ($z/L < 0.2$) has a positive mean transverse velocity component v (i.e., fluid is moving away from the stepped wall rather than toward it). Hence, the segments of the x_u line and the x_b line that are inside this region are not part of the reattachment line/region. Part of the boundary of the primary recirculation region (x_b line) that is downstream from the x_u line develops from the rebound of the jetlike flow impingement, and that fluid ends up reversing its direction and flowing upstream toward the step. The swirling, spanwise, and jetlike flows that develop in this geometry adjacent to the stepped wall make it very difficult to identify, numerically and/or experimentally, a reattachment line/region that can be used for code and/or apparatus validation. However, any one of the lines that have been identified in this figure can be located by using simulated flow and thermal fields and, in principle, can also be measured. Any one of these lines can be used

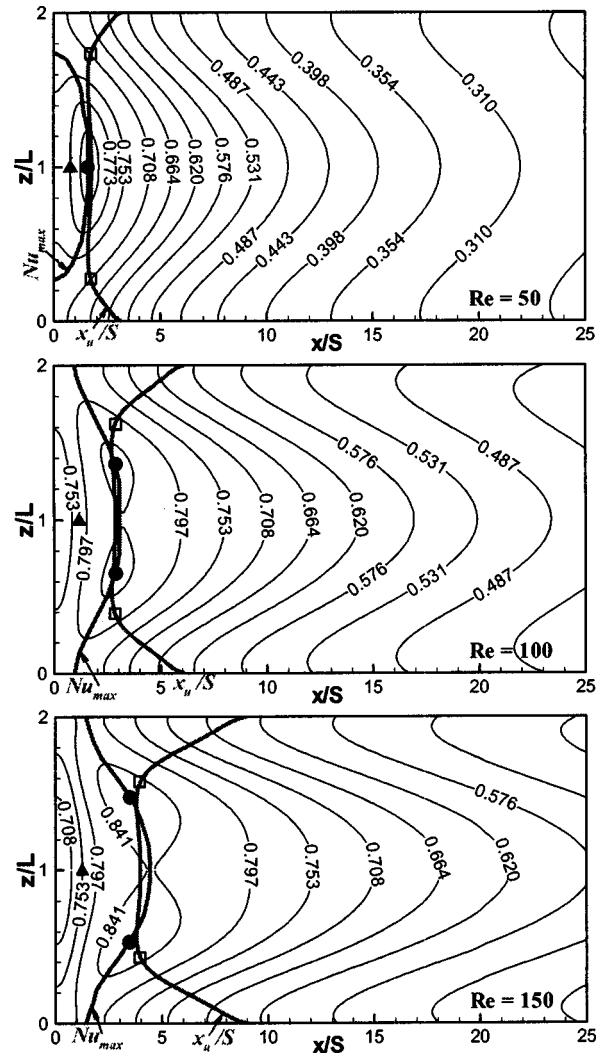


Fig. 5 Distribution of the Nusselt number on the stepped wall (\square jet-impingement, \bullet maximum Nusselt number, \blacktriangle maximum friction coefficient)

for code and/or apparatus validation. The easiest one of these to measure, however, is the location where the gradient of the mean streamwise velocity component is zero ($\partial u/\partial y|_{y=0}=0$) and for that reason it is recommended for use in benchmark studies for this geometry.

The distribution of the Nusselt number ($Nu = q_w S/k(T_w - T_0)$, where T_w is wall temperature) on the stepped wall is shown in Fig. 5. Locations of the maximum Nusselt number Nu_{max} , impingement location of the jetlike flow and the location where the wall shear stress is a maximum are identified in this figure. The spanwise distribution of the line that locates where the Nusselt number is a maximum and the x_u line are also shown in this figure. The x_u line moves further downstream as the Reynolds number increases, and its maximum appears at the sidewalls ($z/L=0$ and 2.0). Similarly the Nu_{max} line moves further downstream from the step and its maximum value moves closer to the sidewalls as the Reynolds number increases. The magnitudes of the maximum Nusselt number for the cases of $Re=50, 100,$ and 150 , are $0.787, 0.837,$ and 0.859 , respectively. Similarly the distributions of the friction coefficient [$C_f = 2\tau_w/\rho u_0^2$, where $\tau_w = \mu\sqrt{(\partial u/\partial y)^2 + (\partial w/\partial y)^2}$] on the stepped wall are shown in Fig. 6. The friction coefficient on the stepped wall develops a maximum at the center width of the duct inside the primary recirculation flow region, and its magnitude decreases to a minimum at the

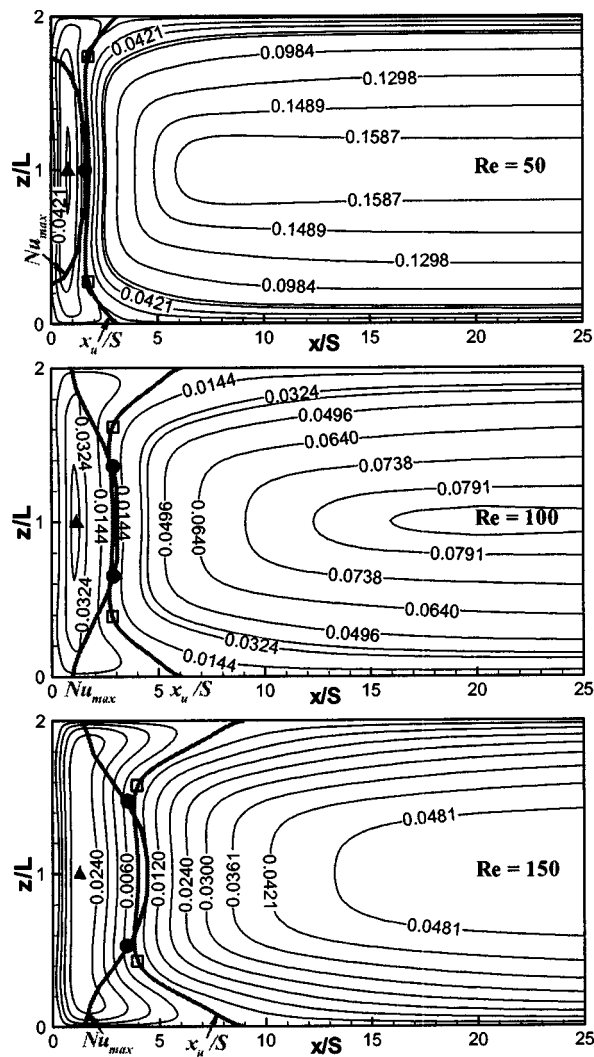


Fig. 6 Distribution of the friction coefficient on the stepped wall (\square jet-impingement, \bullet maximum Nusselt number, \blacktriangle maximum friction coefficient)

reattachment region. Its magnitude then increases gradually as the distance from the step increases in the redeveloping flow region with a maximum developing at the center width of the duct. The x_u line moves further downstream from the step as the Reynolds number increases, but its spanwise distribution does not exhibit the minimum near the sidewall that has been observed for a single backward-facing step flow geometry [2].

Conclusions

Simulations of three-dimensional laminar forced convection in plane symmetric sudden expansion in rectangular duct with an expansion ratio of 2 and an aspect ratio of 4 are presented for Reynolds numbers of 50, 100, and 150. For this Reynolds number range, the flow is steady and symmetric relative to the center

width of the duct. The fluid that is attaching to and/or flowing adjacent to the stepped wall originates at the inlet section from a very narrow region that is adjacent to the sidewall. A swirling jetlike flow develops in the separating shear layer, and a reverse flow region develops near the sidewall. The spanwise distributions of the lines locating the positions where the streamwise wall shear stress is zero (x_u line) are relatively uniform (flat) near the center width of the duct but increase, almost linearly, as they approach the sidewall. The x_u line moves further downstream as the Reynolds number increases, and its maximum appears at the sidewalls. The maximum Nusselt number is located inside the primary recirculation flow region and that location does not coincide with the impingement location of the jetlike flow. Similarly, the Nu_{max} line moves further closer to the sidewalls as the Reynolds number increases. The line locating the outer edge of the primary recirculation flow region is different from the line locating the positions where the streamwise component of the wall shear stress is zero near the sidewall, and neither one of these lines represent the reattachment locations in that region. The strong transverse flow that develops adjacent to the stepped wall makes it very difficult to identify from either simulations and/or measurements the locations of the reattachment region in this geometry.

Acknowledgment

This work was supported in part by a DOE-Basic Energy Sciences Grant No. DE-FG02-03ER46067.

References

- [1] Armaly, B. F., Durst, F., Pereira, J. C. F., and Schonung, B., 1983, "Experimental and Theoretical Investigation of Backward-Facing Step Flow," *J. Fluid Mech.*, **127**, pp. 473–496.
- [2] Nie, J. H., and Armaly, B. F., 2003, "Reattachment of Three-Dimensional Flow Adjacent to Backward-Facing Step," *ASME J. Heat Transfer*, **125**, pp. 422–428.
- [3] Goldstein, R. J., Eriksen, V. L., Olson, R. M., and Eckert, E. R. G., 1970, "Laminar Separation, Reattachment, and Transition of the Flow over Downstream-Facing Step," *ASME J. Heat Transfer*, **92**, pp. 732–741.
- [4] Baughn, J. W., Hoffman, M. A., Takahashi, R. K., and Launder, B. E., 1984, "Local Heat Transfer Downstream of an Abrupt Expansion in a Circular Channel With Constant Wall Heat Flux," *ASME J. Heat Transfer*, **106**, pp. 789–796.
- [5] Durst, F., Melling, A., and Whitelaw, J. H., 1974, "Low Reynolds Number Flow Over a Plane Symmetrical Sudden Expansion," *J. Fluid Mech.*, **64**, pp. 111–128.
- [6] Durst, F., Pereira, J. C. F., and Tropea, C., 1993, "Plane Symmetric Sudden-Expansion Flow at Low Reynolds numbers," *J. Fluid Mech.*, **248**, pp. 567–581.
- [7] Sobey, I. J., and Drazin, P. G., 1986, "Bifurcations of Two-Dimensional Channel Flows," *J. Fluid Mech.*, **171**, pp. 263–287.
- [8] Fearn, R. M., Mullin, T., and Cliffe, K. A., 1990, "Nonlinear Flow Phenomena in a Symmetric Sudden Expansion," *J. Fluid Mech.*, **211**, pp. 595–608.
- [9] Patel, S., and Drikakis, D., 2003, "Numerical Effects on the Prediction of Flow instabilities in Channels With Sudden-Expansion," *Proc. of IMECE'03, ASME-IMECE2003-55616*, CD-ROM, ASME, New York.
- [10] Cherdron, W., Durst, F., and Whitelaw, J. H., 1978, "Asymmetric Flows and Instabilities in Symmetric Ducts with Sudden Expansion," *J. Fluid Mech.*, **84**, pp. 13–31.
- [11] Chiang, T. P., Sheu, T. W. H., and Wang, S. K., 2000, "Side Wall Effects on the Structure of Laminar Flow Over a Plane-Symmetric Sudden Expansion," *Comput. Fluids*, **29**, pp. 467–492.
- [12] Shah, R. K., and London, A. L., 1978, *Laminar Forced Convection in Ducts*, Academic Press, New York.
- [13] Nie, J. H., and Armaly, B. F., 2003, "Three-Dimensional Forced Convection Flow in Plane Symmetric Sudden Expansion," *Proceedings of IMECE'03, ASME-IMECE2003-41428*, CD-ROM, ASME, New York.

The Nonlinear Increase of Nusselt Number With Friction Factor in Fully Developed Laminar Duct Flow

E. Van den Bulck

e-mail: eric.vandenbulck@mech.kuleuven.ac.be

Department of Mechanical Engineering, Katholieke Universiteit Leuven, Celestijnenlaan 300A, B-3001 Heverlee, Belgium

This paper deals with heat transfer in fully developed laminar flow in cylindrical ducts. For this type of flow, the product of friction factor with Reynolds number $f Re$ and the Nusselt number are both constants. It is known that the Nusselt number increases with the shift of boundary condition from constant wall temperature to constant heat flux. Also, the ratio of the Nusselt number to $f Re$ increases when the convexity of the duct is reduced, e.g., a cylinder visavis parallel plates. This paper gives a simple physical explanation for these two phenomena.

[DOI: 10.1115/1.1800511]

Introduction

Many graduate level textbooks discuss the pressure drop and heat transfer for fully developed laminar flow in cylindrical ducts. The books by Kays and Crawford [1] and Bejan [2] give the analytical solutions for circular tubes. The reference book by Kakaç et al. [3] provides full solutions for a large number of different channel cross sections. Table 1 shows representative data for selected geometries that are taken from Kays and London [4]. The analytical and numerical solutions show that, e.g., for a round tube, the Nusselt numbers for the boundary conditions of constant wall temperature (Nu_T) and constant heat flux (Nu_Q) are, respectively, 3.66 and 4.36. For other cross sections, the ratio of both Nusselt numbers varies from 0.78 to 0.92. More remarkable is the variation of the ratio $Nu/(f Re)$ with geometry, where f is the Fanning friction factor and Re is the Reynolds number. With Nu taken for the constant heat flux boundary condition, the ratio $Nu/(f Re)$ varies from 0.23 for triangular ducts to 0.34 for parallel plates. This shift in value for the $Nu/(f Re)$ -ratio with geometry is not without significance as many heat exchangers use elliptical or flat tubes to transfer heat at a reduced pressure drop when compared to round tubes. These facts have been known for a long time and are reported in most heat transfer text books [1–5]. Bejan [2] discusses the applicability of the concept of hydraulic diameter for laminar flow. However, the physical explanation of the variation of the Nusselt number with thermal boundary conditions and the nonlinear increase of Nu with $f Re$ is generally absent. Only Kays and Crawford [1] give a physical explanation for the increase of Nu with the shift of constant temperature to constant heat flux boundary. The following paragraph provides an explanation based upon a simple boundary layer type analysis. The mathematics are such that the analysis could be incorporated in intermediate level heat transfer text books.

Problem Statement

Consider a cylindrical duct with cross section A_c and an internal wall area A which is uniformly distributed along its length L . This duct has a hydraulic diameter given by $D_h = 4A_c/L$. Let x measure the distance along the cylinder axis and y en z are rect-

angular coordinates normal to the surface. Let u represent the axial velocity. The heat transfer is modeled with the transport equation for energy in terms of the fluid temperature T

$$k \left[\frac{\partial^2 T}{\partial y^2} + \frac{\partial^2 T}{\partial z^2} \right] = \rho u c \frac{\partial T}{\partial x} \quad (1)$$

For constant fluid properties, the mean velocity and temperature are defined as

$$u_m = \frac{1}{A_c} \int_{A_c} u \, dy \, dz \quad T_m = \frac{1}{u_m A_c} \int_{A_c} u T \, dy \, dz \quad (2)$$

The cross-sectional averaged energy equation for the duct can be written as

$$\rho u_m c \frac{dT_m}{dx} = \frac{A}{L A_c} h (T_w - T_m) = 4 Nu \frac{k}{D_h^2} (T_w - T_m) \quad (3)$$

where the Nusselt number is introduced as $h D_h / k$. The temperature distribution is written in terms of a dimensionless function ϕ

$$T(x, y, z) = T_w(x, y, z) - (T_w(x, y, z) - T_m(x)) \phi(y/D_h, z/D_h) \quad (4)$$

This function is subject to two boundary conditions

$$\phi|_{\text{wall}} = 0 \quad \text{and} \quad \frac{1}{u_m A_c} \int_{A_c} u \phi \, dy \, dz = 1 \quad (5)$$

Using this function ϕ , the axial derivative of the temperature can be written as

$$\text{constant wall temperature:} \quad \frac{\partial T}{\partial x} = \phi \frac{dT_m}{dx} \quad (6)$$

$$\text{constant wall flux:} \quad \frac{\partial T}{\partial x} = \frac{dT_m}{dx}$$

This last equation is valid because, for laminar flow, the heat transfer coefficient is constant and thus, for a constant heat flux, $T_w - T_m$ is constant.

Boundary Layer Approach

Consider a small region of the duct near the wall. Redefine y to be the local ordinate normal to the wall and directed inward. Define a dimensionless variable η

$$\eta = \frac{y}{D_h} \quad (7)$$

Near the wall, the local temperature distribution can be rewritten in terms of η as

$$T(x, \eta) = T_w - (T_w - T_m(x)) \phi(\eta) \quad \text{with} \quad \phi(0) = 0 \quad (8)$$

Using Eqs. (3) in combination with (6), the transport equation (1) can be written in terms ϕ and η as

$$\frac{d^2 \phi}{d\eta^2} = -4 Nu \frac{u}{u_m} \phi^n \quad (9)$$

where $n=0$ for a constant heat flux boundary and $n=1$ for a constant wall temperature boundary. Near the wall, the velocity can be approximated with a linear profile

$$u = \eta \left. \frac{du}{d\eta} \right|_{\eta=0} \quad (10)$$

where the gradient of the velocity can be found from the definition equation for the friction factor f

$$\mu \left. \frac{du}{dy} \right|_{y=0} = f \frac{\rho u_m^2}{2} \Rightarrow \frac{du}{d\eta} = \frac{f Re}{2} u_m \quad (11)$$

Contributed by the Heat Transfer Division for publication in the JOURNAL OF HEAT TRANSFER. Manuscript received by the Heat Transfer Division March 18, 2004; revision received August 4, 2004. Editor: V. Dhir.

Table 1 Friction factor and Nusselt number for fully developed laminar flow in ducts of various cross-sections

Geometry	$f Re$	Nu_r	Nu_Q	$Nu_Q/f Re$
triangular	13.33	2.47	3.11	0.233
square	14.2	2.98	3.81	0.268
circular	16	3.66	4.384	0.274
rectangular ⁽¹⁾	18.3	4.44	5.33	0.291
rectangular ⁽²⁾	20.6	5.60	6.49	0.315
parallel plates	24	7.54	8.235	0.343

⁽¹⁾aspect ratio 4.

⁽²⁾aspect ratio 8.

The transport equation near the wall (9) can finally be written as

$$\frac{d^2\phi}{d\eta^2} = -2Nu(f Re)\phi^n \eta = -2C\eta \quad \text{with } C = Nu(f Re)\phi^n \quad (12)$$

where the variable C represents the local curvature of the temperature profile ϕ with η . C is proportional to the rate of change in the axial direction of the thermal energy carried by the fluid layers that are adjacent to the wall. To fully appreciate this form of the transport equation, the integral boundary condition of Eq. (5) has to be considered.

Figure 1 shows representative qualitative profiles of $\phi(\eta)$ with the variable C as a parameter. The transport equation tells that the gradient of the cross-wise temperature distribution is maximal at the wall and, as C increases, this gradient decreases faster in the direction of η normal to the wall. Together with the integral boundary condition, i.e., the overall energy balance, this faster decrease has the effect of steepening the temperature distribution near the wall, as indicated in the figure. The Nusselt number is linked to the gradient of the temperature profile at the wall. From the definition of the heat transfer coefficient, it follows that:

$$q = h(T_w - T_m) = k \frac{\partial T}{\partial y} \Rightarrow Nu = \left. \frac{d\phi}{d\eta} \right|_{\eta=0} \quad (13)$$

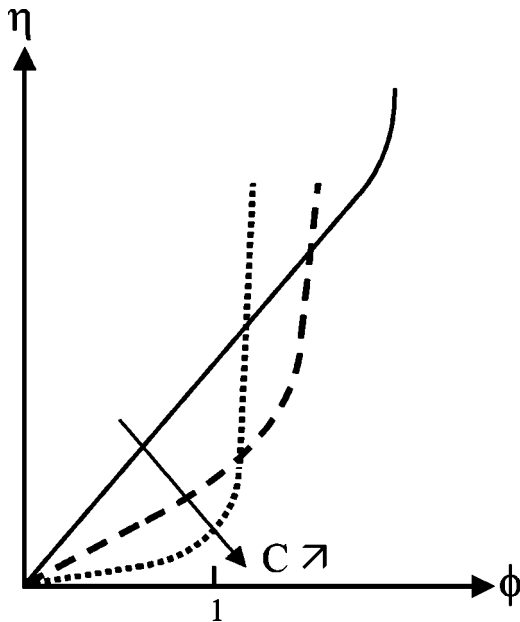


Fig. 1 Change of temperature profile as a function of the distance normal to the wall with the curvature C

As C increases, so does the Nusselt number because of the steepening.

Factors that affect the magnitude of the curvature C are:

1. The thermal boundary condition. Because $\phi=0$ at the wall, $\phi < 1$ near the wall. For $n=1$, this reduces the variable C and thus reduces the gradient at the wall. For $n=0$, the value of ϕ has no effect. Physically, this is explained as follows. With the constant wall temperature boundary condition, the axial rate of change of the thermal energy of the fluid layers adjacent to the wall is smaller than that of the mean flow, and therefore the heat transfer from the wall that is needed to accommodate this axial variation is small. With the constant heat flux boundary condition, this axial rate of change is equal to the rate of change of the mean flow, and therefore the heat transfer is larger.
2. The product $f Re$. As the cross-sectional shape of the duct varies, so does the $f Re$ -value. Compare for instance a circular duct that is deformed into a flat duct. Due to this change of cross section, the product $f Re$ will increase and consequently the variable C will increase and thus the rate of curvature of ϕ will increase. Physically, this means that as $f Re$ increases, the axial rate of change of the energy of the fluid layers adjacent to the wall is increased due to an increase in mass flux. The heat transfer from the wall to accommodate this axial rate of change must therefore increase as well. As a result, the Nusselt number will increase.
3. The Nusselt number. An increase of $f Re$ due to a change in cross section of the duct will increase the curvature of the temperature profile. As consequently the temperature gradient at the wall increases, so does the Nusselt number, which in turn increases the curvature C even more. There exists a sort of cumulative effect. As the heat transfer from the wall increases due to a higher wall shear, the axial rate of change of the energy of the fluid layers adjacent to the wall increases. This increase will lead to a steepening of the temperature profile, which, in turn, increases the heat transfer even more. This cumulative effect explains why the Nusselt number increases more than linear with $f Re$, and thus explains why the factor $Nu/(f Re)$ increases with $f Re$.

Conclusions

The change of Nusselt number with the product $f Re$ and the type of boundary condition is explained with a simple boundary layer approach to the transport equation of energy. It is shown that the Nusselt number increases with the curvature of the cross-wise temperature distribution because the integral energy equation acts a constraint on the overall shape of the temperature profile. It can be easily shown that the boundary condition of constant wall temperature reduces the curvature whereas the constant heat flux boundary condition doesn't. This explains why the Nusselt number changes with the shift in boundary condition. The curvature of the temperature profile is proportional to the velocity gradient, which is characterized by $f Re$, and is proportional to the Nusselt number itself. It is this feedback that explains why the Nusselt number increases more than linear with $f Re$.

Nomenclature

- A_c = cross-sectional area
- A = tube inner wall area
- c = specific heat
- C = curvature parameter
- D_h = hydraulic diameter
- f = Fanning friction factor
- h = heat transfer coefficient
- k = thermal conductivity
- L = axial flow length
- n = boundary type index
- Nu = Nusselt number

Re = Reynolds number
 T = temperature
 u = fluid axial velocity
 x = cartesian ordinate along the cylinder axis
 y = cartesian ordinate normal to the cylinder wall
 z = cartesian ordinate normal to x - y plane
 η = dimensionless distance normal to the wall
 ϕ = dimensionless temperature profile
 ρ = fluid density
 $()_m$ = cross-sectional mean
 $()_w$ = wall

References

- [1] Kays, W. M., and Crawford, M. E., 1980, *Convective Heat and Mass Transfer*, 2nd ed. McGraw-Hill Book Company, New York, Chap. 6.
- [2] Bejan, A., 1984, *Convection Heat Transfer*, John Wiley & Sons, New York, Chap. 3.
- [3] Kakaç, S., Shah, R. K., and Aung, W., 1987, *Handbook of Single-Phase Convective Heat Transfer*, John Wiley & Sons, New York, Chap. 3.
- [4] Kays, W. M., and London, A. L., 1984, *Compact Heat Exchangers*, 3rd ed., Chap. 6, Fig. 6.
- [5] Incropera, F. P., and De Witt, D. P., *Fundamentals of Heat and Mass Transfer*, 3rd ed., Chap. 8.

Convection Velocity of Temperature Fluctuations in a Turbulent Flume

G. Hetsroni

Department of Mechanical Engineering, Technion—Israel Institute of Technology, 3200 Haifa, Israel

I. Tiselj and R. Bergant

“Jožef Stefan” Institute, Jamova 39, 1000 Ljubljana, Slovenia

A. Mosyak and E. Pogrebnyak

Department of Mechanical Engineering, Technion—Israel Institute of Technology, 3200 Haifa, Israel

A numerical investigation of the temperature field in a turbulent flume is presented. We consider the effect of the Prandtl number on the convection velocity of temperature fluctuations in a turbulent boundary layer, and focus also on the effect of the Prandtl number on the connection between the velocity and the temperature fluctuations. Close to the wall, $y^+ < 2$, convection velocities of the temperature fluctuations decrease with an increase in the Prandtl number, i.e., the scale dependence becomes significantly important. In the region $y^+ < 2$ the relation of the convection velocity of the temperature fluctuation to that of the velocity fluctuation may be expressed as $U_{cT}^+ = U_{cu}^+ Pr^{-1/3}$ and $U_{cq}^+ = U_{cu}^+ Pr^{-1/2}$ for isothermal and isoflux wall boundary condition, respectively. [DOI: 10.1115/1.1797032]

Keywords: Heat Transfer, Temperature, Turbulent

1 Introduction

Turbulent thermal or concentration boundary layer evolving on a flat plate has been one of the most important problems in turbulent heat transfer research. In the problem of heat transfer by fluid flow, the Prandtl number can range from the order of unity for gas to hundreds and thousands for oil. In the problem of mass transfer, the Schmidt number can range from unity for gaseous substances in air, to hundreds for salinity in water, and to thousands for color dyes in water. In the case of heat transfer at low and moderate Prandtl (Schmidt) numbers, a significant temperature (concentration) gradient exists not only in the diffusive sublayer but also in the region outside the sublayer. High Prandtl number heat transfer is of special importance in the understanding scalar transfer controlled by turbulent motions very close to the wall.

Mass transfer through the solid boundary of a turbulent channel flow was analyzed by Calmet and Magnaudet [1] using large-eddy simulation (LES) for Schmidt numbers $Sc=1, 100,$ and 200 . The study confirmed the conclusion that high Schmidt-number mass transfer at a solid wall is governed by the large-scale structures observed in planes parallel to the wall in the viscous sublayer. LES of turbulent channel flow for the Schmidt number from 0.1 up to 200 has been performed by Dong et al. [2] to investigate the effect of the Schmidt number on the turbulence behavior. The behavior of the mean and fluctuating concentrations and turbulent mass flux was discussed.

The numerical calculation, can reasonably predict the fluctuating quantities, the correlation's of the fluctuations, and the structures of the scalar field. Yeung et al. [3] used the DNS to study the mass diffusion with Sc up to 4 . Similar studies on passive heat transfer with the Prandtl number $Pr < 10$ were reported by Na et al. [4], Kawamura et al. [5], Lyons et al. [6]. Scalar transport from sources at the wall of a turbulent channel for medium and high Prandtl number fluids was studied by Papavassiliou [7].

Direct numerical simulations of turbulent thermal boundary layers, at $Pr=0.7$, developing on a flat plate with isothermal and isoflux wall boundary conditions were carried out by Kong et al. [8]. It was shown that the behavior of the turbulent wall-normal heat flux is similar to that of the Reynolds shear stress, indicating close correlation between the streamwise velocity and temperature fluctuations. Turbulent temperature boundary layers at $Pr=0.7$ and $Pr=5.4$ have been considered by Tiselj et al. [9] to show how the change in the Prandtl number and in the thermal boundary conditions affects the dissimilarity between the momentum and scalar transport. Na and Hanratty [10] conducted DNS study of passive scalar transport in the immediate vicinity of a wall. The Schmidt number was varied from 1 to 10 . An increase in the Schmidt number was associated with a marked decrease in the frequency of the mass transfer fluctuations. Although the investigation was conducted in an Eulerian frame, the authors proposed that in the region very close to the wall the fluctuations of turbulent scalar field might be connected to convection velocity of near-wall coherent structures.

In many problems of scalar transfer, the dominant mechanism is advective transport in turbulent boundary layer. In these situations it is particularly useful to adopt a Lagrangian viewpoint, with an observer following the motion of the fluid. Lagrangian quantities from numerical simulations, reported in the literature include, for example, the propagation velocity of perturbations in turbulent channel flow Kim and Hussain [11], the structure of turbulent boundary layers, Krogstad and Antonia [12], tracking of coherent thermal structures on a heated wall, Kowalewski et al. [13].

The idea that coherent structures of the temperature field are convected downstream by the mean flow at an average velocity is a useful one in the study of heat-transfer mechanism. That means that the time variations of the temperature field observed at a fixed point in the flow would be approximately the same as those due to convection of an unchanging spatial pattern past the point with the mean convection velocity. Convection velocity depends on the Prandtl number, but the relationship is not presented in the literature.

In the present study we consider the effect of Prandtl number on the convection velocity of temperature fluctuations in a turbulent boundary layer and focus also on the effect of Prandtl number on the connection between the velocity and temperature fluctuations. Apart from fundamental understanding we also aim at providing information on the effect of the thermal wall boundary condition on turbulent scalar field.

2 Numerical Procedure

Infinite flume geometry, Tiselj et al. [9], was used for numerical simulations of turbulent heat transfer. The flow above the infinite heated bottom wall is driven by a constant pressure gradient, whereas the top surface is free. Simulations assume a section of the flow far from inlet, where a steady mean velocity profile is established. Mean wall temperature is increasing linearly in the streamwise direction, however, the mean temperature difference between the wall and bulk of the fluid does not depend on the streamwise coordinate in the simulated domain. These assumptions on the physical model allow implementation of periodic boundary conditions in streamwise and spanwise directions after the constant pressure and temperature gradients are appropriately treated.

With assumptions above the dimensionless Navier-Stokes and energy equations are normalized by the flume height h , the friction

Contributed by the Heat Transfer Division for publication in the JOURNAL OF HEAT TRANSFER. Manuscript received by the Heat Transfer Division October 28, 2003; revision received June 30, 2004. Associate Editor: S. P. Vanka.

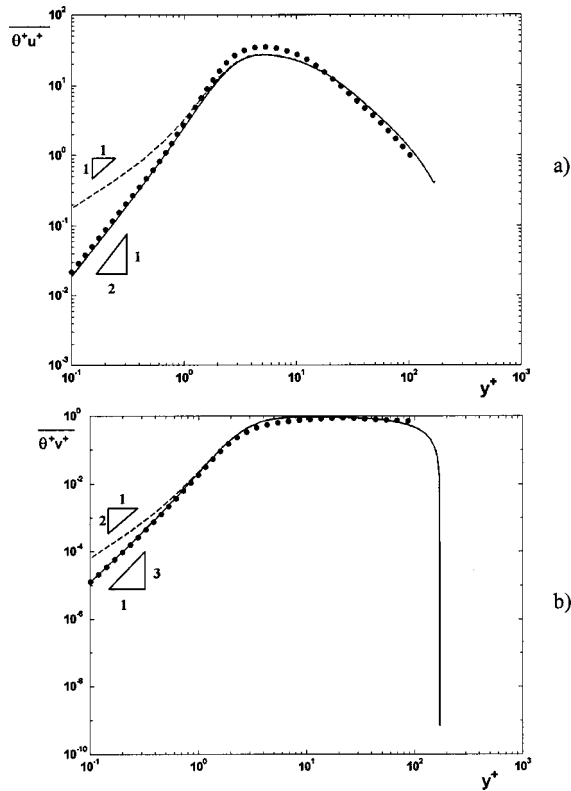


Fig. 1 Turbulent heat flux. $Pr=54$. (a) streamwise heat flux $\overline{\theta^+ u^+}$; and (b) wall-normal heat flux $\overline{\theta^+ v^+}$ (— $T_w = \text{const}$, Dong et al. [2] - - - $q = \text{const}$, Dong et al. [2]).

velocity $u_\tau = \sqrt{\tau_w/\rho}$, and the friction temperature $T_\tau = q_w/(u_\tau \rho c_p)$, the shear stress is defined as $\tau_w = -\mu(du/dy)_w$, q_w is the constant mean wall heat flux, ρ is the density, c_p is the specific heat, μ is the dynamic viscosity, such scaling can be found in the papers of Kasagi [14] or Kawamura [5]. Then the nondimensional equations are given as

$$\nabla \cdot \mathbf{u}^+ = 0 \quad (1)$$

$$\frac{\partial \mathbf{u}^+}{\partial t} = -\nabla \cdot (\mathbf{u}^+ \mathbf{u}^+) + \frac{1}{Re_\tau} \nabla^2 \mathbf{u}^+ - \nabla p + \mathbf{I}_x \quad (2)$$

$$\frac{\partial \theta^+}{\partial t} = -\nabla \cdot (\mathbf{u}^+ \theta^+) + \frac{1}{Re_\tau Pr} \nabla^2 \theta^+ + \frac{u_x^+}{u_B^+} \quad (3)$$

The term \mathbf{I}_x (unit vector in streamwise direction) in Eq. (2) comes from the constant pressure gradient that drives the flow and p represents only the fluctuating part of the pressure. The term u_x^+/u_B^+ in energy Eq. (3) is a compensating term that takes into account linear increase of the mean temperature in the streamwise direction, with instantaneous streamwise component of the velocity u_x^+ , and the mean bulk velocity u_B^+ . Pr is the Prandtl number, $Re_\tau = u_\tau h/\nu$ is the friction Reynolds number.

Dimensionless wall temperature difference is defined as $\theta^+(x, y, z, t) = [\langle T_w \rangle - T(x, y, z, t)]/T_\tau$, with $\langle T_w \rangle$ temperature of the wall averaged over the time, $T(x, y, z, t)$ is the fluid temperature, x, y, z are coordinates in the streamwise, wall-normal and spanwise direction, respectively.

Boundary conditions for the velocity components on the top free surface, parallel to the wall are $du/dz=0$ and $dw/dz=0$, while the wall-normal velocity is $v_{\text{free surface}}=0$. It should be noted that velocity boundary condition at the free surface does not take into account the surface waves. Experiments by Hetsroni et al. [15] and DNS simulations of Lam and Banerjee [16] showed that

this is very close to the reality at low Froude numbers, where surface waves are negligible. No-slip boundary condition is applied at the interface of the wall and the fluid.

Beside velocity boundary conditions, two different thermal boundary conditions were considered at the wall-fluid interface. The first was the isothermal boundary condition (denoted as H1 wall boundary condition):

$$\theta^+(\bar{y} = -1) = 0 \quad (4)$$

and the second was the isoflux boundary condition for dimensionless temperature difference θ (H2 wall boundary condition) with fixed mean wall temperature:

$$\langle \theta^+ \rangle_{x,z,t}(\bar{y} = -1) = 0 \quad (5)$$

and boundary condition for the fluctuation part of temperature θ

$$\frac{d\theta}{dy}(\bar{y} = -1) = Re_\tau Pr \quad (6)$$

where $\bar{y} = y/h$.

Details on both types of boundary conditions and their application can be found in Kong et al. [8] and Tiselj et al. [9].

The free surface was treated as an adiabatic surface: $d\theta^+/dy^+ = 0$ and periodic boundary conditions in the streamwise x and spanwise z -directions were applied for the velocity and temperature fields.

As can be seen from Eqs. (1)–(3), the temperature is assumed to be a passive scalar. Results of the present study consider the systems, where the temperature differences are not too large, while some caution is required for the systems, where the temperature differences are not negligible. Such assumption was used by Kasagi et al. [14], Kawamura et al. [5] and Tiselj et al. [9].

The equations were solved with pseudo-spectral scheme using uniform grid of collocation points and Fourier series in x and z -directions. Chebyshev polynomials are used in the wall-normal direction y , with cosine distribution of the collocation points $y_j = \cos(\pi(j-1)/(N_y-1))$, $j=1, N_y$ that are refined near the wall and the free surface. Numerical procedure and the code of Gavrilakis et al. [17] modified by Lam and Banerjee [16] was used to solve the continuity and momentum equations. The code was later upgraded with energy equation (Tiselj et al. [9]). For the present study, the code was modified with subroutines for calculation of the convection velocities; this modification did not significantly enlarge the CPU time consumption but increased the required physical memory of the computer, as several instantaneous fields were kept in the memory.

In the present study calculations were carried out for $Re_\tau = 171$ in the computational box of $2148 \times 171 \times 537$ wall units (in the x, y and z -direction, respectively). Three different grids $128 \times 65 \times 64$, $200 \times 129 \times 128$, and $256 \times 129 \times 128$, were used for the Prandtl numbers $Pr=1$, $Pr=5.4$, and $Pr=54$, respectively.

The time step for the $Pr=1$ simulation was $0.05124 \nu/u_\tau^2$ and time step of other two runs was $0.02562 \nu/u_\tau^2$. The turbulence characteristics were calculated as an average over time intervals 5124 and 2562 ν/u_τ^2 at $Pr=1$ and $Pr>1$, respectively. It took a longer time interval to obtain statistical steady-state solutions at $Pr=54$ than at $Pr=5.4$ and $Pr=1$. This can be explained by the lower convection velocities in the high Prandtl number turbulent flow (see section on results and discussion).

The resolution for $Pr=1$ and $Pr=5.4$ runs was fine enough to describe both cases as ‘‘Direct Numerical Simulations’’, i.e., all spatial and temporal scales were resolved in these cases (see [5,9,14] for details on the appropriate resolution at given Pr number). The resolution of the third run at $Pr=54$ was sufficient for DNS of the velocity field, but insufficient for the DNS of the thermal field. Numerical simulation of turbulent heat transfer at high Prandtl numbers requires higher resolution due to the smallest temperature scales that are inversely proportional to \sqrt{Pr} . In numerical simulations the velocity field and temperature field at

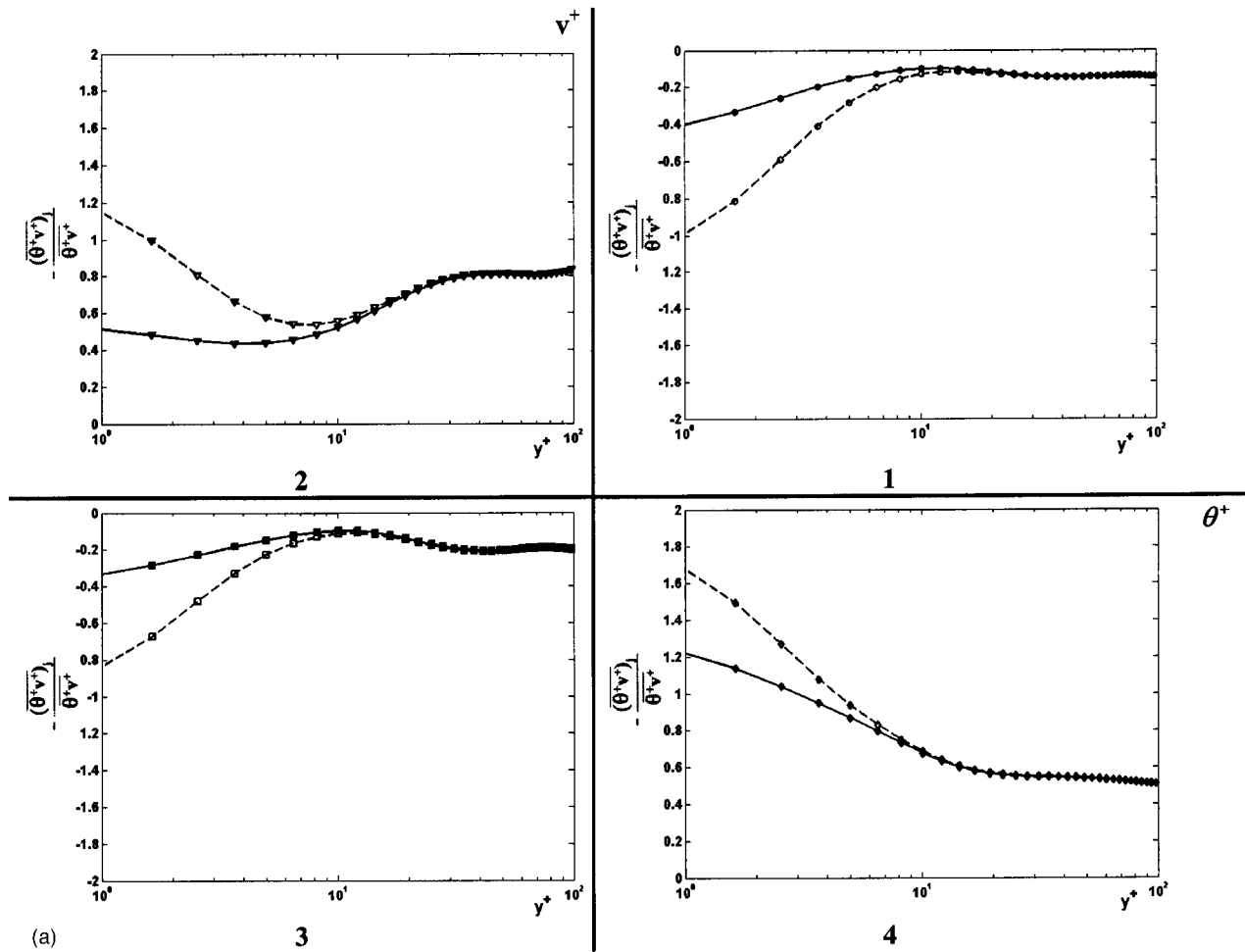


Fig. 2 Fractional contribution of the wall-normal heat flux from each quadrant, $-\overline{(\theta^+ u^+)_j} / \overline{\theta^+ u^+}$: (a) Pr=1, and (b) Pr=54 (solid lines, closed symbols—isothermal wall boundary condition (H1), dashed lines, open symbols—isoflux wall boundary condition (H2))

Pr=1 and Pr=5.4 were described by the accuracy of DNS, and no models for “turbulent viscosity” were needed. The simulation at Pr=54 was performed with DNS resolution for the velocity field and with under-resolved DNS for the temperature field. Such approach is not as accurate as DNS but was found to be very accurate in the study performed at Pr=5.4 by Bergant et al. [18], where DNS results at Pr=5.4 were compared with results of velocity DNS and temperature under-resolved DNS.

The space-time correlations were used to determine convection velocities. In the present work the convection velocity was determined as $U^+ = \Delta x_{\max}^+ / \Delta t^+$. Here, Δx_{\max}^+ is the streamwise separation for which the space-time correlation coefficient is maximum for given time delay Δt^+ . It should be noted that convection velocity derived from this assumption implies a frozen convected pattern. We assumed that the change in the turbulence thermal field between two calculated points is statistically independent of instantaneous temperature fluctuation at the first point. Time delay for the temperature field was chosen according to the Prandtl number. According to Kim and Hussain [11] for convection velocity of the velocity fluctuations the time delay $\Delta t^+ = 18$ was used. This value was also chosen to calculate convection velocity of temperature fluctuation for Pr=1. For the computation of the propagation velocity of the temperature fluctuation for Pr=5.4 and Pr=54 we have used $\Delta t^+ = 10.248$.

3 Results

Turbulent Heat Flux. Figures 1(a,b) show the turbulent streamwise, $\overline{\theta^+ u^+}$, and wall-normal, $\overline{\theta^+ v^+}$, heat flux for Pr=54, respectively. For Pr=54 our calculation of streamwise and wall-normal heat flux agree well with the result of Dong et al. [2] for Sc=50. The data shown in Figs. 1(a,b) were compared with the results of turbulent heat flux for Pr=1 and Pr=5.4 presented by Tiselj et al. [9]. For both streamwise, and wall-normal, turbulent heat fluxes with H1 and H2 wall boundary conditions, the peak value shifts to lower values of y^+ with increasing Prandtl number.

The fluctuating components of the turbulent heat flux are quite different for H1 and H2 thermal wall boundary condition. It may be seen from Figs. 1(a,b) that close to the wall the turbulent streamwise and spanwise heat flux under the isothermal wall boundary condition H1 may be expressed in the following form (Monin and Yaglom) [19]:

$$\overline{\theta^+ u^+} \propto y^{+2} \quad (7)$$

$$\overline{\theta^+ v^+} \propto y^{+3} \quad (8)$$

The isoflux turbulent heat flux H2 may be expressed as Kong et al. [8]:

$$\overline{\theta^+ u^+} \propto y^+ \quad (9)$$

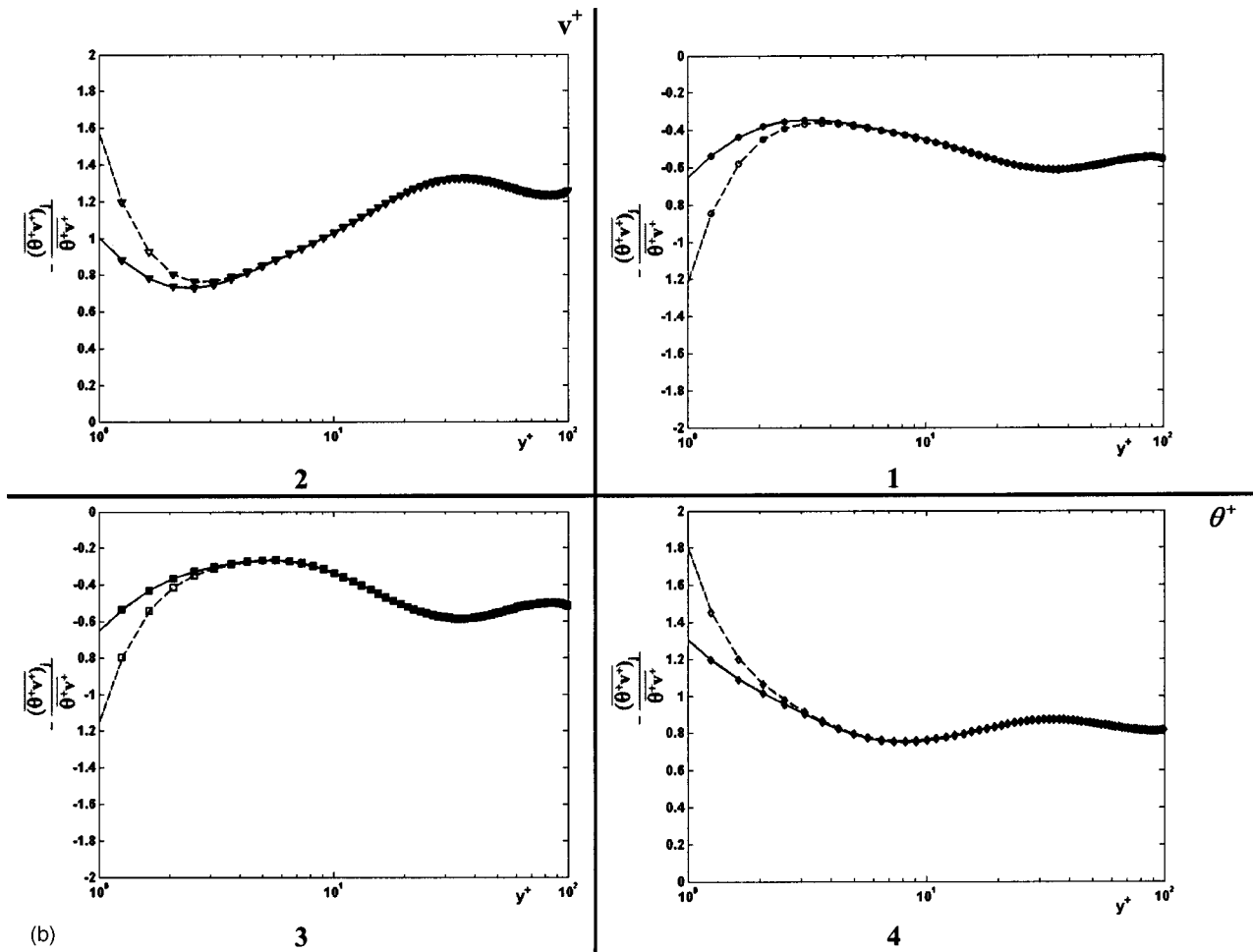


Fig. 2 (continued)

$$\overline{\theta^+ v^+} \propto y^{+2} \quad (10)$$

Quadrant Analysis. Depending on the signs of the fluctuations the instantaneous values of $-(\theta^+ v^+)_j$ get to one of the four quadrants, j , on the planes $-(\theta^+ v^+)_j / (\overline{\theta^+ v^+})$ versus y^+ . Some of these quadrants characterize the seemingly ordered heat transfer in the flow. So quadrant 1 contains values of product $(\theta^+ v^+)$ characterizing the motion of decelerated, and, therefore, hotter liquid from the wall. Quadrant 3 contains the product $(\theta^+ v^+)$ characterizing the inrushes of cold high momentum fluid to the wall. A quadrant analysis was performed to investigate the coherence between the velocity and temperature fluctuations. Figures 2(a,b) show the fractional contributions, $-(\theta^+ v^+)_j / (\overline{\theta^+ v^+})$, from four quadrants to the total wall-normal heat flux. For $Pr=1$ the results agree well with those reported by Kong et al. [8]. In the range of Prandtl number from 1 to 54 the events in the first quadrant ($v^+ > 0, \theta^+ > 0$) and third quadrant ($v^+ < 0, \theta^+ < 0$) are dominant away from the wall. The events in the second quadrant ($v^+ > 0, \theta^+ < 0$) and in the fourth quadrant ($v^+ < 0, \theta^+ > 0$) are dominant near the wall. For $Pr=1$ and $y^+ > 15$, the profiles of the fractional contribution for the isothermal wall are almost the same as for isoflux wall. The location at which the fractional contributions are the same at isothermal and isoflux boundary condition is about $y^+ = 5$ for $Pr=54$. Close to the wall the peak of wall-normal heat flux takes place in the events of velocity and temperature fluctuations have different signs (quadrants 2 and 4). In the proximity of the wall the maximum values of wall-normal heat flux are due to “ordered” heat transfer mechanisms. It includes the motion

of decelerated (and therefore more heated) liquid from the wall into the main flow and inrushes of the liquid with a higher velocity (cooler) to the wall.

Convection Velocities in a Turbulent Boundary Layer. The convection velocities of temperature fluctuations along the channel, U_{cT}^+ , and U_{cq}^+ , are shown in Figs. 3(a–c) for two thermal boundary conditions: isothermal wall, H1, and isoflux wall, H2, with Prandtl number 1, 5.4 and 54, respectively. For comparison, the streamwise component of the convection velocity of the velocity perturbation, U_{cu}^+ , is plotted. The results of behavior of U_{cu}^+ agree quantitatively quite well with data obtained by Kim and Hussain [11]. Figure 3(a) shows that for $Pr=1$ in the outer region of the boundary layer, $y^+ > 15$, the convection velocities of the velocity and the temperature perturbation are about the same and increase with an increase in y^+ . Near the wall, however, all convection velocities do not change at $y^+ < 1$. In Fig. 3(a) we may see that in this region the convection velocity for isothermal wall, U_{cT}^+ , is approximately 10.2, i.e., very close to the convection velocity of the velocity perturbation, U_{cu}^+ . For isoflux wall U_{cq}^+ is about 8.1, which is well below U_{cu}^+ . Figures 3(b) and 3(c) show convection velocities for $Pr=5.4$ and $Pr=54$, respectively. For $Pr=5.4$ the results agree well with those found by Kowalewski et al. [13]. Figures 3(a–c) indicate that in the range $Pr=1–54$ the convection velocity $U_{cT}^+ > U_{cq}^+$. Close to the wall both convection velocities decrease with an increase in the Prandtl number, i.e. scale dependence becomes significantly important. It appears rea-

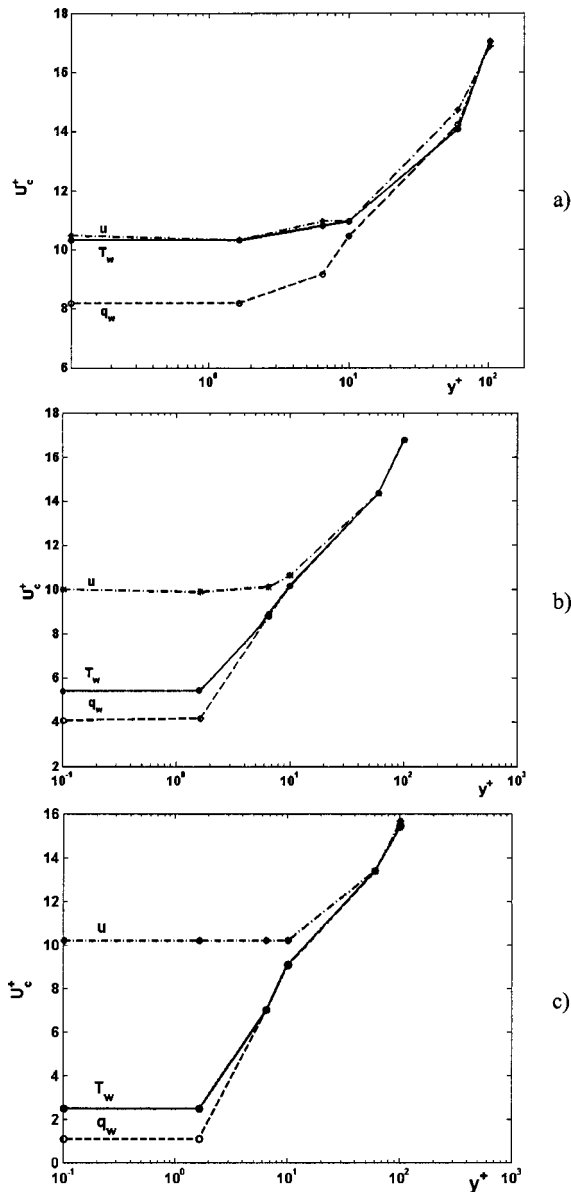


Fig. 3 Convection velocities of the streamwise component of velocity fluctuation, u , convection velocities of temperature fluctuation at isothermal wall boundary condition, T_w , and convection velocities of temperature fluctuation at isoflux wall boundary condition, q_w : (a) $Pr=1$, (b) $Pr=5.4$, and (c) $Pr=54$

reasonable to assume that this scale dependence is responsible for turbulent thermal diffusivity, turbulent Prandtl number and turbulent heat flux.

The thickness of the layer at which the convection velocities for both isothermal and isoflux BC are nearly constant, does not depend on the Prandtl number ($y^+ \approx 2$). This implies that it is not useful to connect a particular type of structure to the length of the region with a constant convection velocity. As the structure evolves and increases in size, it picks up momentum from the large-scale motion. Hence, in the outer layer the average convection velocity of the temperature fluctuations tends toward that of the velocity fluctuations. Figure 4 shows the dependence of U_{cT}^+/U_{cu}^+ and U_{cq}^+/U_{cu}^+ on the Prandtl number in the region $y^+ < 2$. The data may be expressed in the following form:

$$U_{cT}^+ = U_{cu}^+ / Pr^{1/3} \quad (11)$$

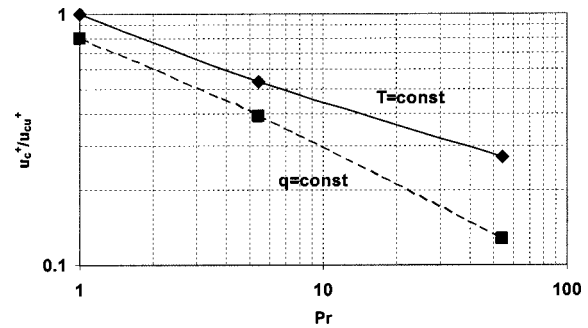


Fig. 4 Dependence of convection velocities of temperature fluctuation on Prandtl number

$$U_{cq}^+ = U_{cu}^+ / Pr^{1/2} \quad (12)$$

4 Conclusions

The distance of the near-wall region, y_{lim}^+ , at which the coefficient of turbulent thermal diffusivity for the isothermal and isoflux BC is proportional to y^{+3} and y^{+2} , respectively, depends on the Prandtl number. At a given Prandtl number the distance of y_{lim}^+ for isoflux wall boundary condition is shorter than that for isothermal BC. For isothermal as well as for isoflux wall boundary condition the value of y_{lim}^+ decreases with an increase in the Prandtl number from $Pr=1$ to $Pr=54$.

Close to the wall, $y^+ < 2$, both convection velocities at isothermal, H1 and isoflux, H2, wall boundary conditions decrease with an increase in the Prandtl number, i.e., scale dependence becomes significantly important. It appears reasonable to assume that this scale dependence is responsible for turbulent eddy conductivity and the statistics of the temperature fields.

The thickness of the turbulent layer $y^+ < 2$, at which the convection velocities for both isothermal and isoflux wall boundary condition are nearly constant, does not depend on the Prandtl number. This implies that it is not useful to connect a particular type of structure to the distance with a constant convection velocity. As the structure evolves and increases in size, it picks up momentum from the large-scale motion. Hence, in the outer layer, the average convection velocity of the temperature fluctuations tends toward that of velocity fluctuations. In the region $y^+ < 2$ the relation of convection velocity of temperature fluctuation to that of velocity fluctuation may be expressed as $U_{cT}^+ = U_{cu}^+ / Pr^{1/3}$ and $U_{cq}^+ = U_{cu}^+ / Pr^{1/2}$ for isothermal and isoflux wall boundary condition, respectively.

Acknowledgments

This research was supported by the Fund for Promotion of Research at the Technion. A. Mosyak was supported by a joint grant from the Committee for Planning and Budgeting of the Council for Higher Education under the framework of the KAMEA PROGRAM, and E. Pogrebnjak was supported by the Center for Absorption in Science, Ministry of Immigrant Absorption State of Israel. I. Tiselj and R. Bergant were supported by Ministry of Science and Technology, Republic of Slovenia.

Nomenclature

Pr	= Prandtl number
$Re_{\tau} = u_{\tau} h / \nu$	= Reynolds number
$T_{\tau} = q_w / u_{\tau} \rho c_p$	= friction temperature
c_p	= specific heat
h	= height of the flume
q_w	= heat flux
p	= pressure
t	= time

u, v, w = streamwise, wall normal and spanwise velocity fluctuations, respectively
 u_τ = friction velocity
 x, y, z = coordinate in the streamwise, wall normal and spanwise direction, respectively

Greek Symbols

τ = shear stress
 ρ = density
 μ = dynamic viscosity
 ν = kinematic viscosity
 θ = temperature fluctuations

Subscripts

cu = convection velocity of velocity fluctuations
 cq = convection velocity of temperature fluctuations at q_w
 = const
 cT = convection velocity of temperature fluctuations at T_w
 = const
 w = wall
 τ = shear

Superscripts

– = average
 + = nondimensional

References

- [1] Calmet, I., and Magnaudet, J., 1997, "Large-Eddy Simulation of High Schmidt Number Mass Transfer in a Turbulent Channel Flow," *Phys. Fluids*, **9**(2), pp. 438–455.
- [2] Dong, Y. H., Lu, X. Y., and Zhuang, L. X., 2003, "Large Eddy Simulation of Turbulent Channel Flow With Mass Transfer at High Schmidt Numbers," *Int. J. Heat Mass Transfer*, **46**, pp. 1529–1539.
- [3] Yeung, P. K., Sykes, M. C., and Vedula, P., 2000, "Direct Numerical Simulation of Differential Diffusion With Schmidt Numbers up to 4.0," *Phys. Fluids*, **12**, pp. 1601–1604.
- [4] Na, Y., Papavassiliou, D. V., and Hanratty, T. J., 1999, "Use of Direct Numerical Simulation to Study the Effect of Prandtl Number on Temperature Field," *Int. J. Heat Fluid Flow*, **20**, pp. 187–195.
- [5] Kawamura, H., Abe, Y., and Matsuo, Y., 1999, "DNS of Turbulent Heat Transfer With Respect to Reynolds and Prandtl Number Effects," *Int. J. Heat Fluid Flow*, **20**, pp. 196–207.
- [6] Lyons, S. I., Hanratty, T. J., and McLaughlin, J. B., 1991, "Direct Numerical Simulation of Passive Heat Transfer in Turbulent Channel Flow," *Int. J. Heat Mass Transfer*, **34**, pp. 1149–1161.
- [7] Papavassiliou, D. V., 2002, "Scalar Dispersion From an Instantaneous Line Source at the Wall of a Turbulent Channel for Medium and High Prandtl Number Fluids," *Int. J. Heat Fluid Flow*, **23**, pp. 161–172.
- [8] Kong, H., Choi, H., and Lee, J. S., 2000, "Direct Numerical Simulation of Turbulent Thermal Boundary Layers," *Phys. Fluids*, **12**, pp. 1–14.
- [9] Tiselj, I., Pogrebnyak, E., Li, C., Mosyak, A., and Hetsroni, G., 2001, "Effect of Wall Boundary Condition on Scalar Transfer in a Fully Developed Turbulent Flume," *Phys. Fluids*, **13**, pp. 1028–1039.
- [10] Na, Y., and Hanratty, T. J., 2000, "Limiting Behavior of Turbulent Scalar Transport Close to a Wall," *Int. J. Heat Mass Transfer*, **43**, pp. 1749–1758.
- [11] Kim, J., and Hussain, F., 1993, "Propagation Velocity of Perturbations in Turbulent Channel Flow," *Phys. Fluids*, **5**, pp. 695–706.
- [12] Krogstad, P. A., and Antonia, R. A., 1994, "Structure of Turbulent Boundary Layers on Smooth and Rough Walls," *J. Fluid Mech.*, **277**, pp. 1–21.
- [13] Kowalewski, T. A., Mosyak, A., and Hetsroni, G., 2003, "Tracking of Coherent Thermal Structures on a Heated Wall 2. DNS Simulation," *Exp. Fluids*, **34**, pp. 390–396.
- [14] Kasagi, N., Tomita, Y., and Kuroda, A., 1992, "Direct Numerical Simulations of Passive Scalar Field in Turbulent Channel Flow," *Trans. ASME Ser. C: J. Heat Transfer*, **114**, pp. 598–606.
- [15] Hetsroni, G., Zakin, J. L., and Mosyak, A., 1997, "Low Speed Streaks in Drag-Reduced Turbulent Flow," *Phys. Fluids*, **9**, p. 2397.
- [16] Lam, K. L., and Banerjee, S., 1988, "Investigation of Turbulent Flow Bounded by a Wall and Free Surface," *Fundamentals of Gas-Liquid Flows*, **72**, pp. 29–38.
- [17] Gavrilakis, S., Tsai, H. M., Voke, P. R., and Leslie, D. C., 1986, "Direct and Large Eddy Simulation of Turbulence," *Notes on Numerical Fluid Mechanics*, **15**, Vieweg, Braunschweig, D.B.R., p. 105.
- [18] Bergant, R., Tiselj, I., and Hetsroni, G., 2001, "Resolution Requirements for Turbulent Flume Heat Transfer DNS at Prandtl Number 5.4," *ASME International Mechanical Engineering Congress and Exposition, IMECE 1*, ASME, New York.
- [19] Monin, A. S., and Yaglom, A. M., 1971, *Statistical Fluid Mechanics*, **1**, MIT, Cambridge, MA.

An Experimental Correlation for Combined Convection and Radiation Between Parallel Vertical Plates

A. S. Krishnan

Research Scholar

C. Balaji

Associate Professor

S. P. Venkateshan¹

Professor

Heat Transfer and Thermal Power Laboratory,

Department of Mechanical Engineering,

Indian Institute of Technology Madras,

Chennai, India

e-mail: spv@iitm.ac.in

Results of an experimental study of natural convection and surface radiation between three parallel vertical plates, symmetrically spaced, with air as the intervening medium are presented. The analysis consists of heating the central plate at different levels and recording the temperatures of both the central and the side plates at steady state conditions. Based on the measurements, a correlation for the maximum temperature excess of the "hot" plate in terms of the emissivity of the central and the side plates, the aspect ratio, and the dimensionless total heat flux is given, valid for a range of emissivity $0.05 \leq \epsilon_c, \epsilon_s \leq 0.85$, aspect ratio $2.38 \leq A \leq 17$, and total heat flux $32 \leq q \leq 1590 \text{ W/m}^2$. Through this, the heat transfer enhancement due to radiation has been succinctly brought out. [DOI: 10.1115/1.1795245]

Keywords: Multi-Mode Heat Transfer, Vertical Plates

Introduction

Natural convection in parallel plate channels occurs in applications such as cooling of electronic equipment and fin-tube baseboard heaters, transformers, and power supplies, with the constraints normally being the space and the temperature, for a given heat duty. The usefulness can be attributed to the simplicity, zero maintenance, and reliability. In most cases, such systems can be approximated to be symmetrically or asymmetrically heated with an isoflux or isothermal boundary together with an adiabatic boundary condition for the adjacent plate. Even so, such an approximation yields results that are accurate within the limits of acceptability from an engineering standpoint.

The classical problem of free convection between vertical flat surfaces has been a field of interest since the 1940s when Elenbaas [1] reported experimental and theoretical analysis on natural convection between isothermal parallel plates and presented an optimization based on maximum heat transfer rate for different plate dimensions, spacing between the plates and the inclination angle. Following him many researchers [2–6] have done experimental and theoretical studies for a wide range of parameters and presented relevant correlations. Experimental and analytical stud-

ies on the optimization of the spacing between two vertical flat plates subjected to free convection cooling also did attract attention of heat transfer researchers [7–12].

However, results pertaining to analysis comprising of combined free convection and surface radiation are relatively new but for Carpenter et al. [13] who presented results of numerical study of this problem. The conjugate nature of such problems was dealt in depth in experimental investigations by Rammohan Rao and Venkateshan [14] for fins and fin assembly and by Balaji and Venkateshan [15], who presented numerical results for open cavities.

From the review of the pertinent literature presented above, it can be inferred that studies of natural convection in the vertical channel geometry has received considerable attention. In spite of this, there exists scope for further investigation of heat transfer characteristics for this kind of geometry. As in most of the experimental studies on natural convection heat transfer between vertical parallel plates, radiation effects have been either nullified by techniques such as mass transfer measurement or accounted for as stray losses. The significance of radiation and its interaction with natural convection has not been brought out. In addition, an expression for the maximum temperature of the plate dissipating heat, as a function of pertinent quantities, is not available.

In this paper, an attempt has been made to develop a correlation for the maximum temperature excess of the hot plate in terms of the total heat flux, the aspect ratio, and the emissivity of the central and the side plates, all in dimensionless form. This has been done for the case of symmetrically spaced and asymmetrically heated vertical parallel plates, cooled by surface radiation and free convection, in ambient air.

Experimental Methodology

The experimental arrangement has been dealt with in detail in Ref. [16]. However, for the sake of completeness a brief description of the same is given. Figure 1 shows a schematic of the end view of the experimental apparatus. It comprises three vertical parallel plates, a central plate, which is heated by a stabilized alternating current power input, and two side plates, one on each side spaced symmetrically on each side of the central plate. The emissivity of the central and the side plates are varied by polishing or having a coat of paint. The side plates are insulated at the back using a nonrubberized cork of thickness 1 in. to simulate adiabatic conditions. The side plates being adiabatic give the most conservative estimate of the heat transfer from the system, as it gives the "worst-case scenario" for the maximum temperature. The emissivity is estimated by the method described in Ref. [17]. The power input to the central plate, the spacing and in turn the aspect ratio and the emissivities of the central and the side plates are the parameters. The range of parameters for which the measurements have been carried out are given in Table 1. The measurement of temperatures are done at steady-state conditions using calibrated "K" type thermocouples and recorded using a data acquisition system. The nondimensionalization of the required variables are done as follows:

$$q = Q/a, \quad (1)$$

$$q^* = Bq/k_f T_\infty, \quad (2)$$

$$A = B/S, \quad (3)$$

$$\theta_{\max} = \Delta T_{\max}/T_\infty. \quad (4)$$

Results and Discussion

For applications, where a given amount of heat needs to be dissipated for given geometrical dimensions, and the surface conditions, viz., the emissivities, although generally not considered, a correlation for the maximum temperature of the hot plate in terms of the relevant parameters would be of significant practical use. Such an attempt has been made. A correlation for the dimensionless maximum temperature excess of the hot plate, in terms of the

¹Author to whom correspondence should be addressed.

Contributed by the Heat Transfer Division for publication in the JOURNAL OF HEAT TRANSFER. Manuscript received by the Heat Transfer Division January 29, 2004; revision received March 17, 2004. Associate Editor: S. Thynell.

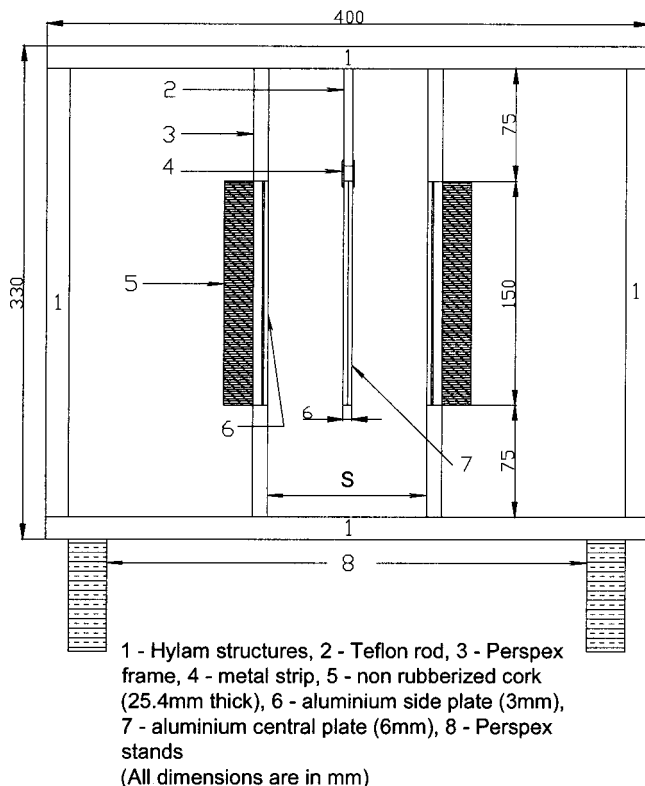


Fig. 1 End view of the experimental arrangement

total heat flux in nondimensional form, aspect ratio, and the emissivity of the central and the side plates has been developed and is as follows:

$$\theta_{\max} = 0.0343(1 + \varepsilon_c)^{-0.484}(1 + \varepsilon_s)^{-0.184} A^{0.08} q^*{}^{0.841} \quad (5)$$

The above equation is based on 308 data, and has a correlation coefficient of 0.998 and a rms error of 0.009. It is to be noted that the right-hand side of the Eq. (5) does contain the ambient temperature in an implicit manner in the dimensionless heat flux term. From Eq. (5), it is clear that the emissivity of the central plate has a stronger effect on θ_{\max} than the emissivity of the side plates, ε_s . Besides, as expected, θ_{\max} decreases with both ε_c and ε_s . The $(1 + \varepsilon)$ form is to take care of the pure natural convection asymptote to the problem, which anyway is very hard to realize. This is a consequence of the fact that emissivity is nonzero for any conceivable surface. θ_{\max} is also a strong, monotonic function of q^* , the exponent being close to unity. The aspect ratio has a finite but mild effect of increasing the θ_{\max} , suggesting that low aspect ratios are better.

Figure 2 shows the parity plot between the measured values and that obtained from the correlation and it may be seen that there is an excellent fit between the correlation and the data without any bias.

For an ideal case wherein the emissivities are forced to zero, the value of the dimensionless temperature excess of the hot plate will

Table 1 Range of parameters

Plate dimensions (all in mm)	250×150×3
Aspect ratio A	2.9–17.9
Channel spacing (mm)	8.5–52.2
Emissivity of central plate, ε_c	0.05–0.85
Emissivity of the side plates, ε_s	0.05–0.85
Prandtl number Pr	0.707
Dimensionless heat flux q^*	0.6–25.6

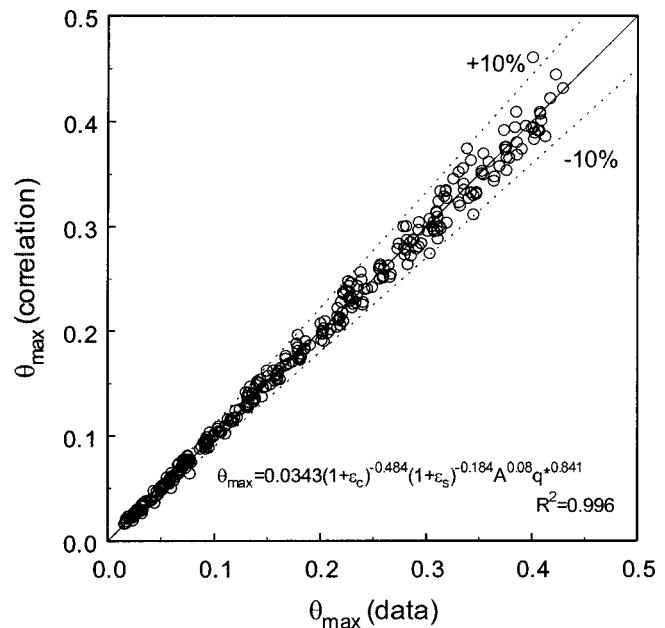


Fig. 2 Parity plot showing agreement of θ_{\max} obtained by correlation with those obtained by measurements

be more than what is given by Eq. (5). A parity plot of such a maximum and the measured values are shown in Fig. 3. This clearly establishes that the dimensionless temperature could be reduced by as much as 60% because of radiation heat transfer. An error analysis was carried out based on Doebelin [18] and the uncertainty in the estimation of the nondimensional temperature excess was found to be less than 1%.

Conclusions

An experimental study of free convection and surface radiation between vertical parallel plates with the central plate heated and the side plates unheated for symmetrical spacing has been presented. A correlation for the dimensionless maximum temperature

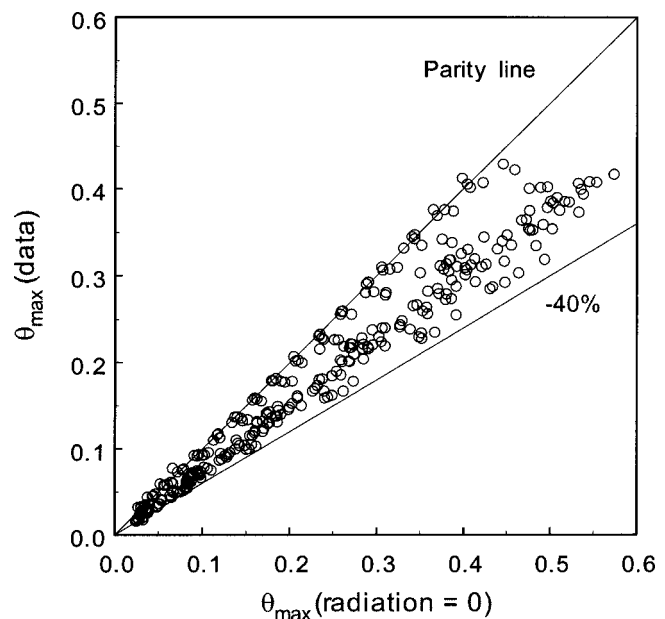


Fig. 3 Parity plot between measured θ_{\max} and θ_{\max} from correlation for $\varepsilon_c, \varepsilon_s = 0$

excess of the hot plate in terms of the emissivities, aspect ratio, and the dimensionless heat flux has been developed. This is expected to be useful from an engineering standpoint. The analysis has intentionally avoided the traditional nondimensional numbers and splitting up of the energy dissipated into convective and the radiative components and has instead set forth through an appropriate nondimensionalization, a result that could be readily used. The effect of radiation has been brought out through a novel plot, and it is seen that radiation reduces the nondimensional temperature excess of the hot plate by as much as 60%. In a typical case of $q = 0.5 \text{ kW/m}^2$, spacing between the plates $S = 0.04 \text{ m}$ and an ambient temperature $T_\infty = 303 \text{ K}$, the maximum temperature of the hot plate reduced from 374 K to 351 K, when the emissivity is increased from 0.05 to 0.85, symmetrically for both the central as well as the side plates, for a plate height of 0.15 m.

Nomenclature

- a = Total surface area of the central plate (m^2)
 A = Aspect ratio B/S
 B = Height of the plate (m)
 k_f = Thermal conductivity of the fluid (W/m K)
 L_c = Characteristic length (m)
 Q = Total heat to be dissipated (W)
 q = Total heat flux (W/m^2)
 q^* = Dimensionless total heat flux $q/(k_f T_\infty / B)$
 S = Spacing between the plates (m)
 $T_{h,\max}$ = Maximum temperature of the hot plate (K)
 T_∞ = Ambient temperature (K)
 ΔT_{\max} = Maximum temperature excess of the hot plate with respect to ambient, $T_{h,\max} - T_\infty$ (K)
 ε_c = Total hemispherical emissivity of the central plate
 ε_s = Total hemispherical emissivity of the side plates
 σ = Stefan-Boltzmann constant, $5.67 \times 10^{-8} \text{ W/m}^2 \text{ K}^4$
 θ_{\max} = Dimensionless temperature excess of the hot plate, $\Delta T_{\max} / T_\infty$

References

- [1] Elenbaas, W., 1942, "Heat Dissipation of Parallel Plates by Free Convection," *Physica (Amsterdam)*, **9**, pp. 1–28.
- [2] Bodoia, J. R., and Osterle, J. F., 1962, "The Development of Free Convection Between Heated Vertical Plates," *ASME J. Heat Transfer*, **84**, pp. 40–44.
- [3] Aung, W., Fletcher, L. S., and Sernas, V., 1972, "Developing Laminar Free Convection Between Vertical Flat Plates With Asymmetric Heating," *Int. J. Heat Mass Transfer*, **15**, pp. 2293–2307.
- [4] Sparrow, E. M., and Bahrami, P. A., 1975, "Experiments on Natural Convection From Vertical Parallel Plates With Either Open or Closed Edges," *ASME J. Heat Transfer*, **102**, pp. 221–227.
- [5] Wirtz, R. A., and Stutzman, R. J., 1982, "Experiments on Free Convection Between Vertical Plates With Symmetric Heating," *ASME J. Heat Transfer*, **104**, pp. 501–507.
- [6] Sparrow, E. M., and Azevedo, L. F., 1985, "Vertical Channel Natural Convection Spanning Between the Fully-Developed Limit and the Single-Plate Boundary-Layer Limit," *Int. J. Heat Mass Transfer*, **28**, pp. 1847–1857.
- [7] Levy, E. K., 1971, "Optimum Plate Spacings for Laminar Free Convection Heat Transfer From Parallel Vertical Isothermal Flat Plates," *ASME J. Heat Transfer*, **93**, pp. 463–465.
- [8] Levy, E. K., Eichen, P. A., Cintani, W. R., and Shaw, R. R., 1975, "Optimum Plate Spacings for Vertical Isothermal Flat Plates: Experimental Verification," *ASME J. Heat Transfer*, **97**, pp. 474–476.
- [9] Bar-Cohen, A., and Rohsenow, W. M., 1984, "Thermally Optimum Spacing of Vertical, Natural Convection Cooled Parallel Plates," *ASME J. Heat Transfer*, **106**, pp. 116–123.
- [10] Bejan, A., 1995, *Convection Heat Transfer*, 2nd ed., Wiley, New York.
- [11] Morrone, B., Campo, A., and Manca, O., 1997, "Optimum Plate Separation in Vertical-Parallel Plate Channels for Natural Convective Flows Incorporation of Large Spaces at Channel Extremes," *Int. J. Heat Mass Transfer*, **40**, pp. 993–1000.
- [12] Bejan, A., 2000, *Shape and Structure, from Engineering to Nature*, Cambridge University Press, Cambridge, U.K.
- [13] Carpenter, J. R., Briggs, D. G., and Sernas, V., 1976, "Combined Radiation and Developing Laminar Free Convection Between Vertical Flat Plates With Asymmetric Heating," *ASME J. Heat Transfer*, **98**, pp. 95–100.
- [14] Rammohan Rao, V., and Venkateshan, S. P., 1992, "Experimental Study of Free Convection and Radiation in Horizontal Fin Arrays," *Int. J. Heat Mass Transfer*, **39**, pp. 779–789.
- [15] Balaji, C., and Venkateshan, S. P., 1994, "Interaction of Surface Radiation With Free Convection in an Open Cavity," *Int. J. Heat Fluid Flow*, **15**, pp. 317–324.
- [16] Krishnan, A. S., Premachandran, B., Balaji, C., and Venkateshan, S. P., "Combined Experimental and Numerical Approaches to Multi-Mode Heat Transfer in Vertical Parallel Plates," *Experimental Thermal Fluid Science* (to be published).
- [17] Krishnan, A. S., Balaji, C., and Venkateshan, S. P., 2003, "A Synergistic Approach to Parameter Estimation in Multi-Mode Heat Transfer," *Int. Commun. Heat Mass Transfer*, **30**, pp. 515–524.
- [18] Doebelin, E. O., 1990, *Measurements Systems—Application and Design*, 4th ed., McGraw-Hill International, Singapore.

Feasibility of High Speed Furnace Drawing of Optical Fibers

Xu Cheng

Yogesh Jaluria

Fellow ASME

e-mail: jaluria@jove.rutgers.edu

Department of Mechanical and Aerospace Engineering,
Rutgers, The State University of New Jersey,
Piscataway, NJ 08854

The domain of operating conditions, in which the optical fiber-drawing process is successful, is an important consideration. Such a domain is mainly determined by the stresses acting on the fiber and by the stability of the process. This paper considers an electrical resistance furnace for fiber drawing and examines conditions for process feasibility. In actual practice, it is known that only certain ranges of furnace temperature and draw speed lead to successful fiber drawing. The results obtained here show that the length of the heated zone and the furnace temperature distribution are other important parameters that can be varied to obtain a feasible process. Physical behavior close to the boundary of the feasible domain is also studied. It is found that the iterative scheme for neck-down profile determination diverges rapidly when the draw temperature is lower than that at the acceptable domain boundary due to the lack of material flow. However, the divergence rate becomes much smaller as the temperature is brought close to the domain boundary. Additional information on the profile determination as one approaches the acceptable region is obtained. It is found that it is computationally expensive and time-consuming to locate the exact boundary of the feasible drawing domain. From the results obtained, along with practical considerations of material rupture, defect concentration, and flow instability, an optimum design of a fiber-drawing system can be obtained for the best fiber quality. [DOI: 10.1115/1.1795246]

Introduction

One of the most widely used methods to draw optical fibers involves continuously feeding a specially fabricated silica glass preform into a cylindrical heating furnace, heating the glass above its softening point of around 1900 K, and pulling it into a fiber of diameter around 125 μm [1]. As the preform proceeds through the heating zone, it narrows down sharply and yields the "neck-down" region, as shown in Fig. 1. The neck-down profile strongly depends on the fiber-drawing conditions and significantly impacts the diameter uniformity, strength, and transmission loss of optical fibers [2,3].

The domain of operating conditions, in which a successful fiber drawing is obtained, is important from both practical and basic considerations. This domain is largely determined by stresses, which may rupture the fiber, and by the stability of the process [2,4]. This paper presents an analytical and numerical study to investigate the feasible domain in a fiber-drawing system. A cylindrical resistance graphite furnace, containing a low-speed aiding argon flow, is chosen. The inert gas flow in the furnace cavity keeps the graphite heating element from oxidation. Transport in the glass and the inert gas, considering a free surface boundary for

the glass, is studied. Thus, a complex thermal analysis, involving conduction, convection, and radiation heat transfer, is necessary to simulate this process. The transport in the two regions is solved to obtain the temperature, velocity, tension, and defect distribution in the glass. The zonal method is used to model the radiative heat transfer in the glass, using the available radiative properties of glass [5–7]. The neck-down profile of the preform is iteratively determined by a force balance at the free-surface interface. It has been seen in practical fiber drawing that only certain combinations of furnace temperature and draw speed result in feasible fiber drawing [8,9]. The length of the heated zone can also be varied to obtain a feasible process. Thus, a feasible or acceptable design of a fiber-drawing system can be determined from the numerical simulation of the process.

The complexity of the physical processes and the exponential variation of glass viscosity with temperature make it difficult to achieve iterative convergence. Thus, several improvements are necessary in existing numerical methods in order to investigate convergence and locate the boundary of the feasible drawing domain. Through numerical experiments, it is possible to determine the dominating factors that affect the feasibility of the process and that may lead to rupture of the fiber. The numerical results must also be considered in terms of the underlying physical mechanisms. All these considerations indicate the importance of investigating the phenomena close to the boundary of the feasible domain.

Analytical and Numerical Modeling

The transport phenomena in a cylindrical graphite furnace are investigated for high-speed optical fiber drawing. A conjugate problem involving the glass and the purge gases is considered. Laminar flow is assumed due to the high viscosity of glass and the typical low velocities of the gas flow. The transport in the two regions is coupled through the boundary conditions at the free surface. Thus, coupled conduction, convection, and radiation heat transfer mechanisms are involved in the analysis. Several earlier papers have presented the analysis and the numerical scheme [4–10] and only a few important aspects are included here for completeness. For further details, these references may be consulted.

The governing equations for axisymmetric conditions, developed in cylindrical coordinates for both the glass and the purge gas, are given as [8]

$$\frac{\partial v}{\partial z} + \frac{1}{r} \frac{\partial(ru)}{\partial r} = 0, \quad (1)$$

$$\frac{\partial v}{\partial t} + u \frac{\partial v}{\partial r} + v \frac{\partial v}{\partial z} = -\frac{1}{\rho} \frac{\partial p}{\partial z} + \frac{1}{r} \frac{\partial}{\partial r} \left[r v \left(\frac{\partial v}{\partial r} + \frac{\partial u}{\partial z} \right) \right] + 2 \frac{\partial}{\partial z} \left[v \left(\frac{\partial v}{\partial r} \right) \right], \quad (2)$$

$$\frac{\partial u}{\partial t} + u \frac{\partial u}{\partial r} + v \frac{\partial u}{\partial z} = -\frac{1}{\rho} \frac{\partial p}{\partial r} + \frac{2}{r} \frac{\partial}{\partial r} \left(r v \frac{\partial u}{\partial r} \right) + \frac{\partial}{\partial z} \left[v \left(\frac{\partial v}{\partial r} + \frac{\partial u}{\partial z} \right) \right] - \frac{2vu}{r^2}, \quad (3)$$

$$\rho C_p \left(\frac{\partial T}{\partial t} + u \frac{\partial T}{\partial r} + v \frac{\partial T}{\partial z} \right) = \frac{1}{r} \frac{\partial}{\partial r} \left(r K \frac{\partial T}{\partial r} \right) + \frac{\partial}{\partial z} \left(K \frac{\partial T}{\partial z} \right) + \Phi + S_r, \quad (4)$$

where, the viscous dissipation term, Φ , is given by

$$\Phi = \mu \left\{ 2 \left[\left(\frac{\partial u}{\partial r} \right)^2 + \left(\frac{u}{r} \right)^2 + \left(\frac{\partial v}{\partial z} \right)^2 \right] + \left(\frac{\partial u}{\partial z} + \frac{\partial v}{\partial r} \right)^2 \right\}. \quad (5)$$

Here, S_r is the radiative source term. The viscous dissipation and the radiative source terms are only kept for the glass flow due to their importance.

Contributed by the Heat Transfer Division for publication in the JOURNAL OF HEAT TRANSFER. Manuscript received by the Heat Transfer Division March 4, 2004; revision received June 10, 2004. Associate Editor: B. Farouk.

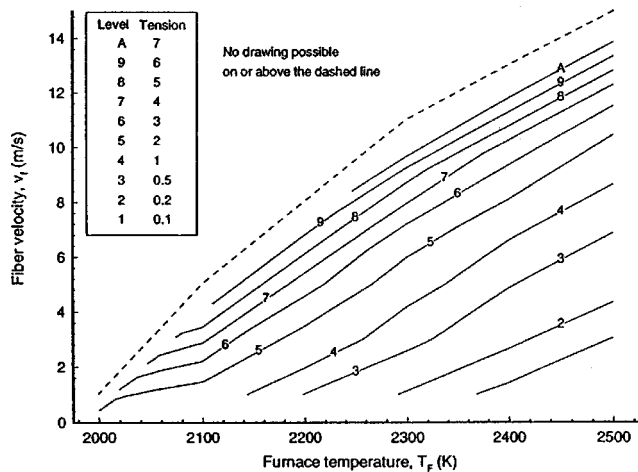


Fig. 2 Results obtained from a feasibility study of the fiber drawing process, in terms of “isotension” contours for the feasible region of fiber drawing

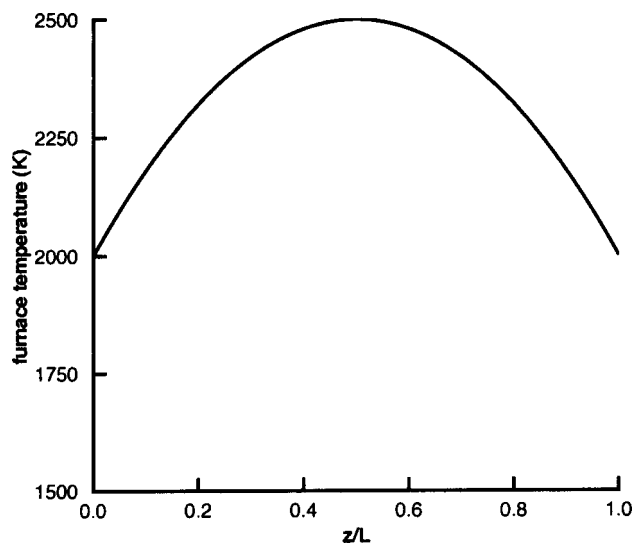


Fig. 3 A parabolic temperature profile specified at the furnace wall

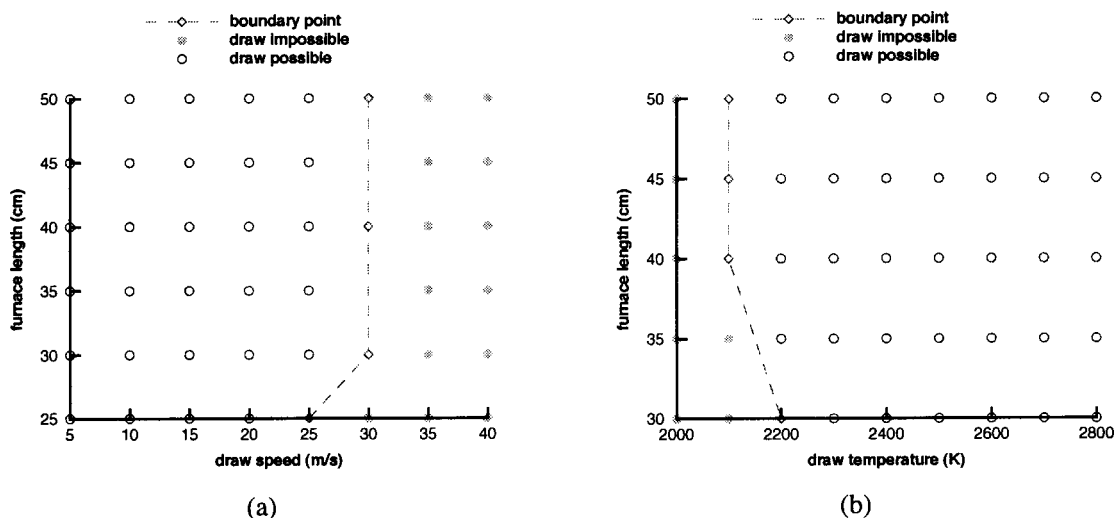


Fig. 4 Feasible domain for a parabolic furnace temperature distribution in terms of (a) the draw speed and the furnace length at a draw temperature of 2500 K, and (b) the draw temperature and the furnace length at a draw speed of 15 m/s

examined separately. The minimum temperature in the distribution is kept fixed, and the maximum temperature is varied and referred to as the furnace or draw temperature.

Fiber drawing for a parabolic temperature profile, as shown Fig. 3, is first studied. Both feasible and infeasible cases are shown in Fig. 4. A feasible region can be easily identified based on a combination of heat-zone length, draw temperature, and draw speed, beyond which the fiber drawing becomes impossible. Clearly, the maximum draw speed at a given maximum furnace temperature could be restricted by the heating-zone length inside the furnace due to the requirement that the temperature in the neck-down region must exceed the softening temperature. Similarly, at a given draw speed, a longer heat zone would allow lower furnace temperature to heat the glass up to the softening point. The latter is a better alternative, since higher temperatures lead to higher concentration of defects and shorter lifespan of a graphite furnace [14]. It is also found from the numerical results on tension that the lower bound of temperature and the upper bound of draw speed are all regulated by viscous rupture, which is a direct result of high draw tension.

A Gaussian temperature distribution is next investigated to obtain the feasible domain. The temperature distribution employed is the one obtained experimentally on an available graphite furnace [15]. The profile has a Gaussian distribution in the middle portion, but has essentially room temperature at the two ends due to water cooling at the ends of the heated zone. This is quite typical of practical furnaces. Either a combination of the furnace length and the draw speed, or of the furnace length and the draw temperature, can be considered to determine feasible parameters for fiber drawing. Figure 5 shows the minimum draw temperatures possible for various heat-zone dimensions, at different draw speeds. Compared to the results in Fig. 4, it is obvious that the feasible domain boundary is quite different due to the changes in the temperature distribution. It is also interesting to see that the boundary of the feasible domain shifts noticeably to the top right when draw speed increases. It indicates that either a higher draw temperature or a longer residence time is needed to make fiber drawing possible at higher draw speeds.

For a realistic fiber-drawing operation, these results are very important, since the parameters in a fiber drawing system, such as draw temperature, draw speed, and heat-zone length, can be identified so that a fiber of desired diameter can be drawn. The fiber quality, in terms of defect concentration, can also be brought in as a consideration [16,17]. However, it must be pointed out that fiber

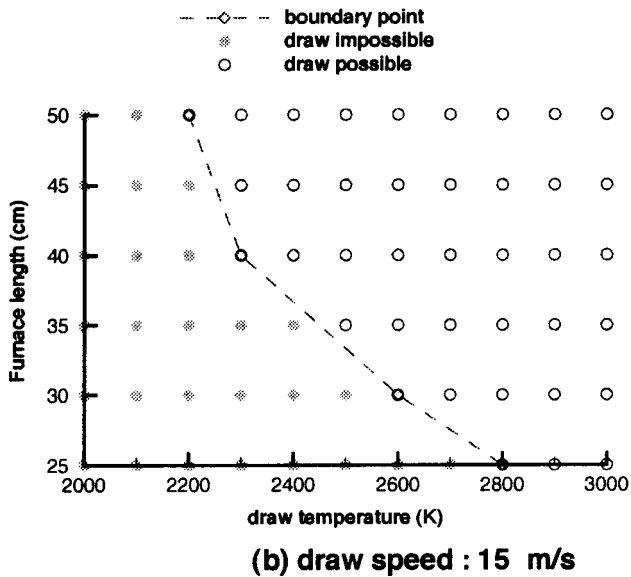
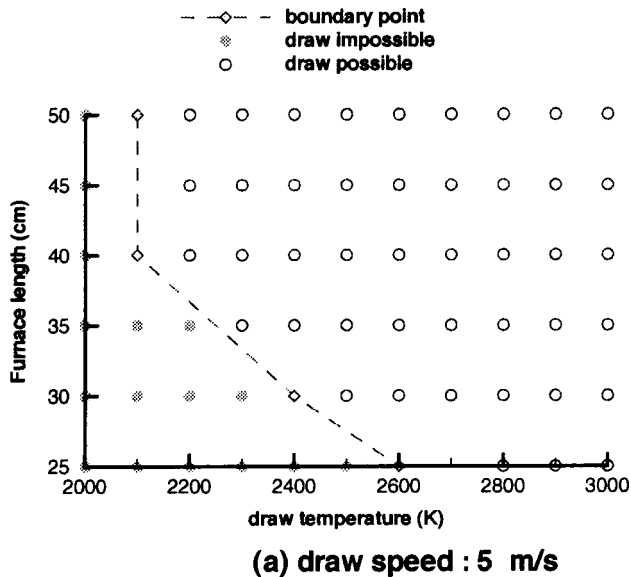


Fig. 5 Comparison of feasible domains at (a) draw speed of 5 m/s, and (b) draw speed of 15 m/s

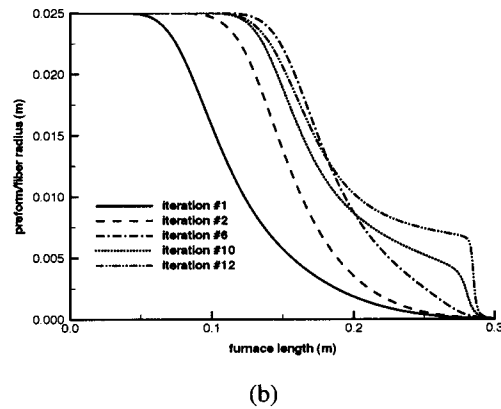
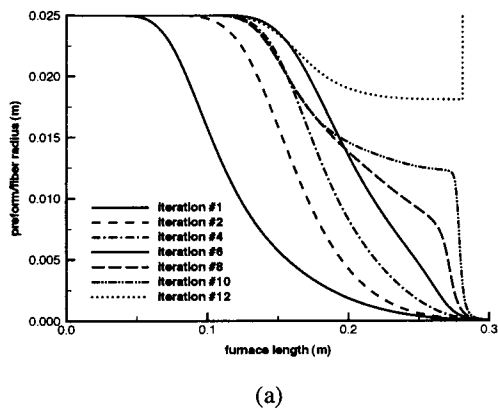


Fig. 6 Neck-down profile corrections for infeasible fiber drawing circumstances at a draw speed of 15 m/s and a furnace temperature of (a) 2200 K, and (b) 2300 K

drawing may never reach the boundaries due to the unacceptable draw tension in practice. Additionally, it is also possible to obtain similar feasibility results for different combinations of other physical and process variables. But, furnace temperature, draw speed, and heat-zone length are investigated here, because these are the most commonly varied parameters in practical systems.

In real life, there are other considerations that must also be taken into account to determine optimum drawing conditions [18]. For example, a very high furnace temperature, together with a very low draw speed, could cause very small draw tension due to the low value of viscosity. The fiber could break into drops because of the very mobile state of glass and the corresponding capillary instability [12]. Under these circumstances, the drawing process also becomes very sensitive to disturbances that are caused by unexpected variations in the drawing parameters. Similarly, the concentrations of various point defects could be very high at combinations of high draw speeds and high draw temperatures. This can also lead to unsatisfactory optical fibers. From these considerations, very high draw speeds or very high draw temperatures are not very desirable as well, even when drawing is feasible in terms of the transport process.

Phenomena at Domain Boundary. As the furnace temperature decreases or as the fiber speed increases, the preform/fiber temperature inevitably drops below the softening point of the fiber material and this eventually makes drawing impossible. The behavior of numerical convergence and physical characteristics are of great basic and applied interest when the drawing parameters are close to the boundary of the feasible domain. On one hand, it is important to know the dominating factors that eventually cause the fiber to break. On the other hand, it is interesting to investigate the characteristics of the numerical algorithm and the iterative procedure in the search for the boundary of the feasible domain.

One typical case involving the draw temperature variation across the boundary of the acceptable domain is presented here. For a 30-cm furnace, the draw temperature is gradually increased, starting from an infeasible drawing point of 2200 K, and finally reaching the feasible boundary at 2600 K. This movement is parallel to the x axis in Fig. 5(b). The iterative evolution of neck-down profiles is compared in Figs. 6 and 7, corresponding to draw temperatures ranging from 2200 to 2600 K.

Several interesting observations can be seen clearly from these results. First, when the draw temperature is far below the temperature at the boundary of the feasible drawing region, the neck-down profile becomes increasingly flat as the iterations proceed due to the lack of material flow. To satisfy the boundary condition of a fixed fiber diameter, it gives rise to an abrupt change in the fiber profile at the lower end of the furnace. Eventually the numerical procedure diverges, as seen in Figs. 6 and 7(a). However,

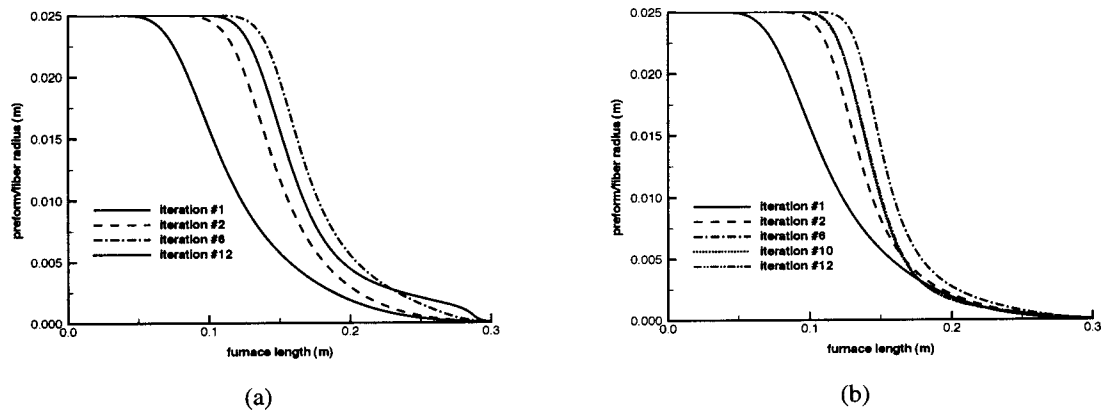


Fig. 7 Neck-down profile corrections at a draw speed of 15 m/s for (a) infeasible fiber drawing circumstance at a furnace temperature of 2400 K, and (b) a feasible fiber drawing circumstance at a furnace temperature of 2600 K

the rate of divergence is very different for various draw temperatures. The iteration diverges much faster at lower draw temperatures that are far away from the feasible boundary, but it diverges much more slowly at higher draw temperatures that are closer to the feasible boundary. As an example, the abrupt change of the profile at 2200 K becomes very obvious after only six neck-down corrections. However, it takes more than eight corrections for 2300 K, and more than ten for 2400 K. Since one correction of the neck-down profile, using the zonal method, requires an expense of 4000 iteration steps, the search for the feasible boundary, therefore, becomes very expensive in terms of computational resources. In fact, it takes more than 50,000 iteration steps to determine that the process is infeasible at 2500 K but feasible at 2600 K.

Once the boundary point is reached, experience shows that the convergence of the numerical iteration process could be alternatively determined by the given number of iterations or neck-down corrections, instead of by specified values of the convergence parameters. From numerical experiments, it is observed that the difference caused by the two control schemes is trivial, especially for feasible cases far away from the domain boundary. In addition, to make the computation economic and feasible, each computational run is checked to locate the boundary points. Interpolation is inevitable for the boundary points, because it is very difficult to develop practical criteria to determine if the numerical process will converge before the iteration finally reaches the steady state.

Numerical experiments also indicate that the temperature in the fiber core below the softening point and the draw tension one order above the practical threshold of 150 g are two direct indicators that the iteration procedure will eventually diverge. The imposed draw tension was calculated as a function of furnace temperature, draw speed, and heat-zone length. The physical phenomenon is identified as viscous rupture. It means that the viscosity of glass material and draw tension increase tremendously and eventually no flow is possible when the temperature is below the softening point. Rupture occurs as tension exceeds the viscous strength of the fiber.

Conclusions

In this paper, the feasible drawing domains are considered under two typical temperature distributions at the draw furnace wall. It is seen that such domains are the direct results of the combinations of three important operating parameters, namely furnace temperature, draw speed, and heating element length. The results show that the upper bound of draw speed and the lower bound of draw temperature can be changed by varying the heat-zone length at the given conditions. It is also found that the temperature dis-

tribution can alter the feasible domain significantly. The domain boundaries are determined by viscous rupture and flow instability.

Physical behavior close to the boundary of a feasible domain is also studied. It is found the iteration diverges more rapidly when the draw temperature is lower than that at the boundary of the acceptable domain due to the lack of material flow. However, the divergence rate becomes much smaller when the temperature gets close to the domain boundary. It is found that it is very expensive, computationally, to locate the exact boundary of the feasible drawing domain. Numerical experiments are used to indicate the dominant parameters and the convergence characteristics of the process.

Acknowledgments

The authors acknowledge the financial support provided by the National Science Foundation, under Grant No. DMI-96-33194, and the computing resources provided by the National Computational Science Alliance (NCSA). The partial support by the Center for Computational Design (CCD) at Rutgers University is also acknowledged. Discussions with Professor C.E. Polymeropoulos are gratefully acknowledged.

Nomenclature

C_p	= Specific heat at constant pressure
F_T	= Draw tension
g	= Magnitude of gravitational acceleration
H	= Mean surface curvature
K	= Thermal conductivity
L	= Height of furnace; length of fiber
R	= Radius of preform, fiber, furnace
r	= Radial coordinate distance
S_r	= Radiative source term
t	= Time
T	= Temperature
T_{melt}	= Glass softening point, typically around 1900 K for silica glass
u	= Radial velocity
v	= Axial velocity
z	= Axial coordinate distance

Greek Symbols

μ	= Dynamic viscosity
ν	= Kinematic viscosity
Φ	= Viscous dissipation
ρ	= Density
ζ	= Surface tension between glass and purge gas

References

- [1] Paek, U. C., and Runk, R. B., 1978, "Physical Behavior of the Neck-down Region during Furnace Drawing of Silica Fibers," *J. Appl. Phys.*, **49**, pp. 4417–4422.
- [2] Paek, U. C., 1999, "Free Drawing and Polymer Coating of Silica Glass Optical Fibers," *ASME J. Heat Transfer*, **121**, pp. 775–788.
- [3] Blyler, Jr., L. L., and Williams, J. C., 1987, "Optical Fiber Drawing and Coating," *AIChE Symp. Ser.*, **83**, pp. 27–28.
- [4] Lee, S. H.-K., and Jaluria, Y., 1997, "Simulation of the Transport Processes in the Neck-Down Region of a Furnace Drawn Optical Fiber," *Int. J. Heat Mass Transfer*, **40**, pp. 843–856.
- [5] Sayles, R., and Caswell, B., 1984, "A Finite Element Analysis of the Upper Jet Region of a Fiber Drawing Flow Field," *Int. J. Heat Mass Transfer*, **27**, pp. 57–67.
- [6] Myers, M. R., 1989, "A Model for Unsteady Analysis of Preform Drawing," *AIChE J.*, **35**, pp. 592–602.
- [7] Yin, Z., and Jaluria, Y., 1997, "Zonal Method to Model Radiative Transport in an Optical Fiber Drawing Furnace," *ASME J. Heat Transfer*, **119**, pp. 597–603.
- [8] Roy Choudhury, S., Jaluria, Y., and Lee, S. H.-K., 1999, "Generation of Neck-Down Profile for Furnace Drawing of Optical fiber," *Numer. Heat Transfer*, **35**, pp. 1–24.
- [9] Yin, Z., and Jaluria, Y., 1998, "Thermal Transport and Material Flow in High Speed Optical Fiber Drawing," *ASME J. Heat Transfer*, **120**, pp. 916–930.
- [10] Roy Choudhury, S. and Jaluria, Y., 1998, "Thermal Transport due to Material and Gas Flow in a Furnace for Drawing an Optical Fiber," *J. Mater. Res.*, **13**, pp. 494–503.
- [11] Cheng, X., and Jaluria, Y., 2002, "Effect of Draw Furnace Geometry on High-Speed Optical Fiber Manufacturing," *Numer. Heat Transfer*, **41**, pp. 757–781.
- [12] Dianov, E. M., Kashin, V. V., Perminov, S. M., Perminova, V. N., Runanov, S. Ya, and Sysoev, S. M., 1988, "The Effects of Different Conditions on the Drawing of Fibers from Preforms," *Glass Technol.*, **29**, pp. 258–262.
- [13] Roy Choudhury, S., and Jaluria, Y., 1998, "Practical Aspects in the Drawing of an Optical Fiber," *J. Mater. Res.*, **13**, pp. 483–493.
- [14] Cheng, X., and Jaluria, Y., 2002, "Thermal Design of Draw Furnace in Optical Fiber Manufacturing," *Heat Transfer 2002, Proc. 12th Int. Heat Transfer Conf.*, Grenoble, France, Elsevier SAS, pp. 839–845.
- [15] Issa, J., Yin, Z., Polymeropoulos, C. E., and Jaluria, Y., 1996, "Temperature Distribution in an Optical Fiber Draw Tower Furnace," *J. Mater. Process. Manuf. Sci.*, **4**, pp. 221–232.
- [16] Yin, Z., and Jaluria, Y., 2000, "Neckdown and Thermally Induced Defects in High Speed Optical Fiber Drawing," *ASME J. Heat Transfer*, **122**, pp. 351–362.
- [17] Jaluria, Y., 2003, "Thermal Processing of Materials: From Basic Research to Engineering," *ASME J. Heat Transfer*, **125**, pp. 957–979.
- [18] Jaluria, Y., 1998, *Design and Optimization of Thermal Systems*, McGraw-Hill, New York.

Importance of Combined Lorentz-Doppler Broadening in High-Temperature Radiative Heat Transfer Applications

Anquan Wang

Michael F. Modest

Fellow ASME

e-mail: mfm6@psu.edu

Department of Mechanical Engineering, Pennsylvania State University, University Park, PA 16802

The importance of combined Lorentz-Doppler (or Voigt) broadening of spectral lines in high-temperature radiative heat transfer applications is investigated. Employing narrow-band transmissivities as the criterion, the critical total pressure below which, and the critical temperature above which Doppler broadening has a significant effect on the absorption coefficient is established for gaseous H₂O and CO₂. [DOI: 10.1115/1.1798951]

Keywords: Gaseous, Heat Transfer, High Temperature, Properties, Radiation

Introduction

The absorption coefficient of a gaseous medium governs the radiative heat transfer rates through it. While the highly oscillating nature of the absorption coefficient along the spectrum makes it computationally expensive to evaluate radiative transfer rates from absorption coefficient data directly by the so-called line-by-line (LBL) approach, modern absorption models, such as narrow-band k -distributions [1,2], spectral line based weighted-sum-of-gray-gases (SLW) [3,4], absorption distribution functions (ADF) [5,6] and full-spectrum k -distributions (FSK) [7–10], were developed based on detailed absorption coefficient data. The LBL approach has been recognized as the most accurate approach to date and has been utilized as a benchmark in radiation calculations.

The absorption coefficient at a specific spectral location is a result of the overlap of nearby spectral lines which are broadened to overlap with each other due to natural line broadening, collision broadening and Doppler broadening [11]. The effect of natural line broadening is fairly small compared to collision broadening, but its shape is identical to that of a collision-broadened line. Generally, natural line broadening and collision broadening are combined, and the combined effect is known as Lorentz broadening. The importance of Lorentz broadening is directly proportional to total pressure, and inversely proportional to the square-root of temperature. Doppler broadening, on the other hand, is independent of pressure and increases with the square-root of temperature. Therefore, Lorentz broadening tends to be dominant at modest-to-high pressures and low-to-moderate temperatures. It follows that, in most engineering applications, such as industrial boilers and combustors as well as gas turbines, Lorentz broadening is the most important broadening mechanism and, therefore, Doppler broadening is usually neglected. On the other hand, in the atmospheric sciences, dealing with extremely low pressures in the upper atmosphere, Doppler broadening becomes important and may even be dominant. Modern high-temperature applications, such as

rocket nozzles and closed-cycle gas turbines, combine both relatively low pressures and high temperatures, such that the importance of Doppler broadening needs to be investigated. The combined effect of Lorentz broadening and Doppler broadening leads to the Voigt line broadening profile. Employing the Voigt profile is much more CPU-time intensive than that of the Lorentz profile, but several fast algorithms for Voigt profile calculations have been developed [12,13].

The purpose of the present note is to investigate under what conditions (i.e., what pressures and temperatures) the Voigt profile should be employed in the absorption coefficient evaluation rather than the Lorentz profile, and to determine the error if the Lorentz profile is used. Currently, water vapor and carbon dioxide, the two major products of hydrocarbon-air combustion, have been studied. The spectral line parameters for the evaluation of the absorption coefficients were obtained from spectroscopic databases: HITEMP 2000 [14] was employed for water vapor, while for carbon dioxide CDSD-1000 [15] was used, which is considered more reliable than HITEMP for temperatures higher than 1000 K [16,17].

Absorption Coefficient Calculation

Evaluation of the absorption coefficient at a specific wavenumber η consists of collecting the contributions of all spectral lines that contribute to that wavenumber, i.e.,

$$\kappa_{\eta} = \sum_i \kappa_i(\eta, \phi_i), \quad (1)$$

where κ_{η} is the absorption coefficient at the wavenumber η , κ_i is the contribution of the spectral line i , and ϕ_i is its line parameter vector containing the line intensity S , the line center wavenumber η_o , the Lorentz broadening half-width b_L , and the Doppler broadening half-width b_D , which are obtained or calculated from the spectroscopic databases. The line shape can be the Lorentz profile [11]

$$\kappa_L = \frac{S}{\pi} \frac{b_L}{(\eta - \eta_o)^2 + b_L^2}, \quad (2)$$

or the Voigt profile [11]

$$\kappa_V = \frac{S b_L}{\pi^{3/2}} \int_{-\infty}^{+\infty} \frac{e^{-x^2} dx}{(\eta - \eta_o - x b_D / \sqrt{\ln 2})^2 + b_L^2}. \quad (3)$$

Unlike the Lorentz profile, the Voigt profile cannot be expressed in a closed form. In the current work, the Humlíček algorithm [13] was employed to evaluate the Voigt profile.

In order to describe the irregularity of the absorption coefficient across the spectrum, κ_{η} must be evaluated from spectroscopic databases at close enough spectral intervals. Since the Lorentz profile always causes weaker overlap between lines and the resulting absorption coefficient is much more oscillating than the Voigt profile with its additional broadening due to Doppler effects, a fine enough wavenumber resolution for the Lorentz profile is also always sufficient for the Voigt profile. As stated earlier, Lorentz broadening (or b_L) is proportional to total pressure. Therefore, a finer wavenumber resolution is needed at lower pressures. Similarly, since b_L is inversely proportional to the square-root of tem-

Table 1 Narrow band division

Spectral range (cm ⁻¹)	Interval (cm ⁻¹)	Number
200–300	10	10
300–4000	25	148
4000–5000	50	20
5000–10,000	100	50
10,000–15,000	250	20
		total: 248

Contributed by the Heat Transfer Division for publication in the JOURNAL OF HEAT TRANSFER. Manuscript received by the Heat Transfer Division February 23, 2004; revision received June 24, 2004. Associate Editor: G. Chen.

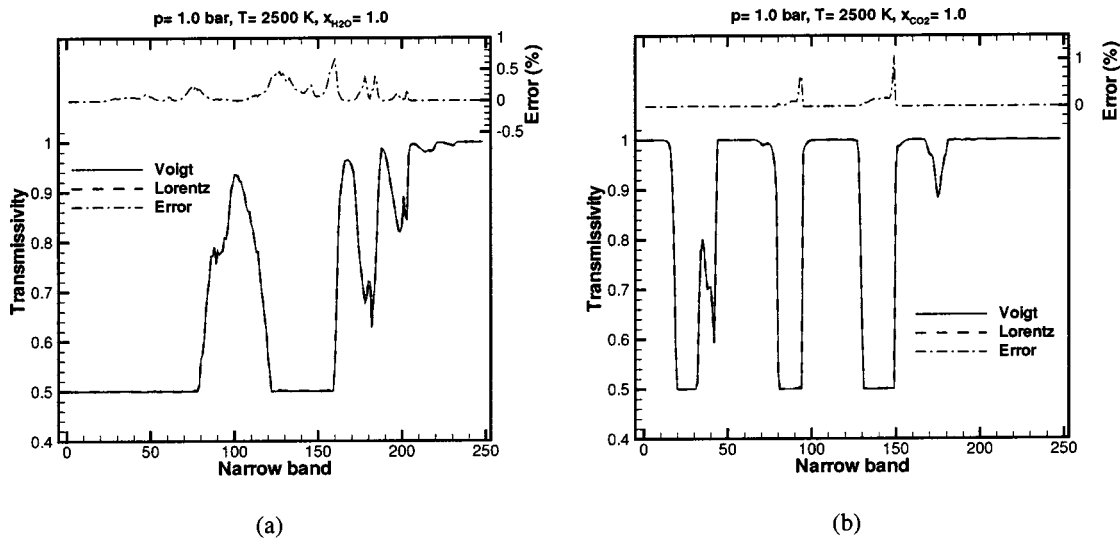


Fig. 1 Narrow-band transmissivity; total pressure $p=1.0$ bar, temperature $T=2500$ K and mole fraction $x=1.0$; errors evaluated according to Eq. (5): (a) water vapor, and (b) carbon dioxide

perature, higher temperatures cause weaker broadening and less overlap. However, as temperature rises, “hot” lines become more important, which induce more overlap between spectral lines. The combined effect leads to a need for higher resolution at high temperatures. In our work, a constant spacing across the entire spectrum was used; the resolution was considered sufficient if, when doubling the resolution, the error of narrow-band mean absorption coefficients stayed below 0.5% in major absorption bands of the entire spectrum, with the Lorentz profile employed. With this criterion, the wavenumber resolution was determined, using the Lorentz profile, for the evaluation of the pressure-based absorption coefficients. Then the same wavenumber resolution was utilized to evaluate the pressure-based absorption coefficients using the Voigt profile.

Narrow-Band Transmissivity

In our work, the effect of line-broadening mechanism on the narrow-band transmissivity has been investigated. A narrow band

is a narrow spectral interval in which the blackbody radiation intensity can be regarded as constant, leading to the definition of narrow-band transmissivity

$$\bar{\tau}_\eta(X) = \frac{\int_{\Delta\eta} I_{b\eta} e^{-\kappa_\eta X} d\eta}{\int_{\Delta\eta} I_{b\eta} d\eta} = \frac{1}{\Delta\eta} \int_{\Delta\eta} e^{-\kappa_\eta X} d\eta, \quad (4)$$

where X is the optical path-length, $\Delta\eta$ is the narrow-band width, and $I_{b\eta}$ is the blackbody intensity (or Planck function).

The entire spectrum was divided into 248 narrow bands as shown in Table 1 [18]. The narrow-band widths were chosen based on the variation of the Planck function and the importance of narrow bands.

Results and Discussion

When comparing the effects of Lorentz and Voigt profiles based on the narrow-band transmissivity, the same optical path-length

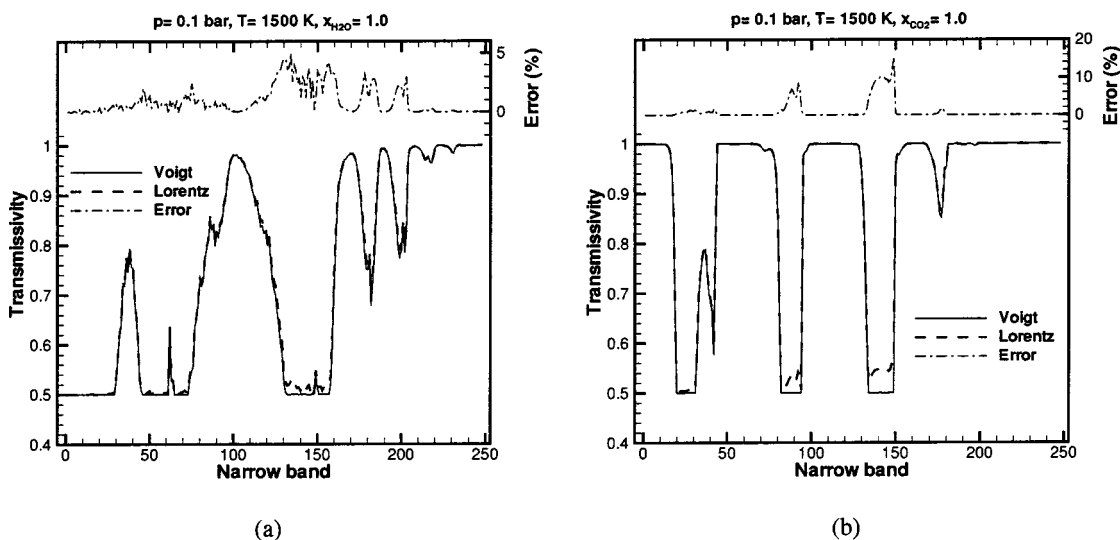


Fig. 2 Narrow-band transmissivity; total pressure $p=0.1$ bar, temperature $T=1500$ K and mole fraction $x=1.0$; errors evaluated according to Eq. (5): (a) water vapor, and (b) carbon dioxide

Table 2 Maximum error of narrow-band transmissivity for H₂O

p (bar)	0.1	0.2	0.3	0.4	0.5	0.7	1.0
T (K)	800	1100	1400	1700	1900	2400	2500
ϵ_{\max} (%)	1.04	0.92	1.00	1.06	0.99	1.01	0.65

should be used in both calculations, and the transmissivities should be adjusted to a moderate value to make the comparison meaningful.

Therefore, for each narrow band a characteristic path-length X_o was chosen, such that the narrow-band transmissivity was 0.5 when the Voigt profile was employed in the absorption coefficient evaluation. For some narrow bands with near-zero absorption coefficient, the necessary path-length to achieve a transmissivity of 0.5 is extremely large ($X_o > 100$ cm-bar), which is unlikely to occur in engineering applications. For such narrow bands, the characteristic path-length was set to $X_o = 100$ cm-bar. Using the characteristic path-length, the transmissivity evaluated from the absorption coefficient of the Lorentz profile was compared to that of the Voigt profile, and the relative error was defined as

$$\epsilon = \frac{(\bar{\tau}_\eta(X_o))_{\text{Lorentz}} - (\bar{\tau}_\eta(X_o))_{\text{Voigt}}}{(\bar{\tau}_\eta(X_o))_{\text{Voigt}}} \times 100\%, \quad (5)$$

where $(\bar{\tau}_\eta(X_o))_{\text{Lorentz}}$ is the narrow-band transmissivity evaluated from the pressure-based absorption coefficient employing the Lorentz profile, and $(\bar{\tau}_\eta(X_o))_{\text{Voigt}}$ is that of the Voigt profile.

Since the mole fraction (x) of the absorbing gas affects the pressure-based absorption coefficient only slightly through its molecular size in collision broadening, the effects of varying the mole fraction are minor. All results presented in this note are for a mole fraction of $x = 1.0$. At other mole fractions, the differences between the Lorentz and the Voigt profiles are slightly smaller.

Figure 1(a) shows the narrow-band transmissivity of H₂O evaluated at the characteristic path-length X_o for a total pressure of 1.0 bar and a temperature of 2500 K. Results of both the Lorentz and Voigt profiles and their differences are presented. Figure 1(b) shows the same results for CO₂ for the same total pressure and temperature. The narrow bands with transmissivity larger than 0.5 are unimportant narrow bands, since their absorption coefficients are so small that, even at $X = 100$ cm-bar, the gas is optically thin. In both figures, the maximum difference between the results for Lorentz and Voigt profiles is approximately 1%, which implies that it is safe to employ the Lorentz profile at 1.0 bar or higher total pressures and any temperature below 2500 K, since the higher the total pressure and the lower the temperature, the more dominant Lorentz broadening becomes. On the other hand, at low pressures the Lorentz profile may cause large errors, as shown in Figs. 2(a) and (b) which were calculated for $p = 0.1$ bar and $T = 1500$ K. Large errors always occur at important narrow bands, i.e., where the transmissivity is 0.5. Therefore, the Voigt profile should be employed in the evaluation of absorption coefficients at such pressures and temperatures.

For H₂O and CO₂ Tables 2 and 3 list some low-pressure (p, T) combinations at which the maximum error of the Lorentz profile is approximately 1.0% in terms of the narrow-band transmissivity. These two tables supply a guideline to determine whether the Lorentz profile can be safely employed at low pressures. For example, for H₂O at $p = 0.1$ bar, the Lorentz profile causes errors of narrow band transmissivity less than 1% if the temperature is

Table 3 Maximum error of narrow-band transmissivity for CO₂

p (bar)	0.1	0.2	0.4	0.5	0.7	1.0
T (K)	500	700	1000	1200	1500	2500
ϵ_{\max} (%)	1.01	1.07	1.03	1.11	0.95	1.06

lower than 800 K. At temperatures higher than 800 K, Doppler broadening becomes more important, leading to larger errors if neglected.

Summary

At low pressures and high temperatures, Doppler broadening tends to become an important spectral line broadening mechanism. The ranges of pressure and temperature, for which the effect of combined Lorentz-Doppler (or Voigt) broadening on the absorption coefficient must be accounted for, has been investigated in this note. Care was taken to evaluate the spectral absorption coefficient with high accuracy from spectroscopic databases. For H₂O and CO₂, based on an optimized optical path-length, the narrow-band transmissivity was evaluated from the absorption coefficients, employing the line shape of either the Lorentz profile (for pure Lorentz broadening) or the Voigt profile (for combined Lorentz-Doppler broadening). The transmissivities from these two broadening mechanisms were compared at various total pressures and temperatures. It was shown that at total pressure of 1.0 bar or higher, Doppler broadening is negligible for all temperatures below 2500 K. For low pressures (less than 1.0 bar), Doppler broadening may become important at high temperatures. The critical temperature above which combined broadening should be employed has been established as a function of pressure for H₂O and CO₂.

Acknowledgment

The authors gratefully acknowledge the financial support of the National Science Foundation under contracts CTS-0112423 and CTS-0121573.

References

- [1] Lacis, A. A., and Oinas, V., 1991, "A Description of the Correlated- k Distribution Method for Modeling Nongray Gaseous Absorption, Thermal Emission, and Multiple Scattering in Vertically Inhomogeneous Atmospheres," *J. Geophys. Res.*, **96**(D5), pp. 9027–9063.
- [2] Goody, R. M., and Yung, Y. L., 1989, *Atmospheric Radiation—Theoretical Basis*, 2nd ed., Oxford University Press, New York.
- [3] Denison, M. K., and Webb, B. W., 1993, "A Spectral Line Based Weighted-Sum-of-Gray-Gases Model for Arbitrary RTE Solvers," *ASME J. Heat Transfer*, **115**, pp. 1004–1012.
- [4] Denison, M. K., and Webb, B. W., 1995, "The Spectral-Line-Based Weighted-Sum-of-Gray-Gases Model in Nonisothermal Nonhomogeneous Media," *ASME J. Heat Transfer*, **117**, pp. 359–365.
- [5] Rivière, Ph., Soufiani, A., Perrin, M. Y., Riad, H., and Gleizes, A., 1996, "Air Mixture Radiative Property Modelling in the Temperature Range 10,000–40,000 K," *J. Quant. Spectrosc. Radiat. Transf.*, **56**, pp. 29–45.
- [6] Pierrot, L., Rivière, Ph., Soufiani, A., and Taine, J., 1999, "A Fictitious-Gas-Based Absorption Distribution Function Global Model for Radiative Transfer in Hot Gases," *J. Quant. Spectrosc. Radiat. Transf.*, **62**, pp. 609–624.
- [7] Modest, M. F., 2003, "Narrow-Band and Full-Spectrum k -Distributions for Radiative Heat Transfer—Correlated- k vs. Scaling Approximation," *J. Quant. Spectrosc. Radiat. Transf.*, **76**(1), pp. 69–83.
- [8] Modest, M. F., and Zhang, H., 2002, "The Full-Spectrum Correlated- k Distribution for Thermal Radiation From Molecular Gas-Particulate Mixtures," *ASME J. Heat Transfer*, **124**(1), pp. 30–38.
- [9] Zhang, H., and Modest, M. F., 2002, "A Multi-Level Full-Spectrum Correlated- k Distribution for Radiative Heat Transfer in Inhomogeneous Gas Mixtures," *J. Quant. Spectrosc. Radiat. Transf.*, **73**(2–5), pp. 349–360.
- [10] Zhang, H., and Modest, M. F., 2003, "Scalable Multi-Group Full-Spectrum Correlated- k Distributions for Radiative Heat Transfer," *ASME J. Heat Transfer*, **125**(3), pp. 454–461.
- [11] Modest, M. F., 2003, *Radiative Heat Transfer*, 2nd ed., Academic Press, New York.
- [12] Hui, A. K., Armstrong, B. H., and Wray, A. A., 1978, "Rapid Computation of the Voigt and Complex Error Functions," *J. Quant. Spectrosc. Radiat. Transf.*, **19**, p. 509.
- [13] Humlíček, J., 1982, "Optimized Computation of the Voigt and Complex Probability Functions," *J. Quant. Spectrosc. Radiat. Transf.*, **27**, p. 437.
- [14] Rothman, L. S., Camy-Peyret, C., Flaud, J.-M., Gamache, R. R., Goldman, A., Goorvitch, D., Hawkins, R. L., Schroeder, J., Selby, J. E. A., and Wattson, R. B., 2000, "HITEMP, the High-Temperature Molecular Spectroscopic Database," available through <http://www.hitran.com>.

- [15] Tashkun, S. A., Perevalov, V. I., Bykov, A. D., Lavrentieva, N. N., and Teffo, J.-L., 2002, "Carbon Dioxide Spectroscopic Databank (CDSDB)," available from <ftp://ftp.iao.ru/pub/CDSDB-1000>.
- [16] Tashkun, S. A., Perevalov, V. I., Teffo, J.-L., Bykov, A. D., and Lavrentieva, N. N., 2003, "CDSDB-1000, the High-Temperature Carbon Dioxide Spectroscopic Databank," *J. Quant. Spectrosc. Radiat. Transf.*, **82**(1–4), pp. 165–196.
- [17] Modest, M. F., and Bharadwaj, S. P., 2002, "High-Resolution, High-Temperature Transmissivity Measurements and Correlations for Carbon Dioxide-Nitrogen Mixtures," *J. Quant. Spectrosc. Radiat. Transf.*, **73**(2–5), pp. 329–338.
- [18] Wang, A., and Modest, M. F., 2004, "High-Accuracy, Compact Database of Narrow-Band k -Distributions for Water Vapor and Carbon Dioxide," *Proceedings of the ICHMT 4th International Symposium on Radiative Transfer*, Mengüç, M. P. and Sclçuk, N., eds., Begell House Inc., New York.

Performance and Optimization Analysis for Fins of Straight Taper With Simultaneous Heat and Mass Transfer

B. Kundu

e-mail: bkundu123@rediffmail.com

Department of Mechanical Engineering, Faculty of Engineering and Technology, Jadavpur University, Kolkata—700 032, India

P. K. Das

e-mail: pkd@iitkgp.ernet.in

Department of Mechanical Engineering, Indian Institute of Technology, Kharagpur—721302, India

An analytical method based on Frobenius power series expansion has been developed for the performance prediction of fully wet fins. Fins of different geometries, namely, longitudinal, annular and spine having both trapezoidal and triangular profiles have been considered. Unlike dry fins, the efficiency and effectiveness of wet fins depend on the fin base temperature and psychrometric condition of the ambient air. A generalized criterion has been derived for the optimization of wet fins having the above geometries. A method for constructing design curves for the optimum fins has also been discussed. [DOI: 10.1115/1.1798911]

Keywords: Analytical, Dehumidification, Finned Surfaces, Heat Exchangers, Optimization

1 Introduction

Extended surfaces or fins are commonly used on the gas side of the heat exchangers to enhance the rate of heat transfer. In general, the energy exchange between the fin and the surrounding gas stream takes place solely by sensible heat transfer. However, in various applications, heat transfer between moist air and the fin is accompanied by diffusion mass transfer of water vapor. This process is common in dehumidifying coils of air conditioners, evaporative air coolers and in environmental control system of aircrafts. In such cases, the fin is termed as a wet fin [1] as there is a thin film of water on it. In the absence of the water film, gas side fins are denoted as dry fins.

In dry fins, the temperature difference between the fin surface and the surrounding fluid acts as the driving force for energy transfer. In wet fins, energy exchange between the fin and air is due to combined heat and mass transfer and it depends on the difference of temperature as well as concentration of water vapor. Fortunately, using psychrometric relationships [2] and the analogy between heat and mass transfer [3], one can establish temperature difference as the net driving force for energy transfer even in case of wet fins [1,2]. Following this methodology, the performance of various fins, namely, rectangular [1,2,4–6], triangular [7], trapezoidal and triangular [8] have been evaluated. Analysis of eccentric annular fins under combined heat and mass transfer has been made by Kazeminejad et al. [9].

Though addition of fins augments the rate of heat transfer, it increases the volume, weight and initial cost of the equipment. In mobile systems, it also increases the running cost, as higher trac-

tive power is needed. Moreover, pressure drop increases with the addition of fins. It is therefore the duty of thermal engineers to see that the addition of fins is justified by a decrease in the total cost. This has prompted numerous studies on optimization of fins. The optimum design of straight rectangular fins and eccentric annular fins for dehumidification has been done by Kilic and Onat [10], and Kazeminejad et al. [9] respectively. In both of these studies, fin thickness has been kept constant. However, it is a known fact that reduction of fin thickness towards the tip gives a considerable saving in fin material. Accordingly, straight taper fins of various geometries, namely, longitudinal, annular and spine [11] are in common use under dry condition.

In the present paper, a unified analysis of straight taper fins has been made for predicting their performance under wet condition. Fins of all the common geometries, namely, longitudinal, annular and spine with both trapezoidal and triangular profiles have been considered. A comparative study on the fin performance has made for dry and wet fins, as well as for wet fins with a variation of thermo-psychrometric parameters. In addition, a generalized scheme is adopted for optimizing the dimensions of the fins such that a constraint of either a given fin volume or a specified heat duty is satisfied.

2 Formulation of Mathematical Model

2.1 Analysis. The geometry of different straight taper fins along with the coordinate systems is shown schematically in Fig. 1. It is assumed that the thermal conductivity of the fin material, the convective heat transfer coefficient and the temperature and relative humidity of the surrounding air are constant. At any point, temperature over the fin cross section is assumed to be constant. It is further assumed that the temperature at the fin tip is below the dew point temperature or in other words the fin is completely wet [1]. In general, the variation of temperature from the tip to base of a fin is rather small in most of the applications for air conditioning. It is customary to approximate the saturation curve as a linear one for such a small temperature interval [1,5]. The specific humidity on the fin surface can then be expressed as $\omega = b_1 + b_2 T$. The constants b_1 and b_2 are determined from the known values of specific humidity and temperature following the procedure of the previous researchers [1,8]. Further, over the fin at every point local thermodynamic equilibrium is considered so that the heat and mass transfer analogy becomes applicable. For the present condition, the outer surface of the fin will be covered by a thin film of condensate. For rigorous analysis, one should explicitly consider the heat and mass transfer of the condensate film, which takes place in a direction normal to the fin axis. However, in a simplified approach [1,2,8] the effect of the condensate film can be incorporated as convective boundary condition of the fin. The transport process can be rendered one-dimensional as is conventionally done for dry fins.

Based on the above assumptions, one dimensional steady state energy equation for three types of fins, namely, longitudinal, annular and spine reduces into a second order ordinary differential equation [1].

$$\frac{d}{dx} \left[y^p (r_i + x)^s \frac{dT}{dx} \right] = \frac{ph(r_i + x)^s y^{p-1}}{k} \sqrt{1 + \left(\frac{dy}{dx} \right)^2} (T - T_a) + \frac{h_m}{h} (\omega - \omega_a) h_{fg} \quad (1)$$

where

longitudinal fin for $p=1, s=0$

annular fin for $p=1, s=1$

spine for $p=2, s=0$.

Contributed by the Heat Transfer Division for publication in the JOURNAL OF HEAT TRANSFER. Manuscript received by the Heat Transfer Division February 7, 2001; revision received June 3, 2004. Associate Editor: G. S. Dulikravich.

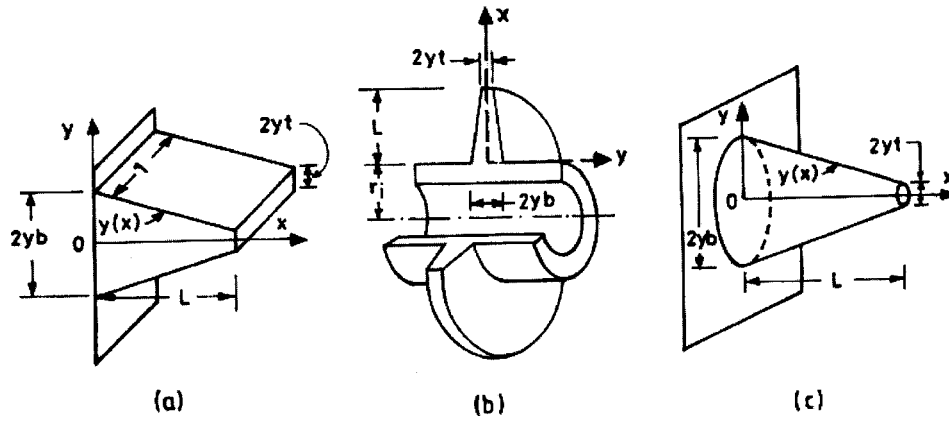


Fig. 1 Schematic diagram of fins with trapezoidal profile: (a) longitudinal, (b) annular, and (c) spine.

Using Chilton Colburn analogy [3], the above equation can be nondimensionalized for either trapezoidal or triangular profiles (Fig. 1) through some algebraic manipulations [11]

$$Y(1-s\alpha Y) \frac{d^2\phi}{dY^2} + [p-(p+1)s\alpha Y] \frac{d\phi}{dY} - Z_1(1-s\alpha Y)\phi = 0 \quad (2)$$

The temperature distribution, and hence the total energy transfer through the fin, are determined solving Eq. (2) subject to the following boundary conditions:

$$\text{at } Y = \begin{cases} 1 & \phi = 1 + \theta_p \\ \lambda & \begin{cases} d\phi/dY = Z_2\phi \\ \phi = \text{finite value} \end{cases} \end{cases} \begin{array}{l} \text{trapezoidal profile} \\ \text{triangular profile} \end{array} \quad (3)$$

A detailed study of singularity of this equation reveals that the power series method of Frobenius would be convergent in the interval of interest [12]. As the indicial equation has two identical roots, both equal to zero, solution of Eq. (2) can be expressed in the following matrix form:

$$\begin{bmatrix} \theta + \theta_p \\ 1 + \theta_p \end{bmatrix} = \begin{bmatrix} F \sum_{n=0}^{\infty} A_n Y^n - E \left(\sum_{n=0}^{\infty} C_n Y^{n-p+1} + F_1 \ln Y \right) \\ \sum_{n=0}^{\infty} A_n Y^n / \sum_{n=0}^{\infty} A_n \end{bmatrix} \begin{array}{l} \text{trapezoidal fin} \\ \text{triangular fin} \end{array} \quad (4)$$

where

$$\begin{bmatrix} E \\ F \end{bmatrix} = \begin{bmatrix} \sum_{n=1}^{\infty} n A_n \lambda^{n-1} - Z_2 \sum_{n=0}^{\infty} A_n \lambda^n \\ F_2 + (p-1)F_3 + (2-p)F_4 \end{bmatrix} \quad (5)$$

and

$$\begin{bmatrix} F_1 \\ F_2 \\ F_3 \\ F_4 \end{bmatrix} = \begin{bmatrix} (p-1) \sum_{n=1}^{\infty} D_n Y^{n-p+1} + (2-p) \sum_{n=0}^{\infty} A_n Y^{n-p+1} \\ \sum_{n=1}^{\infty} (n-p+1) C_n \lambda^{n-p} - Z_2 \sum_{n=1}^{\infty} C_n \lambda^{n-p+1} \\ \sum_{n=1}^{\infty} D_n \lambda^{n-p} + \ln \lambda \left\{ \sum_{n=1}^{\infty} (n-p+1) D_n \lambda^{n-p} - Z_2 \sum_{n=1}^{\infty} D_n \lambda^{n-p+1} \right\} \\ \sum_{n=0}^{\infty} A_n \lambda^{n-p} + \ln \lambda \left\{ \sum_{n=0}^{\infty} (n-p+1) A_n \lambda^{n-p} - Z_2 \sum_{n=0}^{\infty} A_n \lambda^{n-p+1} \right\} \end{bmatrix} \quad (6)$$

The coefficients A_n , C_n , and D_n can be written as follows:

$$\begin{bmatrix} A_0 \\ A_1 \\ \dots \\ A_n \end{bmatrix} = \begin{bmatrix} 1 \\ Z_1/p \\ \dots \\ [A_{n-1}\{s\alpha(n-1)(n+p-1) + Z_1\} - s\alpha Z_1 A_{n-2}]/n(n+p-1) \end{bmatrix} \quad (7)$$

$$\begin{bmatrix} C_0 \\ C_1 \\ \dots \\ C_n \end{bmatrix} = \begin{bmatrix} p-1 \\ s\alpha - (3-p)Z_1 \\ \dots \\ \{n(n-p+1)F_n - (2n-p+1)G_n\}/(n-p+1)^2n^2 \end{bmatrix} \quad (8)$$

$$\begin{bmatrix} D_0 \\ D_2 \\ \dots \\ D_n \end{bmatrix} = \begin{bmatrix} 0 \\ Z_1 \\ \dots \\ \{D_{n-1}[s\alpha(n-2)(n+p-2)+Z_1] - s\alpha Z_1 D_{n-2}\}/(n-1)(n+p-2) \end{bmatrix} \quad (9)$$

where

$$\begin{bmatrix} F_n \\ G_n \end{bmatrix} = \begin{bmatrix} \{ns\alpha(n-p)+Z_1\}C_{n-1} + s\alpha(2n-p)\{(2-p)A_{n-1} + (p-1)D_{n-1}\} - s\alpha Z_1 C_{n-2} \\ \{ns\alpha(n-p)+Z_1\}\{(2-p)A_{n-1} + (p-1)D_{n-1}\} - s\alpha Z_1\{(2-p)A_{n-2} + (p-1)D_{n-2}\} \end{bmatrix} \quad (10)$$

Following the methodology suggested in [8], total rate of heat transfer q , from the fin can be estimated from Eq. (4). The heat transfer q can be nondimensionalized as given in Eq. (11) by the introduction of two dimensionless parameters Φ and Ω .

$$[Q] = \begin{bmatrix} qh^{p-1}p/2(1+s)(T_a - T_b)\pi^{p+s-1}r_i^s k^p \\ Bi^{p-1}\psi(1-\lambda)(1+\theta_p)\Phi/\Omega \end{bmatrix} \quad (11)$$

The expressions of Φ and Ω are given in Eqs. (12) and (13) for trapezoidal and triangular profiles, respectively.

$$[\Phi] = \begin{bmatrix} F \sum_{n=1}^{\infty} nA_n - E \left\{ \sum_{n=1}^{\infty} (n-p+1)C_n + (p-1) \sum_{n=1}^{\infty} D_n + (2-p) \sum_{n=0}^{\infty} A_n \right\} \\ F \sum_{n=0}^{\infty} A_n - E \sum_{n=1}^{\infty} C_n \end{bmatrix} \quad (12)$$

$$[\Phi] = \begin{bmatrix} \sum_{n=1}^{\infty} nA_n \\ \sum_{n=0}^{\infty} A_n \end{bmatrix} \quad (13)$$

The total rate of energy transfer q_i can be estimated assuming the entire fin surface at the fin base condition. And this quantity can be nondimensionalized as

$$[Q_i] = \begin{bmatrix} q_i h^{p-1} p/2(1+s)(T_a - T_b)\pi^{p+s-1} r_i^s k^p \\ \frac{\{Bi^p(1+b_2\xi)/R_i^s\}\{\beta\lambda^{p-1}(1+R_i)^s + [1-\lambda^p - sp\alpha(1-\lambda^{p+1})/(p+1)]\}}{\alpha^s \psi(1-\lambda)^{s+1}} \end{bmatrix} \quad (14)$$

Conventionally, the fin efficiency is expressed as

$$[\eta] = [Q/Q_i] \quad (15)$$

The overall effectiveness (ε) is defined as the ratio of the rate of total heat transfer through fin to that of the same base surface if the fin were not present (q_e).

$$[Q_e] = \begin{bmatrix} q_e h^{p-1} p/2(1+s)(T_a - T_b)\pi^{p+s-1} r_i^s k^p \\ (1+b_2\xi)(1+\theta_p)(Z_0\psi)^{2p} \end{bmatrix} \quad (16)$$

Thus, the overall effectiveness is

$$[\varepsilon] = [Q/Q_e] \quad (17)$$

2.2 Optimization. The volume (V) of all the three types of fins can be expressed in dimensionless form (U)

$$[U] = \begin{bmatrix} Vp h^{p+s+1}/2(1+s)\pi^{p+s-1} k^{p+s+1} \\ \{Bi^{p+s+1}/\psi^{s+1}\alpha^s(1-\lambda)^{s+1}\}\{(1-\lambda^{p+1})/(p+1) - s\alpha(1-\lambda^{p+2})/(p+2)\} \end{bmatrix} \quad (18)$$

From Eqs. (11) and (18), it can be seen that if geometrical parameter λ , outer radius of the tube for annular fin r_i and thermophysical properties are known, both the heat transfer rate and the fin volume are functions of Bi and ψ only. Therefore, it becomes a two variables and one constraint optimization problem where either heat transfer or fin volume can be treated as the constraint. The optimality criteria of present optimization problem can be derived using the Lagrange multiplier technique.

$$[f(Bi, \psi)] = [\partial Q/\partial Bi - \partial Q/\partial \psi] \begin{bmatrix} \partial U/\partial \psi \\ \partial U/\partial Bi \end{bmatrix} = 0 \quad (19)$$

Either the heat transfer Q , or fin volume U , may be taken as the constraint as given in the equation below.

$$[g(\text{Bi}, \psi)] = \left[\begin{array}{c} \text{Bi}^{p-1} \psi (1-\lambda) (1+\theta_p) \Phi / \Omega - Q \\ \{ \text{Bi}^{p+s-1} / \psi^{s+1} \alpha^s (1-\lambda)^{s+1} \} \{ (1-\lambda^{p+1}) / (p+1) - s \alpha (1-\lambda^{p+2}) / (p+2) \} - U \end{array} \right] = \left[\begin{array}{c} 0 \\ 0 \end{array} \right] \quad (20)$$

Equations (19) and (20) are nonlinear and non-homogeneous equations. They can be solved numerically to give the optimum values of Bi and ψ . The generalized Newton-Raphson method [13] has been used for the solution. The initial guess for the roots has been made cautiously to satisfy the convergence criteria [14]. A brief outline of the Newton-Raphson iterative scheme and convergence criteria for the present problem is given below.

$$\begin{bmatrix} \text{Bi}_{j+1} \\ \psi_{j+1} \end{bmatrix} = \begin{bmatrix} \text{Bi}_j \\ \psi_j \end{bmatrix} - [J(\text{Bi}_j, \psi_j)]^{-1} \begin{bmatrix} f(\text{Bi}_j, \psi_j) \\ g(\text{Bi}_j, \psi_j) \end{bmatrix} \quad (21)$$

where, J denotes the Jacobian matrix, which is expressed as

$$[J(\text{Bi}_j, \psi_j)] = \begin{bmatrix} \left[\frac{\partial}{\partial \text{Bi}} f(\text{Bi}, \psi) \right]_j & \left[\frac{\partial}{\partial \psi} f(\text{Bi}, \psi) \right]_j \\ \left[\frac{\partial}{\partial \text{Bi}} g(\text{Bi}, \psi) \right]_j & \left[\frac{\partial}{\partial \psi} g(\text{Bi}, \psi) \right]_j \end{bmatrix} \quad (22)$$

The suffix “ j ” denotes the value at the j th iteration. At each step of this iteration the convergence criteria is selected as follows:

$$\text{Max} \left\{ \left| \frac{\partial \Delta_1}{\partial \text{Bi}} \right|_j + \left| \frac{\partial \Delta_2}{\partial \text{Bi}} \right|_j, \left| \frac{\partial \Delta_1}{\partial \psi} \right|_j + \left| \frac{\partial \Delta_2}{\partial \psi} \right|_j \right\} < 1 \quad (23)$$

where

$$\Delta_1 = \text{Bi} + \left[g(\text{Bi}, \psi) \frac{\partial f(\text{Bi}, \psi)}{\partial \psi} - f(\text{Bi}, \psi) \frac{\partial g(\text{Bi}, \psi)}{\partial \psi} \right] / \det J(\text{Bi}, \psi) \quad (24)$$

and

$$\Delta_2 = \psi + \left[f(\text{Bi}, \psi) \frac{\partial g(\text{Bi}, \psi)}{\partial \text{Bi}} - g(\text{Bi}, \psi) \frac{\partial f(\text{Bi}, \psi)}{\partial \text{Bi}} \right] / \det J(\text{Bi}, \psi) \quad (25)$$

The above process may be repeated to obtain the optimum values of Bi and ψ until a specified convergence (10^{-6} in the present case) is achieved.

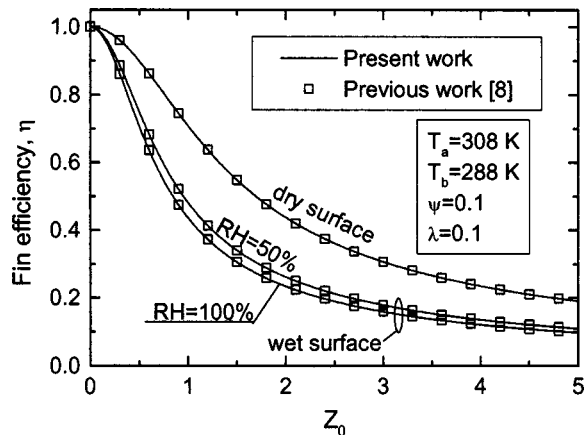


Fig. 2 Comparisons between present and previous results for the longitudinal fin with a trapezoidal profile

3 Results and Discussion

The above analysis can readily be applied for a dry fin if the energy transfer is assumed to take place solely due to sensible heat transfer. This can be done neglecting the mass transfer process (i.e., assigning a zero value to the latent heat) while deriving the energy equation. Such an exercise has been carried out and the excellent agreement of the prediction from the present scheme with the available results of the dry fins indicates its correctness. Further, the present results have been compared with the results available in the existing literature [8] for wet fins. Figure 2 depicts an excellent agreement in the prediction of the efficiency of the wet fins by the present method and that obtained by Bessel functions.

It is well known that the performance of convective dry fins depends only on thermo-geometric parameters. On the other hand, the temperature at the fin base and the psychrometric conditions of the surrounding air strongly influences the performance of wet fins. For demonstration of results, fin base temperature of 285 K and ambient temperature of 305 K have been considered in the present case. Different values of ambient relative humidity have been taken to study its effect on the fin performance.

The variation of performance of a longitudinal fin with both

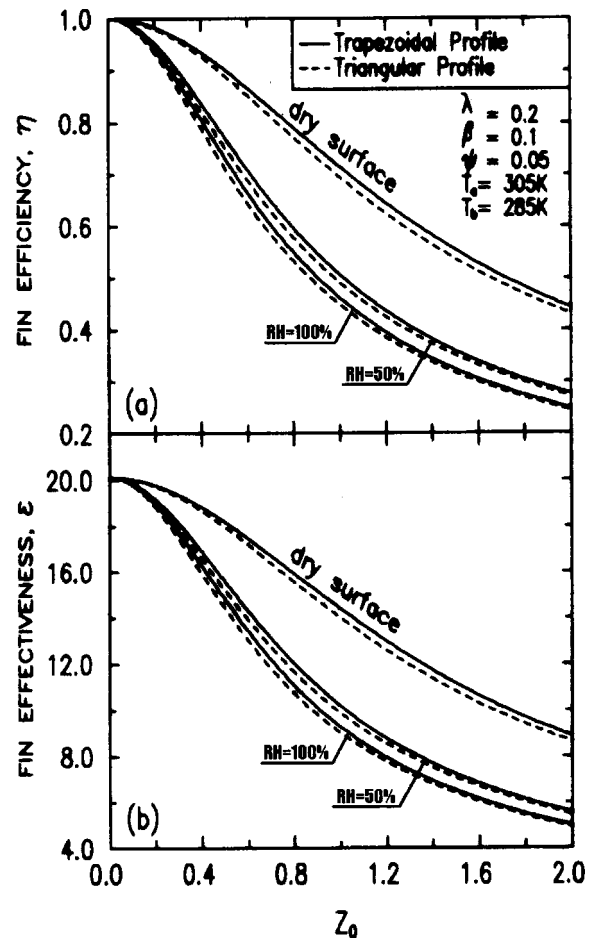


Fig. 3 The effect of dehumidification on the fin performance of a longitudinal fin with trapezoidal profile and comparison with triangular profile: (a) fin efficiency; and (b) fin effectiveness.

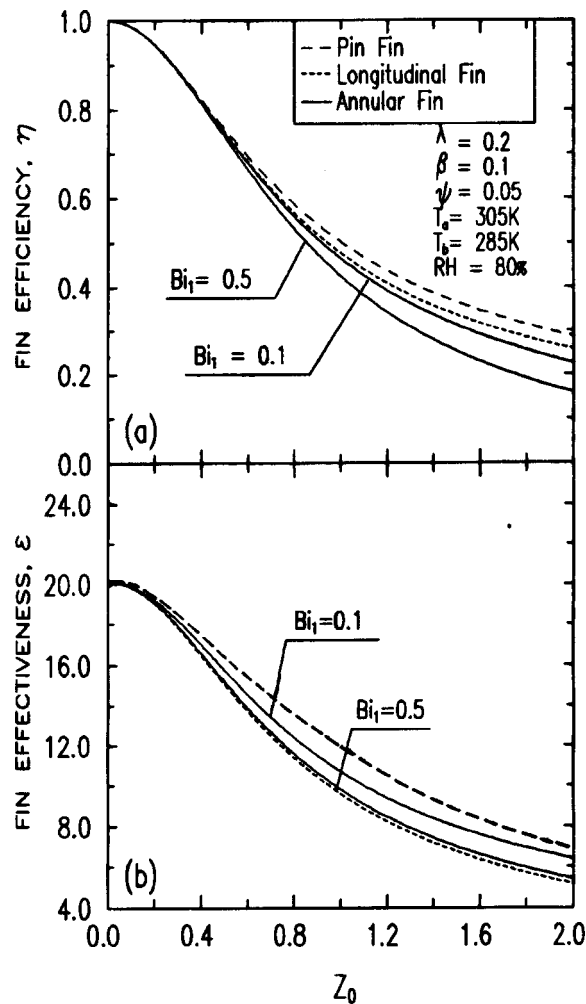


Fig. 4 Comparison of fin performance of different types of wet fins with a trapezoidal profile: (a) fin efficiency; and (b) fin effectiveness.

trapezoidal and triangular profiles is depicted in Fig. 3 as a function of fin parameter Z_0 . Under any circumstances, fin efficiency decreases with increasing value of Z_0 . This trend has also been noticed in all the earlier investigations. The efficiency of a fin with triangular profile is marginally lower than that of its counterpart with a trapezoidal profile. However, it is interesting to note that efficiency of a dry fin is higher than that of a wet fin for the same value of Z_0 . Presence of combined heat and mass transfer increases the longitudinal temperature gradient of wet fins compared to that of dry fins. This results in a decrease in the efficiency of wet fins. Similar observations have also been made by Wu and Bong [1] who has clearly shown that the temperature gradient increases with an increase in relative humidity. As the aspect ratio ψ has been kept constant in the present study, effectiveness curves depict a trend similar to the efficiency curves. Identical trends of efficiency and effectiveness are observed for annular fins and spines.

The thermal performance of the fins having different geometry has been compared in Fig. 4. For identical fin parameter Z_0 , tip thickness parameter λ , aspect ratio ψ , both the efficiency and effectiveness of a spine are slightly higher than those of a longitudinal fin and the difference in the performance parameter increases with Z_0 . The performance of an annular fin can be predicted if additionally one of its radii is specified. In the present work the inner radius is specified non-dimensionally as Bi_1 . It may be noted from Fig. 4 that both the efficiency and effective-

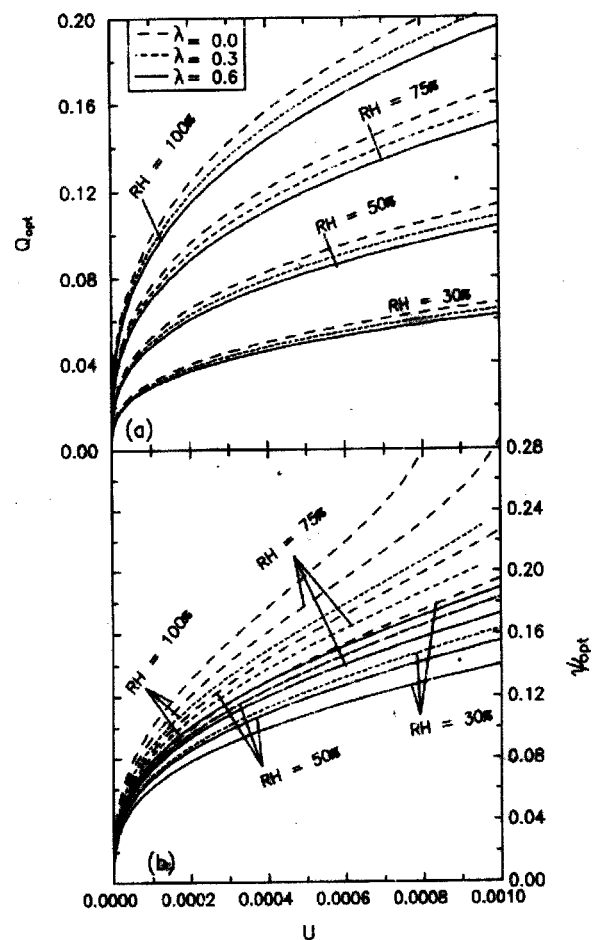


Fig. 5 Design curves for optimum longitudinal wet fins of straight taper profile for $T_a=305$ K, $T_b=285$ K: (a) maximum heat transfer rate; and (b) optimum aspect ratio.

ness of wet annular fin increases with the increase of inner radius. As the total fin length and other geometrical parameters are constant an increase in Bi_1 signifies higher fin surface area. Therefore, the above trend is not unexpected.

Next, an exercise has been made to determine the optimum parameters of straight taper fins. To avoid repetition, results have been shown only for longitudinal fins. Optimum dimensions have been obtained maximizing rate of heat transfer for a given fin volume.

Figure 5(a) shows the total rate of energy transfer from an optimum fin increases rapidly with the increase in relative humidity. The rate of energy transfer also increases with the decrease of the ratio of tip to base thickness λ , hence maximum heat will be transferred from a fin of triangular profile for a given fin volume. However, from the practical considerations often a trapezoidal fin is selected instead of a triangular one. Generally, such a decision is justified, as the variation of the total rate of heat transfer with λ is rather small.

The variation of the optimum ratio of fin base to fin length, ψ_{opt} is depicted in Fig. 5(b) as a function of volume. The ratio is higher for high values of relative humidity and low values of λ , and it also increases with the increase of fin volume. It may be noted that after certain values of fin volume, slope of the curves in Fig. 5(b) increases drastically. One should be cautious in selecting ψ_{opt} in this region. As the ratio of fin base to fin length is very high, one should check the validity of the assumption of one-dimensional heat transfer.

Figure 5 can serve as a design curve for longitudinal fins with triangular and trapezoidal profiles. For any application, if the heat

transfer rate Q , geometrical parameter λ and relative humidity RH are specified, one may locate the optimum design point in Fig. 5(a) and can find the optimum volume. In the next step, all the other geometrical parameters of the fin can be determined from Fig. 5(b). Once such curves are prepared, tedious numerical calculations can be avoided. This may be explained with the help of an example. Determine the optimum dimensions of a longitudinal fin of triangular profile which will transfer 310 W when convective heat transfer coefficient (forced convection), conductivity of the fin material (steel), difference of ambient and base temperature and relative humidity are 100 W/m²K, 55 W/mK, 20 K and 100 percent, respectively. With the help of the above data, initially Q_{opt} is calculated as 0.15. For this known value of Q_{opt} and the given value of relative humidity, one can find out $U=0.00028$ and $\psi_{opt}=0.151$ from the design graphs. Then the optimum Bi can be determined by using Eq. (18). Thus, this gives the optimum values of fin length (L) and semi-base thickness (y_b) as 33 mm and 5 mm, respectively.

4 Conclusions

A generalized analytical technique has been developed for determining the temperature distribution in fully wet fins of trap-ezoidal as well as triangular profile. Fins of three different geometries, namely, longitudinal, annular and spine can be considered with the same formulation. The analysis has been made based on the assumption of a linear relationship between temperature and specific humidity and the method of Frobenius power series expansion has been used to solve the conduction equation. The same analysis may be adopted for dry or partially wet fins. For dry fins, one needs to make the latent heat of phase transformation zero, while for partially wet fins iterative procedure is needed.

It has been demonstrated that the performance of a wet fin is substantially different from that of a dry fin. Unlike the dry fin, the efficiency and effectiveness of wet fins depend on the base temperature and the ambient conditions. Therefore, in later case, the fin performance parameters have only limited significance.

A scheme has also been provided for the optimum design of wet fins. In general, taper fins with small tip to base thickness ratio may be used. In the absence of other restrictions, spines may be preferred to longitudinal fins for identical values of Z_0 , ψ , and λ . Construction of typical design curves has been illustrated taking the example of longitudinal fin. It is seen that, the ratio of base thickness to length of the fin increases with the increase of fin volume. This conclusion may not be valid beyond certain value of Biot number at which the assumption of one-dimensional conduction breaks down. The present analysis has been done for $Bi < 0.1$ as suggested in [15].

Acknowledgment

The valuable suggestions received from all the reviewers are gratefully acknowledged.

Nomenclature

- b_1 = constant, $\omega_b(T_i - T_b) - T_b(\omega_i - \omega_b)/(T_i - T_b)$
 $b_2 = (\omega_i - \omega_b)/(T_i - T_b)$, K⁻¹
 Bi, Bi₁ = Biot numbers, hy_b/k and hr_i/k , respectively
 Bi_t = Biot number based on the tip heat transfer coefficient, $h_t y_b/k$
 C_p = humid specific heat of surrounding air, $C_{pa} + \omega C_{pv}$, J kg⁻¹ K⁻¹
 C_{pa} = specific heat of dry air, J kg⁻¹ K⁻¹
 C_{pv} = specific heat of water vapor, J kg⁻¹ K⁻¹
 f, g = functions defined in Eqs. (18) and (19) respectively
 h = heat transfer coefficient, Wm⁻² K⁻¹
 h_{fg} = latent heat of evaporation of water, Wm⁻²
 J = Jacobian matrix
 k = thermal conductivity of the fin material, Wm⁻¹ K⁻¹

- L = fin length, see Fig. 1, m
 Le = Lewis number
 p, s = constants used in Eq. (1)
 q = actual heat transfer rate through the fin surface, W
 q_e = heat transfer rate through a surface of same size of the fin base, W
 q_i = ideal or maximum heat transfer rate through the fin base, W
 Q = dimensionless actual heat transfer, see Eq. (10)
 Q_e = dimensionless heat transfer, see Eq. (15)
 Q_i = dimensionless ideal heat transfer, see Eq. (13)
 r_i = fin base radius, see Fig. 1, m
 RH = relative humidity
 U = dimensionless fin volume, defined in Eq. (17)
 V = fin volume, m³
 T = temperature, K
 x, y = coordinates starting from the fin base, m
 X, Y = $x/L, y/y_b$, respectively
 y_b = semi-base thickness
 Z_0 = fin parameter, \sqrt{Bi}/ψ
 Z_1 = dimensionless parameter, $pZ_0^2(1+b_2\xi)\sqrt{1+\psi^2(1-\lambda)^2}/(1-\lambda)^2$
 Z_2 = dimensionless parameter, $\beta Z_0^2\psi(1+b_2\xi)/\lambda(1-\lambda)$

Greek symbols

- α = $Bi/[Bi + Bi_1\psi(1-\lambda)]$
 β = tip loss parameter, $Bi_t\lambda/Bi$
 ε = overall fin effectiveness
 η = overall fin efficiency
 θ = dimensionless temperature, $(T_a - T)/(T_a - T_b)$
 θ_p = parameter, $(\omega_a - b_2T_a - b_1)/(T_a - T_b)(1 + b_2\xi)$
 ψ = aspect ratio, y_b/L
 λ = ratio of the tip to base thickness, y_t/y_b
 ϕ = temperature parameter, $\theta + \theta_p$
 ω = specific humidity of air
 ξ = latent heat transfer parameter, $h_{fg}/C_pLe^{2/3}$
 Φ, Ω = parameters defined in Eqs. (11) and (12) for trap-ezoidal and triangular profiles, respectively

Subscripts

- a = ambient
 b = base
 opt = optimum
 t = tip

References

- [1] Wu, G., and Bong, T. Y., 1994, "Overall Efficiency of a Straight Fin With Combined Heat and Mass Transfer," ASHRAE Trans., Part I, pp. 367-374.
- [2] Threlkeld, J. L., 1970, *Thermal Environmental Engineering*, Prentice-Hall, Englewood Cliffs, NJ.
- [3] Chilton, T. H., and Colburn, A. P., 1934, "Mass Transfer (Absorption) Coefficients," Ind. Eng. Chem., **26**, pp. 1183-1187.
- [4] McQuiston, F. C., 1975, "Fin Efficiency With Combined Heat and Mass Transfer," ASHRAE Trans., **81**, pp. 350-355.
- [5] Elmahdy, A. H., and Biggs, R. C., 1983, "Efficiency of Extended Surfaces With Simultaneous Heat and Mass Transfer," ASHRAE Trans., **89**, Part 1A, pp. 135-143.
- [6] Coney, J. E. R., Kazeminejad, H., and Sheppard, C. G. W., 1989, "Dehumidification of Air on a Vertical Rectangular Fin: A Numerical Study," Proc. Inst. Mech. Eng., Part C: Mech. Eng. Sci., **203**, pp. 165-175.
- [7] Toner, A., Killic, A., and Onat, K., 1983, "Comparison of Rectangular and Triangular Fins When Condensation Occurs," *Warne-und Stoffubertragung*, **17**, pp. 65-72.
- [8] Kundu, B., 2002, "Analytical Study of the Effect of Dehumidification of Air on the Performance and Optimization of Straight Tapered Fins," *Int. Commun. Heat Mass Transfer*, **29**, pp. 269-278.
- [9] Kazeminejad, H., Yaghoubi, M. A., and Sepehri, M., 1993, "Effect of Dehumidification of Air on the Performance of Eccentric Circular Fin," *Proc. Inst. Mech. Eng.*, **207**, pp. 141-146.
- [10] Killic, A., and Onat, K., 1981, "The Optimum Shape for Convecting Rectangular Fins When Condensation Occurs," *Warne-und Stoffubertragung*, **15**, pp. 125-133.
- [11] Kundu, B., and Das, P. K., 2002, "Performance Analysis and Optimization of

Straight Taper Fins With Variable Heat Transfer Coefficient," *Int. J. Heat Mass Transfer*, **45**, pp. 4739–4751.

[12] Whittaker, E. L., and Watson, G. N., 1965, *A Course of Modern Analysis*, Cambridge University Press, Cambridge.

[13] Stocker, W. F., 1989, *Design of Thermal System*, McGraw-Hill, New York.

[14] Mathews, J. H., 1998, *Numerical Methods for Mathematics, Science and Engineering*, Prentice-Hall of India Private Limited, New Delhi.

[15] Casarosa, C., and Franco, A., 2001, "On the Optimum Thermal Design of Individual Longitudinal Fins With Rectangular Profile," *Heat Transfer Engineering*, **22**, pp. 51–71.

Numerical and Experimental Investigations of Melting and Solidification Processes of High Melting Point PCM in a Cylindrical Enclosure

Ahmed Elgafy

e-mail: Ahmed.Elgafy@udri.udayton.edu

Osama Mesalhy

University of Dayton Research Institute, 300 College Park, Dayton, OH 45469, USA

Khalid Lafdi

University of Dayton Research Institute, 300 College Park, Dayton, OH 45469, USA
AFRL/MLBC, WPAFB, OH 45433, USA

In the present work, a computational model is developed to investigate and predict the thermal performance of high melting point phase change material during its melting and solidification processes within a cylindrical enclosure. In this model the phases are assumed to be homogeneous and a source term, S , arises from melting or solidification process is considered as a function of the latent heat of fusion and the liquid phase fraction. The numerical model is verified with a test problem and an experiment is performed to assess the validity of the assumptions of it and an agreement between experimental and computational results is achieved. The findings show that utilizing of PCMs of high melting points is a promising technique especially in space applications. [DOI: 10.1115/1.1800492]

Introduction

Heat transfer processes undergoing liquid-solid phase transformation have been of continuing interest for many researchers. Phase Change Materials, (PCMs), have received great consideration in the defense industries for cooling of electronics and in telecommunication equipments to control internal temperature under emergency operating conditions [1]. The problem of phase change of PCMs falls into the category of moving boundary problems. When the PCM changes state, both liquid and solid phases are present and they are separated by the moving interface between them and in this case, the analytical solutions of phase change are mainly based on solving the Stefan moving boundary problems, Crank [2]. A considerable effort has been directed to the mathematical modeling of heat transfer and fluid flow during phase change of pure substances. In general, these can be classified into single-domain and multi-domain models. In multi-domain methods, (moving grid), conservation equations are applied separately to each phase, and continuity of temperature and heat flow conditions are invoked at the solid-liquid interface, Crank [2]. To circumvent this difficulty, transformation of coordinates has to be done. In order to further simplify the computational scheme, two types of approximations have been used by several researchers; a quasi-stationary approximation which is

made by neglecting the motion of the interface in calculating the flow and temperature fields and a quasi-steady approximation which is achieved by neglecting the transient terms in the liquid phase governing equations. On the other hand, in the single-domain (fixed grid) method, a single set of conservation equations and boundary conditions is used for the whole domain comprising the solid and liquid phases, Voller et al. [3]. The interface conditions are accounted for by incorporating suitable source terms in the governing equations. A nodal latent value is assigned to each computational cell according to its temperature. Upon changing phase, the latent heat absorption, or evolution, is reflected as a source or sink term in the energy equation. The zero-velocity condition, which is required as a liquid region turns to solid, is accomplished by adding a source term in the momentum equation. This model is identified as the enthalpy-porosity model. A distinctive advantage of this single-domain model is that it is not necessary to track the interface explicitly; its motion becomes manifest through changes in the liquid fraction. Voller [4] performed a rapid implicit solution technique for enthalpy formulation of conduction controlled phase change problems. Basically, three existing implicit enthalpy schemes are introduced; Shamsundar and Sparrow scheme [5], which is based on Gauss-Seidel point iteration approach, Furzeland scheme [6], which also based on point iteration, and Old-source scheme, which is based on TDMA line-by-line iteration. Ghasemi and Molki [7] employed a fixed-grid enthalpy method to study numerically the melting of an unfixed solid in a square cavity. It was found that at low Rayleigh, and Archimedes numbers, the melting rate and the solid velocity are both very low, and the melting is almost symmetrical. While, higher values of Rayleigh and Archimedes numbers enhance melting and the falling velocity of the solid and distort the symmetry of the interface. Asako et al. [8] employed an enthalpy method to solve transport processes associated with melting of an unfixed rectangular PCM in a low gravitational environment. This method permits the phase change problem in fixed numerical grids, hence eliminating the need for coordinate transformation. The results showed that the melt thickness increases with time and decreases with the increasing of Archimedes number. Also, the rate of solid volume reduction increases with the increasing of Archimedes and Stefan, numbers and in the low-gravitational environments the melting rate is very small. A computational model based on the enthalpy method was performed by Zivkovic and Fujii [9] to simulate the transient behavior of a phase change material. The model was applied for both cylindrical and rectangular geometries and showed a good agreement with the experiment for rectangular case. Rady and Mohanty [10] had applied an enthalpy-porosity fixed grid method to the melting and solidification of pure metals in a rectangular cavity and multi-domain method with a quasi-stationary assumption was applied. The results of the utilized method agreed well with the experimental data.

On the other hand, lot of studies had been carried out to investigate the thermal performance of the PCM in real applications. Lacroix, [11] developed a theoretical model to predict the transient behavior of a shell-and-tube storage unit with PCM on the shell side and the heat transfer fluid (HTF) circulating inside the tube. Results showed that the shell radius, the mass flow rate, and the inlet temperature of the HTF must be chosen carefully in order to optimize the performance of the unit. Patrick and Lacroix [12] studied numerically the thermal behavior of multi-layer heat storage unit. The model is based on the conservation equation of energy for the PCM and the fluid heat transfer. They concluded that the average output heat load during the recovery period is strongly dependent on the minimum operating temperature, mass of PCM, and fluid mass flow rate and temperature. Kurklu et al. [13] developed a numerical model for the prediction of thermal performance of a PCM, polypropylene tube, utilizing air as the heat transfer fluid. They assumed constant physical properties and neglected the heat loss or gain. They predicted the amount of heat energy used to increase the temperature of the PCM during the

Contributed by the Heat Transfer Division for publication in the JOURNAL OF HEAT TRANSFER. Manuscript received by the Heat Transfer Division August 19, 2003; revision received May 5, 2004. Associate Editor: V. Prasad.

phase change process to be about 3.5 percent of the total energy stored. Jianfeng et al. [14] studied experimentally the charging process of a cylindrical heat storage capsule filled with three different phase change materials. The results showed that the using of multiple PCMs enhances the charging rate of the PCM storage. Casano and Piva [15] presented numerical and experimental investigations of a periodic phase-change process dominated by heat conduction. In the experimental arrangement a plane slab of PCM is periodically heated from above by applying a sinusoidal heat flow. A one-dimensional control volume computer code had been developed for the solution of the corresponding mathematical model. The comparison between numerical prediction and experimental data showed good agreement.

From the previous literature, it is obvious that the current practice is to utilize paraffins, gallium, waxes, etc., as PCMs and materials of these types have low melting points and low latent heat. Space applications of an advanced power system in sunshade operating conditions require the system to have high efficiency, reliability, low specific weight, and low life cost cycle. This system must continuously provide electrical power by collecting and storing thermal energy that is later converted to electrical power. The collected solar thermal energy is stored in a heat receiver that consists of containers holding a phase change material. As a matter of status, the utilized PCM must have high melting temperature and latent heat to achieve the thermal storing requirements.

The objective of the present work is to investigate and predict experimentally and numerically, the thermal performance of high melting point phase change material during its melting and solidification processes within a cylindrical enclosure.

1 Computational Formulation

The physical system consists of a vertical cylindrical enclosure filled with a PCM of high melting point. This system is supposed to be insulated from the bottom and receives heat flux from the top and sides. The mathematical model formulated to represent the physical system is based on the following assumptions: the PCM is homogeneous, isotropic and axisymmetrical, the thermo-physical properties are constant in each phase, and the mechanical energy for the volume change during phase change is ignored. Another assumption is that, the heat transfer is controlled by conduction and the thermal conductivity of the liquid phase is modified to account for the convection effect,

$$\frac{k_e}{k_l} = C_l R a^{n_1}$$

where C_l and n_1 are constants determined experimentally given by Lacroix [11] and these constants are set equal to 0.099 and 0.25, respectively, for cylindrical geometries.

1.1 Governing Equations. The problem is governed by the conservation of the total enthalpy, H

$$\frac{\partial(\rho H)}{\partial t} + \nabla \cdot J = 0$$

where H represents the sensible and latent heats, $H = c \cdot T + f \cdot L$

By considering the assumption of constant properties, the equation can be written as

$$\rho c \frac{\partial T}{\partial t} + \nabla \cdot J = S \quad (1)$$

where J is the diffusion flux vector

$$J = -k \nabla T \quad (2)$$

and, S is a source term arises from melting and solidification process. This source term takes the following form:

$$S = -\rho L \frac{\partial f}{\partial t} \quad (3)$$

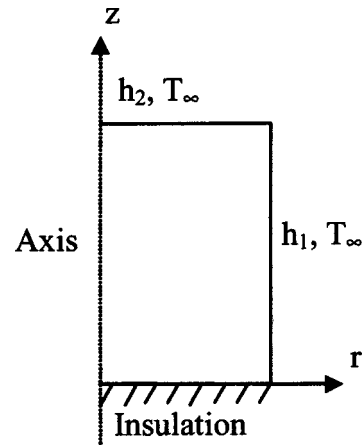


Fig. 1 Physical domain and boundary conditions

L is the latent heat of fusion, and f is the liquid phase fraction.

During the cooling process, the PCM is supposed to be cooled by natural convection and radiation. The Nusselt number on the sidewall is assumed to take the following relation introduced by Incropera and Dewitt [16]:

$$Nu_z = \left[\frac{g \beta_{\text{air}} (T_b - T_{\infty}) z^3}{4 \nu_{\text{air}}^2} \right]^{1/4} Y(\text{Pr}) \quad (4)$$

where the function

$$Y(\text{Pr}) = \frac{0.75 \text{Pr}^{1/2}}{(0.609 + 1.221 \text{Pr}^{1/2} + 1.238 \text{Pr})^{1/4}}$$

While Nusselt number for the upper surface can be obtained from the relation

$$Nu_D = 0.54 Ra_D^{1/4}$$

1.2 Physical Domain. A diagram of the physical domain and boundary conditions is shown in Fig. 1. The sample of the PCM has a cylindrical shape and dimensions of $l/D = 1$ with 10 cm diameter. The value of T_{∞} is taken according to the temperature attained in the furnace. The heat transfer from the furnace wall to the sample is considered to take place by natural convection and radiation. The thermo-physical properties for the considered phase change material are listed at Table 1.

1.3 Numerical Procedure. The heat diffusion equation is solved using finite difference based on control volume approach. The numerical domain is divided into small control volumes. The finite difference equation is obtained by integrating the heat diffusion equation over each control volume. The control volume is shown in Fig. 2, the volume of the control volume is $(2\pi r \Delta r \Delta z)$.

$$\int \rho c \frac{\partial T}{\partial t} dV = - \int \nabla \cdot J dV + \int S dV \quad (5)$$

Table 1 Thermophysical properties of the considered PCM

Property	Value
Density	2600 (kg/m ³)
Specific heat	1562 (J/kg.K)
Melting point	1121 (K)
Latent heat of fusion	1043.6 (kJ/kg)
Thermal conductivity	14.2 (W/m.K)
Thermal Expansion	34.4*10 ⁻⁶ (1/K)
Dynamic viscosity	0.015 (Pa.sec)

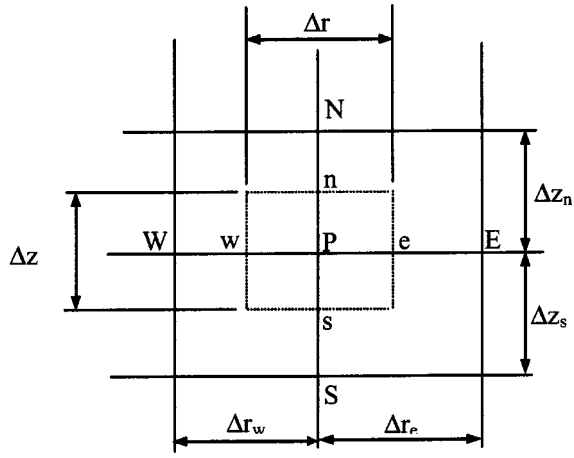
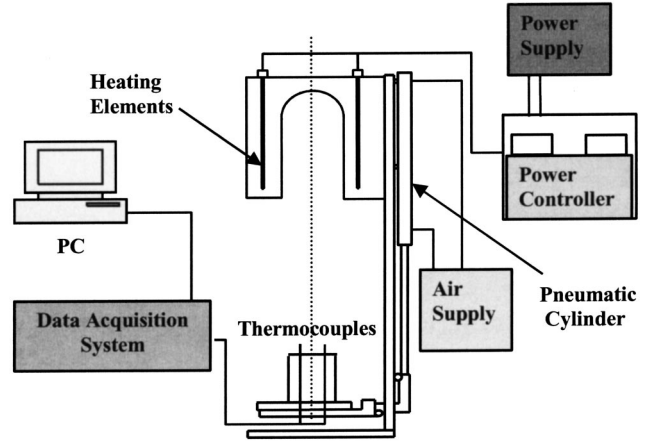


Fig. 2 Control volume around node P



Experimental Setup

Fig. 4 Experimental setup

$\rho c [T^{n+1} - T^n / \Delta t] dv = -\sum_{f=n,s,e,w} J_f \cdot A_f + \bar{S} dv$, where $J = -k \nabla T$ and \bar{S} is the average value of the source term at point P. The first term in the right hand side can be set as

$$\sum_{f=n,s,e,w} J_f \cdot A_f = -k_e A_e \frac{T_E - T_P}{\Delta z_e} + k_w A_w \frac{T_P - T_W}{\Delta z_w} - k_n A_n \frac{T_N - T_P}{\Delta r_n} + k_s A_s \frac{T_P - T_S}{\Delta r_s} \quad (6)$$

After arranging the finite difference equation, it will take the following form:

$$a_p^o T_P^{n+1} = a_E T_E^n + a_W T_W^n + a_N T_N^n + a_S T_S^n + (a_p^o - (a_E + a_W + a_N + a_S)) T_P^n + \rho L \frac{f_p^n - f_p^{n+1}}{\Delta t} \Delta V \quad (7)$$

where $(n+1)$ refers to time $(t + \Delta t)$, n refers to time (t) and,

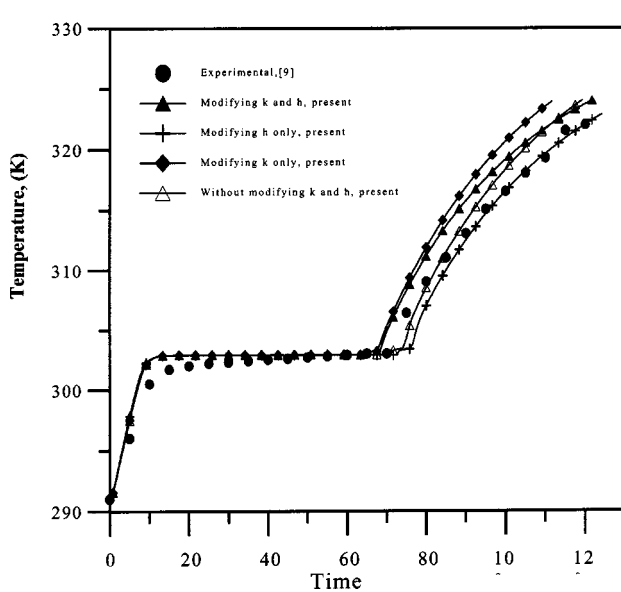


Fig. 3 Verification of the present model with Zivkovic and Fujii findings [9]

$$a_E = \frac{k_e r_e \Delta r}{\Delta z_e} \quad a_W = \frac{k_w r_r \Delta r}{\Delta z_w} \quad a_N = \frac{k_n r_n \Delta z}{\Delta r_n} \quad a_S = \frac{k_s r_s \Delta z}{\Delta r_s} \quad a_p = \frac{\rho \Delta V}{\Delta t} \quad (8)$$

The time step is calculated from the following expression to satisfy the stability condition:

$$\Delta t \leq 0.5 \frac{1}{\alpha / (dz)^2 + \alpha / (dr)^2} \quad (9)$$

At the time of phase change, i.e., $0 < f < 1$, it is assumed that the temperature will remain constant and all the heat diffusion fluxes to or from the control volume will be used to change the phase. By equating T_p^n and T_p^{n+1} during the phase change process, Eq. (7) will take the following form:

$$a_E T_E^n + a_W T_W^n + a_N T_N^n + a_S T_S^n - (a_E + a_W + a_N + a_S) T_p^n = \rho L \frac{f_p^{n+1} - f_p^n}{\Delta t} \Delta V \quad (10)$$

The updated liquid fraction (f^{n+1}) is subjected to the following constraints to prevent getting unreasonable values

$$\text{and } f^{n+1} = \begin{cases} 0 & \text{if } f^{n+1} < 0 \\ 1 & \text{if } f^{n+1} > 1 \end{cases}$$

The calculations begin from the second point in r and z -direction. The values of temperatures at the boundary points are calculated by applying energy balance at the control volume beside the boundary. For the cylindrical surface, the temperature at the boundary is calculated by solving the following equation by simple iteration.

$$T_b = \frac{h_1 R T_\infty + (k T_{b-1} / \ln(R / (R - \Delta r))) + \sigma \epsilon R (T_\infty^4 - T_b^4)}{h_1 R + k / \ln(R / (R - \Delta r))}$$

Similarly the top surface from

$$T_b = \frac{h_2 T_\infty + (k T_{b-1} / dz) + \sigma \epsilon (T_\infty^4 - T_b^4)}{h_2 + (k / dz)}$$

where T_{b-1} is the temperature of the point beside the boundary.

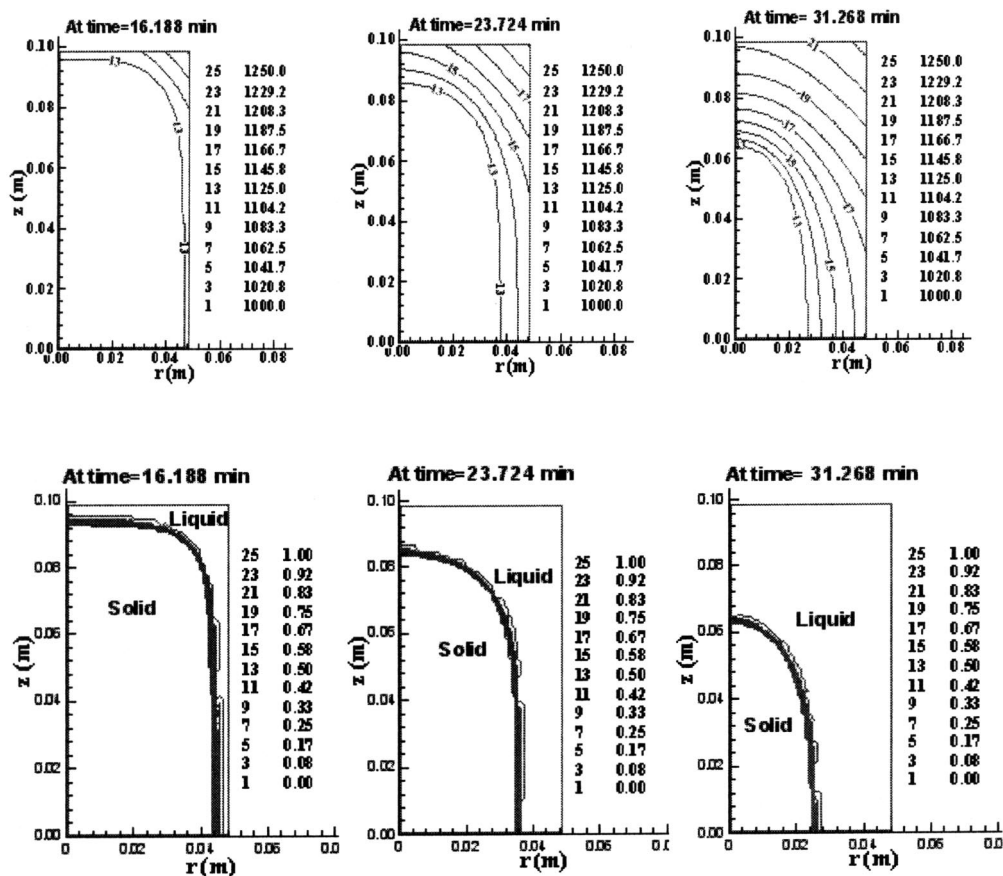


Fig. 5 Temperature and liquid fraction contours during heating process

2 Grid Size and Model Verification

The grid size is changed up to 100×50 and it is found that this grid size is sufficient for the present case of study. The validity of the present model is first verified with the experimental findings obtained by Zivkovic and Fujii [9]. The present model is modified to predict the rectangular geometry of their model and a compar-

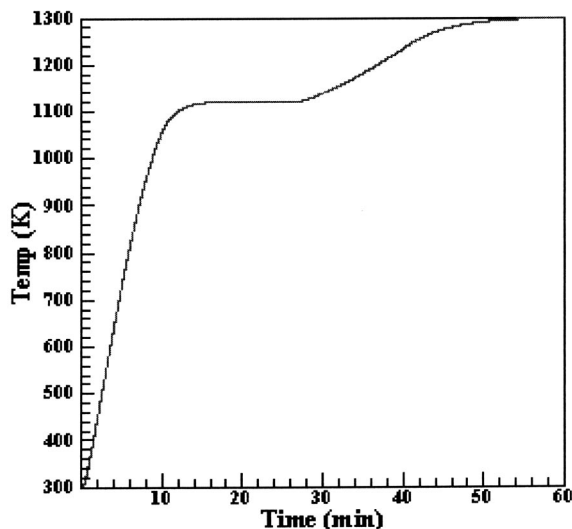


Fig. 6 Temperature time history for heating process at $z = 0.5 L$ and $r = 0.6 R$

ative study is performed. Figure 3 shows a comparison between predicted results of the present numerical model and the experimental results obtained by [9]. Several trials have been done:

1. With neglecting the effect of convection in liquid melt and keeping the heat transfer constant coefficient h (without modifying k and h).
2. Adding the effect of natural convection in the liquid region by modifying the value of (k) for the liquid phase.
3. Modifying the convection heat transfer coefficient by calculating the Grashof number based on $(T_{\infty} - T_b)$ instead of $(T_{\infty} - T_{melt})$.
4. By modifying both k and h .

As shown in Fig. 3, the present model shows a good agreement with the experimental findings obtained by Zivkovic and Fujii [9]. Also, from the figure, one can see that the most appropriate model is the fourth one, in which both k and h are modified. This model is used in all subsequent calculations for present work and the heat transfer coefficient is changed by calculating the Nusselt number each time step as a function of the temperature difference between the PCM and the ambient temperature.

3 Experimental

To investigate experimentally the melting and solidification processes of the utilized PCM, which has a melting point of 1121 K, a mass of 36 gram from it is introduced in a cylindrical Alumina enclosure of 3.6 cm diameter and 2 cm height while, the top and the bottom of it are well insulated. The enclosure is then introduced inside a furnace to attain the needed heat for its melting process. The experimental setup, as shown in Fig. 4, consists of a well-controlled furnace equipped of 10-molybdenum disili-

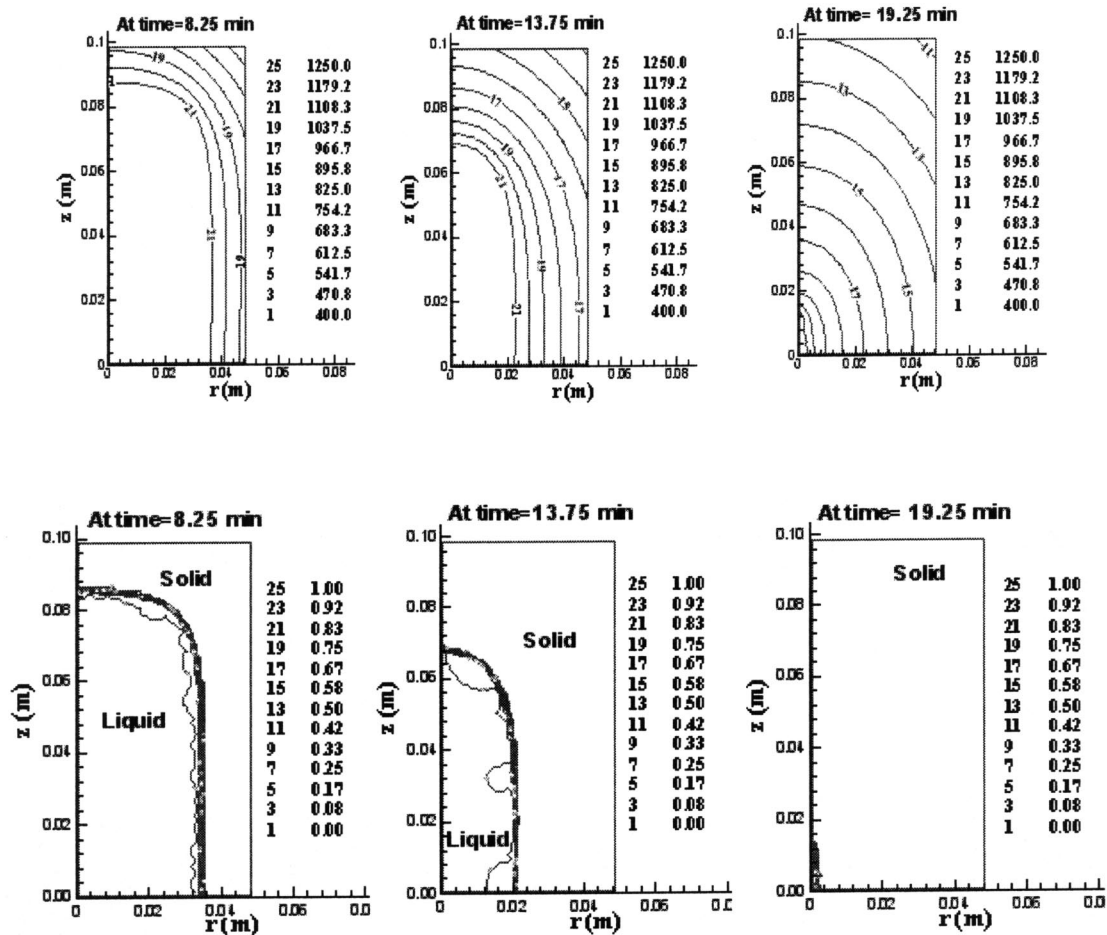


Fig. 7 Temperature and liquid fraction contours during cooling process

cide heating elements. These elements are uniformly spaced in a full circle around the interior furnace wall to achieve a uniform heat distribution. The maximum attainable temperature of the furnace is 1900 K and the interior temperature of it is kept at 1200 K. A complete airlift mechanism, pneumatic system, with top and bottom plugs is supplied to the furnace to attain a variable environment to the test sample and in case of cooling process; the ambient temperature is 300 K. The temperature distribution inside and outside the enclosure is measured by means of multiple thermocouples, and a Data Acquisition System is used to convert the thermocouples output to a PC through a standard RS-232 asynchronous serial communication.

4 Results and Discussion

The present numerical model is proposed to predict the thermal performance of high melting point material during its melting and solidification processes in a cylindrical enclosure. The initial temperature of the specimen is assumed to be, $T_i = 300$ K and the specimen is placed in a furnace where the temperature is kept constant and above the melting point of the PCM. At early stages, sensible heat is stored at the PCM, while its temperature increases from T_i to its melting point. During this period, the liquid fraction, f , remains null as the PCM is still in its solid phase. As the temperature increases the melting triggers and begins at the interior intersection of the side and top walls of the specimen where, the PCM receives the maximum heat flux. By continuous proceeding, the liquid fraction increases with time and once the PCM is entirely melted, energy is stored by sensible heat and the temperature begins to increase again.

In the cooling process, the specimen is removed from the furnace and is exposed to the atmospheric temperature; 300 K. The heat transfer during the cooling process is mainly occurs by natural convection and radiation. First, the PCM will begin to cool and lose the sensible heat until it reaches to the melting temperature. The solidification begins at the lower corner of the cylinder where the free convection heat transfer coefficient is a maximum. The solidification will continue to grow from the top and side walls of the enclosure until all the PCM changes entirely to the solid phase.

The thermal performance of the PCM can be explained in terms of some design and operating condition parameters. These parameters could be the size of the PCM, the heat transfer surface area, and the cooling process. It is found that the two parameters which best characterize the overall performance of the unit are the total energy stored and the output heat release. The output heat release can be defined as the output heat released from the PCM during the cooling process.

The predicted temperature contours and liquid phase fraction during the heating process are shown in Fig. 5, where the temperature contours are represented at the upper part of the figure and the liquid phase fraction are represented at the lower part of it. From the figure one can see that, the temperature starts to increase at the intersection of the top and side walls of the specimen. When the temperature reaches the melting point and the sample begins to melt, the interface between the liquid and solid makes as insulation. This is because of all the heat, which comes from the furnace, is used just to change the phase. The solid part of the

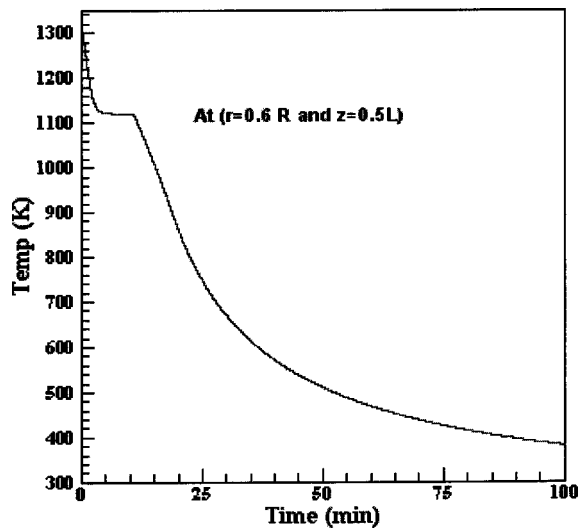


Fig. 8 Temperature time history for cooling process at $z = 0.5 L$ and $r = 0.6 R$

PCM stays at constant temperature and equals to its melting point. This is also obvious in the contours of the liquid fraction.

The predicted temperature history at the point of coordinates ($z = 0.5 \times \text{length}$ and $r = 0.6$ radius) is shown in Fig. 6, which illustrates that, the temperature is increased with high rate at the beginning of the heating process and during the phase change, the temperature keeps constant. At the end of the heating process, the temperature increase rate decreases because of the decreasing of the temperature difference between the sample and the furnace temperature.

During the cooling process the predicted temperature and liquid fraction contours are shown in Fig. 7, where the temperature contours are represented at the upper part of the figure and the liquid phase fraction are represented at the lower part of it. Opposite to the heating process, the temperature begins to decrease at the side and top surfaces of the sample while the solid liquid interface moving to the bottom surface and to the center.

Figure 8 represents the predicted temperature time history during the solidification process. From the figure it is obvious that the high temperature decreases at the beginning of cooling and the constancy of temperature during phase-change can be observed.

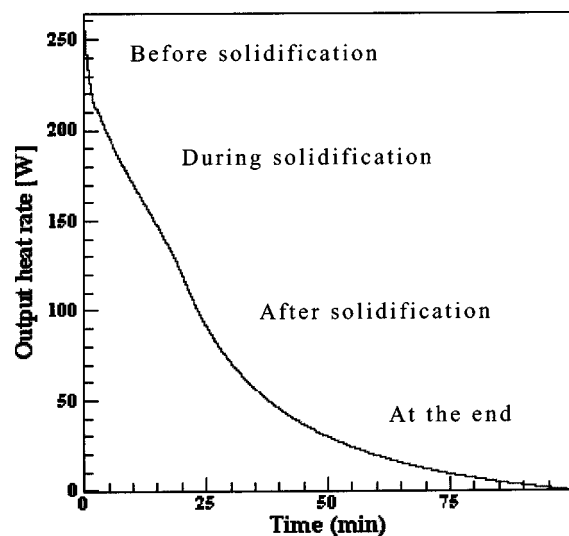


Fig. 9 Rate of heat release during cooling process

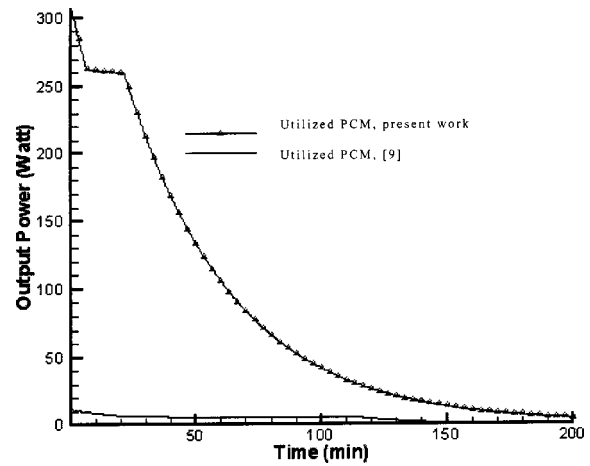


Fig. 10 The output power realized during the solidification process from utilized PCM of present work and from utilized PCM of [9]

Figure 9 shows the predicted heat release rate from the sample at the cooling process. The rate of heat release differs from one period to another. As shown from the figure, the rate of heat release can be divided into four regions. At the beginning, the heat release decreases so fast with a high rate due to the temperature decrease in the sample at the beginning. When the PCM begins to change to solid, the heat release decrease rate decreases because of the energy stored as latent heat in the PCM. After the solidification has completed the rate increases again. At the end of the cooling process, the heat release decreases due to the decrease in temperature difference between the sample surface and the atmosphere.

Figure 10 represents a comparative study for the output power realized through the solidification process from low melting point material, [9] and high melting point material, present work. From the figure one can see that, the output power realized from the solidification of the high melting point material is extremely high than that from the low melting point material.

To compare the numerical and experimental findings of the present work, a modification in the physical domain of the numerical model is performed to fit the geometry and boundary conditions of the experimental setup. A comparison between numerical and experimental values of the temperature at the center of the present test enclosure with time during melting and solidification

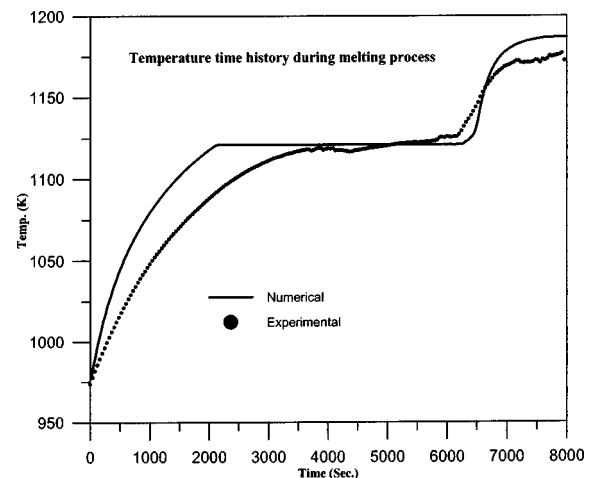


Fig. 11 Variation of temperature at the center of the test enclosure with time during the melting process of the utilized PCM

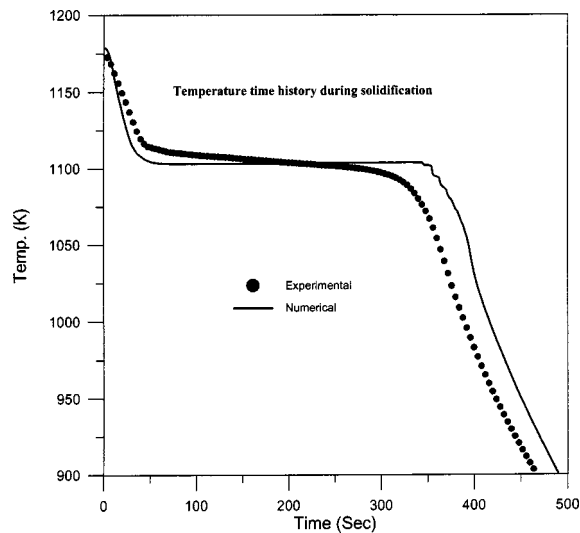


Fig. 12 Variation of temperature at the center of the test enclosure with time during the solidification process of the utilized PCM

processes of the utilized PCM, $T_{\text{melt}} = 1121$ K, is shown in Figs. 11 and 12 respectively. From the figures, it can be concluded that an agreement between numerical and experimental results is achieved within experimental uncertainties. The deviation between experimental and numerical findings could be explained by the heat losses during the melting and solidification processes due to imperfect system insulation.

5 Conclusions

A computational model for the prediction of the thermal behavior of high melting point material during its melting and solidification processes within a cylindrical enclosure has been presented. The model rests on solving the heat equation and making energy conservation between the PCM and atmosphere. Results show that the heat release from this material during its solidification is very high. The decrease rate of heat release shows some improvements during the phase change process due to the high latent heat of fusion of the utilized material. The performance of the present model is verified with the experimental findings obtained by another work and a comparative study was performed and showed good agreement. An experiment was performed to validate the present case of study and the predicted numerical results show good agreement with the experimental findings.

Acknowledgment

This work was sponsored by the US Air Force Materials Laboratory under the research contract # F33615-00-D-5006.

Nomenclature

A	= area [m^2]
Ar	= Archimedes number
c	= specific heat [$\text{J/kg}\cdot\text{K}$]
D	= diameter [m]
f	= liquid fraction
g	= gravity acceleration [m/s^2]
h	= heat transfer coefficient [$\text{W/m}^2\cdot\text{K}$]
J	= heat diffusion flux [W/m^2]
k	= thermal conductivity [$\text{W/m}\cdot\text{K}$]
l	= enclosure height [m]
L	= latent heat of fusion [J/kg]

Nu	= Nusselt number
r	= distance in radial direction [m]
R	= radius [m]
Ra	= Rayleigh number
Pr	= Prandtl number
Ste	= Stefan number
t	= time [s]
T	= temperature [K]
V	= volume [m^3]
z	= distance in axial direction [m]

Greek letters

α	= thermal diffusivity [m^2/s]
β	= thermal expansion coefficient [$1/\text{K}$]
Δr	= grid size in radial direction [m]
Δt	= time step [s]
Δz	= grid size in axial direction [m]
ν	= kinematic viscosity [m^2/s]
ρ	= density [kg/m^3]
σ	= Stefan-Boltzmann constant
ε	= emissivity

Subscripts

b	= at boundary
$b-1$	= before boundary
e	= effective
f	= face (n,s,e,w) north, south, east, and west
i	= initial
l	= liquid
∞	= ambient value

References

- [1] Harris, K. T., Haji-Sheikh, A., and Agwu Nnanna, A. G., 2001, "Phase-Change Phenomena in Porous Media—A Non-Local Thermal Equilibrium Model," *Int. J. Heat Mass Transfer*, **44**, pp. 1619–1625.
- [2] Crank, J., 1984, *Free and Moving Boundary Problems*, Clarendon Press, Oxford.
- [3] Voller, V. R., Swaminathan, C. R., and Thoma, B. G., 1990, "Fixed Grid Techniques for Phase Change Problems: Review," *Int. J. Numer. Methods Eng.*, **30**, pp. 875–898.
- [4] Voller, V. R., 1990, "Fast Implicit Finite-Difference Method for the Analysis of Phase Change Problem," *Numer. Heat Transfer, Part B*, **17**, pp. 155–169.
- [5] Shamsunder, N., and Sparrow, E. M., 1975, "Analysis of Multi-Dimensional Conduction Phase Change via the Enthalpy Model," *ASME J. Heat Transfer*, **97**, pp. 330–340.
- [6] Furzeland, R. M., 1980, "A Comparative Study of Numerical Methods for Moving Boundary Problems," *J. Inst. Math. Appl.*, **19**, pp. 411–429.
- [7] Ghasemi, B., and Molki, M., 1999, "Melting of Unfixed Solids in Square Cavities," *Int. J. Heat Fluid Flow*, **20**, pp. 446–452.
- [8] Asako, Y., Faghri, M., Charmchi, M., and Bahrami, P. A., 1994, "Numerical Solution for Melting of Unfixed Rectangular Phase-Change Material Under Low-Gravity Environment," *Numer. Heat Transfer, Part A*, **25**, pp. 191–208.
- [9] Zivkovic, B., and Fujii, I., 2001, "An Analysis of Isothermal Phase Change of Phase Change Material Within Rectangular and Cylindrical Containers," *Sol. Energy*, **70**(1), pp. 51–61.
- [10] Rady, M. A., and Mohanty, A. K., 1996, "Natural Convection During Melting and Solidification of Pure Metals in a Cavity," *Numer. Heat Transfer, Part A*, **29**, pp. 49–63.
- [11] Lacroix, M., 1993, "Numerical Simulation of a Shell-and-Tube Latent Heat Thermal Energy Storage Unit," *Sol. Energy*, **50**(4), pp. 357–367.
- [12] Patrick, B., and Lacroix, M., 1998, "Numerical Simulation of a Multi-Layer Latent Heat Thermal Energy Storage System," *Int. J. Energy Res.*, **22**, pp. 1–15.
- [13] Kurklu, A., Wheldon, A., and Hadley, P., 1996, "Mathematical Modeling of the Thermal Performance of a Phase-Change Material (PCM) Store: Cooling Cycle," *Journal of Applied Thermal Engineering*, **16**(7), pp. 613–623.
- [14] Jianfeng, W., Ouyang, Y., and Chen, G., 2001, "Experimental Study of Charging Process of a Cylindrical Heat Storage Capsule Employing Multiple-Phase-Change Materials," *Int. J. Energy Res.*, **25**, pp. 439–447.
- [15] Casano, G., and Piva, S., 2002, "Experimental and Numerical Investigation of the Steady Periodic Solid-Liquid Phase-Change Heat Transfer," *Int. J. Heat Mass Transfer*, **45**, pp. 4181–4190.
- [16] Incropera, F. P., and Dewitt, D. P., 2001, *Fundamentals of Heat and Mass Transfer*, fourth ed., Wiley, New York.